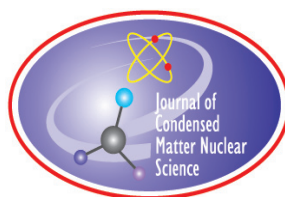


JOURNAL OF CONDENSED MATTER NUCLEAR SCIENCE

Experiments and Methods in Cold Fusion

VOLUME 4, February 2011



JOURNAL OF CONDENSED MATTER NUCLEAR SCIENCE

Experiments and Methods in Cold Fusion

Editor-in-Chief

Jean-Paul Biberian
Marseille, France

Editorial Board

Peter Hagelstein
MIT, USA

Xing Zhong Li
Tsinghua University, China

Edmund Storms
KivaLabs, LLC, USA

George Miley
*Fusion Studies Laboratory,
University of Illinois, USA*

Michael McKubre
SRI International, USA

Akito Takahashi
Osaka University, Japan

JOURNAL OF CONDENSED MATTER NUCLEAR SCIENCE

Volume 4, February 2011

© 2011 ISCMNS. All rights reserved.

This journal and the individual contributions contained in it are protected under copyright by ISCMNS and the following terms and conditions apply.

Electronic usage or storage of data

JCMNS is an open-access scientific journal and no special permissions or fees are required to download for personal non-commercial use or for teaching purposes in an educational institution.

All other uses including printing, copying, distribution require the written consent of ISCMNS.

Permission of the ISCMNS and payment of a fee are required for photocopying, including multiple or systematic copying, copying for advertising or promotional purposes, resale, and all forms of document delivery.

Permissions may be sought directly from ISCMNS, E-mail: CMNSEditor@iscmns.org. For further details you may also visit our web site: <http://www.iscmns.org/CMNS/>

Members of ISCMNS may reproduce the table of contents or prepare lists of articles for internal circulation within their institutions.

Orders, claims, author inquiries and journal inquiries

Please contact the Editor in Chief, CMNSEditor@iscmns.org or webmaster@iscmns.org



JOURNAL OF CONDENSED MATTER NUCLEAR SCIENCE

Volume 4

2011

CONTENTS

PREFACE

REVIEW ARTICLE

Hot and Cold Fusion for Energy Generation 1
David J. Nagel

RESEARCH ARTICLES

What is Real about Cold Fusion and What Explanations are Plausible? 17
Edmund Storms and Brian Scanlan

Cold Fusion, LENR, CMNS, FPE: One Perspective on the State of the Science Based on Measurements Made at SRI 32
Michael C.H. McKubre and Francis L. Tanzella

Measurements of Excess Power Effects In Pd/D₂O Systems Using a New Isoperibolic Calorimeter 45
M.H. Miles and M. Fleischmann

Heat Evolution from Pd Nano-powders Exposed to High-pressure Hydrogen Isotopes and Associated Radiation Measurements 56
Akira Kitamura, Akito Takahashi, Reiko Seto and Yushi Fujita

Absorption Capacity and Heat Evolution with Loading of Hydrogen Isotope Gases for Pd Nanopowder and Pd/Ceramics Nanocomposite 69
T. Hioki, H. Azuma, T. Nishi, A. Itoh, S. Hibi, J. Gao, T. Motohiro and J. Kasagi

Codeposition Methods: A Search for Enabling Factors <i>Dennis Letts</i>	81
Impact of an Applied Magnetic Field on a High Impedance Dual Anode LANR Device <i>Mitchell R. Swartz</i>	93
Detection of Abnormal Quantity of Hydrogen upon Electrical Explosion of Titanium Foil in a Liquid <i>Leonid I. Urutskoev, Dmitry V. Filippov, Anri A. Rukhadze and Larion A. Lebedev</i>	106
Studies on Anomalous Phenomena of D/Pd Systems using a Gas-loading Process – A Stride Towards Neutrino Detection <i>Zhan M. Dong, Chang L. Liang, Bin Liu, Qing M. Wei, Jian Tian, Shu X. Zheng, Jin Z. Yu and Xing Z. Li</i>	119
Observation of Low Energy Nuclear Transmutation Reactions Induced by Deuterium Permeation through Multilayer Pd and CaO thin Film <i>Y. Iwamura, T. Itoh, N. Yamazaki, J. Kasagi, Y. Terada, T. Ishikawa, D. Sekiba, H. Yonemura and K. Fukutani</i>	132
Low-energy Nuclear Reactions and Transmutation of Stable and Radioactive Isotopes in Growing Biological Systems <i>Vladimir I. Vysotskii and Alla A. Kornilova</i>	146
Neutron Emission in Bursts and Hot Spots: Signature of Micro-Nuclear Explosions? <i>Mahadeva Srinivasan</i>	168
Review of Twenty Years of LENR Research Using Pd/D Co-deposition? <i>Pamela A. Mosier-Boss, Jack Y. Dea, Frank E. Gordon, Lawrence P.G. Forsley and Melvin H. Miles</i>	173
Bose–Einstein Condensate Theory of Deuteron Fusion in Metal <i>Yeong E. Kim</i>	188
Energy Exchange Using Spin-Boson Models with Infinite Loss <i>P.L. Hagelstein and I.U. Chaudhary</i>	202
Concerning the Role of Electromagnetism in Low-energy Nuclear Reactions <i>Scott R. Chubb</i>	213
Weight of Evidence for the Fleischmann–Pons Effect <i>Rodney Johnson and Michael Melich</i>	225

Tunneling Beneath the ${}^4\text{He}^*$ Fragmentation Energy <i>Andrew Meulenberg and Krityunjai P. Sinha</i>	241
Ultra-High Density Deuteron-cluster Electrode for Low-energy Nuclear Reactions <i>George H. Miley, Xiaoling Yang and Heinrich Hora</i>	256
Progress in Condensed Cluster Fusion Theory <i>Akito Takahashi</i>	269
Inhibition of LENR by Hydrogen within Gas-loaded Systems <i>Dennis Cravens</i>	282
Dynamics in Pd–H(D) Systems <i>Antonella De Ninno</i>	291
Model for Sonofusion <i>Roger S. Stringham</i>	304

PREFACE

This special volume includes the proceedings of the March 2010, New Energy Technology Symposium held at the 239th American Chemical Society National Meeting and Exposition in San Francisco. These proceedings were to be published as a book by AIP Publishing, a branch of the American Institute of Physics. Jan Marwan, the editor of the book did an excellent job. All papers were ready for printing, when AIP Publishing without any reason cancelled the work. They did so based on an evaluation of the contents that drove them to exercise their right to decline publishing the proceedings and materials as an AIP publication. In fact, even though no precise argument was given for the cancellation, it is obvious that some people from AIP Publishing triggered the change. They might have realized that by publishing papers related to Condensed Matter Nuclear Science, they were actually supporting Cold Fusion. Mainstream science does not accept this field as genuine. After more than twenty years of research by hundreds of scientists worldwide, the change is extremely slow. The proceedings edited by Jan Marwan were of excellent scientific quality, and could not be challenged on these grounds, and AIP Publishing made their decision using their legal right of controlling what is acceptable to them. It is my pleasure to publish these proceedings as a special volume of the *Journal of Condensed Matter Nuclear Science*. No change has been made from the original papers; they have been solely adapted to the format of the journal, including the following preface by Jan Marwan.

Jean-Paul Biberian
February 2011

The year 1989, Martin Fleischmann and Stanley Pons announced, to great fanfare, excess heat without harmful neutron emissions or strong gamma radiation involving electrochemical cells using heavy water and palladium. Their significant claims have held strong in spite of chagrin and criticism from many people in the scientific community.

In recent years, Low-Energy Nuclear Reactions (LENR), within the field of condensed matter nuclear science, have begun to attract widespread attention. The LENR is now regarded as a potential alternative and renewable energy source to confront climate change and energy scarcity. The aim of the research is to collect experimental findings for LENR in order to present reasonable explanations and a conclusive theoretical basis for a practical working model.

Palladium is well known to absorb large quantities of hydrogen/deuterium into the bulk metal where the nuclei, electrochemically inserted, occupy interstitial octahedral/tetrahedral sites dependent on the specific palladium–hydride phase. Using this approach, Martin Fleischmann raised the idea of electrochemically inserting deuterium into bulk palladium, hoping to increase the probability of deuterium nuclei reacting and colliding efficiently. Based on this idea, in 1989 in Salt Lake City, Utah, Martin Fleischmann together with his colleague Stanley Pons designed an experiment involving an electrochemical cell using a heavy water solution with the corresponding electrolyte and palladium as the electrode, in order to generate nuclear fusion within the metal lattice. The energetic output generated after a long-term electrolysis-over a couple of days-was found to be significant. From this, Fleischmann concluded that nuclear fusion of deuterium nuclei inside the bulk palladium metal had occurred.

Because this reaction, initially named “cold fusion”, seemed to offer an opportunity solve energy problems in the future, it instantly raised widespread attention. As a result, many quickly came to regard “cold fusion” as one of the most important topics confronting the scientific community.

Research scientists from all over the world, after learning of the news announcement, attempted to replicate the experiment in their labs. Unfortunately, most of them lacked crucial information about the experiment. This, together with the well-known contradiction in physics that deuterons are unlikely to collide efficiently at room temperature

because of the enormous amount of energy required to overcome the Coulomb barrier, caused mainstream science to dismiss the entire subject as error.

Twenty years later, we can see that progress came slowly but steadily. The few scientists who maintained an open interest and continuing commitment to explore the unknown had to contend with the shame and disgrace of being associated with a field of science that had been labeled as illegitimate.

Some of the LENR scientists have worked on replications of the original Fleischmann–Pons electrolysis experiment. Many others have explored new ground, performing experiments with deuterium gas and a variety of approaches. Many of these approaches and effects go well beyond the initial Fleischmann–Pons electrolytic effect.

These determined pioneers have set out to determine and evaluate the experimental parameters that may play a significant role in this process and to give plausible explanations to theoretical approaches. Given their negligible budgets, the work they have done and the understanding they have acquired of the “cold fusion”/LENR process is especially impressive, compared to the standard set by results obtained by thousands of generously funded scientists working in the “hot fusion” field. This suggests a promising research topic to discover and exploit perhaps the most auspicious alternative energy source. With limited funding and maximum resistance from science orthodoxy, the LENR scientists succeeded, regardless of the small and at times non-existent research budgets available to them. Their efforts are characterized by hard work and intensive research performed in their mostly privately funded labs. LENR scientists have remained isolated and separated from mainstream science often working in loneliness, without acknowledgement and recognition.

That was the past. The research has now achieved notable recognition as a new legitimate field of science. LENR is now poised to become a significant addition to the future of science.

Although LENR may become an option to provide energy for private households, industry and the transportation sector, running the economy on the basis of intensive use of a raw material as costly as palladium is impractical and, in the long term, perhaps impossible. Therefore, in the future LENR studies using less expensive metals such as nickel etc, are more likely to be considered as the materials on which to run a true hydrogen economy.

Considering the accelerating energy crisis, growing worldwide demands for increased energy, and geopolitical instabilities stemming from control of energy sources for a global economy, the possibilities suggested by LENR come at an ideal time. We are beginning to see this historic science development find inclusion as a research topic in university Chemistry and Physics classes worldwide. Although the promises of the field remain illusive, the interest in this exciting new field is nevertheless being received enthusiastically.

LENR does not appear to fit into current scientific understanding, and it raises uncomfortable questions about current and historical understandings of nuclear physics. The path forward will require new openness, receptivity, and tolerance. It may require flexibility on the part of orthodox physics to learn from LENR researchers. It may also require LENR researchers to learn from orthodox physics. Together, the disciplines of chemistry and physics are developing and will continue to build the foundation of a new field of science.

This Proceeding based on the New Energy Technology Symposium is a summary of selected experimental and theoretical research performed over the last 21 years that gives profound and unambiguous evidence for low-energy nuclear reactions (LENR), historically known as “cold fusion.” From the experimental papers presented, the reader will discern clear evidence for excess heat, tritium and neutron emission, helium production, and nuclear transmutation of the host metal. And, from the theory papers, presented, the reader will learn of a variety of reasonable explanations to approach the understanding of the experimental behavior. In part, some authors will reveal how to design LENR devices based on the experimental results obtained over the last 21 years.

*Jan Marwan
February 2011*



Review Article

Hot and Cold Fusion for Energy Generation

David J. Nagel *

The George Washington University, Washington, DC 20052, USA

Abstract

Sixty years of research on hot fusion have cost more than \$ 20 B. Only one of the dozens of experiments has barely reached breakeven, the point at which the energy produced is equal to the energy spent for its production. Twenty years of work on “cold fusion” cost less than \$ 0.2 B. Energy amplifications exceeding 10 for the palladium–deuterium system, and more than 100 for the nickel–hydrogen system, have been reported, but not verified. Hot fusion is understood and may result in large power plants in several decades. “Cold fusion”, now called Low-Energy Nuclear Reactions (LENR), remains a scientific mystery. If adequately funded, LENR could lead to safe, non-radioactive, green, small, distributed nuclear energy sources in less than two or three decades, well before hot fusion can produce commercial power.

© 2011 ISCMNS. All rights reserved.

Keywords: Cold fusion, Condensed matter nuclear science, Fusion energy generation, Hot fusion, Low-energy nuclear reactions, Nuclear energy generation

PACS: 25.10.+s

1. Introduction

There are many enduring concerns in the modern world. Energy is certainly one of them. The relentless increase in the world’s population, and the increase in the per capita use of energy in most countries, both force attention to old and new sources of energy. More and more people are on average needing more and more energy.

It is possible to group sources of energy into four categories. The first category includes materials and technologies that are already heavily used. They are three types of fossil fuels, coal, oil, and gas, and nuclear fission in large reactors. Overall, these established sources of energy provide over 90% of the power in the US. The environmental drawbacks of fossil fuels are well known. Nuclear fission is relatively benign environmentally, and is beginning to make a comeback in the US after three decades of stagnation.

The second group is often called “alternative” sources. They include “renewable” reservoirs of energy, notably solar, wind, and tidal energies, as well as hydroelectric and geothermal sources, and biomass. Most of these sources

*E-mail: nagel@gwu.edu

of energy tend to be best in particular regions, which are rarely near high population density areas. Hence, long power lines are needed to deliver the energy from such sources to consumers. Solar and wind energy have grown rapidly in recent years. Continued growth can be expected in the coming decades as the prices of both photovoltaic devices and wind generators continue to decline. In the US, these alternative sources provide less than 10% of the country's energy needs. Few people expect them to grow enough in the near future to significantly erode the large fractional positions of the sources in the first category. Growth of alternative energy sources will be mostly absorbed by increasing population and the growing demand for more energy per individual.

The third group of energy sources is distinguished by two characteristics, well-established experimental demonstrations and a lack of commercialization. Included in this category are hot and cold nuclear fusion, the subjects of this paper. Hot fusion due to the energetic collisions of light nuclei is well understood theoretically, as well as robustly demonstrated experimentally. The nuclei of main interest are the heavy isotopes of Hydrogen (H), namely Deuterium (D) and Tritium (T). The characteristics and history of hot fusion are sketched in Section 2.

“Cold fusion” is the historic name for the ability to produce nuclear reactions at relatively low energies (temperatures). The name is, at least, misleading and may be entirely wrong. The topic is now called Low Energy Nuclear Reactions (LENR) by many researchers. It is part of the field of Condensed Matter Nuclear Science [1]. The subject is well established experimentally, but not understood theoretically. The features and history of LENR constitute the third section of this paper. Both hot fusion and LENR are fields of scientific research now. They are decades away from commercialization, and later, possibly becoming of fractional importance as energy sources for both developed and developing countries.

The last of the groups of energy sources is populated by a few concepts, which have yet to be robustly demonstrated as energy generators, but may someday become such sources. That is, there is little or no experimental basis for believing now that they will emerge as sources of energy on any time scale. The best known conceivable source in this class is probably Zero Point Energy (ZPE) [2]. The idea behind ZPE is to draw energy from the large reservoir of fluctuations in all of space. Reports of demonstrations of such postulated effects and sources should be monitored. However, from engineering and commercial perspectives, it is unrealistic to expect the emergence of practical ZPE or other such energy sources for a half-century.

Another way to put into perspective the variety of power generators is to consider the source of their energy. Fossil and biomass fuels release energy by the occurrence of chemical reactions. There are several types of nuclear reactions that also yield energy, and they will be considered below. The remaining currently practical energy sources depend on three general reservoirs of energy, the motion of matter (wind, falling water and tides), thermally hot matter (geothermal and solar thermal) and light (solar photovoltaic). The focus here is on existing and potential nuclear sources of energy. But, since they involve reactions, as do the burning of various fuels, we can usefully compare chemical and nuclear energy sources.

Table 1 is a summary of the means of initiating reactions, their propagation and the possibility of fast energy releases for the different types of reactions. Of the four types of listed reactions, the least is known about LENR.

It should be noted that the situation for fission reactions is qualitatively different than that for fusion reactions in two ways. First, spontaneous radioactive decay can result in fission of a few heavy nuclides. Second, neutron-induced fission, as in ordinary nuclear reactors, does not involve an electrostatic barrier because the neutrons are not charged and, hence, are not subject to Coulomb repulsion. However, there are two primary requirements for sustained neutron-induced fission reactions to produce energy. The first is that the neutrons incident on a heavy nucleus must have appropriate energies, called thermal energies, because they are low in equivalent temperature. The second is that the heavy nuclides have to be sufficiently numerous and close enough to each other to use the neutrons emitted during fission reactions to induce other fissions. Control rods in fission reactors absorb neutrons to tune the rate of reactions and the power output. In short, the requirements of supplying energy for most chemical and nuclear reactions do not apply to neutron-induced fission reactions. But, they have these other requirements on neutron energies, and the density,

mass and arrangement of the nuclear fuel.

Before reviewing hot and “cold” fusion, it is worth considering the recent data on the sources and uses of energy in the US, shown in Fig. 1 [3]. Focusing on the US is done simply because the information is conveniently available, and that country is a disproportionately large consumer of energy. The dominance of coal, oil, and gas as chemical energy sources is clear from this diagram. The three primary uses of energy are shown as (a) residential and commercial, (b) industrial and (c) transportation. Non-fuel uses are mainly chemical processes, such as production of plastics. Despite all the recent emphasis on electric cars, the use of electricity for transportation was fractionally minuscule in 2002. Another very large-scale feature of the diagram is the fact that over half of the energy is unusable due to thermodynamic and other inefficiencies, such as heat leaks and electrical resistances. It is clear that energy conservation is attractive and relatively near-term way to help somewhat to balance the energy “books”. But, it cannot be a total solution to the energy needs of any one country or the world.

In 2002, nuclear fission contributed somewhat over 8% of the total energy source, and lead to about 20% of the US electricity generation. In France, almost 80% of electricity is generated by nuclear fission energy. The US is finally embarking on the construction of new fission reactors as old reactors retire and the use of electricity continues to grow. The US Department of Energy projects that the country will need 28% more electricity by 2035. Maintaining the current 20% nuclear fraction would require building about one reactor per year starting in 2016 [4].

Nuclear reactions other than fission, including hot fusion and LENR, are now where fission reactors were over 50 years ago. Even if their development, demonstration and commercialization proceeded quickly, they are decades away from starting to impact the energy balances in the US and elsewhere.

Section 2 summarizes the characteristics, history and status of hot fusion. Similar factors for LENR constitute in Section 3.

2. Hot Fusion

2.1. Background on nuclear reactions

Nuclei can be grouped into two major classes, stable nuclei and radioactive nuclei, which decay at rates characterized by a half-life. The spontaneous decay of a single radioactive nucleus is not strictly a nuclear reaction because two nuclei or quanta do not come together to react. There are many types of nuclear reactions that do involve the interaction of two nuclei (or nuclei and neutrons or gamma rays). The number of possible binary nuclear reactions can be simply computed. Since there are 256 stable isotopes for 80 of the elements in the periodic table, the number of possible reactions of stable nuclei is the square of 256, or 65,536 [5]. Reactions of unstable nuclei are possible, so the total number of potential nuclear reactions is very large, possibly exceeding 1,00,000. An interactive chart of the stable and unstable nuclides is on the web [6].

Table 1. Comparison of the initiation, propagation and runaway scenarios for chemical, fission, fusion and low-energy nuclear reactions. Fusion reactions can be produced in accelerator experiments, but they have no prospect of being practical energy sources. Tokamaks are the primary machines for production and confinement of very hot plasmas. Eventual commercial power plants for fusion energy will be Tokamaks. They might attain burning conditions some day. HAD represents “Heat After Death”, the production of energy in a LENR experiment after the input energy is terminated.

Reactions initiated by		Propagating reactions	Runaway reactions
Chemical	Flame	Burning	Explosions
Fission	Slow neutrons	In nuclear reactors	Atomic bombs
Fusion	Very hot plasmas	Possibly in Tokamaks	Hydrogen bombs
LENR	Unknown	Possibly HAD	Unknown

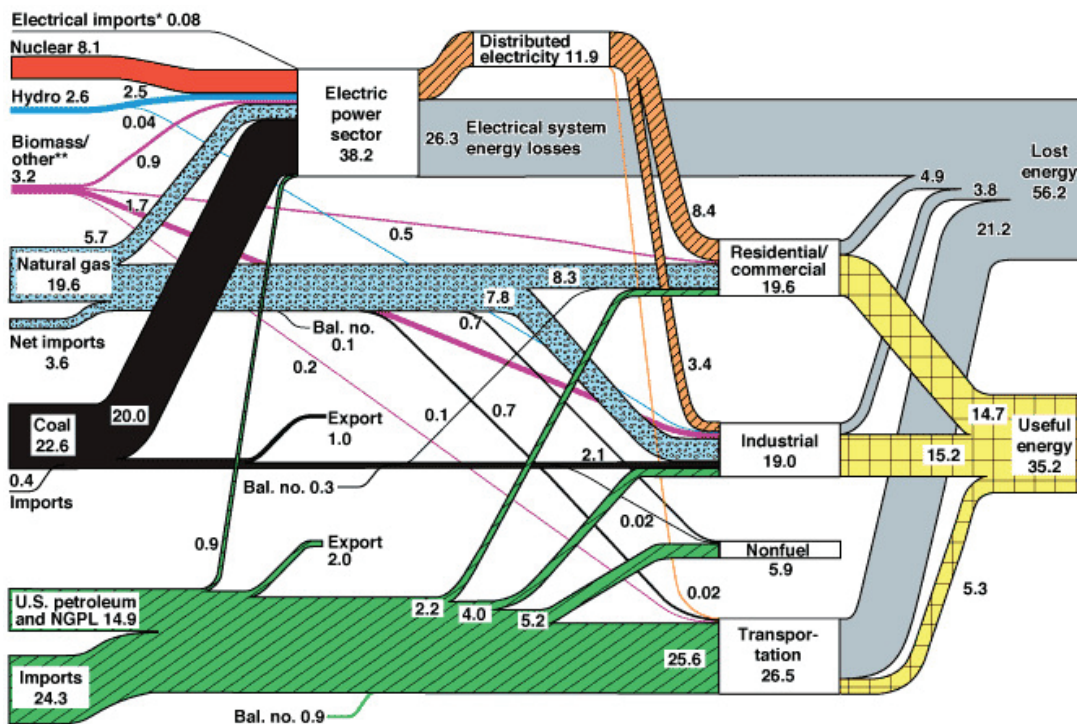


Figure 1. Diagram showing the sources (left) and sinks (right) of energy in the US for the year 2002 [3]. Since it happened for that year, the US energy consumption was about 97 quads, the numbers on this graphic are approximately percentage points. “Biomass/Other” (3.2 quads) includes wood, waste, alcohol, geothermal, solar and wind sources. A quad is an energy unit equal to 10^{15} British Thermal Units (BTU) or 1.055×10^{18} J. Equivalents of 1 quad are conveniently available on Wikipedia: http://en.wikipedia.org/wiki/Quad_%28energy%29.

Most of the possible binary reactions are simply termed nuclear reactions. However, reactions at the extremes of light and heavy elements are of practical interest and have special names. Both of these types of reactions are generally exothermic, that is, they yield energy. The splitting of heavy nuclei, notably isotopes of uranium and plutonium, due to neutron impact is termed fission, as already noted. It is the basis of the over 400 nuclear power reactors now in use around the world [7]. Fission power reactors already have a history of over a half-century. The reactions of very light nuclei go by the name of fusion. Fusion reactions are the basis of hypothetical large power plants that might become productive in a few decades.

Fusion reactions were initially studied using directed ion beams striking targets in accelerator experiments. When it became possible to heat and confine very hot plasmas, in which the random thermal motions of ions have sufficient momenta to induce nuclear reactions, energy production from multi-million degree plasmas could be sought. The very hot nuclei have to be confined, so the plasma does not cool, and net energy production results. This is done in either of two primary ways. The first uses very strong magnetic fields to restrain rather dilute plasmas, so it is called “magnetic fusion”. The second involves producing conditions in very dense materials that can lead to significant numbers of fusion reactions before the plasma explodes and cools. The inertia of the ions provides a short time before the plasma is too cold to support hot fusion reactions, so this method is called “inertial fusion”. Such fusion can be induced by very high-power lasers or by electrical discharges.

Two equivalent units are used to characterize ion kinetic energies (for beams or in plasmas) or ion temperatures (in plasmas). Ion kinetic energies are usually expressed in electron volts (eV). Plasma temperatures are given in degrees Kelvin (K). In plasmas, there are distributions of the kinetic energies for all of the particles. The hotter the plasma, the higher is the maximum of the distribution in energy terms. The conversion factor between kinetic energies and plasma temperatures is $1 \text{ eV} = 11,604 \text{ K}$. Hence, a particle energy of 1 eV (the energy obtained by one electron accelerated by a potential drop of 1 V) is equivalent to the peak energies of particles in a plasma with a temperature of 11,604 K. The surface of the sun has a temperature of about 6000 K, or roughly 0.5 eV, for example.

2.2. Hot fusion reactions

There are many types of fusion reactions between the isotopes of hydrogen, helium, lithium and beryllium. We consider two of them, first, fusion between two deuterons, because of its envisioned relevance to LENR, and then deuterium–tritium fusion, because of its practical importance for hot fusion energy production. Figure 2 shows cartoons of the particles involved in two D–D reactions and the variation of reaction probabilities (cross sections) with kinetic energy for these two reactions [8]. Note that D–D fusion requires higher energies and has much lower cross sections compared to D–T fusion. Fusion between two deuterons is not a practical approach to hot fusion because relatively high energies (temperatures) are required. By contrast a deuteron and triton have peak reaction rates at much lower energies. This greatly relieves the requirements for both heating and confining the plasma in which the particle kinetic energies are

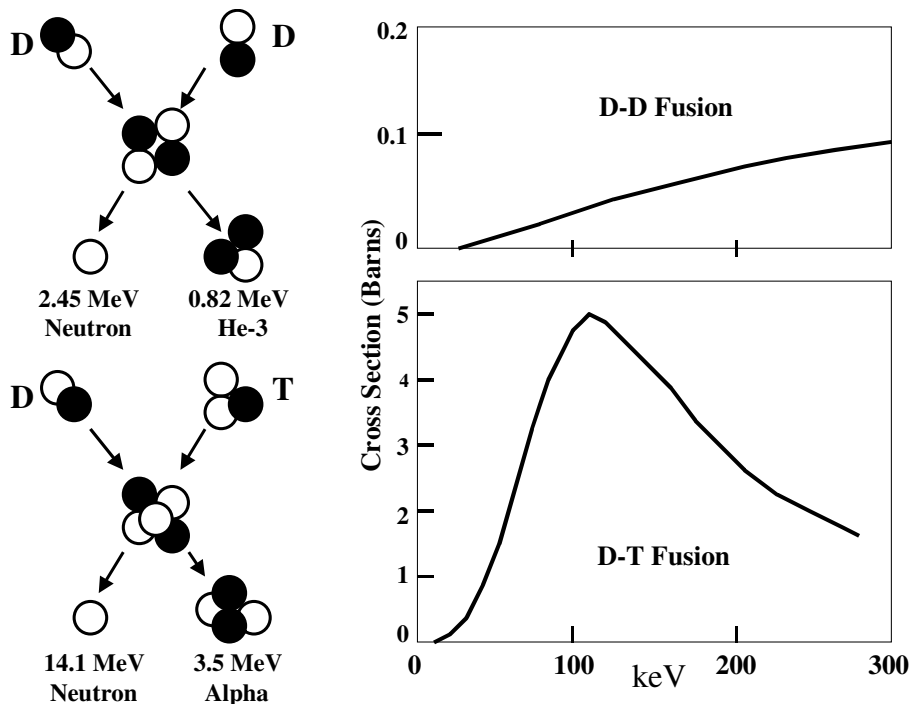


Figure 2. *Top left:* A schematic showing the particles and exit energies for one branch of D–D fusion. Table 2 provides all the outcomes of D–D fusion. Protons are shown in black and neutrons in white. *Bottom left:* A schematic of the reactants, product particles, and exit energies, for D–T fusion. *Right top and bottom:* The cross sections for D–D and D–T fusion. One Barn is 10^{-24} cm^2 .

great enough for power production.

The term fusion, as applied to reactions of two deuterons, is actually somewhat odd. Consider the outcomes of D–D reactions shown in Table 2. In almost all of the deuteron–deuteron “fusion” reactions, the incoming nuclei do not fuse in the ordinary sense of the word. For only one reaction in 10 million is there actual fusion (joining) of the two deuterons to form a helium nucleus, which is called an alpha particle. Then, the excess energy is emitted as a 23.5 MeV gamma ray. Most of the time, the energy that is produced by D–D reactions is carried off kinetically by the reaction products. Table 2 also contains the particle and energy accounting for D–T fusion, which will be used in potential commercial hot fusion power plants.

2.3. The Lawson criterion and progress in hot fusion

The “fusion” of light elements in very hot plasmas is understood both conceptually and quantitatively. This permits the computation of the conditions which must be met to produce energy, that is, to get out more energy than is needed to produce and maintain the plasma. There are three critical plasma parameters, the density, the temperature and the lifetime. The density is crucial because higher densities lead to more frequent collisions and, hence, more reactions. The temperature is important because it determines the particle velocities and, hence, the energies with which they collide. Those energies in turn determine the reaction cross sections, as shown in Fig. 2. The plasma lifetime is significant because it measures the time available for fusion reactions. If it is very short, the same energy is needed to create the plasma, but there are relatively few reactions. That is, there is no hope of net energy production for short-lived magnetically confined plasmas. The challenge to plasma physicists and engineers is to achieve high values of all three critical parameters simultaneously within a Tokamak.

In 1955, Lawson derived the criterion that bears his name. It was published in 1957 and applies to deuterium–tritium fusion. He found that the triple product of density, temperature and plasma lifetime must exceed 10^{21} to achieve energy breakeven. The units are m^{-3} for density, keV for temperature, and seconds for time. A compact derivation of the Lawson Criterion is available on the web [9]. Steady increases in the triple product have been achieved in the last half century in large and expensive hot plasma experiments. That history is shown in Fig. 3 along with a similar curve for growth in the number of transistors in leading-edge microelectronics and the energy of accelerators for high-energy physics [10]. It appears that the Japan Torus (JT-60) experiments have already achieved the Lawson Criterion. However, the values for the JT-60 device are based on deuterium–deuterium experiments. Were those experiments done instead with deuterium–tritium plasmas, an energy gain of 25% was calculated. Tritium is expensive and radioactive, so it was not used in the JT-60 experiments.

While progress in both hot fusion research and microelectronics might appear similar, there is a vast difference in the impact of both trends. To date, all of the high temperature plasma devices were energy sinks, requiring more energy to run than they produced. Figure 4 shows the annual costs of hot fusion research in the US [11]. They total to over \$ 20 B in current USD for the second half of the last century. There has been no energy return on investments in hot fusion yet. Such will probably be the case for another few decades. Financial returns for past funding of hot fusion are

Table 2. The branching ratios (fractions), and the emitted quanta and their energies (in MeV), for the fusion of two Deuterons (D) with three outcomes, and the fusion of a deuteron and triton (T) with one outcome. Alpha is short for Alpha Particle, the nucleus of a Helium atom.

Reaction	Partners	Fraction	Emitted	Energy	Emitted	Energy
D	D	0.5	Neutron	2.45	He-3	0.82
D	D	0.5	Proton	3.03	H-3	1.01
D	D	10^{-7}	Alpha	0.082	Gamma	23.5
D	T	1.0	Neutron	14.1	Alpha	3.51

even more remote.

By contrast, the progress in microelectronics has enabled the computer and communication revolutions, which have created vast new industries and already changed the world. The amount of value from production and use of computers of all sizes, and the internet and wireless industries, is immense and may be inestimable. Even if hot fusion succeeds grandly on a scale of a few decades, it might attain only a niche status in the overall generation of energy. That is, it must compete with many other energy sources. Meanwhile, the melding of information technology and humans will have advanced greatly.

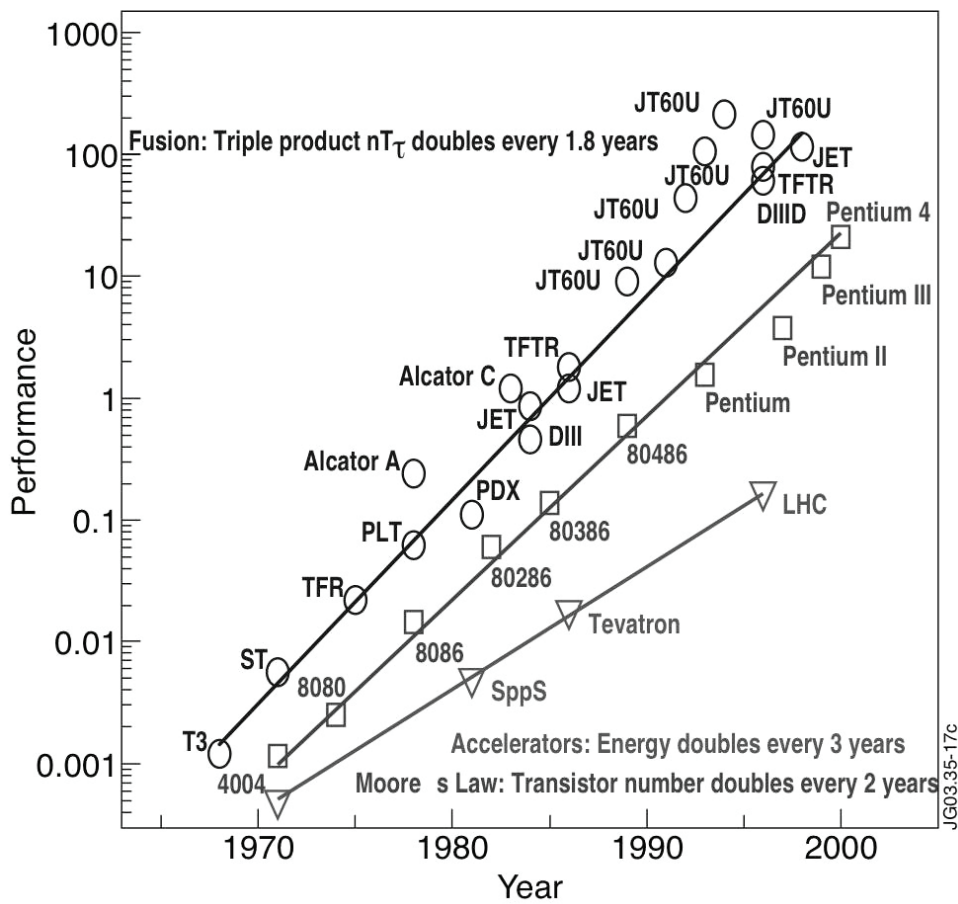


Figure 3. History of the increase in the Lawson Triple Product, the number of transistors on computer chips (Moore's law) and the energy of particle accelerators [10]. The Lawson Criterion is achieved at the value of 100 on the left-hand vertical scale of this graph. High-energy particle accelerators advance slower than the other technologies because of the immense cost per facility.

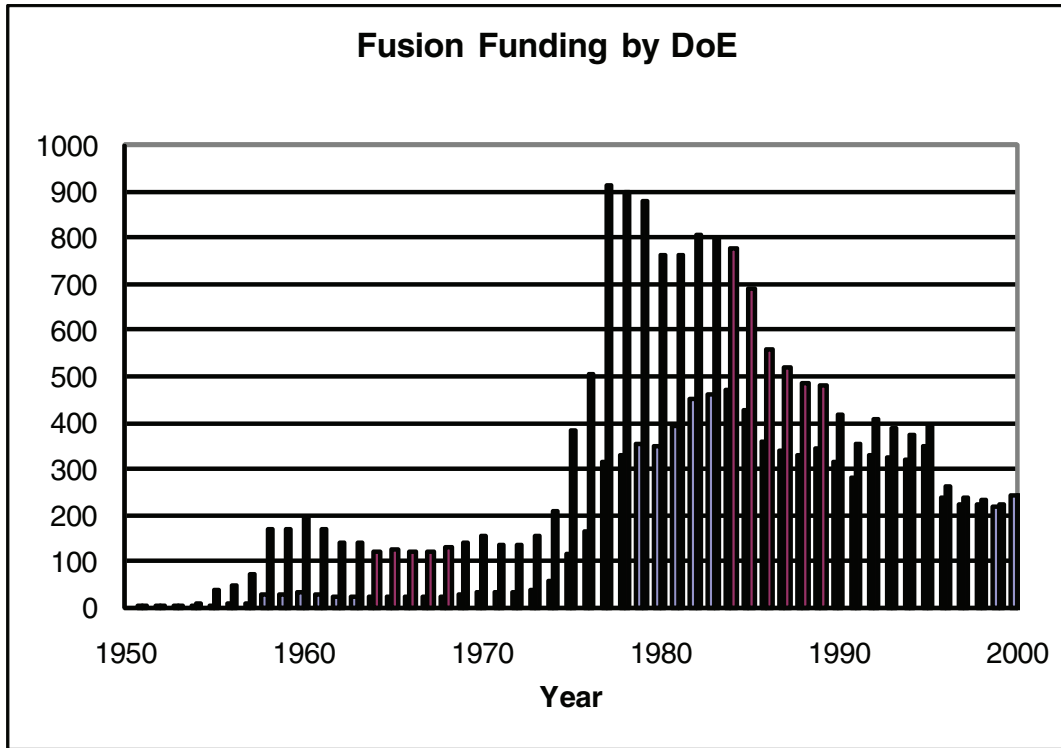


Figure 4. History of the funding of hot fusion research by the US Department of Energy over five decades at the end of the last century [11]. The vertical axis is millions of USD. The shorter bars for each year are actual (“then year”) dollars. The longer bars are inflation-adjusted to the year 2000. The effect of the oil price shock in the early 1970s due to decisions of the Organization of Petroleum Exporting Countries is evident.

2.4. Status and prognosis for hot fusion research

Having reviewed the history of hot fusion, what is its current status and expected progress in the coming decades? Table 3 gives a terse history and prognosis for the major current and planned hot fusion machines.

Figure 5 shows the largest magnetic and laser inertial machines for hot fusion research. The total capital and

Table 3. Actual and projected energy gains for experimental Tokamaks with D-T plasmas. The value for JT-60 was computed for D-T plasmas based on its actual performance with D-D plasmas. The years for the projected machines are conservative. That is, building and successful operation of ITER, DEMO and PROTO may occur substantially later than shown. The energy gain goal for PROTO, if it is actually to be built, is to be determined (TBD).

Machine	Goal	Year	Energy gain	Reference
JET	Research	1997	0.7	[12]
JT-60	Breakeven	1998	“1.25”	[13]
ITER	Ignition of burning	>2020	10	[14]
DEMO	Steady-state electricity generation	>2030	25	[15]
PROTO	Prototype commercial power sation	>2040	TBD	[16]

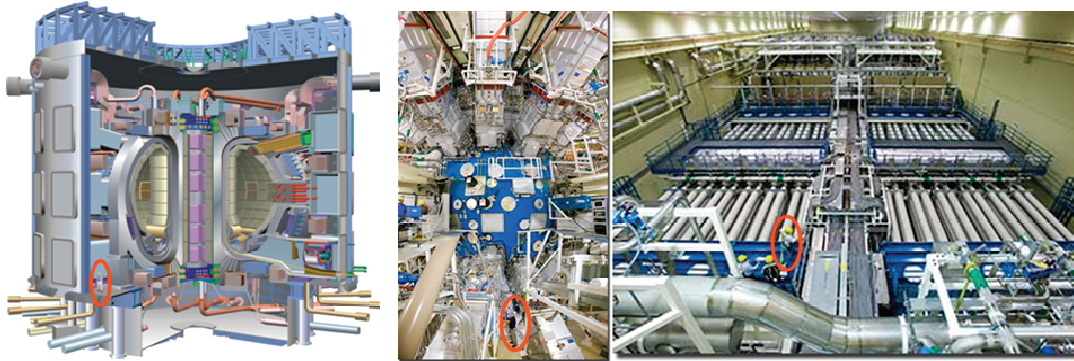


Figure 5. *Left:* Drawing of the International Thermonuclear Experimental Reactor, a Tokamak hot fusion facility being built in France [17]. *Center:* Photograph of the laser target chamber for the US National Ignition Facility (NIF), an inertial fusion facility in early operation at the Lawrence Livermore National Laboratory. *Right:* Photograph of one of the two 400-foot-long NIF laser bays [18]. The ovals indicate people in the drawing for ITER and the pictures for NIF.

operational cost of these facilities is very great. The projected costs for International Thermonuclear Experimental Reactor (ITER) exceed \$ 15 B. Those for the US National Ignition Facility (NIF) will likely be greater than \$ 3 B. Neither machine will produce useable energy, let alone electricity.

There are many potential scenarios in the long-term competition for part of the escalating energy market. Assuming that hot fusion does achieve energy gain values high enough to be commercially valuable, its large central power plants might augment or replace some fission reactors. Mining of uranium might yield fission fuels for centuries. The deuterium fuel for hot fusion is available from water, and would be adequate for millennia. However, large hot fusion reactors will be expensive to operate and they will produce nuclear waste. So, it is also possible that increased use of distributed solar and wind energy will keep hot fusion nuclear reactors from ever becoming a major source of energy. Recent and largely unenthusiastic perspectives on the history, status and prospects for hot fusion are available [19,20].

Imagine that it is 100 years ago, and the subject was transportation rather than energy. Arguments over possible outcomes were similar to current uncertainties over the future of nuclear and other sources of energy. What would be the types of engines for moving people and goods? The sizes, configurations and number of cylinders were central issues. The best fuels were also uncertain. Now we know two things. The first is that almost all options under consideration at the outset of the transportation revolution have some role to play currently. The second is that fast turbines, which enable modern jet airline transportation, were not a major part of the historic discussion in the early 1900s. Water turbines were common and gas turbines were demonstrated. However, the materials needed for high-speed gas turbines were not available a century ago. Will anything emerge in the field of energy production, as did fast turbines in the field of transportation? Could it be Low-Energy Nuclear Reactions? If so, when might that happen?

3. Low-energy Nuclear Reactions

3.1. Background

The term “low energy” is part of LENR because of the fact that it is possible to induce nuclear reactions at energies and equivalent temperatures that are dramatically lower than those needed for ordinary nuclear reactions, fusion included. We noted in the last section that energies of at least tens of keV, that is, temperatures exceeding 100s of millions of degrees K are needed to overcome the Coulomb barrier for fusion reactions to occur. Much higher energies are needed

for nuclei with higher charges. But, it has been found experimentally that it is possible to induce exothermic LENR in both light and heavy ions at rather ordinary temperatures. The corresponding energies are well below 0.1 eV.

Many books give myriad details on LENR. A useful compilation is on the web [21]. The architecture of this section is similar to that of the last section on hot fusion. The goal of the section is to give highlights on the characteristics, status and prognosis for LENR.

3.2. Types of LENR

In very general terms, the specific materials, the equipment and the protocols in LENR experiments have varied widely. Materials in LENR experiments are quite diverse. But, in all cases, either a proton or deuteron is loaded on to or into a solid lattice. The hydrogen isotopes can come from a liquid (electrochemical loading), a gas (high pressure and elevated temperature loading), a plasma (mostly glow discharges, but also arcs) or an ion beam (from an accelerator).

The material system used by Fleischmann and Pons in the pioneering experiments in the late 1980s was Pd as the solid lattice and deuterium as the hydrogen isotope. Most of the experimental work in the field has been done using this system, including electrochemical, gas, plasma and beam loading. Early in the field, some experimenters worked with the Ni and H system and reported getting excess heat, indicative of nuclear reactions. This system has also been the core of numerous experiments, but many fewer than for the Pd–D combination.

The signatures of nuclear reactions are also varied, but can be categorized. The first and most important is the generation of heat at levels far beyond what can be explained chemically. Energy output is the most likely to be a practically important result of LENR. It is the focus of this paper. We will survey energy gains for the Pd–D and Ni–H systems below.

There are other measured signals that indicate nuclear reactions can occur at low temperatures. One is “nuclear ash”, the elemental residues of the reactions. Helium and tritium are the dominant examples of nuclear reaction products. There are several reports of a correlation between heat and helium production in LENR experiments. The first was by Miles [22]. The most detailed was by McKubre and his colleagues [23]. The correlation of heat and helium remains contentious, as do most aspects of LENR, both experimental and theoretical.

The production of heavy elements in LENR experiments has been widely reported. The term “transmutation” is applied to this kind of output from LENR. In 2003, Miley compiled a list of 15 laboratories in six countries, which reported transmutations in LENR experiments [24]. Such experiments are difficult because they require trace element analyses both before and after the LENR experiments. Such analyses are generally complex and expensive.

Fast charged particles, which also cannot be produced chemically, have been observed by many investigators. For example, Lipson and his colleagues reported the emission and measurement of 3 MeV protons and 11–20 MeV alpha particles from Pd/PdOD_x and TiD_x [25].

Besides heat, nuclear ash and energetic particles, there are some infrequently measured low-energy phenomena that can also be interpreted as evidence of nuclear reactions. They include the emission of sound and infrared radiation, and the production of micro-craters. Such measurements must be verified in experiments that involve parametric variations of the materials and conditions used. Until then, they provide only weak but suggestive evidence for LENR.

The variety of means to load hydrogen isotopes onto and into a lattice and the classes of ensuing measurements is given schematically in Fig. 6. It must be emphasized that the number of experiments that can be classified into each of the 16 boxes varies greatly. Most work has been done with electrochemical loading from liquids and heat measurements using a wide variety of calorimeters.

3.3. Criteria for LENR

We saw that there are three critical plasma parameters, the density, the temperature and the lifetime, for energy production in hot fusion. The Lawson Criterion gives the requirements on the Triple Product of these three factors quantitatively

Input Processes: Loading a Solid	Output (Measurements)			
	Excess Heat	Nuclear Products	Prompt Radiation	Sound or Infrared
Liquids: Electrochemical	Dark	Medium	Light	Light
Gases: Thermodynamic	Light	Medium	Light	Light
Plasmas: Kinetic	Light	Medium	Light	Light
Beams: Kinetic	Light	Light	Light	Light

Figure 6. The four means to bring together a solid lattice and hydrogen isotopes (left side) and the four classes of measurements that indicate the occurrence of LENR (top row). The darker shading indicates the combinations with the most experiments.

for net energy production by D–T fusion. The question naturally arises: are the conditions for LENR known similarly, and are they quantified? In other words, is there the equivalent of a Lawson Criterion for LENR? The answer now is no. The fundamental roadblock is the lack of understanding of LENR, both conceptually and quantitatively. Around two dozen theories of LENR have been published, but none of them has been adequately tested against the results of LENR experiments. The present lack of theoretical understanding does not mean that a criterion specifying quantitative conditions for achievement of LENR will never be developed. In fact, there has been major progress toward the development of such a criterion.

The most fundamental requirement for the occurrence of LENR seems to be the need for a solid lattice to be the host for the protons or deuterons. This is in stark contrast to the situation for energetic and high temperature nuclear reactions. In beam experiments, the lattice provides a holder for target nuclei, but is not a requirement for the occurrence of nuclear reactions. Put another way, crossed ion beams in a vacuum system also lead to high-energy nuclear reactions. In hot plasmas, there is no lattice because the particle energies are sufficiently great to melt, vaporize and ionize the atoms that might initially be part of a solid lattice.

There has been much discussion about the location of the sites at which LENR occur. It is not finally decided whether LENR occur only on the surfaces of lattices, only within them or in both locations. Much evidence indicates that surface reactions are dominant, but there is no consensus. Similarly, many studies have employed materials with particle sizes on micrometer and nanometer scales, in addition to the millimeter-scale electrodes usually used in LENR experiments. Several experiments indicate that the use of nano-scale particles favors the production of LENR, but here also the “jury is still out”. Despite all these uncertainties, there is a good start on determining the criteria required for production of LENR.

McKubre and his colleagues have done over 100,000 h of precision calorimetry in LENR experiments. They presented [26] a provocative relationship based on their measurements, which gives the variations in excess power P_{xs} in electrochemical LENR experiments with three quantities, which will be defined in the following paragraphs. K is an unknown proportionality constant in this equation.

$$P_{xs} = K(I - I_0)^2(X - X_0)dx/dt.$$

The first factor in the McKubre equation is the value of the electrochemical current density I passing through the cylindrical cathode surface beyond a value near $100 \text{ mA/cm}^2 = I_0$. It was found that P_{xs} scales with $(I-I_0)^2$. Experimental current densities about an order of magnitude greater than 100 mA/cm^2 have been employed. The maximum values of I are not well defined. Power supplies capable of delivering very large currents can be built, so there is no imminent equipment limit. Heating of electrochemical cells might be the first factor that limits the increase of electrical current density. But, heating has been shown to favor excess power production in some experiments.

The second parameter is the loading factor, specifically, the ratio of the number of deuterons to the number of Pd atoms within a Pd cathode, that is, $X = D/\text{Pd}$. The excess power scales linearly with values of X in excess of $0.85 = X_0$. It has been difficult to achieve and maintain values for X substantially above unity in electrochemical experiments. Then, $(X-X_0)$ is near 0.15. Other (non-electrochemical) experiments have reported values for X near 2. Hence, $(X-X_0)$ can range from zero to somewhat above unity.

The third parameter in the equation for the Pd–D electrolytic system is the rate of change of the loading X . The higher dX/dt , where t = time, the higher the excess power. In the experiments that lead to the discovery that P_{xs} scales linearly with the rate of change of the loading factor, the value of dX/dt was not a control parameter. It varied capriciously, leading to the observed correlation. If there were, indeed, some way to willfully increase the rate of loading ($+dX/dt$) and deloading ($-dX/dt$) for D in Pd, P_{xs} might be enhanced. But, it is not easy to estimate the maximum achievable values. The rate of diffusion of D in Pd might provide an extreme limit on the values of dX/dt . But, that rate is remarkably high. The rate of ingress and egress of D is clamped to the electrochemical current. Possibly, the use of power supplies that rapidly vary their applied currents for constant voltage (potentiostatic) electrolysis, would favor large values of dX/dt and, hence, high values of P_{xs} .

The above conditions on loading, current density through a cathode surface and rate of change of loading are probably necessary, but not sufficient conditions for full control of LENR in electrochemical experiments. Analogous criteria for gas, plasma and beam loading experiments remain to be developed.

We must note that a criterion, or rather multiple criteria, for the occurrence of LENR is not the same as some measure of ways to optimize the production of energy by LENR. While the Lawson break-even criterion for energy production in hot fusion is available, a recipe for optimization of hot fusion energy production does not exist now. There are inevitable limits on hot plasma densities, temperatures and lifetimes. Until these limits and trade-offs between them are known, it is not possible to provide the conditions for optimization of hot fusion energy production. The situation is similar to the operation and efficiency of an automobile. It is relatively easy to state what is needed to make a car work. It is more complex to ascertain how to get the best gas mileage, which depends on both the design and the operation of a car. In short, now we are waiting for the complete criteria for occurrence of LENR. Knowledge of the conditions for net energy production and for optimization of energy production may not be available for several years, or even longer.

3.4. Status of LENR

3.4.1. *The palladium–deuterium system*

There are about three dozen experimental papers on the Pd–D system, which present the values for both the output and input energies, so an energy gain can be computed. For most of them, the energy gains (energy out divided by energy in) are less than 1.5. Such relatively low values raise questions about the possibility of chemical effects, and experimental errors, especially drifts in long-term experiments. A short summary of a few of the more noteworthy measured LENR energy gains is given in Table 4. None of these experiments has been adequately replicated. Note that the first two of these experiments involve relative small (<1 MJ) energies.

3.4.2. The nickel–hydrogen system

The field of LENR was started with Pd–D experiments, and most of the experiments in the field have been done with that system. However, there have been many reports on experiments with the Ni–H system, which first got attention in the early 1990s. It is attractive since Ni is much cheaper than Pd and H₂O is also less expensive than D₂O. In the recent past, Focardi and Rossi have reported spectacular energy gains in the range from 80 to somewhat over 400 from Ni–H experiments [30]. They tabulated the results of six experiments during the period from mid-2008 to mid-2009. Figure 7 is a plot of their reported input and output energies.

There are three remarkable features of these data from the Ni–H system. The first is the immense energy amplification factors. Ordinarily, a factor of 25 is adequate for commercialization of an energy source. That gain is enough to overcome thermodynamic, conversion and transmission losses. Gains in the range of 80–400 bode well for the practical applications of LENR.

The second noteworthy factor is the relatively large amounts of energies going in and out of the system. Pd–D experiments rarely have powers exceeding 100 W as input and output, and integrated excess energies seldom exceed 1 MJ. The highest of the Focardi–Rossi input energy exceeds 30 MJ with the associated output energy in the 3 GJ range. These are very large values for LENR experiments. The last important feature of the new Ni–H data in Fig. 7 is the approximate linearity of the output energy with the input energy. This indicates that, with some thermal lag, the input energy may be the much-needed control parameter for LENR energy source output.

The important power–time histories (power input and output) from the Rossi Ni–H experiments are not available. Additional information on this provocative work is in an international patent application [31]. However, that application does not teach how to produce LENR and realize high energy gains. The immense reported gains for the Ni–H system share an unfortunate feature with the high energy gains in the Pd–D system. They have not been reproduced by other experimenters nor even robustly verified.

4. Conclusion

The overall contrast between hot and “cold” fusion is remarkable. It is a fact of scientific history that hot fusion experiments have been conducted for 60 years by hundreds of physicists and engineers at a cost exceeding \$ 20 B. But, they have barely achieved energy breakeven. Experiments having costs, which will double the investment in hot fusion, are planned for the next few decades. Both their uncertain outcomes, and competition from other sources, make the eventual practical importance of hot fusion inscrutable.

Hot fusion is understood scientifically, and a great deal of the engineering needed to realize hot fusion power plants is already done. It is possible that large central hot fusion power plants might be supplying electrical power before 2050, a century after research in the area took off. Like current fission power plants, the grid will be used to distribute power that huge hot fusion plants might eventually produce. Their operation will activate large amounts of materials near the plasmas, which will be heavily bombarded by neutrons. Hence, future hot fusion plants will leave behind significant radioactive waste, as do present fission plants.

In stark contrast, LENR (then called “cold fusion”) experiments reached breakeven after less than 10 years of experimentation by two people, Fleischmann and Pons. The total cost of LENR research to date is probably well under

Table 4. Reports of high-energy amplifications from some Pd–D LENR experiments.

Authors	Year	Energy in (kJ)	Energy out (kJ)	Energy gain	Ref.
Fleischman and Pons	1991	22.5	102.5	4.5	[27]
Sun, Zhang and Guo	2003	28.3	131	4.6	[28]
Dardick et al.	2003			6.7	[29]

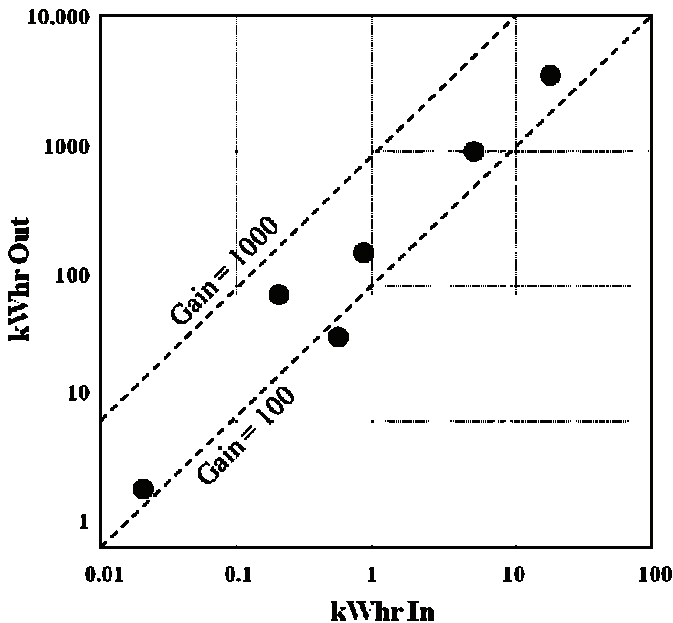


Figure 7. The output energies as a function of input energies reported in the recent Focardi–Rossi paper [30]. 1 kWh = 3.6 MJ. The very high gain values are noteworthy. If they are verified or reproduced, they would prove to be historic.

\$ 0.2 B. Very little support is available for LENR at present. Given that the field has the potential to produce a new and clean source of energy, this situation is anomalous. If practical sources based on LENR are promising, why is the scientific study of LENR not being pushed hard? The most fundamental reason is lack of attention by the mainstream scientific community. Funding agencies, major investors, patenting organizations, and the editors of both scientific journals and magazines, are all waiting for the scientific community to adequately engage the voluminous literature on LENR and then legitimize the field as a part of science. However, few scientists with the appropriate expertise are willing to thoroughly examine the available information. And, several well-recognized ex-scientists continue to disparage the field for unknown reasons.

LENR are not understood now. None of the many theories has been adequately tested. However, the empirical database in the field, which is mostly public, makes it possible to contemplate the following possibilities.

- The new sources would be safe during their operation because LENR do not emit high intensities of dangerous prompt radiation (neutrons or gamma rays).
- There is ample experimental evidence that LENR do not produce significant residual radioactivity, so generators based on these reactions would not generate dangerous waste.
- No green house gases are emitted during the operation of LENR experiments.
- LENR generators do not have to be big or expensive. However, they might be scalable for larger applications, both mobile and fixed.
- The sources could be distributed, even powering individual homes and, hence, relieving the electrical distribution grid of some load.

The sizes of potential LENR sources of power and energy are naturally key to possible applications. Now, neither the

physical size nor the power output of potential LENR sources is clear. Some people envision such sources being the size of batteries for personal electronics. They might be desk sized and supply enough power for an individual home. Powers ranging from watts to more than kilowatts have been discussed. One of the main issues for commercial LENR power sources is already known from experience with fuel cells. The ancillary equipment for electronic, fluidic and thermal functions can be relatively complex. Put another way, even if a vessel in which LENR could be confidently produced at an attractive cost were available now, engineering it into widely useful and reliable products would be challenging.

While it is possible to project the performance of magnetically confined hot fusion experiments, this cannot be done now for LENR experiments. Until reproducibility and controllability of such experiments are improved, and the active mechanisms are understood, confident theoretical scaling of LENR power and energy gains will remain essentially impossible. However, despite the current shortcomings for LENR, the prospect of many applications, in addition to the vexing scientific riddles in the field, should spur research. One application in particular could be historic. The production of clean water by either desalination of seawater or distillation of contaminated river waters would have immense global health benefits. The availability of distributed sources of nuclear energy for clean water production is a wonderful vision for the future of LENR.

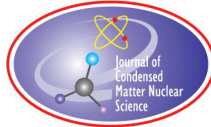
Acknowledgements

Dr. Jan Marwan suggested this article. His initiative was timely and is appreciated. Amal Al Katrib is thanked for providing information on the published energy gains in the Pd–D system. Paul Fleury and Chia-Pin Chang provided useful comments on the manuscript. Their gracious assistance is recalled with pleasure.

References

- [1] The International Society for Condensed Matter Nuclear Science. <http://www.iscmns.org>. Accessed 24 June 2010.
- [2] T. Valone, Zero Point Energy: The Fuel of the Future, Integrity Research Institute, Beltsville MD, 2008.
- [3] https://publicaffairs.llnl.gov/news/energy/content/energy/energy_archive/energy_flow_2002/ USEnFlow02-quads.pdf. Accessed 24 June 2010.
- [4] <http://www.nei.org/keyissues/newnuclearplants/>. Accessed 24 June 2010.
- [5] http://en.wikipedia.org/wiki/Stable_isotope. Accessed 24 June 2010.
- [6] <http://www.nndc.bnl.gov/chart/>. Accessed 24 June 2010.
- [7] <http://www.euronuclear.org/info/encyclopedia/n/nuclear-power-plant-world-wide.htm>. Accessed 24 June 2010.
- [8] X.Z. Li, Q.M. Wei, B. Liu, *Nuclear Fusion* **48** (2008) 1–6.
- [9] http://www-fusion-magnetique.cea.fr/gb/fusion/physique/demo_ntt.htm. Accessed 24 June 2010.
- [10] http://iter.rma.ac.be/en/img/MooresLaw_EN.jpg. Accessed 24 June 2010.
- [11] D.J. Nagel, *Program Strategy for Low Energy Nuclear Reactions*, Infinite Energy Magazine, Issue 69, 2006, <http://www.infinite-energy.com/iemagazine/issue69/programstudy.html>. Accessed 24 June 2010.
- [12] "Joint European Torus", http://en.wikipedia.org/wiki/Joint_European_Torus. Accessed 24 June 2010.
- [13] <http://www-jt60.naka.jaea.go.jp/english/jt60/project/html/history.html>. Accessed 24 June 2010.
- [14] "International Thermonuclear Experimental Reactor", <http://www.ITER.org/>. Accessed 24 June 2010.
- [15] <http://en.wikipedia.org/wiki/DEMO>. Accessed 24 June 2010.
- [16] <http://www.energyresearch.nl/energy-options/nuclear-fusion/research/research-of-nuclear-fusionby- demo/>. Accessed 24 June 2010.
- [17] <http://gk.ps.uci.edu/gsep/>. Accessed 24 June 2010.
- [18] https://publicaffairs.llnl.gov/news/news_releases/2009/NR-NNSA-09-03-06.html. Accessed 24 June 2010.
- [19] M. Moyer, Fusion's False Dawn, *Scientific American* **302** (2010) 50–57.
- [20] C. Seife, *Sun in a Bottle: The Strange History of Fusion and the Science of Wishful Thinking*, Viking Adult, New York, 2008.

- [21] <http://www.newenergytimes.com/v2/books/books.shtml>. Accessed 24 June 2010.
- [22] M. Miles et al., Heat and Helium Production in Cold Fusion Experiments, in *The Science of Cold Fusion*, T. Bressani, E. Del Guidice, G. Preparata (eds), Societa Italiana de Fisica, Bologna, 1991, pp. 363–372.
- [23] M.C.H. McKubre et al., New Physical Effects in Metal Deuterides, in *Condensed Matter Nuclear Science*, J.-P. Biberian (ed.), World Scientific, New York, 2006, pp. 23–59.
- [24] G. Miley, P.J. Shrestha, Review of Transmutation Reactions in Solids, in *Condensed Matter Nuclear Science*, P.L. Hagelstein, S.R. Chubb (eds.), World Scientific, New York, 2006, pp. 361–378.
- [25] A. Lipson et al., Charged Particle Emission during Electron Beam Bombardment of Deuterium Subsystem in Pd and Ti-Deuteride Targets, in *Proc. of the 14th International Conference on Condensed Matter Nuclear Science*, D.J. Nagel, M.E. Melich (eds.), 2010, in press.
- [26] M.C.H. McKubre et al., Concerning the Reproducibility of Excess Power Production, in *Proc. of the 5th International Conference on Cold Fusion*, S. Pons (ed.), International Conference on Cold Fusion, Valbonne France, 1995, pp. 17–33.
- [27] M. Fleischmann, S. Pons, Calorimetry of the PD Ed2O System; from Simplicity to Complications to Simplicity, in *Frontiers of Cold Fusion*, H. Ikegami (ed.), Universal Academy Press, Tokyo, 1993, pp. 47–66.
- [28] Y. Sun, Q. Zhang, Q. Guo, The crystal change and ‘excess heat’ produced by long time electrolysis of heavy water with titanium cathode, *Chinese J. Atomic and Molecular Phys.* **20** (1) (2003) 69–74.
- [29] I. Dardik et al., Intensification of Low Energy Nuclear Reactions Using Superwave Excitation, in *Condensed Matter Nuclear Science*, P.L. Hagelstein, S.R. Chubb (eds.), World Scientific, New York, 2006, pp. 61–71.
- [30] S. Focardi, A. Rossi, A new energy source from nuclear fusion, http://www.journal-ofnuclear-physics.com/files/Rossi-Focardi_paper.pdf, 2010. Accessed 25 June 2010.
- [31] A. Rossi, Method And Apparatus For Carrying Out Nickel And Hydrogen Exothermal Reactions, World Intellectual Property Association WO 2009/125444 A1, 2010. Accessed 25 June 2010.



Research Article

What is Real about Cold Fusion and What Explanations are Plausible?

Edmund Storms *

Kiva Labs, 2140 Paseo Ponderosa, Santa Fe, NM 87501, USA

Brian Scanlan

Kiva Labs, 277 Old Church Rd, Greenwich, CT, USA

Abstract

Experimental observations are now available to test rational theories and models about the cold fusion effect. Some of these informations are summarized and used to draw logical inferences about the requirements a plausible theory must satisfy. A model based on the role of super-clusters is proposed.

© 2011 ISCMNS. All rights reserved.

Keywords: Cluster, Cold fusion, Fusion, Nuclear reaction

PACS: 89.3J

1. Introduction

The field of study commonly called cold fusion started in 1989 with the announcement by Profs. Fleischmann and Pons [1] of unusually large heat production in an electrolytic cell containing deuterium. At the time, the reported experimental results were too general to give much confidence in the claims for a fusion reaction between deuterons in palladium. Over the last 20 years, this situation has changed remarkably thanks to steady research in over eight countries. The question now is which part of this large data set can be believed and used to understand the mechanism that results in fusion and transmutation reactions.

To explain the anomalous results, a successful theory or model must be related to a unique physical and/or chemical environment because the nuclear reactions apparently cannot occur without this condition being present. Once this novel condition forms, a nuclear reaction can release its energy into the environment by several different processes. These can be proposed to including emission of energetic radiation. This radiation has been difficult to detect because most is absorbed before reaching a detector. Nevertheless, various nuclear products accumulate in the material and

*E-mail: storms2@ix.netcom.com

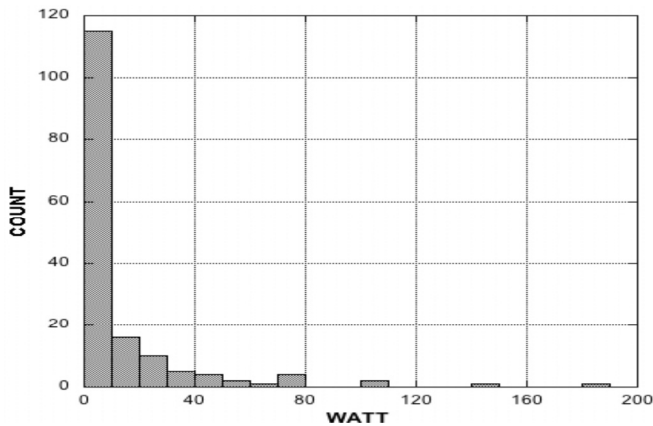


Figure 1. Histogram of power production using the electrolytic method.

these have been detected in significant amounts. Incremental transfer of energy directly to the surrounding atoms has also been suggested without emission of detectable radiation.

This is not a review or evaluation of proposed theories. Hopefully, the approach used in this paper will encourage theoreticians to evaluate their own ideas. In addition, this paper accepts the effect as being real and is not a critique or review of published work. A few well-documented studies are cited to provide a general understanding of the cold fusion effect. Each of these observations suggests several questions that must be addressed and logically connected by any theory. A mechanism is described that meets this requirement.

2. Discussion

Several indications of a novel process have been discovered. These have a range of acceptance and importance with heat generation being the most accepted and important. For this energy to result from a nuclear reaction, nuclear products must be found. At the present time, these products include, helium-4, tritium, transmutation products from various target elements, and energetic radiation. These are listed and discussed in the order of decreasing amount. So far, only helium production is quantitatively related to heat production. Other products, such as radiation may be present in amounts consistent with heat production but are difficult to detect due to their limited range in experimental conditions.

2.1. Heat

Energy production in excess of any known chemical reaction is the major indication of a novel nuclear reaction taking place. The number of successful efforts is too large to list here, but can be found in the book by Storms [2]. The histogram (Fig. 1) summarizes the amount of heat produced using the electrolytic method pioneered by Fleischmann and Pons. While many studies produced only a few watts of extra power, a significant number produced large and easily measured amounts of power. Furthermore, a single value is used from each paper even though many successful results are frequently described in the paper. “What kind of reaction can generate MJ of energy in a simple chemical system along with production of radiation and additional elements”? This question is addressed in a later section.

Where in a sample is this energy produced? McKubre et al. used the following equation to describe excess power (EP) obtained from wire cathodes in a Fleischmann–Pons electrolytic cell [3,4].

$$EP = M(x - x_0)^2(i - i_0) \frac{dx}{dt},$$

Table 1. Reactions resulting from fusion involving energetic deuterons.

$d + d = {}^3\text{He}$ (0.82 MeV) + n (2.45 MeV)
$d + t = n$ (14.01 MeV) + ${}^4\text{He}$ (3.5 MeV)
$d + d = p$ (3.02 MeV) + t (1.01 MeV)
$d + p = {}^3\text{He} + \text{gamma}$ (5.5 MeV)
$d + d = {}^4\text{He} + \text{gamma}$ (23.5 MeV)

where x_o is the critical average D/Pd of the bulk cathode, x the actual average composition, i the actual average current density, i_o the critical average I/cm^2 , dx/dt is the variation in composition. This equation can be expanded by

$$M = nA, \text{ where "A" is the number of nuclear active sites having 'n' efficiency.}$$

The heat producing reaction favors locations where the deuteron concentration is greatest, which is affected to some degree by applied current density and rate of composition change. This location exists at the surface of the cathode in an electrolytic cell and on the surface of nanoparticles. The deuterium concentration becomes especially great on the surface of a cathode as the bulk composition approaches unity and on the surface of nanoparticles as they become smaller. In fact, the composition at the surface of a cathode has been measured [5,6] and the D/Pd ratio is found to be at least 1.5, which indicates the presence of another phase having a perfect-lattice D/Pd ratio greater than unity — perhaps as great as 2. [7] Abrupt changes in the temperature coefficient of resistivity at $\text{D}/\text{Pd} = 1$ also indicate the presence of another phase having a larger ideal lattice composition. [8,9] In addition to having a large D/Pd ratio, the surface of an electrolytic cathode contains lithium [10] and other advantageous impurities. Consequently, a theory based on β -PdD in bulk material is not addressing the true active environment, which is a complex alloy containing Li, Pd, D and other elements of unknown kind and amount, all with a very non-uniform distribution. Such surfaces also frequently contain significant oxygen because the stability of the Li-O bond prevents its reduction by hydrogen generated at the electrode.

2.2. Products of nuclear reactions

Although some anomalous energy is produced when ordinary hydrogen [11] or water [12] is used, the d-d fusion reaction has been and continues to be the center of attention. Many laboratories investigating cold fusion searched for products expected from hot fusion, but without success. For example, the expected neutrons are occasionally detected, but these are not associated with heat production either in time or in magnitude. Tritium is occasionally detected in small quantity, but again it is not associated with heat production.

A nuclear reaction between two nuclei must produce at least two products, which are required to carry away the energy and momentum. Fusion reactions involving deuterons are known to result in the paths listed in Table 1, with each producing the required two products. The first two reaction paths are found in equal amount when enough energy is applied to force two deuterium nuclei through the Coulomb barrier, i.e. hot fusion.

According to the third possible reaction path resulting in helium production, 23.5 MeV gamma radiation would be produced and easily detected. Failure to find this radiation supported considerable skepticism, but did not stop a search for helium at a few laboratories.

2.3. Helium

Helium has been detected on many occasions in cold fusion cells, in both the gas and the palladium cathode, and shown to have a relationship to the amount of heat measured. Two independent measurements are compared in Fig. 2. Many other studies show a clear correlation between heat and helium production, but without giving quantitative

values. To properly understand these measurements, a few qualifications must be accepted. Normally, only the amount of He released into the gas stream is measured. McKubre et al. [13] and Matsunaka et al. [14] show that this quantity represents only part of the total amount of He produced since it omits any helium trapped in the solid Pd cathode. Although the amount trapped can be variable, depending on how deep into the surface helium forms, the round number value is about 50%. Both studies compared in Fig. 2 are consistent within expected uncertainty with the expected energy value after this 50% loss is applied. Taking all measurements into account and applying this potential loss of helium, Storms [2] proposed a value of 25 ± 5 MeV for the energy produced by formation of each helium nucleus, which is consistent with the energy expected to result from d-d fusion.

Explanations have been suggested that involve addition of deuterons, protons, or neutrons to isotopes of lithium to generate helium. None of these reactions produce enough energy per He atom to be consistent with the measurements.

2.4. Tritium

Many examples of tritium production have been reported occasionally in electrolytic cells and during gas discharge [15,16] as reviewed by Storms [2]. Since tritium is seldom measured, it may be underreported. However, it is nevertheless rare. The amount found is always too small to generate detectable heat, but sufficient to demonstrate an unexpected nuclear process. When the neutron/tritium ratio is measured, it is always found to be very small — in the range between 10^{-9} and 10^{-6} . Consequently, tritium does not result from the normal hot fusion reaction.

Bockris [17] reported interruption of tritium production when the electrolytic cell was shaken, suggesting the source is dendrites on the cathode surface that are removed by agitation. These later reformed to continue production. Surface examination showed deposits of copper from wires within the cell. Claytor et al. [16] have been increasingly successful in producing tritium using pulsed DC discharge between alloys of palladium in deuterium gas. This process is very sensitive to the composition of the alloy and also generates dendrites.

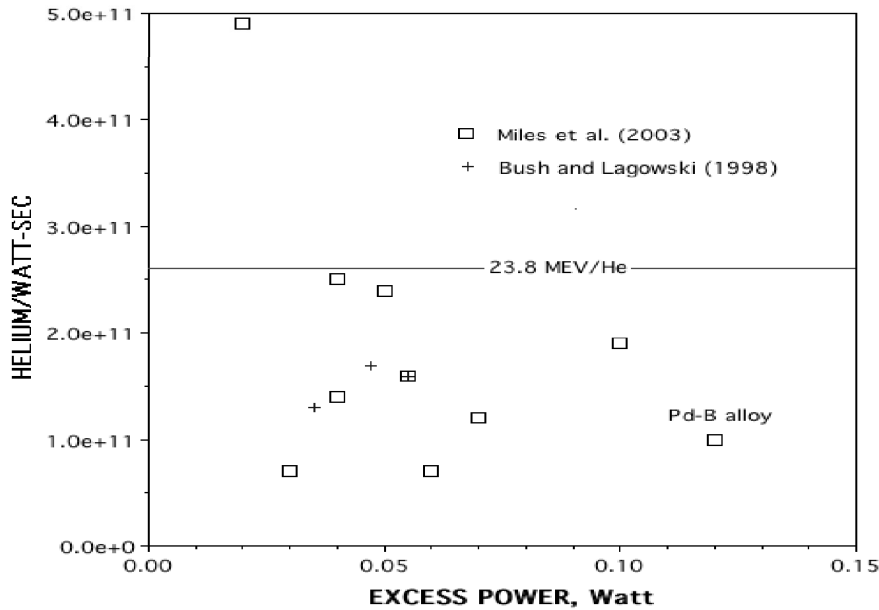


Figure 2. Helium atoms/joule vs excess power. Two independent studies are compared.

Table 2. Observed transmutation reactions reported by Iwamura et al.

$d + d = {}^3\text{He}$ (0.82 MeV) + n (2.45 MeV)
$\text{Ba} + 6d = \text{Sm} + ?, Q = 67.6 \text{ MeV}$
$\text{Sr} + 4d = \text{Mo} + ?, Q = 53.4 \text{ MeV}$
$\text{Cs} + 2d = \text{La} + ?, Q = \sim 24 \text{ MeV}$
$\text{Cs} + 4d = \text{Pr} + ?, Q = 50.5 \text{ MeV}$

Tritium is unique because it is one of the very rare radioactive elements produced by the process. A useful theory must account for its occasional presence.

2.5. Transmutation

Isotopes and elements not present in the initial environment are reported. [2] While the elements or isotopes may have been present initially as contamination, this argument cannot be applied successfully to all such claims. Two studies stand out in showing that clusters of deuterons might be involved in such transmutation reactions. Iwamura et al. [18–22], in a series of papers, claimed to detect the reactions shown in Table 3. Clusters containing as many as six deuterons are found to enter the nucleus as a unit. However, several aspects of this work require explanation. As shown in Fig. 3, the target nuclei are deposited on a 400 Å thick surface layer of palladium that lies on a layer of CaO, a presumed catalyst. How does the cluster get from the catalyst to the target and why do the clusters not react with the intervening palladium? How is the significant energy communicated to the environment? Clearly, something must be emitted that is not detected, as indicated by the question mark in Table 3.

The second study involves the work of Miley et al. [25,26]. His experiments employ SIMS, AES, EDX and NAA for analysis. The work is based on the use of thin films of nickel and/or palladium deposited on an inert substrate, with a small amount of platinum as an impurity from the anode and perhaps a little sulfur as an impurity from the electrolyte because the electrolyte contained Li_2SO_4 in H_2O . Elemental analysis was made before and after electrolytic action. Although it is safe to assume some of the detected elements resulted either from contamination, migration to the surface from within the sample, or from error in analysis, the general pattern appears to be real. The study showed a region of atoms having high concentration from about mass 106 (Pd) to mass 130; from mass 195 (Pt) to mass 210; and from about mass 25 (S?) to mass 32. The region around nickel (58) shows elements on both the high mass and the low mass sides of this potential target element. Transmutation requires addition of something to the target, which leaves elements on the low-mass side unexplained. Addition of neutrons, protons or deuterons to Pd is explored next as a potential explanation.

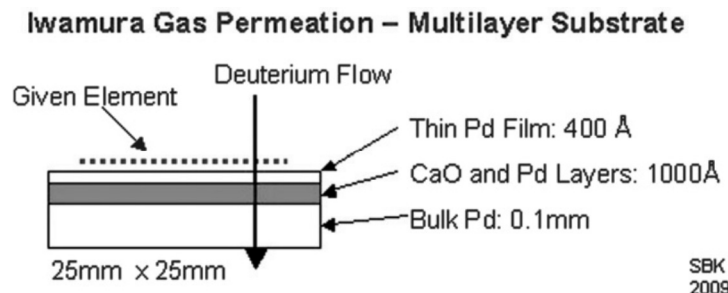


Figure 3. Simplified cross-section representation of the Iwamura experiment. Figure provided by Steve Krivit [23,24].

Figure 4 shows the position of the stable isotopes near palladium with respect to their atomic number and atomic weight. If neutrons were added to palladium, the resulting isotopes would follow a horizontal line on the figure and eventually produce beta emitters. These have half-lives that decrease from minutes to milliseconds as more neutrons are added. To produce the observed elements near mass 130, a series of decays from parent to daughter would have to take place over a significant length of time as each isotope decayed to another radioactive isotope with gradually increasing atomic number. In addition, the expected radioactivity is rarely detected even though this would be an easy measurement. Therefore, it is possible to conclude that transmutation does not result from neutron addition from any source.

If protons were added to palladium, the resulting isotopes would follow a line parallel to the one shown on the figure labeled protons. The mass of the heaviest stable isotope is 114 before unstable isotopes are produced, which are not high enough to explain the full range reported.

Only addition of deuterons, as indicated by the line labeled “add deuteron”, result in the full range of observed stable isotopes. This same process can be applied to nickel, platinum and sulfur to give the same conclusion in spite of the fact that water containing the normal amount of deuterium was used. Apparently, only deuterons, regardless of having a relatively low concentration in normal water, produce active deuteron clusters.

In the case of elements having a mass less than nickel, these cannot result from a reaction with deuterons or any other particle. These elements might result from fission of nuclei after addition of deuterons to palladium, as has been suggested by other authors. Apparently, release of additional energy to form the very stable nuclei at and near iron allows fission to take place. The consequence of this proposed process is summarized in Table 5. Since no radioactive isotopes have been found to result from transmutation, it is safe to assume only stable isotopes are formed by the fission process, shown in bold. Except for Ag, stable isotopes result only by the addition of an even number of deuterons up to 10. No stable isotopes are formed by larger additions. However, a few unstable isotopes, shown in italic, can release additional energy by splitting into the elements listed at the bottom of the table. In other words, stable isotopes remain whole and certain unstable (radioactive) isotopes might fission while conserving total mass and total atomic number. The quantity of each transmutation or fission product is determined by the abundance of the target isotope and unknown selection rules.

Although this approach does not prove elements near iron result from fission, it does show that such a process is consistent with the atomic numbers and weights resulting after deuteron addition to palladium. One of many examples of experimental evidence for this process is shown in Fig. 5, based on an electrolytic study by Mizuno [27,28] who used

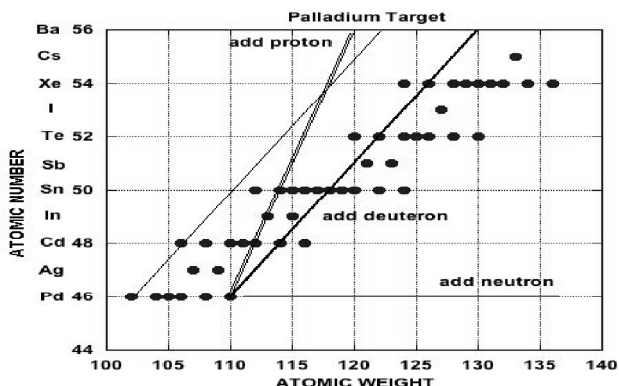


Figure 4. Stable elements as a function of atomic weight and atomic number near palladium. Lines show the result of adding neutrons, protons, or deuterons to palladium.

Table 3. Summary of isotopes made by adding deuterons to palladium.

Element	Pd	Ag	Cd	In	Sn	Sb	Te	I	Xe	Cs	Ba	La	Ce
Atomic number	46	47	48	49	50	51	52	53	54	55	56	57	58
#D	0	1	2	3	4	5	6	7	8	9	10	11	12
Atomic weight	102	104	106	<i>108</i>	<i>110</i>	<i>112</i>	<i>114</i>	<i>116</i>	<i>118</i>	<i>120</i>	<i>122</i>	<i>124</i>	<i>126</i>
	104	106	108	110	112	114	116	118	120	122	124	126	128
	105	107	109	111	113	115	117	119	121	123	125	127	129
	106	108	110	112	114	116	118	120	122	124	126	128	130
	108	110	112	114	116	118	120	122	124	126	128	130	132
	110	122	114	116	118	120	122	124	126	128	130	132	134
Fission elements	Ti+ Co	2 Mn	Ti+Ni	Fe+Mn	2 Fe	Fe+Co	2 Co	Ni+Co	2 Ni	Ni+Cu	2 Cu		

#D is the number deuterons added.

Bold indicates stable isotopes.

Italic indicates radioactive and produces stable isotopes after fission.

Normal indicates radioactive and produces radioactive isotopes after fission.

a Pd cathode, Pt anode, and an electrolyte containing D₂O. These elements are located within a few tens of microns of the surface and hide a substantial portion of the underlying palladium.

2.6. Energetic radiation

Nuclear reactions are expected to produce radiation that can be used to determine the nature of the reaction. For many years, failure to detect expected radiation was a reason for skepticism and frustration. At the very least, X-ray radiation should be detected from the slowing-down process of energetic particle emission and gamma radiation. Both should be detectable well away from the source using simple detectors such as film or Geiger-Mueller counters. Such radiation has been reported occasionally, although its magnitude is much smaller than required to explain heat or transmutation products.

Charged particles have a much shorter range and must be sought very close to the source. Until CR-39 was used, detection was not possible in electrolytic cells although such radiation was found during gas discharge using other kinds of detectors. The apparent absence of such radiation encouraged people to propose mechanisms that did not require energetic emissions. The characteristics of detected radiation must now be examined carefully to determine whether

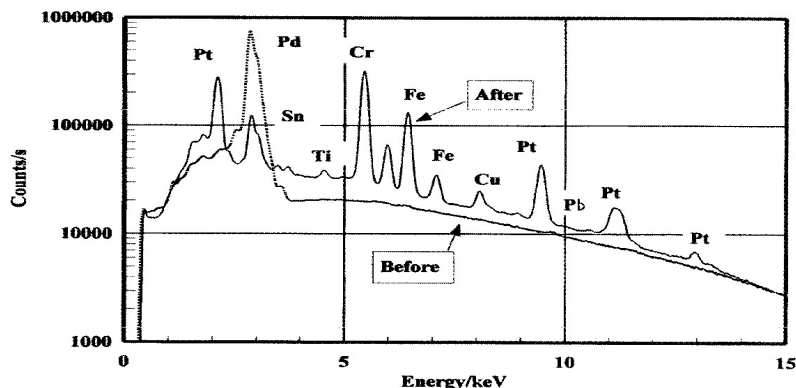


Figure 5. EDX examination of a palladium cathode before and after electrolysis [27].

these mechanisms are necessary and to discover exactly how the nuclear energy is dissipated. Because different energy is applied and different detectors are used, radiation from electrolysis and gas discharge are discussed separately.

2.6.1. X-ray emission during electrolysis

Electrolysis involves so little energy that emission of X-radiation from processes other than nuclear is unexpected, yet such radiation has been reported many times. This provides one more clear indication of a nuclear reaction being the source of the anomalous energy.

The X-ray emission from electrolytic cathodes using dental X-ray film revealed a point source that appeared to be well focused [29]. When X-ray energy is measured, the results are consistent with K- α radiation from elements present on the surface along with some Bremsstrahlung [30–32]. The radiation flux correlates with the amount of heat being produced [33,34]. However, the measured flux is very low, no doubt caused by absorption in the cell wall as calculated by Violante et al. [35]. Bursts of radiation reveal the erratic nature of the process, a fact that is not visible in the heat measurement because the large time constant typical of calorimeters smoothes the process. A process that can eject an electron from a K- α state, which for Pd requires about 19 keV, must be considered

2.6.2. Particle emission during electrolysis

After many failed attempts, particles of various kinds having a range of energies are found during electrolysis using D₂O. Because their range is very short, detection requires placing CR-39 very close to the cathode. Passage of energetic particles modifies the plastic, producing a pit when some plastic is dissolved away by subsequent application of concentrated NaOH. The energy and type of radiation can be estimated from the size and shape of the pit.

Mosier-Boss et al. [36] found pits on pieces of CR-39 after exposure to radiation from cathodes made from three different metals. Each was subjected to electrolysis in D₂O + LiCl + PdCl₂ in the same cell while Pd was deposited on each metal surface. The front side of the CR-39 shows the effect of what are identified as alpha particles with energy near 1 MeV and pits on the backside are produced by radiation identified as neutrons. The silver cathode (Ag), which readily absorbs neutrons, did not generate radiation that is able to penetrate to the backside.

Lipson et al. [37] constructed an electrolytic cell with a cathode made by oxidizing Pd and plating one side with gold. This was reacted with deuterium using the electrolytic method and placed next to a silicon barrier detector while under vacuum. The energy of particles emitted during removal of deuterium is shown in Fig. 6. Notice most particles have energy near 0.7 MeV, with a rapid drop in number at higher values. Lower energies may be present, depending on where the lower detection-limit was set. Some of the peaks near 8 MeV might be caused by radon. Although the particles were identified as alpha, this conclusion is questionable, which also raises doubts about the assigned energy. Nevertheless, the emitted particles appear to have a range of energy with most having low energy. Based on the small flux, apparently only a very small part of the sample was active.

In contrast to evidence for conventional particles having relatively low energy, Oriani and Fisher [38,39] used CR-39 to detect particles able to cause secondary reactions well outside of the apparatus. These are detected within the electrolytic cell as well as up to 8 cm from the cathode after having passed through the electrolyte and glass. As suggested by Kowalski [40], these might be energetic neutral particles emitted from an unconventional source.

2.6.3. Particle emission during gas discharge

Particles emitted from the cathode during and after low-voltage gas discharge in D₂ have been detected using a silicon barrier detector (SBD), from which energy can be determined after the kind of particle is identified using absorbers. Energy is reduced by an amount proportional to the absorber mass-density that depends on the kind of particle being

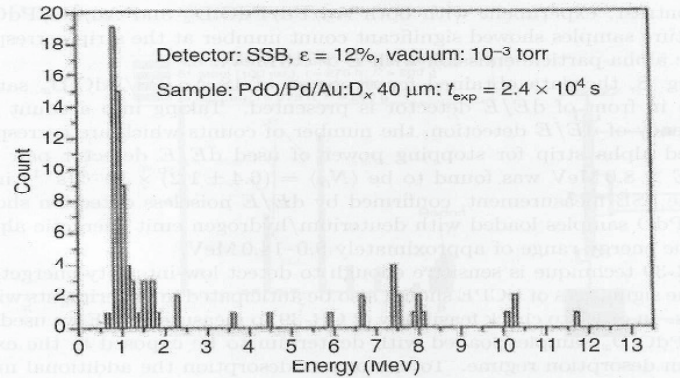


Figure 6. Particles emitted from PdD as deuterium is removed [37].

detected. Alphas are easy to identify this way but protons and deuterons are more difficult to differentiate from each other because they have similar absorption characteristics.

Karabut et al. [41] produced a discharge in D₂ using a Pd cathode and less than 500 V. Immediately after the discharge was stopped, the spectrum shown in Fig. 7 was recorded using a silicon barrier detector. The radiation at 3.5 MeV was identified as alpha using absorbers. Presumably, this radiation resulted from a nuclear reaction as the deuterium content slowly decreased from the rate produced by the discharge.

Too much electrical noise prevented the spectrum from being recorded during discharge. This delayed reaction, so called life-after-death, was explored by Savvatimova [42] by measuring the total current produced by emitted ions and by observing exposure of X-ray film. Evidence for strange radiation having extraordinary penetrating power was also found, similar to reports by Oriani and Fisher [43], Matsumoto [44], and Lochak and Urutskoev [45].

Storms and Scanlan [46] (Fig. 8) observed an energetic particle spectrum during discharge in D₂ at 794 V using a silicon barrier detector. The particles were tentatively identified as deuterons and distinguished from electrical noise using absorbers. The lowest energy that could be measured was about 0.5 MeV, with decreasing numbers of particles with greater energy, similar to the behavior found by Karabut et al. [41]. The question is, “What process produces this type of energy spectrum”?

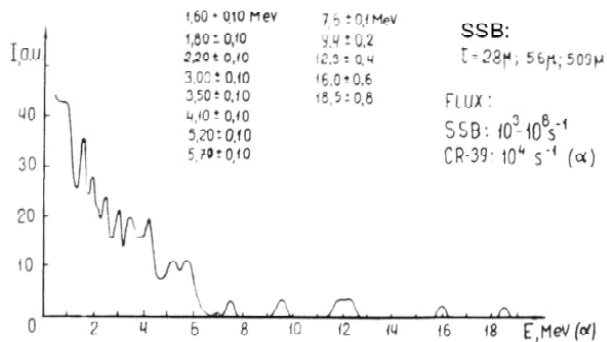


Figure 7. Energy of particles emitted immediately after discharge in D₂ was stopped [41].

3. General Requirements of Theory

A comprehensive theory has been slow to develop because several ad hoc assumptions are required to explain the “impossible” behaviors. Now that the field has a large body of experimental data, a rational basis exists to reject or accept many proposed theories. This understanding is summarized below.

The nuclear reactions occur where deuterium concentration is the greatest, which includes the surface of electrolyzing cathodes and the surface of nanoparticles of certain metals and alloys. These environments have very little relationship to the properties of b-PdD, which have been used as the basis for many mechanisms. In addition, the nuclear-active environment (NAE) has additional unknown features that are rare to form. These facts need to be applied to a proposed theory.

The major heat producing reaction is unconventional fusion between deuterons to produce helium-4, which can occur at rates in excess of 10^{12} He/second as bursts. Helium results in preference to the other products because a mechanism is available in a solid to dissipate the resulting energy and achieve a product having the lowest energy. In contrast, the only mechanism available in plasma to create helium requires emission of gamma radiation, which is rare. Consequently, the other less-energetic paths are taken in plasma because they can use energetic particles to dissipate energy, as summarized in Table 1.

Other possible but rare reactions involve additions of multiple deuterons to nuclei of various elements in the NAE, i.e. transmutation and production of tritium. Formation of radioactive elements other than tritium is rare but not impossible. Neutrons do not play a role in these reactions, neither as reactants nor as products. Protons have a limited role and deuterons are the main reactant.

Energy is released from these reactions by energetic particles without gamma emission. The energy of these particles is smaller than expected to result from the proposed source reaction and is too small to allow detection except very close to the source. Some energy might be absorbed directly into the lattice, but this process has no direct evidence and might have no importance once all of the particle emissions have been identified. Some of the particles have strange properties, making identification even more difficult.

Regardless of the reaction, the resulting particle energy can produce secondary reactions, resulting in neutron and/or gamma emission, if their energy is above critical values. Failure to detect significant amounts of such radiation indicates existence of a mechanism that can reduce the energy below these values. Measurements show that the observed particle energy is well below the energy released by a fusion or transmutation reaction. This realization places emphasis on

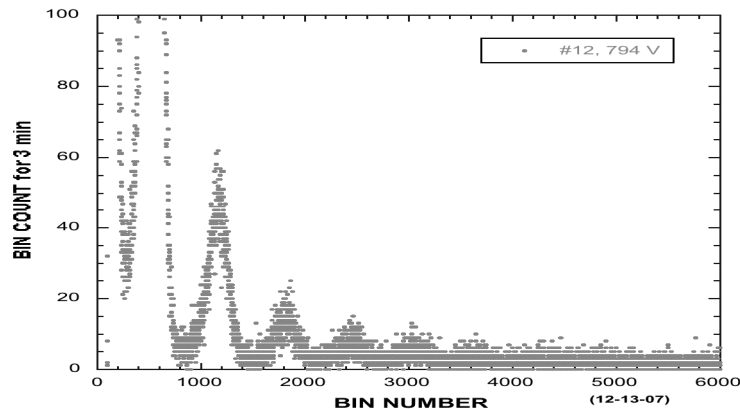


Figure 8. Spectrum of particles emitted during DC discharge at 794V in D₂ [46].

the low-end of the energy range as location of important particle energy and indicates the need for a process that can reduce energy to these low values.

A plausible theory must also be consistent with general scientific understanding. To get over a barrier, energy must be concentrated to a level equal to the barrier height. If the concept of tunneling is used, the energy must be high enough to produce the observed reaction rate. Accelerating the nuclei, as used to produce hot fusion, can achieve this result, but with some unintended consequences within the lattice. The atomic structure will not tolerate local high-energy without it being absorbed by various processes before it can reach levels required to affect nuclear interactions. Consequently, concentration of local energy is not possible. Instead, an exothermic reaction must occur for the process to be spontaneous and must be localized on a group of deuterons, called the active structure (AS) located within the NAE. This cluster allows multiple deuterons to enter a nucleus at the same time and cause the observed transmutation. This assumed process leads to several logical consequences. As energy is lost from the AS, electrons in the AS become more stable, hence increasingly less affected by the presence of a nearby nuclear charge. This allows them to remain fixed in locations, orbits, or energy levels that can hide the combined nuclear charge of the AS. Once this total charge is sufficiently hidden, the AS can approach and enter another nucleus, whether this is a deuteron or a heavier element. In other words, a two-step process is required. The first step involves incremental loss of energy until a special structure is sufficiently stable to overcome a Coulomb barrier. This process gives off energy that accelerates the reaction without requiring additional energy from the environment. Once this structure forms, a nuclear reaction occurs as the second step with a large release of energy that further accelerates the process. What type of mechanism might be consistent with these requirements?

4. Summary of Proposed Mechanism

The model is based on the assumption that a change must take place in a material for the nuclear reactions to be initiated. In other words, the required conditions are not present in normal material. This change must be identified along with all the consequences. This requirement is addressed as follows:

Two basic questions, in addition to the requirements noted above, need to be addressed by any theory. These are, “How can multiple deuterons enter a nucleus with high atomic number and how is the energy resulting from this reaction dissipated into the environment”? One possible answer is the involvement of deuterium clusters in both processes. While involvement of small clusters has been suggested in the past by several authors [47,48], this model solves a couple of problems by proposing the clusters have a large number of members, called in this paper “super-clusters” having a size that is described by the number of deuterons present, so-called number-size. However, the proposed size is less than clusters having 306 members as proposed by Miley. This concept is applied first to the transmutation reaction and then to fusion.

Up to 10 deuterons apparently can enter a nucleus. For this to happen as a single event, all must be at the same place at the same time. For all members of the cluster to enter at the same time, they also must be located close together compared to nuclear dimensions and their nuclear charge must be hidden from the target nuclei. These requirements imply existence of an unusual bonding state that can form within a group of deuterons. The nature of this state will not be discussed here, but will be a subject for future papers.

Clusters of deuterons are proposed to form by an exothermic reaction requiring a catalyst or template. Once the basic structure of the cluster has formed on the surface of this special material, it detaches and diffuses in random directions within the solid lattice. Initially, this seed structure cannot cause fusion or transmutation because it has not released enough energy. Energy is released in small units as each deuteron is added, causing the effective nuclear charge of the assembly to be increasingly hidden. For example, in the Iwamura study, cluster seeds form on the surface of the CaO and these diffused through 400 Å of Pd to the surface where target nuclei have been deposited. During the trip, the seeds grow in number-size as they encounter an increasing concentration of deuterons streaming in the opposite direction.

A transmutation reaction is only possible after the number-size has increased enough to hide the nuclear charge of the assembly and to reduce the physical size comparable to that of the target nucleus. Presumably, in the Iwamura study, clusters do not become active until they reach the deposited targets, where reaction with the deposited targets as well as with the much more numerous palladium nuclei become possible. A similar process might occur in studies [49–56] during which deuterium is simply allowed to diffuse through palladium, which produces a small amount of heat and transmutation products.

This special material is rare so that cold fusion occurs infrequently and only when and where the material is present. The observed delay in starting power production is proposed to be caused by slow formation of this material and slow growth of clusters to a reactive number-size. The rate of cluster growth is influenced by the concentrations of AS and deuterons. Therefore, nuclear reactions will have the highest rate where deuteron concentration is greatest. This concentration determines how fast cluster size increases and the probability of an active cluster finding a deuteron with which to fuse one of its members.

The AS is slow to form because it is a complex combination of certain atoms that seldom result in the required structure. Several different combinations of several different elements are probably active, all in the form of nanoparticles. Consequently, the NAE is located on the surface of nanoparticles that are formed on a surface or present after having been placed in the apparatus fully formed. Naturally, not all such particles are active. As a result, the amount of power produced by a cell is highly variable, as is observed. Power output will also be highly variable over short and long times, as observed, because active clusters will be destroyed by energy release and new ones will have to form by a random process. The challenge is to identify nature of the active nanoparticle and to make these in large amounts. Only then can the effect be made reproducible and a source of significant power.

Once a cluster reacts with a target nucleus, how is the considerable energy dissipated? If the cluster has more members than can be fully absorbed by the target, the extra members are proposed to carry away the energy. The number of extra members would have to be large enough so that the energy of each emitted deuteron is too small to cause significant secondary reactions. Furthermore, a transmutation reaction would have to be impossible before this large number had been achieved to prevent this requirement from being violated. Therefore, the nuclear charge must be increasingly hidden as the number-size increases and a critical number, determined by the charge on the target nuclei, must be reached before reaction is possible.

The probability of a fusion reaction between a cluster and a deuteron is expected to increase as number-size increases, resulting in competition between further increase in number-size and the fusion reaction. Therefore, fusion will have a higher rate than does transmutation and compete with transmutation by removing clusters that might grow enough members to cause transmutation. However, even a fusion reaction will require the cluster to be large enough to avoid secondary reactions. Because a random range of number-sizes are expected to react, the energy of emitted deuterons is expected to have a range of values, from ones that are difficult to detect to a few that are energetic enough to produce secondary reactions, similar to the spectrum of particle energy shown in Figs. 6–8. This range is expected to be sensitive to conditions and applied energy, which might explain the observed wide range of reported energies for detected particles. Also, some of the emitted particles might be neutral or be a fragment of the original cluster, which would complicate identification and measurement of energy. A cluster fragment, if it retains the unique bonding characteristics, might not be stopped easily by matter and could explain the behavior of reported “strange” radiation.

The proposed model is still very incomplete and ignores many observations. Nevertheless, the logic suggests a new way to look at the problem that might be helpful in development of more complete models.

References

- [1] M. Fleischmann, S. Pons, M. Hawkins, Electrochemically induced nuclear fusion of deuterium, *J. Electroanal. Chem.* **261** (1989) 301 and errata in Vol. 263.

- [2] E.K. Storms, *The Science of Low Energy Nuclear Reaction*, World Scientific, Singapore, 2007, p. 312.
- [3] M.C.H. McKubre et al., Concerning reproducibility of excess power production, in *5th International Conference on Cold Fusion*, Monte-Carlo, Monaco, IMRA, Europe, Sophia Antipolis Cedex, France, 1995.
- [4] M.C. McKubre et al., Replication of condensed matter heat production, in *ACS Symposium Series 998, Low-Energy Nuclear Reactions Sourcebook*, J. Marwan, S.B. Krivit (Eds.), American Chemical Society, Washington, DC, 2008, p. 219.
- [5] E.K. Storms, Relationship between open-circuit-voltage and heat production in a Pons–Fleischmann cell, in *The Seventh International Conference on Cold Fusion*, Vancouver, Canada, ENECO Inc., Salt Lake City, UT, 1998.
- [6] M. Yanokura et al., An approach to the cold fusion through hydrogen isotopes analysis by the heavy ion Rutherford scattering, *Chem. Lett.* **18** (1989) 2197.
- [7] E. Storms, The nature of the energy-active state in Pd–D, in *II Workshop on the Loading of Hydrogen/Deuterium in Metals*, Characterization of Materials and Related Phenomena, Asti, Italy, 1995.
- [8] A. Spallone et al., An overview of experimental studies on H/Pd over-loading with thin Pd wires and different electrolytic solutions, in *11th International Conference on Cold Fusion*, Marseilles, France, World Scientific, Singapore, 2004.
- [9] M.C. McKubre, F. Tanzella, Using resistivity to measure H/Pd and D/Pd loading, Method and significance, in *Condensed Matter Nuclear Science, ICCF-12*, Yokohama, Japan, World Scientific, Singapore, 2005.
- [10] N. Asami et al., Material behaviour of highly deuterium loaded palladium by electrolysis, in *Sixth International Conference on Cold Fusion, Progress in New Hydrogen Energy*, Lake Toya, Hokkaido, Japan, New Energy and Industrial Technology Development Organization, Tokyo Institute of Technology, Tokyo, Japan, 1996.
- [11] S. Focardi et al. Evidence of electromagnetic radiation from Ni–H systems, in *11th International Conference on Cold Fusion*, Marseilles, France, World Scientific, Singapore, 2004.
- [12] T. Mizuno et al., Production of heat during plasma electrolysis, *Jpn. J. Appl. Phys. A* **39** (2000) 6055.
- [13] M.C. McKubre, F. Tanzella, P. Tripodi, Evidence of d–d fusion products in experiments conducted with palladium at near ambient temperatures, *Trans. Am. Nucl. Soc.* **83** (2000) 367.
- [14] M. Matsunaka et al., Studies of coherent deuteron fusion and related nuclear reactions in solid, in *The 9th International Conference on Cold Fusion, Condensed Matter Nuclear Science*, Tsinghua Univ., Beijing, China, 2002.
- [15] V.A. Alekseev et al., Tritium production in the interaction of dense streams of deuterium plasma with metal surfaces, *Tech. Phys. Lett.* **21** (1995) 231.
- [16] T.N. Claytor, D.D. Jackson, D.G. Tuggle, Tritium production from a low voltage deuterium discharge of palladium and other metals, *J. New Energy* **1**(1) (1996) 111.
- [17] C.-C. Chien et al., On an electrode producing massive quantities of tritium and helium, *J. Electroanal. Chem.* **338** (1992) 189.
- [18] Y. Iwamura et al., Detection of anomalous elements, X-ray and excess heat induced by continuous diffusion of deuterium through multi-layer cathode (Pd/CaO/Pd), *Infinite Energy* **4**(20) (1998) 56.
- [19] Y. Iwamura et al., Correlation between behavior of deuterium in palladium and occurrence of nuclear reactions observed by simultaneous measurement of excess heat and nuclear products, in *Sixth International Conference on Cold Fusion, Progress in New Hydrogen Energy*, Lake Toya, Hokkaido, Japan, Lake Toya, Hokkaido, Japan, 1996.
- [20] Y. Iwamura et al., Detection of anomalous elements, X-ray, and excess heat in a D2–Pd system and its interpretation by the electron-induced nuclear reaction model, *Fusion Technol.* **33** (1998) 476.
- [21] Y. Iwamura et al., Observation of nuclear transmutation reactions induced by D2 gas permeation through Pd complexes, in *ICCF-11, International Conference on Condensed Matter Nuclear Science*, Marseilles, France, World Scientific, Singapore, 2004.
- [22] Y. Iwamura et al., Observation of surface distribution of products by X-ray fluorescence spectrometry during D2 gas permeation through Pd cathodes, in *Condensed Matter Nuclear Science, ICCF-12*, Yokohama, Japan, World Scientific, Singapore, 2005.
- [23] S.B. Krivit, J. Marwan, A new look at low-energy nuclear reaction research, *J. Environ. Monit.* **11** (2009) 1731.
- [24] Y. Iwamura, M. Sakano, T. Itoh, Elemental analysis of Pd complexes: effects of D2 gas permeation, *Jpn. J. Appl. Phys. A* **41**(7) (2002) 4642.
- [25] G.H. Miley, J.A. Patterson, Nuclear transmutations in thin-film nickel coatings undergoing electrolysis, *J. New Energy* **1**(3) (1996) 5.
- [26] G. Miley, Characteristics of reaction product patterns in thin metallic films experiments, in *Asti Workshop on Anomalies in Hydrogen/Deuterium Loaded Metals*, Villa Riccardi, Rocca d’Arazzo, Italy, Italian Phys. Soc., 1997.

- [27] T. Mizuno, *Nuclear Transmutation: The Reality of Cold Fusion*, Concord, NH, Infinite Energy Press, 1998, p. 151.
- [28] T. Mizuno et al., Confirmation of the changes of isotopic distribution for the elements on palladium cathode after strong electrolysis in D₂O solutions, *Int. J. Soc. Mat. Eng. Resources* 6(1) (1998) 45.
- [29] S. Szpak, P.A. Mosier-Boss, J.J. Smith, On the behavior of Pd deposited in the presence of evolving deuterium, *J. Electroanal. Chem.* **302** (1991) 255.
- [30] Y. Iwamura et al., Characteristic X-ray and neutron emissions from electrochemically deuterated palladium, in *5th International Conference on Cold Fusion*, Monte-Carlo, Monaco, IMRA Europe, Sophia Antipolis Cedex, France, 1995.
- [31] V. Violante et al., X-ray emission during electrolysis of light water on palladium and nickel thin films, in *The 9th International Conference on Cold Fusion, Condensed Matter Nuclear Science*, Tsinghua Univ., Tsinghua Univ. Press, Beijing, China, 2002.
- [32] R.T. Bush, R.D. Eagleton, Experimental studies supporting the transmission resonance model for cold fusion in light water: II. Correlation of X-Ray emission with excess power, in *Third International Conference on Cold Fusion, "Frontiers of Cold Fusion"*, Nagoya, Japan, Universal Academy Press Inc., Tokyo, Japan, 1992.
- [33] S. Szpak, P.A. Mosier-Boss, J.J. Smith, On the behavior of the cathodically polarized Pd/D system: Search for emanating radiation, *Phys. Lett. A* **210** (1996) 382, 34. S. Szpak, P.A. Mosier-Boss, Nuclear and thermal events associated with Pd + D co-deposition, *J. New Energy* 1(3) (1996) 54.
- [34] V. Violante et al., Search for nuclear ashes In electrochemical experiments, in *Tenth International Conference on Cold Fusion*, Cambridge, MA, World Scientific, Singapore, 2003.
- [35] P.A. Mosier-Boss et al., Detection of energetic particles and neutrons emitted during Pd/D codeposition, in *ACS Symposium Series 998, Low-Energy Nuclear Reactions Sourcebook*, J. Marwan, S.B. Krivit (Eds.), 2008, American Chemical Society, Washington, DC, 2008, p. 311.
- [36] A.G. Lipson et al., Energetic charged particles emission from hydrogen-loaded Pd and Ti cathodes and its enhancement by He-4 implantation, in *11th International Conference on Cold Fusion*, Marseilles, France, World Scientific, Singapore, 2004.
- [37] J.C. Fisher, External radiation produced by electrolysis — A work in progress, in *8th International Workshop on Anomalies in Hydrogen/Deuterium Loaded Metals*, Catania, Sicily, Italy, The International Society for Condensed Matter Science, 2007.
- [38] R.A. Oriani, J.C. Fisher, Nuclear reactions produced in an operating electrolytic cell, in *11th International Conference on Cold Fusion*, Marseilles, France, World Scientific, Singapore, 2004.
- [39] L. Kowalski, On emission of nuclear particles caused by electrolysis, in *8th International Workshop on Anomalies in Hydrogen/Deuterium Loaded Metals*, Catania, Sicily, Italy, The International Society for Condensed Matter Science, 2007.
- [40] A.B. Karabut, Y.R. Kucherov, I.B. Savvatimova, Nuclear product ratio for glow discharge in deuterium, *Phys. Lett. A* **170** (1992) 265.
- [41] I. Savvatimova, Reproducibility of experiments in glow discharge and processes accompanying deuterium ions bombardment, in *8th International Conference on Cold Fusion*, Lerici (La Spezia), Italy, Italian Physical Society, Bologna, Italy, 2000.
- [42] R.A. Oriani, J.C. Fisher, Energetic charged particles produced during electrolysis, in *Tenth International Conference on Cold Fusion*, Cambridge, MA, World Scientific, Singapore, 2003.
- [43] T. Matsumoto, Experiments of underwater spark discharge with pinched electrodes, *J. New Energy* **1**(4) (1996) 79.
- [44] G. Lochak, L. Urutskoev, Low-energy nuclear reactions and the leptonic monopole, in *11th International Conference on Cold Fusion*, Marseilles, France, World Scientific, Singapore, 2004.
- [45] E.K. Storms, B. Scanlan, Detection of radiation from LENR, in *ICCF-14*, Washington, DC, www.LENR.org., 2008.
- [46] A. Takahashi, Mechanism of deuteron cluster fusion by EQPET model, in *Tenth International Conference on Cold Fusion*, Cambridge, MA, World Scientific, Singapore, 2003.
- [47] G. Miley et al., Cluster reactions in low energy nuclear reactions (LENR), in *8th International Workshop on Anomalies in Hydrogen/Deuterium Loaded Metals*, Catania, Sicily, Italy, The International Society for Condensed Matter Science, 2007.
- [48] X.Z. Li et al., "Super-absorption" — correlation between deuterium flux and excess heat, in *The 9th International Conference on Cold Fusion, Condensed Matter Nuclear Science*, 2002. Tsinghua Univ., Tsinghua Univ. Press, Beijing, China, 2002.
- [49] G.S. Qiao et al., Nuclear transmutation in a gas-loading system, *J. New Energy* **2**(2) (1997) 48.
- [50] G.S. Qiao et al., Nuclear products in a gas-loading D/Pd and H/Pd system, in *The Seventh International Conference on Cold Fusion*, Vancouver, Canada, 1998.
- [51] Q.-M. Wei et al., Element analysis of the surface layer on the Pd and Pd–Y alloy after deuterium permeation, in *8th International Workshop on Anomalies in Hydrogen/Deuterium Loaded Metals*, Catania, Sicily, Italy, The International Society for Condensed

Matter Science, 2007.

- [52] J. Tian et al., Anomalous heat flow and its correlation with deuterium flux in a gas-loading deuterium–palladium system, in *The 9th International Conference on Cold Fusion, Condensed Matter Nuclear Science*, Tsinghua Univ., Tsinghua Univ. Press, Beijing, China, 2002.
- [53] W. Wu et al., Anomalous heat effect during permeation of deuterium gas through the palladium tube, in *The 9th International Conference on Cold Fusion, Condensed Matter Nuclear Science*, Tsinghua Univ., Tsinghua Univ. Press, Beijing, China, 2002.
- [54] B. Liu et al. "Excess heat" induced by deuterium flux in palladium film, in *Condensed Matter Nuclear Science, ICCF-12*, Yokohama, Japan, World Scientific, Singapore, 2005.
- [55] B. Liu et al., "Excess heat" in a gas-loaded D/Pd system with pumping inside palladium tube, in *8th International Workshop on Anomalies in Hydrogen/Deuterium Loaded Metals*, Catania, Sicily, Italy, The International Society for Condensed Matter Science, 2007.



Research Article

Cold Fusion, LENR, CMNS, FPE: One Perspective on the State of the Science Based on Measurements Made at SRI

Michael C.H. McKubre * and Francis L. Tanzella

SRI International, Menlo Park, CA 94025, USA

Abstract

Our object is to clarify in non-specialist terms what is known and what is understood in the general field of so called Low-Energy or Lattice Enhanced Nuclear Reactions (LENR). It is also crucial and timely to expose and elaborate what objections or reservations exist with regard to these new understandings. In essence, we are concerned with the answers to the following three questions: What do we think we know? Why do we think we know it? Why do doubts still exist in the broader scientific community? Progress in the LENR field will be reviewed with primary focus on the experimental work performed at SRI by and with its close collaborators with a view to defining experiments based non-traditional understandings of new physical effects in metal deuterides. Particular attention is directed to the Fleischmann–Pons Effect, nuclear level heat from the deuterium–palladium, and the associated nuclear products: ^4He , ^3He and ^3H .

© 2011 ISCMNS. All rights reserved.

Keywords: Calorimetry, Cold fusion, Excess heat

PACS:

1. Introduction

After 21 years of continuous study and tens of millions of research dollars spent worldwide it is appropriate to examine the basis for, and confidence in what has been learned since the public announcements of a prospective new effect in March 1989. One fact that seems irrefutable is the existence of a heat effect in the electrolytic deuterium–palladium system that is quantitatively consistent with nuclear, but not chemical heat production. Now established as the Fleischmann–Pons Effect (or FPE) several tasks require further study:

- (i) Certain identification of the pathway from reactant (presumed to be D) to primary product (observed in some experiments to be ^4He).
- (ii) Quantitative or upper bound definition of the products of secondary or tertiary reactions.
- (iii) Complete development of a mechanistic and quantitatively predictive physical and mathematical model for the reaction process.

*E-mail: michael.mckubre@sri.com

- (iv) Evaluation of potential applications of any new phenomena.

2. Excess Heat

The Fleischmann–Pons Effect is defined as the production of nuclear level heat from the electrochemical stimulation of the D₂O–Pd. This effect has been observed by hundreds of people in dozens of laboratories around the world, and published in hundreds or thousands of papers as recently reviewed [1,2]. In fact, the very breadth of diversity in experiment and calorimeter choice has contributed to a perceived irreproducibility (although the primary cause of apparent irreproducibility is the lack of measurement and control of variables critical to the effect).

The Fleischmann–Pons effect is produced under difficult-to-achieve but (now) relatively well-defined conditions in the cathodic stimulus of Pd (and alloy) electrodes in heavy water electrolytes (see [2]). Early failures to observe the effect can be attributed to inadequacies or deficiencies¹ in electrochemical and/or metallurgical protocols and the failure to anticipate the threshold nature of the phenomenon, particularly the thresholds of high D/Pd loading (>0.9) and long time initiation (>100 h for bulk Pd wire cathodes). Electrochemistry takes place at an electrified interface between two “difficult” material phases (solid and liquid), neither of which are fully under our control.

Stimulation of the excess heat effect is often observed to be prompted by changes in experimental conditions. Fleischmann and Pons [3] noticed in their initial work that the excess heat effect was occasionally initiated or improved with the application of a heat pulse, which can be considered as a transient change in conditions within the present argument. At SRI, one of the techniques used with success to initiate a heat pulse was to alter the current density, either through sudden changes or ramps. In later work a highly modulated current waveform was used to accomplish simultaneously the conditions of high deuterium loading and flux, following the pioneering work of Dardik [4].

Quantitative evidence indicating that deuterium flux plays an important role in determining the excess heat in a Fleischmann–Pons cell was found at SRI [5]. A purely empirical function was found to describe the excess heat observed for 1 mm diameter Pd cathodes. After initiation, excess power was found to be proportional to the product of three terms: (i) the square of the loading above a threshold value $(x - x^{\circ})^2$ (see Fig. 1); (ii) the electrochemical current above a threshold (see Fig. 2) and (iii) the flux of deuterium through the interface, irrespective of direction, measured as the time derivative of the average D loading, $|\delta x / \delta t|$ (see Fig. 3).

Figure 3 presents data showing the correlation of measured excess power with the amplitude of a ~ 2 h near-sinusoidal loading oscillation. Experiments appear to show that deuterium flux plays an important role in excess power production, independent of whether it is incoming, outgoing, axial, or traversing.

An important criterion coupled with excess heat production is the ability of a cathode to *sustain* high D/Pd loading. A variety of evidence supports the notion that the excess heat effect occurs at or very near the electrified electrolyte interface. Nevertheless the maximum *bulk* loading achieved by a cathode tells us something about *whether* (or not) a Pd D_x cathode is going to produce excess. Figure 4 plots the incidence of unsuccessful and successful excess heat producing experiments versus the maximum D/Pd loading achieved by the cathode *at any time* during the experiment. In some experiments the maximum heat was produced at times other than maximum loading; the statistically important feature appears to be *capacity* to obtain high loading. To get more information about when and how much heat is produced² we need to have more information about conditions of surface stimulation (current, laser, etc.) and surface dynamics (deuterium flux).

Four important understandings developed from intensive studies at SRI of deuterium loading and calorimetry [6–9]:

- (i) Irreproducibility in FPE experiments can be fully or at least sufficiently explained in terms of the electrochemistry of loading D into Pd.

¹In most cases early null or unintelligible results were caused more by an artificial sense of urgency than intrinsic core incompetence.

²More accurately, heat rate or power.

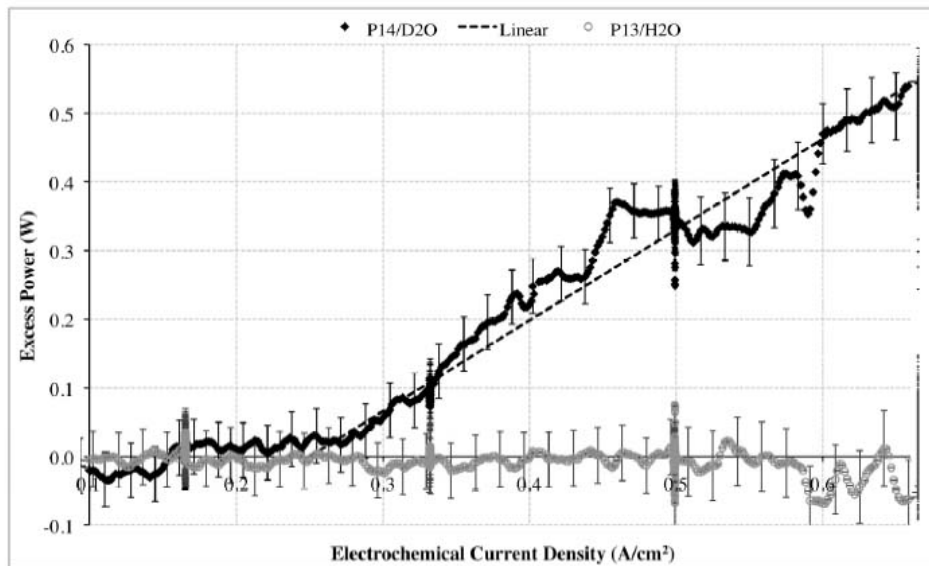


Figure 1. The effect of electrochemical current density on excess heat production in FPE experiments.

- (ii) In the absence of a measure or knowledge of the D/Pd loading the experimenter has no basis to judge whether an experiment could or should have produced excess heat.
- (iii) After basic precautions are taken the irreproducibility of loading and interfacial kinetics is not largely or even primarily controlled by the electrolyte or the electrochemistry, it is controlled by the bulk palladium metallurgy.

An empirical and near quantitative understanding of the measured magnitude of excess heat effects, and more particularly of the failure to achieve the FPE, can be obtained from measurements made of the controlling variables, and the failure to achieve critical threshold values.

3. Pathway Identification

3.1. Near quantitative

Much effort has been devoted to the search for reaction products that could be associated with the excess heat. It soon became clear that there are insufficient chemical reaction products to account for the excess heat by several orders of magnitude. Attention has been directed to the search for nuclear products in amounts commensurate with the energy measured. The problem is more difficult than in the case of chemical reactions as no similar processes are known.

Searches for neutrons, tritons, and other energetic emissions in quantitative association with the excess heat effect have been uniformly unsuccessful. The primary nuclear reaction pathway identified or hypothesized to be associated with excess heat results is the production of ${}^4\text{He}$. Observations of this ${}^4\text{He}$ appear to be solid and reproducible although experiment difficulties have reduced the number of successful ${}^4\text{He}$ reports far below the number of reliable excess heat results. Miles and Bush were the first to demonstrate semi-quantitative correlation between the rates of creation of ${}^4\text{He}$ and excess heat [10]. That effect has now been observed in a number of laboratories around the world [10–14] including SRI [9,15].

The simplest imagined nuclear reaction consistent with the thermal signature of the observed effect is the net reaction of two deuterons to produce ${}^4\text{He}$ with overall energy release ~ 23.8 MeV. It is this overall reaction against which Miles and Bush (and subsequent experimentalists) tested their quantitative observations. It has long been widely recognized by those active in FPE research and skeptics alike that this reaction cannot (and need not) proceed at low energies in the lattice by the same mechanism as the elementary process of “hot fusion” in isolation of all other matter.

Although measurements have been made of product ${}^4\text{He}$ at close to the 24 MeV Q -value [9,14,15], issues possibly associated with lattice retention always have resulted in larger measured energy values (or correspondingly smaller amounts of ${}^4\text{He}$). In addition, in no case has it been possible to perform a rigorous D, ${}^4\text{He}$ mass balance to identify the reactant as well as the product. Unless or until the FPE is used on an industrial scale to produce heat it will remain experimentally impossible to measure or even observe the tiny consumption of a very leaky gas (D_2) and isotope that is present ubiquitously in water.

It is also worth noting that several imaginative alternative nuclear reaction schemes have been proposed that produce ${}^4\text{He}$ at approximately the 24 MeV Q -value of dd fusion [2]. A large number of possible nuclear reactions also exist involving the known and expected constituents of the FPE metal/electrolyte system that produce ${}^4\text{He}$ with Q -values different from the ~ 24 MeV of dd fusion value (typically less). These putative and potential nuclear-reactive elements include: Li, B, C, N, O, Na, Ca, Pd, and all their natural isotopes. While in principle easier to undertake a quantitative mass balance of minority constituents such as Li and B, a rigorous tracking of reactant and product concentrations before, during and following an accurately measured heat release has yet to be performed.

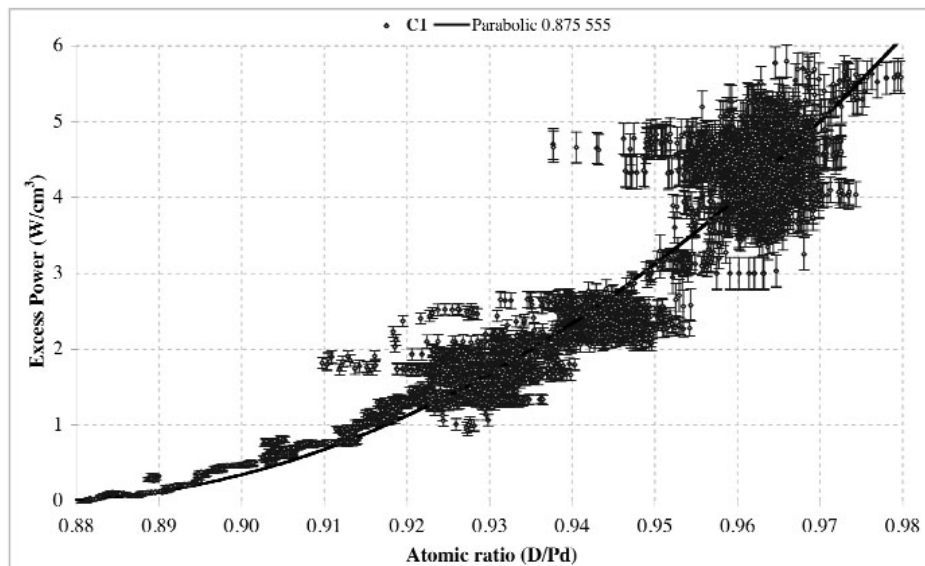


Figure 2. The effect of deuterium loading on excess heat production in FPE experiments.

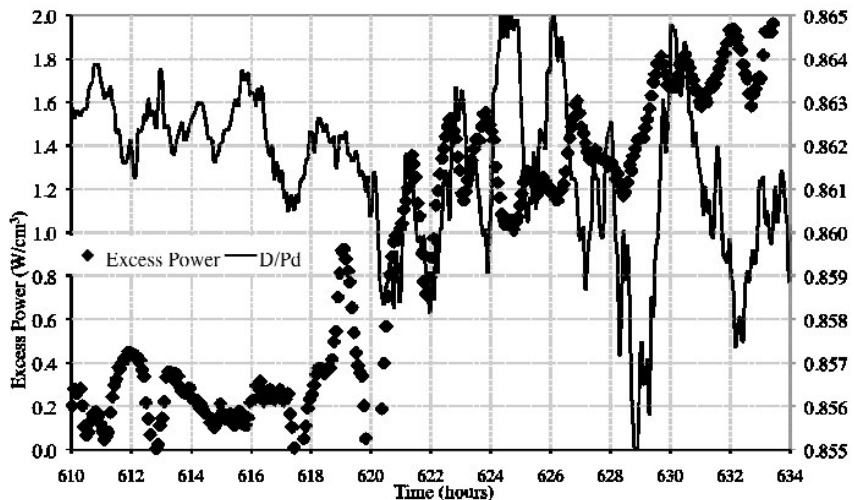


Figure 3. Correlation of excess power and deuterium flux for 1 mm dia. Pd cathode in FPE experiments.

3.2. Associated products (ash)

Additional products have been claimed of secondary reactions such as those that produce ash³ in chemical combustion. First amongst the secondary reaction products is tritium⁴. This isotope appears both temporally and quantitatively uncorrelated with excess heat production, but is clearly created in a number of experiments. Considerable discussion of this can be found in the excellent review by Storms [2].

Rather than being the dominant observable product (together with neutrons) in a putative dd fusion reaction, tritium is generally created at times when excess heat production is not observed and is not expected. On the rare occasions when heat and tritium production are observed in the same experiment at similar times, the tritium yield is 4–6 orders of magnitude less than that expected for a dd fusion heat effect.

Tritium is relatively easily observed. It is present at very low-background levels in most laboratories, and can be unambiguously identified by three different commonly employed methods: liquid scintillation in the liquid phase; direct beta observation in the gas using proportional counters or ionization chambers; mass spectrometric measurement of the rate of production of ³He via ³H decay. All three methods have been used in FPE studies, increasing the reliability and confidence in tritium observation. Other isotopic effects also have been reported, proposed and reviewed [2].

3.3. Mechanism and theory

At present there is no consensus among those in the field as to what physical mechanism is responsible for the effect although many propositions are under active discussion and significant progress is being made [16]. Nuclear reactions in the rarified environment of high-energy beams or plasmas are generally understood in terms of local energy and

³The term “nuclear ash” was originally applied not to the parasitic processes of reaction (by analogy with chemical combustion) but to mean the products of heat generating reactions (either observed or absent). This is equivalent to describing the products of chemical combustion, CO₂ and H₂O, as ash. Like helium, both are gases and neither can be considered as ash. The ashes of chemical combustion are the oxidation products of trace metal impurities and the residuum of already oxidized fuel inclusions.

⁴As a gas, tritium cannot be an ash.

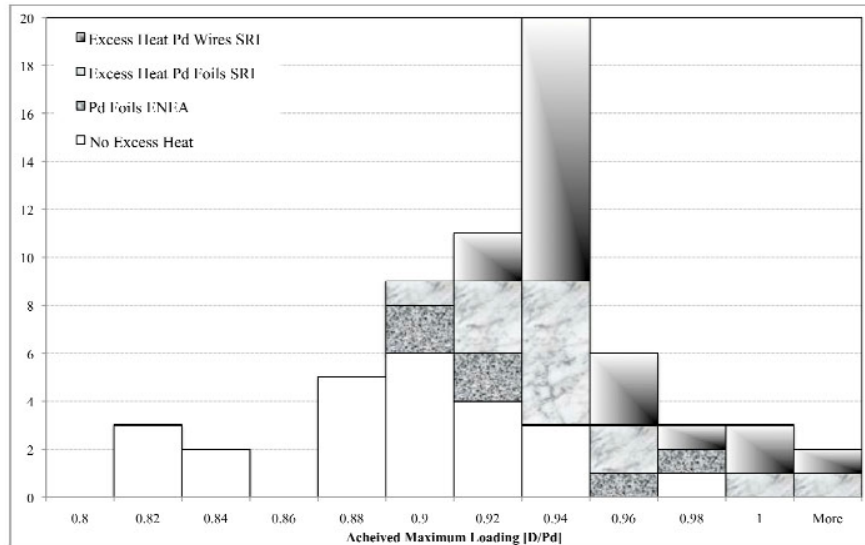


Figure 4. No heat (white) and successful excess heat experiments as a function of maximum D/Pd loading achieved in the FPE experiment.

momentum conservation in an assumed closed system encompassing only the putative reaction volume. It is not clear to what extent such simple considerations will prove to apply to nuclear reactions in solid lattices or in any form of condensed matter where the reactants and products are not isolated from their environment but are integral parts of the extended coherent system, the wave structure of the lattice.

4. Calorimetry: Measurement of Excess Heat

By simple consideration of energy scales and experiment duration the needs of so called “cold fusion” calorimeters are so different from those intended for use studying brief chemical reactions that, while valuable as a guide to basic principles, very little of value can be learned from studying that community, and little reference will be made to them here. The generation of mass flow, or more generically heat balance calorimeters under discussion here, were constructed to achieve confidence and give credence to a result that was not believed. Fleischmann et al. [3], and others had reported results of a nuclear level heat effect resulting from the *extensive electrochemical insertion of deuterium into palladium* cathodes over an *extended period of time* by means of electrolysis of heavy water in heavily alkaline conditions.

If true, this result was seen by some as a potential energy source, or at the very least a new potentially interesting physical effect. By others it was viewed as an unwelcome diversion of attention which was criticized as “irreproducible” or the result of unspecified “inaccuracies”. With regard to the second, apparently informed statements were made that “all calorimeters” were “intrinsically inaccurate”, an assertion that early pioneers of chemical thermodynamics in the early 20-th and even late 19-th century would have found puzzling. In this climate, however, the challenges to the second-generation FPE calorimeters were threefold:

- To allow reproducible demonstration of the effect — whether it be real or the consequence of (unidentified) systematic error.
- To exhibit proven levels of accuracy, over sufficient periods to quantify heat generation consistent with the FPE.

- (iii) The operating principal must be sufficiently simple to allow an open-minded non-specialist to visualize the full range of potential error.

The SRI calorimeters were designed and constructed [8,9] with 10 requirements.

1. As conceptually simple, first-principals devices based on the first law of thermodynamics ⁵.
2. With a requirement to maintain complete control of the critical chemical and electrochemical operating parameters, including cell temperature.
3. To accommodate a large dynamic range of heat input and output anticipated to be ~ 100 mW – 100 W (later extended to 500 W).
4. To permit complete, on-line monitoring of all important physical, chemical, electrochemical and thermal variables.
5. With multiple measurement redundancy of variables critical to calorimetry (e.g. temperature).
6. So that heat was measured accurately, equally and completely, independent of its source position within the calorimeter.
7. To allow high precision (the greater of 10 mW or 0.1% of power input) and high and stable accuracy for operating times as long as 1000 h.
8. To operate as closely as possible to the (thermal) steady state, thus simplifying calorimetric data analysis.
9. With sufficient time resolution to permit simple non-steady state analysis allowing source reconstruction of possible thermal transients.
10. Such that known sources of potential systematic error yield conservative estimates of “excess” heat.

One means of calorimetry was considered (in 1989) best able to meet the above-listed requirements. Often called mass flow calorimetry because of its emphasis on heat convected by a moving fluid mass, Heat Balance Calorimetry is accomplished by monitoring the heat gained or lost by the heat transfer fluid as follows:

$$Q_o = \delta m/\delta t C_{ps}(T_o - T_i), \quad (1)$$

where Q_o is the process heating (output) power (W), $\delta m/\delta t$ the mass flow of heat transfer fluid (kg/s), C_{ps} the specific heat of heat transfer fluid (J/(kg K)), T_i , the inlet temperature of heat transfer fluid (K), and T_o is the outlet temperature of heat transfer fluid (K).

As written, Eq. (1) has no calorimeter-dependent calibration requirements. Given independent, fundamental calibrated references for mass and time (hence $\delta m/\delta t$) and temperature (or temperature difference), and independent accurately known properties of the mass transport fluid, then the measurement of Q is absolute. This calibration independence is very important. Drifts in calorimeter “calibration constant” are the greatest cause of concern and error potential in FPE experiments that must survive hundreds of hours of intense electrolysis before the effect is seen that may last thousands of years ⁶.

Input power to an electrochemical cell operating thermodynamically closed is simply the product of the electrochemical current and the voltage measured at the calorimetric boundary (i.e. at a point on the surface that is neither inside nor outside). To meet requirements 2 and 8 above allowing independent control of electrolyte temperature and steady state operation it is necessary to add an input electrical Joule heater to complement the electrochemical power input. In this configuration,

⁵It is interesting to note that our widespread and deep trust in this law, is based exactly on our confidence in calorimetric accuracy.

⁶The effect of drift was eliminated and turned to advantage in the heat flow calorimeters designed by Fleischmann and Pons by daily, automated Joule calibration pulses. The presence of drift and rather clumsy handling of it essentially invalidated several early null results (sometimes classified as “negative”) as the position of the “baseline” was adjusted daily and arbitrarily.

$$Q_i = I_{EC} V_{EC} + I_J V_J, \quad (2)$$

we define as excess power the difference between the calorimetrically determined heating output power and the sum of power input,

$$Q_{XS} = Q_o - Q_i. \quad (3)$$

Note that Q_{XS} may have either sign. Negative “excess” is possible, although this condition has never been observed in any mass flow calorimetry performed at SRI in studies of the FPE except under transient condition as will be discussed shortly.

4.1. Departures from ideality

To obtain accuracies higher than $\sim 1\%$, two factors affecting calorimeter performance must be taken into account.

4.1.1. Thermal efficiency

Equation (1) accounts for heat removed from the calorimeter by convection of the thermal transfer fluid. Heat may also penetrate the calorimeter boundary by conductive exchange with the ambient. Of particular concern are metallic wires and pipes. If the environment is configured in such a way that the ambient is the inlet temperature, then Eq. (1) can be simply rewritten to include a conductive loss term, k ,

$$Q_o = ((\delta m/\delta t)C_{ps} + k)(T_i - T_o). \quad (4)$$

Since k is a calorimeter specific constant that does require calibration, it is important that it be kept small to approach first principals operation. By careful insulation, controlled geometry and selection of the fluid flow rate, k was typically less than 1% of $\delta m/\delta t C_{ps}$ in the SRI mass flow calorimeters. Because k is defined by geometry, it is also very unlikely to change and was observed to be stable.

In high-temperature operation one should expect radiative in addition to conductive transport. No such non-linear term has been observed or required in the mass flow studies so far performed at SRI or by our close collaborators. In high-temperature studies [4] performed at Energetics reflective surfaces were used to minimize radiative heat transport.

4.1.2. Thermal time constant

Input power is measured effectively and instantaneously while the calorimetric output thermal power responds with the thermal time constant(s) of the calorimeter. To make accurate subtraction of $Q_o - Q_i$ in order to calculate Q_{XS} at the same instant and thus improve (instantaneous) accuracy and permit study of thermal transients, it is necessary to apply one or a series of exponential filters to Q_i so that the terms on the right-hand side of Eq. [3] refer to the same time of measurement.

Although other heat transfer processes might be considered, three terms dominate the transfer of electrochemical cell heat out of the calorimeter:

- (a) Communication by conduction of electrochemical cell heat to the moving heat transfer fluid.
- (b) Convective transport of the heated fluid element to the outlet temperature sensors.

- (c) Convective thermal dilution of this heat due to the incoming mass flow at constant rate and constant (cooler) temperature.

Terms (a) and (c) depend exponentially on time. In all calorimeters studied at SRI the time constant for (a) and (b) were substantially less than for (c) and it was found sufficient to adopt a single level of exponential filtering with the following form.

$$\Delta Q = \sum_{\Delta t=0}^t \Delta Q_{i,\Delta t} (1 - e^{-\Delta t/\tau}), \quad (5)$$

where Δt is the time interval of measurement and τ is the composite time constant.

It is important to remember that the form of the non-steady-state correction is such that, while this can significantly improve calorimetric precision, it cannot affect the accuracy of total excess energy generation. The round trip integral effect is zero given the same initial and final conditions.

4.2. Practical implementation

The calorimeter shown in Fig. 5 was designed to accommodate a hermetically sealed quartz (fused silica) cell body. All components structural or otherwise inside the cell in contact with either electrolyte or vapor were manufactured of SiO_2 , Al_2O_3 , PTFE, Pt or Pd. Internal recombination and thus thermodynamic closure, was provided by either Pt or Pd on Al_2O_3 recombination catalyst suspended above a PTFE conic section designed to prevent electrolyte splash damage and allow the condensed recombinate (either H_2O or D_2O) to wash deposits back into the electrolyte. The working volume was $\sim 30 \text{ cm}^3$. Using this materials selection and design geometry, these cells are capable of sustained operation in 1 M base at currents above 1 A for periods over 1000 h.

The hermetic design of the electrochemical cell allows for full immersion in the mass flow fluid so that the moving mass of calorimetry fluid (in this case air saturated water) can remove heat efficiently from each of five geometrically disperse heat sources:

1. The product of the electrochemical current flow and the cathode interfacial impedance and any excess heat source located at the cathode.
2. The product of the current flow and the electrolyte resistance path located within the electrolyte volume between cathode and anode (or anodes).
3. The product of the current flow and the anode interfacial impedance.
4. The heat of recombination of H_2 and O_2 or D_2 and O_2 at the recombination catalyst located in the volume of recombiner near the top of the cell.
5. The product of the current in a Joule heater used for power compensation and calibration, located in an axially symmetric cylindrical shell immediately outside and intimately contacting the cell wall.

These enumerated terms significantly and differently couple to the calorimeter and outside environment. In a well-stirred electrolyte as exists above relatively modest current densities, the first three terms constitute effectively a single volume source. In the steady state the recombination thermal power is equal to the electrochemical current times the thermoneutral voltage of 1.48 V for H_2O or 1.53 V for D_2O . The Joule heater, while axially symmetric with the electrolyte volumetric heat source, is closer and therefore temporally and thermally better coupled to the convecting mass flow fluid. By enveloping the cell in the flow as shown in Fig. 5 we were able to establish within better than 0.1% (1 ppt) that the measurement of heat (the output power) was independent of its source within the calorimeter. This degree of position insensitivity is very difficult to achieve in calorimeters employing internal heat exchangers to remove calorimetric heat.

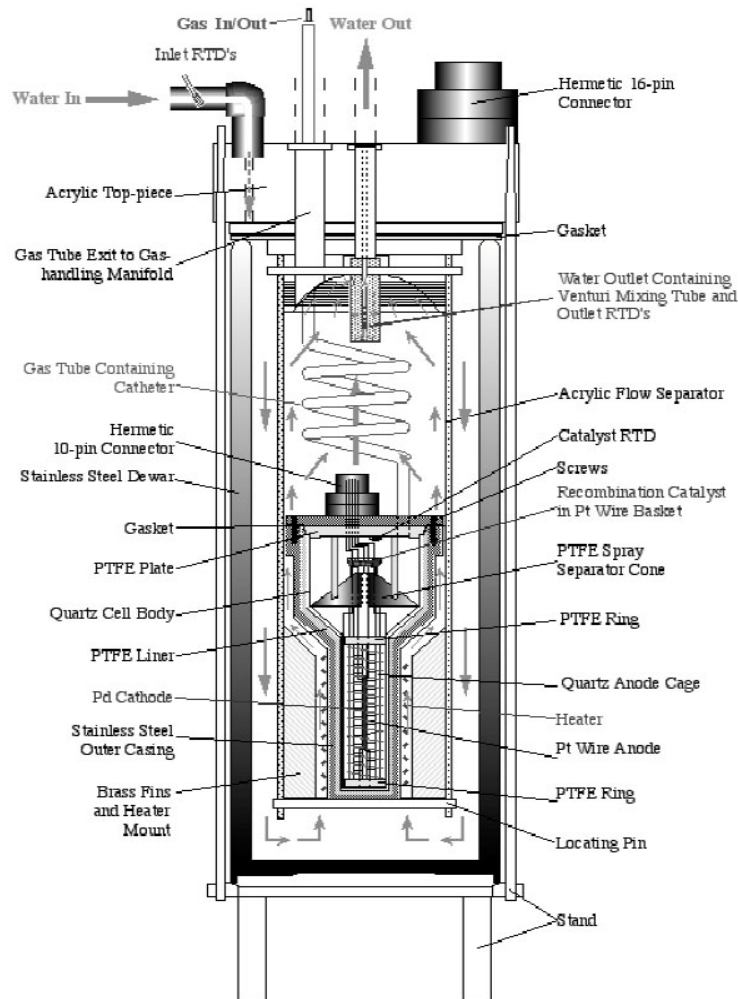


Figure 5. SRI Labyrinth Mass Flow Calorimeter containing hermetically sealed fused silica cell for FPE electrochemical and calorimetric studies. The calorimeter operates immersed in a thermally well-regulated water bath.

Several other features of the calorimeter shown in Fig. 5 merit further discussion. In employing Eq. (4) with a single conductive loss term, k , it is necessary to ensure that the calorimeter experiences a single, stable thermal ambient environment. The calorimeter was submerged inside a large ($\sim 1 \text{ m}^3$), water bath that was well stirred and well regulated⁷. This bath was placed in the center of an isolated, temperature controlled room. The mass flow fluid (water) was drawn from the bath past two inlet RTD sensors placed directly in the flow stream. The flow enters the head of the calorimeter through a flow distribution header and channels down through the annular volume between

⁷Temperature gradients and variability both short and long term were maintained below $\pm 3 \text{ mK}$. A Quartz Crystal reference thermometer [HP Model 2804A] was maintained as a temperature standard in this bath.

the inner wall of a 2-liter stainless steel dewar and a thermally insulating barrier to form a flow labyrinth reversing direction at the bottom to flow past the submersed electrochemical cell. The electrical leads from the cell were dressed in the reverse direction from a hermetic connector at the top of the cell to another at the top of the calorimeter. The purpose of this arrangement is to minimize conductive heat loss radially from the cell and along the electrical leads used for electrochemical control and measurement. Heat leaving by these paths is picked up in the incoming fluid and is delivered to the outlet sensors for measurement.

The final feature of the calorimeter is the hemispherically domed insulating head that houses the outlet temperature sensors. The hemispherical shape was designed to minimize the formation of thermal “pockets” at higher or lower temperature than the average. The mass flow fluid flows through a small hole at the highest accessible point of the hemisphere to enter the outer annulus of a small flow labyrinth containing a venturi (helical) flow mixer. Turning the corner this flow enters a small axial flow channel designed to ensure good mixing at the operating mass flow rate (typically ~ 1 g/s).

These flow precautions were taken to ensure that the outlet temperatures measured represent an accurate average value in the fluid flow. The outlet temperature sensors were situated within the axial outflow channel, directly in contact with the outgoing fluid. Two RTD sensors were used, identical to the two at the inlet, to provide a redundant measurement of ΔT . In some experiments two additional thermistor sensors were used at the outlet to provide a redundancy of measurement method.

An FMI QV-OSSY constant displacement pump was used to draw water from the top of the calorimeter through a standard heat exchanger to ensure constant mass flow. This flow was then pumped directly into a reservoir placed on a Setra 5000L electronic balance that was polled periodically by the data acquisition system to measure the mass flow rate as $\Delta m/\Delta t$. When the balance reservoir is filled a siphon automatically forms and empties the vessel rapidly⁸.

4.3. Brief consideration of errors

Excess power is calculated as the difference between the output power and the input power

$$Q_{XS} = Q_o - Q_i = (\Delta m/\Delta t C_{ps} + k)(T_i - T_o) - I_{EC} V_{EC} - I_J V_J. \quad (6)$$

Temperatures were measured using 100 Ω platinum resistance temperature devices (RTD's) so that to first order,

$$T = T^\circ + (R - R^\circ)/\alpha R^\circ, \quad (7)$$

where α is the (known) temperature coefficient of resistance for Pt, and R° is the sensor resistance at some known temperature (typically 0°C).

A complete error propagation model has been developed for the calorimeter shown in Fig. 5; the basic elements are reproduced below. Errors propagate from mis-measurement of each of the terms. The constants and variables needed to measure Q_{XS} and its uncertainty may be divided into three classes:

1. Measured variables: Δm , Δt , R , I and V .
2. Predetermined constants: C_{ps} , α and R° .
3. The calorimeter inefficiency: k .

Measurements of mass, time, resistance, current and voltage rely on the calibration accuracy of the instruments being used. At SRI the instruments used for the purposes were periodically calibrated to accuracies better than 1 part

⁸This normally disrupts only one, and at most determinations of $\Delta m/\Delta t$. In general the flows were very stable but redundant mass flow measurements occasionally were used for added accuracy.

per 1000 (<1 ppt) and typically better than 1 part in 10,000. Measuring R° with the same instrument used to measure R further increases measurement accuracy. Systematic errors in the calorimetry critical temperature difference tend to reduce since this depends on the difference of resistances measured with the same meter at almost identical times.

The heat capacity of air-saturated water and the temperature coefficient of Pt resistance are well measured constants. It should be noted that these are not constant with temperature; for accuracies better than 1 ppt it is necessary to take account of the fact that the outlet temperature may vary over a considerable range, affecting both C_{ps} and α .

What remains is the conductive loss term or calorimeter thermal inefficiency, k . Three factors contribute to reducing the inaccuracy in this term and increase its long-term stability and thus influence on overall calorimeter accuracy.

- (a) By design and selection of mass flow rate k is maintained to be a small fraction of $\Delta m/\Delta t C_{ps}$. Typically this constant was held to contribute $\sim 1\%$ or less of the output power and it can be measured easily with better than $\pm 10\%$ accuracy thus contributing <1 ppt.
- (b) The method of calibration using a Joule heater pulse determines k in terms of the other predetermined constants. In this way the cumulative error is reduced and recalibration can be performed at any time (in the absence of excess power) using a Joule heater pulse.
- (c) The value of k is determined by the geometry and materials properties of heat conduction pathways. With the calorimeter isolated in the constant temperature bath these are not likely to change, and were not observed to do so.

For the Labyrinth Mass Flow Calorimeter shown in Fig. 5 the maximum error in the typical operating range of input power and mass flow rates ($Q_i = 5\text{--}20\text{ W}$, $\partial m/\partial t \sim 1\text{ g/s}$) was $\pm 0.35\%$ of Q_i . The largest source of error in practice is mismeasurement of the average temperature of the outgoing fluid stream due to flow streaming. Care must be taken to ensure good flow mixing and the avoidance of particulates in the flow stream.

5. Conclusions

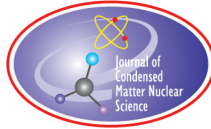
With some attention to detail heat balance calorimeters based on the mass flow of water are capable and robust instruments that combine the desirable features of simplicity of design and calorimetric analysis, adequate accuracy, high long-term stability and low initial materials and operating costs. By these criteria such devices are well suited to studies of the FPE and have been widely employed with considerable success. Mass flow calorimeters are conceptually simple, first principles devices based on the first law of thermodynamics. They are able to accommodate and operate nearly linearly over a large dynamic range of heat input and output, extending easily to 500 W while maintaining better than 1% accuracy. Designs are available to permit the measurement of heat accurately, equally and completely, independent of its source position within the calorimeter.

The base of experimental support of the FPE is far broader than the interpretation of thermal signatures from mass flow calorimeters. In recent reviews [1,2] and in a full session devoted to the topic at ICCF14, a range of potent calorimetric methods have been reviewed with reference to FPE studies. Although varied in result and quality the (increasing) totality of an observable effect outside of known physics seems unimpeachable based on the heat effects alone, thus supporting the original claims of Fleischmann, Pons and Hawkins [3].

Of perhaps greater significance the support and identified existence of new physical effects does not rely on extreme heat effects alone. Numerous investigators have sought and, in many cases, found ${}^4\text{He}$ in different environments including in the gas phase, dissolved or trapped in the cathode metal, and emitted as charged particles [1]. In 8–10 cases the appearance of ${}^4\text{He}$ correlates to a high degree with the production of excess heat, offering strong support to the idea that the new physical effect is of nuclear origin.

References

- [1] P.L. Hagelstein, M.C.H. McKubre, D.J. Nagel, T.A. Chubb, R.J. Hekman, New effects in metal deuterides, in *11th International Conference on Cold Fusion*, J-P. Biberian (ed.), Marseilles, France, 2004, pp. 23.
- [2] E. Storms, *The Science of Low Energy Nuclear Reactions*, World Scientific, Singapore, 2007.
- [3] M. Fleischmann, S. Pons, M. Hawkins, *J. Electroanal. Chem.* **201** (1989) 301; Errata, **263** (1990) 187. See also M. Fleischmann, S. Pons, M.W. Anderson, L.J. Li, M. Hawkins, *J. Electroanal. Chem.* **287** (1990) 293.
- [4] I. Dardik, H. Branover, A. El-Boher, D. Gazit, E. Golbreich, E. Greenspan, A. Kapusta, B. Khachatorov, V. Krakov, S. Lesin, B. Michailovitch, G. Shani, T. Zilov, Intensification of low energy nuclear reactions using superwave excitation, in *Tenth International Conference on Cold Fusion*, P.L. Hagelstein, World Scientific, Cambridge, MA, 2003, pp. 61.
- [5] M.C.H. McKubre, S. Crouch-Baker, A.K. Hauser, S.I. Smedley, F.L. Tanzella, M.S. Williams, S.S. Wing, Concerning reproducibility of excess power production, in *5th International Conference on Cold Fusion*, S. Pons, IMRA Europe, Sophia Antipolis Cedex, France, Monte-Carlo, Monaco, 1995, p. 17.
- [6] M.C.H. McKubre, R.C. Rocha-Filho, S.I. Smedley, F.L. Tanzella, S. Crouch-Baker, T.O. Passell, J. Santucci, Isothermal flow calorimetric investigations of the D/Pd system, in *The Science of Cold Fusion*, T. Bressani, E. Del Giudice, G. Preparata (eds.), Conference Proceedings, Vol. 33, Italian Physical Society, Bologna, 1992, p. 419.
- [7] M.C.H. McKubre, S. Crouch-Baker, R.C. Rocha-Filho, S.I. Smedley, F.L.S. Tanzella, T.O. Passell, J. Santucci, Isothermal flow calorimetric investigations of the D/Pd and H/D systems, *J. Electroanal. Chem.* **368** (1994) 55.
- [8] M.C.H. McKubre, S. Crouch-Baker, S.I. Smedley, F.L. Tanzella, M. Williams, S. Wing, M. Maly-Schreiber, R.C. Rocha-Filho, P.C. Searson, J.G. Pronko, D.A. Koehler, Development of Advanced Concepts for Nuclear Processes in Deuterated Metals, EPRI Report TR-104195, August 1994.
- [9] M.C.H. McKubre, S. Crouch-Baker, A. Hauser, N. Jevtic, S.I. Smedley, F.L. Tanzella, M. Williams, S. Wing, Development of Energy Production Systems from Heat Produced in Deuterated Metals, Final Report on EPRI Contract 3170-23, 1995.
- [10] M.H. Miles, B. Bush, Search for Anomalous Effects Involving Excess Power and Helium during D₂O Electrolysis using palladium cathodes, in *3rd International Conference on Cold Fusion*, H. Ikegami, Nagoya, Japan, 1992, p. 189.
- [11] D. Gozzi, R. Caputo, P.L. Cignini, M. Tomellini, G. Gigli, G. Balducci, E. Cisban, S. Frullani, F. Garibaldi, M. Jodice, G.M. Urciuoli, Excess heat and nuclear product measurements in cold fusion electrochemical cells, in *4th International Conference on Cold Fusion*, T.O. Passell, Lahaina, USA, Vol. 1, 1993, p. 2–1.
- [12] E. Botta, R. Bracco, T. Bressani, D. Calvo, V. Cela, C. Fanara, U. Ferracin, F. Iazzi, Search for 4He production from Pd/D systems in gas phase, in *5th International Conference on Cold Fusion*, S. Pons, IMRA Europe, Sophia Antipolis Cedex, France, Monte-Carlo, Monaco, 1995, p. 233.
- [13] Y. Arata, Y-C. Zhang, Helium (⁴He, ³He) within deuterated Pd-black, *Proc. Japan Acad.* **73B** (1997) 1.
- [14] M. Apicella, E. Castagna, L. Capobianco, L. D'Aulerio, G. Mazzitelli, F. Sarto, A. Rosada, E. Santoro, V. Violante, M.C.H. McKubre, F. Tanzella, C. Sibilia, Some Recent Results at ENEA, *Proceedings of the 12th International Conference on Condensed Matter Nuclear Science*, Yokohama, Japan, 2005.
- [15] M.C.H. McKubre, F.L. Tanzella, T. Tripodi, P.L. Hagelstein, The emergence of a coherent explanation for anomalies observed in D/Pd and H/Pd systems; evidence for ⁴He and ³H production, in *8th International Conference on Cold Fusion*, F. Scaramuzzi, Lerici, Italy, 2000, p. 3.
- [16] P.L. Hagelstein, I.U. Chaudhary, Arguments for dideuterium near monovacancies in PdD, submitted to the proceedings of the *15th International Conference on Cold Fusion*, V. Violante, ENEA, Frascati, Italy, 2009.



Research Article

Measurements of Excess Power Effects In Pd/D₂O Systems Using a New Isoperibolic Calorimeter

M.H. Miles *

Dixie State College, St. George, UT 84770, USA

M. Fleischmann

Bury Lodge, Duck Street, Tisbury, Salisbury, Wilts SP3 6LJ, UK

Abstract

Relatively inexpensive isoperibolic calorimeters have been designed and constructed with the goal of obtaining a constant heat transfer coefficient that is insensitive to normal changes in the electrolyte level during electrolysis. Four prototypes were constructed from copper tubing and used different insulating materials. Preliminary tests on two of these new calorimeters show excellent stability for the cell temperature measurements, stable heat transfer coefficients during electrolysis, and precise power measurements. Initial applications include nitrate electrolytes and co-deposition systems. There was no evidence for any shuttle reactions in these experiments.

© 2011 ISCMNS. All rights reserved.

Keywords: Co-deposition, Electrolysis, Heat capacity, Heat conduction, Nitrates, Shuttle reactions, Temperature, Thermistors

1. Introduction: Design Considerations

An important goal for isoperibolic calorimeters is a constant heat transfer coefficient that does not change as the electrolyte level decreases due to the electrolysis and evaporation. All measurements could then be evaluated with a single, predetermined value for the heat transfer coefficient. The placement of the thermistors in a secondary compartment outside the cell has been shown to minimize the cell electrolyte level effect [1–4]. This type of calorimeter can then be modeled as a fluid in which the electrochemical cell serves as a heating element for the substance in the adjacent compartment.

The size of the calorimetric system must be carefully considered in the design. Large systems give slower electrolyte level changes along with larger heat capacities and time constants. Small calorimetric cells yield faster electrolyte level changes and smaller heat capacities and time constants, but their small cell volumes require more frequent makeup of H₂O or D₂O additions. The heat transfer coefficient will also increase with the surface area of the calorimetric system.

*E-mail: melmiles1@juno.com

Adequate stirring of the cell contents by the electrolysis gases requires thin, tall cells where the cell diameter does not exceed 3 or 4 cm. All these factors were carefully considered in selecting design features for these new isoperibolic calorimeters.

Desired features of isoperibolic calorimeters include simple construction and low costs, heat transfer mainly by either conduction or by radiation (Dewar type), and a wide dynamic range from 20°C to boiling for the cell temperature with cell input power levels ranging from 0 to 10 W. This requires heat transfer coefficients near $k_C = 0.13 \text{ W/K}$ if the heat transfer is by conduction or near $k_R = 0.83 \times 10^{-9} \text{ W/K}^4$ if the heat transfer is by radiation (Dewar). Because of the simpler construction and lower costs, isoperibolic calorimeters providing heat transfer by conduction were selected rather than Dewar cells. It should be noted, however, that a Dewar design fitted with a metallic conductive cylinder insert containing two thermistors and the glass electrochemical cell has also been proposed (see Fig. A.27 of Ref. [5]). Although this calorimetric design has never been constructed, it would likely have provided a constant radiative heat transfer coefficient that would be independent of the electrolyte level (p. 26 of Ref. [5]).

2. Experimental Details of the Calorimetric Design

Four prototype isoperibolic calorimeters (A, B, C, and D) have been constructed from commercial copper tubing and copper end caps, and two (A, B) have been tested. Each calorimeter consisted of two completely isolated copper cylinders. The outer copper cylinder for each calorimeter had a 5.1 cm (2.0 in) diameter and a 28 cm height. The inner copper cylinder (3.2 cm × 20 cm) was completely separated from the outer cylinder by the insulating material consisting of either pipe foam insulation (Cell A) or of tightly packed Oregon timber sawdust (Cell B). The glass electrochemical cell (2.5 cm × 20 cm) was a large commercial glass test tube (Kimax). This test tube cell was positioned inside the inner copper cylinder and filled 2/3 full using 50.0 mL of the selected electrolyte. Two thermistors were positioned on opposite sides of the outer wall of the glass tube with each thermistor level with the center of the cathode used. Thermal contact between the glass cell and the inner copper tube was provided by Mobil-1 (5–30 W) synthetic motor oil (50 mL) as the heat conducting fluid. The Mobil-1 oil has a reported density of 0.80 g/mL at 15°C and a heat capacity of 210 J/g K at 80°C. This 50 mL of Mobil-1 oil filled the secondary chamber well above the cell electrolyte level. It is expected that this calorimetric design will provide for high cell operating temperatures up to the boiling point of the selected electrolyte solution.

3. Review of Equations for Isoperibolic Calorimetry

The mathematical equations that model isoperibolic calorimetry have been presented elsewhere [5–8], thus this will only be a brief review. Full details are given in Appendix A1. The fundamental modeling equation is

$$P_{\text{calor}} = P_{\text{EI}} + P_H + P_X + P_C + P_R + P_{\text{gas}} + P_W, \quad (1)$$

where these individual power terms have all been defined elsewhere [5–8] as well as in Appendix A2. Equation (1) represents a differential equation because

$$P_{\text{calor}} = C_p M \frac{dT}{dt}, \quad (2)$$

where $C_p M$ (J/K) is the heat capacity of the calorimetric system consisting of the molar heat capacity (C_p) of H_2O or D_2O in J/K mol and the number of equivalent moles (M) of the H_2O or D_2O that would yield this heat capacity.

It is useful in initial calculations to assume that there is no anomalous excess power, $P_X = 0$, thus Eq. (1) becomes

$$P_{\text{calor}} = P_{\text{EI}} + P_H + 0 + P'_C + P_R + P_{\text{gas}} + P_W. \quad (3)$$

The simple subtraction of Eq. (3) from Eq. (1) yields

$$0 = P_X + P_C - P'_C = P_X - k_C \Delta T + k'_C \Delta T \quad (4)$$

or

$$P_X = (k_C - k'_C)\Delta T, \quad (5)$$

where $\Delta T = T - T_b$. Therefore, the difference between the true conductive heat transfer coefficient (k_C) and the pseudo-heat transfer coefficient (k'_C) obtained by assuming $P_X = 0$ provides for a simple calculation of the actual excess power via Eq. (5). All of the power terms in Eq. (1), however, should be considered in the determination of k'_C .

4. Experimental Results

The use of this new isoperibolic calorimetric design requires the evaluation of the conductive heat transfer coefficient, k_C , and the heat capacity, $C_p M$, of the calorimetric system (see Appendix A1). Several experiments using H_2O control electrolytes yielded $k_C = 0.164 \text{ W/K}$ for Cell A and $k_C = 0.133 \text{ W/K}$ for Cell B.

These cells differ only by the use of foam insulation in Cell A and packed sawdust insulation in Cell B.

4.1. Heat capacity/differential and integral equations

The experimental cooling curve obtained by simply turning off the cell current provides a convenient method for determining the heat capacity, $C_p M$, of the calorimetric system. For a H_2O control experiment at zero current, Eq. (1) becomes

$$C_p M \frac{dT}{dt} = -k_C(T - T_b). \quad (6)$$

This differential equation can be rearranged to

$$\frac{dT}{(T - T_b)} = -(k_C/C_p M)dt \quad (7)$$

and then integrated to yield

$$-\ln(T - T_b)/(T_0 - T_b) = (k_C/C_p M)t. \quad (8)$$

This integrated equation is of the form $y = mx$ where the slope (m) is given by $m = k_C/C_p M$.

The experimental cooling curve for Cell B using a H_2O control is present in Fig. 1, where T_2 is the cell temperature measured by thermistor 2. This figure shows the expected exponential decrease of $T_2 - T_b$ with time. Figure 2 shows the same data using the integrated Eq. (8). The slope $m = 0.01752 \text{ min}^{-1} = 2.920 \times 10^{-4} \text{ s}^{-1}$. Therefore $C_p M = k_C/m = 456 \text{ J/K}$. The water equivalent that would give this same heat capacity is 6.06 mol ($C_p = 75.291 \text{ J/mol K}$ for H_2O). The heat capacity of the system can also be calculated using the differential equation (Eq. (6)) directly, but this is considerably less accurate because of the estimate of dT/dt . From Eq. (6), $C_p M = -k_C(T - T_b)/dT/dt$. Table 1 presents the value for $C_p M$ obtained directly from Fig. 1 at 10, 30, and 65 min. The three values calculated for $C_p M$ range from 427 to 485 J/K with a mean of $457 \pm 29 \text{ J/K}$. It is obvious that more accurate results for $C_p M$ are obtained by use of the integrated equation (Eq. (8)) where the results can be displayed in a straight line form (Fig. 2). The same is true for all isoperibolic calorimetric results using Eq. (1). Numerical integration of the experimental calorimetric data along with casting them into the straight line form, $y = mx + b$, gives the most accurate results as previously reported [5-9].

The time constants for Cells A and B can be readily calculated once k_C and $C_p M$ are known because $\tau = C_p M/k_C$. This yields $\tau = 3420 \text{ s}$ or 57 min for Cell B and 46 min for Cell A.

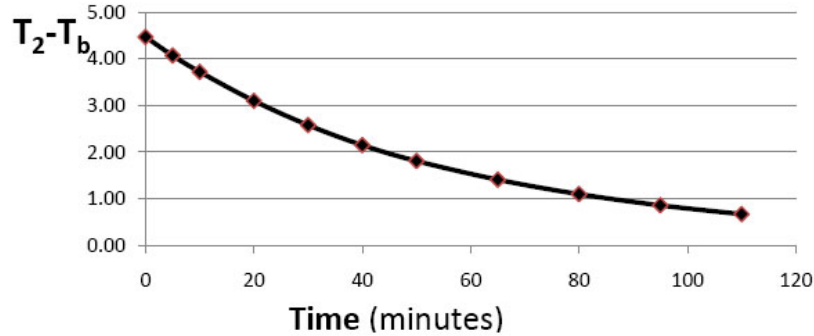


Figure 1. Experimental cooling curve for Cell B.

4.2. Estimated heat capacity

The heat capacity of the cell can also be estimated by considering the heat capacity of all materials in the cell or in contact with the cell that undergo the same temperature changes. These calculations give 208 J/K for the 50.0 mL of H₂O used, 133 J/K for the 344 g of the inner copper cylinder, 84 J/K for 50 mL of Mobil-1 oil, 31 J/K for 42 g of the glass cell, and 2 J/K for the copper cathode, platinum wire, palladium and nickel present. The calculated total of 458 J/K is close to the measured value for $C_p M$. For a cell filled with 50.0 mL of D₂O giving 233 J/K, the calculated total for $C_p M$ would be 483 J/K. Methods for minimizing the effect of errors for $C_p M$ have been previously presented [3,7].

4.3. Detection of “Heat After Death” effects

It should be noted that cooling curves such as Figs. 1 and 2 provide a useful method for determining lingering excess power effects or “heat-after-death” when electrolysis ceases in active D₂O/Pd experiments. Cell cooling that departs from Eq. (8) or Fig. 2 would be readily apparent. Such studies of cooling curve behavior are planned for future D₂O/Pd experiments. A previous study of Pd-B/D₂O in a Dewar type cell showed marked deviations from the expected cooling curve behavior (see pp. 22–23 and Figs. A.23 and A.24 of Ref. [5]). For heat transfer by radiation with no excess power present, Eq. (1) becomes

$$C_p M dT/dt = -k_R (T^4 - T_b^4), \quad (9)$$

Table 1. Heat capacity ($C_p M$) for Cell B calculated from the cooling Curve of Fig. 1 using the differential equation (Eq. (8)).

T (min)	dT _{cell} /dt (K/min)	T - T _b (K)	C _p M (J/K)
10	-10.8×10^{-4}	3.72	458
30	-8.03×10^{-4}	2.58	427
65	-3.87×10^{-4}	1.41	485

Mean $C_p M = 457 \pm 29$ J/K

when the current is off. The rearrangement and integration of this differential equation yields

$$\ln(T + T_b)(T_0 - T_b)/(T_0 + T_b)(T - T_b) + 2 \tan^{-1}(T/T_b) - 2 \tan^{-1}(T_0/T_b) = 4T_b^3 k_R t / C_p M. \quad (10)$$

Although more complicated than Eq. (8) for heat transfer by conduction, the use of Eq. (10) for Dewar cells in a previous Pd-B study readily shows the presence of the “heat-after-death” effect [5].

4.4. Experimental Tests for Shuttle Reactions

Potassium nitrate (KNO_3) has been widely used for years by electrochemists as an inert supporting electrolyte. However, it has been proposed that shuttle reactions involving nitrates may give false excess power effects [10]. Theoretically, the nitrate ion may be reduced at the cathode to form various gaseous nitrogen oxides, nitrite ions (NO_2^-), or even N_2 or NH_4^+ . With the use of special electrocatalysts and conditions, some electrochemical reduction of nitrates is possible [11]. In molten nitrates ($\text{LiNO}_3-\text{KNO}_3$) at elevated temperatures (250°C), there exists a large 4.5 V electrostability region between the reduction of lithium ions and the oxidation of nitrate ions [12,13]. This demonstrates the stability of the nitrate ion even at high temperatures. The anodic limit for the nitrate melt is the oxidation of the nitrate ion, $\text{NO}_3^- \rightarrow \text{NO} + \text{O}_2 + \text{e}^-$, followed by the further reaction of NO with oxygen to form brown NO_2 gas [12].

Because of the proposed shuttle reactions involving nitrates [10], an initial study using this new isoperibolic calorimeter was the investigation of 0.154 M KNO_3 in Cell B. This study used a platinum wire cathode (1 mm \times 15 mm) and a platinum coil anode. The $\text{H}_2\text{O} + 0.154 \text{ M KNO}_3/\text{Pt}$ system was investigated over several days of electrolysis at currents of 80, 100, and 150 mA. These were no measurable excess power effects. The correct value of $k'_C = 0.133 \text{ W/K}$ was obtained using Cell B and assuming $P_X = 0$. Therefore $k_C - k'_C = 0$ and $P_X = 0$ from Eq. (5). Recent cyclic voltammetric studies on $\text{KNO}_3+\text{NaNO}_2$ have confirmed that there are no reversible reactions involving nitrates or nitrites that could act as shuttle reactions.

The measured pH of the 0.154 M KNO_3 solution, however, changed from near neutral initially (pH = 7.02) to pH = 10.24 at the end of this study. Any electrochemical reaction of NO_3^- ions to form a neutral product such as NO_2 , NO or N_2 results in the production of OH^- ions to maintain electroneutrality. For the total of 27,626 C used in this study, the observed pH change could be explained by 0.003% of the current being consumed by the reaction of NO_3^- to form a neutral product. The remaining 99.997% of the current was apparently consumed by the expected H_2O electrolysis. The electrochemical reaction of nitrates would, therefore, change the thermoneutral potential (E_H)

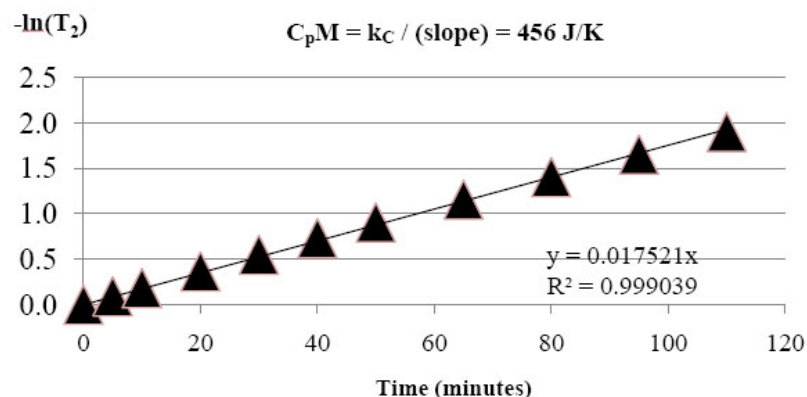


Figure 2. Cooling curve data of Fig. 1 using the integrated equation where $-\ln(T_2)$ represents the left-hand side of Eq. (8).

by only 4.4×10^{-5} V. At the highest current used (150 mA), this nitrate reaction would give a calorimetric error of $(4.4 \times 10^{-5}$ V)(0.150 A) = 6.6×10^{-6} W or less than 0.007 mW. Therefore, based on this study of 0.154 M KNO₃/Pt, the use of KNO₃ as an inert electrolyte in calorimetric studies would be justified. In a related experiment using 0.158 M KNO₃+0.0577 M NaNO₂, 99.992% of the current (90,720 C) was consumed by H₂O electrolysis. There are no shuttle reactions involving nitrates or nitrites that would give a false excess power effect. In both experiments, the volume of H₂O consumed was larger than the theoretical amount based on Faraday's law, and this provides further evidence against shuttle reactions.

4.5. Co-deposition/light water controls

This new calorimeter was also used to study the 0.15 M NH₄Cl + 0.15 M NH₄OH + 0.025 M PdCl₂ co-deposition system in H₂O. Complete results are given elsewhere [14]. In this case, a chemical excess power effect was detected early in the experiment due to the solution becoming acidic (pH = 1.25) resulting in chlorine evolution and the formation of nitrogen trichloride (NCl₃). Similar excess power effects were measured by the Naval Research Laboratory (NRL) for this same system using a Seebeck calorimeter [15]. With further electrolysis, the solution becomes more basic, chlorine evolution ceases, the NCl₃ dissipates, and normal calorimetric results are observed [14].

In a new study, NH₄Cl + NH₄OH + PdCl₂ co-deposition was repeated, but following the palladium co-deposition onto a copper cathode, sufficient LiOH was added to maintain a basic pH. This provided a very stable electrolysis system with no chlorine or NCl₃ formation. The electrolysis of this system using a high current of 400 mA gave evidence for a stable cell constant that was independent of the electrolyte level. The results for this study in Cell B are given in Table 2. The mean cell constant over almost 5 h of electrolysis was $\langle k_2 \rangle = 0.1324 \pm 0.000069$ W/K. The cell constants never varied by more than ± 0.0001 W/K from the mean value. This is the best evidence to date for an isoperibolic calorimetric cell where the electrolyte level does not affect the cell constant. We were, therefore, successful in attaining our major goal for this new isoperibolic calorimeter.

Table 2. Calorimetric data summary for Cell B with $I = 400$ mA using the PdCl₂ + NH₄Cl + NH₄OH + LiOH electrolyte.

Time	$-E_{\text{cell}}$ (V)	P_{EI} (W)	ΔT_2 (K)	k_2 (W/K)
2:29	5.122	1.4564	11.000	0.1324
2:44	5.121	1.4560	10.995	0.1324
4:01	5.110	1.4516	10.970	0.1323
4:53	5.103	1.4488	10.935	0.1325
5:51	5.094	1.4452	10.915	0.1324
6:46	5.088	1.4428	10.900	0.1324
7:19	5.083	1.4408	10.890	0.1323

The change in the cell voltage with time (t , min) in Table 2 gives the linear relationship $E_{\text{cell}} = -5.122458 + 1.36 \times 10^{-4}t$ ($R_2 = 0.9988$). This is the expected behavior for water electrolysis if there are no shuttle reactions or anomalous F-P effects. The steady electrolysis of water at constant current gradually increases the electrolyte concentration and decreases the IR (resistive heating) component of the cell voltage. The changes in both P_{EI} and ΔT_2 (Table 2) are directly related to the changes in E_{cell} when there are no anomalous effects.

4.6. Co-deposition/heavy water studies

Two calorimetric studies of co-deposition have been completed using heavy water and deuterated compounds. Chlorine evolution and the related NCl_3 formation were avoided by the use of $\text{PdCl}_2 + \text{ND}_4\text{Cl} + \text{ND}_4\text{OD} + \text{LiOD/D}_2\text{O}$ similar to the very stable H_2O study shown in Table 2. Excess power effects were measured in both experiments using an electrolysis current of 100 mA. For example, $k'_C = 0.09585 \text{ W/K}$ with $\Delta T = 2.15 \text{ K}$, thus from Eq. (5), $P_X = 80 \text{ mW}$. Typically, the excess power ranged from 75 to 105 mW in both experiments. However, the excess power gradually decreased to near zero in both experiments after several days of electrolysis. It was later found that the deposited palladium had become detached from the copper cathode substrate and fell to the bottom of the cell in both experiments resulting in the palladium becoming electrochemically isolated. New experiments are planned where the copper cathode will be positioned close to the cell bottom, thus any detached palladium will remain in electrical contact with the cathode.

5. Summary of Results

New isoperibolic calorimeters that are relatively inexpensive have been designed, constructed, and tested using several different electrolyte systems. These calorimeters show stable heat transfer coefficients that do not change during electrolysis at high cell currents over long time periods. Initial studies have shown excess power effects for the $\text{ND}_4\text{Cl} + \text{ND}_4\text{OD} + \text{PdCl}_2 + \text{LiOD/D}_2\text{O}$ co-deposition system. No excess power was measured in the corresponding H_2O control study.

Shuttle reactions have been proposed by NRL as an explanation for excess power in co-deposition systems [10]. In our studies, neither calorimetric nor electrochemical measurements have detected any shuttle reactions involving nitrates or nitrites. Similar results were obtained in studies of chlorates [14]. Furthermore, no excess power was observed for the $\text{NH}_4\text{Cl} + \text{NH}_4\text{OH} + \text{PdCl}_2 + \text{LiOH/H}_2\text{O}$ control co-deposition system. Another paper in preparation [16] will focus on co-deposition experiments and the absence of any experimental evidence for the shuttle reaction hypothesis for excess power in co-deposition systems.

Acknowledgements

Financial help in the design and construction of these new calorimeters is acknowledged by M.H.M. from an anonymous fund at the Denver Foundation via Dixie State College. Steve Tetz of Wolf Creek, Oregon performed the actual construction of the four calorimetric cells. Portions of this work were presented at ICCF-15 in Rome, Italy [17].

Appendix A1. Calorimetric Equations

Treating the isoperibolic calorimetric cell as the system of interest, the First Law of Thermodynamics expressed as power (J/s or W) becomes

$$P_{\text{calor}}(t) = P_{\text{EI}}(t) + P_{\text{H}}(t) + P_{\text{X}}(t) + P_{\text{gas}}(t) + P_{\text{R}}(t) + P_{\text{C}}(t) + P_{\text{W}}(t). \quad (\text{A.1})$$

By definition, P_{calor} is the power for the calorimetric cell, P_{EI} the electrochemical power, P_{H} the internal heater power, P_{X} any anomalous excess power, P_{gas} the power carried away by the gas stream exiting the open cell ($\text{D}_2, \text{O}_2, \text{D}_2\text{O}$ vapor), P_{R} the net power transferred by radiation between the cell and water bath, P_{C} is the power transferred by conduction, and P_{W} represents the rate of pressure-volume work by the generated electrolysis gases (D_2, O_2). Because both the cell temperature and cell voltage change with time during electrolysis, most of the terms in Eq. (A.1) also vary with the time (t). The internal heater power, P_{H} , will be zero except for the time period between turning the heater on (t_1) and off (t_2). Typical values for P_{H} , when on, are either 0.2000 W or 0.2500 W. There are often time periods where P_{X} is zero or constant. As usual in thermodynamics, positive quantities represent power added to the system (calorimetric cell) and negative quantities represent power given off by the system to the surroundings.

The mathematical expressions for the terms in Eq. (A.1) are as follows:

$$P_{\text{calor}} = C_p M (dT/dt), \quad (\text{A.2})$$

$$P_{\text{EI}} = (E - E_H) I, \quad (\text{A.3})$$

$$P_{\text{gas}} = -(I/F) \{ [0.5C_{p,D_2} + 0.25C_{p,O_2} + 0.75(\mathbf{P}/(\mathbf{P}^* - \mathbf{P}))C_{p,D_2O(g)}] \Delta T + 0.75(\mathbf{P}/(\mathbf{P}^* - \mathbf{P}))L \}, \text{ where } \Delta T = T - T_b, \quad (\text{A.4})$$

$$P_R = -k_R f(T), \text{ where } f(T) = T^4 - T_b^4, \quad (\text{A.5})$$

$$P_C = -k_C (T - T_b), \quad (\text{A.6})$$

$$P_W = -RT(dn_g/dt) = -RT(0.75I/F). \quad (\text{A.7})$$

For this new isoperibolic calorimeter, the heat transfer will be mostly by conduction, hence P_R will be small and negligible compared with P_C .

The pressure terms in Eq. (A.4) are bolded to minimize confusion with any power terms. Under normal constant current (I) operation, the terms T , E , ΔT , and \mathbf{P} will vary with time, t . The change of the cell temperature with time, as given by P_{calor} in Eq. (A.2), makes Eq. (A.1) a nonlinear, inhomogeneous differential equation. Although this differential equation can be used directly, numerical integration yields more accurate results (see Fig. 2). The P_{calor} term is obviously larger when the cell temperature is changing more rapidly such as when D_2O is replenished or when the internal heater is turned on (t_1) or off (t_2). The small progressive decrease with time for the cell temperature (Table 2) is due to the progressive increase of the electrolyte concentration due to electrolysis resulting in an increasing ionic conductance and hence a decreasing cell voltage and input power (Eq. (A.3)) as shown in Table 2.

The most complicated term, P_{gas} , is generally small except when the cell temperature exceeds 70°C. The electrolysis reaction



consumes 0.5 mol of D_2O and produces 0.5 mol of D_2 gas and 0.25 mol of O_2 gas per Faraday, F (96485.3415 C mol⁻¹). The 0.75 mol total of electrolysis gases generated per Faraday also carry away D_2O vapor due to the equilibrium vapor pressure of D_2O in the cell, $\mathbf{P} = \mathbf{P}_{D_2O(g)}$. Using Dalton's law of partial pressures, the moles of $D_2O(g)$ carried away per Faraday are given by

$$\text{moles } D_2O(g) = 0.75(\mathbf{P}/(\mathbf{P}_{D_2} + \mathbf{P}_{O_2})) = 0.75(\mathbf{P}/(\mathbf{P}^* - \mathbf{P})), \quad (\text{A.9})$$

where the gas pressure within the cell, \mathbf{P}^* , is expressed by

$$\mathbf{P}^* = \mathbf{P}_{D_2(g)} + \mathbf{P}_{O_2(g)} + \mathbf{P}_{D_2O(g)} \quad (\text{A.10})$$

and is close to the atmospheric pressure for this open system. This \mathbf{P}^* term dictates the monitoring of the atmospheric pressure for highly accurate calorimetric measurements, but this has not been done by most laboratories. The largest term for P_{gas} results from the large enthalpy of vaporization of D_2O , $L = 41678.9 \text{ J/mol}$ at 101.42°C. Therefore, simpler versions of Eq. (A.4) are often used such as

$$P_{\text{gas}} = -(0.75I/F)(\mathbf{P}/(\mathbf{P}^* - \mathbf{P}))[(C_{p,D_2O(g)} - C_{p,D_2O(l)})\Delta T + L]. \quad (\text{A.11})$$

Assuming $I = 0.2000 \text{ A}$ and $T_b = 22.00^\circ\text{C}$, the P_{gas} term is -5.6489 mW at $T = 40.00^\circ\text{C}$ and increases to -57.8253 mW at $T = 80.00^\circ\text{C}$. The term involving the enthalpy of vaporization (L) contributes -4.9103 mW (86.92%) and -52.9857 mW (91.63%), respectively, at these two cell temperatures. The electrolysis of D_2O in the calorimeter causes the equivalent moles (M) to change with time

$$M = M^{\circ} - (1 + \beta) \gamma I t / 2F, \quad (\text{A.12})$$

where I is the constant current, β is the fraction of D_2O lost by evaporation, and γ is the current efficiency for electrolysis. Thus, a more exact expression used in earlier publication by Fleischmann and Pons is

$$P_{\text{calor}} = C_p d/dt(M\Delta T) = C_p M(d\Delta T/dt) + C_p \Delta T(dM/dt) \quad (\text{A.13})$$

or equivalently

$$P_{\text{calor}} = C_p [M^\circ - (l + \beta)\gamma It/2F](d\Delta T/dt) - C_p \Delta T(l + \beta)\gamma I/2F, \quad (\text{A.14})$$

where $\Delta T = T - T_b$. For constant T_b , $d\Delta T/dt = dT/dt$. Except for small cells and large currents, the simpler Eq. (A.2) is adequate.

In chemical kinetics, the differential equations for the rates of the reactions are seldom used because the integrated expressions are much more accurate. The use of numerical integration of the calorimetric data also results in greater accuracy. Integrals can be numerically evaluated by using the mean value of the function and the integration limits. Mathematically,

$$\int_a^b f(x)dx = (b - a)\langle f(x) \rangle, \quad (\text{A.15})$$

where a and b are the integration limits and $\langle f(x) \rangle$ is the mean value of the function. Other approximate integration methods can also be used such as Simpson's Rule or the Trapezoidal Rule, but only Eq. (A.15) is, strictly speaking, correct in that it agrees with the mathematical definition of an integral. The Trapezoidal Rule, however, allows integration around the discontinuities at $t = t_1$ and $t = t_2$. The integrals of power over selected time periods give units of energy (J).

The required heat capacities at constant pressure (C_p), enthalpy of vaporization of D_2O (L), the vapor pressure of D_2O (\mathbf{P}), and the thermoneutral potential (E_H) are available from thermodynamic tables at 25°C (298.15 K) and standard pressure. The temperature dependence of these calorimetric parameters at standard atmospheric pressure can be calculated from the following equations where T is the Kelvin temperature ($^\circ\text{C} + 273.15$).

$$L = 85263.9 - 173.429T + 0.2586T^2 - 1.91913 \times 10^{-4}T^3 - 1805569T^{-1} \quad (\text{in J/mol}^{-1}), \quad (\text{A.16})$$

$$E_H = 1.5318346 - 0.0002067(T - 273.15) \quad (\text{in V}), \quad (\text{A.17})$$

$$\begin{aligned} \log \mathbf{P} = & 35.47686 - 3343.93T^{-1} - 10.9 \log T + 0.0041645T \\ & + 9.14056/(197.397 - T) \quad (\mathbf{P} \text{ in atm}), \end{aligned} \quad (\text{A.18})$$

$$\begin{aligned} C_{p,\text{D}_2\text{O}_{(l)}} = & 200.13 - 495.9 \times 10^{-3}T + 573.07 \times 10^{-6}T^2 \\ & - 16.765 \times 10^5 T^{-2} \quad (\text{in J mol}^{-1}\text{K}^{-1}), \end{aligned} \quad (\text{A.19})$$

$$\begin{aligned} C_{p,\text{D}_2\text{O}_{(g)}} = & 26.7006 + 21.2897 \times 10^{-3}T + 2.66774 \times 10^{-6}T^2 \\ & + 1.2907 \times 10^5 T^{-2} \quad (\text{in J mol}^{-1}\text{K}^{-1}), \end{aligned} \quad (\text{A.20})$$

$$\begin{aligned} C_{p,\text{D}_2\text{(g)}} = & 28.9778 - 1.49226 \times 10^{-3}T + 4.14779 \times 10^{-6}T^2 \\ & + 0.26544 \times 10^5 T^{-2} \quad (\text{in J mol}^{-1}\text{K}^{-1}), \end{aligned} \quad (\text{A.21})$$

$$\begin{aligned} C_{p,\text{O}_2\text{(g)}} = & 23.1436 + 18.2628 \times 10^{-3}T - 6.605 \times 10^{-6}T^2 \\ & + 1.2118 \times 10^5 T^{-2} \quad (\text{in J mol}^{-1}\text{K}^{-1}). \end{aligned} \quad (\text{A.22})$$

At a typical cell temperature of 60°C (333.15 K) and standard pressure, these calculated values are $L = 43672 \text{ J mol}^{-1}$, $E_H = 1.5194V$, $\mathbf{P} = 0.18317 \text{ atm}$, $C_{p,D_2O_{(l)}} = 83.420 \text{ J mol}^{-1}\text{K}^{-1}$, $C_{p,D_2O_{(g)}} = 34.660 \text{ J mol}^{-1}\text{K}^{-1}$, $C_{p,D_2O_{(g)}} = 29.180 \text{ J mol}^{-1}\text{K}^{-1}$, and $C_{p,O_{2(g)}} = 29.587 \text{ J mol}^{-1}\text{K}^{-1}$.

Equations (A.16)–(A.22) look daunting, but they can be handled readily by computers (Excel). These equations, along with Eqs. (A.2)–(A.7), were always used with the China Lake calorimetry [18].

Appendix A2. List of Symbols

C_p	Heat capacity at constant pressure, $\text{JK}^{-1}\text{mol}^{-1}$
E	Cell potential, V
E_H	Thermoneutral potential, V
F	Faraday constant, 96 485.3415 C mol $^{-1}$
I	Cell current, A
k_C	Conductive heat transfer coefficient, WK^{-1}
k'_C	Pseudo-conductive heat transfer coefficient, WK^{-1}
k_R	Radiative heat transfer coefficient, WK^{-4}
L	Enthalpy of evaporation for D_2O , J mol^{-1}
n_g	Moles of electrolysis gases, mol
M	Water equivalent of the calorimetric cell, mol
P	Partial pressure of D_2O , Pa
P^*	Atmospheric pressure, Pa
P_C	Power transferred by conduction, W
P_{calor}	Rate of enthalpy change within the calorimeter, W
P_{EI}	Power input due to electrolysis, W
P_{gas}	Rate of enthalpy transport by the gas stream, W
P_H	Power input due to the calibration heater, W
P_R	Power transferred by radiation, W
P_W	Rate of pressure–volume work by the generated gases, W
P_X	Excess power generated, W
R	Gas constant, $8.314472 \text{ JK}^{-1} \text{ mol}^{-1}$
T_b	Temperature of water bath, K
T	Temperature of cell, K
ΔT	$T - T_b$, K
$f(T)$	$T^4 - T_b^4$, K^4
β	Fraction of D_2O lost by evaporation, dimensionless
γ	Current efficiency for electrolysis, dimensionless

References

- [1] M.H. Miles, K.H. Park, D.E. Stillwell, *J. Fusion Energy* **9** (1990) 333.
- [2] M.H. Miles, K.H. Park, D.E. Stilwell, *J. Electroanal. Chem.* **296** (1990) 409.
- [3] M.H. Miles, B.F. Bush, D.E. Stilwell, *J. Phys. Chem.* **98** (1994) 1948.
- [4] M.H. Miles, *J. Electroanal. Chem.* **482** (2000) 55.
- [5] M.H. Miles, M. Fleischmann, M.A. Imam, Calorimetric Analysis of a Heavy Water Electrolysis Experiment Using a Pd-B Alloy Cathode, NRL/MR/6320-01-8526, March 26, 2001.
- [6] M. Fleischmann, S. Pons, M.W. Anderson, L.J. Li, M. Hawkins, *J. Electroanal. Chem.* **287** (1990) 293.

- [7] M. Fleischmann, M.H. Miles, *Proceeding of ICCF-10*, P.L. Hagelstein, S.R. Chubb (eds.), Cambridge, 2003, pp. 247–268.
- [8] M.H. Miles, M. Fleischmann, *Low-Energy Nuclear Reactions Sourcebook*, J Marwan, S.B. Krivit (eds.), ACS Symposium Series, Vol. 998, 2008, pp. 153–171.
- [9] M.H. Miles, M. Fleischmann, Proceedings of ICCF-14, Washington DC, 2008, submitted.
- [10] D.A. Kidwell, K. Grabowski, NRL, Email communications. Note: We have not been able to obtain any experimental evidence from NRL that supports their claim for shuttle reactions, 2009.
- [11] F.V. Andrade, L.J. Deiner, H. Varela, J.F.R. de Castro, I.A. Rodrigues, F.C. Nart, *J. Electrochem. Soc.* **154** (2007) F159.
- [12] M.H. Miles, J.R. Alston, A.J. Davenport, A.A. Grumet, Low Melting Electrolytes for Thermal Batteries, SBIR Phase I Final Report, October 31, 2007.
- [13] M.H. Miles, Chloride-Free Thermal Batteries Using Molten Nitrate Electrolytes, U.S. Patent No. 7,629,075 B2, December 8, 2009.
- [14] M.H. Miles, *ICCF-15 Proceedings*, Rome, Italy, ENEA (ed.), 2009, submitted.
- [15] D. Knies, NRL, E-mail communication, 2009.
- [16] M.H. Miles, Chemical and Electrochemical Studies of Co-Deposition Systems in H₂O and D₂O, American Chemical Society Meeting, San Francisco, CA, March 21–25, 2010, in Preparation.
- [17] M.H. Miles, M. Fleischmann, *ICCF-15 Proceedings*, Rome, Italy, ENEA (ed.), 2009, submitted.
- [18] M.H. Miles, B.F. Bush, K.B. Johnson, Anomalous Effects in Deuterated Systems, NAWCWPNS TP 8302, September, 1996.



Research Article

Heat Evolution from Pd Nano-powders Exposed to High-pressure Hydrogen Isotopes and Associated Radiation Measurements

Akira Kitamura ^{*}, Yu Sasaki, Yuki Miyoshi and Akira Taniike

Division of Marine Engineering, Graduate School of Maritime Sciences, Kobe University, Higashinadaku, Kobe 658-0022, Japan

Akito Takahashi, Reiko Seto and Yushi Fujita

Technova Inc., Uchisaiwaicho 1-1-1, Chiyodaku, Tokyo, Japan

Abstract

Using a twin system for hydrogen absorption, experiments on heat evolution and charged particle generation by D₂ (H₂) gas absorption in nano-sized Pd powders were done for the 0.1 μ m. Pd powder, the Pd-black, and the mixed oxides of Pd-Zr, Pd-Ni-Zr and Ni-Zr. It has been found that the D(H)/Pd loading ratio and the absorption energy per D (H) is an increasing function of fineness of the sample surface. The Pd-Zr oxide nano-composites showed anomalously large energies of hydrogen isotope absorption as well as large loading ratio in the phase of deuteride/hydride formation. Although the samples were deteriorated by the repeated baking-hydrogenation cycles, an artificial oxidation of the PZ and the PNZ samples recovered the excellent original performances, and gave hydride formation energies of 1.5–2.3 eV/D and 1.5–2.0 eV/H, which are anomalously high compared with values for bulk Pd metal. In the second phase after the deuteride formation, the Pd-Zr and Pd-Ni-Zr oxide composites charged exclusively with D₂ sometimes gave significantly positive output, which should be subjected to repeated investigation. Nuclear reaction products including energetic charged-particles for a possible cause of the phenomena were examined using a variety of nuclear diagnostics. © 2011 ISCMNS. All rights reserved.

Keywords: Anomalous heat, Charged particle measurement, Deuterium absorption, D/Pd loading ratio, Forced oxidation, Isotope effect, Pd-Zr nano-powder, Recovery of performance

PACS: 89.20.-a

1. Introduction

Arata and Zhang recently reported that highly pure D₂ gas charging of Pd nanopowders in the form of Pd/ZrO₂ nano-composite induced significantly higher temperatures inside the reactor vessel than at the outside wall continuing for more than 50 h, while runs with H₂ gas showed almost no temperature difference [1]. To verify that the excess heat

^{*}E-mail: kitamura@maritime.kobe-u.ac.jp

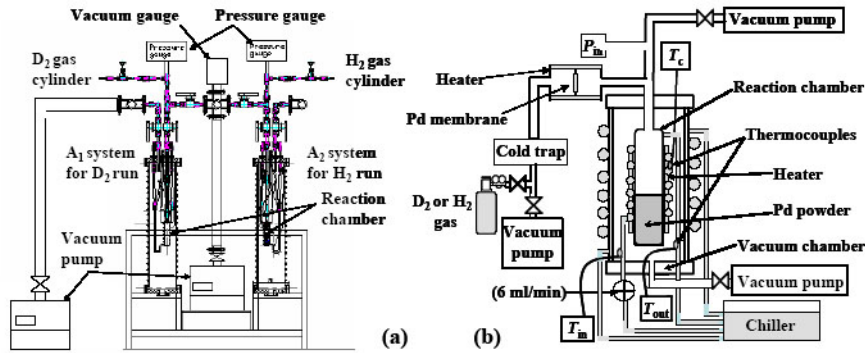


Figure 1. (a) Reduced view of the $A_1 \cdot A_2$ twin system, and (b) functional view of A_1 used in the early stage of the present research. The Pd membrane filter for flow rate control is replaced by a mechanical needle valve, ‘Super Needle’.

originated in a nuclear process, a quadrupole mass spectrometer was employed to show the existence of ${}^4\text{He}$ as nuclear ash in the vessel and in the powder after the charging. The charging system is a sophisticated, yet simplified, version of the previous-generation DS reactor [2]. Successful replications using systems similar to the DS reactor with Pd-black have been reported [3,4].

However, few reports on the replication experiments producing heat and ${}^4\text{He}$ with the new configuration have published yet in spite of extreme importance of the phenomenon. It is crucial to confirm the phenomenon of heat and ${}^4\text{He}$ generation with fully quantitative reliability.

We have constructed an experimental system to replicate the phenomenon and to investigate the underlying physics. The system is composed of two identical reaction chambers, an $A_1 \cdot A_2$ twin system, equipped with calorimetry setups, and a B-system for nuclear diagnostics. We report here the results of heat measurements as well as charged particle measurements under deuterium/hydrogen absorption by a variety of Pd nano-powders, covering our former results [11–13] and newer results.

2. Experimental Apparatus for Calorimetry

The D_2/H_2 absorption system is composed of two identical chambers (an $A_1 \cdot A_2$ twin system): one for a D_2 gas foreground run, and the other for H_2 gas background run. As shown in Fig. 1, each part has an inner reaction chamber containing Pd powder and an outer chamber that is evacuated to provide thermal insulation for calorimetry. A sheath heater and a cooling water pipe made of copper are wound on the outer surface of the reaction chamber for baking the sample powder and for flow calorimetry to estimate the heat production rate, respectively. A pair of thermocouples is provided for the flow calorimetry by measuring the temperature difference between the inlet and the outlet of the cooling water.

The D_2 gas is nominally 99.5% pure and the H_2 is 99.998% pure. In the early stage of the present research, flow rate control of D_2/H_2 gas purified through a liquid-nitrogen cold trap was made with a Pd membrane filter which also serves as an additional purifier. The Pd membrane (0.2 mm-t, 99.95%) separates the evacuated reaction chamber (50 cm^3) and the gas reservoir filled with D_2/H_2 at 1 MPa. The gas permeation rate is controllable between 0.1 and 25 sccm by varying the membrane temperature from room temperature to 900 K. However, it was replaced in the latter half of the experiments by a mechanical needle valve, ‘Super Needle’, because the precision of adjustment of the membrane temperature was found to be rather poor.

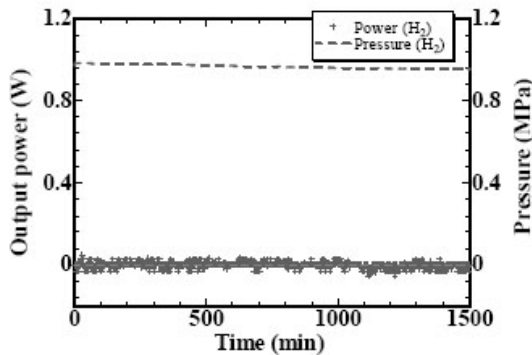


Figure 2. Blank run with no sample powder.

In expectation of occurrence of some nuclear phenomena, a neutron dose rate meter and a scintillation probe for γ -ray detection are located just outside the outer chambers. All parameters measured are stored in a PC with an acquisition period of 1 min.

As a calibration of the flow calorimeter, we measured the heat recovery rate under a variety of conditions; with input power of 1, 3, 6 and 10 W, and D₂ gas pressure of 0, 0.1, 0.3 and 1.0 MPa in the reaction chamber. The coolant flow rate was 6 cm³/min in all cases. The heat recovery rate was found to be almost independent of the pressure and the input power, and the averaged value is $(63.1 \pm 5.8)\%$. Temperature response to a stepwise variation of the input power was found to be expressed as a simple exponential function with a time constant of 5.2 min.

We examined temperature uncertainty and drift, with no sample powder put in the A₁ chamber filled with H₂ gas at a pressure of 1 MPa. The inlet–outlet temperature difference and the output power deduced from it showed short-term fluctuation as shown in Fig. 2. If we regard an experimental error in the present system as the standard deviation of the longitudinal data, the error or the uncertainty for the output power and the integrated output energy measured for the A₁ · A₂ system is evaluated to be 0.014 W and 0.83 kJ for 1000-min acquisition. In the prototype system A₀, which had the larger time constant and smaller sensitivity of heat measurement, and was used in the first stage experiments with the 0.1- μ m ϕ Pd powder and the Pd-black [5], a temperature drift observed sometimes resulted in the larger error of 4.0 kJ for 1000-min run.

In the following, the run number is designated by “G-PN#M”, with G, P, N and M being the gas species, the powder species, powder ID, and the number of repeated use, respectively. The powder species include PP (Pd powder with particle diameter of 0.1 μ m and a purity of 99.5%), PB (Pd-black with a particle size of “300 mesh” and purity of 99.9%), PZ (mixed oxides of Pd-Zr), PNZ (mixed oxides of Pd-Ni · Zr) and PN (mixed oxides of Ni-Zr). For example, “D-PB2#3” represents the third absorption run with D₂ using a Pd-black sample “2” following evacuation and baking after two cycles of evacuation-baking-absorption. All D₂/H₂ gas absorption runs described below were conducted at room temperature.

Three kinds of mixed oxide samples, PZ, PNZ and NZ, were fabricated by Santoku Corporation, Kobe, Japan. The physical properties of these samples are tabulated in Table 1. The PZ samples have an average particle size of 7.7–20 μ m, a specific surface area of 37–41 m²/g, and an average Pd grain size of 10.7–8.3 nm. Since X-ray diffraction measurements of the PZ sample have revealed presence of PdO, we have to assume that 10 g of the sample contains 3.0–3.3 g of Pd depending on the degree of oxidation of Pd. In the sample PNZ, substantial part of Pd is replaced by Ni also in the form of NiO with a molar fraction of about 25%, while Pd is completely replaced by Ni with a larger

Table 1. Physical properties of Pd-Ni-Zr oxide samples prepared by Santoku Corp. The fraction depends on the degree of oxidation of Pd, i.e., the ratio of PdO to Pd.

Sample name	PZ	PNZ	NZ
Lot number	081030	090529-1	090609-1
	090609-2		
Molar fraction	Pd	0.346	0.105
	Ni		0.253
	Zr	0.654	0.642
	O	1.31–1.65	1.54–1.64
Weight fraction	Pd	0.314–0.299	0.103–0.101
	Ni		0.135–0.133
	Zr	0.508–0.485	0.537–0.529
	O	0.178–0.215	0.537–0.237
Average particle size (mm)	7.7	20.3	23.7
Specific surface area (m ² /g)	37.1	41.3	35.2
Average grain size (nm)	10.7	8.3	7.4
			(Ni) 23.2

grain size of 23 nm in the sample NZ. In the following analysis of the data for the PZ samples, we use an average value of 0.314 for the weight fraction of Pd, which introduces a systematic error of about 5% to the values of the loading ratio D(H)/Pd and the first phase absorption energy E_{1st} which is considered to be equal to the heat of solution or the hydride formation energy Q_D (Q_H). In the present paper the word “hydride” stands for the deuteride and the hydride in the customary sense.

3. Results of Calorimetry

3.1. 0.1- μ m ϕ Pd powder (PP)

First of all, we describe absorption runs using the A₀ system for 5 g of commercially available 0.1- μ m ϕ Pd powder. The reaction chamber filled with the powder was evacuated and heated for baking at 430 K. Then highly pure D₂ or H₂ gas was introduced into the reaction chamber through the Pd membrane filter. The results for the case of D₂ and H₂ absorption are compared in Fig. 3(a). After the gas is introduced, pressure does not begin to rise for a while. During this phase (the first phase) the Pd powder absorbs almost all of the D₂ (H₂) gas atoms as they flow in, and heat is released as a result of adsorption and formation of deuterides (hydrides). After about 30 min, the powder almost stops absorbing gas; the gas pressure begins to rise, and the heat release from deuteride (hydride) formation subsides. This is the beginning of the second phase, and the gas flow rate in the first phase is evaluated from the rate of the pressure increase. From the flow rate multiplied by the duration of the first phase, loading is estimated to reach PdD_{0.46} (PdH_{0.45}). The loading ratios, i.e., H(D)/Pd values, might be smaller by about 30% than those evaluated at the final pressure of 1 MPa, since the pressure is still low at this moment. This possible underestimation of the loading ratio would lead to overestimation of the first phase absorption energy E_{1st} calculated as follows by the same amount.

The output power is integrated over the first phase to give the output energies of 0.10 kJ/g-Pd(D) and 0.08 kJ/g-Pd(H), which are divided by the loading ratio of 0.46 and 0.45 to give the first phase absorption energy E_{1st} or the hydride formation energy Q_D of 0.24 eV/atom-D and Q_H of 0.20 eV/atom-H, respectively. The values appear to be somewhat larger than those found in the literature [6–10]. However, they are consistent with each other, when we take into account that the differential heat of solution is a decreasing function of the loading ratio; $Q_H = 0.15, 0.12, 0.070$, and 0.061 eV/H for H/Pd ratio of 0.5, 0.55, 0.6 and 0.65 [9,10]. The difference between D and H, the isotope effect, is rather large, but is not considered to be anomalous, since we find $Q_D/Q_H = 1.25$ in [9]. The difference is even considered to be meaningless in view of the experimental error shown by the values following ‘±’ in the fifth column.

On the other hand, the output energy in the second phase, i.e., the output power integrated over the second phase

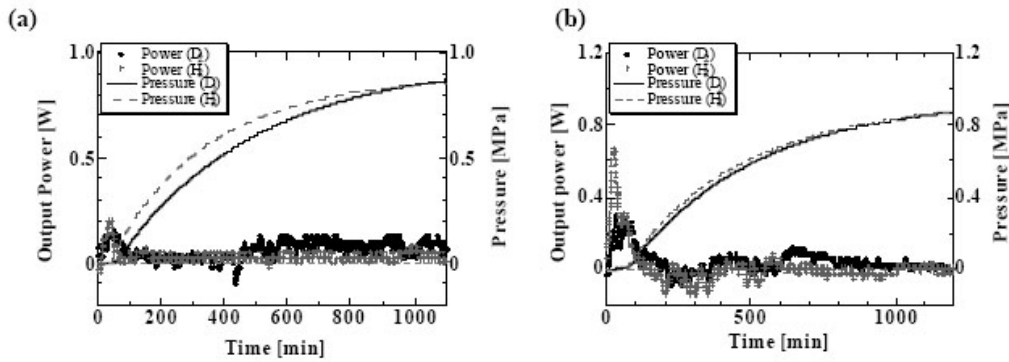


Figure 3. Evolution of heat and pressure in the vessel after pumping D_2 gas or H_2 gas; (a) $0.1\text{-}\mu\text{m}\phi$ Pd powder (D-PP1#1 and H-PP2#1), (b) 300-mesh Pd-black (D-PB1#1 and H-PB2#1).

with duration of 1,400 min, is smaller than the experimental error mentioned above, and is therefore meaningless. The results are summarized in Table 2, which includes those for the Pd-black sample described below.

3.2. 300-Mesh Pd-black (PB)

The second kind of the sample tested is commercially available, 300-mesh Pd-black whose surface has a kind of nano-scale fractal structure finer than the $0.1\text{-}\mu\text{m}\phi$ Pd powder. The performance of the Pd-black absorption of D_2 using the A₀ system is compared with that of H_2 in Fig. 3(b). It is very interesting to note that: (1) much higher loading to $PdD_{0.82}$ or $PdH_{0.78}$ is realized, and (2) the output energies in the first phase, $E_{1st} = (0.68\pm 0.12)$ eV/atom-D and (0.63 ± 0.11) eV/atom-H, are 2–3 times larger than those for the $0.1\text{-}\mu\text{m}\phi$ Pd powder and those found in the literature [6–10]. On the other hand, the output energy of 8.3 ± 4.5 kJ (2.6 ± 1.4 kJ/g-Pd) in the second phase of D_2 absorption appears to be larger than that in the case of H_2 . The difference, however, is only marginal compared with the above-mentioned error due to the temperature drift of 5.5 kJ in the present case.

Using the improved twin system A₁·A₂, we compared the performance of the Pd-black sample PB3 with a prolonged duration of the second phase of 4,500 min, which was subjected to repeated use with the sample baking before absorption at 440 K for 3 h (No. 2), or at 570 K for 1 h (No. 3). The results are shown in the sixth row through the eighth in Table 2.

Table 2. Comparison of absorption runs for the $0.1\text{-}\mu\text{m}\phi$ Pd powder (PP), and the 300-mesh Pd-black (PB).

Run	Weight (g)	Pd weight (g)	First phase				Second phase	
			Flow rate (sccm)	Specific output energy E_1 (kJ/g-Pd)	D/Pd or H/Pd	E_{1st} per D or H atom (Q_D or Q_H) (eV)	Specific output energy E_2 (kJ/g-Pd)	
D-PP1#1	5	5	3.5	0.10 ± 0.07	0.46	0.24	0.52 ± 0.83	
D-PP1#2	5	5	4.3	0.10 ± 0.05	0.43	0.26	0.79 ± 0.88	
H-PP2#1	5	5	6.8	0.08 ± 0.003	0.45	0.20	0.53 ± 0.8	
D-PB1#1	3.2	3.2	3.5	0.54 ± 0.10	0.85	0.70	2.6 ± 1.4	
H-PB2#1	3.6	3.6	5.6	0.45 ± 0.08	0.78	0.63	-0.62 ± 1.3	
D-PB3#1	20	20	2.9	0.47 ± 0.06	0.78	0.66	0.06 ± 0.02	
D-PB3#2	20	20	0.8	0.17 ± 0.03	0.23	0.82	0.17 ± 0.13	
H-PB4#2	20	20	1.9	0.16 ± 0.01	0.22	0.80	0.68 ± 0.23	

First we notice that the first run (D-PB3#1) has essentially the same D/Pd ratio and the output energy E_{1st} as that for the A_0 system. Second, the repeated use retains almost the same or even higher output energy E_{1st} in spite of the significantly smaller D(H)/Pd ratio. This interesting fact could be related to some structural change of the sample. The SEM photograph of the sample indicates an image of clumping-together of the sample flakes and disappearance of the fine structure on the scale of several tens of nm. This point will be discussed in detail later elsewhere. As for the second phase, we have little to discuss, when we take into account that they are comparable to the error of 4.0 kJ/1000-min mentioned above for the A_0 system.

3.3. Mixed oxides of Pd-Zr (PZ)

Now we describe the performance of the mixed oxides of Pd-Zr that are thought to have an even finer mesoscopic structure. The results of fourteen runs using PZ samples are summarized in Table 3. These include runs with virgin PZ samples (No. 1) and used PZ samples (Nos. 2 and 3). Using the A_1 - A_2 twin system, the runs H-PZ(2n) No. 1 were performed simultaneously with D-PZ(2n – 1) No. 1, where $n = 1, 2, 3$ and 5. The A_1 subsystem was used for D-PZ1, D-PZ3, D-PZ9 and H-PZ6, and the A_2 subsystem for H-PZ2, H-PZ4, H-PZ10 and D-PZ5. Note that the subsystem was permuted for D-PZ5 and H-PZ6 intentionally to confirm that which reaction chamber to choose does not matter. The PZ sample used was 10 g or 14 g, and the baking temperature was 570 K for 3 h. The output energy in the second phase is the power integrated over 1,600 min. Examples of the evolution of the output power and the pressure for runs D-PZ1#1 and H-PZ2#1 are shown in Fig. 4.

To deduce the values of D/Pd (H/Pd), we have assumed that the pressure change is caused solely by consumption of D_2 (H_2) gas due to the formation of PdD (PdH). As mentioned earlier, some fractions of Pd atoms in the Pd-Zr oxide samples may be in the form of PdO. X-ray diffraction measurements after D (H) absorption experiments have revealed almost perfect reduction to Pd to replace D_2 (H_2) by D_2O (H_2O) molecules. If the D_2O (H_2O) molecules happen to condense into the liquid phase to give almost no contribution to the gas pressure, the reduction of PdO could lead to overestimation of the amount of the D_2 (H_2) gas absorbed by Pd, and therefore of the values of D/Pd (H/Pd). However, the sample is in vacuum, and therefore the water molecules will remain in the gas phase at least until we evaluate the

Table 3. Comparison of absorption runs for the Pd-Zr nano-composite (PZ).

Run	Weight (g)	Pd weight (g)	First phase		D/Pd or H/Pd	Second phase	
			Flow rate (sccm)	Specific output energy E_1 (kJ/g-Pd)		E_{1st} per D or H atom (eV)	Specific output energy E_2 (kJ/g-Pd)
D-PZ1#1	10	3.14	1.76	2.30±0.06	1.03	2.47	2.09±0.90
H-PZ2#1	10	3.14	2.29	1.17±0.04	0.95	1.35	-1.69±0.91
D-PZ3#1	10	3.14	1.85	2.10±0.06	1.03	2.26	2.11±0.80
H-PZ4#1	10	3.14	2.93	1.63±0.03	0.82	2.19	-0.11±0.80
D-PZ3#2	10	3.14	1.66	0.05±0.01	0.28	0.20	2.49±0.67
H-PZ4#2	10	3.14	2.79	0.20±0.02	0.29	0.77	0.62±0.67
D-PZ3#3	10	3.14	1.69	0.10±0.02	0.24	0.48	0.21±0.40
H-PZ4#3	10	3.14	2.99	0.17±0.01	0.25	0.73	0.11±0.40
D-PZ5#1	10	3.14	2.02	2.28±0.05	1.00	2.52	0.40±0.48
H-PZ6#1	10	3.14	6.23	2.34±0.03	1.35	1.91	-0.08±0.48
D-PZ5#3	10	3.14	9.93	0.16±0.01	0.24	0.74	-0.50±0.48
H-PZ6#3	10	3.14	10.69	0.27±0.01	0.29	1.02	-0.07±0.48
D-PZ9#1	14	4.41	6.42	2.33±0.02	1.34	1.92	0.87±0.34
H-PZ10#1	14	4.41	20.49	2.18±0.01	0.97	2.48	0.87±0.34
D-PZ#1 avrg	—	—	—	2.25±0.10	1.10±0.16	2.29±0.27	1.37±0.87
H-PZ#1 avrg	—	—	—	1.83±0.53	1.03±0.23	1.98±0.48	-0.25±1.06

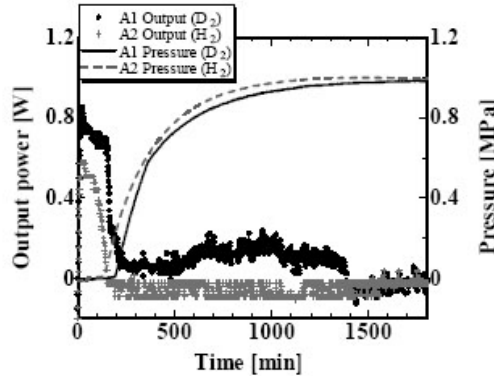


Figure 4. Evolution of heat and pressure in the vessel after pumping D₂ gas or H₂ gas for mixed oxides of Pd and Zr (D-PZ1#1 and H-PZ2#1).

rate of pressure increase, which, multiplied by the duration of the first phase, is used to calculate the amount of D₂ (H₂) gas absorbed into the sample. Therefore, there is little chance to overestimate the amount of the gas absorbed for the formation of PdD(H), since the same volume of D₂O (H₂O) is liberated in the gas phase in exchange for consumption of D₂ (H₂) for the PdO reduction.

To evaluate the values of Q_D or Q_H, we have to know the extent to which the Pd atoms are oxidized. For this purpose, assuming that a fraction x of the Pd atoms are oxidized, we examine reduction of PdO_x followed by production of x D₂O (x H₂O) and PdD_y (PdH_y). The total reaction energies are evaluated to be $(1.69x + Q_{Dy})$ eV/atom-Pd and $(1.63x + Q_{Hy})$ eV/atom-Pd, respectively. The values of Q_D and Q_H for the bulk Pd cited from the references [6–10] lie in the range from 0.2 to 0.7 eV. Since we do not know the values of x for the given samples, we leave E_{1st} in the seventh column in Table 3, and do not dare to obtain the values of Q_D and Q_H from the measured quantities for the moment. This point will be discussed later in this subsection.

We notice in Table 3 the following three facts in the first phase of the No. 1 runs, i.e., for virgin samples: (1) very large D/Pd (H/Pd) ratio of about 1.1 ± 0.2 (1.0 ± 0.2) that are even higher than those for the PB samples, (2) surprisingly large $E_{1st} = (2.3 \pm 0.3)$ eV (D) and (2.0 ± 0.5) eV (H) on average, and (3) a modest isotope effect in E_{1st} consistent with those for $0.1\text{-}\mu\text{m}\phi$ powder and Pd-black; the difference does not exceed the error range determined from the standard deviations in contrast to our former report [11–13] which does not include the runs D(H)-PZ9(10) No. 1.

On the other hand, for used samples, i.e., in the runs with the run numbers 2 and 3, we observe smaller D/Pd (H/Pd) ratios which are essentially the same as those for the used PB samples mentioned in the preceding subsection, and E_{1st} values similar to those for PB and PP samples with a few exceptions. It is inferred that these are due to the clumping-together effect mentioned above for the PB samples. TEM photographs of the samples taken by the courtesy of the Nuclear Science and Engineering Institute and Particulate Systems Research Center at the University of Missouri-Colombia showed that the Pd nano-particles are bunched together to form clusters consisting of tens to hundreds of Pd nano-particles. The absorption–desorption or heating–cooling history of the sample might have a crucial effect on the hydrogen absorption characteristics.

We have anomalously large absorption energies and loading ratios in the present mesoscopic system of virgin Pd-Zr oxides. It should be mentioned here that we cannot assume large contribution of ZrO₂ to these quantities. This is because the NZ samples fabricated in the same way as the PZ samples absorb essentially no D₂ (H₂) gas, and there is no output energy, as described in the next subsection.

Next, to examine the contribution of PdO reduction to E_{1st} , the used PZ1 and PZ2 samples were artificially oxidized

Table 4. Artificial oxidation to find the D(H) absorption energy for the Pd-Zr nano-composite (PZ). It is assumed that the reaction proceeds via oxygen pickup from PdO_x followed by hydridation to PdD_y (PdH_y), i.e. $\text{PdO}_x + (x + y/2)\text{D}_2 \rightarrow x\text{D}_2\text{O} + \text{PdD}_y$, the absorption energy Q_D (Q_H) is calculated from the relationship; $E_{1\text{st},y} = Q_{\text{red},x} + Q_{D(H),y}$ (eV/Pd), where the reduction energy $Q_{\text{red}} = 1.69$ (1.63) eV for D (H) is assumed: (m), (c) and (a) mean “measured”, “calculated” and “assumed”, respectively.

Run	First phase						Second phase	Remarks
	Flow rate (sccm)	Specific output energy E_1 (kJ/g-Pd)	D/Pd or H/Pd (= y)	$E_{1\text{st}}$ per D/H atom (eV)	O/Pd (= x)	Q_D or Q_H (eV/D(H))		
D-PZ1#3	7.88	1.45±0.01	0.97 (m)	1.73 (m)	0.081 (m)	1.59 (c)	1.37±1.28	Artificially oxidized
H-PZ2#3	12.12	0.89±0.01	0.65 (m)	1.57 (m)	0.048 (m)	1.45 (c)	0.29±1.28	
D-PZ*#1 avrg	—	2.25±0.10	1.10 (m)	2.29 (m)	0.459 (c)	1.59 (a)	1.08±0.67	Q_D and Q_H assumed.
H-PZ*#1 avrg	—	1.83±0.53	1.03 (m)	1.98 (m)	0.334 (c)	1.45 (a)	-0.63 ± 1.34	

by keeping them in O_2 atmosphere. The sample vessel was initially filled with O_2 gas at a pressure of 0.1 MPa, and kept at a temperature of 470 K for 33 h without supplying additional O_2 gas into the closed vessel. Assuming that the samples had no oxygen before this process, the extent of the sample oxidation, i.e., x for PdO_x , was calculated from the pressure drop in the reaction vessel. The values of x were rather modest, below 10%, which are given in the sixth column in Table 4.

The D_2 (H_2) absorption runs after the oxidation, D-PZ1#3 and H-PZ2#3, showed substantial recovery of D(H)/Pd and $E_{1\text{st}}$, as shown in the upper two rows in Table 4. Since we know the values of x for these samples, we can eliminate the reduction energy from $E_{1\text{st}}$ to obtain the hydride formation energy, Q_D (Q_H). It is assumed here that the reaction proceeds via oxygen pickup from PdO_x followed by hydridation to PdD_y or PdH_y ; $\text{PdO}_x + (x + y/2)\text{D}_2 \rightarrow x\text{D}_2\text{O} + \text{PdD}_y$, or $\text{PdO}_x + (x + y/2)\text{H}_2 \rightarrow x\text{H}_2\text{O} + \text{PdH}_y$. The hydride formation energy Q_D (Q_H) is calculated from a relationship; $E_{1\text{st},y} = Q_{\text{red},x} + Q_{D(H),y}$ (eV/Pd), where the reduction energy $Q_{\text{red}} = 1.69$ (1.63) eV for D(H) is assumed. In the table, (m), (c) and (a) stand for “measured”, “calculated” and “assumed”, respectively. It is found that the hydride formation energies, $Q_D = 1.59$ eV and $Q_H = 1.45$ eV, are about twice as large as those for the PB samples, and about 6~7 times larger than for the PP samples or the published values for the bulk Pd.

Once we know Q_D (Q_H), we can estimate x for the PZ samples using the same relationship, under the assumption that the hydride formation energies Q_D and Q_H remain unchanged after the oxidation process. These are shown in the lower two rows in Table 4. We see that rather reasonable values of $x = 0.46$ –0.33 are obtained.

Finally, we examine the second-phase heat evolution. We have negative values for the specific output energy E_2 in some runs mainly using H_2 , as seen in Tables 2 and 3. This should be considered to be due to a possible baseline shift of the thermocouple signal. In contrast to the runs with H_2 , positive output signals exceeding the error range have been observed in several runs with D_2 , as typically shown in Fig. 4. This implies that some nuclear process could be involved, although the values are only marginal in view of the negative value observed in H-PZ2#1. These points should be subjected to further investigation.

3.4. Mixed oxides of Pd-Ni-Zr (PNZ) and Ni-Zr (NZ)

Next, the performances of the mixed oxide samples PNZ and NZ are described. The former type of the mixture was used in [1], and was found, they say, to give the best performance for the “excess” heat generation. The results of eight runs using the PNZ samples are summarized in the upper eight rows in Table 5. Similar to the runs using the PZ samples, the runs H-PNZ2#m were performed simultaneously with D-PNZ1#m, where $m = 1, 2, 3$ and 4. The samples PNZ1 and PNZ2 remained in each reaction chamber during these runs. Table 5 also includes the results of two runs using the NZ samples in the last two rows. The PNZ or NZ samples used were 10 g or 20 g, each containing 1.02 g or 0 g of Pd, respectively. The processing conditions for baking and oxidation were similar to those for the PZ samples.

We see that the loading ratio, $D(H)/Pd$, and the output energy in the first phase, E_{1st} , evaluated for one $D(H)$ atom are essentially the same as those for the PZ sample. Also similar to the PZ sample is the much smaller $D(H)/Pd$ ratio in the No. 2 runs. At the first glance, these facts mean that Ni has no contribution to the heat evolution. However, some features similar to those for the PNZ sample are observed. One is that E_{1st} does not significantly decrease in the No. 2 runs.

The other is the effect of artificial oxidation of the sample. The oxidation provides a distinguished recovery of the high values of E_{1st} and a modest recovery of the $D(H)/Pd$ ratios, as can be seen in the Nos. 5–8 runs with artificial oxidation of the used samples. Similar to the PZ sample, the modest oxidation of 3–6% has induced a modest recovery of $D(H)/Pd$ and a pronounced recovery of E_{1st} to the initial values. As has been done for the PZ sample, Q_D (Q_H) is calculated from the known values of x to find even higher values than for the PZ sample. Again, we apply the mean values of Q_D (Q_H) to estimate x for the virgin samples to confirm reasonable values of x . The same procedure is applied to the reused samples supplied for the No. 2 runs. The values of x are negative but nearly equal to zero, which implies that the above procedure is quite reasonable.

Concerning the NZ sample, we have observed definitely no interval with $p = 0$ nor any positive outlet–inlet temperature difference; the NZ sample gives negligibly small $D(H)$ absorption rate and heat evolution. This fact confirms that not only Ni in the present samples has only a second-order effect on the hydrogen absorption and heat evolution but also that the ZrO_2 matrix has no effect on the hydrogen absorption nor heat evolution. We confirm also that the sample NZ has negligible amount of impurity elements except oxygen. The same is true also for the PZ and the PNZ samples, since these samples were fabricated using the same recipe. These points assure validity of the statements made for the PZ and the PNZ samples in the preceding subsections.

For the PNZ sample we have observed a positive output signal in the second phase exceeding the error range recorded for more than two days. We have to look into a possible zero-level drift of the thermocouple signal, before concluding a positive output power in the second phase.

3.5. Summary of heat measurements

We claim in the present work that;

- (1) The absorption energy E_{1st} increases in function of the fineness of the sample surface, and these samples are ranging from the $0.1\text{-}\mu\text{m}\phi$ Pd powder (PP), the 300-mesh Pd-black (PB) and the oxide composites of Pd-Zr

Table 5. Results of runs using samples containing Ni, PNZ and NZ. The same procedure was applied to obtain Q_D and Q_H for Nos. and runs, and to estimate x for Nos. 1 and 2 runs.

Run	First phase						Second phase	Remarks
	Flow rate (sccm)	Specific output energy E_1 (kJ/g-Pd)	D/Pd or H/Pd ($= y$)	E_{1st} per D/H atom (eV)	O/Pd ($= x$)	Q_D or Q_H (eV/D(H))		
D-PNZ1#1	5.57	1.74 ± 0.03	0.94 (m)	2.05 (m)	0.156 (c)	1.77 (a)	1.01 ± 0.45	$Q_D(Q_H)$ assumed to calculate x
H-PNZ2#1	11.12	1.86 ± 0.03	0.94 (m)	2.19 (m)	0.262 (c)	1.73 (a)	0.10 ± 0.45	
D-PNZ1#2	5.37	0.12 ± 0.03	0.10 (m)	1.28 (m)	-0.029 (c)	1.77 (a)	5.78 ± 3.18	
H-PNZ2#2	11.37	0.14 ± 0.03	0.11 (m)	1.44 (m)	-0.019 (c)	1.73 (a)	2.18 ± 3.18	
D-PNZ1#3	5.21	0.73 ± 0.02	0.39 (m)	2.09 (m)	0.044 (m)	1.89 (c)	0.91 ± 0.72	Artificially oxidized
H-PNZ2#3	11.14	0.75 ± 0.02	0.41 (m)	2.01 (m)	0.032 (m)	1.89 (c)	-0.66 ± 0.72	
D-PNZ1#4	5.43	0.84 ± 0.03	0.50 (m)	1.85 (m)	0.063 (m)	1.64 (c)	-0.31 ± 1.83	
H-PNZ2#4	12.01	0.87 ± 0.02	0.56 (m)	1.72 (m)	0.047 (m)	1.58 (c)	-0.03 ± 1.85	
D-NZ1#2	7.01	0.0 (Ni)	0.0 (/Ni)	—	—	—	0.0 (/Ni)	
H-NZ2#2	13.05	0.0 (Ni)	0.0 (/Ni)	—	—	—	0.0 (/Ni)	

(PZ) or Pd·Ni·Zr (PNZ).

- (2) For the PB sample, the loading ratios D/Pd = 0.82 or H/Pd = 0.78 and the output energies in the first phase, $E_{1st} = (0.68 \pm 0.12)$ eV/atom-D or (0.63 ± 0.11) eV/atom-H, were both 2–3 times larger than those for the $0.1\text{-}\mu\text{m}\phi$ Pd powder and those found in the literature.
- (3) The PZ sample shows an outstanding performance concerning the high loading ratios D/Pd = 1.1 ± 0.2 and H/Pd = 1.0 ± 0.2 , as well as the high absorption energies E_{1st} , or the deuteride (hydride) formation energy Q_D and Q_H ranging from 1.5 to 2.3 eV/D and from 1.5 to 2.0 eV/H depending on how much fraction of the PdO_x reduction energy is included in the measured values of E_{1st} .
- (4) The outstanding performance of the PZ sample, which deteriorates because of its repeated use and/or the baking treatment, is shown to be restored significantly by oxidizing a small amount (only less than 10%) of the sample.
- (5) The PNZ sample exhibits a performance similar to that shown for the PZ sample, when evaluated from the values per one Pd atom. It shows an even more pronounced recovery after the oxidizing process.
- (6) The NZ sample absorbs no hydrogen isotopes.
- (7) As for the second phase, we have positive output exceeding the error range for the deuterium runs employing both the virgin PZ and the used PZ samples and the PNZ sample, which should be confirmed by further investigation.

4. Search for Reaction Products

4.1. Neutron and gamma-ray measurement and residual activity

Among possible nuclear reaction products, neutrons and γ rays could be detectable outside the gas absorption chamber. During the absorption runs using the $\text{A}_1\text{-}\text{A}_2$ system, these were simultaneously monitored with a BF_3 neutron dose rate meter and a scintillation probe for γ ray detection, respectively, with a solid angle of about 0.2 and 0.1 sr [11–13]. Radio activity of some samples after the absorption runs was also measured with use of an imaging plate. However, we have not succeeded in finding meaningful signals in these measurements.

4.2. System B for charged particle measurement

To detect energetic charged particles is the most convincing method to demonstrate the existence of the nuclear phenomenon. The charged particles have a mean free path or a range too small to allow measurements outside the chamber wall. An experimental system shown schematically in Fig. 5 was prepared for charged particle measurements independent on the $\text{A}_1\text{-}\text{A}_2$ heat measurement system. A solid state detector, a Si surface barrier detector (SSBD) or an ion implanted Si detector (IISD), is located inside the reaction chamber containing a sample holder on which tens of milligrams of the Pd·Zr oxide complex samples are mounted. A sheath heater is wound around the holder for sample baking, and the holder temperature is measured with an alumel–chromel thermocouple attached to the side of the holder. During the sample baking a retractable thermal-shield plate is inserted between the sample and the SSBD/IISD to avoid its deterioration by heating. Energy calibration of the SSBD/IISD is done with the use of an ^{241}Am checking source placed on the retractable shield. During the calibration and before deuterium absorption runs, the chamber is evacuated by a TMP-diaphragm pumping kit. The deuterium gas is introduced into the reaction chamber through a liquid nitrogen cold trap and a “Super needle” valve which enables precise control of the gas flow rate.

4.3. Examples of the Measurement

In the initial stage of this study, we used an SSBD with a depletion layer thickness of $200\text{ }\mu\text{m}$ and the used sample PZ1. The energy spectra recorded during a 5-day run DPZ1# 3B through D-PZ1#4B and evolution of the counting are shown in Fig. 6(a) and (b), respectively.

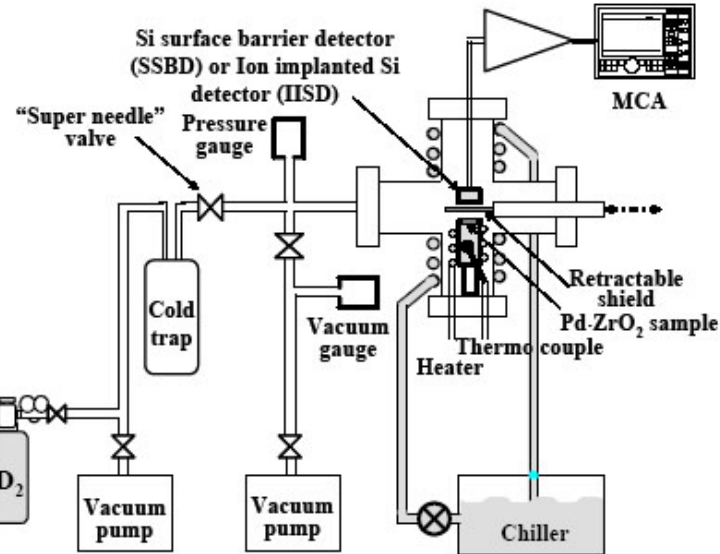


Figure 5. Schematic of the system B for particle measurement.

We see several counts within the energy range from 2 to 4 MeV and a few counts from 7 to 9 MeV. Although these counts could be due to charged particles, we cannot rule out the possibility that this might be caused by electronic noise induced by mechanical shock or oscillation. It is shown in Fig. 6(b) that these counts increase during the period of time at which the pressure changes. Although it is fascinating to imagine that some nuclear events may occur when deuterium atoms flow into/out of the Pd lattice, we cannot conclude it at present.

It is known that any SSBD suffers from deterioration or breakdown when it is used in hydrogen atmosphere. The output pulse height from the SSBD used in the run D-PZ1#3B through D-PZ1#4B was reduced by a factor of about

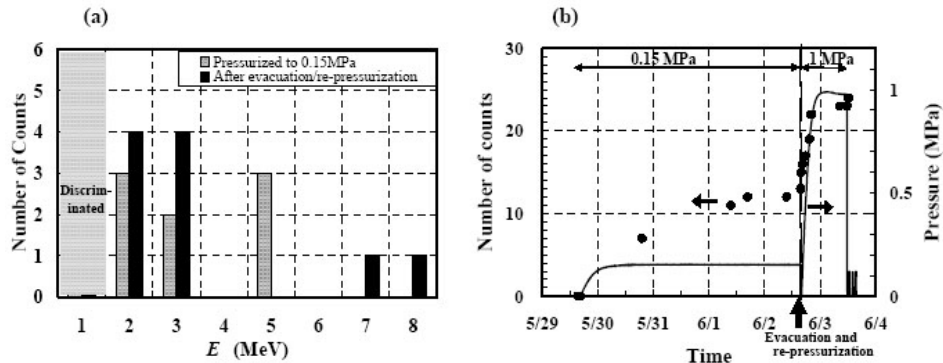


Figure 6. (a) Spectra recorded by SSBD with a 200- μ m-thick depletion layer and (b) Evolution of counting in the "1–12 MeV" range of the spectra measured by the SSBD during the run DPZ1# 3B through D-PZ1#4B.

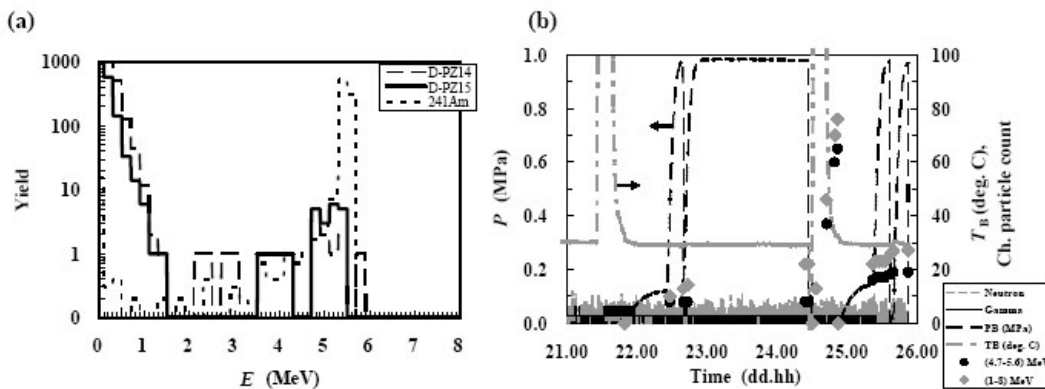


Figure 7. (a) Spectra recorded by the IISD with a 500- μm -thick depletion layer and (b) Evolution of pressure and IISD counting and other radiations during the runs D-PZ14#1B through D-PZ15#2B.

30% and the FWHM increased by a factor of about 5. Although the deteriorated characteristics was stabilized after the initial use for several hundred hours, it was better to abandon it in succeeding runs using virgin samples. We used an IISD with a depletion layer thickness of 500 μm which is known to endure use in hydrogen atmosphere.

Figure 7(a) and (b) show the energy spectra and evolution of pressure and counting of the IISD and other radiations monitored outside the reaction chamber during the runs of D-PZ14#1B, D-PZ15#1B and D-PZ15#2B. The broken line in (a) shows the spectrum of ^{241}Am - α particles used for energy calibration of the detectors. We observe several tens of counts within the energy range of 2–5 MeV during these runs. In (b) the IISD countings are integrated over the runs D-PZ14#1B, D-PZ15#1B–2B, and the baking period. They are reset between the operations.

The integrated IISD counting increased during the baking period between D-PZ14#1B and D-PZ15#1B, which is largely occupied (85%) by the signals lying in the energy range of 4.7–5.6 MeV. This indicates that the upper surface of the retractable shield plate is contaminated by ^{241}Am . From the active surface of the IISD we could see the contamination spot in case of insufficient retraction of the shield plate during the runs. This can account for the increase of the counting also during the runs D-PZ14#1B and DPZ15# 1B–2B.

As shown in Fig. 7(a), the spectra during these runs are a little different from that of the ^{241}Am - α particles, which is also indicated by the difference between the counting in the energy range of 1–8 MeV and that in the range of 4.7–5.6 MeV. The energy shift of the ^{241}Am - α particles by about 0.8 MeV is consistent with the energy loss of 5.486 MeV α -particles in a 5 mm.MPa hydrogen gas. We see again, however, a tendency that the counting increases during the phase of pressure change. It could be possible that the signals lying in the energy range of 2.0–4.5 MeV originate in charged particles emitted by nuclear effects in the sample.

4.4. Summary of charged particle measurements in gas charging system

We have observed several tens of counts within the 1–10 MeV range, which appeared to be emitted coincidentally with pressure change. However, we cannot rule out the possibility that they are due to electronic noise or contamination of ^{241}Am . Up to now, we have no firm evidence of charged particle emission, nor burst of high energy particles corresponding quantitatively to any heat observed in the A₁·A₂ twin system. There remains a possibility that the conditions including the gas pumping were not suitable for the possible excess heat evolution. We are planning to detect X-rays as another candidate to evidence the reaction products.

5. Concluding Remarks

Using the twin system, characteristics of deuterium/hydrogen absorption and accompanying heat generation have been compared for different types of Pd powders; the $0.1\text{-}\mu\text{m}\phi$ Pd powder, the Pd-black, and the mixed oxides of Pd-Zr, Pd-Ni-Zr and Ni-Zr. It has been found that the D(H)/Pd ratio and the absorption energy increase in function of fineness of the sample surface.

The Pd-Zr oxide nano-composites showed anomalously large energies of hydrogen isotope absorption exceeding 2.0 eV as well as large loading ratio exceeding 1.0 in the phase of deuteride/hydride formation. Although the samples were deteriorated by the repeated baking-hydrogenation cycle, an artificial oxidation of the PZ and the PNZ samples recovered the excellent performance of these samples, giving the hydride formation energy of 1.5–2.3 eV/D and 1.5–2.0 eV/H depending on how much fraction of the PdO_x reduction energy is included in the measured values of $E_{1\text{s}}$.

In the second phase after the deuteride formation, the Pd-Zr and Pd-Ni-Zr oxide composites charged exclusively with D_2 sometimes gave significantly positive output, which requires further investigation.

There might be a yet-unknown atomic/electronic process governing the first-phase phenomenon in the present mesoscopic system, or the concept of “atom clusters” [14] might be applied. However, it seems rather difficult to assume that such a large isotope effect observed especially in the second-phase is only due to electron transfer within the process of adsorption and/or hydride formation. Nuclear effects could be one of the candidates responsible for this phenomenon. The 4D-TSC fusion model [15, 16] is one of the most probable scenarios.

References

- [1] Y. Arata, Y. Zhang, The special report on research project for creation of new energy, *J. High Temp. Soc.* (1) (2008).
- [2] Y. Arata, Y. Zhang, *Condensed Matter Nuclear Science, Proc. 12th Int. Conf. on Cold Fusion*, A. Takahashi, Y. Iwamura, K. Ota (eds.), World Scientific, Singapore, 2006, pp.44–54.
- [3] V.A. Kirkinskii, A.I. Kumelnikov, *Proc. ICCF13*, Sochi, Publisher Center MATI, Moscow, 2007, ISBN 978-5-93271-428-7, pp.43–46.
- [4] J.P. Biberian, N. Armanet, *ibid.* pp.170–180.
- [5] T. Nohmi, Y. Sasaki, T. Yamaguchi, A. Taniike, A. Kitamura, A. Takahashi, R. Seto, Y. Fujita, <http://www.ler-canr.org/>; to be published in *Proc. 14th Int. Conf. Condensed Matter Nuclear Science (ICCF14)*, Washington, DC, 2008.
- [6] G. Alefeld, J. Voelkl (eds.), *Hydrogen in Metals II -Topics in Applied Physics*, Vol. 29, Springer, Berlin, 1978.
- [7] A. Koiwai, A. Itoh, T. Hioki, Japan Patent 2005-21860 (P2005-21860A).
- [8] C. P. Chang et al., *Int. J. Hydrogen Energy* **16** (1991) 491.
- [9] M.M. Antonova, *Sboistva Gidriedov Metallov, Properties of Metal-hydrides*, Naukova Dumka, Kiev, 1975; translated by NissoTsushinsha, Wakayama, 1976 (in Japanese).
- [10] Y. Fukai, K. Tanaka, H. Uchida, *Hydrogen and Metals*, Uchida Rokakuho, Tokyo, 1998 (in Japanese).
- [11] Y. Sasaki, A. Kitamura, T. Nohmi, Y. Miyoshi, A. Taniike, A. Takahashi, R. Seto, Y. Fujita, *Proc. 9th Meeting of Japan CF-Research Society*, 2009, pp. 29–34; <http://www.lenrcanr.org/acrobat/SasakiYdeuteriumg.pdf>.
- [12] A. Takahashi, A. Kitamura, T. Nohmi, Y. Sasaki, Y. Miyoshi, A. Taniike, R. Seto, Y. Fujita, *Proc. 9th Meeting of Japan CF-Research Society*, 2009, pp. 35–41; <http://www.lenrcanr.org/acrobat/TakahashiAdeuteriumg.pdf>.
- [13] A. Kitamura, T. Nohmi, Y. Sasaki, A. Taniike, A. Takahashi, R. Seto, Y. Fujita, *Phys. Lett. A*, **373** (2009) 3109–3112.
- [14] H. Fujita, *J. High Temp. Soc.* **24** (1998) 272.
- [15] A. Takahashi, The basics of deuteron cluster dynamics as shown by a Langevin equation, in *LENR Source-Book*, Vol. 2, J. Marwan, S. Krivit (eds.), Washington DC, American Chemical Society, 2009, pp. 193–217.
- [16] A. Takahashi, *J. Condensed Matter Nucl. Sci.* **2** (2009) 33–44.



Research Article

Absorption Capacity and Heat Evolution with Loading of Hydrogen Isotope Gases for Pd Nanopowder and Pd/Ceramics Nanocomposite

T. Hioki ^{*}H. Azuma, T. Nishi, A. Itoh, S. Hibi, J. Gao and T. Motohiro

Toyota Central Research and Development Laboratories Inc., Nagakute, Aichi 480-1192, Japan

J. Kasagi

Research Center for Electron Photon Science, Tohoku University, Sendai 982-0826, Japan

Abstract

Using Sievert's method, the hydrogen (/deuterium) absorption capacity was measured for Pd nanopowder with particle size 10–20 nm and for Pd- γ Al₂O₃ nanocomposites with Pd particle size 2–5 nm. In order to eliminate the influence of oxidized Pd particles on the absorption capacity, measurements were repeated three or four times without exposing the samples to air. For both nano-Pd materials, the absorption capacity at 1 MPa was found to be slightly smaller than that of Pd bulk. The difference in the absorption capacity between hydrogen and deuterium, i.e., the isotope effect, was negligible within the experimental error. It was found that the average size of the Pd particles was significantly increased after the repeated measurements of the absorption capacity. The heat generated upon pressurizing the materials with deuterium or hydrogen up to 1 MPa was measured using a flow calorimeter. Similar to the measurements of absorption capacity, the heat measurements were also conducted repeatedly. The observed heat generation was composed of two stages, i.e., the first stage during pressurizing the samples from 0 to 1 MPa and the second stage, where the sample was kept under a fixed pressure of 1 MPa. The heat generated in the first stage was much larger at the time of the first measurement than at the second or third. The heat generated in the first stage was largely explained by taking into account two chemical reactions, i.e., the water formation reaction and the deuteride formation reaction. It was noted that in the second stage, where the heat generated from chemical reactions was hardly expected to occur, a small heat power was observed intermittently. This heat evolution was observed frequently when the samples were loaded with deuterium.

© 2011 ISCMNS. All rights reserved.

Keywords: Calorimeter, CMNS, Deuterium absorption, Heat evolution, Hydrogen storage, Pd nanoparticle

PACS: 25.45.-z, 65.80.-g, 81.07.Bc, 81.07.Wx, 88.30.R-

^{*}E-mail: hioki@mosk.tytlabs.co.jp

1. Introduction

It has recently been recognized that nanometer scale structures of Pd or nanometer size Pd particles are essential to successfully observe low energy nuclear phenomena in condensed matter. Iwamura et al. have used nanometer-size multi-layers of CaO and Pd and have reported an observation of nuclear transmutation from Sr to Mo and Cs to Pr, as a result of deuterium permeation through the multi-layer structure [1]. Dardik et al. have achieved a high reproducibility of excess heat generation by using the ultrasonically excited “Super Wave” electrolysis technique [2]. In their experiments, a high deuterium loading has been obtained, i.e., D/Pd, the number of absorbed deuterium atoms to Pd atoms, is larger than 0.95. The remarkable increase in the deuterium loading has been attributed to increasing the surface area of the Pd cathode as well as cleaning and activating the cathode surface as a result of the ultrasonic excitation [2]. It has long been known that attaining a D/Pd ratio larger than 0.88 is favorable to observe excess heat in electrochemical loading of Pd with deuterium [3].

Arata and Zhang have recently reported that by simply loading a nano-Pd–ZrO₂ system with deuterium gas, heat generation due to a nuclear reaction is observed [4]. They have also observed a remarkable increase of ⁴He in the gas sampled from the powder after the loading experiments, suggesting that the heat is generated as a result of the D–D nuclear reaction that yields ⁴He as ash. For nano-Pd–ZrO₂ systems, a high value of H/Pd has been reported and attributed to interfacial hydrogen spillover effect [5]. Kitamura et al. have constructed a twin type flow calorimeter system to quantitatively evaluate the heat reported by Arata and Zhang, and have observed anomalously large energies of hydrogen isotope gas absorption as well as large D/Pd and H/Pd ratios of about 1.1 [6].

In this study, in order to clarify the relationship between Pd particle size and hydrogen (/deuterium) absorption capacity, the volumetric method or Sievert's method was employed and the pressure-composition isotherms were measured for Pd nanopowder and nanoPd- γ Al₂O₃ composites. A flow calorimeter was constructed and used to evaluate the heat generated upon pressurizing the materials with hydrogen isotope gases. In order to identify the properties of metallic Pd nanoparticles, efforts were made to separate the influences of oxidized Pd on the absorption capacity and heat evolution, i.e., both quantities were measured repeatedly three or four times, without exposing the samples to air. Prior to each cycle of measurement, the samples were heat treated in vacuum to remove the adsorbed molecules or to completely eliminate the hydrogen or deuterium absorbed in the preceding measurement. The degree of oxidation of Pd nanoparticles was estimated from the results of the repeated measurements of the absorption capacity and was used to evaluate the heat generated from chemical reactions.

2. Experimental

2.1. Materials

The materials were Pd nanopowder and Pd nanocomposite. The Pd nanopowder (TMAY4030) was commercially obtained from Tanaka Kikinzoku Kogyo. The Pd- γ Al₂O₃ composites with Pd concentrations of 13 and 20 wt% were prepared by impregnating the γ Al₂O₃ support of specific surface area 90 m²/g with an aqueous solution of Pd(NO₃)₂, followed by drying in the ambient atmosphere and subsequent heating at 773 K for 2 h in the air. By transmission electron microscopy (TEM) observation, the size of the Pd (/PdO) particles was determined to be 10–20 and 2–5 nm for the Pd nanopowder and the nanoPd- γ Al₂O₃ composites, respectively.

2.2. Hydrogen/deuterium storage capacity

The hydrogen (/deuterium) absorption behavior up to 1 MPa was investigated using a pressure-composition isotherm apparatus (Suzuki Shokan Co. Ltd.). The amount of the measured samples was about 3 g of Pd. The purity of hydrogen and deuterium gases was 99.99999% and 99.995%, respectively.

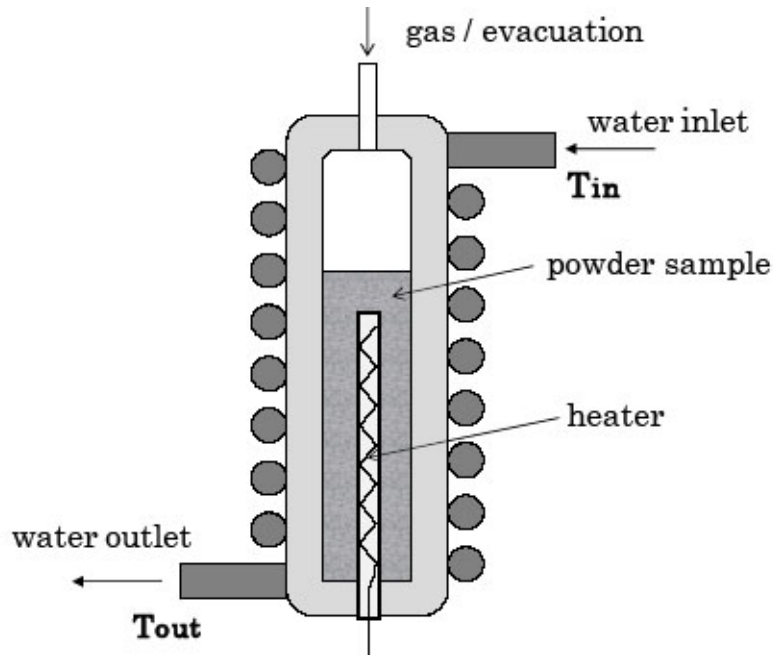


Figure 1. Schematic of the calorimeter.

2.3. Calorimetry

A flow calorimeter was constructed and used to measure the heat evolution upon pressurizing the samples with hydrogen isotope gases. A schematic of the calorimeter is shown in Fig. 1. Thermocouples of alumel–chromel were used to measure the temperature difference, $T_{\text{out}} - T_{\text{in}}$, between the inlet and outlet of the cooling water. The flow rate of water, f , was measured using a Coriolis force-type flow meter.

The temperature difference and the flow rate of water were registered every 30 s, and used to calculate the heat power P_{out} , following the equation,

$$P_{\text{out}} = C(T_{\text{out}} - T_{\text{in}})f/r, \quad (1)$$

where C is the specific heat of water and r the recovery rate of heat. An electric heater was mounted at the center of the sample vessel. The value of r was determined experimentally so that P_{out} was equal to the electric input power P_{in} under conditions where no heat source other than the electric heater existed. The value of r was almost independent of the species of the used gas (H_2 , D_2 and He), the gas pressure of 0–1 MPa, and the value of P_{in} in the range of 1–5 W. It was dependent on the flow rate of water. An example of r as a function of f is shown in Fig. 2, where the sample vessel was mounted with Pd nanopowder of 26 g and pressurized with He of 0.85 MPa. In the present study, r was fixed to be 55%, because f used in this study was 6–7 ml/min. The fluctuation and the drift of the measured output power were examined under a condition where Pd powder of 26 g was loaded with He up to 1 MPa. The result is shown in Fig. 3. In order to suppress the drift, the calorimeter system was thermally insulated from the ambient atmosphere. The accuracy of the calorimeter was ± 50 mW. The gases were supplied into the sample vessel through a needle valve and a mass flow controller. The flow rate of gas was about 20 ml/min.

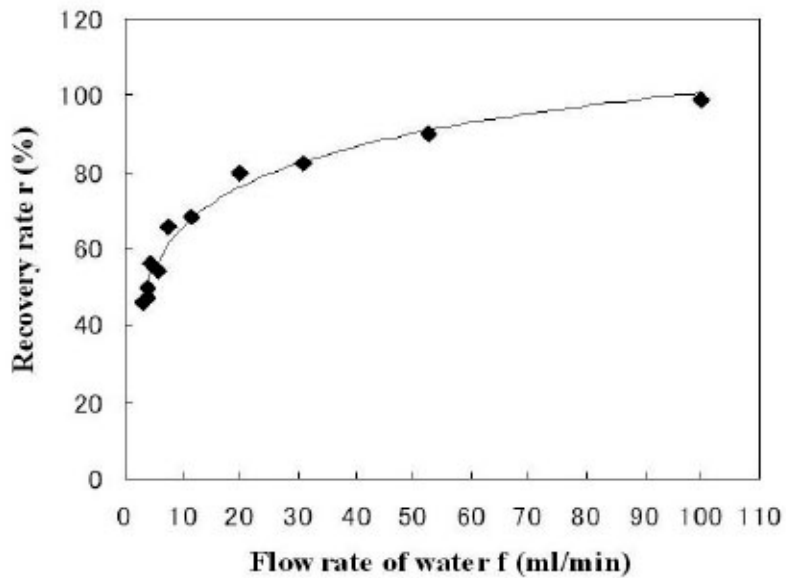


Figure 2. Recovery rate (r) as a function of flow rate (f) for Pd nanopowder AY4030 of 26 g under a He gas pressure of 0.85 MPa. The electric input power was 1.5 W or 0.66 W. The solid line is drawn to connect the data points smoothly.

3. Results and Discussion

3.1. Deuterium/hydrogen storage capacity

Pressure-composition (PC) isotherms at 300 K for Pd nanopowder AY4030 and 13 wt%Pd- γ Al₂O₃ composite are shown in Figs. 4 and 5, respectively. The measurements were conducted four times repeatedly. The first, second, and

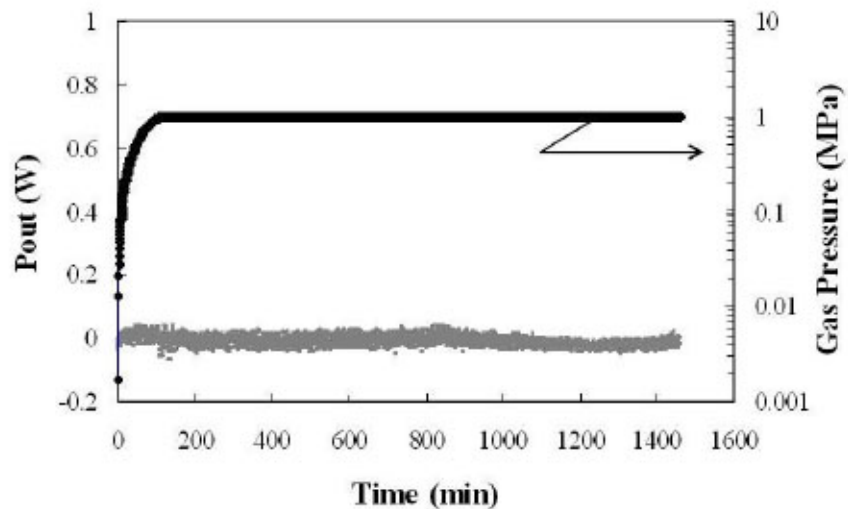


Figure 3. Output power and He gas pressure as a function of time for Pd nanopowder of 26 g.

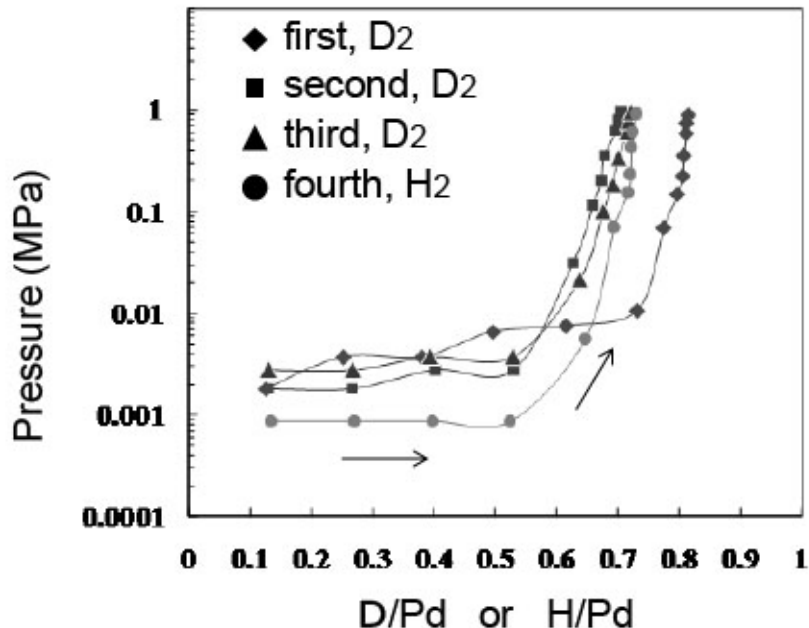


Figure 4. PC isotherms of Pd nanoparticles AY4030. Isotherms were measured four times repeatedly. The arrows show the sequence of the measurements.

third loadings were with deuterium gas and the fourth loading was with hydrogen gas. Prior to each measurement, the sample was heated in vacuum at 523 K for 2 h in order to remove adsorbed molecules (first) or to completely remove the deuterium absorbed in the preceding measurement (second, third, and fourth).

It is seen in Fig. 4 that the apparent D/Pd value at 1 MPa for the first measurement is 0.82. This value is considerably larger than those of the second (0.69) and the third (0.70) measurements. This difference is attributed to the fact that in the first measurement, the surface layer of Pd particles is initially oxidized and this oxide layer is reduced to metallic Pd during the first time loading with deuterium gas. From the measured difference, the number of Pd atoms in the form of PdO for the as-received powder is estimated to be about 6 at.% to the total number of Pd atoms.

The difference in the apparent absorption capacity between the first and second measurements is much more remarkable for the composite sample, as seen in Fig. 5. The apparent D/Pd value at 1 MPa in the first loading with D₂ is 2.7, while the values in the second and third loadings are about 0.71. The apparent D/Pd value of 2.7 in the first measurement is understood if we assume that all the Pd in the sample is oxidized, i.e., in the chemical state of PdO. Then, if the sample is exposed to deuterium or hydrogen, the following water formation reaction and deuteride (/hydride) formation reaction will proceed.



Reaction (2) gives an apparent D/Pd value of 2, while reaction (3) gives the true value of D/Pd. In the second and third loadings, only reaction (3) is expected to occur, and D/Pd for this sample is 0.71 from the experiment. Because both reactions (2) and (3) occur in the first loading, an apparent D/Pd value of about 2.7 should be obtained.

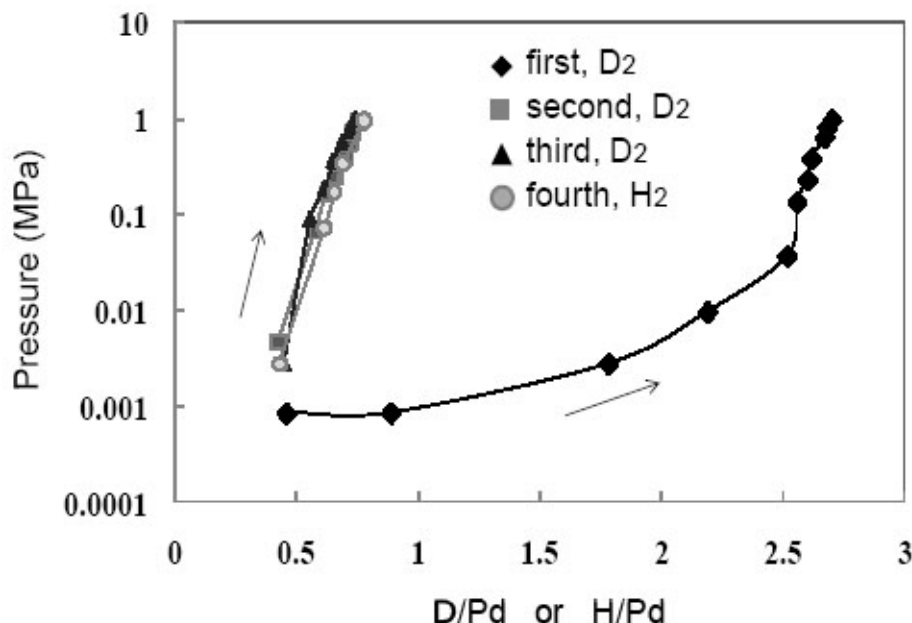


Figure 5. PC isotherms of 13 wt.%Pd- γ Al₂O₃. Isotherms were measured four times repeatedly. The arrows show the sequence of the measurements.

In order to confirm the chemical composition of the sample, the X-ray diffraction pattern was taken for 13 wt.%Pd- γ Al₂O₃ after the heat treatment in vacuum at 523 K for 2 h. The diffraction pattern clearly showed that the sample consisted of PdO and γ Al₂O₃, while the diffraction pattern for the sample after the four-fold PC measurements showed that the sample consisted of metallic Pd and γ Al₂O₃. In Table 1, the results of the absorption capacity at 1 MPa are summarized.

PC isotherms were also measured three times with hydrogen gas for 13 wt.%Pd- and 20 wt.%Pd- γ Al₂O₃ and for Pd bulk in the form of a 0.1 mm thick-foil. The results are summarized in Table 2.

As seen in Table 2, large differences in the absorption capacity between the first and the second loading with hydrogen are observed for the two composite samples, whereas no difference for the Pd foil can be seen. The absorption capacity for the foil sample agrees well with the literature value for Pd bulk [7].

From these results, it has been demonstrated that the PdO in the Pd nanopowder and nanocomposites easily reduces to metallic Pd, once it is exposed to deuterium or hydrogen. In the second, third, and fourth loadings, the measured values of absorption capacity are for metallic Pd particles. It is seen from Table 1 that the deuterium absorption capacity of Pd nanopowder AY4030 is almost the same as that of 13 wt.%Pd- γ Al₂O₃. It is also seen that the value of H/Pd at the fourth measurement almost agrees with the D/Pd value in the second or third measurement for both the Pd powder

Table 1. The order of measurement cycles and D/Pd (or H/Pd) at 300 K under 1 MPa.

	First (D ₂)	Second (D ₂)	Third (D ₂)	Fourth (H ₂)
nanoPd (AY4030)	0.82±0.02	0.69±0.02	0.70±0.02	0.71±0.02
13 wt.%Pd-Al ₂ O ₃	2.7±0.2	0.71±0.02	0.72±0.02	0.72±0.02

Table 2. The order of measurement cycle and H/Pd at 300 K under 1 MPa.

	First (H ₂)	Second (H ₂)	Third (H ₂)
13 wt.%Pd-Al ₂ O ₃	2.8±0.2	0.69±0.02	0.71±0.02
20 wt.%Pd-Al ₂ O ₃	2.4±0.2	0.68±0.02	0.70±0.02
Pd bulk (foil)	0.74±0.02	0.74±0.02	0.74±0.02

and the composite sample. Therefore, the isotope effect of these materials is negligible within the experimental error, as far as the absorption capacity at 1 MPa is concerned. Furthermore, it is noted from Tables 1 and 2 that the hydrogen absorption capacity for all the nanoPd materials used in the present study is slightly smaller compared to the value of Pd bulk.

Figure 6 compares the TEM images for the as-received Pd powder AY-4030 and the powder after the four cyclic measurements of absorption capacity. The average size of the Pd particles is initially 10–20 nm, whereas that of the Pd particles after the measurements is about 50 nm. The local temperature at the contact point of assembling Pd particles will rise significantly with the heat of reaction (2) and/or (3). This local temperature rise may cause the observed growth of the Pd particles.

Similar growth of Pd nanoparticles is also observed for the composite sample, as shown in Fig. 7. The size of PdO for the as-synthesized 13 wt.%Pd- γ Al₂O₃ is 2–5 nm, whereas the size of Pd particles after the four cyclic measurements of absorption capacity is 2–15 nm. Therefore, the growth of Pd particles in the nanocomposite material is suppressed compared to that in the Pd nanopowder, although the heat generated with the loading of hydrogen or deuterium is much larger for the nearly 100% oxidized Pd particles of the composite, as described later. In the composite sample, Pd particles of the smallest size i.e., 2 nm, are still observed after the exposure to deuterium and hydrogen. It is probable that the Pd particles formed in the pores of γ Al₂O₃ are hard to grow owing to the separation of Pd particles by the wall of Al₂O₃.

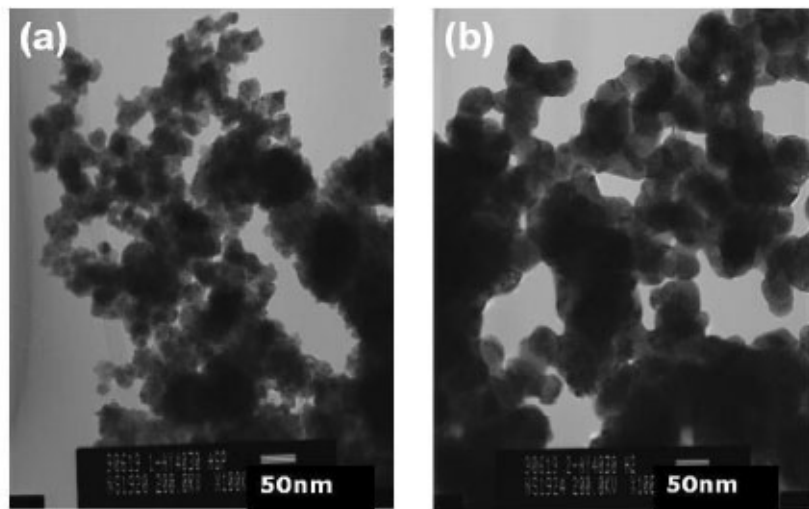


Figure 6. TEM images of Pd nanopowder AY4030; (a) as-received, (b) after four cycle measurements of absorption capacity.

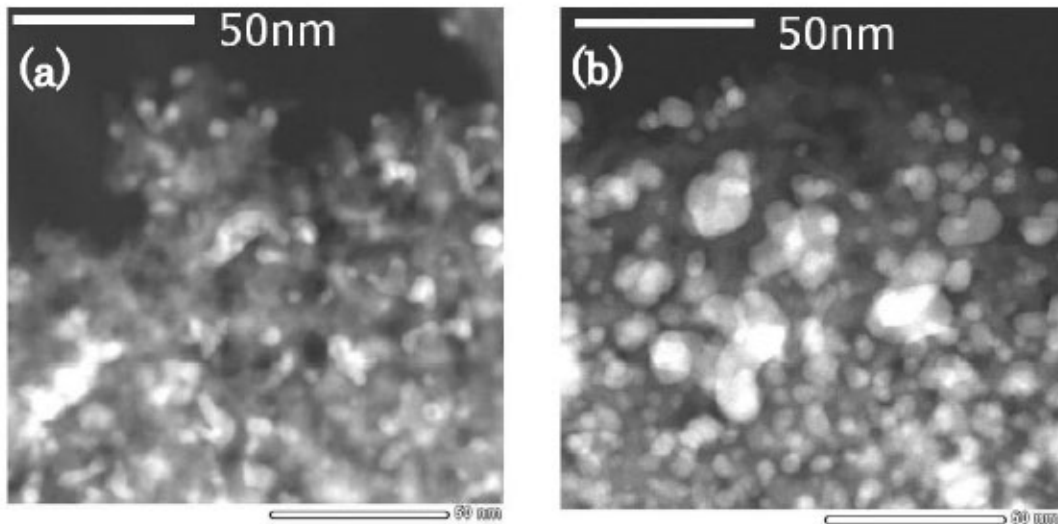


Figure 7. Scanning TEM images of 13 wt.%Pd- γ Al₂O₃; (a) as-synthesized, (b) after four cycle measurements of absorption capacity. The white spots are PdO (a) or Pd (b).

3.2. Heat evolution associated with loading of hydrogen isotope gases

3.2.1. Heat evolution during pressurizing up to 1 MPa (the first stage)

Figure 8 shows the thermal output power as a function of time for 20 wt.%Pd- γ Al₂O₃. The amount of the sample mounted in the sample vessel was 42.5 g, i.e., 8.5 g of Pd. The sample was first evacuated, heated up to 523 K, maintained at this temperature for 2 h, and cooled to room temperature. Then, the sample was loaded with deuterium. The gas pressure as a function of time is also shown in Fig. 8.

Here, we define the first stage as the period from the beginning of gas loading to the time at which the gas pressure reaches 1 MPa, the second stage as the period where the pressure is kept constant at 1 MPa. After the first measurement of heat evolution, the sample was again evacuated, heated up to 523 K, maintained at this temperature for 2 h in order to eliminate the absorbed deuterium completely. Then, the sample was subjected to the second loading with D₂ at room temperature. Similarly, the third loading was conducted with H₂. In Fig. 8, it is seen that heat evolution in the first stage is significant and especially the heat evolution in the first loading is much larger compared to those of the second and the third loadings. This behavior is quite similar to the deuterium absorption capacity shown in Fig. 5.

Therefore, the heat evolution in the first loading is related with the chemical reactions (2) and (3).

Similarly, three cycles of heat measurement were also performed for Pd powder AY4030 of 26 g. In Fig. 9, the heat generated in the first stage is summarized for both Pd powder and 20 wt.%Pd- γ Al₂O₃ and compared to the values estimated from the chemical reactions (2) and (3).

For the estimation, ΔH (water) and ΔH (deuteride) were taken as -178 kJ/mol Pd [8] and -40 kJ/mol H₂ [9], respectively. It was assumed that ΔH (deuteride) = ΔH (hydride). From the results of Tables 1 and 2, it was assumed that 6 at.% of Pd was initially PdO for AY4030 and 85% for 20 wt.%Pd- γ Al₂O₃. In the first loading, the chemical reactions of both (2) and (3) were taken into account, in the second and the third loading only the chemical reaction (3). It is seen in Fig. 9 that the heat generated in the first stage is largely explained by the chemical reactions.

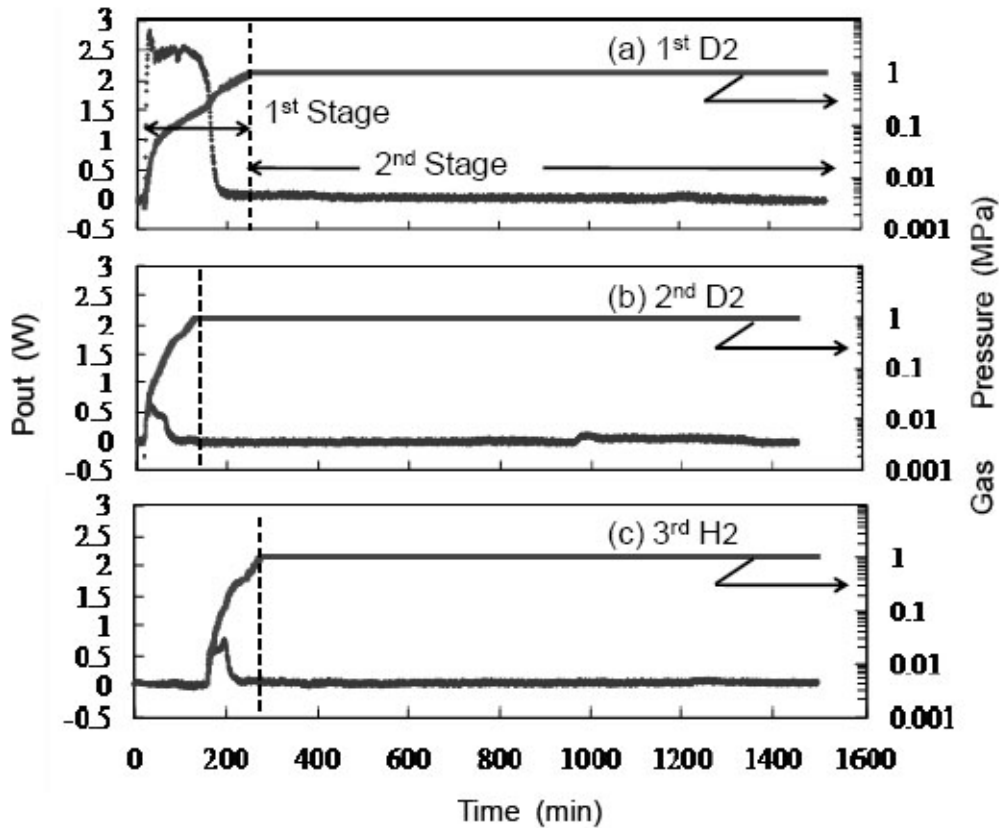


Figure 8. Heat power and gas pressure as a function of time for 20 wt.%Pd- γ Al₂O₃; (a) the first cycle loading with D₂, (b) the second cycle loading with D₂, (c) the third cycle loading with hydrogen.

3.2.2. Heat evolution under constant pressure (the second stage)

The chemical reactions associated with loading the Pd nanoparticle systems with hydrogen isotope gases up to 1 MPa are considered to cease until the pressure reaches 1 MPa. Therefore, in the second stage where the gas pressure is kept constant at 1 MPa, no chemical reactions are expected to occur. In Fig. 10, the same data as in Fig. 8 are shown with P_{out} magnified by 10 times.

As seen in Fig. 10, in the first and the second loading with D₂, an output power as small as 0.05–0.1 W is observed for a period of about three and six hours, respectively. On the other hand, as seen in Fig. 10(c), no such anomalous heat evolution is observed in the third loading with H₂.

Similarly, the results for the Pd nanopowder sample of 26 g are shown in Fig. 11. As indicated in the figure, similar heat evolution in the second stage is also observed for the Pd nanopowder sample only under deuterium gas pressure. Therefore, it cannot be ruled out that this anomalous heat evolution in the second stage is of nuclear origin, as reported by Arata and Zhang [4] and by Kitamura et al. [6]. However, in this study, the observed anomalous heat power is as small as 0.05–0.10 W, which is close to the detection limit (± 50 mW) of the calorimeter used here. Therefore, in order

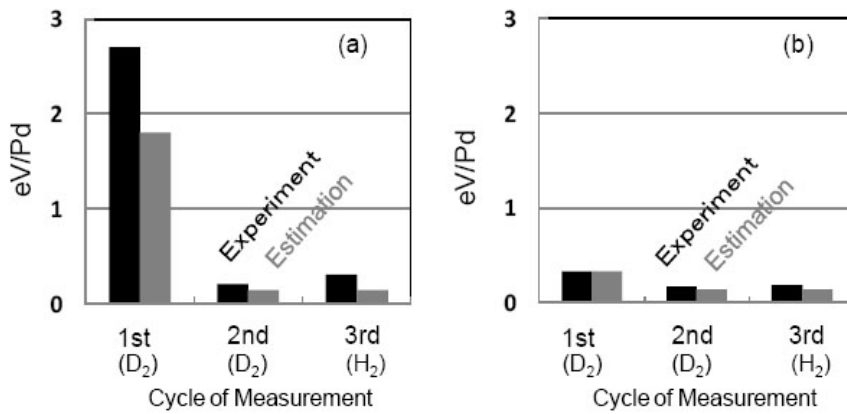


Figure 9. Variation of heat generated in the first stage with cycle of measurement for (a) 20 wt.%Pd- γ Al₂O₃ and (b) Pd nanopowder AY4030. Experimental values are compared to the estimated ones.

to clarify the origin of the anomalous heat power in the second stage, it is necessary to increase the output power and/or to improve the accuracy of the calorimeter.

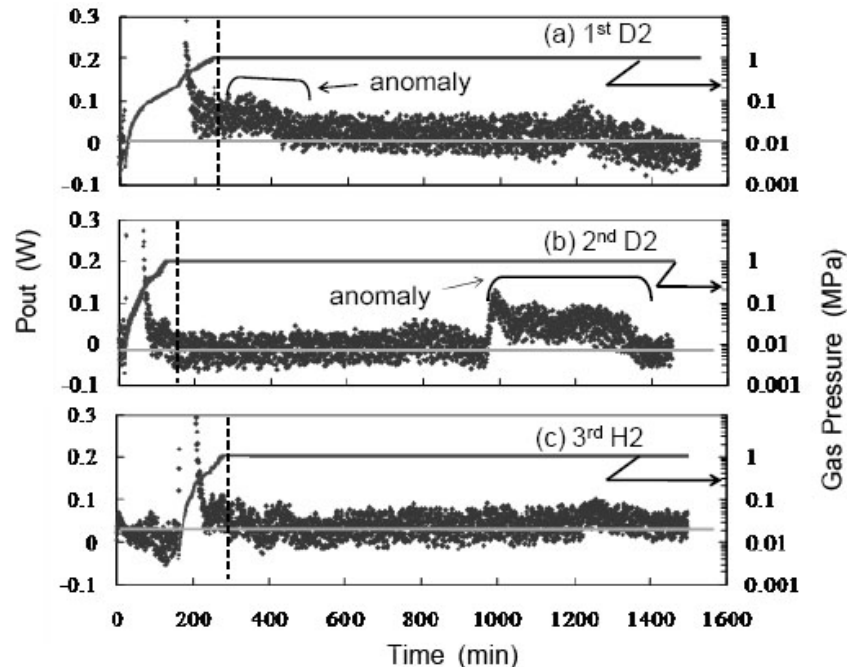


Figure 10. The same data as in Fig. 8 are displayed with the vertical axis enlarged by 10-fold. The vertical dotted lines indicate the boundary of the first stage and the second stage, and the horizontal gray lines the zero level of P_{out} .

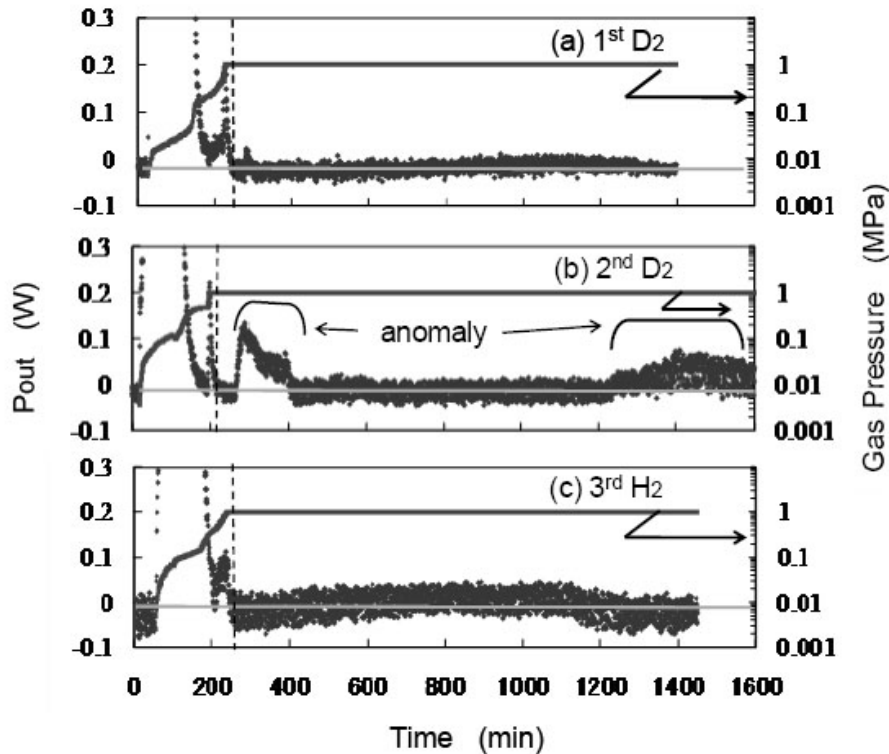


Figure 11. Heat power and gas pressure as a function of time for Pd nanopowder AY4030; (a) the first cycle loading with D₂, (b) the second cycle loading with D₂, and (c) the third cycle loading with H₂. The vertical dotted lines indicate the boundary of the first stage and the second stage, and the horizontal gray lines the zero level of P_{out} .

4. Conclusion

- (1) For Pd nanoparticle systems, Pd particles are often partially or wholly oxidized, and the oxidized Pd, i.e., PdO, gives a large value of apparent absorption capacity of hydrogen isotope gases. When they are wholly oxidized, the apparent absorption capacity at 1 MPa and ambient temperature is about 2.7, which is larger than that of Pd bulk by about 3.6 times.
- (2) When they are partially oxidized, the degree of oxidization, i.e., the ratio of the oxidized Pd atoms to the total Pd atoms is estimated from the difference in the apparent and the real values of the hydrogen absorption capacity.
- (3) Nanoparticles of PdO were reduced to metallic Pd particles, once they were exposed to hydrogen isotope gases at ambient temperature. Therefore, if measurements of absorption capacity are performed repeatedly without exposing the sample in air, the results at the time of the second measurement give the real values of hydrogen absorption capacity for metallic Pd particles. The real values of hydrogen/deuterium absorption capacity at 1 MPa for the nano-Pd materials used in the present study were slightly smaller than that of Pd bulk.
- (4) After four cyclic measurements of deuterium/hydrogen absorption capacity at 300 K, i.e., after four cycles of loading and degassing of hydrogen isotope gases, the average size of the Pd particles increased significantly compared to that of initial particles. The extent of the grain growth for the Pd nanopowder was larger than that

for the Pd- γ Al₂O₃ nanocomposite.

- (5) Similar to the absorption capacity, the heat generated in the first stage also depended strongly on the degree of oxidation of Pd nano-particles. The measured values of heat are largely explained by taking into account the water formation reaction and the hydride formation reaction.
- (6) In the second stage, where no chemical reaction was expected to occur, an output power as small as 0.05–0.1 W was observed intermittently for a period of a few to several hours. The events of such anomalous heat generation were frequently observed for the loading with deuterium for both samples of Pd nanopowder and Pd- γ Al₂O₃ nanocomposite.

Acknowledgements

We thank N. Suzuki for TEM observations, M. Hatanaka for help in preparing the materials, S. Towata, K. Aoki, T. Noritake, M. Matsumoto, and K. Miwa for discussions on hydrogen absorption capacity and for help in the measurements. Discussions on heat evolution with A. Kitamura of Kobe University and A. Takahashi of Technova Inc. were helpful. We also thank N. Nakamura of Toyota Motor Corporation for encouragement.

References

- [1] Y. Iwamura, M. Sakano, T. Itoh, *Jpn. J. Appl. Phys.* **41** (2002) 4642–4650.
- [2] I. Dardik, T. Zilov, H. Branover, A. El-Boher, E. Greenspan, B. Khachaturov, V. Krakov, S. Lesin, A. Shapiro, M. Tsirlin, Ultrasonically-excited electrolysis experiments at energetics technologies, in: Proceedings of the 14th International Conference on Condensed Matter Nuclear Science, Washington DC, 2008.
- [3] M. McKubre, F. Tanzella, P.L. Hagelstein, K. Mullican, M. Trevithick, The need for triggering in cold fusion reactions, in: Proceedings of the 10th International Conference on Condensed Matter Nuclear Science, Cambridge, Massachusetts, 2003, pp.199–212.
- [4] Y. Arata, Y. Zhang, *J. High Temp. Soc.* **34** (2008) 85–93.
- [5] S. Yamaura, K. Sasamori, H. Kimura, A. Inoue, *J. Mater. Res.* **17** (2002) 1329–1334.
- [6] A. Kitamura, T. Nohmi, Y. Sasaki, A. Taniike, A. Takahashi, R. Seto, Y. Fujita, *Phys. Let. A* **373** (2009) 3109–3112.
- [7] E. Wicke, H. Brodowsky, in: *Hydrogen in Metals II*, G. Alefeld, J. Volkl (eds.), Springer, Berlin, 1978, p. 81.
- [8] HSC Chemistry 6.1, Chemical Simulation and Reaction Software with Extensive Thermo-chemical Database, Outokumpu Research, Oy, Finland, 2007.
- [9] Y. Fukai, K. Tanaka, Y. Uchida, Suiso to Kinzoku, Uchida Rokakuho Publishing Co. Ltd., Tokyo, 1998, p. 38 (Jpn).



Research Article

Codeposition Methods: A Search for Enabling Factors

Dennis Letts*

12015 Ladrido Lane, Austin, TX 78727, USA
Web: <http://www.letlabs.org>

Abstract

This paper is a preliminary report on results obtained from a series of experiments conducted April–September 2009. The experiments were designed to test for excess power using the basic methods disclosed in 1991 by Szpak, Mossier-Boss and Smith. A large and repeatable excess power signal was observed and the efforts to test mundane explanations for the signal are described. The design, fabrication and calibration methods of a new type of Seebeck calorimeter used for these experiments are also disclosed.

© 2011 ISCMNS. All rights reserved.

Keywords: Excess power, Palladium, Seebeck calorimeter

PACS: *****

1. Introduction

The field of Condensed Matter Nuclear Science (CMNS) began March 23, 1989 with the controversial name of Cold Fusion; the field quickly gained a negative reputation in the mainstream scientific community because the effects claimed in the original paper by Fleischmann, Pons, Hawkins were not easily reproduced [1]. In this seminal paper, the authors claimed that when a deuterated palladium cathode was electrolyzed in lithium deuteroxide, the cell produced more thermal power than was provided by the DC electrical input power. The observed cathode power densities were commensurate with nuclear power densities, leading to claims of a room temperature nuclear process and a scientific controversy that has persisted for two decades.

Producing the power gain observed in the Fleischmann and Pons experiments required considerable skill and patience. In the early years of 1989–1990, excess power results were sporadic and required many weeks of electrolysis to observe. In 1990–1991 Dr. Stanislaw Szpak, working at the Naval Ocean Systems Center in San Diego, California (SPAWAR-SSC), developed a codeposition method designed to deposit palladium and deuterium concurrently onto a metal substrate, typically copper or gold foil.

Szpak claimed that this method created the conditions to produce the Fleischmann–Pons excess power effect without a long incubation period. It was claimed that codeposition methods provide for a fresh ever-expanding cathode surface

*lettslab@sbcglobal.net

and non-steady-state conditions. The need to provide a uniform current density for high deuterium loading was also eliminated. Szpak and his co-workers tested mainly for temperature gains, reporting that the cathode remained 2–4°C hotter than the electrolyte. Claims for elevated levels of tritium in the deuterium-based electrolyte were also made [2].

Over the years, several researchers have attempted to reproduce the Szpak methods but success has not been uniform. Dr. Melvin Miles has arguably been the most successful and has reported positive excess power results in several papers such as Ref. [3]. Experiments reported in 1996 by the Naval Research Laboratory (NRL) in Washington, DC did not produce significant excess power results, but their reported calorimetric errors for these codeposition experiments were ± 200 mW [4]. For many years, the SPAWAR-SSC group in San Diego has reported evidence from CR39 studies supporting the claim that nuclear reactions can result from codeposition methods [5].

In 2008 Dr. Michael Melich contacted the author and several other experienced researchers in the field of CMNS with specific codeposition experience and publication histories, inviting them to attempt reproduction of the codeposition heat effect. The project was funded through the Naval Research Laboratory for six months. The project required that each researcher design and build a calorimeter with at least a 3% level of precision and then attempt to produce credible levels of excess power using Szpak's codeposition methods. This paper reports on the author's efforts to meet the goals of this project.

2. The Seebeck Cell Calorimeter

The Seebeck Cell Calorimeter was designed to provide calorimetry at a 1% level of precision. Seebeck calorimeters have been used in the CMNS field for several years. Dr. Edmund Storms has written several papers about building and working with Seebeck calorimeters [6]. Storms' approach has been to build a box lined with thermoelectric converters (TECs) and then to place the cell under test inside the box. As heat flows out through the TECs, a voltage is produced that can be calibrated to scale with power dissipated in the cell. To function properly, the cold side of the TECs must be kept at a constant temperature so the voltage can be calibrated reliably. Storms and others have traditionally used water coupling to keep the cold side of the TECs at a constant temperature. This method, while effective, is not very portable or affordable. Water coupling is a technical challenge and requires expensive bulky equipment. The approach used in this study relies on air coupling to keep the cool side of the TECs at a constant temperature (Fig. 1).

The Seebeck Cell Calorimeter is shown in Fig 1. The laser view port is also visible, providing access for cathode inspection and laser stimulation. The area of the view port is $\sim 4\%$ of the total surface area of the calorimeter. In the center of the laser view port is a detector for an optical spectrometer used for laser tuning. The 4-inch DC brushless fan provides a strong air flow up the axis of the heat sinks. Two thermistors are secured in the aluminum trough to provide feedback for controlling air temperature to within $\pm 0.02^\circ\text{C}$. Highly conductive thermal epoxy (Duralco 128) provides good thermal transfer but is not electrically conductive.

The core of the calorimeter is a square piece of borosilicate glass 15 cm long and 45 mm on each side (Friederich & Dimmock, #BST45-200). Wall thickness is 2 mm. A square Teflon lid provides sealing for the electrochemical cell and support for up to nine electrode holders/thermistors probes. The Teflon lid provides pass through holes for thermistors (Digi-Key, 2250 Ohm, #615-1000-ND), an immersion heater, a gas vent tube, an anode, a main cathode, a calibration cathode, and a siphon tube so that the electrolyte can be changed during operation without loss of precision (Fig. 2).

Two copper plates are epoxied to the outside of the cell wall, the magnets are epoxied to the copper plates and the TECs are epoxied to the magnets. The copper plates provide an optional high voltage electric field; the two magnets provide a 500 G magnetic field at the cathode (United Nuclear, two 2" \times 1/4" plate magnets). The copper plates are electrically insulated by the Duralco 128 epoxy. A 25 \times 50 mm viewport provides visual and laser access to the cathode during operation without loss of calorimetric precision. The 50 \times 50 mm TECs (Thermal Enterprises, EBay store, #TEC310117657888) are epoxied directly to the electrochemical cell except the area containing the copper plates and magnets, providing rapid heat transfer properties and thermal equilibration. The thermal epoxy used was Duralco 128



Figure 1. The Seebeck Cell Calorimeter is shown inside a temperature controlled enclosure on top of a rack with a fan to provide vigorous air stirring and a consistent airflow over the heat sinks attached to the TECs and the cell walls. Airflow temperature is controlled to $\pm 0.02^\circ\text{C}$, stability is $\pm 0.01\text{ W}$.

with 10% flexibilizer (Cotronics Corp., # 105RF-1) added to avoid thermal expansion damage (Fig. 3).

The final steps in the calorimeter fabrication process are shown in Figs. 3 and 5. The heat sinks (Custom Thermo-electric, #HS54541401) shown in Fig. 3 provide good thermal coupling to the well-controlled airflow. The heat sinks help maintain the cold side temperature of the TECs at a constant value. The simple calorimeter stand shown in Fig. 5 was made from off-the-shelf parts available at most hardware/electronics stores.

3. Calorimeter Performance and Calibration

The calorimeter was completed and installed in a temperature-controlled enclosure for calibration. The enclosure is an Avanti wine cooler that has been modified by adding a Nichrome wire heater and brushless DC fans to stir the air vigorously. The enclosure temperature was set to 32°C and controlled to within $\pm 0.02^\circ\text{C}$. 100 mL of LIOH electrolyte was mixed to a concentration of 0.15 M and a platinum foil cathode $8 \times 10 \times 0.25\text{ mm}$ was used. The anode was a coil of platinum wire with an inside diameter of 12 mm and five turns over the cathode length. An immersion heater was in the

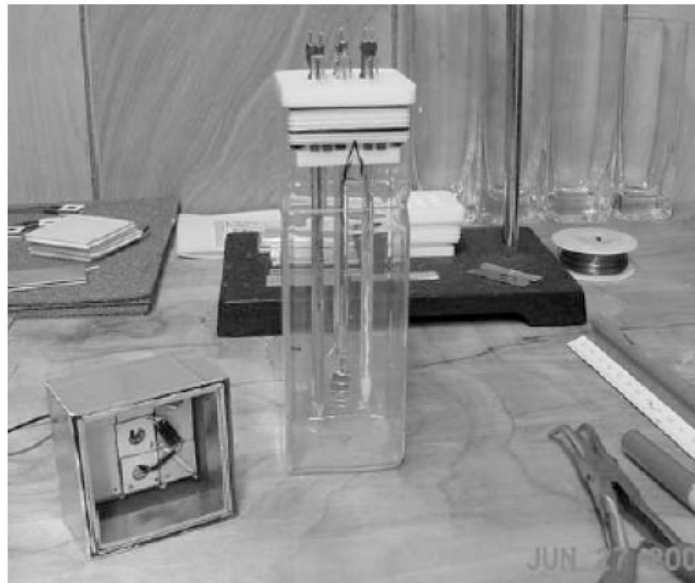


Figure 2. The electrode holders and thermistor probes are 5 mm diameter sealed glass tubes. Hook up wire is 0.5 mm platinum wire spot welded to copper wire sealed inside the glass tubes. The platinum wire is sealed against the soft glass tubing making an airtight seal.

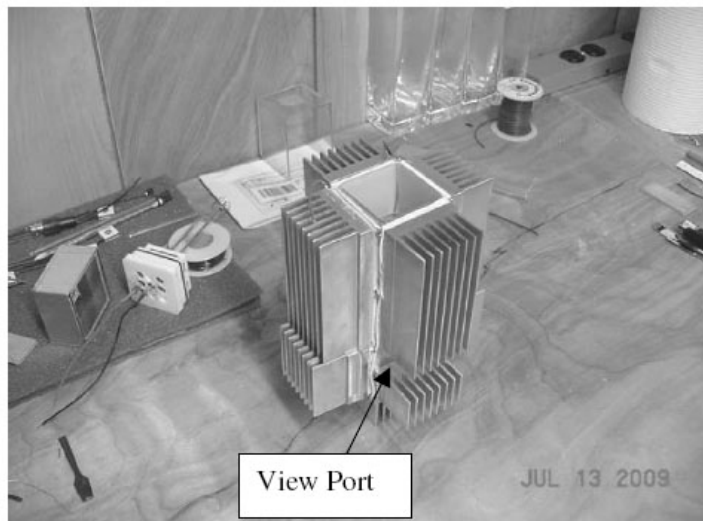


Figure 3. Aluminum heat sinks were epoxied to the TECs for air-coupled temperature control. The heat sinks conduct heat out of the cell so efficiently that the calorimeter can handle high electrical power input. The calorimeter has been tested 0–20 W and demonstrated a 1% level of precision.

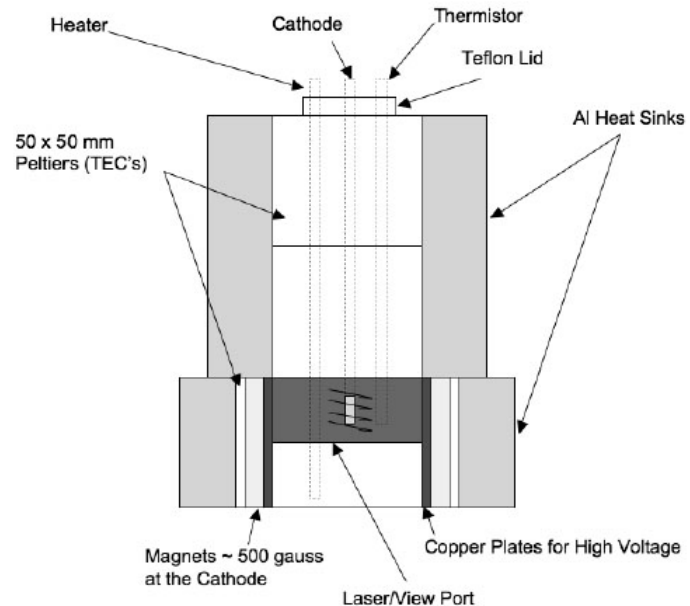


Figure 4. A schematic of the Seebeck cell calorimeter in cut-away view.

cell and provided constant DC power at 11 W to keep the cell temperature about 45°C so the recombiners would work



Figure 5. A rack was constructed from commonly available parts; the aluminum trough was perforated to allow uniform air flow over the heat sinks. Two thermistors were placed in the aluminum trough to provide precise control of the air temperature as it flows over the heat sinks.

properly. A calibration was performed from 0 to 4 W of electrolysis power. The cell was closed and recombination of the gases was provided by alumina pellets coated with 0.5% platinum. The cell was not mechanically stirred, although the external magnetic field provided some degree of stirring. The following calibration plot resulted (Fig. 6).

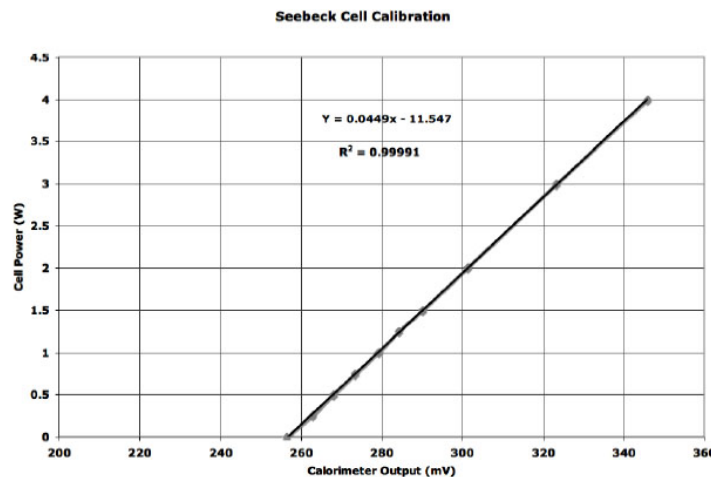


Figure 6. The calorimeter voltage output over 0–4 W is linear and has an R -squared of 0.9999; The presence of the immersion heater at a constant 11 W produces a 256 mV signal when electrolysis power is zero. Calibrations were made with electrolysis power; when resistance power of a few watts was added to electrolysis power, the calorimeter reported a power balance within 1%.

Calibration revealed that this calorimeter requires re-calibration when the cell is opened for maintenance or a new experiment is started; if the cell lid is not opened, then an existing calibration will hold for many weeks, longer than the routine maintenance interval of the calorimeter. The calorimeter has a 10 min time constant, so a thorough calibration can be completed in 30 h. The results of a typical calibration are shown in Fig. 7.

4. Calorimeter Properties

- Precision $\sim 1\%$.
- Time constant ~ 10 min.
- Time to reach equilibrium ~ 6 time constants.
- Sensitivity ~ 5 mW.
- Operational stability during electrolysis ± 0.01 W.
- Stability duration > 72 h at ± 0.01 W.
- Power range tested 0–20 W.
- Calorimeter permits changing cathodes during operation.
- Calorimeter permits removing/replacing electrolyte during operation.
- Calorimeter provides a viewing/laser access port without precision loss.
- Calorimeter provides high voltage capability for electric field application.
- Calorimeter provides a magnetic field of ~ 500 G at the cathode.
- Calorimeter provides nine holes in the cell lid for probes/electrodes.
- Calorimeter provides an in-cell resistance heater for checking calibration.

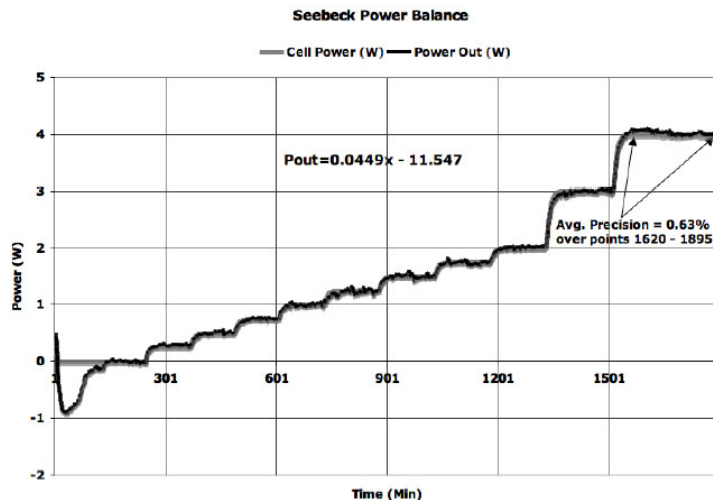


Figure 7. This plot demonstrates that the fitting equation provides for a good input/output power balance over the tested range of 0–4 W; Precision = $(P_{out} - P_{in})/P_{in}$ at $\sim 1\%$.

- Low cost $\sim \$2000$.
- Portable—weighs a few pounds and occupies less than 1 ft³.

5. Experimental Results

Two experiments will be discussed in this paper, NRL681 and NRL684; both experiments produced an excess power signal, ranging from 175 to 250 mW. Subject to further testing, the origin of the excess power signal appears to be nonchemical.

The schematic shown in Fig. 8 is typical for experiments NRL681 and NRL684d; the key features are external magnets, a second cathode for calibration, an immersion heater and a siphon (not visible) located in the left rear of the cell to allow replacement of the electrolyte during the experiment. All cells were closed and gases recombined using 1/8 inch alumina pellets coated with 0.5% platinum reduced (Alpha Aesar, #89106). The recombiner pellets were placed in a 1/8 inch groove in the Teflon lid as shown in Fig. 8. The recombiners worked well as long as cell temperature was maintained between 45 and 50°C. A bubbler containing spent electrolyte was used to monitor recombiner activity.

Experiment NRL681 cathode was a copper substrate plated with gold for approximately 5 min at 3 V, 0.2 A. The cathode was $8 \times 10 \times 0.6$ mm, the anode was a coil of 0.999 Pt wire with an inside diameter of 12 mm (Fig. 9), and the electrolyte used was 0.15 M LiCl, 0.025 M PdCl₂ in 100 mL of 99.9% D₂O from Aldrich.

These experiments differed slightly from Szpak's original protocol. Codeposition experiments normally use bare copper cathodes, electrolyte with twice the concentration and begin electrolysis using very low currents for about a week. This long low-current period plates the palladium smoothly onto the cathode; current is increased when the electrolyte has become clear, indicating that palladium has plated onto the cathode.

The protocol for NRL681 and NRL684 applied electrolysis of 3 W immediately, reaching 6 V at 0.5 A without a slow ramp up. A magnetic field of 500 G was always present. Experience soon showed that the concentration of the electrolyte needed to be reduced by 50% because the palladium build-up on the cathode was excessive. Szpak's protocol was changed slightly because gold plating was less expensive than gold foil and high voltage/current produces a coarse

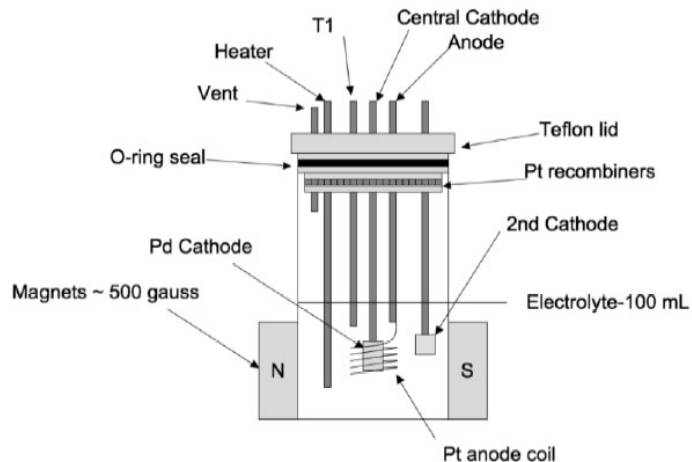


Figure 8. The schematic shown is typical for NRL681 and NRL684. Titanium proved to be a good inert material for the second cathode. It depicts only the cell and magnets for clarity. Details showing the TECs, copper plates and aluminum fins have been suppressed. More details are shown in Fig. 4.

layer of palladium containing many vacancies, which Hagelstein has conjectured might be helpful in the production of excess power. The author was further motivated to use high voltage and gold-plated copper cathodes throughout the entire experiment because Dr. Dennis Cravens followed the low voltage protocol on bare copper cathodes and obtained a null result. Elevated temperature in this series of experiments might also be an enabling factor in the observation of excess power. Temperature was maintained at 45–50°C to improve recombiner function in the closed cells.

Interval 1 of Fig. 10 shows a good zero power balance. Interval 2, resistance heater power to 3 W and power balance to within 1% precision. Interval 3, electrolysis power to 3 W, excess power observed ~175 mW. Interval 4,

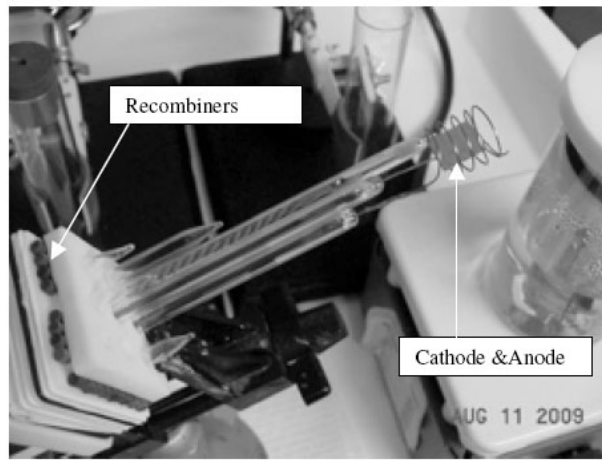


Figure 9. The cell lid, recombiners, sealed glass electrode holders and cathode/anode are shown following the gold plating process, typical for NRL681.

electrolysis power to 1 W, power balance to within 1%. Interval 5, resistance heater at 1 W, power balance to within 1%. Interval 6, zero power balance to within 1%.

Experiment NRL681 was a very clear demonstration that the Seebeck Cell Calorimeter had long-term stability and could show a good power balance. However, NRL681 left open the possibility that the effect was chemical in origin or was due to the presence of an immersion heater used to keep the cell at 40°C.

Experiment NRL684d was designed to permit changing or repositioning of the electrodes and removal/replacement of the electrolyte while the experiment is running. This can be done without changing calorimeter performance or calibration. The cathode used for NRL684d was a $4 \times 10 \times 0.6$ mm Cu substrate plated with Au for 5 min at 3 V, 0.2 A. The anode coil was 0.999 Pt wire with an ID of 12 mm. Electrolyte was 0.15 M LiCl and 0.025 M PdCl_2 in 100 mL of 99.9% D_2O . A 5 mm glass tube 16 cm long was located in the left rear of the cell to remove/replace electrolyte during the experiment. Cathode width was reduced from previous experiments so the cathode can be withdrawn through the 5 mm lid pass-through during the experiment.

This permits testing different cathode materials very quickly without changing calorimeter performance or calibration. Over a 30 h period, NRL684d produced the result shown in Fig. 11:

Interval 1 of Fig. 11, the Ti cathode was electrolyzed in hole No. 5 at 3 W; the gold plated copper cathode was in hole No. 3 without electrolysis power. Power was in balance to within 1%. Interval 2, electrolysis power was switched to the gold plated copper cathode in hole No. 3 outside of the anode coil. After a transient disturbance due to switching cathodes, power came into balance within 1%. Interval 3, exchanged electrodes. The Au plated Cu cathode was put into hole No. 5, inside the Pt anode coil. However, electrolysis power continued to the inert Ti cathode now located in hole No. 3. Again power was in balance to within 1%. Interval 4, electrolysis was diverted to the gold plated copper cathode now located in hole No. 5 inside the Pt anode coil. An excess power signal of 250 mW appeared very quickly and cell temperature increased at the same time by 4–5°C. The excess power signal and cell temperature remained elevated, producing ~ 5 kJ of excess energy. Interval 5, a pump was activated near point 1210 to remove the deuterium-based electrolyte and replace it with hydrogen-based electrolyte of identical volume and concentration as that used at the start of the experiment. As seen in Fig. 11, the excess power signal declined over a nine-hour period. Normally, equilibrium is re-established in about 1 h. Possible explanations might be the presence of a non-chemical exothermic process or a calorimeter error. Future experiments will attempt to clarify this issue.

NRL684d made some credibility advances over NRL681. For example, the inert Ti cathode was electrolyzed in the

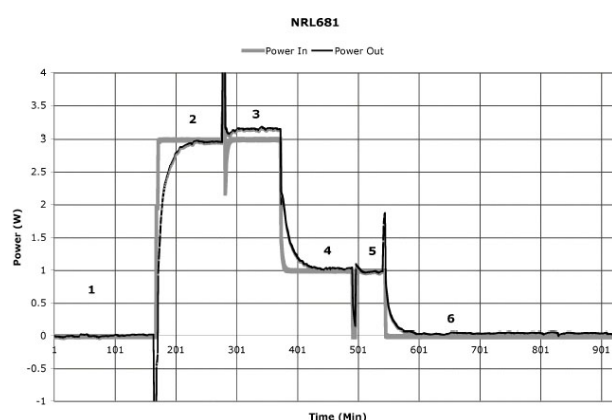


Figure 10. This plot shows that the calorimeter reports a power balance at all intervals except No. 3; during this interval the gold plated copper cathode was electrolyzed at 6 V, 0.5 A and ~ 175 mW of excess power was observed.

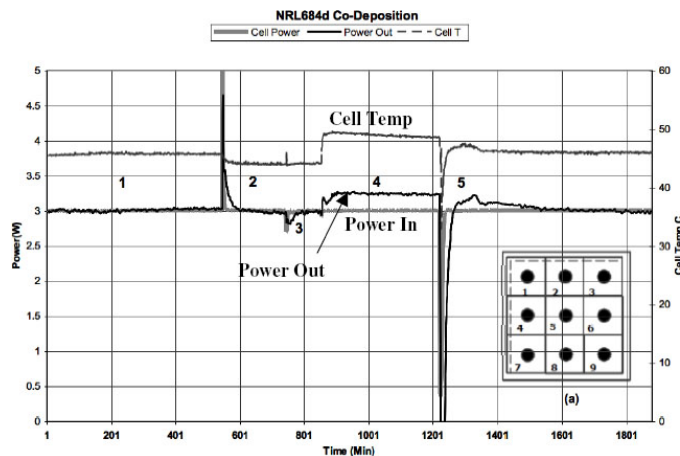


Figure 11. This plot shows a 30 h test consisting of five intervals producing a good power balance at all intervals except No. 4. During this interval the gold plated copper cathode was electrolyzed inside the anode coil and produced a 250 mW excess power signal. The inset (a) shows the lid configuration for this experiment.

same location and manner as the gold plated copper cathode, yet only the gold plated copper cathode produced excess power when electrolyzed inside the Pt anode coil, indicating that the calorimeter was functioning properly. Further, the excess power signal appeared when electrolyzed in a deuterium-based electrolyte but declined slowly to zero when deuterium was replaced with light hydrogen, suggesting the signal might be non-chemical in origin.

6. Discussion

While great care was taken during the experiments to avoid the creation of false positives, the possibility of error was always considered. Colleagues have made several suggestions for sources of effect-producing errors. Most have been tested and shown to be a non factor. One suggestion, made by Dr. Ken Grabowski from NRL, remains open. His concern was that the single immersion heater might create a hot spot within the calorimeter, in turn causing a false positive. This idea was tested briefly by turning off the immersion heater and increasing the enclosure temperature to provide an operating temperature of 45°C. Under these conditions, the excess power signal did not appear. However, the experiment was not conducted with fresh electrolyte and that may have been a factor. The immersion heater was turned back on during the follow-up experiment and the excess power signal returned very slowly, inconsistent with previous experiments. The effect of the immersion heater was tested several times with an inert cathode in an inert electrolyte (LIOH) and the false positive was never observed. If the use of an immersion heater is the source of a false positive, it seems reasonable to expect that the effect would be observed in all types of electrolytes but it is not. The effect is observed only in deuterium-based electrolyte.

Since this calorimeter is a new design, it seemed prudent to study how heat is evolved inside the Seebeck Cell Calorimeter when electrolysis is performed using inert electrodes and electrolyte. Thermistors were placed in holes 1,3,7, and 9 while duplicating the protocol shown in interval 4 of Fig. 11. Two temperature gradient contour maps are shown in Fig. 12a and b.

In Fig. 12a, the immersion heater was off while 3 W of electrolysis was applied to the platinum cathode in hole 5 (center), resulting in a small gradient running from the lower left corner to the upper right corner. Figure 12b shows the gradient when an 11 W resistance heater was turned on in hole 4 plus 3 W of electrolysis power applied to the cathode

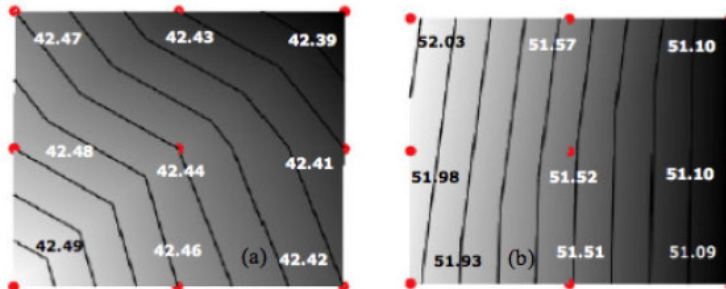


Figure 12. (a and b). The contour plots show temperature gradients produced during electrolysis of a platinum (inert) cathode in LIOH. Thermistors were placed in each of the cell lid corners at holes 1, 3, 7 and 9. The other five temperatures are simply averages from adjacent thermistor probes. The heater is in hole 4, left side center of the cell. Temperatures are in Celsius.

in hole 5. With the resistance heater on, a moderate thermal gradient was produced from left to right across the cell (Fig. 12b). Even with the thermal gradient, the calorimeter produced a power balance at 3 and 14 W (Fig. 13).

7. Enabling Factors

Overall, the claims of Szpak and his co-workers were observed in this series of experiments – codeposition methods produced a significant and repeatable excess power signal that appeared without a long incubation period. The excess power signal appeared only when using deuterium-based electrolyte and was strongest when the cathode was gold plated copper. A new observation was made – the robust excess power signal only appeared when the gold plated copper cathode was electrolyzed inside the anode coil. When electrolyzed outside the anode coil, a null result was normally observed.

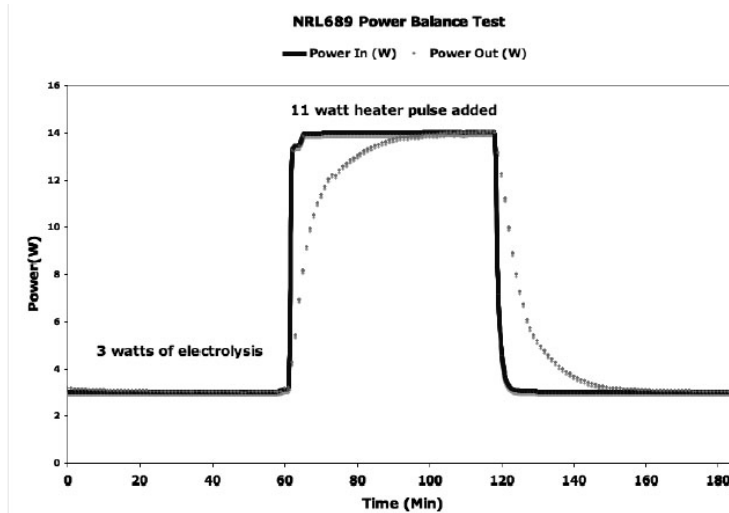


Figure 13. This plot shows the calorimeter is not affected by temperature gradients. The contour map of Fig. 12a relates to the intervals 0–60 and 120–180 min when the immersion heater is off. The interval 60–120 min relates to the contour map shown in Fig. 12b when the heater is on.

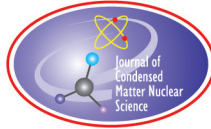
Additional experiments are underway using fresh materials and will attempt to clarify the role of various factors in the production of excess power using codeposition methods. The enabling factors under consideration are the gold plated surface, the external magnetic field, the role of the anode, plating palladium at high current/voltage initially, and the role of the immersion heater as a possible source of error.

Acknowledgements

The author thanks Drs. Graham Hubler, David Knies and Ken Grabowski for project management, Dr. Michael Melich for constant guidance, Breed and Harvel Associates for contracting services, Drs. Melvin Eisner and Melvin Miles for sharing accumulated wisdom. The author is also grateful to Drs. Dennis Cravens, Peter Hagelstein, Pam Mosier-Boss, Francis Tanzella, Scott Chubb for reviewing experimental results and Michael Ronalter for calorimeter glass work. The preliminary results and conclusions presented are the sole responsibility of the author.

References

- [1] S. Pons, M. Fleischmann, M. Hawkins, *J. Electroanal. Chem.* **261** (1989) 301–308.
- [2] S. Szpak, P.A. Mosier-Boss, J.J. Smith, *J. Electroanal. Chem.* **302** (1991) 273.
- [3] M. Miles, P.A. Mosier-Boss, M. Fleischmann, Thermal behavior of polarized Pd/D electrodes prepared by co-deposition, *The Ninth International Conference on Cold Fusion*, Beijing, China, 2002.
- [4] D. Dominguez, P. Hagans, M. Imam, A summary of NRL research on anomalous effects in deuterated palladium electrochemical systems, NRL/MR/6170-96-7803, Washington DC, 1996.
- [5] P.A. Mosier-Boss et al., Detection of energetic particles and neutrons emitted During Pd/D Co- deposition, in *Low-energy Nuclear Reactions Sourcebook*, J. Marwan, S. Krivit (eds.), Oxford University Press, Oxford, 2008.
- [6] E. Storms, How to make a cheap and effective Seebeck calorimeter, in *Condensed Matter Nuclear Science-2003, Tenth International Conference on Cold Fusion Conference Proceedings*, P. Hagelstein, S. Chubb (eds.), Cambridge, MA, 2003, pp. 269–272.



Research Article

Impact of an Applied Magnetic Field on a High Impedance Dual Anode LANR Device

Mitchell R. Swartz *

JET Energy Inc., Massachusetts, USA

Abstract

This paper reports on the impact of an applied magnetic field intensity on LANR solution electrical resistance and an analysis of its role in metal deuteride loading and LANR performance. A dual anode PHUSOR®-type Pd/D₂O/Au LANR device was driven at its optimal operating point, with two electrical current sources; to drive, and examine by 4-terminal electrical resistance, the loaded PdD_x cathode. An applied magnetic field ~0.3 T increases the LANR solution's electrical resistance ~10–17% with a time constant in minutes. The incremental resistance increase to an applied H-field is greatest at low loading current. The incremental resistance increase from an applied H-field is greatest with the applied H-field perpendicular to the driving electrical field (E-field) intensity. The modified LANR deuteron loading rate equation indicates that an applied magnetic field intensity increases deuteron loading in a LANR system by the increasing solution resistance and limiting undesired gas evolving reactions.

© 2011 ISCMNS. All rights reserved.

Keywords: Deuterium, Deuterons, Excess heat, Excess power gain, Flux, Lattice assisted nuclear reactions, Loading, Metamaterials, Nanostructures, Optimal operating point, Palladium

PACS: 28.52.-s, 72.15.-v, 75.30.-m

1. Lattice Assisted Nuclear Reactions

Lattice assisted nuclear reactions (LANR) use hydrogen-loaded alloys to enable near room temperature deuterium fusion and other nuclear reactions [1–49] using deuterons as fuel. Technologies which increase LANR excess energy production include thermal power spectroscopy [4], optimal operating point operation [1,3,4,24], the use of high electrical impedance solutions [3,4], metamaterial shapes [1,32] and nanostructures [1,37,60]. Correctly driven, LANR metamaterial nanostructured devices exhibit excess heat, excess heat flow, and non-thermal near infrared (NT-NIR) emission linked to both [34]. LANRs generated (“excess”) power densities range from ~7 (1989 announcement) to 80–10,000 W/cm³, today. Over time, the magnitude of generated excess power yields significant excess heat, and material changes which are wrought on the electrode, such as volcano-like pits [8,18,19].

At LANRs “core” are deuterons which are tightly packed into binary (“highly loaded”) metals and metallic nanostructures by an applied electric field or elevated gas pressure which supply deuterons in heavy water or gaseous deuterium.

*E-mail: mica@theworld.com

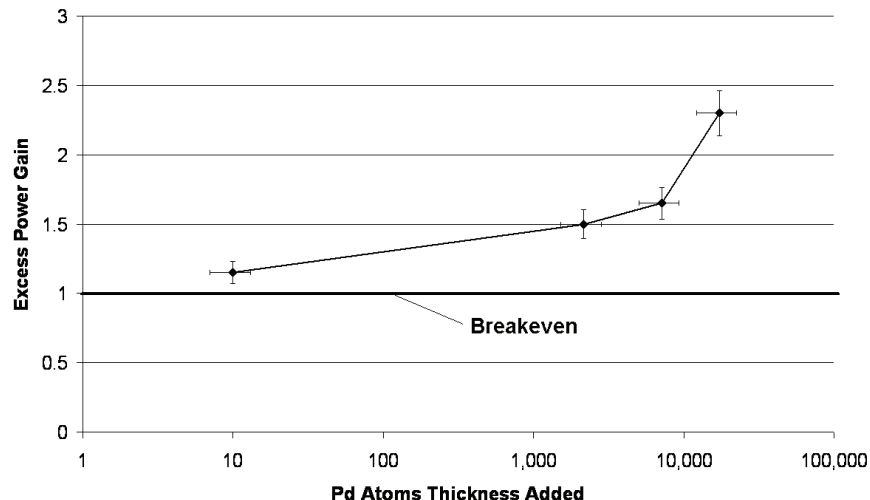


Figure 1. Excess Heat Correlated With Pd Codepositional Thickness Such high impedance metamaterial nanostructured LANR devices have shown power gains more than 200% and short term power gains to $\sim 8000\%$ [1,2], compared to input energy and to input energy transferred to conventional dissipative devices.

With control of LANR devices by precise nanostructure fabrication, metamaterial shape selection using high impedance (“High-Z”) PHUSOR®-type LANR devices in very high electrical resistivity (the real part of the complex impedance, with units of ohms) D₂O, control of D-flux and post D-loading flux, there is a higher likelihood of achieving LANRs impressive energy gain, and with time integration – excess heat, with fairly good reproducibility.

Dual anode PHUSOR® LANR devices (DAP) use two anodes. The first is for preparation of the codepositional surface and solution, and the second is used to drive the active surface [37,68]. Investigations of DAP LANR devices (Fig. 1) have demonstrated that nanostructures are important in LANR with sizes involving circa 10 atoms or more in size. Corroboration of this fact includes experimental results in codeposition [25] and non-thermal near IR (NT NIR; Fig. 3) emissions [34]. The curve in Fig. 1 demonstrates with experimental evidence that LANR excess heat is correlated with the size of the Pd–D nanostructures, which can be considerable (Fig. 2). Figure 1 shows the monotonic increase in excess heat from LANR as the codepositional layer was increased in size over loaded palladium, apparently beginning with nanosize structures in temperature (degrees centigrade, delta-T) for both the ohmic thermal control and the DAP PHUSOR® type LANR device. The input power normalized delta-T was used to compare the LANR and control (ohmic) systems over varying input powers. Sites 1 and 2 represent two sites within the active LANR cell. Site 3 was located at the ohmic (joule) control, consisting of a carbon resistor. In Fig. 2, over time, electrical power was first delivered to the control and then to the LANR device. The important point is that Fig. 2 demonstrates an LANR power gain of $\sim 8000\%$.

By imaging near infra-red, Fig. 3 shows a distribution of LANR activity over the surface of an LANR device, consistent with nanostructures. It shows the emission of near-IR from the electrodes when excess heat is only observed and the active electrodes operated at their optimal operating point (OOP; [1,2,57]), and then the nonthermal near IR emission (NT-NIR) is linked and specific to the LANR devices’ excess heat production and not its physical temperature [34]. This results from the temperature-related shift from hot fusion’s penetrating ionizing radiation to LANR’s skin-depth-locked infrared radiation [50]. Unlike hot fusion or plasma systems, bremsstrahlung radiant power density falls from 0.05 to 0.28 (hot fusion) to $1.4\text{--}8.1 \times 10^{-10}$ for LANR. The delivered X-ray dose at 1 m decreases by incredible 18–

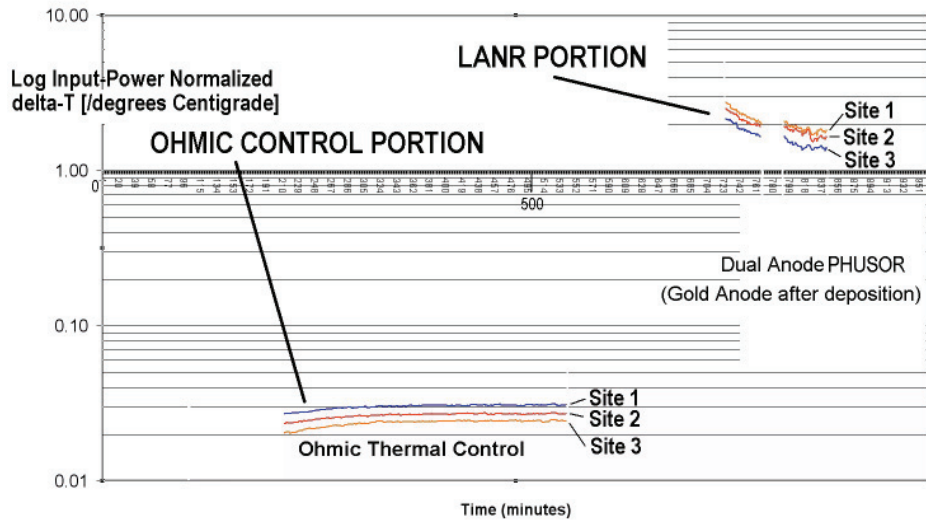


Figure 2. Input power normalized delta- T curves for DAP PHUSOR[®] LANR Fig. 2 shows the transient output of one DAP ($\text{Pd}^*/\text{D}_2\text{O}-\text{Pd}(\text{OD})_2/\text{Au}$ Dual Anode PHUSOR[®]-type) LANR device. The graph shows the input power-normalized change.

23 orders of magnitude from 3.1×10^{19} Grays (hot fusion) to $\sim 2 \times 10^{-4}$ Grays for LANR. In addition, the temperature difference also causes the output spectrum of the Bremsstrahlung radiation to be shifted to the near infra-red, consistent with the NIR emission of LANR systems at their OOP. Figure 3 shows three visible and nearinfrared (NIR) views of a DAP codeposition PHUSOR[®]-type LANR device in heavy water. The platinum anode is seen in the background. The DAP PHUSOR[®] is located in both images (~ 7.7 mM $\text{Pd}(\text{OD})_2$). The inset view is in ordinary light, the other two (from a slightly different angle of observation) are in the near infrared (NIR). The image on the left precedes (“off”), and the one on the right is after activation and generation of excess heat of the PHUSOR[®]-type LANR system.

Given these LANR reactions, there has been much interest in the application of magnetic field intensities to LANR

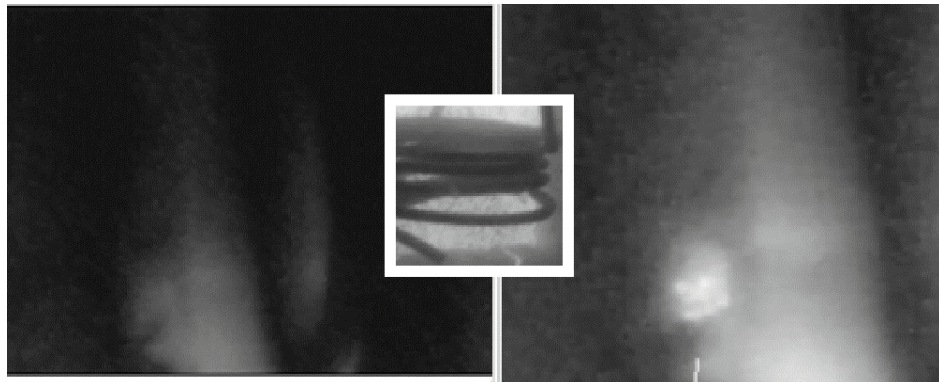


Figure 3. Near-infrared images of DAP LANR cell, before and after activation, with close-up of cathode in visible light (inset) – after Swartz (2010; Ref. [34]).

systems. Dr. Pamela Mosier-Boss et al. at SPAWAR have reported morphology changes on the cathode with an applied magnetic field intensity [19]. For reasons that will become clear in the Interpretation section, because of the complex impact of laser irradiation of LANR cathodes upon solution electrical resistance and power gain [33], we elected to first report on the effect of those applied magnetic field intensities on LANR solution's electrical conductivity because that material parameter is decisive in the success of LANR systems.

2. Experimental Details

The six terminal LANR codepositional high impedance device used here was a DAP LANR device (Dual anode PHUSOR®-Type LANR device; Pd/D₂O, Pd(OD)₂/Pt–Au). It contain nanostructures whose preparation, assembly, and driving is complicated and described elsewhere [1,2, 3,4,34,35,37]. The LANR cathodes were prepared from 99.98+% Pd [Alfa Aesar, Ward Hill, MA], 1.0 mm diameter, ~ 4 – 7 turns on a spiral of ~1.3 cm diameter, with a gap separation from the anode arranged in a Pd/D₂O/Pt or Pd/D₂O/Au configuration (Pt 99.998%). The solution was 7.7 mM Pd(OD)₂ in low paramagnetic high electrical resistivity heavy water (deuterium oxide, low paramagnetic, 99.99%, Cambridge Isotope Laboratories, Andover MA) with no additional electrolyte. For the DAP devices, palladium is laid down from a sacrificial anode upon the surface of a palladium cathode. Then, the palladium anode is removed, and replaced by a gold wire anode to stop the further laying down of further palladium nanostructure upon the palladium cathode. Interestingly, we have reported a new phenomenon during codepositional layering of the DAP cathode. This consists of a dynamic instability oscillation, an electrohydrodynamic Rayleigh–Bernard instability associated with the layering. The time constant was circa 15 min per cycle, but this was irregular, with three to five cycles occurring in a 60 min period. Contamination remains a major problem, with excess heat devastatingly quenched by decreasing electrical resistance of the solution [2–4] the effects on the cathode can be minimized. Contaminants appear from both electrode and container degradation and leaching, from atmospheric contamination, and after temperature cycling. These all inexorably, unintentionally, add to the electrolytic solution decreasing the level of deuteron loading, the rate of loading as well, and the maximum heat producing activity. The heavy water is hygroscopic, therefore kept physically isolated from the air by seals, including several layers of Parafilm M (American National Can, Menasha, WI) and paraffin. All leads near the solution were covered with electrically insulating tubes (medical grade silicone, Teflon, or proprietary materials) used to electrically isolate wires. We continue to avoid chlorine or chloride because of possible explosions from visible light ignition susceptibility, which results because the activation energy with chlorine is only ~17 μ J.

The loading of the palladium from the heavy water, and driving of the reactions through the two electrodes within the reaction container was obtained by controlled electric current source, or a Keithley 225 at low input, with $\pm 1\%$ accuracy. Electrical voltage sources included HP/Harrison 6525A for transsample potentials up to 3000 V ($\sim \pm 0.5\%$ accuracy). All connections isolated, when possible, with Keithley electrometers for computer isolation. To allow 4-terminal electrical resistance measurements within the loaded PdD_x cathode, a first Keithley 225 electric current source was used to drive the cell, and load the cathode, and then a second Keithley 225 electric current source was used to drive the electrical current portion of the four terminal electrical resistivity measurement of the palladium. The data from voltage, current, temperatures at multiple sites of the solution, and outside of the cell, the 4-terminal measurement of the cathode's internal electrical conductivity, additional calibration thermometry and other measurements were sampled at 0.20 Hz, usually 1 Hz, 22+ bits resolution (Omega OMB-DaqTemp, voltage accuracy 0.015 ± 0.005 V, temperature accuracy $< 0.6^\circ\text{C}$) and recorded by computed DAQ. To minimize quantization noise, 1 min moving averages were sometimes made. The noise power of the calorimeter is in the range of ~1–30 mW. The noise power of the Keithley current sources is ~10 nW. Input power is defined as VI . There is no thermo-neutral correction in denominator. Therefore, the observed power is a lower limit. The instantaneous power gain [power amplification factor (nondimensional)] is defined as $P_{\text{out}}/P_{\text{in}}$, as calibrated by at least one electrical joule control (ohmic resistor) and time integrated for validation. The excess energy, when present, is defined as $(P_{\text{output}} - P_{\text{input}}) \times \text{time}$.

The amount of output energy is interfered from the heat released producing a temperature rise, which is then compared to the input energy. Temperature measurements are made by specialized electrically insulated thermocouples [(accuracy ± 0.8 K, precision ± 0.1 K), RTD and other sensors. Probes were calibrated by Omega IcePoint Cell and core temperatures were maintained by feedback control using a Yellow Spring Thermal Controller Model 72 (bandwidth of 0.2 K) within a Honeywell water circulation zone controlled room (± 2.5 K). Thermocouples and other temperature sensors decorated the periphery of the cell, and a multicompartiment calorimeter was used. There was an additional heat-flow probe at the periphery outside of the core. To minimize contamination, the majority of temperature measurements were outside of the inner core container. Calorimetry is augmented by heat flow measurement, electricity production using thermoelectrics, and LANR-driven motors. Outputs are calibrated by ohmic (thermal) controls, and dual ohmic (calorimeter) controls, to evaluate, and certify possible excess heat. Additional calibration has included adequate Nyquist sampling, time-integration, thermal ohmic controls, waveform reconstruction, noise measurement, and other techniques [2–4]. During the experiment, an attempt was made to determine, first, the impact of the direction of the electrical current used for the 4-terminal measurements along the cathode, and second, the impact of the direction of the applied magnetic field intensity obtained from neodymium magnets. The stationary applied magnetic field intensity was circa 0.3 T, and the field was directed either parallel or perpendicular to the applied electric field intensity used to load and drive the LANR device.

3. Results -- Magnetic Fields

Within the DAP (Dual Anode PHUSOR[®]-type Pd/D₂O/Au LANR) device, solution resistances ranged from 800,000 Ω initially to ~ 5000 Ω . The 4-terminal cathodes measurements of electrical resistance of the loaded metal ranged from ~ 50 to 120 m Ω . For the DAP device, the excess heat was measured as the thickness increased to $\sim 17,000$ atoms deep (Fig. 1). At that time, the solution was 7.7 mM Pd(OD)₂, and the open circuit voltage, V_{oc} , used to determine the effectivity of LANR [2,3], was 1.46 V. The Pd^{*}/D₂O-Pd(OD)₂/Au PHUSOR[®]-type system has an initial cell resistance of circa 868 k Ω , which fell to circa 48.3 k Ω upon final preparation.

For the DAP (Dual Anode PHUSOR[®]-type Pd/D₂O/Au LANR device), applying a static magnetic field to the LANR system increased the solution's electrical resistance by 10–17%. This is shown in Fig. 4. The increase in solution electrical resistance was greatest at lower levels of electrical driving of the LANR system (1 mA vs. 10 mA). The increase in solution electrical resistance was greatest when the applied magnetic field was perpendicular to the driving electrical field intensity.

Figure 5 shows the time course of the changes to the magnetic field intensity. The time constant was on the order of minutes.

4. Interpretation – Deuteron Fluxes in LANR

An applied magnetic field in LANR can effect the resistance of the solution, and as will be shown below, that increased resistance can increase metal deuteride loading. Relevant to this analysis were our past studies which examined the impact of laser irradiation on LANR cathodes and reported, in 2003, that it decreases the solution electrical resistance and increases LANR excess heat, but decreases LANR power gain.

Deuteron flux is a key issue in LANR. Nernst calculations of the activities of the electrolyte [51,52] adjacent to a metal electrode have been applied to LANR to derive distributions of deuterium in palladium and the solution. However, because the LANR systems are not at equilibrium, such Nernst calculations are generally not applicable [53,54]. By contrast, unaffected by non-equilibrium, the quasi-1-dimensional (Q1D) model of deuteron loading [53] has been used to analyze deuteron populations and deuteron flow. It has foundation in the known dielectric properties of materials

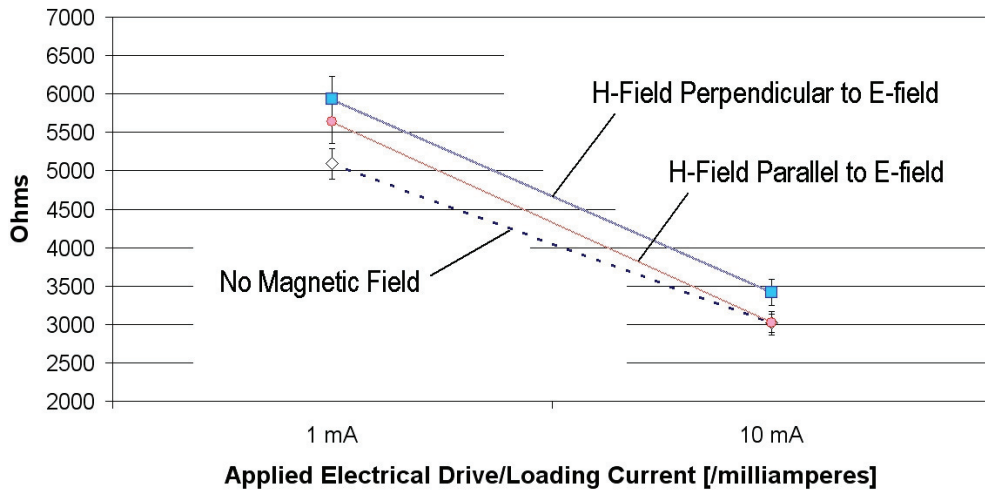


Figure 4. Effect of applied H-field on DAP PHUSOR®- LANR device's solution electrical resistance.

[55] and continuum electromechanics [56], and has generated the deuteron-flux equations which explain the reason for LANR's difficulty – and the road to success.

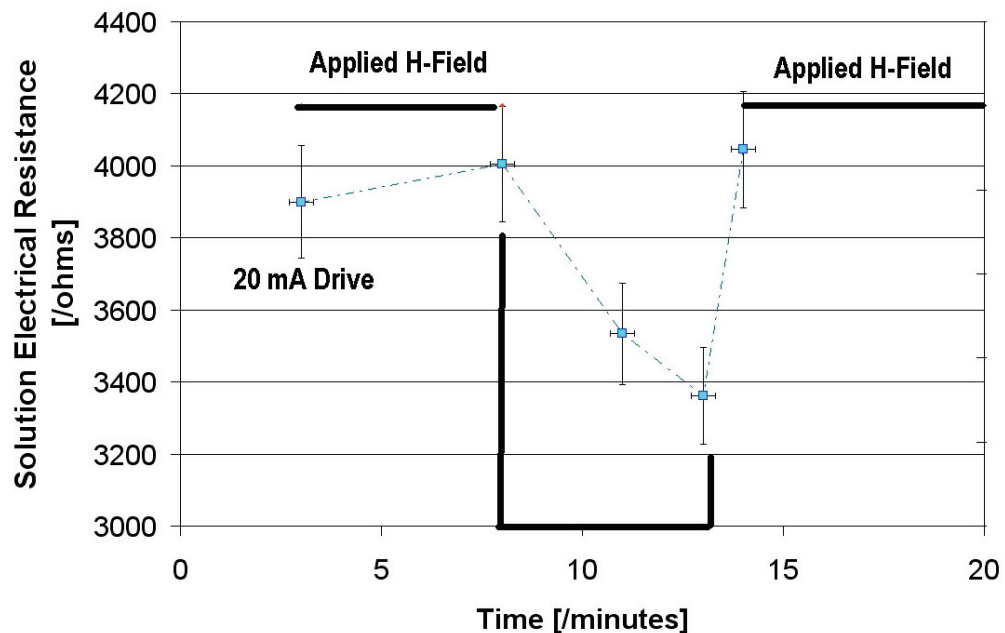


Figure 5. Time course of solution electrical resistance after change of applied H-field.

Several different deuteron populations and fluxes must be distinguished [57] at the surface of the low hydrogen-overvoltage palladium, with its surface highly populated with atomic, diatomic (D_2), and bulk-entering deuterons [1,32]. The deuteron fluxes are seen on the left of Fig. 6, which is a schematic, simplified, representation of the anode, solution, and a portion of the cathode along with five types of deuteron fluxes involved in LANR.

The deuteron fluxes are deuteron cationic flow in the solution (J_D), and the four types of deuteron flux in the loaded palladium cathodic lattice (J_E , J_G , J_F , and J_{IP}). The latter are the entry of deuterons to the metal lattice (“loading”, J_E), movement to gas (D_2) evolution (“bubble formation”, J_G), intrapalladial deuteron flux (J_{IP}) flow through the metal (generated by metamaterials), and an extremely tiny loss by the desired fusion reactions (J_F). There is conservation of deuterons with the exception of a loss (J_F) to all putative fusion reactions, which are extremely small, when present.

As Fig. 6 shows, cationic deuteron flux (J_D) brings deuterons to the cathode surface to create a cathodic fall and double layer before the electrode surface. It begins far from the cathode surface, in the deuterium oxide (heavy water) located between the electrodes, where the deuterons are tightly bound to oxygen atoms as D_2O . In the absence of significant solution convection, the flux of deuterons (J_D) results from diffusion down concentration gradients and electrophoretic drift by the applied electric field [53,54,56,58].

$$J_D = -B_D \frac{d[D(z, t)]}{dz} - \mu_D [D(z, t)] \frac{d\Phi}{dz}, \quad (1)$$

J_D depends on deuteron diffusivity (B_D) and electrophoretic mobility (D), and the applied electric field intensity. At any molecular site across the heavy water solution, the applied electrical energy is a tiny fraction compared to $k_B T$, so the deuterons migrate by drift ellipsoids of L- and D-deuteron defects in the applied electric field creating a ferroelectric inscription [58,59]. This D-defect conduction/polarization process augments other charge carriers, ionic drift, space charge polarization and clathrates. The resultant D-defect migration produces a “cathodic fall” of deuterons and a E-field contraction so that most of the voltage drop is at the interface in front of the electrode surface. This concentration polarization may produce very large local electric field intensities, possibly ranging from 10^4 to 10^7 V/cm [53,54].

From the concentration polarization of deuterons before the cathode, at the inner boundary of the double layer, intermolecular deuteron transfer from the heavy water solution to the metal surface is controlled and limited by electron-limited transfer, which leaves an atomic deuteron on the metal surface. The transfer mechanisms to the palladium surface are driven by infrared vibrations and microwave rotations [33,59], creating a solution photosensitivity which produces a photo-activated increase of excess energy and loss of power gain [33].

On the metal surface, the plethora of atomic deuterons either enter the metal (“are loaded”) forming a binary alloy [60–67], or remain on the surface, or form diatomic deuterium gas bubbles (D_2). As a result, palladium has its

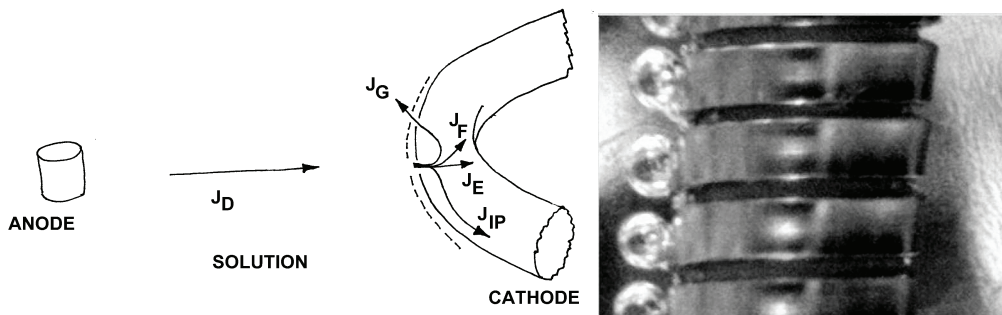


Figure 6. Deuteron Fluxes in LANR (a) Left – Schematic of deuteron fluxes, from solution to loaded metal. (b) Right – Close-up of active LANR cathode (after Swartz 2006, Ref. [17]).

surface populated with atomic (D) and diatomic deuterium (D_2). Any deuterons which enter the metal are electrically neutralized ('dressed') by a partial electronic cloud, shielding their charge (in a Born–Oppenheimer approximation) [37]. The deuterons drift along dislocations and through the lattice and its vacancies, falling from shallow to deeper located binding sites. There is competing obstruction by ordinary hydrogen and other materials at interfaces and grain boundary dislocations. The gas bubbles (D_2) are undesirable producing low dielectric constant layers in front of the electrode, obstructing the electrical circuit. As derived elsewhere [53], after solving the partial differential equations, and using conservation of mass, and numerically dividing each deuteron flux (J_E , J_G , and J_F) by the local deuteron concentration to yield the first-order deuteron flow rates, k_E , k_G , and k_F (with units of cm/s, respectively), Eq. (2) is the deuteron flux equation of LANR. Numerically, k_E might be in the range of 0.5–30 μ A, and the concentration of (D) is circa 50 M.

$$\kappa_E = \mu_D E - (\kappa_g + \kappa_f). \quad (2)$$

Equation (2) is the deuteron loading rate equation. It relates cathodic deuteron gain from the applied electric field to the loss of deuterons from gas evolution and fusion, and teaches many things. The deuteron loading rate equation shows that the deuteron gain of the lattice [through the first order loading flux rate (k_E)] is dependent upon the applied electric field *minus* the flux rate losses of deuterons from gas evolution (k_G) and fusion (k_F). The deuteron loading rate equation, Eq. (2), reveals that desired LANR reactions are quenched by electrolysis, which is opposite conventional "wisdom" that LANR is 'fusion by electrolysis'. Equation (2) also heralds that LANR can be missed by insufficient loading, contamination (effecting k_E , by protons or salt) and by the evolution of D_2 gas, which all inhibit the desired LANR reactions [53,1,2] and leading to the optimal operating point manifolds. This quenching is of prime importance.

Equation (2) can be modified to Eq. (3), the modified deuteron loading rate equation, by substituting into it the Einstein relation. There are many important lessons for LANR.

$$k_E = \frac{B_D q V}{L[k_B T]} - (\kappa_g + \kappa_f). \quad (3)$$

The first term now has geometric and material factors. B_D is the diffusivity of the deuteron. $k_B T$ is the Boltzmann's constant and temperature. q is the electronic charge, and V is the driving applied voltage. Most importantly, dominating the first term is the ratio of two energies (the applied electric energy organizing the deuterons divided by $k_B T$, thermal disorder). This energy ratio is decisive in controlling the deuteron loading flux in palladium – and thus LANR. Successful LANR experiments reflect the 'war' between applied electrical energy which is organizing the deuterons versus their randomization by thermal disorganization.

The second term includes the first-order deuteron loss rates by gas evolution and the desired fusion process(es). The minus sign means that the second term heralds that competitive gas evolving reactions at the metal electrode surface can destroy (quench) the desired reactions. The first-order loading flux rate constant (k_E) is dependent upon the applied electric field intensity minus the first-order gas loss rate constant resulting from gas (D_2) evolution at the cathode (k_G). This implication is exactly opposite conventional "wisdom" that LANR is 'fusion by electrolysis' [1–4]. LANR can be missed by insufficient loading, contamination (effecting k_E , by protons or salt), and by the evolution of D_2 gas, which all inhibit ("quench") the desired LANR reactions [3,4]. Note that Eq. (3) with the Einstein relation is similar to some flux equations from solid state physics, so there is the question of similarity of deuterons and their holes in Pd to holes and electrons in semiconductor materials.

5. Interpretation – Impact on Loading Rate

We believe the applied magnetic field intensity directly changes the loading rate of deuterons in to a metal deuteride. The following explains the reasons, and derives the equations demonstrating the relationship. Consider the role of

cathodic photo-irradiation in LANR. In addition to entry into the skin depth layer of the metal, a part of the impact is due to reflection off the cathode back into the double layer. Deuteron injection into the palladium increases (activation energy of ~ 14 kcal per mol) from microwave rotation and IR vibration for the intermolecular transfer of deuterons to the Pd [33]. Hagelstein, Letts and Cravens [11,12] have also reported both single and dual photon impacts on cathodes as increasing excess heat. As we reported, there is a small and reproducible photo-incremental increase in both the power gain and in the observed excess heat from the coherent irradiation of the cathode, even when heating effects of the beam were included in the calibration. Near the OOP, the optical irradiation increased the excess power from 84.7 ± 10 to 95.5 ± 12 mW. For ~ 250 mW input electrical power, the irradiation increased the excess power from 79.8 ± 7.6 to 93.3 ± 6.3 mW. Beyond the OOP, the impact of coherent non-ionizing radiation upon the cathode is small compared to dark heat production (power gain 1.49 ± 0.005 in the dark, 1.50 ± 0.005 for the laser irradiation, for input power levels which produce 400 mW excess heat). Incremental photoinduced excess power was observed only in the presence of a functioning active loaded cathode. This photoinduced excess power may be a lower limit. Issues of good optical path geometry, angle of penetration, active irradiated cathodic area, possible double layer interactions, interference with low dielectric constant bubbles formed and skin depth penetration remain relevant and suggest that the actual impact of laser irradiation may be greater.

We discovered that the effects are partially extra-cathodic. Therein lies the “rub”. Even though there is an incremental photo-thermoelectric increase in excess heat production changing the net excess power from 1.7 to 1.8 ± 0.1 W, with optical irradiation of the cathode and surrounding solution, there is an additional change. Irradiation of the cathode necessarily results in irradiation of the solution and a photoinduced decrease in the Pt/D₂O/Pd electrical resistance which increased the input electrical power dissipated (not excess). Optical irradiation of the cathodic volume and surrounding solution produces a photoinduced decrease in the effective cell-solution electrical resistance (55–51 k Ω). This increases the input electrical power for the same applied voltage. Because of the relationship between power gain (non-dimensional), excess power and input electrical power (watts), there follows a photoinduced decrease of the power gain, which is noticeable at higher input electrical power levels (2.4–2.3, for 1.3 W input).

This paradoxical decrease in the power gain heralds conduction/polarization pathways which lead away from some desired reactions. Exactly why this occurs can be understood by analysis of the modified loading flux equation. Examination of the LANR loading rate equations reveals that there are at least two ways the applied magnetic field can interact in the solution, through the ordering energy ratio and diffusivity of deuterons at the surface (first term), and through the solution resistance (second term).

Assuming a Faradaic efficiency for gas formation of ξ_g per electron, an electric current I , and accounting for the Faraday ratio to the mole, F , then

$$K_g \approx \frac{\xi_g I}{F A [D^+]} \quad (4)$$

Substituting the electrical admittance with electrical conductivity with geometric factors, yields

$$K_g \approx \frac{\xi_g \sigma_{D_2O} V}{F L [D^+]} \quad (5)$$

As a result, the modified LANR loading rate equation becomes

$$k_e \cong \frac{B_D q V}{L k_B T} - \frac{\xi_g \sigma_C V}{F L [D^+]} \quad (6)$$

The term σ_C/L can be replaced by $1/AR$ (A is the area, R is the solution electrical resistance (ohms)). R is in the denominator of the second term. This is a very important equation because, first, the first-order loading rate decreases (“is quenched”) with increasing solution electrical conductivity (or decreasing electrical resistance). This equation predicts the response of LANR to an applied magnetic field intensity in an LANR system. If the applied magnetic field

intensity is sufficient, this term may dominate, actually increasing the system performance. Increasing the solution electrical resistance (R) increases LANR loading. The converse, through the second term can end all loading and LANR performance.

Second, in addition, the changes in vectors from the applied magnetic field intensity, with the observed decreased electrophoretic mobility, may be the etiology of some of the morphologies reported by Szpak, Gordon and Mosier-Boss [47,19,41].

6. Conclusion – Possibility of Increased Loading

An applied magnetic field (~ 0.3 T) to the high impedance DAP (Dual anode PHUSOR(R) type) LANR system increases the LANR solution's electrical resistance $\sim 10\text{--}17\%$. The time constant for change was on the order of minutes. The incremental resistance increase to an applied H-field is greatest at low input loading and driving electrical currents. The incremental resistance increase to an applied H-field is greatest with the applied H-field perpendicular to the applied driving electrical field (E-field) intensity.

The modified LANR loading rate equation indicates that an applied H-field may increase loading in a LANR system by increasing solution resistance. Our past studies, which examined the impact of laser irradiation on LANR cathodes has taught us that any change of solution electrical resistance will directly impact LANR performances through the modified deuteron loading rate equation.

In this paper, it is shown that if an applied magnetic field intensity is sufficient, especially perpendicular to the applied electric field intensity and at lower electrical driving currents, an increase in system performance is expected from increased loading, resulting from an increase in solution electrical resistance. In the future, we anticipate reporting and discussing the observed and expected findings in LANR systems, with various arrangements of applied magnetic field intensities.

Acknowledgments

The author thanks Gayle Verner for her meticulous help, and Larry Parker Forsley for presenting this lecture, and Jeffrey Tolleson, Alan Weinberg, Alex Frank, Charles Entenmann, John Thompson, Peter Hagelstein, Brian Ahern, Pamela Mosier-Boss, Scott Chubb, Jeffrey Driscoll, Richard Kramer, Michael Staker, Jan Marwan, Steven Olasky, Robert Smith, for their critique, valued ideas, suggestions, and JET Energy, Incorporated and New Energy Foundation for contributing to support this effort. PHUSOR® is a registered trademark of JET Energy Inc. Images are copyright 2010 JET Energy, Incorporated. All rights reserved. Protected by US Patents D596,724; D413,659; and other patents pending.

References

- [1] Swartz, M.R. Survey of the Observed Excess Energy and Emissions in Lattice Assisted Nuclear Reactions, *J. Scientific Exploration* 23(4) (2009) 419–436.
- [2] Swartz, M.R. Excess Power Gain using High Impedance and Codepositional LANR Devices Monitored by Calorimetry, Heat Flow, and Paired Stirling Engines, *Proceedings of the 14th International Conference on Condensed Matter Nuclear Science and the 14th International Conference on Cold Fusion* (ICCF-14), 10–15 August 2008, Washington, DC, David J. Nagel and Michael E. Melich (eds.), ISBN: 978-0-578-06694-3, 2010, p. 123.
- [3] Swartz, M., G. Verner, Excess Heat from Low Electrical Conductivity Heavy Water Spiral-Wound Pd/D₂O/Pt and Pd/D₂O-PdCl₂/Pt Devices, *Condensed Matter Nuclear Science, Proceedings of ICCF-10*, (eds.) P.L. Hagelstein, S.Chubb, World Scientific, Singapore, pp. 29–44; 45–54, 2006. ISBN 981-256-564-6.
- [4] Swartz, M., Consistency of the Biphasic Nature of Excess Enthalpy in Solid State Anomalous Phenomena with the Quasi-1-Dimensional Model of Isotope Loading into a Material, *Fusion Technol.* 31 (1997) 63–74.

- [5] Arata, Y., Y.C. Zhang, Anomalous Production of Gaseous ${}^4\text{He}$ at the Inside of DS-Cathode During D_2 -Electrolysis, *Proc. Jpn. Acad. Ser. B* **75** (1999) 281; Arata, Y., Y.C. Zhang, Observation of Anomalous Heat Release and Helium-4 Production from Highly Deuterated Fine Particles, *Jpn. J. Appl. Phys.* **38**(2) (1999) L774; Arata, Y., Y. Zhang, The Establishment of Solid Nuclear Fusion Reactor, *J. High Temp. Soc.* **34**(2) (2008) 85.
- [6] Celani, F. et al., Deuteron Electromigration in Thin Pd Wires Coated With Nano-Particles: Evidence for Ultra-Fast Deuterium Loading and Anomalous, Large Thermal Effects, in *ICCF-14 International Conference on Condensed Matter Nuclear Science*, Washington, DC, 2008.
- [7] Dardik, I., H. Branover, A. El-Boher, D. Gazit, E. Golbreich, E. Greenspan, A. Kapusta, B. Khachatorov, V. Krakov, S. Lesin, B. Michailovitch, G. Shani, T. Zilov, Intensification of Low Energy Nuclear Reactions Using Superwave Excitation, *Proceedings of the 10th International Conference on Cold Fusion*, Peter L. Hagelstein, Scott, R. Chubb (eds.), World Scientific, NJ, ISBN 981-256-564-6, 2006, p. 61.
- [8] Dash, J., D.S. Silver, Surface Studies After Loading Metals With Hydrogen And/Or Deuterium, *13th Conf. CMNS 2007*. Sochi, Russia; Dash, J., S. Miguet, Microanalysis of Pd Cathodes after Electrolysis in Aqueous Acids, *J. New Energy* **1**(1) (1996) 23.
- [9] Fleischmann, M., S. Pons, Electrochemically Induced Nuclear Fusion of Deuterium, *J. Electroanal. Chem.* **261** (1989) 301–308, erratum, **263** (1989) 187; M. Fleischmann, S. Pons, Some comments on the paper Analysis of Experiments on Calorimetry of LiOD/ D_2O Electrochemical Cells, R.H. Wilson et al., *J. Electroanal. Chem.* **332** (1992) 1*, *J. Electroanal. Chem.* **332** (1992) 33–53, M. Fleischmann, S. Pons, Calorimetry of the Pd- D_2O system: from simplicity via complications to simplicity, *Phys. Lett. A* **176** (1993) 118–129, M. Fleischmann, S. Pons, M. Anderson, L.J. Li, M. Hawkins, Calorimetry of the palladium–deuterium-heavy water System, *Electroanal. Chem.* **287** (1990) 293.
- [10] Iwamura, Y., M. Sakano, T. Itoh, Elemental Analysis of Pd Complexes: Effects of D_2 Gas Permeation, *Jpn. J. Appl. Phys. A* **41** (2002) 4642, Iwamura, Y. et al., Observation Of Surface Distribution Of Products By X-Ray Fluorescence Spectrometry During D_2 Gas Permeation Through Pd Complexes, in *The 12th International Conference on Condensed Matter Nuclear Science*. Yokohama, Japan, 2005.
- [11] Letts D., D. Cravens, Laser Stimulation of Deuterated Palladium: Past and Present, *Proceedings of the 10th International Conference on Cold Fusion*, Peter L. Hagelstein, Scott, R. Chubb (eds.), World Scientific, NJ, ISBN 981-256-564-6, 2006, pp. 171, 159.
- [12] Letts, D., P.L. Hagelstein, Stimulation of Optical Phonons in Deuterated Palladium, in *ICCF-14 International Conference on Condensed Matter Nuclear Science*, Washington, DC, 2008; Letts, D., D. Cravens, P.L. Hagelstein, Thermal Changes in Palladium Deuteride Induced by Laser Beat Frequencies, in *Low-Energy Nuclear Reactions Sourcebook*, J. Marwan, S. Krivit (eds.), 2008.
- [13] McKubre, M., F. Tanzella, P. Hagelstein, K. Mullican, M. Trevithick, The Need for Triggering in Cold Fusion Reactions, *Proc. 10th International Conf. on Cold Fusion*, Peter L. Hagelstein, Scott, R. Chubb (eds.), World Scientific, NJ, ISBN 981-256-564-6, 2006, p. 199.
- [14] Miles, M.H., R.A. Hollins, B.F.Bush, J.J. Lagowski, R.E. Miles, Correlation of excess power and helium production during D_2O and H_2O electrolysis, *J. Electroanal. Chem.* **346** (1993) 99–117.
- [15] Miles, M.H., B.F.Bush, Heat and Helium Measurements in Deuterated Palladium, *Trans. Fusion Technol.* **26** (1994) 156–159.
- [16] Miles, M.H. et al. Calorimetric Analysis of a Heavy Water Electrolysis Experiment Using a Pd-B Alloy Cathode, Naval Research Laboratory Report NRL/MR/6320-01-8526, pp. 155, March 16, 2001.
- [17] Miley, G.H., G. Narne, T. Woo, Use of combined NAA and SIMS analyses for impurity level isotope detection. *J. Radioanal. Nucl. Chem.* **263**(3) (2005) 691–696, Miley, G.H., J. Shrestha, Transmutation Reactions and Associated LENR Effects in Solids, in *Low-Energy Nuclear Reactions Sourcebook*, J. Marwan, S. Krivit (eds.), Oxford University Press, Oxford, 2008.
- [18] Mosier-Boss, P.A., S. Szpak, 'The Pd/nH System: Transport Processes and Development of Thermal Instabilities, *Il Nuovo Cimento* **112A** (1999) 577–585.
- [19] Mosier-Boss, P.A., S. Szpak, F.E. Gordon, L.P.G. Forsley, Use of CR-39 in Pd/D Co-Deposition Experiments, *Euro. Phys. J.Appl. Phys.* **40** (2007) 293–303.
- [20] Mosier-Boss, P.A., S. Szpak, F.Gordon, L.P.Forsley, Triple Tracks in CR-39 Evidence of Energetic Neutrons, *Naturwissenschaften* **96** (2009) 135–142.
- [21] Pons, S., Fleischmann, M., Heat After Death, *Proc. ICCF-4*, Maui, EPRI TR104188-V2, vol. 2, 1994, pp. 8–1, *Trans. Fusion Technol.* **26** (4T, Part 2) (1994) 87.

[22] Srinivasan, M. et al., Tritium and Excess Heat Generation During Electrolysis of Aqueous Solutions of Alkali Salts with Nickel Cathode, *Frontiers of Cold Fusion*, H. Ikegami (ed.), *Proceedings of the Third International Conference on Cold Fusion*, October 21–25, 1992, Universal Academy Press, Tokyo, pp. 123–138.

[23] Stringham, R., *Cavitation and Fusion, ICCF-10*, Cambridge, MA, 2003.

[24] Swartz, M., Can a Pd/D₂O/Pt Device be Made Portable to Demonstrate the Optimal Operating Point?, *Condensed Matter Nuclear Science, Proceedings of ICCF-10*, Peter L. Hagelstein, Scott, R. Chubb (eds.), World Scientific Publishing, NJ, 2006, pp. 29–44; 45–54. ISBN 981-256-564-6.

[25] Swartz, M., Codeposition Of Palladium And Deuterium, *Fusion Technol.* **32** (1997) 126–130.

[26] Swartz, M., Noise Measurement in cold fusion systems, *J. New Energy* **2** (2) (1997) 56–61.

[27] Swartz, M., Patterns of Failure in Cold Fusion Experiments, *Proc. 33RD Intersociety Engineering Conference on Energy Conversion*, IECEC-98-I229, CO, Aug. 1998.

[28] Swartz, M., Patterns of Success in Research Involving Low-Energy Nuclear Reactions, *Infinite Energy* **31** (2000) 46–48.

[29] Swartz, M., The Impact of Heavy Water (D₂O) on Nickel-Light Water LANR Systems, *Proc. of the 9th International Conference on Cold Fusion*, Beijing, China, Xing Z. Li (ed.), pp. 335–342, May 2002.

[30] Swartz, M., G. Verner, Dual Ohmic Controls Improve Understanding of ‘Heat after Death’, *Trans. Amer. Nucl. Society* **93** (2005) 891–892. ISSN:0003-018X.

[31] M. Swartz, G. Verner, Two Sites of Cold Fusion Reactions Viewed by their Evanescent Tardive Thermal Power, Abstract of ICCF-11, 2004; M. Swartz, Kinetics and Lumped Parameter Model of Excess Tardive Thermal Power, Mitchell Swartz, APS (2005).

[32] Swartz, M., G. Verner, Metamaterial Function of Cathodes Producing Hydrogen Energy and Deuteron Flux, in *ICCF-14 International Conference on Condensed Matter Nuclear Science*, 10–15 August 2008, Washington, DC, David J. Nagel and Michael E. Melich (eds.), ISBN: 978-0-578-06694-3, 2010, p. 458. .

[33] Swartz, M., G. Verner, Photoinduced Excess Heat from Laser-Irradiated Electrically-Polarized Palladium Cathodes in D₂O, *Condensed Matter Nuclear Science, Proc. ICCF-10*, Peter L. Hagelstein, Scott Chubb (eds.), NJ, 2006, pp. 213–226. ISBN 981-256-564-6.

[34] Swartz, M., G. Verner, A. Weinberg, Non-Thermal Near-IR Emission Linked with Excess Power Gain in High Impedance and Codeposition PHUSOR-LANR Devices, in *ICCF-14 International Conference on Condensed Matter Nuclear Science*, 10–15 August 2008, Washington, DC, David J. Nagel and Michael E. Melich (eds.), ISBN: 978-0-578-06694-3, 2010, p. 343.

[35] Swartz, M., Improved Electrolytic Reactor Performance Using pi-Notch System Operation and Gold Anodes, *Trans. American Nuclear Association*, Nashville, Tenn Meeting, (ISSN:0003-018X publisher LaGrange, Ill) Vol. 78, 1998, pp. 84–85.

[36] Swartz, M.R., Breakeven from LANR PHUSOR Device Systems: Relative Limitations of Thermal Loss in Feedback Loop, in *ICCF-14 International Conference on Condensed Matter Nuclear Science*, D. J. Nagel and M. E. Melich (eds.), 2010.

[37] Swartz, M.R., Excess Heat and Electrical Characteristics of Type B Anode-Plate High Impedance PHUSOR-type LANR Devices, *J. Scientific Exploration*, American Chemical Society, Salt Lake City, UT, 2010, in press.

[38] Szpak S., P.A. Mosier-Boss, ‘On the Behavior of the Cathodically Polarized Pd/D System: a Response to Vigier’s Comments, *Phys. Letts. A* **221** (1996) 141–143, Szpak S., P.A. Mosier-Boss, S.R. Scharber, J.J. Smith, Cyclic Voltammetry of Pd+D Codeposition, *J. Electroanal. Chem.* **380** (1995) 1–6.

[39] Szpak S., P.A. Mosier-Boss, J.J. Smith, Deuterium Uptake During Pd–D Codeposition, *J. Electroanal. Chem.* **379** (1994) 121–127.

[40] Szpak S., P.A. Mosier-Boss, F.E. Gordon, Further Evidence of Nuclear Reactions in the Pd/D Lattice: Emission of Charged Particles, *Naturwissenschaften* **94** (2007) 511–514.

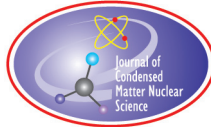
[41] Szpak S., P.A. Mosier-Boss, C. Young, F.E. Gordon, Evidence of Nuclear Reactions in the Pd Lattice, *Naturwissenschaften* **92** (2005) 394–397.

[42] Szpak S., P.A. Mosier-Boss, S.R. Scharber, J.J. Smith, Charging of the Pd/nH System: Role of the Interphase, *J. Electroanal. Chem.* **337** (1992) 147–163.

[43] Szpak S., P.A. Mosier-Boss, M.H. Miles, M. Fleischmann, Thermal Behavior of Polarized Pd/D Electrodes Prepared by Co-Deposition, *Thermochim. Acta* **410** (2004) 101–107.

[44] Szpak S., P.A. Mosier-Boss, J.J. Smith, On the Behavior of the Cathodically Polarized Pd/D System: Search for Emanating Radiation, *Phys. Letts. A* **210** (1996) 382–390.

- [45] Szpak S., P.A. Mosier-Boss, J.J. Smith, On the Behavior of Pd Deposited in the Presence of Evolving Deuterium, *J. Electroanal. Chem.* **302** (1991) 255–260.
- [46] Szpak S., P.A. Mosier-Boss, R.D. Boss, J.J. Smith, On the Behavior of the Pd/D System: Evidence for Tritium Production, *Fusion Technol.* **33** (1998) 38–51.
- [47] Szpak, S. et al., The effect of an external electric field on surface morphology of codeposited Pd/D films, *J. Electroanal. Chem.* **580** (2005) 284–290.
- [48] Violante, V., E. Castagna, C. Sibilia, S. Paoloni, F. Sarto, Analysis of Mi-Hydride Thin Film After Surface Plasmons Generation by Laser Technique, *Proceedings of the 10th International Conference on Cold Fusion*, Peter L. Hagelstein, Scott, R. Chubb (eds.), World Scientific, NJ, ISBN 981-256-564-6, 2006, pp. 405, 421.
- [49] Will, F.G., K. Cedzynska, D.C. Linton, Tritium Generation in Palladium Cathodes with High Deuterium Loading, *Trans. Fusion Technol.* **26** (1994) 209–213, Reproducible tritium generation in electrochemical cells employing palladium cathodes with high deuterium loading, *J. Electroanal. Chem.* **360** (1993) 161–176.
- [50] Swartz, M., G. Verner, Bremsstrahlung in Hot and Cold Fusion, *J. New Energy* **3**(4) (1999) 90–101.
- [51] H. H. Uhlig, *Corrosion and Corrosion Control*, Wiley, New York, 1971.
- [52] J. O'M Bockris, A.K.N. Reddy, *Modern Electrochemistry*, Plenum Press, New York, 1970.
- [53] Swartz, M., Quasi-One-Dimensional Model of Electrochemical Loading of Isotopic Fuel into a Metal, *Fusion Technol.* **22**(2) (1992) 296–300.
- [54] Swartz, M., Isotopic Fuel Loading Coupled to Reactions At an Electrode, *Fusion Technol.* **26**(4T) (1994) 74–77.
- [55] A. Von Hippel, *Dielectric Materials and Applications*, MIT Press, Cambridge, 1954.
- [56] J.R. Melcher, *Continuum Electromechanics*, MIT Press, Cambridge, 1981.
- [57] Swartz, M., Generality of Optimal Operating Point Behavior in Low Energy Nuclear Systems, *J. New Energy* **4**(2) 218–228. (1999).
- [58] Swartz, M., Dances with Protons - Ferroelectric Inscriptions in Water/Ice Relevant to Cold Fusion and Some Energy Systems, *Infinite Energy* **44** (2002).
- [59] A. Von Hippel, D.B. Knoll, W.B. Westphal, Transfer of Protons through 'Pure' Ice 1h Single Crystals, *J. Chem. Phys.* **54** (1971) 134, 145.
- [60] Swartz, M.R., Optimal Operating Point Manifolds in Active, Loaded Palladium Linked to Three Distinct Physical Regions, in *ICCF-14 International Conference on Condensed Matter Nuclear Science*, Washington, DC, 2010, in press.
- [61] Hampel, C.A., *Rare Metal Handbook*, Reinhold Pub., NY, 1954.
- [62] Hansen, M., K. Anderko, *Constitution of Binary Alloys*, McGraw-Hill, NY, 1958.
- [63] Swartz, M., Catastrophic Active Medium Hypothesis of Cold Fusion, Fourth International Conference on Cold Fusion, Vol. 4, Sponsored by EPRI and the Office of Naval Research, 1994, Swartz, M., Hydrogen Redistribution By Catastrophic Desorption In Select Transition Metals, *J. New Energy* **1**(4) (1997) 26–33.
- [64] Papaconstantopoulos, D.A., B.M. Klein et al., Band structure and superconductivity of PdD_x and PdH_x, *Phys. Rev.* **17**(1) (1977) 141150.
- [65] Wicke, E., H. Brodowsky, Hydrogen in Palladium and Palladium Alloys, *Hydrogen in Metals II*, G. Alefeld, J. Volkl, (eds.), Springer, Berlin, 1978.
- [66] Teichler, H., Theory of hydrogen hopping dynamics including hydrogen-lattice correlations, *J. Less-Common Metals* **172–174** (1991) 548–556.
- [67] Klein, B.M., R. E. Cohen, Anharmonicity and the inverse isotope effect in the palladiumhydrogen system, *Phys. Rev. B* **45**(21) (1992) 405.
- [68] Swartz, M., US Patent Application 07/339,976, 1989.



Research Article

Detection of Abnormal Quantity of Hydrogen upon Electrical Explosion of Titanium Foil in a Liquid

Leonid I. Urutskoev * and Dmitry V. Filippov

RECOM, National Research Center "Kurchatov Institute", Moscow, Russia and Moscow State University of Printing Arts, Moscow, Russia

Anri A. Rukhadze

General Physics Institute (Russian Academy Of Sciences), Moscow, Russia

Larion A. Lebedev

State Research and Development Center for Expertise of Projects and Technologies, Moscow, Russia

Abstract

Experimental studies of pulse electrical explosion of thin titanium foils in water, with discharge power of ~ 0.2 GW are described. Production of a considerable amount of molecular hydrogen is revealed whose origin cannot be explained either by water decomposition or by known chemical reactions. A nuclear mechanism for the formation of the observed molecular hydrogen upon electric explosion is hypothesized. Emphasis is laid on some measurements confirming the hypothesis.
© 2011 ISCMNS. All rights reserved.

Keywords: Electrical explosion, Hydrogen

PACS: 52.80.W_q

1. Introduction

It has long been known that high-current electrical explosions of metal wires in liquid produce strong magnetic fields ($H \sim 1$ MGs) and high pulse pressures ($P \sim 10^5$ atm) [1,2]. Meanwhile, there is no doubt that such strong external fields can significantly change the probability of nuclear decays and even the conditions of nuclear stability [3].

In this connection, in our previous works we studied the electric explosions of metal foils in uranium salt solutions [4, 5] in order to detect experimentally the effect of ionization and strong magnetic fields on the change in the β -decay periods. During these experiments we studied the gas phase of such electric explosions (i.e., the gases resulting from these explosions). The analysis of the gas mixtures showed an abnormally high content of hydrogen. A thorough

*E-mail: urleon@ya.ru

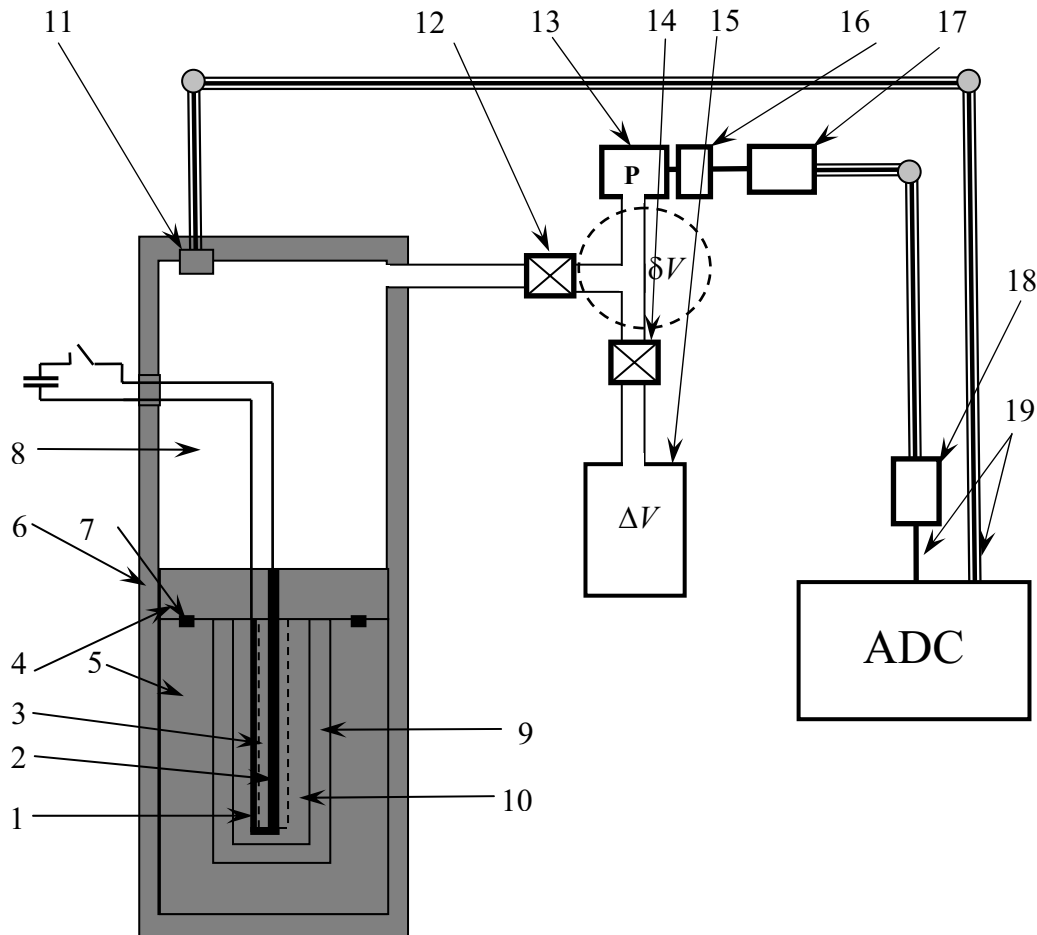


Figure 1. Schematic drawing of experimental setup. (1) Titanium foil; (2) Titanium electrode; (3) Insulator; (4) Lid; (5) Interior of the explosion chamber; (6) Stainless steel frame; (7) Sealing; (8) Gas-collecting chamber; (9) Disposable beaker; (10) Liquid; (11) Piezoelectric total pressure sensor; (12) Valve; (13) Polarographic sensor DV-16 of hydrogen partial pressure; (14) Valve; (15) Calibrated gas-collecting volume; (16) Signal amplifier; (17) Voltage–frequency signal transducer; (18) Frequency–voltage signal transducer; (19) Cable.

investigation of this phenomenon required more than 500 experiments and took about 4 years. The results of this research are outlined in the present paper.

2. Description of the Experimental Setup

The experimental setup consisted of two (2) capacitor banks with $C = 2.5 \times 10^{-3}$ F each. One bank was charged to $+4.8$ kV and the second one was charged to -4.8 kV (relative to the ground potential). Under maximum voltage, the energy reserve of the setup was $W \sim 50$ kJ. Two vacuum solid-state spark-gaps of trigatron type were used as commutators; they were ignited by specially designed devices. The current pulse of each bank lasted for $T \sim 120$ μ s and its amplitude was about $I_0 \sim 120$ kA. The electric pulse was transported from each bank through four coaxial

cables with the inductance $L = 0.4 \mu\text{H}$. The current was measured by coaxial shunts and the voltage was measured by a divider, which were described in detail previously (together with oscillogram data of the electrical current and voltage) [4,5]. Analog oscilloscopes and high-speed analog-to-digital transformers connected to computers were used to record the electric signals. The recording equipment was located in a shielding room at a ~ 40 m distance to avoid electromagnetic disturbance.

In this experimental series, each bank worked to its own electrical load which was a titanium foil 1 (Fig. 1) resistance-welded to a bulk titanium electrode 2. Figure 1 shows one of the two explosion chambers where a Teflon insulator 3 was mounted between the bulk electrode and the foil and, hence, the welded foil served as a cable armoring short-circuited to the cable central core. The electrodes were fixed to the dielectric insulator 4 as shown in the figure, which was made either of polyethylene or Teflon depending on the experimental purpose. Simultaneously, this insulator served as a packing element for the explosion chamber. The amount of the titanium foil (loading) varied in different experiments from one to four stripes, each being $\Delta = 50 \mu\text{m}$ thick, 1 cm wide and $L = 4.0$ cm long. The weight of each stripe was $m = (90 \pm 5) \times 10^{-3}$ g.

The interior of the explosion chamber 5 was made of polyethylene (or Teflon) and placed in the lower part of a firm body made of stainless steel 6, which provided tightness in all experiments. All the sealing elements were made of nonhydrogenous materials. The tightness of the explosion chamber itself was provided by sealing 7 of the lid 4. The power input was through the upper part of the metallic container, which served also as a $V = 3.125$ l gas-collecting chamber 8. The gas-collecting chamber was required as the attempts to hold the gases back in the explosion chamber failed, resulting only in the mechanical destruction of the explosion chamber.

The interior of the explosion chamber 5 contained a disposable Teflon (or polyethylene) beaker 9 filled with liquid 10. The central electrode bearing the foil welded to it was immersed in the liquid. At the instant of electric explosion, beaker 9 was subjected to the greatest mechanical deformation. Teflon beakers were even mechanically destroyed. Therefore, the use of this construction element significantly increased the service life of the basic part 5 of the explosion chamber. The volume of the liquid (in the main part of the experiments) was $v \sim 18 \text{ cm}^3$. The liquids used were either de-ionized doubly distilled water or certified heavy water 99.8% (D_2O).

At the instant of electric explosion, the pressure in the chamber rapidly increased and the resulting gas broke through the sealing 7 into the gas collecting chamber 8. A pressure sensor 11 was located in the upper part of the gas collector, and also a branch pipe connected through valve 12 to the partial hydrogen pressure sensor 13 and through valve 14 to the calibrated gas collecting volume 15 ($\Delta V = 250 \text{ cm}^3$) whose function will be discussed below. Before installation, the gas collecting volume had been evacuated down to the 2×10^{-2} Torr pressure. The gas collecting chamber had been evacuated before the electric explosion down to a pressure of several Torr, purged with argon several times, and then filled with high-purity argon until the pressure was $P = 1.5$ atm. This procedure minimized the influence of atmospheric gases on the results of measurements.

3. Procedure of Measurements

We used both standard procedures (solid-state laser mass spectrometry, gas chromatography, gas mass spectroscopy, electron microscopy) and methods specially developed for this particular experiment (measuring the relative hydrogen content, optical method, and a procedure for producing calibration H/D gas mixtures).

3.1. Procedure of hydrogen partial pressure measurements

Since the results of measuring the amount of produced hydrogen are of great importance for the present research, this method will be analyzed most thoroughly. The method involved the following measuring instruments: a hydrogen partial pressure sensor, a total pressure sensor, a block of electronics, an analog-to-digital converter (ADC), and a

computer. A polarographic DV-16 sensor (produced by the JSC “Insovt”, St.-Petersburg) [6] was used as a partial hydrogen pressure sensor. The sensor operation was based on the linear dependence of the diffusion current running in the polarographic cell on the partial pressure of electrolyte-dissolved hydrogen. Our tests showed that the sensor response function depended on two parameters: the hydrogen partial pressure P_H and the total pressure P_0 in the mixture. Note that in the pressure range $1 \text{ atm} < P_0 < 2.5 \text{ atm}$, the dependence $U_{PH} = f(P_0)$ was not strong, but a special calibration procedure was needed to increase the accuracy of measurements.

The experimental conditions required the transfer of information on the measured parameter by a considerable distance (by more than 30 m), which resulted in overlapping between noise and the useful signal. Furthermore, at the instant of electric explosion, high-voltage discharges are very likely to get onto the hydrogen sensor circuits. With the use of galvanic coupling in the direct current, this can cause failure of the entire measurement system. The problem was solved by converting the measured voltage into frequency. The error (nonlinearity) in the signal voltage-to-frequency conversion was $\pm 0.03\%$, the error (nonlinearity) of the reverse (frequency-to-voltage) conversion being $\pm 0.06\%$, which is much less than the hydrogen meter basic error of $\pm 1.5\%$.

A SIEMENS SITRANS P Serie Z, Typ 7MF 1564 piezoelectric sensor was used to measure the total gas mixture pressure in the chamber. The electric signal U_{P_0} from the sensor was taken directly to the AD converter. The linearity of the sensor, along with the whole tract, was verified by a standard manometer. The calibration showed that the measuring system was linear with good approximation up to $\sim 0.1\%$, which is even higher than guaranteed by the manufacturer.

After an electric explosion of foil, the pressure in the gas-collecting chamber became $P_0 \sim 2 \text{ atm}$ and was measured by pressure sensor 11 (Fig. 1). At the instant of “shot”, valve 12 was shut off, which was dictated by service characteristics of the hydrogen sensor. This sensor lost operability upon both a sharp pressure jump and forevacuum evacuation. The valve 14 was also closed, thus separating the calibrated volume 15 from the chamber working volume. The use of the calibrated volume 15 is needed within this method because the air present between valves 12, 14 and pressure sensor 13 (see Fig. 1) cannot be pumped out of the “dead space” $\delta V \sim 18 \text{ cm}^3$. Thus, the dead space δV turned out to be filled with air at atmospheric pressure. Therefore, after valve 12 was opened and δV was thus combined with the main space, the partial gas pressures started to slowly equalize due to the rather slow diffusion through the membrane. This resulted in a long time required for establishing the equilibrium between the measured gas volume V_0 and the hydrogen sensor. As a consequence, the time required for the one measurement was too long.

The measuring procedure was as follows. To reduce the time it took for hydrogen pressure sensor to be equilibrated, valve 14 was opened and the gas was “pressed” into the volume δV . In this case, the stationary mode was established in the hydrogen partial pressure sensor within only $\sim 30 \text{ min}$.

Next, the valve to the hydrogen-pressure sensor was closed (step 2), and the calibration volume and the hydrogen sensor were detached. The calibrated volume was again pumped out to 10^{-2} Torr , and then the partial pressure was measured several times.

Assuming the process to be isothermal, we can readily write the relations between the pressures of the i and $i + 1$ iteration steps:

$$\begin{aligned} P_0^i &= P_0^{i+1} \left(\frac{V_0 + \Delta V}{V_0} \right) + \frac{\delta V}{V_0} (P_0^{i+1} - P_a), \\ P_H^i &= P_H^{i+1} \left(\frac{V_0 + \Delta V + \delta V}{V_0} \right), \end{aligned} \quad (1)$$

where P is pressure in atmospheres and $P_a = 1 \text{ atm}$ is atmospheric pressure.

Since at each step the relative hydrogen content depends on the initial relative hydrogen content γ^0 and the known

volumes

$$\gamma^{i+1} = \frac{P_H^{i+1}}{P_0^{i+1}} = \gamma^i \left(1 + \frac{P_a \delta V}{P_0^i V_0} \right)^{-1}, \quad (2)$$

we obtain n measurements of one and the same quantity γ^0 . The advantage of such a method lies in the decrease, due to averaging, of the measurement error caused by the weak dependence of the readings of the hydrogen partial pressure sensor on the total gas-mixture pressure P_0 . To make sure that the method works well, we prepared a calibration mixture (83% Ar + 17% H₂). The hydrogen concentration was measured by the above-described method with a no less than one percent error.

To make certain that the elaborated method of hydrogen percentage measurement is linear in the concentration range of interest, we prepared (Ar + H₂) mixtures of different concentrations. The calibration mixture composition was determined using a gas chromatograph. We found that within the range 5% < γ < 30%, the response function was linear depending on γ .

Our method also made it possible to measure slow variations of relative hydrogen content during several days. The method is insensitive to the replacement of H₂ by D₂ or HD.

3.2. Procedure of chromatographic analysis

Gas chromatography was used, on the one hand, to verify the abovedescribed method for determining the specific hydrogen content in the gas mixture under study and, on the other hand, to perform a qualitative and quantitative analysis of the gas mixture. We used an LCM-80 gas chromatograph, which had three sorption columns. The analysis was carried out at a temperature of 40°C in isothermal mode. The analyzed mixture components were detected by a detector based on the thermal conductivity of separate gas-mixture components. The quantitative composition of the gas mixture was calculated by the absolute calibration method from chromatographic peak areas (for gaseous components CH₄, C₂H₄, C₂H₂, and CO₂).

Standard gas mixtures were used for calibration with respect to hydrogen, nitrogen, and CO. We either made calibration the same day as the gas samples were tested or used the calibration of the previous analysis. The method did not permit measurement of hydrogen isotopic distribution.

3.3. Procedure of solid-state laser mass spectrometry

We used laser mass spectrometry here only to determine the oxidation state of the titanium powder formed from the foil as a result of explosion. This information was necessary for the correct account of the amount of oxygen absorbed by titanium. In other words, the method was aimed at determining the n value in the TiO _{n} formula in each experiment. In addition, we were interested in the isotopic distribution of titanium contained in the powder. Therefore, to determine the element and isotope compositions of the liquid and metal foil remainders, we chose laser mass-spectrometry which, given sufficient sensitivity (10^{-4} – 10^{-5} at.%), shows an error of 10–15% in determining the amount of trace impurities.

The validity of the measurements was permanently checked through both the standard alloy samples and certified geological samples.

3.4. Procedure of gas mass spectrometry

Gas mass spectrometry was also needed for two purposes. First, it duplicated the gas chromatographer measurements, and therefore, when extracted from the same removable containers and already measured on the gas chromatograph, the gas was examined using the gas mass spectrometer. Second, this method was very important for finding the isotopic

distribution of hydrogen atoms in the gas mixture due to electric explosion in experiments with liquid represented by heavy water.

The method rested upon a time-of-flight quadrupole unipolar MMC-1A mass-spectrometer described in greater detail in [7], which allowed determination of components with atomic mass of 1–400. The test with standard gas mixtures showed that this method operated within a 5% error in the entire mass range of interest. In some cases, to check correctness of measurement correlations for the second, third and fourth masses (H_2 , HD , D_2) we used a gas mass spectrometer with magnetic focusing. The obtained results showed good agreement. Masses above 44 (CO_2) were not observed in the tested gas samples to within 5% precision.

3.5. Spectral analysis

Optical spectroscopy was chosen as a duplicate method for a qualitative elemental analysis and semi-quantitative isotopic analysis of hydrogen. For this purpose, a special setup was designed. This setup made it possible to obtain and investigate the radiation spectrum of high-frequency discharge occurring in the gas flow. In order to avoid “pollutions” of an investigated optical spectrum by “impurity” hydrogen, vacuum rubber seals were only used where gas containers were attached to the analytical system and also where the setup was connected to the forevacuum pump.

For the same purpose liquid nitrogen traps, which froze out vapors from water-containing liquids were placed upstream and downstream of the discharge area. These liquids are normally contained in forevacuum pump oil, the vacuumvalve lubricant, and can get into the gas volume when a gas sample is taken from the experimental setup. To avoid accumulation in the high-frequency discharge area of impurities, which could be due to microcracks and vessel degassing, the discharge was implemented in a stream of the analyzed gasses. The maximum pressure of the remaining gas in the setup space was nearly 10^{-3} Torr, while the gas flow pressure during the discharge was ~ 3.0 Torr. We shall see below that these measures sufficed to avoid alien impurities in the gas under investigation.

The gas was excited in a gas tube with a high-frequency Tesla generator. The occurring optical radiation was gathered by a quartz objective and focused on 1:1 scale onto the slit of a spectrograph with the diffraction grating (PGS-2). Dispersion of the device in the area under study was 7.3 \AA/mm . All of the experimental procedures are described in more details in [8].

4. Experimental Results

4.1. Basic results

As has been said above, the ionized gas is produced at the instant of foil electric explosion and breaks through the seals from the explosion chamber to the prechamber. For constant parameters of the experiment, namely, load mass, foil type, explosion chamber geometry, type of liquid, current, etc., the pressure jump was by one and the same value. For example, for the Ti load mass $m_{Ti} = 180 \text{ mg}$, the pressure jump was $\Delta P = 0.42 \pm 0.04 \text{ atm}$ which, when converted to the chamber volume, made up $\Delta N = 3.4 \times 10^{22}$ atoms. At first glance, this result may seem to be absolutely natural because it is common knowledge that an electric charge running through water must generate hydrogen and oxygen. But it should be taken into account that an electric charge stored in a capacitor bank amounted to $Q \sim 11 \text{ C}$ and the Faraday number is $F \sim 96\,500 \text{ C/mol}$.

Note that the reproducibility of the effect in these experiments depends on many factors which at first glance may seem insignificant. However, it took us about two years to attain satisfactory reproducibility of the results.

As has already been noted, when the capacitor bank was actuated, the currents and voltages under electric load and the signals from the piezoelectric pressure sensor were recorded. The signal from the pressure sensor branched consistently and then was digitized through two different analog-to-digital converters (ADC). The signal digitization frequency was $v = 0.2 \text{ MHz}$ for the first (“fast”) ADC signal and $v = 10 \text{ Hz}$ for the second (“slow”) ADC. Typical

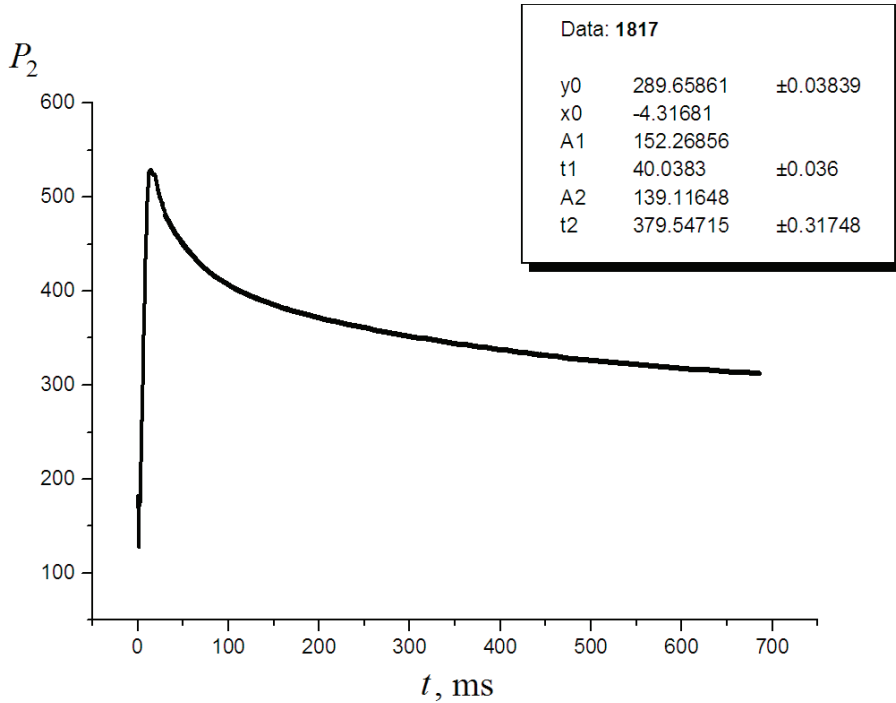


Figure 2. (a) Signal from fast ADC.

signals from both ADCs are illustrated in Fig. 2. Each of the signals is well approximated by the two exponents:

$$P(t) = y_0 + A_1 \exp\left(\frac{t - t_0}{t_1}\right) + A_2 \exp\left(\frac{t - t_0}{t_2}\right). \quad (3)$$

The characteristic exponent periods for the first signal are $T_1 \sim 40$ ms and $T_2 \sim 0.3$ s and for the second signal $T_2 \sim 0.3$ s and $T_3 \sim 3.2$ s. One can thus see that the time behavior of pressure is characterized by three time scales. This issue has not been thoroughly studied here, but we may assume the first exponent period $T_1 \sim 40$ ms to be due to radiative cooling, the second one $T_2 \sim 0.3$ s to be due to transition gas-dynamical processes, and the third period $T_3 \sim 3.2$ s to result from heat conductivity. The amplification rate and the amplitude of the signal in Fig. 2 were indicative, although quite indirectly, of the gas gain intensity. And the signal from the slow ADC (Fig. 3) made it possible to control the chamber tightness after the “shot” and the hydrogen partial pressure measurement (see Fig. 3). Figure 3 shows that in 20–30 s after an electrical pulse all transition processes mainly terminate and the pressure becomes stationary.

At the early stage of our present research the main effort was directed to investigate the chemical composition of the gas formed upon a titanium foil electric explosion. Several minutes after the explosion, i.e., when the pressure and temperature in the gas-collecting chamber had already reached their stationary values, the hydrogen partial pressure in the produced gas mixture was measured by the method described above. After that, the gas was sampled to the calibrated volume and analyzed using the gas chromatograph. Table 1 presents typical data from gas chromatography. The table shows that the basic component, except the ballast gas argon, is hydrogen. One can notice the absence of oxygen beyond the method sensitivity limits.

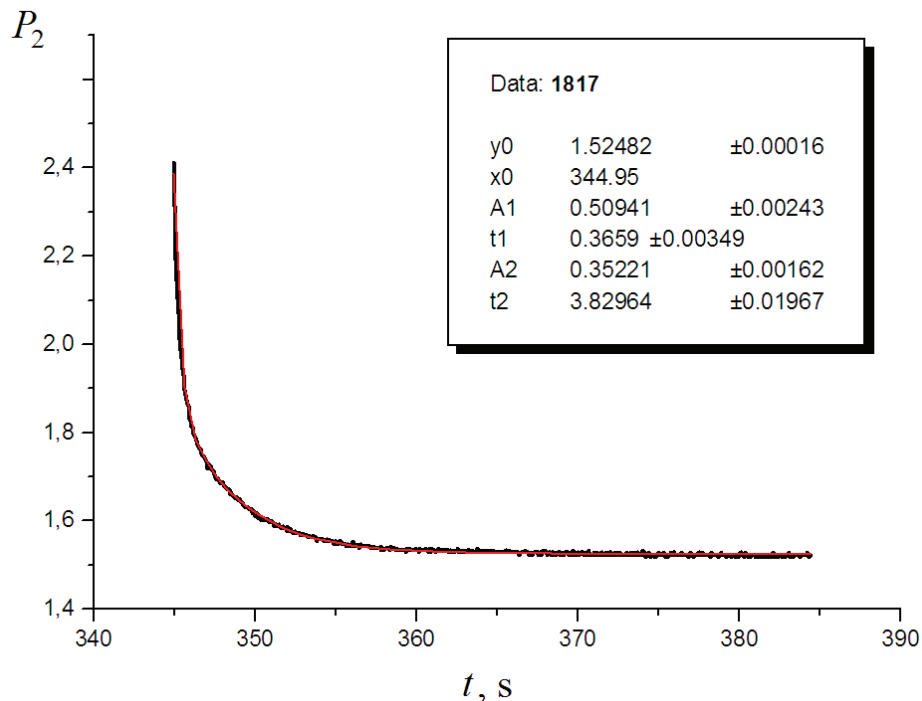


Figure 3. (b) Signal from slow ADC.

Table 2 gives comparison of the values of measured relative H₂ content in the gas mixture obtained with a gas chromatograph and a polarization sensor for one series of experiments, where Ar was also used as the ballast gas. We note that argon chemical “purity” was 99.8%. The table demonstrates good coincidence of the results obtained by two different methods. And, nevertheless, to make sure that the gas chromatograph yields a correct chemical composition

Table 1. Typical result of gas chromatograph measurements.

Element	%
H ₂	13.97
O ₂	<0.3
N ₂	0.6
CO	3.62
Ar	80.85
CO ₂	0.4
CH ₄	<0.02
C ₂ H ₆	<0.03
C ₂ H ₄	<0.04
C ₃ H ₈ , C ₃ H ₆	<0.1
C ₂ H ₂	<0.07
Σ	100

of the mixture, some of the gas samples were simultaneously analyzed using a gas mass spectrometer. The gas mass spectrometer also showed (within the method sensitivity) the absence of free oxygen.

The coincidence of the results of measurements taken within different methods implies that the anomalously large amount of hydrogen and the absence of oxygen are not due to erroneous measurements. Simple conversion of the relative hydrogen content with allowance for the chamber volume and the total pressure shows that during a pulse ~ 0.9 l of hydrogen is generated (under normal conditions) in each chamber. This result is rather stable, reliable, and verified in a large number of experiments. Thus, if we assume that the registered hydrogen is a result of chemical or pyrolytic water decomposition, the question arises: where did the oxygen disappear? In other words, 0.9 l of atomic oxygen due to water decomposition must have been absorbed by the chamber surface without producing a notable amount of molecular oxygen. And as follows from Fig. 3, this mechanism must be actuated within the first seconds because after that the pressure lowering stops.

4.2. Analysis of the chemical mechanism of hydrogen production

To try and examine the physical mechanism of hydrogen production, it was necessary to establish the balance in oxygen. An insignificant part of oxygen was found in the gas sample in the form of CO and CO₂, and this amount of oxygen could readily be taken into account in the general balance. The reason for the absence of free oxygen could also be oxidation of the titanium electrode and exploded foil. Neither isolation of the titanium electrode from water using Teflon nor replacement of the Ti electrodes by metal electrodes possessing lower oxidability (stainless steel, cobalt, etc.) has led to observation of oxygen in the generated gas.

As concerns titanium foil oxidation, this channel of oxygen binding was allowed for by the solid-state mass spectrometry method. To this end, we examined the foil remainders and measured the Ti/O ratio. As a result of numerous measurements it was found that titanium was oxidized to the formula TiOn ($n = 1.4 \pm 0.2$). This means that some of the Ti was oxidized to TiO₂ and some to TiO. It is worthy of notice that the titanium oxidation state depends on the mass of the applied load, and this fact was also taken into account in the general balance in oxygen.

For example, for the load mass $m = 180$ mg, one mole of H₂O yields $(2.3 \pm 0.16) \times 10^{22}$ H₂ molecules upon electric explosion. NO₂ = $(8.7 \pm 0.9) \times 10^{21}$ oxygen atoms were found in the gas samples in the form of CO and CO₂. The origin of these molecules may well be explained by pyrolytic decomposition of water with subsequent formation of carbon oxides upon addition of oxygen atoms to the carbon contained, e.g., in polyethylene. When oxidized, the titanium foil binds NO₂ = $(3.3 \pm 0.6) \times 10^{21}$ atoms. Hence, the oxygen balance fails almost by half, i.e., almost 0.5. of hydrogen does not meet the corresponding oxygen atoms.

We have analyzed the dependence of hydrogen output on the titanium foil mass. A series of no less than seven experiments was carried out for each foil mass, and the averaged results are presented in Fig. 4. The triangular points refer to the total amount of detected hydrogen, and the round points are for hydrogen of non-chemical origin. The values of standard deviation smaller than the point size were not plotted. In view of the pulsed character of the process, the reproducibility of our experiments can be thought of as satisfactory. The figure shows that the amount of non-chemically produced hydrogen does not virtually depend on the titanium foil mass. Noteworthy is the fact that when averaged, the standard deviation values for the lower points appeared to be smaller than those for the initial measurements of the total amount of hydrogen (i.e., for the upper points). Furthermore, the number of hydrogen molecules due to a non-chemical

Table 2. Measured values of relative hydrogen content obtained using gas chromatography and polarization sensor for the series of experiments with loading $m_{\text{Ti}} = 180$ mg.

No.	1830	1829	1828	1826	1825	1824	1823	1822	Average
Polarogr.	15.76	16.89	14.2	14.0	17.9	19.5	16.8	13.4	14.4
Gas. chrom.	17.4	15.4	16.4	14.1	18.5	16.8	16.4	12.8	13.7

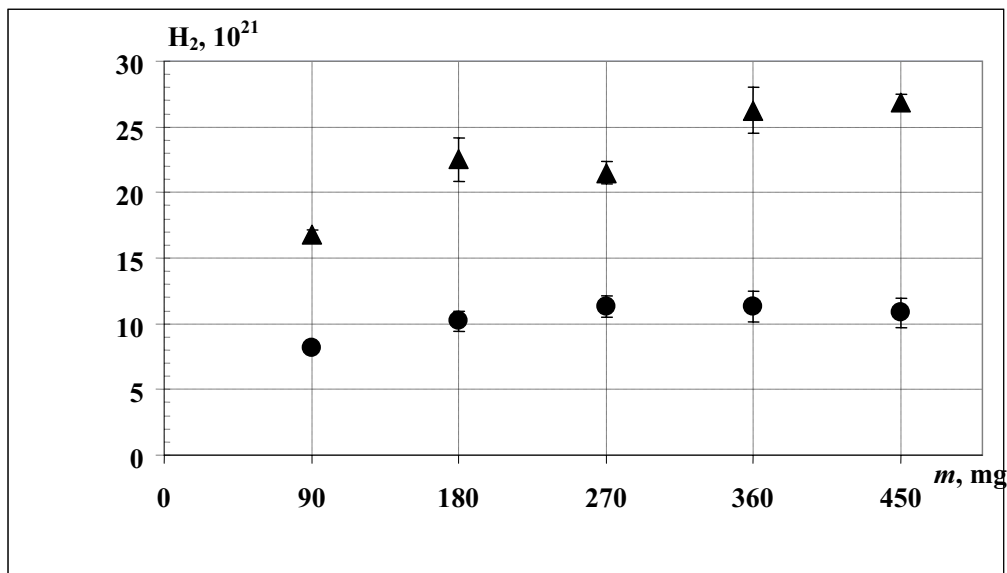


Figure 4. Dependence of the amount of hydrogen on the foil mass: triangles show the registered amount of hydrogen, circles show the amount of hydrogen whose origin cannot be explained by the chemical or pyrolytic mechanism of production.

mechanism is $N = 10^{22}$ to a good accuracy irrespective of the foil mass. In other words, this mechanism is more reproducible and so-to-say “fundamental” than the foil chemical oxidation.

The imbalance in oxygen cannot, of course, be a strong argument for drawing conclusions, but it was a stimulus for seeking the mechanism of “impurity” hydrogen origin.

4.3. Search for “impurity” hydrogen sources

4.3.1. Titanium foil

The titanium foil used in the experiments was the first to be tested as “impurity”-hydrogen generator. It is common knowledge that titanium can be saturated with hydrogen to the ratio of almost 1:1. However, most physicists unfortunately forget that this can only be achieved through titanium heating to a high temperature in hydrogen atmosphere. Although spontaneous titanium saturation with hydrogen seems to be improbable, we have nevertheless verified such a possibility experimentally.

The analysis of results of measurements of qualitative structure and quantity of gas impurity allowed asserting that:

- (1) One gram of the initial titanium foil contains $\sim 0.2 \times 10^{19}$ molecules of H_2 .
- (2) The gases contained in the initial foil are impurities located for the most part on the surface rather than in the bulk.

In more detail the results of these measurements are described in [7, 8].

Thus, the results presented imply that the experimentally observed anomalous amount of hydrogen cannot be explained by its presence in the initial foil.

Table 3. Dependence of the amount of hydrogen on the inner beaker diameters.

<i>D</i> (mm)	20	40	60	“Chem”
<i>H</i> ₂ (%)	16.0	9.0	6.8	6.7

4.3.2. Polyethylene

Polyethylene contained in the constructional elements of the explosion chamber could have been another probable source of hydrogen. To check the validity of this assumption, all the polyethylene-containing constructional elements inside the tight chamber frame were replaced by those made of Teflon. We conducted several series of experiments with all other experimental conditions (foil mass, the amount of water, ballast gas pressure, etc.) equal. The experiments gave the following result: the hydrogen content was (16.1±2.2)% in the “polyethylene” surrounding and (14.0±0.6)% for the “Teflon”. This showed that the polyethylene elements of the explosion chamber construction were not the source of the observed hydrogen. The small difference in the hydrogen percentage was certainly insufficient to explain the registered amount of hydrogen. Hence, even if polyethylene is the source of hydrogen, it is responsible for very small amounts. It should be noted that when made of Teflon, the disposable beaker 9 (Fig. 1) failed to withstand the high pressure caused by the electric explosion in the chamber and was destroyed, thus increasing the explosion chamber radius. And we shall see below that the diameter of the inner beaker had a very notable effect on the amount of produced hydrogen. When the entire lower part of the explosion chamber (i.e., elements 5 and 9 in Fig. 1) was made of an integral piece of Teflon (as an integral constructional element), the difference between the two series of experiments in the amount of produced hydrogen was quite insignificant.

4.3.3. Other sources

To finally exclude the hypothesis of “impurity” origin of hydrogen, we undertook the following series of experiments. We increased the inner beaker (9, Fig. 1) diameter, which was typically 20 mm, and accordingly the volume of doubly distilled water increased. All the other construction parts were left unchanged. Dielectric polyethylene parts were used in these experiments. The foil mass remained the same in the entire series of experiments. The percentage of produced hydrogen for different inner beaker diameters is shown in Table 3. With increasing beaker diameter the explosion chamber pressure falls, which is obviously the reason for the sharp decrease in the amount of produced hydrogen. The last column of the table shows that hydrogen percentage can be due to titanium oxidation and to allowance for CO and CO₂ gases. In other words, that amount of hydrogen has a clear chemical origin. All the values in the table have an almost $\sigma_m \sim 1\%$ mean error. Table 3 shows that with an increase in the beaker diameter up to 40 mm the entire observed hydrogen can already be thought of as having a chemical origin.

All the results presented above suggest that the hydrogen produced at the moment of electric explosion is due to a process yet unknown to us, and its origin cannot be explained by the chemical or “impurity” mechanism. We believe that the observed hydrogen is of nuclear origin.

4.4. Verification of the nuclear hypothesis

To verify the hypothesis, we conducted experiments using “heavy” water (D₂O) instead of doubly distilled water. We used water containing 99.8% of D₂O. The pressure jump and the measured hydrogen percentage differed insignificantly from the experiments with ordinary water. This circumstance suggests that at the moment of electric explosion all processes progressed almost identically in both cases. The idea of experiments with heavy water was as follows. If part of the hydrogen is of nuclear origin, it will not change upon replacement of H by D. Thus, the problem was reduced to determination in a gas sample of a relative H and D content in the produced mixture. We note that the experiments

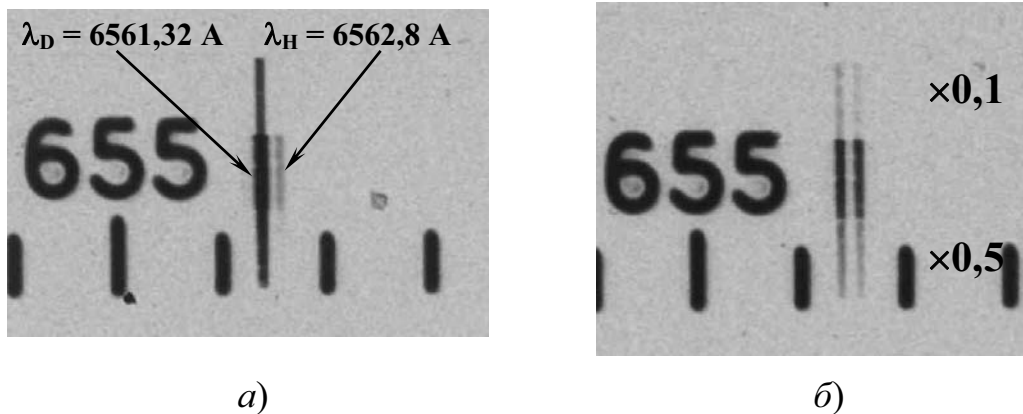


Figure 5. Fragment of the optical spectrum recorded with depressions of 10% and 50%: a) control; b) experiment.

with heavy water were carried out exclusively in a Teflon explosion chamber. All the sample intakes were preliminarily pumped out carefully, and the walls were heated to exclude the presence of moisture.

To solve this problem, we used two methods, namely, optical spectrometry and gas mass spectrometry. To verify the optical method, we first prepared a gas calibration mixture containing 94% of D and 6% of H. Using the above-described optical method, we measured the ratio of intensities H_α and D_α as well as H_β and D_β for the calibration mixture to obtain the values of 95% of D and 5% of H.

A fragment of the calibration optical spectrum is presented in Fig. 5a. Such good agreement between the results of optical measurements with the hydrogen concentration values in the calibration mixture means that the optical setup itself contains no “impurity” hydrogen sources. So, we have made sure that the optical method is correct. Figure 5b shows, as an example, a fragment of the optical spectrum of the investigated gas mixture. The hydrogen-to-deuterium ratio measured in this experiment from the optical line ratio made up $D/H=1/1$. Approximately the same D to H ratio was obtained for this experiment using a gas mass analyzer: $D_2/HD/H_2 = 0.5/0.25/0.25$.

5. Discussion

- (1) We have reliably established that an electric explosion of titanium foil in water induces production of a considerable amount of molecular hydrogen ($NH_2 \sim 2 \times 10^{22}$ molecules). The origin of about half of this amount cannot be attributed to water decomposition.
- (2) Careful search of the “impurity” hydrogen source was not crowned with success.
- (3) The authors advanced a hypothesis on the nuclear mechanism of the origin of observed molecular hydrogen and obtained some results to back up the hypothesis.

We should emphasize that by using the words “nuclear mechanism” we, of course, mean neither the nuclear fission nor the nuclear fusion mechanism, at least in their traditional sense. The temperature of plasma produced upon electric explosion is, too low (it is close to the solar corona temperature [4]), and such class of nuclear reactions is impossible in the present experiments. At the same time, on the basis of our preceding experiments [4, 9, 10] we believe that in conditions of dense low-temperature nonequilibrium plasma, an absolutely new class of nuclear reactions may proceed in the absence of strong interactions. The main difference between the hypothetic nuclear reactions and the generally known ones is the assumption concerning their collective mechanism of interaction. We should note that in plasma

physics, the role of collective interactions has long been thoroughly investigated and is beyond question, whereas in nuclear physics such a hypothesis seems to be very extravagant.

6. Conclusion

It is significant that although our results of relative hydrogen and deuterium content measurements seem to be reliable, in our opinion they cannot underlie the final conclusion concerning the nuclear origin of observed hydrogen. The final conclusion will require additional research. However, it is much more likely that the hydrogen described in our experiments has nuclear rather than chemical origin caused by some disregarded chemical processes.

Acknowledgements

The authors are deeply indebted to I.A. Egorov for financial support of the present study and to A.I. Abramov who took up all administrative duties to provide the whole of the research process. We are grateful to the workers of “Kurchatov Institute” RSC Elesin L.A., Dorovskoi V.M., Stolyarov V.L., Djemkin S.N., Novoselov B.N., and Kuznetsov V.L. for conducting numerous measurements. We would also like to thank the workers of “RECOM” for their many-years’ labor and mention those without whose active participation it would have been absolutely impossible to carry out the experiments: Gulyaev A. A., Petrushko S.V., Petrushko V.D., Strashko P. F., Shevchenko V.L., Gaverdovsky A. B., Bayushkin V.N., Sergeev E.N., Govorun A.P., and Popelev E.N.

The experiments were carried out at “RECOM” (a subsidiary of I.V. Kurchatov Institute of Atomic Energy) in the Institute of Atomic Energy since 2004 and were stopped in 2007 for a reason not worthy of discussion within a scientific paper.

References

- [1] W.G. Chace and H.K. Moore (eds.), *Exploding wires*, Plenum Press, New York, 1962.
- [2] Y. Bakshaev et al., *Plasma Phys. Rep.* **27** (2001) 1039; A. Velikovich et al., *Phys. Plasmas* **14** (2007) 022706.
- [3] L.I. Urutskoev, D.V. Filippov, *Physics-Uspekhi* **47** (2004) 1257.
- [4] L.I. Urutskoev, V.I. Liksonov, V.G. Tsinoev, *Ann. Fond. L. de Broglie* **27** (2002) 701.
- [5] A.G. Volkovich et al., *Ann. Fond. L. de Broglie* **30** (2005) 63.
- [6] www.insovt.ru
- [7] V. M. Dorovskoj et al., *Prikladnaya fizika* 2006 (4), 28 [in Russian].
- [8] L. I. Urutskoev, D. V. Filippov, A. A. Rukhadze et al., The research of gas phase under electrical titan foil explosion in liquid. Preprint (Institute of General Physics of the RAS, Moscow, 2009) [in Russian].
- [9] D. V. Filippov, L. I. Urutskoev, *Ann. Fond. L. de Broglie* **29** (2004) 1187.
- [10] D. Priem, G. Racineux, G. Lochak et al., *Ann. Fond. L. de Broglie* **33** (2008) 129.



Research Article

Studies on Anomalous Phenomena of D/Pd Systems using a Gas-loading Process – A Stride Towards Neutrino Detection

Zhan M. Dong, Chang L. Liang, Bin Liu, Qing M. Wei, Jian Tian,
Shu X. Zheng, Jin Z. Yu and Xing Z. Li*

Department of Physics, Tsinghua University, Beijing 100084, China

Abstract

A brief review of 20 years of experiments at Tsinghua University confirms anomalous phenomena during gas loading in D/Pd systems. A scale-up of the experiment would make it feasible to test the hypothesis that neutrinos are emitted during these phenomena (the “neutrino conjecture”).

© 2011 ISCMNS. All rights reserved.

Keywords: Deuterium/Palladium system, Gas-loading, Neutrino detection, Pumping effect

PACS: 89.30.Jj, 89.90.+n, 88.20.fn, 88.85.mh

1. Introduction

Condensed matter nuclear science research has been conducted for 20 years at Tsinghua University. It started from both electrolysis and gas-loading experiments, but later we worked on gas-loading experiments mainly because of the following theoretical consideration: If the charged particles react, there must be some charged nuclear products, due to the conservation of electrical charge. Hence, we should try to detect charged particles instead of neutron or gamma radiation, in order to confirm this anomalous phenomenon. The gas loading cell is much more favorable for charged particle detection. The first successful experiment used CR-39 to detect charged particle emission from a palladium foil after thermal cycling at high deuterium pressure [1]. At the same time the first theoretical efforts were initiated to explain the tunneling through the Coulomb barrier, and the puzzle of “excess heat without commensurate radiation” [2] (“thunder without lightning”).

After 1995, our gas-loading experiments were switched from low-temperature, high-pressure to high-temperature, low-pressure in order to improve reproducibility (i.e. switched from (77 K, 9 atm.) to (180°C, 0.8 atm.)). Our motivation was mainly

*E-mail: lxz-dmp@tsinghua.edu.cn

- Pons' presentation in ICCF-4, "Heat after death" [3].
- The paper by Oats and Flanagan on gas loading at high temperature with high reproducibility [4].
- Manduchi's gas loading experiments at high temperature [5].

It appears that gas-loading has higher reproducibility with less dependence on materials.

Our gas-loading experiments started from the goal of high loading ratio in terms of a hot tungsten wire. It led to the studies of

- The pumping effect [6].
- A simple calorimeter configuration [7].
- Nuclear transmutation in a gas-loading H/Pd system [8].
- Correlation between deuterium flux and heat flow at temperatures higher than the boiling point of heavy water [9].
- Gas-loading systems with international collaborations [10–13].

The selective resonant tunneling model has successfully explained the puzzle of excess heat without strong radiation [14], corrected the mistakes in D–T hot fusion data [15], and further improved the formula for six major hot fusion cross-sections [16]. Indeed, these hot fusion data justified the selective resonant tunneling model. Moreover, this model explained the "heat after death" phenomena, three-deuteron fusion reactions [17], and the asymmetry in cooling and heating processes, this led us to find the correlation between deuterium flux and heat flow directly. Based on this model, a conjecture on neutrino emission from palladium deuteride has been proposed [18], and a self-sustaining heat generator using deuterium flux has been outlined [19].

The recent gas-loading experiments at room temperature showed that (1) neutrino emission should be detectable in a palladium tube system with 2 W excess heat running for 7 days, (2) a 30 m long palladium tube (diameter 3 mm, 0.1 mm wall thickness) might be enough to build the first demonstration for a self-sustaining heat generator.

2. Nuclear Tracks in CR-39 (1989–1998)

After the Santa Fe workshop in 1989, it was clear that the neutron or gamma radiation from palladium deuteride must be very weak. Hence, the confirmation of the nuclear nature of this anomalous phenomenon should be based on charged particle detection with low noise and good long-term stability. A CR-39 Solid State Nuclear Track Detector was suggested by the Institute of Nuclear Technology of Tsinghua University. The Institute of Atomic Energy of China kindly provided the high quality CR-39 detectors, and the Institute of High Energy Physics, Chinese Academy of Science, calibrated them using its accelerator.

A graduate student devoted one year to running the gas-loading experiment (thermal cycling in a liquid nitrogen dewar). The positive result was published in the Provo workshop (1990) and in the first AIP Proceedings on this subject [1]. It led to the Chinese involvement in the International Advisory Committee, with help from Professor Scaramuzzi, who was an advocate of gas-loading technology at low temperature. Figures 1(a), (f), and (g) are nuclear tracks from the palladium foils after deuterium loading. Figure 1(d) and (e) are controls using hydrogen instead of deuterium gas, or using deuterium gas with no palladium foil. Figure 1(b) is a comparison with a CR-39 chip radiated by an americium radioactive source, which emitted α -particles of ~ 5 MeV energy. The numbers in parenthesis are the batch numbers. Figure 1(c) shows the surface effect on charged particle emission. The surface cleaning procedures using aqua regia might have caused the negative result. The reproducibility was still poor, although batches 6 and 7 both produced positive results. Price [20] also found a negative result. Thus, reproducibility was the key issue at the beginning of the gas loading studies.

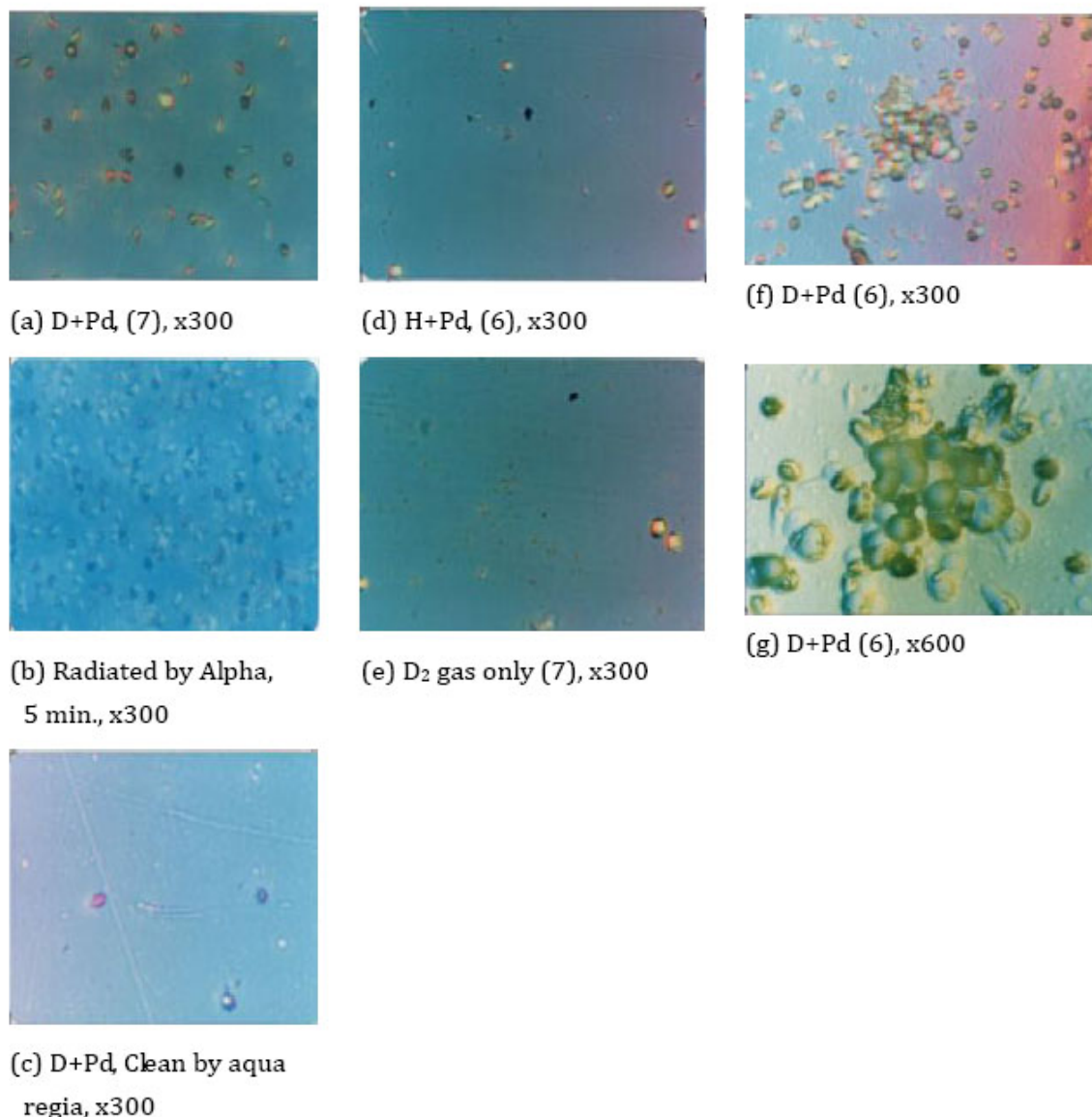


Figure 1. (a) D₂ + Pd, (7), $\times 300$. (b) Radiated by α -particle source (Am) 5 min, $\times 300$. (c) Clean by aqua regia, $\times 300$. (d) H₂ + Pd,(6), $\times 300$. (e) D₂ gas only, (7), $\times 300$. (f) D₂ + Pd,(6) $\times 300$. (g) D₂ + Pd, (6), $\times 600$.

3. Gas-Loading Pd Wire in a Dewar – Pumping Effect

High loading ratio was reportedly good for reproducibility. Materials problems were considered to be a key issue for high loading ratio by several researchers. However, Italian scientists [5] published their successful gas-loading work

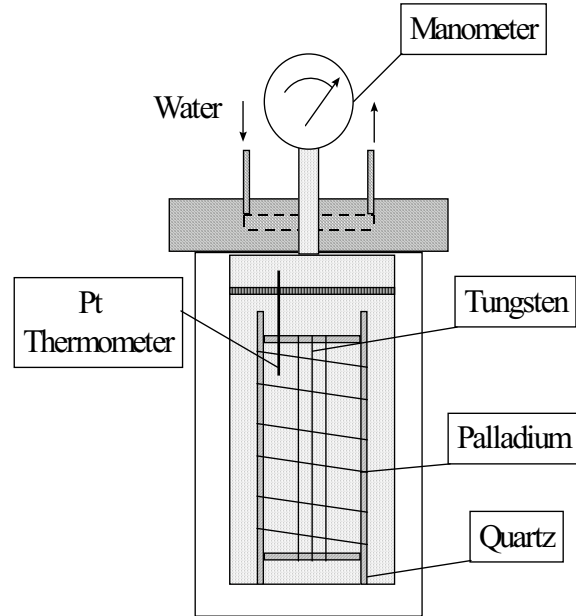


Figure 2. Gas-loading dewar with a long-thin Pd wire and a tungsten heating wire.

with materials from various resources. Oats and Flanagan [4] also claimed that high loading ratio might be achieved using their gas-loading cell without any concern about materials. Hence, a gas-loading cell was constructed in 1995 (Fig. 2) at Tsinghua University.

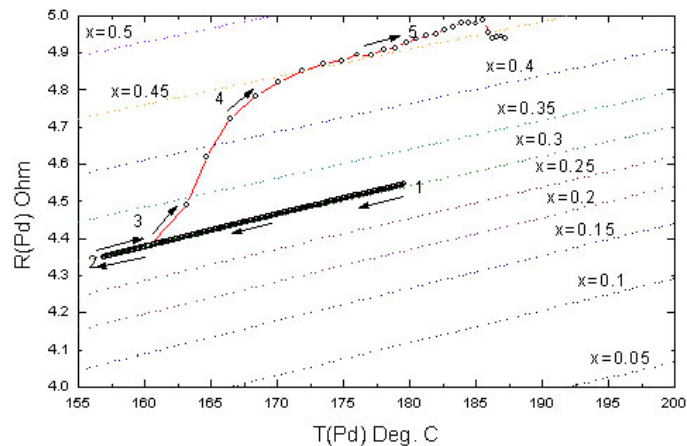


Figure 3. Pumping at 160°C induced a jump in loading ratio(constant current mode).

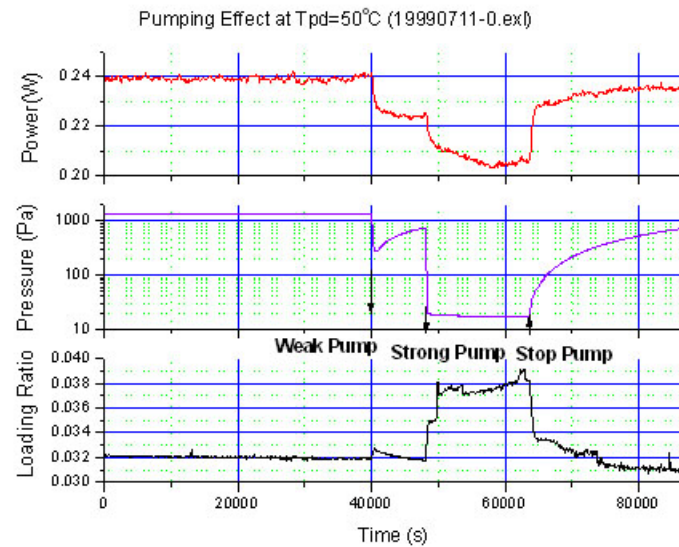


Figure 4. Necessary heating power to keep constant temperature is not a function of pressure, but directly related to pumping rate.

A long-thin palladium wire (250 mm long \times 0.34 mm diameter) was wound on a quartz frame and sealed in a stainless steel dewar. A tungsten wire (0.1 mm diameter) was wound on the same quartz frame to provide a high

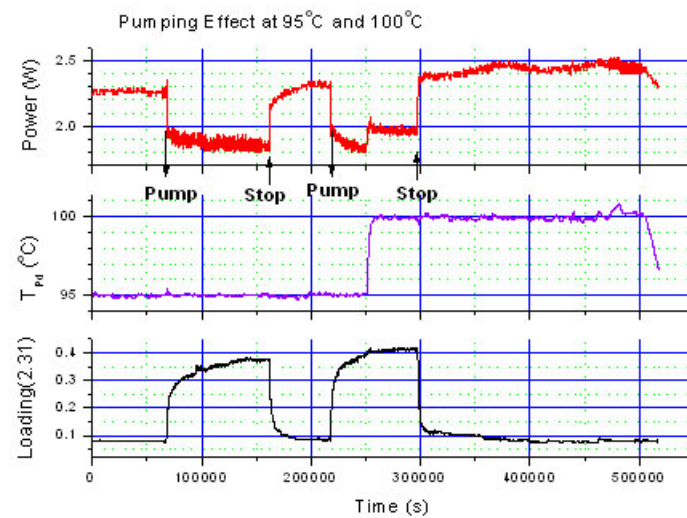


Figure 5. Excess heat under constant T_{pd} , 1998,12,13–17. (5_days7.xls).

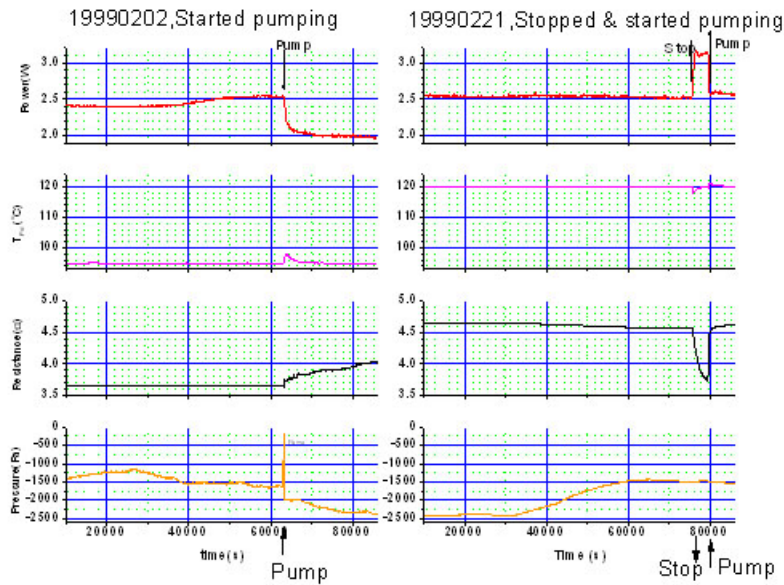


Figure 6. Pumping effect after 20 days at 120°C.

chemical potential of hydrogen atoms from the dissociation of hydrogen molecules. It was designed mainly for the study of the loading ratio; however, its operation led to an unexpected result: the pumping effect. It helped us to discover a correlation between deuterium flux and heat flow.

When we heat the palladium wire, we might anticipate that the loading ratio $x = D/Pd$ would drop if the pressure is reduced. However, the experiments showed that the loading ratio did not drop. Absorption occurs at high temperatures even if the pressure is lower than one atmosphere. In our gas-loading experiments, a pumping effect appeared in the D/Pd system. When the palladium wire was heated by electrical current its resistance was recorded to monitor the gas loading ratio. The resistance of a palladium wire depends on both its loading ratio and temperature. Figure 3 shows the resistance of the palladium wire, $R(Pd)$, as a function of its temperature, T_{Pd} , and loading ratio. Each dotted line shows the resistance as a function of T_{Pd} for a specific value of x . When we kept the electrical current in the Pd wire, $I(Pd)$, constant and changed the temperature of the dewar wall (T_w), then T_{Pd} changed to keep the thermal flow in balance with the electrical power input. The loading ratio was not changed when T_{Pd} dropped from point 1 (180°C) to point 2 (157°C) and rose from points 2 to 3 gradually. Starting the pump at point 3 introduced a jump in x from 0.3 to 0.45 (points 3 to 4). The time between two adjacent data points was only 10 s, so it was a quick jump. This jump was followed by a temperature rise due to the enhancement of the electrical power input in constant $I(Pd)$ mode (points 4–5).

This behavior appeared every time the pump was started. It was first thought (mistakenly) that this jump in resistance was induced by a positive feed-back mechanism as follows. The pumping reduced the gas pressure, so its thermal conductivity was reduced, and T_{Pd} increased. The increase of T_{Pd} would cause further increase of the resistance; hence, the electrical power input would be enhanced and it would cause further increase of T_{Pd} .

However, this feedback mechanism is not supported by the time behavior of the Pd wire resistance. Figure 3 shows that the resistance jumped much faster than the temperature rise at the onset (point 3). It was first a jump in loading

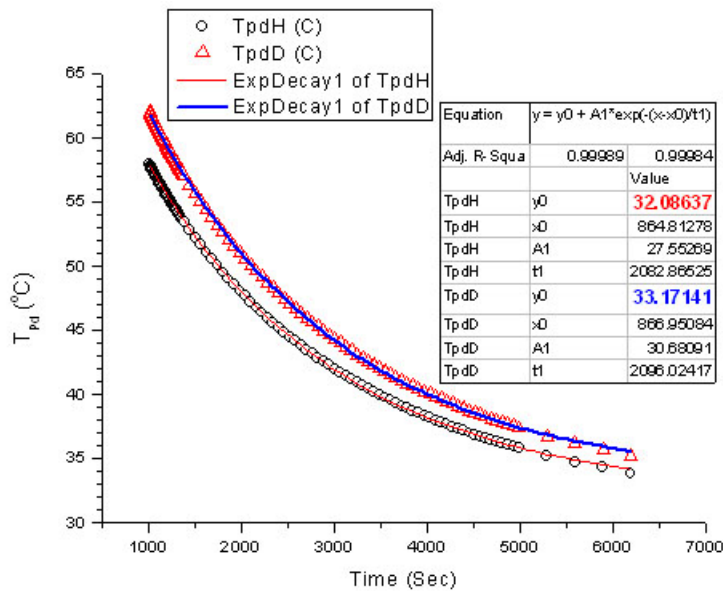


Figure 7. Exponential cooling behavior for D/Pd and H/Pd systems.

ratio, followed by an increase in temperature. Nevertheless, we were most interested in whether there was any “excess heat” accompanying this jump in loading ratio. Thus we have to eliminate first the temperature effect on the electrical resistance of Pd wire, and the effect of temperature on heat radiation.

New experiments were run in a constant temperature mode to avoid the temperature effects on electrical resistance and on heat radiation. Even if we assume that the heat transfer coefficient does not change at this pressure, we have to distinguish the heat of the electrical power input from the “excess heat” (if any). A computer-controlled power supply was used to keep T_{Pd} constant. A tiny Pt thermistor was attached to the palladium wire to monitor T_{Pd} , which could be preset to a fixed value using a computer program. In this way, we eliminated temperature effects during the pumping; however, we still observed the drop in heating power, P_h , needed to keep T_{Pd} constant.

When we started pumping the deuterium dewar at 40,000 s, the power necessary to keep $T_{\text{Pd}} = 50^\circ\text{C}$ dropped quickly (Fig. 4). One might suspect that the drop in deuterium gas pressure reduces the heat conductivity and hence, the necessary electrical power. This explanation is not correct.

When the pressure in the dewar increased slowly from 250 to 800 Pa the heating power, P_h did not increase with the pressure at all. When we increased the pumping rate again at 48,000 s, P_h dropped suddenly again. It is clearly shown that the P_h is a function of pumping rate but not a function of pressure in the dewar. Particularly, when we stopped the pumping at 63,000 s, P_h jumped up quickly, although the gas pressure was still very low in the dewar. These data exclude the possibility of explaining the jump of P_h as a jump in heat transfer coefficient. Indeed, the sudden change in P_h is possibly an evidence of “excess heat”. Assuming a constant heat transfer coefficient, this drop of P_h corresponds to an “excess heat” of 0.035 W, it is about 15% of the input power (0.24 W). The volume of the Pd wire is about 0.237 cm^3 ; hence, the power density is on the order of 0.15 W/ cm^3 at 50°C.

Based on the high temperature electrolysis experiments, we might anticipate that the “excess heat” would be enhanced at higher temperature. Figure 5 showed similar data at 95°C and 100°C. When T_{Pd} was kept constant, the

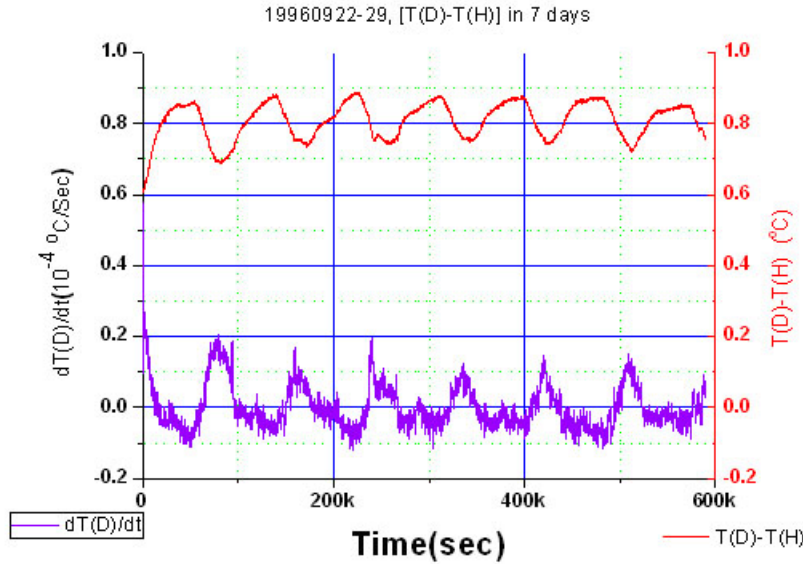


Figure 8. Temperature difference between D/Pd and H/Pd systems.

pumping at 69,000 s introduced a resistance jump and a power drop again. Since the T_{Pd} was kept constant, the change in resistance was attributed to loading, and the change in power was due to the “excess heat”. When the electrical power dropped from 2.28 to 1.84 W, the Pd temperature was still kept at $95 \pm 0.5^\circ\text{C}$. If the heat transfer coefficient did not change during the pumping; then, the “excess heat” power was about 0.44 W, which is 19% of the power input. When the pumping was stopped at 1,60,000 s, the necessary power jumped back to 2.3 W. This effect was reproduced

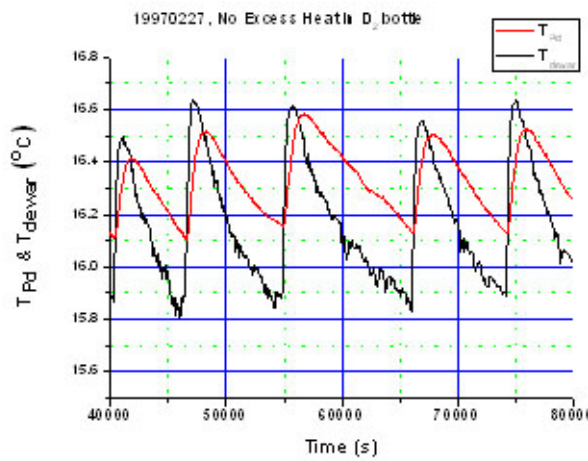


Figure 9. Temperature of palladium wire and dewar when there was no excess heat.

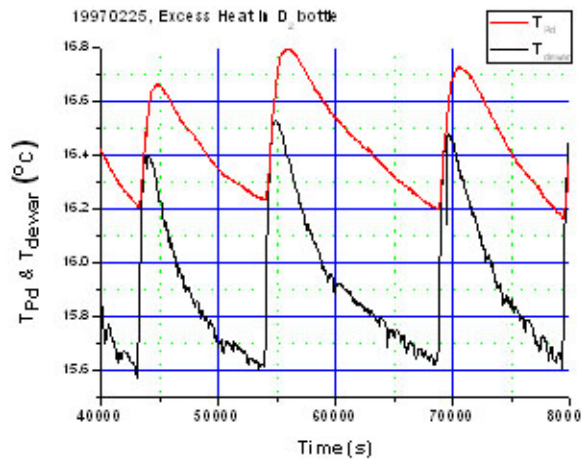


Figure 10. Temperature of palladium wire and dewar when there was excess heat.

the next day, at 2,18,000 s the necessary power dropped again to 1.84 W due to the pumping. There were two jumps in power at 2,50,000 and 2,97,000 s, respectively. They were different in nature. The first power jump at 2,50,000 s was due to the computer program setting. We required that T_{Pd} should be raised from 95°C to 100°C at 2,50,000 s; the computer increased the power input to meet this requirement. However, at 2,97,000 s we stopped pumping, and the power jumped up instantly to keep $T_{\text{Pd}} = 100^{\circ}\text{C}$. The power densities for this “excess heat” near 95°C and 100°C are about 1.8 and 2.1 W/cm³, respectively.

We have extended this experiment to $T_{\text{Pd}} = 120^{\circ}\text{C}$, and kept pumping for as long as 20 days. The P_h value was kept low until the pumping was stopped after 20 days. The corresponding “excess heat” power was 0.6 W at 120°C (greater than 2.5 W/cm³). Figure 6 shows this pumping effect after pumping 20 days. This experiment was started on February 2, 1999 near 95°C, the pumping reduced the heating power from 2.5 to 2.0 W (the plot on the top-left). After pumping 20 days, the temperature had been raised to 120°C by increasing heating power to 2.5 W (the plot on the top-right). On February 21, 1999 near 120°C, stopping the pumping enhanced the necessary heating power to 3.1 W; then, the pumping again reduced the heating power back to the 2.5 W level. The computer-controlled temperature was maintained at the preset level (second row of plots). The resistance of the palladium wire increased every time we started pumping (third row of plots). The fourth row clearly shows that the pressure did not change much after pumping 20 days, because there was very low deuterium gas left in the vacuum vessel. However, the pumping effect still existed vigorously. It might imply that pumping effect was related to the property of palladium wire (near the surface layers). It is not related to a reduction of the heat transfer coefficient.

4. Difference Between D/Pd and H/Pd Systems

It was a prevailing trend in 1990’s to test the difference between D/Pd and H/Pd systems. Our long-thin palladium wire loading vessels provided a convenient calorimeter for this purpose, because we put the long-thin palladium wire frame inside a dewar to get higher temperature with much lower heating power. We made a pair of twin loading systems. They were heated by tungsten wires with same electrical current. The parameters for these twin systems are listed in Table 1.

Figure 7 shows the cooling feature of these twin systems. The values of T_{Pd} are changing with time. Both cooling

curves may be fit with an exponential,

$$y = y_0 + A_1 \exp[-(x - x_0)/t_1]. \quad (1)$$

Here, y is the temperature of palladium wire, and the x is the time. This exponential behavior implies that this system may be described by a heat transfer equation with three parameters (C, k, S):

$$C \frac{dT_{pd}}{dt} = -k(T_{pd} - T_{room}) + S, \quad (2)$$

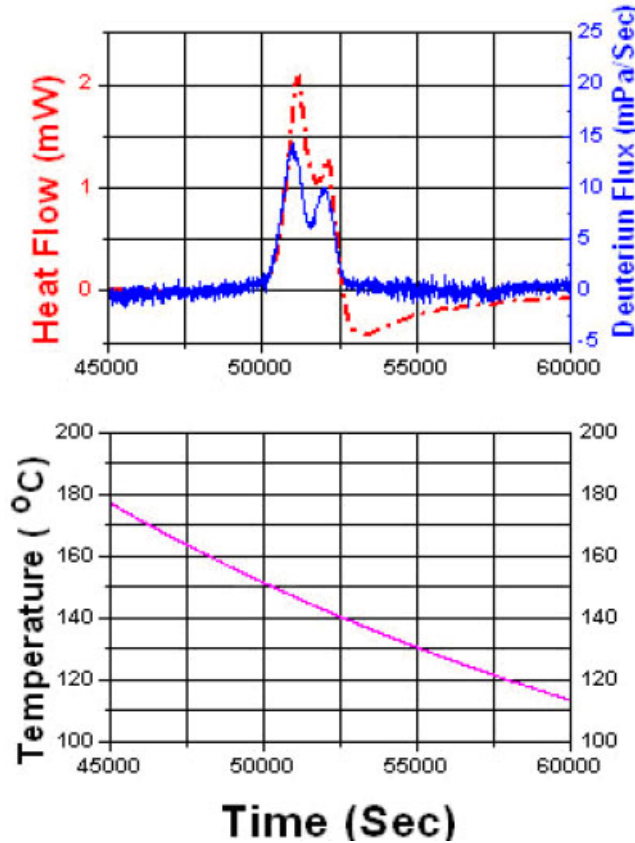


Figure 11. Correlation between heat flow and deuterium flux.

Table 1. Parameters of twin systems for gas-loading.

	D/Pd	H/Pd
Weight of Pd wire (g)	2.846	2.844
Resistance of tungsten wire (Ω)	4.1	4.3
Vacuum pressure before filling (Pa)	10^{-3}	10^{-3}
Filling pressure(mmHg)	600(D)	600(H)

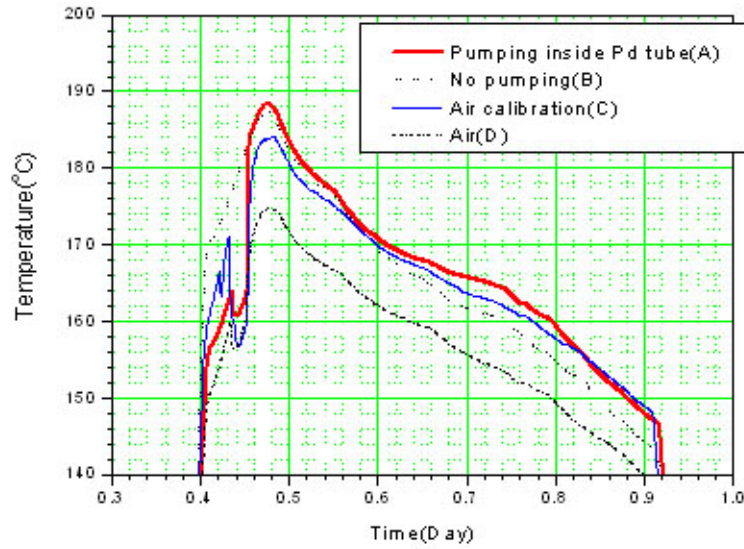


Figure 12. Comparison among 4 cooling cases shows the excess heat correlated with pumping effect.

Here C is the heat capacity of the system, k is the heat transfer coefficient and S is the heat source (if any). From the parameters of the fitting curves, we find that

$$y_0 = T_{\text{room}} + \frac{S}{k}, \quad t_1 = \frac{C}{k}. \quad (3)$$

In Fig. 7, the triangles are for the D/Pd system, and the circles are for the H/Pd system. The difference in y_0 implies different S for D/Pd and H/Pd systems, respectively, because T_{room} , k , and C are almost the same for D/Pd and H/Pd systems. Qualitatively, we may say that the D/Pd bottle is hotter than H/Pd bottle by 1.1°C . From Fig. 4, we know that 0.24 W may raise the T_{Pd} from room temperature (30°C) to 50°C ; therefore, 1.1°C might correspond an excess heat source of 12 mW in the D/Pd system.(roughly, 50 mW/cm^3) Usually, the first question one may ask is the calibration of the thermistors. Can we eliminate the possibility of a thermistor problem? (Was the temperature difference just caused by thermistor error?). Fortunately we measured the temperature difference between D/Pd and H/Pd systems for 7 days (Fig. 8). It was not constant, but varies with the derivative of the temperature (dT_{Pd}/dt). The temperature difference, $[T(\text{D})-T(\text{H})]_{\text{Pd}}$ (the thick line and the right ordinate) reaches a maximum when (dT_{Pd}/dt) (the thin line and the left ordinate) reaches a minimum. This is consistent with the selective resonant tunneling model. It seems that the D/Pd bottle is always warmer than H/Pd bottle. This is not an error in the thermistors. It should be noticed that the time scale is expanded to 6,00,000 s, the temperature is almost in equilibrium with the environment at every instant. One more piece of evidence is from the D/Pd bottle itself. Figures 9 and 10 show the temperature of palladium wire and the temperature of the dewar when we put the dewar in the water bath of a thermostat. Due to the heater in the thermostat, which acted intermittently, the temperature of the dewar varied around a pre-set value. When the D/Pd bottle had no heater inside, T_{Pd} was supposed to vary with the dewar. When there was no excess heat inside the D/Pd bottle, the temperature of palladium wire increased only if $T_{\text{dewar}} > T_{\text{Pd}}$; and the temperature of palladium wire decreased only

if $T_{\text{dewar}} < T_{\text{Pd}}$. This is clearly shown in Fig. 9: The T_{Pd} (solid line) went up whenever T_{dewar} (dotted line) was higher than T_{Pd} , and T_{Pd} (solid line) turned downwards whenever T_{dewar} (dotted line) was lower than T_{Pd} . Hence the interception points of the T_{Pd} and T_{dewar} curves are always at the peak of the solid line or at the bottom of the valley of the solid line (i.e. $dT_{\text{Pd}}/dt = 0$ at $T_{\text{Pd}} = T_{\text{dewar}}$). When Fig. 9 shows that the calibration of thermistor T_{Pd} and T_{dewar} was correct, Fig. 10 shows that there had to be excess heat inside the D/Pd bottle on Feb. 25, 1997, because T_{Pd} was increasing even if T_{Pd} was higher than T_{dewar} .

5. Correlation Between D₂ Flux and Heat Flow

A decisive experiment was conducted in 2000 in collaboration with the Department of Chemistry at Tsinghua University where the high precision calorimeter (C-80D) was located. The most important feature of the C-80D calorimeter is that it is based on the Seebeck effect; hence, it eliminated any concern about the change of the heat transfer coefficient during the pumping. The C-80D, imported from France (SETARAM), has such high precision that it is able to detect one microwatt heat flow from its reaction vessel. When we put a piece of sealed palladium tube inside the reaction vessel of the C-80D calorimeter, and pumped out the deuterium gas from outside of the Pd tube, the deuterium gas inside the Pd tube permeated through the thin wall of the Pd tube. The pressure in the vessel was determined by the balance between the deuterium flux and the pumping rate. The change in the deuterium flux is detected by the deuterium pressure in the vessel.

We found that the heat flow in C-80D was accompanied by a change of deuterium pressure in the vessel while the pump was working continuously. In Fig. 11, the thick line shows the heat flow recorded by the C-80D calorimeter, and the thin line shows the derivative of the pressure. The two peaks in heat flow were correlated with the two peaks in the deuterium flux. This phenomenon was observed when the heater in the C-80D was turned off, and the temperature of the vessel was cooling down slowly through 150°C to 140°C. The selective resonant tunneling theory predicted that the excess heat would be observed preferably in the slow cooling process, because the slow cooling down process might elongate the time in the resonance. We did observe this asymmetry in the cooling and heating processes.

Figure 12 shows the scale-up of this pumping effect. The length of the palladium tube was lengthened from 26 to 200 mm, and single Pd tube configuration was changed to a bundle of 5 Pd tubes. Under the same situation (room temperature, pattern of heating power, gas pressure, etc.) the temperature of Pd tube was monitored during the cooling processes. There were 4 different cooling cases: A, Cooling in the deuterium gas and pumping inside the Pd tube; B, Cooling in the deuterium gas without pumping; C, Cooling in the air and with 1 W inner heater on the Pd tube for calibration; D, Cooling in the air with inner heater off. It is evident that the temperature of Pd tube was the highest in case A; and temperature of the Pd tube was the lowest in case D although the heat transfer coefficient of deuterium gas was supposed to be greater than that of air. The temperature of the Pd tube for case B was lower, it implied that the pumping inside the Pd tube was very important for this excess heat. The calibration using inner heater on the Pd tube (case C) gave a rough estimate of the power of excess heat. It was on the order of 1 W, and it lasted 10 h.

6. A Stride Towards Neutrino Detection

The neutrino detector at the Neutrino Science Research Center in Japan requires a minimum neutrino flux for its operation. On the surface of the big liquid scintillator sphere, there has to be at least 10^6 neutrinos per cm^2 per second. For this 14 m diameter sphere, it requires a source of 10^{12} neutrinos/s at the center of the sphere. If each neutrino accompanies 10 MeV reaction energy; then, 1 W reaction energy just provides the necessary neutrino flux for detection. We know that most of the reaction energy is carried away by neutrinos [18], only the heavy charged particles leave their energy in the palladium deuteride—the excess heat. The excess heat is from the recoil energy of the neutrino emission. Hence, we might expect even many more neutrinos from 1 W excess heat ($\sim 10^{15}$ neutrinos/s). If the detection of neutrinos is successful; then, nuclear energy without nuclear contamination will have been demonstrated.

If we scrutinize the “excess heat” data in the past 20 years, the highest “excess power” density with long enough time was the “heat after death” in 1994 [3]. In average, the “excess power” density was estimated to be 3.7 kW/cm^3 in 3 h. Hence each atom of reactant released $\sim 220 \text{ eV}$ only. This is on the order of recoil energy. It confirms that most of the reaction energy is carried away by neutrinos. Indeed this is the physics basis of “nuclear energy without nuclear contamination”.

Acknowledgments

This research is supported by the Ministry of Education, The Ministry of Science and Technology (Fundamental Research Division), Natural Science Foundation of China (#10145004, #10475045), The China Association for Science and Technology, and Tsinghua University (Basic Research Fund (985-III)), National Basic Research Program of China (2009CB226113).

References

- [1] X.Z. Li et al. The precursor Of *Cold Fusion* phenomenon in deuterium/solid systems, in *Anomalous Nuclear Effects in Deuterium/Solid Systems –Provo*, Utah, 1990, S.E. Jones et al. (eds.), AIP Conference Proceedings 228, New York, 1991, pp. 419–429.
- [2] X.Z. Li, *J. New Energy* **1**(4) (1996) 44–54.
- [3] S. Pons, M. Fleischmann, Heat after death, *Tans. Fusion Technol.* **26** (1994) 87–95; M. Fleischmann, S. Pons, Calorimetry of the Pd-D₂O system: from simplicity via complications to simplicity, *Phys. Lett. A* **176** (1993) 118–129.
- [4] W.A.Oats, Ted B. Flanagan, *Nature Phys. Sci.* **231** (1971) 19.
- [5] C. Manduchi et al., *IL Nuovo Cimento* **107A** (2) (1994) 171–183.
- [6] X.Z. Li et al., Pumping effect–reproducible excess heat in a gas-loading D/Pd system, in *Condensed Matter Nuclear Science, Proceedings of ICCF-9*, X.Z. Li (ed.), Tsinghua Press, Beijing, 2002, pp. 197–201.
- [7] X.Z. Li et al., Excess heat measurement in gas-loading D/Pd system, *Proceedings in New Hydrogen Energy*, M. Okamoto (ed.), Vol. 2, 1996, pp. 455–462.
- [8] G.S. Qiao et al., Nuclear products in a gas-loading D/Pd and H/Pd system, *Proceedings of ICCF-7*, ENECO (ed.), 1998, pp.314–318.
- [9] X.Z. Li et al. *J. Phys. D: Appl. Phys.* **36** (2003) 3095–3097.
- [10] T.O. Passell, Evidence for lithium-6 depletion in Pd exposed to gaseous deuterium and hydrogen, in *Condensed Matter Nuclear Science, Proceedings of ICCF-9*, X.Z. Li (ed.), Tsinghua Press, Beijing, 2002, pp. 299–304.
- [11] J.P. Biberian et al., Excess heat production during D₂ diffusion through palladium, *Proceedings of ICCF-13*, Yu.N. Bazhutov (ed.), 2007.
- [12] Q.M. Wei et al., in *Condensed Matter Nuclear Science , Proceedings of ICCF-11*, J.P. Biberian (ed.), World Scientific, New Jersey, 2004, pp. 351–358.
- [13] B. Liu et al., Excess heat induced by deuterium flux in palladium film, in *Condensed Matter Nuclear Science, Proceedings of ICCF-12*, A. Takahashi et al. (eds.), World Scientific, New Jersey, 2005, pp.75–79.
- [14] X.Z. Li et al., *Phys. Rev. C* **61** (2000) 024610.
- [15] X.Z. Li, *Fusion Sci. Techol.* **41** (2002) 63.
- [16] X.Z. Li, *Nucl. Fusion* **48** (2008) 125003.
- [17] J. Kasagi. *J. Phys. Soc. Japan* **64**(3) (1995) 777–783.
- [18] X.Z. Li et al., The conjecture of the neutrino emission from the metal hydrides, *J. Condensed Matter Nucl. Sci.* **1** (2007) 11–15.
- [19] X.Z. Li et al., Exploring a self-Sustaining heater without strong nuclear radiation, in *Proceedings of ICCF-14*, D. Nagel et al. (eds.), 2008.
- [20] P.B. Price et al., *Phys. Rev. Lett.* **63** (1989) 1926–1929.



Research Article

Observation of Low Energy Nuclear Transmutation Reactions Induced by Deuterium Permeation through Multilayer Pd and CaO thin Film

Y. Iwamura ^{*}T. Itoh and N. Yamazaki

Advanced Technology Research Center, Mitsubishi Heavy Industries Ltd., Yokohama, Japan

J. Kasagi

Research Center for Electron Photon Science, Tohoku University, Sendai, Japan

Y. Terada

Japan Synchrotron Radiation Research Institute (JASRI), Hyogo, Japan

T. Ishikawa

RIKEN SPring-8 Center, Hyogo, Japan

D. Sekiba

Research Facility Center for Science and Technology, University of Tsukuba, Ibaraki, Japan

H. Yonemura and K. Fukutani

Institute of Industrial Science, University of Tokyo, Tokyo, Japan

Abstract

Low energy nuclear transmutations in condensed matter have been observed in the nano-structured Pd multilayer complex, which are composed of Pd and CaO thin film and Pd substrate, induced by D₂ gas permeation through Pd multilayer complexes. Permeation of deuterium is attained by exposing one side of the Pd complex to D₂ gas while keeping the other side under vacuum conditions. Transmutation reactions of Cs into Pr, Ba into Sm were observed. Especially, transmutation of Cs into Pr has been confirmed by “in-situ” measurements using x-ray fluorescence spectrometry (XRF) at SPring-8 in Japan. Similar experiments have been performed by some researchers and positive results have been obtained in some cases. However, more systematic experiments and theoretical approaches are required to make clear the nature of this phenomenon.

© 2011 ISCMNS. All rights reserved.

Keywords: CaO, Deuterium, D₂ gas, Multilayer, Nano-structure, Pd, Permeation, Thin film, Time of flight mass spectrometry, Transmutation, X-ray fluorescence, X-ray photoelectron spectrometry

PACS: 82.80.Pv, 81.07.-b, 68.65.Ac, 68.47.De, 29.30.Kv.

^{*}E-mail: yasuhiro_iwamura@mhi.co.jp

1. Introduction

Transmutation reactions in nano-structured material have been observed in Pd complexes which are composed of Pd and CaO thin film and Pd substrate, induced by D₂ gas permeation[1–7]. Experimental data that indicates the presence of transmutation have been accumulated and experimental conditions for inducing low energy transmutation reactions are gradually becoming clear, although it is difficult to make theoretical explanations to this phenomenon and systematic experimental study is still insufficient.

Figure 1 shows schematic of our experimental method. Our approach can be characterized by the permeation of D₂ gas through the nano-structured Pd complex and the addition of an element that is specifically targeted to be transmuted.

Permeation of deuterium, the first feature, is attained by exposing one side of the Pd multilayer thin film to D₂ gas while maintaining the other side under vacuum conditions. On the D₂ gas side of the Pd complex, dissociative absorption causes the separation of D₂ molecules into D atoms, which diffuse through the Pd metal toward the vacuum side, where they emerge from the Pd metal, combine and are released as D₂ gas.

The second feature is the addition of an element targeted to be transmuted. Our sample is a Pd complex composed of bulk Pd on the bottom, alternating CaO and Pd layers, and a Pd thin film on top. After fabricating a Pd complex, Cs, Ba, Sr or other element is deposited on the surface of the top thin Pd layer. We can observe transmutation of the added elements.

In other words, with this experimental method, we can provide a deuterium flux through the Pd multilayer thin film on which an element is placed as a target to be transmuted. We perform elemental analyses of the given elements after D₂ gas permeation by exhausting the D₂ chamber.

2. Experimental

Fabrication of Pd complex is basically the same as before [1–6]. Preparation of the multilayer Pd thin film is shown in Fig. 2a. A Pd was washed with acetone and annealed in vacuum ($<10^{-5}$ Pa) at 900°C for 10 h. It was then cooled to room temperature in furnace and washed with aqua regia to remove impurities on the surface of the Pd plate. The surface of the plate was covered by layers of CaO and Pd, which were obtained by five times alternately sputtering 2-nm-thick CaO and 20-nm thick Pd layers. Then a 40 nm-thick Pd layer was sputtered on the surface of the CaO

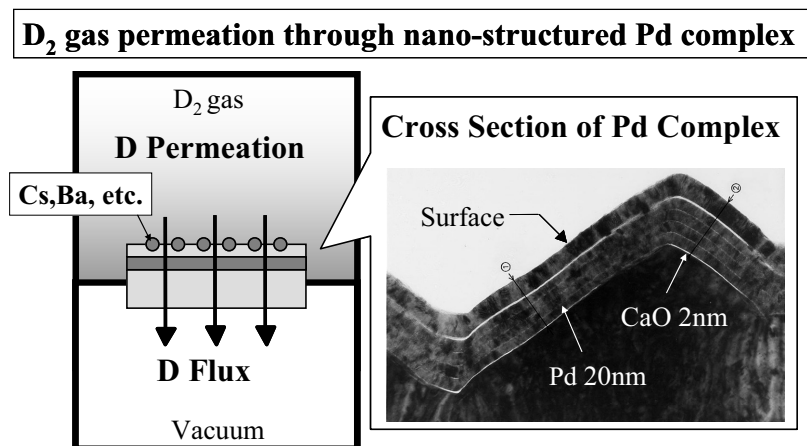
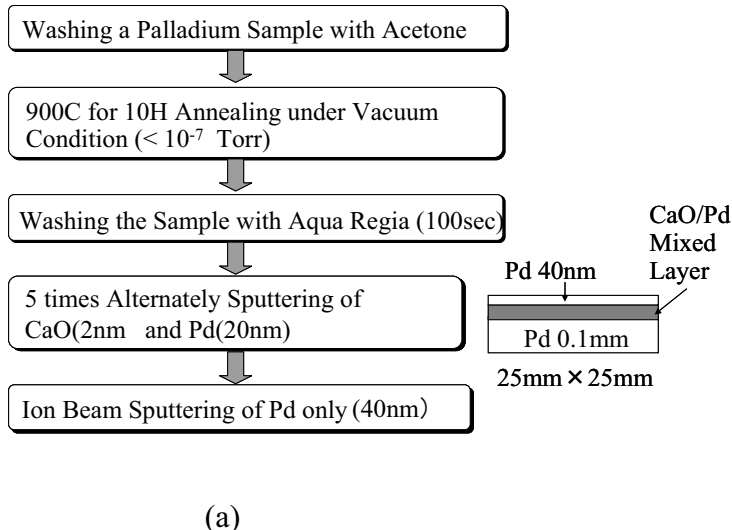


Figure 1. Schematic of our experimental approach.



(a)

Figure 2. (a) Preparation of Pd multilayer thin film, (b) cross-sectional view of the fabricated sample by TEM.

and Pd layers. These processes were performed by the Ar ion beam sputtering method or the magnetron sputtering method. After fabricating a Pd complex, Cs was deposited on the surface of the thin Pd layer. Cs was deposited by the electrochemical method or the ion implantation method. In the case of SPring-8 experiments, Cs was given by the ion beam implantation method (voltage: 5 kV, dose: $2.5 - 5 \times 10^{14}/\text{cm}^2$).

Cross-sectional view of the fabricated Pd multilayer sample is shown in Fig. 2b. The white lines in the photograph correspond to CaO. We can see that the sample is correctly fabricated by our procedure.

Originally, we used an experimental apparatus with X-ray Photoelectron Spectrometry (XPS) shown in Fig. 3a. Elemental changes on Pd complexes were measured by XPS without taking them out of the vacuum chamber, to prevent contamination from outside of the chamber. Using this experimental set-up, transmutation reactions of Cs into Pr and Sr into Mo were observed. In the case of transmutation experiments of Ba into Sm, the XPS in the chamber was not available at that time so the samples were analyzed before and after D_2 permeation using XPS or Secondary Ion Mass Spectrometry (SIMS).

Figure 3(b) shows the experimental setup for in-situ measurement at SPring-8, which is one of the largest synchrotron radiation facilities, located in the west part of Japan. This setup enables us to observe elemental changes during D_2 gas permeation by X-ray fluorescence spectrometry (XRF). Synchrotron orbital radiation X-ray (5.97 keV) is introduced into the permeation chamber through a Be window and attacks on the surface of Pd complex sample. X-ray intensity is about from 10^{12} to 10^{13} photons/s. Cs-L and Pr-L lines can be detected by a Silicon Drift Detector (SDD). The SDD is covered by a Cl filter which is used for the absorption of intense Pd-L X-ray. XRF was performed during D_2 permeation in-situ at the beginning and the end of the experimental runs.

3. Results and Discussion

Transmutations of various elements were tried in our laboratory. In this paper, transmutation of Cs into Pr, Ba into Sm, measurement of distribution of products, the role of CaO, key factors in permeation experiments and replication experiments are described.

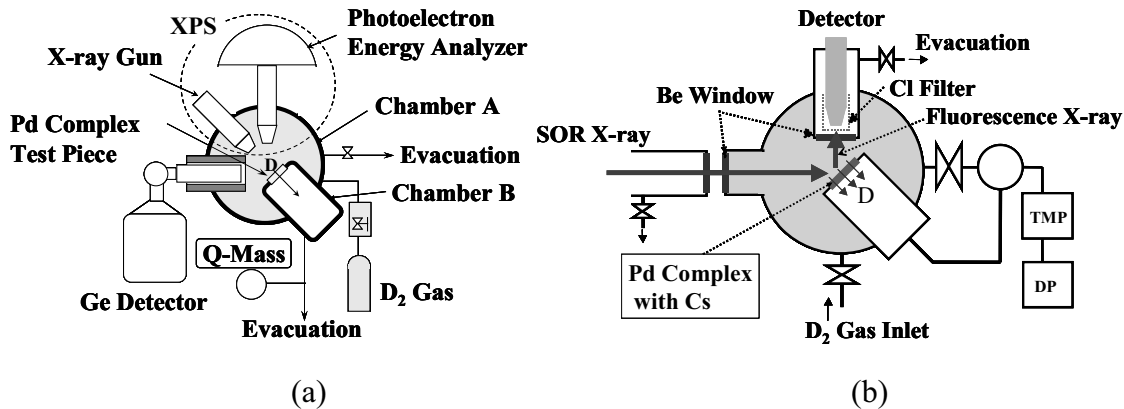


Figure 3. Experimental set-ups for permeation experiments. (a) Original apparatus with XPS [1]. (b) In-situ experimental setup at Spring-8 [2].

4. Transmutation of Cs into Pr

Figure 4 shows the first observation of transmutation reaction from Cs into Pr using the experimental set-up shown in Fig. 3a. Results for two runs are shown as examples. There was no Pr at the beginning of the experiments. The number of Cs atoms decreased while Pr atoms increased as experimental time went by. The number of atoms were evaluated by XPS spectra. Amount of deuterium permeation was proportional to the elapsed time. After 120 h, the number of Pr atoms exceeded that of Cs atoms.

As the control experiments, (1) H₂ gas permeation experiments using the same Pd multilayer samples (Pd/CaO/Pd), (2) D₂ gas permeation using the same Pd multilayer samples (Pd/CaO/Pd) without Cs, and (3) D₂ gas permeation using the Pd sample without CaO were performed. These control experiments were performed under the same temperature

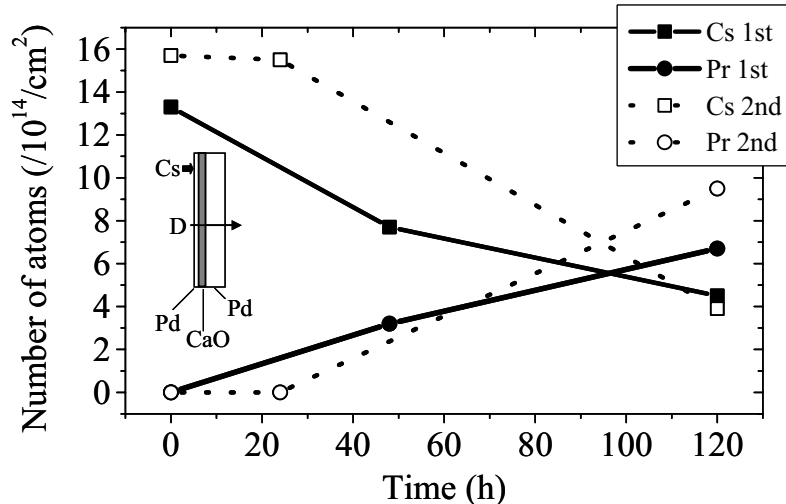


Figure 4. Observed transmutation reactions from Cs into Pr [1].

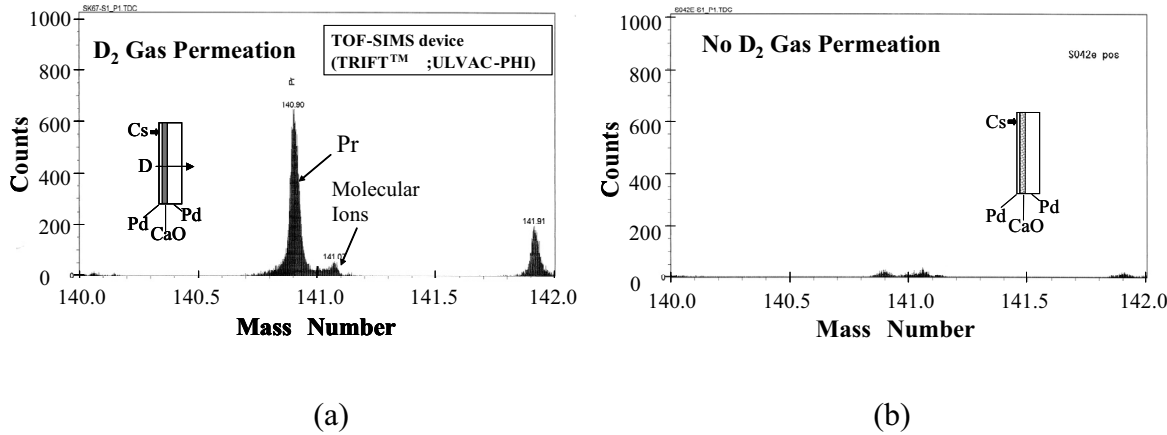


Figure 5. Pr detection by TOF-SIMS analysis [4].

and pressure as foreground experiments. No Pr was detected in all the control experiments. It suggests that both deuterium and nano-structured Pd multilayer with CaO are necessary factor to observe transmutation reactions.

Pr, the transmuted product from Cs, was confirmed by many element analysis methods. Identification of Pr by Time of Flight Secondary Ion Mass Spectrometry (TOF-SIMS) is illustrated in Fig. 5. The TOF-SIMS device is a model TRIFIT™ II made by ULVAC-PHI. Figure 5a shows the mass number distribution of the Pd complex (Pd/CaO/Pd) after D₂ gas permeation, and Fig. 5b is for the Pd complex without D₂ gas permeation. The TOF-SIMS can distinguish small mass difference so that Pr and molecular ions can be clearly separated, as shown in the upper figure. It is confirmed that Pr is detected only for the permeated sample.

The existence of Pr was confirmed by X-ray Absorption Near Edge Structure (XANES), Inductively Coupled Plasma Mass Spectrometry (ICP-MS) and XRF [2–4]. According to ICP-MS, detected Pr ranged from 0.1 to 100 ng [4].

On the next stage, we tried in-situ measurements with XRF to obtain more confident results. An example of detection of Pr by in-situ measurement is shown in Fig. 6. Initial (before D₂ gas permeation) and final (after D₂ gas permeation) XRF spectra are plotted. Cs was injected by the ion beam implantation method (voltage: 5 kV, dose: $2.5 \times 10^{14}/\text{cm}^2$). In this case, we use 1 mm square X-ray beam. The Cs peaks decreased and the Pr peak emerged after D₂ gas permeation at the shown point in Fig. 6. It can be seen that transmutation of Cs into Pr occurred at this point. However, no Cs was changed and no Pr was seen except this point in the case of this sample. Pr distribution for this sample was measured using micro-sized X-ray as described later.

5. Transmutation of Ba into Sm

We tried Ba transmutation experiments using natural Ba and mass 137 enriched Ba. Natural Ba was deposited by the electrochemical method with 10 mM Ba(OH)₂ solution. And mass number 137 enriched Ba was deposited by electrochemical method with 7.3 mM Ba(NO₃)₂ solution. Applied voltage was 1 V and the time was 10 s as the same as Cs or Sr experiment [1].

Figure 7 shows XPS spectra for the Pd complex after deuterium permeation for 2 weeks with natural Ba. Sm 3d spectra are shown in Fig. 7a. The measurements were done twice to make sure measurement reproducibility and clear Sm spectra were obtained in both measurements. XPS full spectrum is shown in Fig. 7b. Pd, Ba, C(surface impurity) and Sm 3d and Sm 4d peaks can be seen.

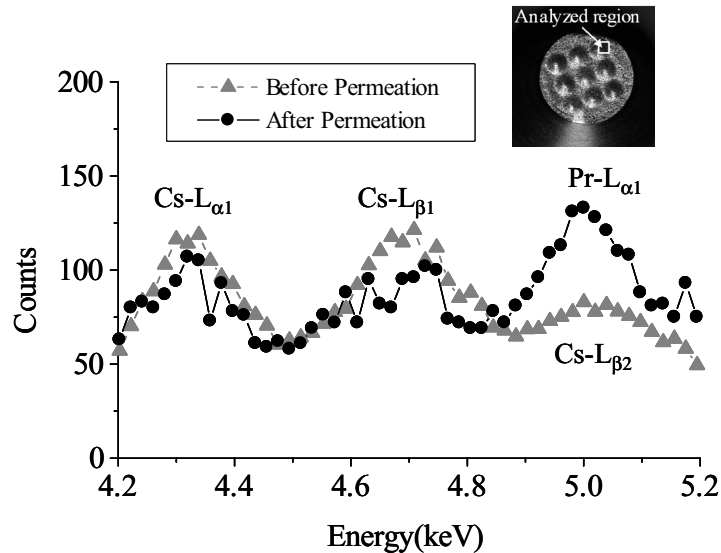


Figure 6. Detection of Pr by an in-situ experiment at SPring-8 [2].

In order to investigate the Sm isotopic distribution, we analyzed the detected Sm by SIMS. Natural abundance of Sm and SIMS spectrum of the detected Sm are shown in Table 1 and Fig. 8, respectively. Natural Sm has seven isotopes and the largest isotope is ^{152}Sm . However, natural Sm SIMS spectra cannot be seen in Fig. 8, although clear XPS spectra for Sm were obtained on this sample. In Fig. 8, “after permeation” means the Pd multilayer thin film with natural Ba after D_2 permeation and “before permeation” means the Pd multilayer thin film with natural Ba without D_2 permeation. Mass number 150 for “after permeation” is one order larger than “before permeation” in Fig. 8. This mass

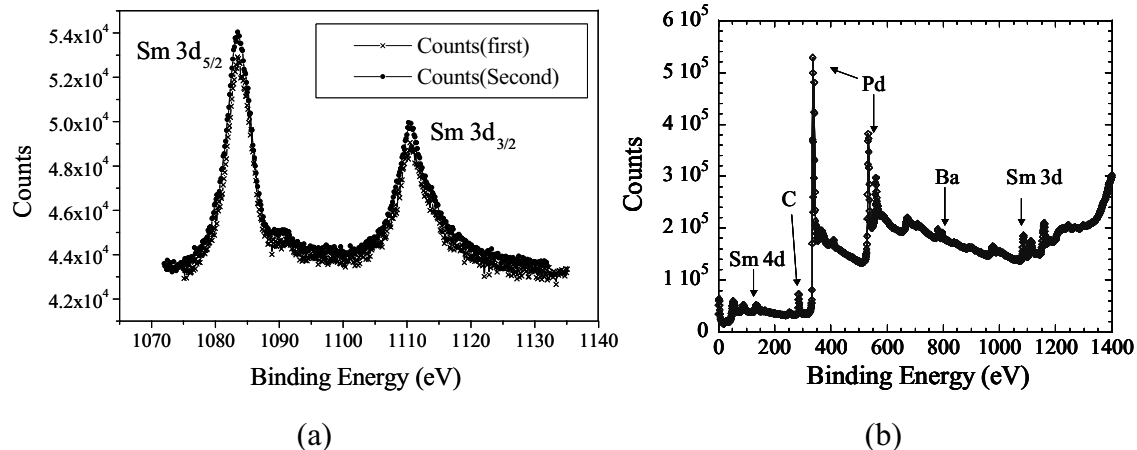


Figure 7. Detected Sm XPS spectra after D_2 gas permeation through a Pd complex deposited with natural Ba; (a) XPS spectra for Sm 3d, (b) Full XPS spectrum [3].

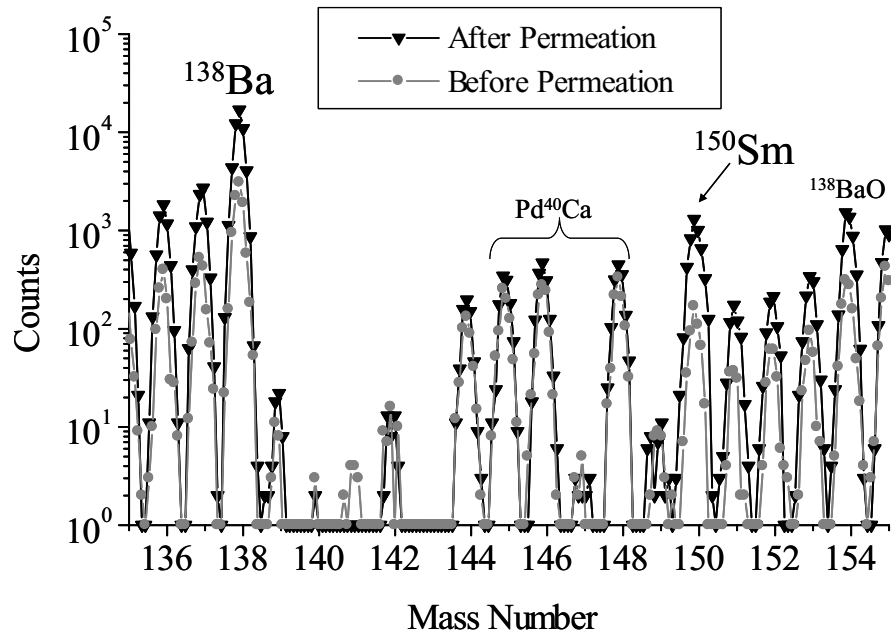


Figure 8. SIMS spectra for Pd complexes with natural Ba [3].

number must have been derived from ^{150}Sm according to the XPS analysis.

Let us consider these spectra in Fig. 8 using Table 2 that examines the effects of molecular ions. ^{138}Ba signal for “before permeation” and “after permeation” does not match. We consider this is because of non-uniformity of Ba deposition. Pd^{40}Ca molecular ion peaks for “before permeation” and “after permeation” are nearly equal. Both $^{110}\text{Pd}(12\%)^{40}\text{Ca}$ and $^{134}\text{Ba}(2.4\%)^{16}\text{O}$ are candidates for mass 150.

In the case of $^{110}\text{Pd}(12\%)^{40}\text{Ca}$, $^{110}\text{Pd}^{40}\text{Ca}$ cannot explain the large mass 150 since the signal for $^{110}\text{Pd}(12\%)^{40}\text{Ca}$ must be lower than $^{106}\text{Pd}(27\%)^{40}\text{Ca}$ and mass 146 is smaller than mass 150.

In the case of $^{134}\text{Ba}(2.4\%)^{16}\text{O}$, the signal of $^{134}\text{Ba}(2.4\%)^{16}\text{O}$ must be one order lower than the signal of $^{138}\text{Ba}(71.7\%)^{16}\text{O}$. However, the mass 150 for the “after permeation” is the same order as $^{138}\text{Ba}(71.7\%)^{16}\text{O}$. Therefore the contribution of $^{134}\text{Ba}(2.4\%)^{16}\text{O}$ cannot explain the mass 150 signal.

Now we consider about the effect of ^{12}C ion. Mass 150 can be created numerically with the combination of ^{138}Ba and ^{12}C . If $^{138}\text{Ba}^{12}\text{C}$ might be created, then $^{137}\text{Ba}^{12}\text{C}$ (mass 149) and $^{136}\text{Ba}^{12}\text{C}$ (mass 148) should be created. However, we cannot see any increase of mass 149 and 148 in the “after permeation” signals in Fig. 8. This fact indicates that BaC molecular ions have almost no effects on the SIMS spectra. Therefore the large mass 150 signal cannot be explained by $^{138}\text{Ba}^{12}\text{C}$ formation..

Based on these SIMS considerations and XPS results, it is reasonable that mass 150 for the permeated sample is

Table 1. Natural abundance of Sm.

^{144}Sm	^{147}Sm	^{148}Sm	^{149}Sm	^{150}Sm	^{152}Sm	^{154}Sm
3.2%	15.1%	11.3%	13.8%	7.5%	26.6%	22.5%

Table 2. Examination of molecular ions.

Pd	Pd ^{40}Ca	Ba	BaO
102(1%)	142	130(0.1%)	146
104 (11%)	144	132(0.1%)	148
105 (22%)	145	134(2.4%)	150
106 (27%)	146	135(6.6%)	151
108 (26%)	148	136(7.8%)	152
110 (12%)	150	137(11.3%)	153
		138(71.7%)	154
		130(0.1%)	146

derived from Sm. It is strongly suggested that ^{150}Sm exists on the Pd complex after D_2 gas permeation.

In the case of the 137 enriched Ba deposition sample, we could not obtain clear XPS spectra. However, we obtained SIMS data that showed the increase of mass 149. Figure 9 shows two SIMS spectra for Pd complexes with 137 enriched Ba after D_2 permeation. About one order increase of mass 149 was observed in the both experiments of Nos. 1 and 2. Table 2 indicates that mass 149 cannot be created by Pd ^{40}Ca and Ba^{16}O . $^{137}\text{Ba}^{12}\text{C}$ also cannot explain because BaC molecular ions have almost no effects on the SIMS spectra as described before. These facts imply that ^{149}Sm exists on the Pd complex if we consider that Sm spectra were obtained by XPS using natural Ba. The 149 mass increase might be caused by ^{149}Sm .

Figure 10 shows the mass correlation between given and detected elements. If we put ^{138}Ba on the nano-structured Pd film, we obtain ^{150}Sm by D_2 gas permeation. And if we set ^{137}Ba on the Pd complex, we obtain ^{149}Sm , if we assume that the mass 149 increase of the SIMS spectra are caused by Sm. The observed transmutation reactions of Ba into Sm belong to a reaction category in which the increase of mass number is 12 and the increase of atomic number is 6. Nuclear transmutation induced by our experimental method is not limited to the category in which the increase of mass number is 8 and the increase of atomic number is 4 ($\text{Cs} \rightarrow \text{Pr, Sr} \rightarrow \text{Mo}$).

We might say that the transmutation of Cs into Pr belongs to 2α capture type reaction and the transmutation of Ba into Sm to 3α . At present, it is just a speculation; however, it is important that a certain rule can be noticed for this deuterium permeation transmutation.

6. Distribution of Products

Surface distribution of Cs and Pr were measured by the strong synchrotron radiation X-ray at Spring-8. The X-ray was divided by slits and we got rectangular micro X-ray beam. 500-micron, 100-micron and 50-micron X-ray beams were applied for our measurement. The Pd sample was attached on an $X-Y$ stage that could be moved by stepping motors and so 2-dimensional XRF spectra could be obtained. Surface images could be taken by a microscope that was equipped for this 2-dimensional XRF spectrum analysis.

Figure 11 shows surface distribution of Pr and XRF spectra obtained by 100-micron X-ray beam at the point where transmutation of Cs into Pr was observed by the in-situ measurement described in Fig. 6. The amount of Pr changed greatly depending on the locations of the Pd surface. Pr was localized at the specific points as shown in Fig. 11. Surface image for the corresponding region is shown in Fig. 11b. No clear correlation between the localized Pr and surface image could be observed.

These experimental results suggest that transmutation reaction rate varies depending on the Pd surface region. Some uncertain factors, presumably relating to condensed matter effects in the present Pd/D/CaO system, must make a lot of effects on the rate or the process of the reactions. In order to make clear the uncertain factors, it would be necessary to use smaller X-ray beam, although it would take much more time for XRF measurement.

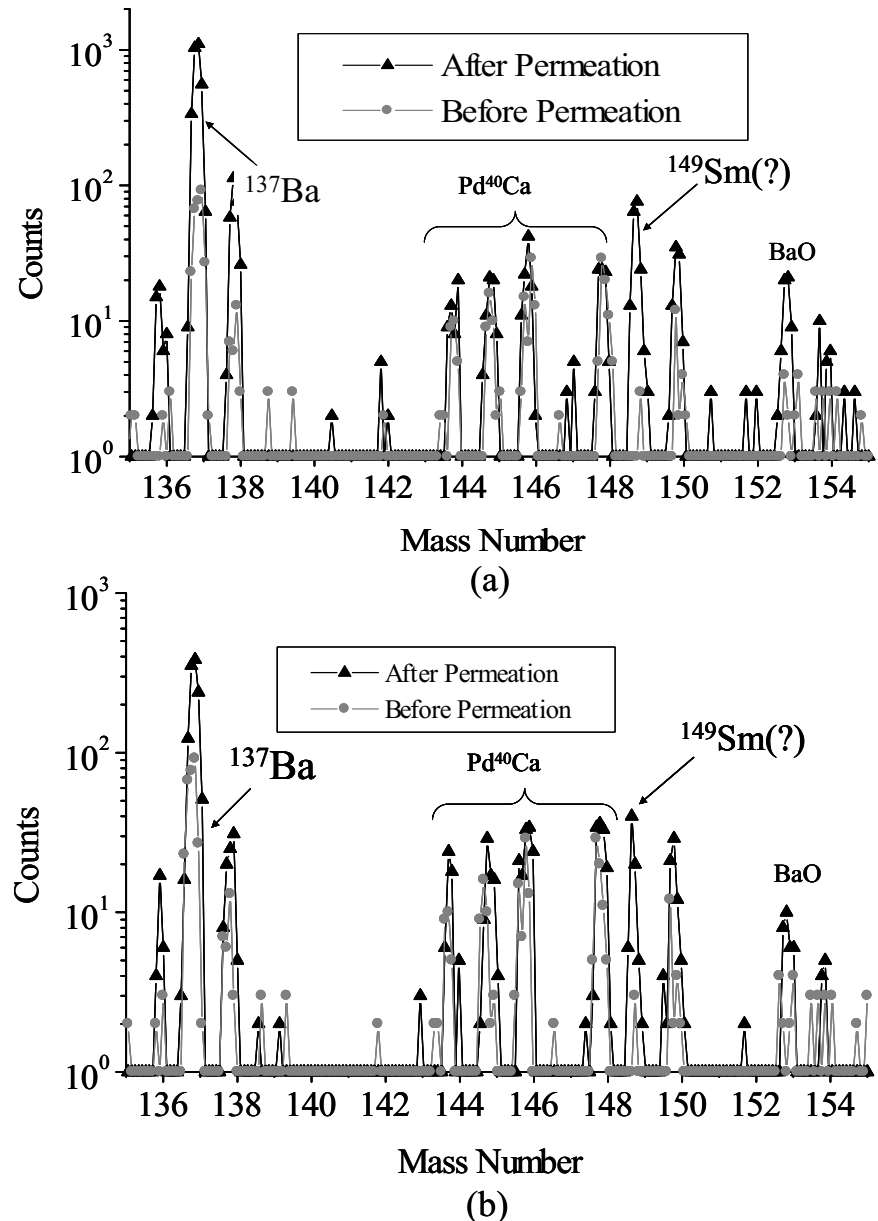


Figure 9. SIMS spectra for Pd complexes with 137 enriched Ba; (a) Spectrum for No. 1 experiment, (b) Spectrum for No. 2 experiment [3].

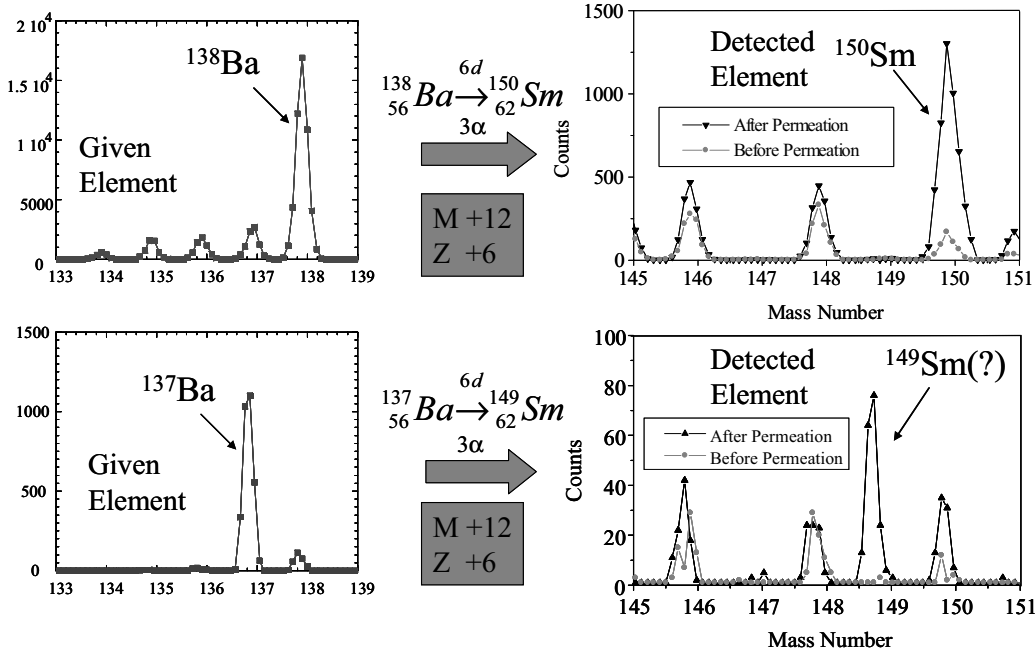


Figure 10. Mass correlation between given and detected elements [3].

Depth profiles of Cs and Pr were plotted in Fig.12. XPS analysis was applied to Fig.12. Cs was injected into all the Pd complex samples by the ion implantation method. The relation between the sputtering time and the real depth was estimated in advance using a Pd thin film on Si substrate; thickness of the Pd thin film is known.

The Cs and Pr depth profiles for the Pd complex without permeation show normal and reasonable result as shown in Fig. 12. Cs decreases continuously from the surface and there is no Pr in the sample before permeation. On the other hand, Cs decreases and Pr increases within 10 nm region from the top surface. Cs depth profiles in the both samples are nearly equal in deep area. This supports that Cs transmutation reaction into Pr occurs in the near surface region up to 10 nm.

Figure 12 also shows that Cs atoms do not diffuse and migrate with D₂ gas permeation under our experimental conditions. Therefore it is very difficult to postulate that the detected Pr was a concentrated impurity that migrated from the whole Pd multilayer sample.

7. Role of CaO

The authors do not have a definite explanation for the role of the CaO layers in the nano-structured Pd multilayer thin film at present. We have two kinds of explanations for the effects of CaO. The first effect is the increase of deuterium density in the Pd multilayer thin film and the second is the effect for modifying the electronic state of top Pd layer. D⁺ ion bombardment experiments suggest the first effect and the correlation between intermediate material and transmutation reactions implies the second effect.

D⁺ ion bombardment experiment using a Pd complex was performed at Tohoku University. Low energy D⁺ ion beam from 2.5 to 10 keV irradiates the surface of metal and induces D(d, p)T reactions. Proton yield obtained $\delta E - E$ counter telescope and its energy dependence enable us to estimate screening potential and deuterium density [8]. As

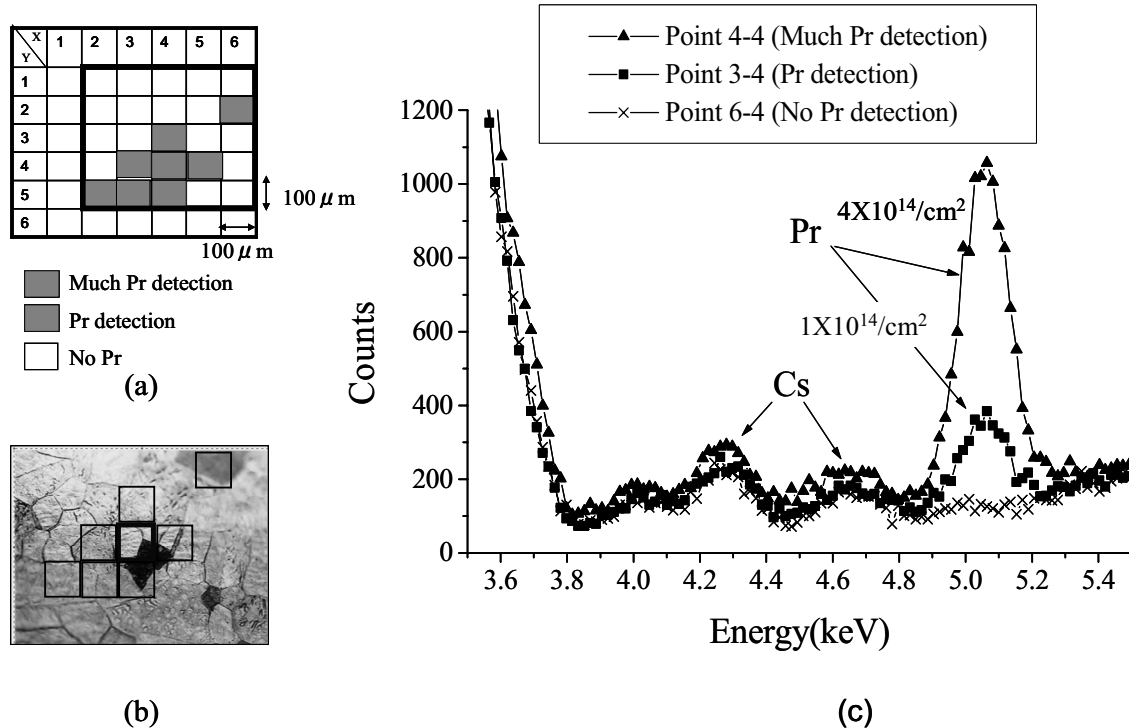


Figure 11. Surface distribution of Pr using 100-micron X-ray beams. (a) Mapping of Pr by 100-micron beam at the point where Pr was detected by in-situ measurement. (b) Surface image of the sample corresponding to XRF spectra. (c) XRF spectra for three different points [2].

we can see in Fig.13, deuterium density of Pd complex (Pd/CaO) is about one order larger than normal Pd. It suggests that the nano-structured Pd multilayer film contains more deuterium than normal bulk Pd.

When we replaced CaO with MgO, we did not obtain any positive results; we could not observe any transmutation reactions as shown in Table 3. It means that MgO cannot work instead of CaO. Three cases out of the three experiments using MgO show no Pr by ICP-MS measurements, although D₂ gas Flow rates were enough (2–3 sccm) in all cases.

However, if we replaced CaO with Y₂O₃, we could observe transmutation reactions from Cs to Pr. In other words, Y₂O₃ works like CaO. Work functions for MgO, Y₂O₃ and CaO are shown in the Table 3. Although it is difficult to make conclusive results, the existence of low work function of intermediate material might have some effects to induce transmutation. Anyway, we should continue to make systematic researches to make clear how the CaO layers work.

Table 3. Correlation between intermediate material in Pd multilayer film and transmutation results.

Intermediate Material	Work function (eV)	Results for analysis after permeation
MgO	3.3	No Pr (3 cases)
Y ₂ O ₃	2.2	Pr detected (3 cases)
CaO	1.2	Pr detected (>100 cases)

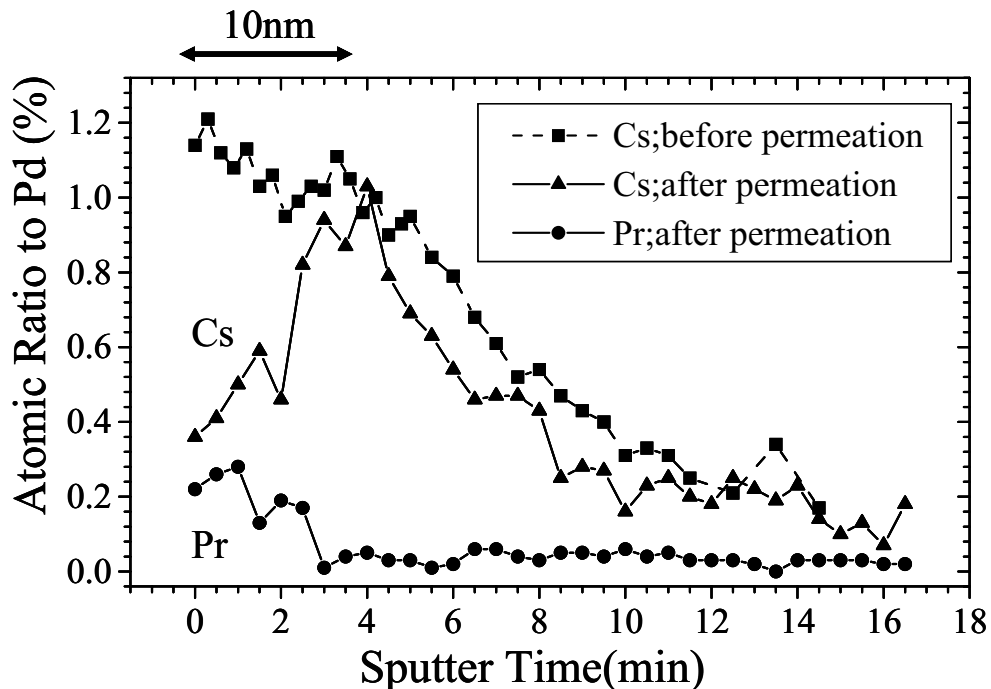


Figure 12. Depth profile of Cs and Pr for samples after D_2 permeation and without permeation [3].

8. Key factors in permeation experiments

Transmutation reactions induced by deuterium permeation through nano-structured multilayer Pd were observed for Cs and Ba as described in this paper. Transmutation caused by other elements, for example, Sr, Ca, Na and Li were also observed, though a number of experiments and a number of analysis cross checks are not necessarily enough for these elements. Of course, there are some elements that we could not observe any anomalous transmutation reactions. Based on these experimental results, alkali and alkaline earth elements seem to be transmutable.

There are no established theories that can explain the experimental results without any assumptions, although some interesting models and theories have been proposed [9,10]. The observed transmutation processes must belong to a new category of nuclear reactions in condensed matter. We should continue to work in order to make clear the nature of this new phenomenon experimentally with theoretical approaches. Identification of key experimental factors to induce transmutation reactions would be important to make progress. And more essential factors, such as local deuteron density and electronic structure of Pd–CaO–D system, should be clarified.

The followings are the candidates for key factors in permeation experiments. (1) Deuterium flux through Pd multilayer, (2) target element, (3) local deuterium density, (4) nano-size or nano-structure, (5) temperature, and (6) work function of the intermediate layer. These factors are derived from experimental results obtained so far.

We are now trying to make clear the effect of (3) local deuterium density. A resonance nuclear reaction [11] would give us precise depth profile deuterium near surface. At this moment, we succeed to measure hydrogen 3-dimensional profiles under high pressure (~ 1 bar) using ^{15}N ion beam. Local hydrogen density will be able to be detected during permeation through nano-structured Pd multilayer thin film.

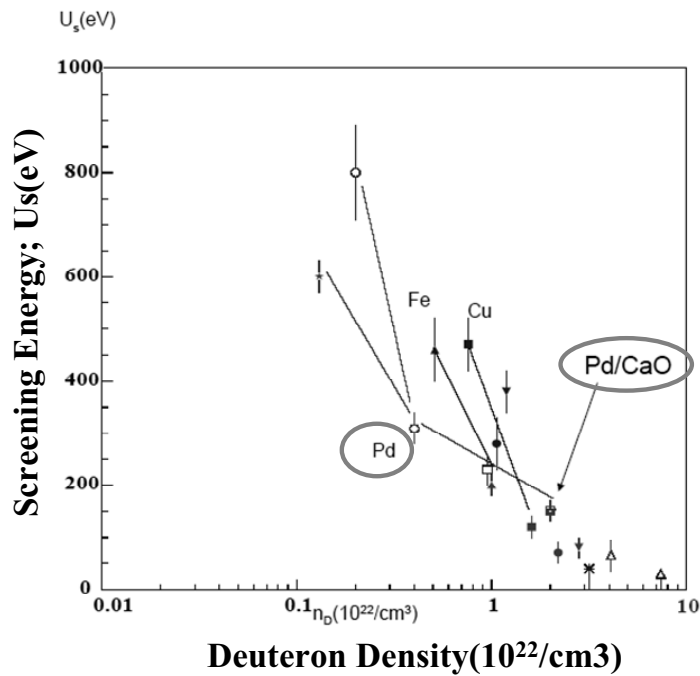


Figure 13. Density measured by D^+ ion bombardment experiment at Tohoku University [3].

9. Replication Experiments

Replication experiments have been performed in some universities or institutes mainly in Japan. T. Higashiyama et al. of Osaka University observed transmutation of Cs into Pr in 2003 [12]. H. Yamada et al. performed similar experiments using Cs and detected increase of mass number 137 by TOF-SIMS. They used a couple of nano-structured Pd multilayer thin film and observed the increase of mass number 141 (corresponding to Pr) only when ^{133}Cs was given on the Pd sample [13]. T. Hioki et al., the researchers of Toyota Central R&D Labs, recently presented that they detected Pr from the permeated Pd sample using SOR X-ray at Spring-8 and the detected Pr was confirmed by TOF-SIMS [14].

It is not easy to obtain positive results in replication experiments since necessary experimental factors are not completely clarified. Details of experimental conditions can be often varied. If the difference would influence the phenomenon, it might be difficult to observe the same transmutation reactions as ours.

These above replication observations provide important information concerning about the nature of this phenomenon. Their samples were independently fabricated except in the experiments at Osaka University and fabrication conditions, for example, Pd dimension or fabrication method, were different. Nevertheless, similar results were observed. We should investigate how the experimental parameters influence the transmutation reactions more intensively.

10. Concluding Remarks

Low energy nuclear transmutations in condensed matter have been observed in the nano-structured Pd multilayer complex. Transmutation reactions of Cs into Pr, Ba into Sm were observed. Especially, transmutation of Cs into Pr has been confirmed by “in-situ” measurements using XRF at SPring-8 in Japan. Replication experiments have

been performed by some researchers and similar results have been obtained in some cases. However, nature of this phenomenon is not clear at present; we should continue to identify the key experimental factors to induce transmutation reactions experimentally with theoretical approaches.

Acknowledgments

This work is supported by Japan Synchrotron Radiation Research Institute (JASRI) and the Thermal & Electric Energy Technology Foundation (TEET). The authors would like acknowledge Prof. A.Takahashi, Dr.F. Clelani Prof. M. Melich, Dr. K. Grabowski, Dr. C. Catalina, Dr. D. Kidwell for their supports and valuable discussions.

References

- [1] Y. Iwamura, M. Sakano, T. Itoh, *Jpn. J. Appl. Phys.* **41** (2002) 4642–4648.
- [2] Y. Iwamura et al., *Proceedings of 12th International Conference on Condensed Matter Nuclear Science*, A. Takahashi et al. (eds.), Condensed Matter Nuclear Science, World Scientific, New Jersey, 2006, pp. 178–187.
- [3] Y. Iwamura et al., *Proceedings of 11th International Conference on Condensed Matter Nuclear Science*, J.P. Biberian (ed.), Condensed Matter Nuclear Science, World Scientific, New Jersey, 2004, pp. 339–350.
- [4] Y. Iwamura et al., *Proceedings of 10th International Conference on Condensed Matter Nuclear Science*, P.H. Hagelstein et al. (eds.), Condensed Matter Nuclear Science, World Scientific, New Jersey, 2006, pp. 435–446.
- [5] Y. Iwamura et al., *Proceedings of 9th International Conference on Cold Fusion*, X.Z. Li (ed.), Tsinghua University Press, Beijing, 2002, pp. 141–146.
- [6] Y. Iwamura et al., *Proceedings of 8th International Conference on Cold Fusion*, F.Scaramuzzi (ed.) , SIF Conf. Proceeding, Vol. 70, Rome, 2001, pp. 141–146.
- [7] Y. Iwamura, T. Itoh, N. Gotoh, I. Toyoda, *Fusion Technol.* **33** (1998) 476–492.
- [8] J. Kasagi, H. Yuki, T. Baba, T. Noda, T. Ohtsuki, A.G. Lipson, *J. Phys. Soc. Jpn.* **71** (2002) 2881–288.
- [9] A. Takahashi, *J. Condensed Matter Nucl. Sci.* **33** (2009) 33–44.
- [10] A. Widom, L. Larsen, *Eur. Phys. J. C* **46** (2006) 107.
- [11] D. Sekiba et al., *Nucl. Instr. and Meth. B* **266** (2008) 4027–4036.
- [12] T. Higashiyama et al., *Proceedings of 10th International Conference on Condensed Matter Nuclear Science*, P.H. Hagelstein et al. (eds.), Condensed Matter Nuclear Science, World Scientific, New Jersey, 2006, pp. 447–454.
- [13] H. Yamada et al., *Proceedings of 12th International Conference on Condensed Matter Nuclear Science*, A. Takahashi et al. (eds.), Condensed Matter Nuclear Science, World Scientific, New Jersey, 2006, pp. 196–205.
- [14] T. Hioki, Private communication.



Research Article

Low-energy Nuclear Reactions and Transmutation of Stable and Radioactive Isotopes in Growing Biological Systems

Vladimir I. Vysotskii *

Kiev National Shevchenko University, 01033 Vladimirskaya Str, 64 Kiev, Ukraine

Alla A. Kornilova

Moscow Lomonosov's State University, 119899 Moscow, Russia

Abstract

The report presents the results of combined (Mössbauer and mass-spectroscopy) qualifying examinations of stable isotope transmutation processes in growing microbiological cultures, in the iron-region of atomic masses. It is shown that transmutation during the process of growth of microbiological cultures, at optimal conditions in microbiological associations, is 20 times more effective than the same transmutation process in the form of "One-line" (clean) microbiological cultures. In the work, the process of direct, controlled decontamination of highly active intermediate lifetime and long-lived reactor isotopes through the process of growing microbiological associations has been studied. For the first time, an accelerated deactivation rate is observed that is 35 times larger than the controlled deactivation of the Cs^{137} isotope. A theoretical model of low-energy nuclear transmutation in biological objects is discussed also.

© 2011 ISCMNS. All rights reserved.

Keywords: Isotope transmutation, Low-energy reaction, Microbiological association

PACS: 25.45.-z; 25.60.Pj; 25.70.Jj; 28.41.Kw; 87.85.M-

1. Introduction and Foundation of the Effect of Isotopes Transmutation in Biological Systems

The problem of transmutation of stable and active isotopes in biological systems is one of the most mysterious in modern nuclear physics. The hypothesis about the possibility of nuclear transmutation of chemical elements and their isotopes in physical, biological and geological systems with low energy of relative movement of interacting nuclei has been frequently discussed during the last decades [1,2]. Interest toward this issue grew after systematic study of the phenomenon of cold nuclear fusion (CNF) based on dd-reactions in solid systems.

*E-mail: viv@vhome.kiev.ua

In our opinion, there are no reasons to consider the process of transformation of isotopes and elements in biological transmutation to be separate and different from the general physical forms of nuclear transmutation that can occur from comparable forms of transformation of isotopes through transmutation, that can occur through alternative processes, governed by the laws of physics. We believe that all the observed isotopic effects (in case they are real and supported by adequate and reliable measurements) can be characterized as the “regular” process of transmutation of isotopes and elements, which occurs in biological systems, and the efficacy of which is determined precisely by the specific characteristics and behavior of such systems.

While analyzing the problem of transmutation of isotopes in growing biological cultures (especially the case of transmutation with generation of isotopes of such chemical elements which are not required by a growing culture in normal conditions) many additional specific questions arise. The most important of them: “Why does a growing culture need this kind of process; How is the process accomplished; Can this process be controlled?”

In the distant future, more refined studies will provide more complete and potentially full and final answers to these questions. The authors recognize the complexities of this problem. Our thesis can be interpreted only as one possible solution, based on our understanding of the problem. Being consistent with our position of objective regularity of such a process, we must note that an explanation ought to be sought among the known laws of physics, chemistry, and biology.

In our opinion, the process of transmutation is evolution’s answer to the global dilemma – how is it possible to combine development and adaptation of biological objects, each one of which contains a genetically predetermined set of elements, with a random character and dissimilar distribution of elements in the outer environment, as well as constant environmental changes? This process occurs in places, where there is competition based on the stereochemical analogy (at least in transporting and fermentation systems). The area, where this competition takes place determines the area where transmutation itself is performed. Can we point to a specific spot, or set of conditions, where this ingenious nuclear reaction process takes place? Possibly, there could be many such places or sets of conditions (otherwise, reactions could be such rare events that they would be impossible to detect). Also note, that transmutation occurs with a higher probability in structural parts of biological objects, which are subjected to dynamic influences (zone of growth, non-stationary transport systems, and dynamic response systems to any kind of agitation etc.).

The physical aspects of transmutation processes are related to general problems of low-energy nuclear reactions. Currently, there are over 400 works, in which – with various degrees of agreement and disagreement – different physical models are presented, capable, according to their authors, of explaining the phenomenon of “cold nuclear synthesis,” or, at least, of providing a framework for finding ways to explain these kinds of effects. Our point of view with respect to explaining this problem has been presented in our books [1,2]. We think that in the case of dynamic (growing) biological systems, the most effective mechanism, which was suggested [3] and discussed [4] in 1994–1996, is capable of removing – for a brief time – the influence of the Coulomb barrier of a nuclear reaction occurring in a large number of non-stationary potential wells with a structure that is close to being parabolic in volume of any growing biological system. This mechanism will be discussed below.

2. Experimental Investigation of Fusion of Ironregion Stable Isotopes in Optimal Growing Microbiological Associations

About 10–15 years ago we have studied the process of transmutation of stable isotopes in growing “one-line” (one type, “clean”) microbiological cultures like *Escherichia coli* or *Saccharomyces cerevisiae* in two kinds of nuclear reactions [4,5]



It was shown that the transmutation process during the growth of such microbiological cultures had taken place, but its effectiveness had been low. Expressed in relative units (defined by the ratio between accumulated number of

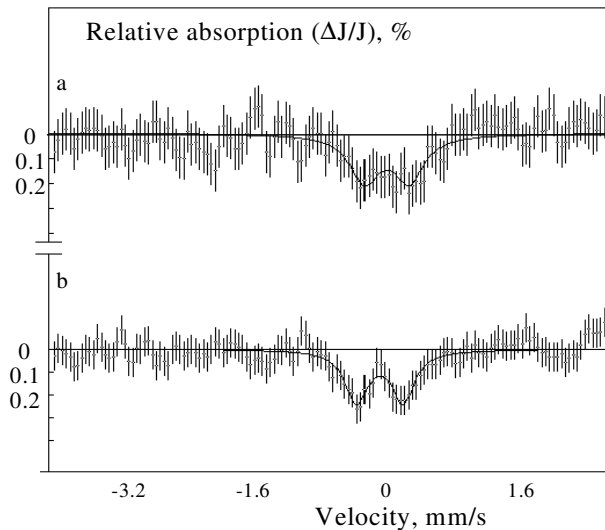


Figure 1. (a) and (b) are Mossbauer spectra of grown identical cultures in different flasks. Culture *Saccharomyces cerevisiae* grown in D₂O in presence of Mn⁵⁵ isotopes.

$N(\text{Fe}^{57})$ of Fe⁵⁷ nuclei to the number $N(\text{Mn}^{55})$ of Mn⁵⁵ nuclei) the rate (λ) of Fe⁵⁷ production

$$\lambda = N(\text{Fe}^{57})/N(\text{Mn}^{55})\Delta t \approx 10^{-8}\text{s}^{-1}$$

(synthesized Fe⁵⁷ nuclei/s and per single Mn⁵⁵ nucleus) in the case of the reaction with light isotope Mn⁵⁵ + d² = Fe⁵⁷, and $\lambda \approx 10^{10}\text{s}^{-1}$ in the reaction for the middle range mass isotopes Na²³ + P³¹ = Fe⁵⁴. The typical Mossbauer spectrum of “one-line” *Saccharomyces cerevisiae* culture, grown in D₂O with the presence of Mn⁵⁵ isotope [1,2,4], is presented in Fig. 1.

The low-relative amplitude of Mossbauer resonance ($\Delta J/J \approx 0.2\%$) in these experiments was the result of low-absolute and relative concentration of created Fe⁵⁷ isotope in the culture. There are two main reasons of low effectiveness of nuclear transmutation in “one-line” microbiological cultures:

- The relatively low efficiency for creating these reactions is the result of the narrow interval of optimal functional individual characteristics for initiating nuclear activity in any “one-line” type of culture. Each of the “one-line” cultures individually requires a set of specific conditions (temperature, hydrogen ion exponent pH, balanced contents of nutrient medium, etc.) for achieving optimal metabolic conditions during the complete period of growth. Such conditions are often absent in real experiments.
- During the growth of a “one-line” culture, we hypothesize that processes involving forms of auto-intoxication of nutrient media by metabolic products take place. This hypothesis is consistent with forms of growth impairment.

In contrast to these “one-line” cultures, during the last year we have investigated microbiological associates that include great numbers of types of different cultures.

The base of “microbial catalyst-transmutor” (MCT) compound that was used is the microbe syntrophic associations of thousands of different kinds of microorganisms that are in the state of complete symbiosis [2,6,7]. These microorganisms appertain to different physiological groups that represent practically the whole variety of the microbe

metabolism and relevantly all kinds of microbe accumulation mechanisms. We postulate that the state of complete symbiosis of the syntropic associations results from the possibility of maximal adaptation of the microorganisms' association in response to changes in any external. These cultures are in a state of natural complete symbiosis and grow as a total correlated multisystem. There are a lot of different types of intraspecific and interspecific stimulated and symbiotic connections between different cultures in the volume of syntrophic associations. This microbiological multisystem adequately reacts to modifications of exterior requirements, to composition of nutrient medium and to biochemical properties of a system because of metabolic growth and transmutation processes. The spectrum of their functional characteristics (including resistance to aggressive environment and methods of synergetic adaptation to this environment) is very wide. We believe that it should be expected that this would lead to high efficiency/effectiveness for stimulating transmutation processes. This model is presented in symbolic form in Fig. 2.

The MCT compound involves special granules that include:

- Concentrated biomass of metabolically active microorganisms (microbe syntrophin association).
- Organic sources of carbon and energy, phosphorus, nitrogen, etc.
- Gluing substances that keep all components in the form of granules stable in water solutions, for a long period of time, subjected to some, possibly many, external conditions.

The general aim of that investigation was to find biotechnology based ways for effective isotope transmutations. The possibility of a potential reaction, $Mn^{55} + d^2 = Fe^{57}$, with heavy water in growing MCT was investigated in the system. This was initiated starting from a more general form of reaction of the form,

“ $D_2O + Mn^{55} + MCT +$ additional isotope components”.

The control experiments were conducted in another system

“ $H_2O + Mn^{55} + MCT +$ the same additional isotope components”.

A typical series of experiments on nuclear transmutation of isotopes in growing microbiological cultures involved simultaneous growing of separated parts of the same culture in several (usually four) flasks (see Fig. 3).

The first and the second flask contained basic (constant) ingredients: sugar-salt nutrient medium on the basis of light water (H_2O) both with and without $MnSO_4$. In the third flask, the nutrient medium was prepared from the same basic ingredients on the basis of heavy water (D_2O), but without $MnSO_4$. Accordingly, the fourth dish contained nutrient medium with all the ingredients necessary for the culture's growth as well as $MnSO_4$, required for transmutation, and was prepared on the basis of heavy water (D_2O).

From the list of nutrient media, necessary for growing cultures, it can be seen that the isotopic composition necessary for achieving transmutation was in only one (optimized by the isotopic and elementary content) – the fourth flask.

The method of cross-combinations of the nutrient media ingredients has allowed excluding a possible influence of the admixed Fe^{57} isotope on the result of these experiments. In particular, if the Fe^{57} isotope was present, in the form of admixture, in light or heavy water, as part of basic salts, and was also part of the flasks glass, or contained in the air, that isotope would be extracted during the culture's growth and detected in all flasks (including the experiments in flasks 1–3) after growing the culture.

If the Fe^{57} isotope were found only in heavy water, it would be detected in the cultures grown in flasks 3 and 4. If it was present in $MnSO_4$, it would also be detected in the cultures grown in flasks 2 and 4.

Such series of experiments were performed for various cultures, with different growth periods (24, 48, and 72 h) and growth modes. All cultures were grown in the thermostat with the optimal temperature of 32°C. It was discovered, that growing cultures in the media based on heavy water requires continuous stirring of the medium throughout the whole time of growth.

After each series, the substance that was obtained was collected, cleaned in distilled H_2O water and dried. The dried substance in the form of unstructured granules (like peat) were separated using a non-iron containing instrument, ground to a powder and placed in the same amounts in the Mossbauer spectrometer. The mass of the dried biological

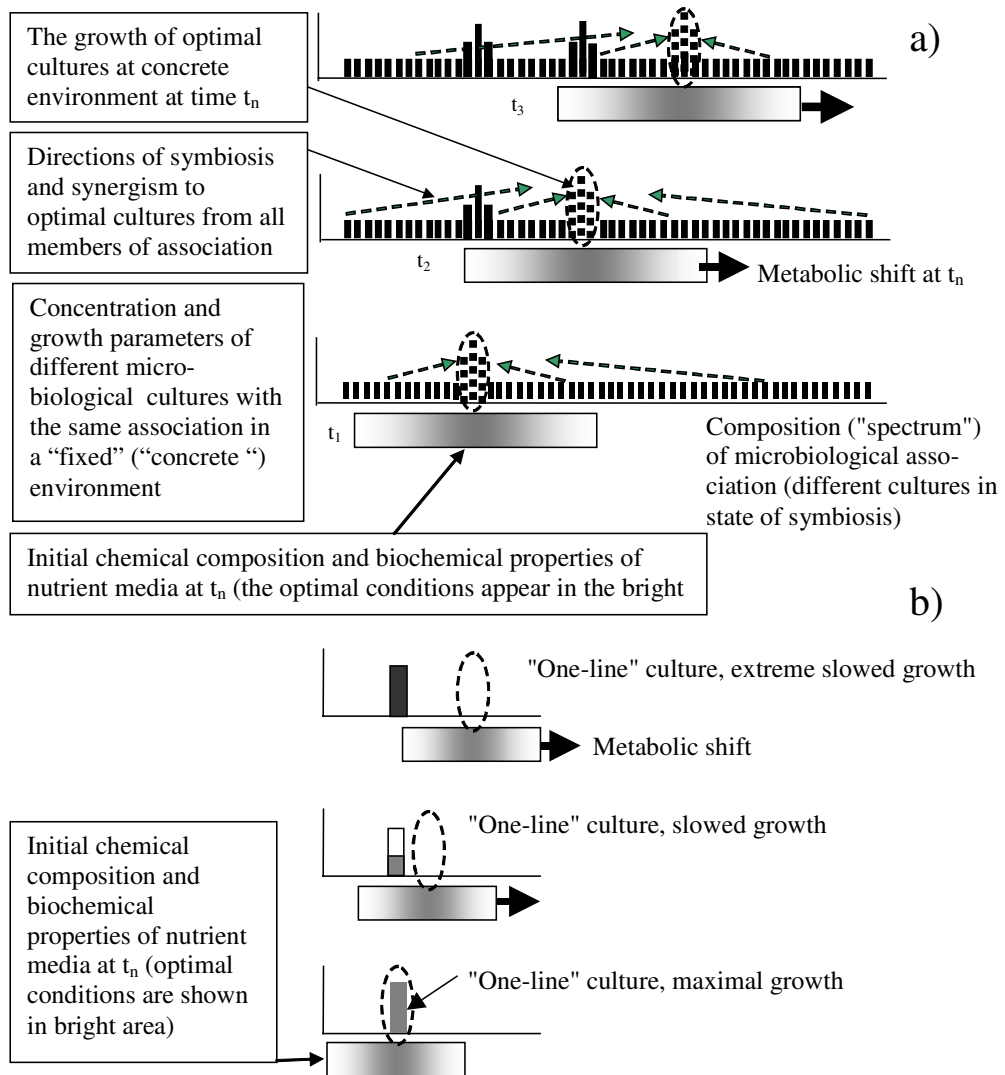


Figure 2. Changes in the directions of symbiosis and synergism in microbiological association (case a) to optimal growing cultures involving changes in types of chemical composition and biochemical properties of nutrient media and environment. Changes in types of optimal cultures is the result of metabolic shifts of chemical composition and biochemical properties of nutrient media. The case (b) presents the process of growth impairment in "one-line" culture with metabolic shifts.

substance, that was investigated, was about 0.3 g.

The results of the Mossbauer measurements of the optimally dried biological substances are presented in Fig. 1 ("one-line" culture) and Fig. 4 (MCT compound (microbiological association)).

In this last experiment with microbiological association, the large amplitude of the Mossbauer resonance

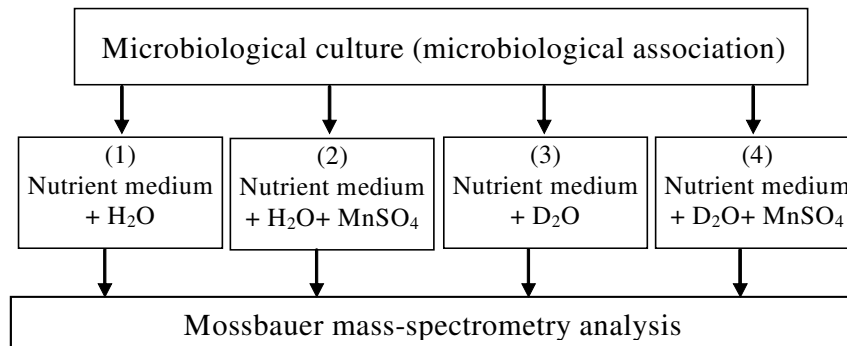


Figure 3. The scheme of “cross-experiments” for studying the effect of nuclear transmutation of isotopes in growing microbiological cultures.

$(\Delta J_{\max}/J_{\text{transmut}}) \approx 3.4\%$) at the same mass of the investigated dried biological substance was observed and measured.

The total, relative number of Fe^{57} nuclei that was created was about 10^{17} nuclei per 1 g of grown and dried biological substances [1,2,7], which is between 10 and 20 times more than the comparable, relative, maximal number of Fe^{57} nuclei that is created in “one-line” grown and dried cultures [1,2,4]. The total mass of Fe^{57} isotopes that is created is about 10^{-5} g per each g of dried biological substance. The efficiency has increased, in particular, because the association has been allowed to grow during a 20 day period. “One-line” cultures cannot be grown for such a long period of time in heavy water because of “self-intoxication” of the medium by the metabolic products (in our former experiments [4] the “one-line” *Escherichia coli* culture was grown during a 72 h period).

The relative efficiency rate λ of such forms of transmutation (the coefficient of transmutation) is the following:
 $\lambda \approx (0.5 - 1) \times 10^{-6}$ (synthesized Fe^{57} nuclei per s and per single Mn^{55} nucleus).

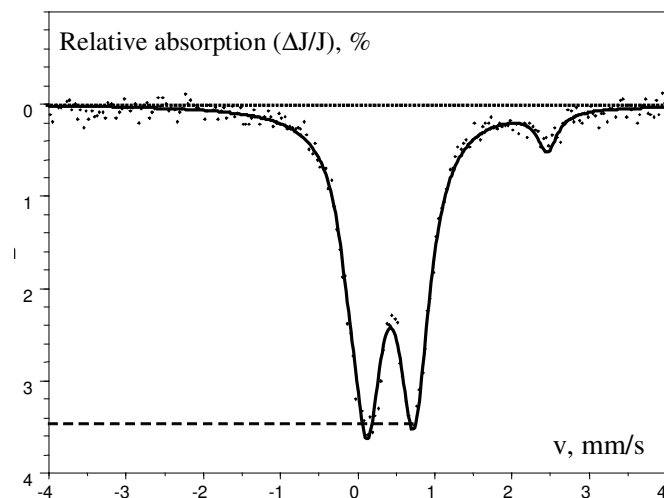


Figure 4. Mossbauer spectra of microbiological MCT grown in nutrient medium in presence of D_2O and Mn^{55} isotope: $\Delta J_{\max}/J \approx 3.4\%$ is the magnitude of the Mossbauer resonance.

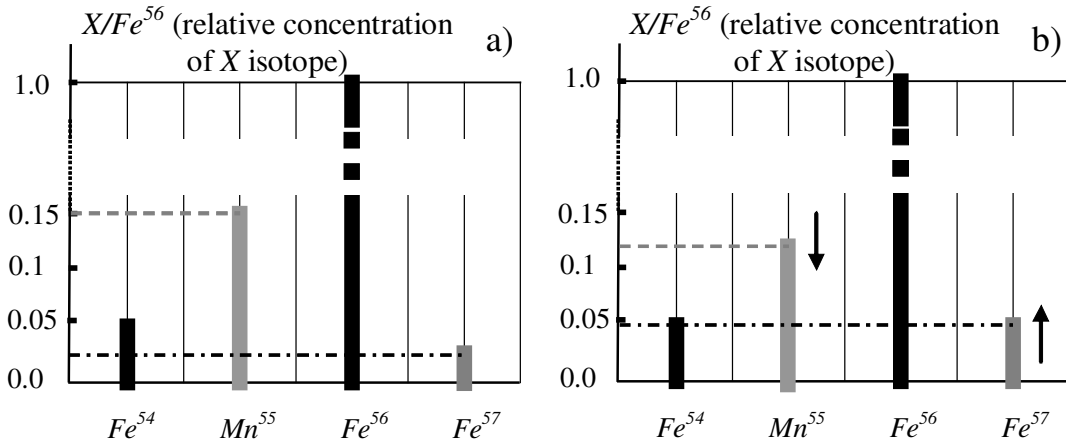


Figure 5. Mass-spectrum of iron-region of microbiological associations (dried biological substances) that were grown in control nutrient medium with H_2O and Mn^{55} (case a) and in experimental nutrient medium with D_2O and the same quantity of Mn^{55} isotope (case b). Here $X = Fe^{54}; Mn^{55}; Fe^{57}$. The process of increasing (\uparrow) concentration of Fe^{57} isotopes is accompanied by decreasing (\downarrow) concentration of Mn^{55} isotopes.

For verification of these results, additional examinations of the isotopic ratio of the same dried biological substances (both control and transmuted) were conducted by Thermal Ion Mass Spectroscopy (TIMS), <<Finnigan>> MAT-262.

The results of TIMS measurements presented in Fig. 5 and in Table 1.

The amount of Fe^{57} isotopes that are created are approximately the same in the cases of Mossbauer resonant gamma-spectroscopy and TIMS measurements (concentrations of Fe^{57} isotopes that are created increase by factors of 2–3).

The effectiveness of isotope transmutation during the process of growth of microbiological associations at optimal conditions increases by factors of 10–20 times more than the effectiveness of the same transmutation in “one-line” (clean) microbiological cultures.

The structure and half-width of Mossbauer spectra of control and transmuted microbiological associations are identical. So, the process of transmutation does not appear to change the spatial structure of the growing biological culture. Created and natural Fe are identical in the biochemical sense!

Decrease in the amount of the additional Mn^{55} isotope in the transmutation flask is synchronized with the creation of Fe^{57} isotopes in the same flask. This appears to provide proof of nuclear synthesis in processes associated with a “growing” biological system!

3. Experiments on Controlled Decontamination of Intermediate and Long-Lived Active Isotopes in Biological Cells

Next steps of the investigation were related to the process of direct controlled decontamination of a highly active water mixture of selected different intermediate and long-lived active isotopes by action of the same growing microbiological systems MCT. The process of decontamination (deactivation) of radioactive waste through the action of growth in microbiological systems is connected with transmutation of active nuclei to different non-radioactive isotopes during growth and metabolic processes involving MCT granules.

Table 1. Parameters of mass-spectroscopy investigation of control and transmuted cultures.

Isotope (natural concentration)	Natural isotopic ratio (in relation to Fe^{56})	Concentration in dried biological substance in control experiment: $\text{H}_2\text{O} + \text{MnSO}_4 + \text{nutrient}$ medium (normalized)	Isotopic ratio in control biological substance	Concentration in dried biological substance in experiment on transmutation: $\text{D}_2\text{O} + \text{MnSO}_4 + \text{nutrient}$ medium, (normalized)	Isotopic ratio in the experiment on transmutation
Mn^{55} , 100%	--	0.15 ± 0.012	$\text{Mn}^{55}/\text{Fe}^{57} = 6.6$	0.13 ± 0.012	$\text{Mn}^{55}/\text{Fe}^{57} = 7.7$
Fe^{56} , 91.7%	1	1	1	1	1
Fe^{57} , 2.2 %	$\text{Fe}^{56}/\text{Fe}^{57} = 41.7$	0.024 ± 0.002	$\text{Fe}^{56}/\text{Fe}^{57} = 42.5$	0.051 ± 0.003	$\text{Fe}^{56}/\text{Fe}^{57} = 19.5$

3.1. Controlled decontamination of intermediate lifetime reactor isotopes

In our work [6], we studied the process of the accelerated decay of activity of reactor water from first contour of water–water atomic reactor of the Kiev Institute of Nuclear Research. The water with total activity about 10–4 Curie/L contained highly active isotopes (e.g., Na^{24} , K^{40} , Co^{60} , Sr^{91} , I^{131} , Xe^{135} , Ba^{140} , La^{140} , Ce^{141} , and Np^{239}).

The spectrum of gamma-radiation of this water is presented in Fig. 6.

For the first time we observed the fast utilization of several kinds of active isotopes to nonradioactive nuclei in the flasks that contained MCT.

The results of the investigation of the time-dependent activity $Q(t)$ of the same reactor Ba^{140} , La^{140} and Co^{60} isotopes in the experiment on transmutation (activity is Q_{cultures}) and in the control one (Q_{control}) are presented in Fig. 7.

For the first time we have observed accelerated utilization (decrease of radioactivity) of radioactive La^{140} and Ba^{140} isotopes in the flasks that contained MCT during the time of the experiment (during 30 days)!

Studied La^{140} isotope has intermediate life-time $\tau_{\text{La}} = 40.3$ h and is a non-stable daughter isotope of Ba^{140} radioactive isotope that has a life-time of about $\tau_{\text{Ba}} = 12.7$ days and the following decay $\text{Ba}^{140} \rightarrow \text{La}^{140} + \beta^-$.

Initial activities of the Ba^{140} and La^{140} isotopes (on the 10th day after extraction of water from the active zone of the nuclear reactor) were $Q_{\text{Ba}^{140}} \approx 1.46 \times 10^{-7}$ Curie / L and $Q_{\text{La}^{140}} \approx 2.31 \times 10^{-7}$ Curie / L. A possible path for Ba^{140} isotope transmutation is



. These reactions are energetically favorable and the reaction energy is positive.

The Sm^{2+} and Ca^{2+} ions are chemically alike and have approximately the same ionic radii of divalent state ($R_{\text{Sm}} \approx 1.2 \text{ \AA}$, $R_{\text{Ca}} \approx 1.06 \text{ \AA}$). The substituted element Ca is among several vitally necessary elements. Ions of created Sm^{2+} elements can substitute Ca^{2+} ions while microbiological cultures are growing [1,2]. Probability of such substitution during the process of growing the biological culture is high because the initial concentration of the Ca element in MCT is low.

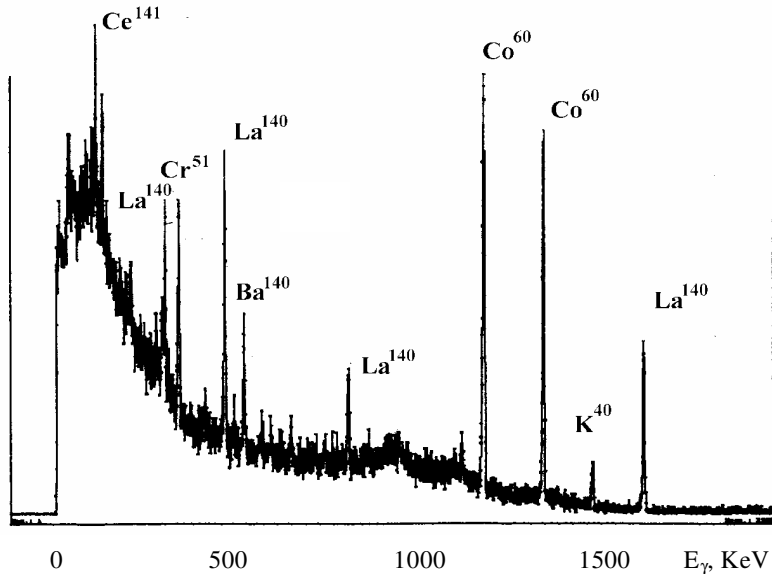


Figure 6. Spectrum of gamma-radiation of distilled water from first contour of water–water atomic reactor 10th day after extraction from the active zone.

3.2. Controlled decontamination of long-lived reactor Cs¹³⁷ isotopes in biological cells

The investigation of controlled decontamination of the long-lived reactor Cs¹³⁷ isotope [7] has been carried out, based on using the identical distilled water but with a process that involves Cs¹³⁷ with an activity of 2×10^4 bq. In the experiments, eight identical closed glass flasks with very thin walls and with 10 ml of the same active water in each were used (see Fig. 8). The MCT compound was placed in seven glass flasks.

In six different flasks, different pure K, Ca, Na, Fe, Mg, and P salts as single admixture were added to the active water. These chemical elements are vitally necessary for any cultures. Each of these specific replacements completely blocks all possible transmutation channels, in which any of the biochemical analogs of the specific chemical element can be used. Two additional flasks were used for control experiments: one flask contained the active water and MCT (but without additional salts) and in another one was only active water (without salts and MCT).

The cultures were grown at the temperature of 20°C. Activity of all closed flasks was measured every 7 days by precise large amplitudes using a Ge detector. The results to show the change of the relative activity $Q(t)/Q(0)$ of the isotopes are presented in Fig. 9 and Table 2.

We have observed increased rates of decay (more precisely accelerated rate of utilization) of Cs¹³⁷ isotopes in all experiments with MCT and in the presence of different additional salts during 100 days! In the control experiment (flask

Table 2. Deactivation of different active isotopes in optimal experiment (MCT + active water with presence of Cs¹³⁷ + CaCO₃ salt).

Isotope, energy of gamma radiation	Start	End of experiments (in 100 days)			Natural decay per 100 days	Change (N ₂ –N ₁)/N ₂
	N ₁ , registered events per 10 ³ s	N ₂ , registered events per 10 ³ s	Error (absolute/relative)			
Cs ¹³⁷ , 661.7 keV	2,66,900	2,16,800	±478(±0.2%)	–0.6 %	–24 %	

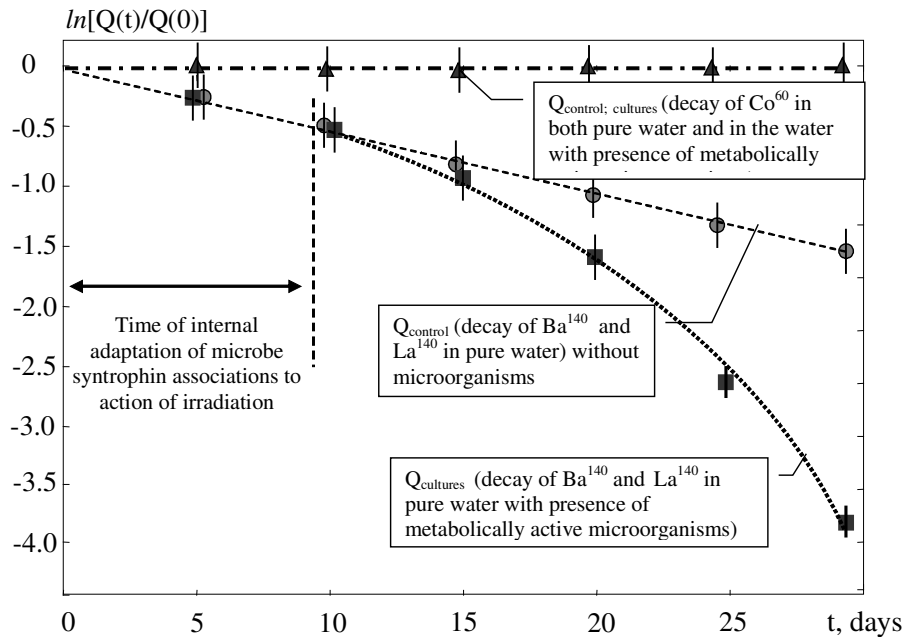


Figure 7. Activity $Q(t)$ of the same reactor Ba^{140} , La^{140} and Co^{60} isotopes in the experiment on transmutation (activity Q_{cultures} in pure reactor water in presence of metabolically active microorganisms) and in the control one (activity Q_{control} in the same pure reactor water without microorganisms). t is the time after extraction of radioactive water from the active zone of reactor.

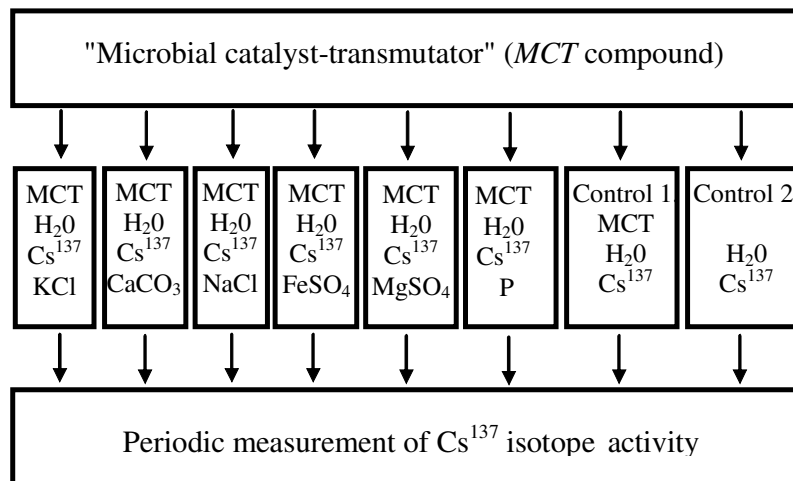


Figure 8. Study of utilization of active isotopes at different conditions.

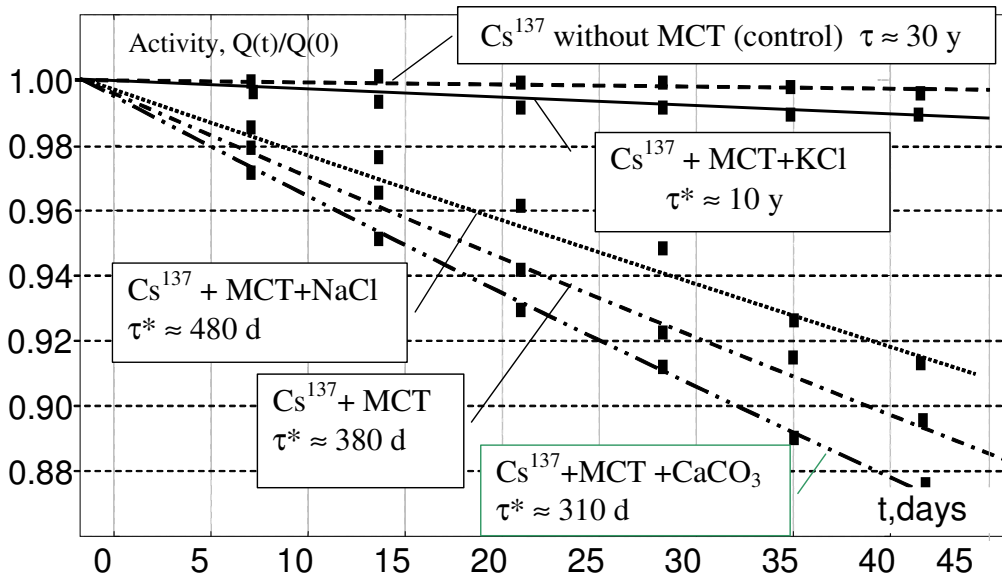


Figure 9. Accelerated deactivation (accelerated rates of decay) of Cs^{137} isotope in “biological cells” in presence of different chemical elements.

with active water but without MCT), the “usual” law of nuclear decay applies, and the life-time was about 30 years. The most rapidly increasing decay rate, which occurred with effective lifetime $\tau^* \approx 310$ days (involving an increase in rate, and decrease in lifetime by a factor of 35 times) was observed in the presence of Ca salt! In the presence of an abnormal (redundant) quantity of potassium in the nutritive media, the process of Cesium transmutation becomes very weak and the life-time of the decay was 10 years.

A possible reaction of radioactive Cs^{137} isotope utilization is



The result of this reaction is the creation of a stable Ba^{138} isotope.

What is the reason and sense of this reaction for microcultures?

Each metal has its peculiar oxidizing-reconstructive and/or stereochemical analogue among vital microelements, adapted to the particular culture, which are well represented components in microorganisms’ metabolism (K^+ , Na^+ , Mg^{2+} and others). The oxidizing-reconstructive analogy, or redox analogy, implies proximity or parity of redox potentials of reconstructive reactions of a metal and a macro element; stereochemical – proximity or parity of ionic radii of a metal and a macro element. One of the consequences of the stereochemical analogy and redox analogy is the non-peculiar nature of interaction of microorganisms with metals. Receptor and transporting and oxidizing-reconstructive systems of a microbial cell make “errors” due to proximity of values of ionic radii or redox potentials of a metal and a macro element, and therefore a metal is either accumulated by a microbial cell in a non-peculiar way (by “non-peculiar” we mean accumulation of metals by microorganisms not adapted to them) or it is reconstructed (often with generation of insoluble in water compounds). Some metals are capable of both accumulation and reconstruction by microorganisms. Due to the non-peculiar nature of the aforementioned processes, metals should interact with microorganisms, not adapted to them. Stereochemical analogy presumes proximity or parity of ionic radii of a metal and a macro element. Microorganisms react with metals because of this stereochemical analogy.

The Ba^{2+} and K^+ ions are chemically alike and have approximately the same ionic radius of the associated ionic state ($R_{\text{Ba}} \approx 1.4 \text{ \AA}$, $R_{\text{K}} \approx 1.33 \text{ \AA}$). We speculate that substitution of the element K can result in one, among several, vitally necessary elements. Ba^{2+} ions can be created, in principle (as in the last reaction) by substituting elements involving K^+ ions in metabolic processes while microbiological cultures are growing. This substitution is potentially more effective than the “direct” replacement of Potassium for Cesium because the ionic radius of Cesium is $R_{\text{Cs}} \approx 1.65\text{--}1.69 \text{ \AA}$ which is larger than the ionic radius of $R_{\text{K}} \approx 1.33 \text{ \AA}$ of Potassium. These ions can replace each other in transporting ions through a membrane to a cell (e.g. [8]). A lot is known of such replacements for different ions.

What is the reason for increasing the efficiency of transmutation by increasing the concentrations of calcium? These phenomena are probably connected with general problems of metabolic processes involving microbiological cultures. Optimal growth of microcultures takes place when a balanced relation of micro elements occurs. The phenomenon of low-energy transmutation of chemical elements and isotopes in biological systems and creating conditions for sustaining it is based upon the heuristic proposition that if some of the required elements or microelements are not present in the living environment (or nutrient media), then, given that certain pre-requisites are met, it will be synthesized as a result of the transmutation. In fact, such an approach unambiguously suggests that the ratio of all the necessary elements in each type of living organisms is fixed.

These results reveal a non-trivial nature of interactions of different microelements. By changing the makeup of the nutrient medium, it is possible to control the speed of a culture’s growth. Lacking at least one of the microelements in the nutrient medium hinders the development of the entire biological object.

4. The Possible Theoretical Model of Coulomb Barrier Suppression in Dynamical Physical and Biological Systems

To our opinion the process of isotope transmutation in biological systems occurs according to strict laws of physics, but it is induced by certain features of growing biological objects’ structure. According to this postulation let us consider briefly the possible mechanisms of nuclei interaction that contribute to effective nuclear transmutation reactions with the formation of Fe^{57} isotope.

It is evident that tunnelling quantum processes can not provide a great probability of nuclear transmutation (e.g. for D_2 molecule the probability of “usual” tunnelling dd-fusion is $\lambda_{\text{d+d}} \approx 10^{-70} \text{ s}^{-1}$). We would like to note that all relations for the probability of the tunnel effect have been obtained on the basis of the stationary Schrodinger equation and therefore, relate only to stationary interaction of the nuclei, although the process itself is never stationary. Non-stationary nature of any interaction is evident from the fact that a system of interacting nuclei has its own history and has been formed at some point in the past.

We assume that the most effective action in this case would be the one provided by the mechanism proposed in [3], which is capable of providing a short term elimination of the Coulomb barrier of the pair reaction in dynamical micropotential holes with the structure that is close to parabolic. In such holes the structure of quantum levels is equidistant and is characterized by the spectrum

$$E_n = \hbar\omega_0(n + 3/2), \quad n = 0, 1, 2, \dots$$

Let the Mn atom be in the center of such a hole. Due to dissociation processes, the hydrophilic compound has a great quantity of free d-deutons (at $T = 300 \text{ K}$ dissociation probability is $\eta \approx 10^{-10}$). When a deuteron gets into the hole due to diffusion, a complex Mn+d appears in the hole. In the free space this complex would correspond to a quasimolecule $(\text{MnD})^+$. In the quantum system the situation is more complicated. This complicity is connected to the fact that in such a system the energy of the nucleus interaction $V(r)$ is a sign-variable distance function (see Fig. 10 for a plot of function $r^2 V(r)$ which is important for the calculation of diagonal matrix elements).

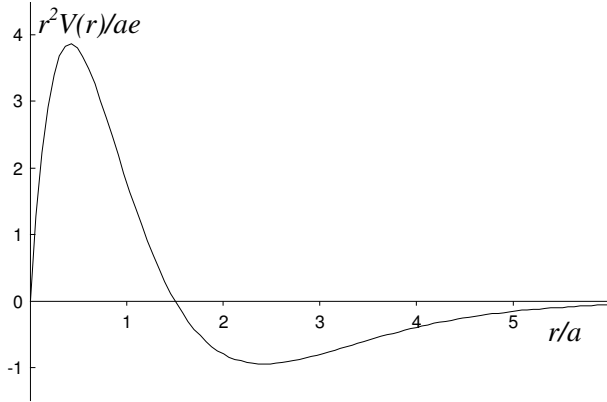


Figure 10. Structure of interaction energy $r^2 V(r)$ in Mn-d system.

For distances $r \ll a \equiv h^2/m_e e^2$ the energy $V(r)$ is similar to the energy of the p–e–d system and $V(r) < 0$. In the region of intermediate distances $a/Z \equiv < r < a$ this energy is defined by the Thomas–Fermi approximation

$$V(r) = (Ze^2/r)\xi(rZ^{1/3}/0.885a) \quad \text{and} \quad V(r) > 0.$$

In the region of small distances $r \ll a/Z$ nucleus interaction corresponds to pure Coulomb repulsion of bare nuclei and $V(r) = Ze^2/r > 0$.

Can this energy be a small correction that does not influence the character of nuclei movement in a quantum system? This is the most important question.

According to the first order of non-stationary perturbation theory, to fulfill such condition the diagonal matrix elements V_{mm} of interaction energy should be small and the probability of interlayer transitions

$$W_{nk} = (2\pi/h)^2 |V_{nk}(\omega_{nk})|^2 = (2\pi/h)^2 |V_{nk}|^2 \left\{ \frac{\sin(\omega_{nk}\tau/2)}{(\omega_{nk}/2)} \right\}^2$$

caused by this interaction should also be small.

Here

$$V_{nk}(\omega) = \int_{\infty}^{\infty} V_{nk}(t) e^{i\omega t} dt,$$

$$V_{nk}(t) = V_{nk}, 0 \leq t \leq \tau; V_{nk} = \int \int \int \Psi_n^*(\vec{r}) \hat{V}(\vec{r}) d^3r \equiv 4\pi \int \Psi_n^*(r) V(r) \Psi_k(r) r^2 dr,$$

$$|V_{nk}(\omega)| = |V_{nk}| \left| \frac{\sin(\omega\tau/2)}{(\omega/2)} \right|.$$

The probability of interlayer transition in the regarded parabolic potential becomes equal to zero automatically at the moments $\tau_s = 2\pi s/\omega_0$, $s = 1, 2, 3, \dots$, when frequencies of all possible interlayer transitions $\omega_{nk} = 2\pi s/\omega_0$ correspond to zeroes of the spectral density of perturbation energy $V_{nk}(\omega_{nk}) = 0$ (see Fig. 11)

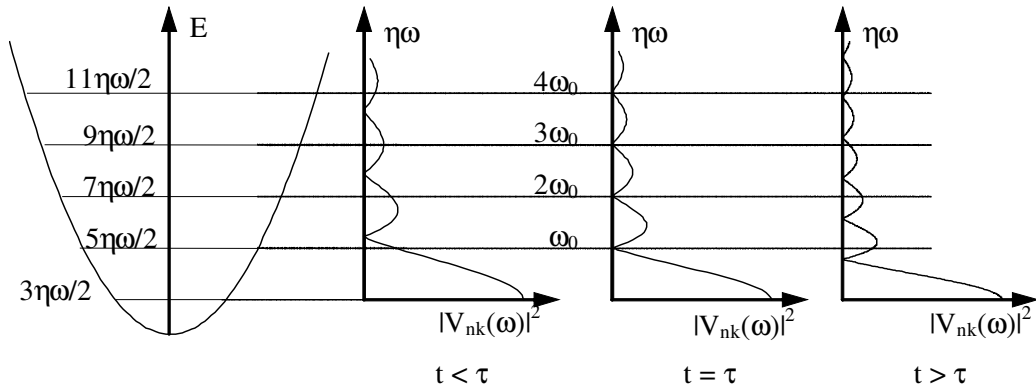


Figure 11. Correlation between energy spectrum of quantum levels E_n and spectral density $|V_{nk}(\omega)|^2$ of perturbation energy $V(r)$ for short ($t < \tau$), optimal ($t = \tau$) and long ($t > \tau$) duration of $\text{Mn}^{55} - \text{d}^2$ nuclear interaction.

At such conditions inter-particle interaction completely disappears and the deuteron wave function $\Psi_n(r)$ is determined only by properties of the quantized potential field.

For zeroing of diagonal matrix elements of the interaction energy $V(r)$

$$V_{nn} = 4\pi \int_0^{R_{\text{opt}}} |\Psi_n(r)|^2 V(r) r^2 dr \rightarrow 0.$$

(which is a sign-variable function of inter-nucleus distance) the optimal size R_{opt} of the hole is needed. In [1–4] it was shown that in the case of Mn–d system, $R_{\text{opt}} \approx 4 \text{ \AA}$.

If all above mentioned conditions are satisfied, the independent from Mn quantizing of the deuteron in the hole takes place. In this case the wave function of deuteron $\Psi_n(0)$ in all even states is different from zero in the center of the hole (at $r = 0$), where the Mn nucleus is located. This leads to a high probability of nuclear fusion. The rate of nuclear synthesis (probability of reaction per unit of time for one pair of interacting nuclei) is equal

$$\lambda_{\text{Mn}^{55} + \text{d}^2} = \Lambda |\Psi_n(r = 0)|^2.$$

Here, $\Lambda = S(E)h/\pi Me^2$ is the constant of nuclear $\text{Mn}^{55} - \text{d}^2$ interaction; $S(E)$ is the astrophysical nuclear factor depending on a matrix element of the nuclear interaction energy of particles; M is the reduced mass of interacting nuclei. $S(E)$ is the slowly changing function of energy, which is constant $S(E) = S_0$ for low relative energy of interacting particles in the case of non-resonance nuclear reactions.

As can be seen from the given scenario of the process, optimal size and shape of quantizing structures are needed for such non-barrier nucleus interaction. The exact parameters of these structures are very difficult to calculate. The situation substantially improves when the hole parameters are slowly changing, inevitably passing through optimal value. This situation is realized in growing microbiological cultures. During the growth process the replication of DNA, formation of membranes, cells and other bio-molecular objects takes place. In this case in the area of growth inter-atomic potential holes with slowly changing sizes are consistently appearing. If a Mn atom and a deuteron are randomly met in such a changing hole, conditions for a new Fe^{57} isotope fusion will be satisfied.

We hope that the given mechanism satisfactorily describes the basic properties of nuclear transmutation processes, which have been observed in discussed experiments.

References

- [1] V.I. Vysotskii, A.A. Kornilova, *Nuclear Fusion and Transmutation of Isotopes in Biological Systems*, MIR Publishing, Moscow, 2003.
- [2] V.I. Vysotskii, A.A. Kornilova, *Nuclear Transmutation of Stable and Radioactive Isotopes in Biological Systems*, Pentagon Press, India, 2009.
- [3] V.I. Vysotskii, Conditions and mechanism of nonbarrier double-particle fusion in potential pit in crystals, in: *Proceedings of Forth International Conference on Cold Fusion*, Vol. 4, 1994, pp. 20.2–20.5.
- [4] V.I. Vysotskii, A.A. Kornilova, I.I. Samoylenko, Experimental discovery of the phenomenon of low-energy nuclear transmutation of isotopes ($Mn^{55} \rightarrow Fe^{57}$) in growing biological cultures, in: *Proceedings of Sixth Intern. Conference on Cold Fusion*, Vol. 2, 1996, pp. 687–693.
- [5] V.I. Vysotskii, A.A. Kornilova, I.I. Samoylenko, Observation and massspectroscopy study of controlled transmutation of intermediate mass isotopes in growing biological cultures, *Infinite Energy* 6(36) (2001) 64–68.
- [6] V.I. Vysotskii, A. Odintsov, V.N. Pavlovich, A.B. Tashyrev, A.A. Kornilova, Experiments on controlled decontamination of water mixture of different long lived active isotopes in biological cells, in: *Proceedings of 11th International Conference on Condensed Matter Nuclear Science*, World Scientific, Singapore, 2006, pp. 530–536.
- [7] V.I. Vysotskii, A.B. Tashyrev, A.A. Kornilova, Experimental observation and modeling of Cs-137 isotope deactivation and stable isotopes transmutation in biological cells, in: *Low Energy Nuclear reactions Sourcebook*, Jan Marwan, Steven B. Krivit (eds.), ACS Symposium Series 998, Washington DC, 2008, pp. 295–303.
- [8] J. Van Brunt, J.H. Caldwell, F.M. Harold, Circulation of potassium across the plasma embrane of *Blastocladiella emersonii*: K-chanel, *J. Bacteriol.* 150(3) (1982) 1449–1561.



Neutron Emission in Bursts and Hot Spots: Signature of Micro-Nuclear Explosions?

Mahadeva Srinivasan ^{*,†}

(Retired) Bhabha Atomic Research Centre (BARC), Trombay, Mumbai, India

Abstract

Within a few months of the Fleischmann Pons announcement of 1989 several independent groups at BARC had confirmed the production of neutrons and tritium in a variety of electrolytic cells. Among the many findings of the BARC groups were the first hint of the neutron to tritium branching ratio anomaly, namely that tritium production is several orders of magnitude higher than that of neutrons, that neutrons and tritium are probably being emitted simultaneously and that at least in the case of titanium targets, the generated tritium is found to be entrenched in highly localized “hot spots”. But the most intriguing observation of all was that neutrons appeared to be emitted in sharp bursts of up to 10^3 neutrons per event. An integrated view of all these findings taken together led to the speculation that perhaps up to 10^{10} – 10^{12} tritons each were being generated in the form of micro-nuclear explosions, with neutron emission being only a minor side reaction in the process. Whatever the nature of the phenomenon, it seemed to be occurring in a highly localized fashion, both in space and time. Since those early days however the aspect of spatially localized occurrence of nuclear reactions has gained further acceptance through the concept of “Nuclear Active Environment”. The observation of thermal hot spots, micro-craters and isolated regions wherein transmutation products are concentrated on the cathode surface has reinforced the suspicion that the phenomenon is spatially localized. But how reliable is the evidence for localization in time? This review revisits our early neutron multiplicity measurements since it appears that confirmation of multiple neutron production is possibly the only handle we have to establish the temporal localization feature and thereby give some insight into the possible occurrence of micro-nuclear explosions which in turn would have a tremendous bearing on the nature of the theoretical mechanism governing these LENR reactions.

© 2011 ISCMNS. All rights reserved.

Keywords: Hot spots, Micro-nuclear explosion, Neutron bursts, Statistics, Tritium

PACS:

^{*}E-mail: chino37@gmail.com

[†]Present address: 25/15, Rukmani Road, Kalakshetra Colony, Besant Nagar, Chennai 600090, India

1. Introduction

Two decades of wide ranging studies has shown that low-energy nuclear reactions take place primarily on the surface rather than in the bulk metal. The growing preference for thin films, small diameter wires, nano-powders, etc., is an indication of this. Further there is convergence of perception that even on the surface, these reactions occur only at certain special locations referred to as “Nuclear Active Environment” (NAE) [1], which are thought to be created during the dynamic transport of deuterons (or protons) in and out of the metal, often initiated by some type of triggering mechanism. However, the exact nature of the NAE continues to be elusive.

In the present paper, we wish to bring into the conversation the aspect of “localized time” in addition to localized space, governing the occurrence of these reactions. In other words we raise questions regarding the temporal characteristics of the NAE. It is reasonable to expect that NAEs will not all be created simultaneously and uniformly over the entire host metal surface and also, once created, would not be able to continue catalyzing nuclear reactions “for ever”. Thus, it may be postulated that NAEs are continuously generated and destroyed and during their “lifetime” they trigger a certain number of nuclear reactions. A pertinent question that then arises is: what could be the order of magnitude of the lifetime of the NAEs? Could it be possible that their lifetimes is as small as nanoseconds or micro-seconds?

This line of thinking leads us to postulate that the LENR phenomenon could comprise of a series of “bursts” of nuclear reactions, each burst composed of “ x ” numbers of nuclear reactions generated by an NAE site during its lifetime. What could be the temporal characteristics of the reactions *within* a single nuclear “burst”? Could these individual reactions be “chain correlated”, with each new reaction being triggered by the previous one or an “exotic” agent or particle responsible for catalyzing these reactions? Alternately the entire “ x ” numbers of reactions could all take place simultaneously in a coherent fashion, in a “flash”. In either case it would have the characteristics of a micro-nuclear explosion.

These speculative considerations are not entirely imaginative but arise out of the multiplicity distribution of neutron counts measurements that our group had carried out during the first few years following the Fleischmann–Pons announcement, with both electrolytically loaded Pd cathodes as well as gas loaded Ti targets. These early measurements led us to conclude, even as far back as 1989 [2], that micro-nuclear explosions are possibly responsible for the generation of tritium in highly localized hot spots. In this paper we first review the sequence of experimental findings that led us to such a conclusion and then go on to examine whether there is any case for extending the concept of micro-nuclear explosions to other nuclear reactions that have also been observed in the LENR field. An abridged version of the present paper was earlier published in the proceedings of ICCF 15 held at Rome in October 2009 [3].

2. Summary of the Early BARC Findings

Within days of the Fleischman–Pons announcement in March 1989 a dozen independent groups from various divisions of BARC set up electrolytic cells using whatever materials were readily available. Clear evidence was obtained for the production of neutrons and tritium, signatures of the occurrence fusion reactions, but with the difference that tritium production was higher by several orders of magnitude as compared to neutrons. A comprehensive overview of these early BARC results in which over 50 researchers were involved [4] has just been re-published [5]. The main findings are summarized below.

2.1. BARC finding No. 1: branching ratio anomaly

Majority of the BARC cells produced both neutrons and tritium [6] with the neutron to tritium yield ratio being in the range of $\sim 10^{-7}$ rather than the expected value of unity. BARC groups were among the first to publish [2] this unexpected feature of neutron and tritium production in electrolytic cells. This so-called “branching ratio anomaly” has since been observed by several other groups also, even using devices where in the deuterium loading into titanium

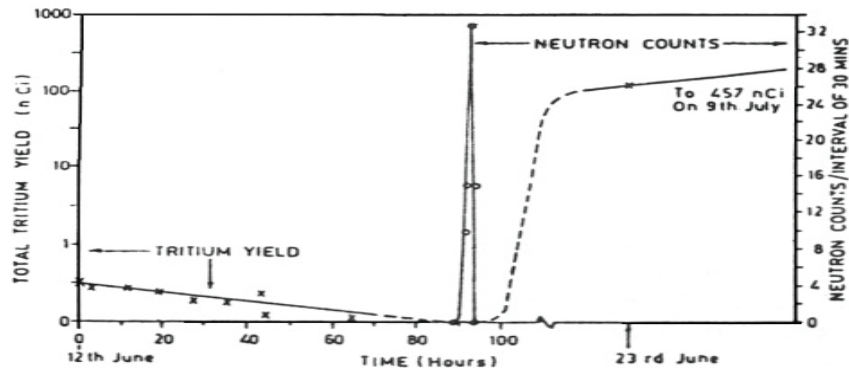


Figure 1. Concomitant generation of neutrons and tritium during run 2 of the first Milton Roy cell.

samples was carried out by gas loading methods. The branching ratio anomaly essentially signifies that on an average one neutron is generated for every 10 million tritons. Surprisingly neutron and tritium production was also noticed in a couple of instances even after the cell current had been switched off in the case of electrolytic cells or with unperturbed TiD_2 targets just sitting on the table, a behavior which has since come to be alluded as “life after death” in CMNS literature.

2.2. BARC finding No. 2: simultaneous production of neutrons and tritium

In electrolysis experiments neutron yield is measured online using standard neutron pulse detector set ups (BF_3 counters, proton recoil type scintillator, etc.), while tritium production is measured off line employing liquid scintillation techniques, with the electrolyte being sampled typically once or twice a day or at times once in a few days. In the BARC experiments it was noted that invariably the tritium levels indicated a jump only after one or more neutron emission “spikes” had been detected. Figures 1 and 2 reproduced from [6] bring out this behavior.

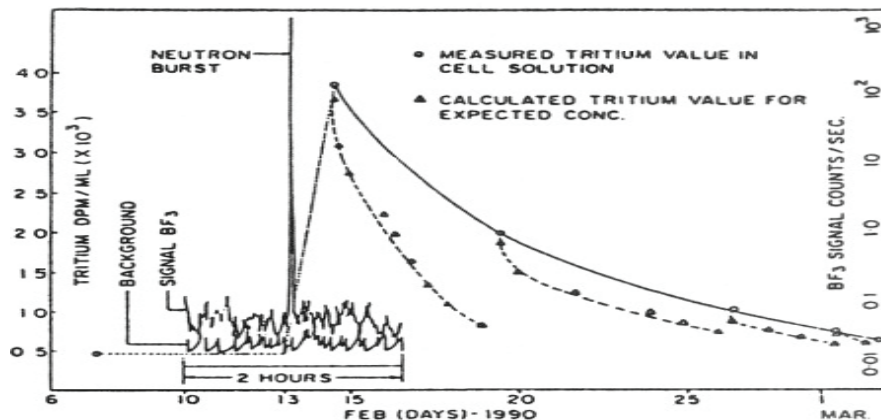


Figure 2. Increase of tritium concentration in electrolyte following a neutron spike in ROMG cell.

It was inferred from these that neutrons and tritium are probably produced simultaneously. Simultaneity in time would also imply co-generation at the same spatial location as a product of the same event; it is difficult to conceive of a mechanism responsible for concomitant generation from spatially separated sites since otherwise we are faced with an action-at-a-distance problem.

2.3. BARC finding No. 3: multiplicity distribution of neutron emission

BARC groups were the first [2,7] and perhaps the only group so far to have carried out a detailed experimental analysis of the statistical characteristics of the neutrons emitted by LENR devices. The question we asked ourselves was: Are the neutrons put out by these devices being emitted one at a time following Poisson statistics or are they emitted in bunches of 2, 10 or 100 s? We were inspired to ask such a question primarily because one of us had, decades earlier, carried out a Masters degree thesis study on the neutron density (or flux) fluctuations in a zero-energy experimental fission reactor using the so called Feynmann alpha technique [8]. He had the experimental background and familiarity with the statistical analysis methodology to quickly set up the hardware to measure the multiplicity distribution of neutron emission. The details of this are elaborated on further in a later Section in view of its central importance to the main theme of the present paper.

The results of neutron multiplicity studies, repeated with many different LENR devices, clearly indicated that a non negligible fraction (6.5–25%) of the neutrons produced were in bunches of 20–400, the exact fraction and magnitude of the bunches being dependent on the efficiency of the neutron detection set up, the characteristics of the LENR device and the nature of the deuterium loaded metal. The intriguing question raised by this finding which has puzzled this author for the last two decades is: what could be the mechanism by which such bunched neutron generation takes place?

2.3.1. *Implication of BARC Findings 1–3 taken together*

If for every neutron produced 10 million tritons are generated “simultaneously” and if say a 100 neutrons are emitted in a bunch then it could be logically concluded that 10^9 tritons are produced in the form of a micro-nuclear explosion. In this context we have already considered arguments which suggest that all this must be taking place at a highly localized site, because otherwise we would be obliged to invoke an appropriate action-at-a-distance mechanism. In the following it is shown that this is precisely what the autoradiographic images seem to indicate.

2.4. BARC finding No. 4: tritium found mainly in hot spots in gas loaded Ti targets

BARC groups deployed autoradiography as a very powerful tool to identify the location of tritium embedded in deuterated titanium targets [9,10]. The samples were placed close to but not touching medical x-ray films giving exposure times in the region of 20–60 h. Both deuterium loaded and hydrogen loaded palladium and titanium samples were investigated. We also carried out a number of basic studies to understand the mechanism of production of images in photographic films deploying various thin absorbers between the target and the photographic film. Such experiments clearly ruled out the possibility that these images could be artifacts caused by chemical reaction of the metallic sample being in direct contact with the emulsion of the photographic film. Besides, in the case of titanium targets, the presence of tritium in the surface layers of the target could be cross checked by measuring the 4.5 keV Ti K- α X-ray, as well as the direct measurement of the 18 keV tritium β s [11]. In the case of Pd samples however the threshold for production of Pd K- α X-ray is too high for the 18 keV tritium β s and only direct counting of the tritium β particles could be adopted.

It was thus conclusively established in a variety of gas/plasma loaded titanium target experiments that in the case of machined (cold worked) samples, the tritium generated by low-energy nuclear reaction processes is invariably lodged in lattice defect spots and crevices where the metal was subject to severe cold working (along outer edges for example) [11].

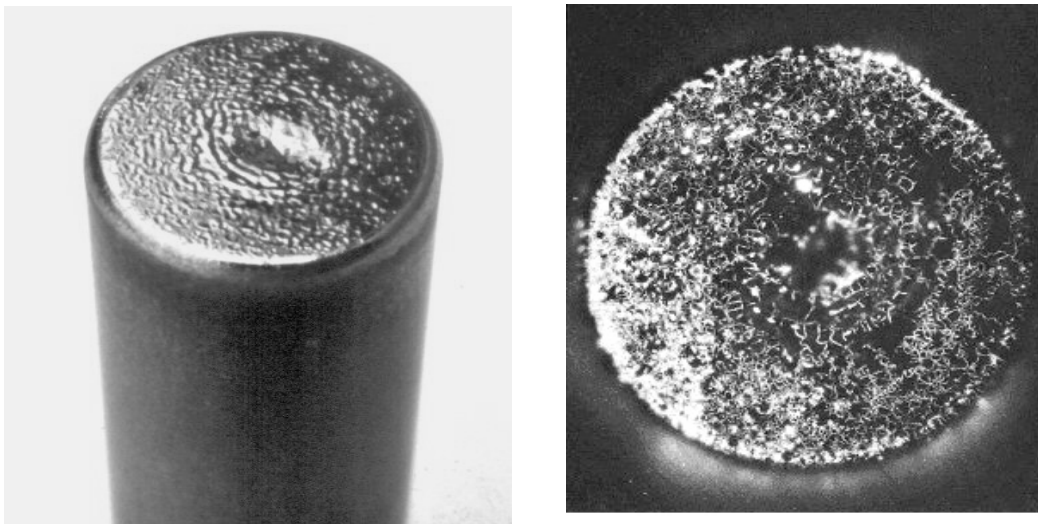


Figure 3. Photograph (*left*) and autoradiograph (*right*) of the top surface of titanium anode rod TA1 after 50 discharge shots.

The plasma focus anodes which were subject to several charge discharge shots in particular gave spectacular images of the top surface [13]. Figure 3 shows both a photograph and an autoradiographic image of the top surface of titanium anode rod TA1.

Figure 4 which gives the autoradiographs of the same rod repeatedly measured again and again over a period of 5 years brings out the remarkable reproducibility of the images indicating that tritium remains entrenched in the same spot in titanium for years together. Similar observations were made in the autoradiographic images of deuterated Ti disc samples and also titanium shavings loaded by gas loading methods [10]. This finding further supports our conclusion that the tritium must have in fact been generated at these “hot spots” and did not migrate and accumulate there after being produced elsewhere.

Thus, as already pointed out, although the first three “BARC findings” alone are adequate to support the micro-nuclear explosion hypothesis the characteristic spotty autoradiographic images in titanium further strengthens this speculation .

3. Brief Review of the Neutron Multiplicity Measurements

3.1. Basis of time resolved detection of individual neutrons of a simultaneously emitted burst

When a bunch of simultaneously produced fast neutrons impinges on a large hydrogenous moderator assembly in which one or more thermal neutron detectors such as BF_3 or He^3 gas proportional counters are embedded, because of the statistical time spread (typically about $25 \mu\text{s}$) that occurs during the neutron slowing down process, a certain fraction of the total number of neutrons emitted get separately and individually detected in a time resolved manner, the exact fraction depending on the geometrical efficiency and other factors. The resultant time series of electronic pulses issuing from the neutron detector tubes can then be analyzed for its statistical properties, especially the degree of departure from Poisson characteristics, in order to yield information on the neutron multiplicity spectrum.

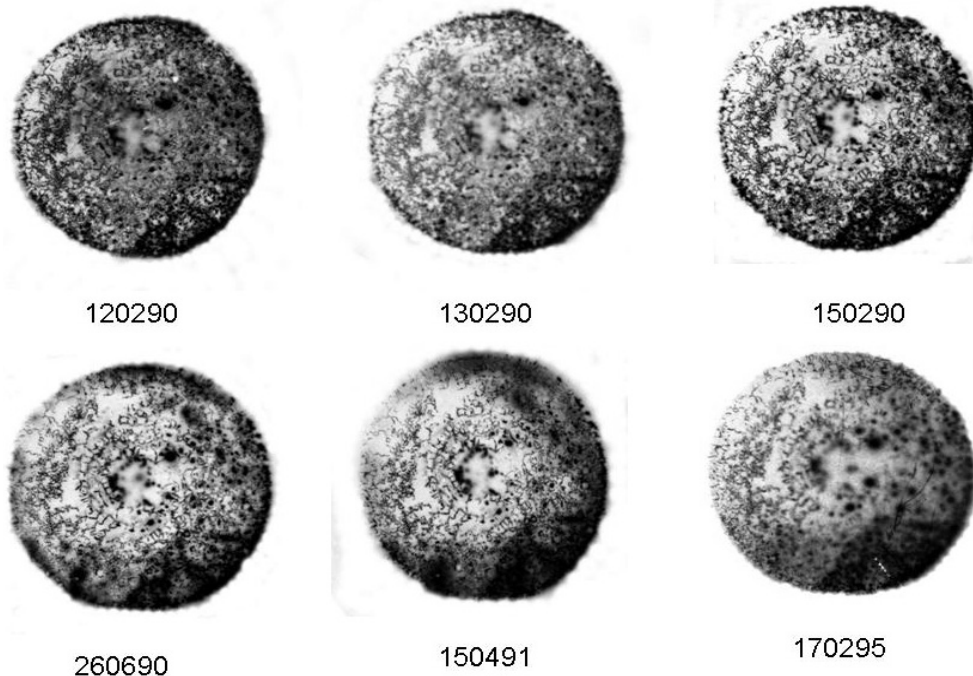


Figure 4. Repeat autoradiographs of titanium anode rod TA1 over five-year period: Dates of measurement are given under each radiograph.

3.2. Experimental techniques for statistical analysis

Two different techniques were used to determine the statistical characteristics of the pulse train issuing from the BF_3 or He^3 neutron counter banks. In the first method the frequency distribution of counts in 20 ms (or 10 ms) time bins was recorded [7]. In each sweep of the pulse train there were 1000 such bins, with a 280 ms separation between the 20 ms bins (as required by the data acquisition system), consuming in all a real time duration of 5 min per 1000 bin sweep. The duration of the counting interval was set in the 10–20 ms region and was dictated by the technical specifications of the computerized data acquisition system which was readily available at that time.

The second approach to measuring the statistical characteristics of the pulse train was an adaptation of the “artificial dead time” method [7,13] developed originally for investigating neutron density fluctuations in experimental fission reactors [8,14] as well as for the passive neutron assay of plutonium in the safeguards field [15,16]. When more than one neutron from a neutron burst is registered by the BF_3 or He^3 detectors (embedded inside a neutron moderator block), the corresponding electronic pulses will all be time correlated and closely spaced within about 100 μs of each other. In such events the second, third and subsequent pulses of the “family of pulses” are diverted by a 100 μs wide “artificial dead time gate” into a separate “burst counts analyzer”, while the leading pulses are totalized separately. The computerized burst counts analyzer then carries out a frequency of counts analysis to give the multiplicity spectrum of the neutron counts.

Table 1. Theoretical Prediction of frequency distribution of counts for random (Poisson) and burst neutron events for typical sets of experimental parameters

Multiplicity of counts	Frequency of counts in 20 ms intervals for 10^5 samples					
	Poisson events		Bunched events ($S = 10^{-2}$ per s)			
	$N_0 = 0.3$ cps	$N_0 = 3.0$ cps	$v = 100$	$v = 100$	$v = 500$	$v = 500$
			$\varepsilon = 0.005$	$\varepsilon = 0.015$	$\varepsilon = 0.005$	$\varepsilon = 0.015$
			$Sv\varepsilon = 0.005$	$Sv\varepsilon = 0.015$	$Sv\varepsilon = 0.025$	$Sv\varepsilon = 0.075$
0	99940	99402	99992	99984	99980	99980
1	60	597	6.1	6.6	4.00	0.07
2	$\sim 10^{-2}$	1.7	1.5	5.0	5.1	0.3
3	$\sim 10^{-9}$	$\sim 10^{-2}$	0.2	2.5	4.2	0.8
4	$\sim 10^{-9}$	$\sim 10^{-5}$	0.03	1.0	2.3	1.5
5	$\sim 10^{-13}$	$\sim 10^{-8}$	0.003	0.33	1.3	2.2

3.3. Theoretical considerations

For a purely random (Poisson) pulse series wherein N_0 is the average count rate and τ is the counting bin time interval (in this case 20 ms) and for the case when $N_0\tau$ is $\ll 1$, the probability of registering one count in a single 20 ms interval is $N_0\tau$, while $[(N_0\tau)^2]/2!$ gives the probability of getting doubles, $[(N_0\tau)^3]/3!$ that of getting a multiplicity of three counts and so on. Note that the probability of getting higher order multiplicity counts decreases steadily, since $N_0\tau$ is much less than unity.

If now there are ζ burst events per second generating v neutrons per burst, superimposed on the random background and the neutron detection efficiency is ε , then the contribution of the burst events to the overall count rate would be $\zeta v\varepsilon$. The probability of getting r counts in time τ from burst events is governed by a binomial distribution. Table 1 reproduced from [17] gives numerical examples with typical parameters for the expected frequency distribution of counts for random and bunched neutronic events. The main point brought out is that whereas for random events and low-count rates, the probability of getting doubles, triples, etc. is extremely small, in the case of burst events these probabilities are non-negligible. It is noteworthy that for burst events the peak of the multiplicity distribution actually shifts to higher multiplicity values as the product $v\varepsilon$ increases. Thus when the product $v\varepsilon$ exceeds unity (as for example when a bunch of 500 neutrons are emitted in a single event and detection efficiency ε is 1.5% in which case the magnitude of product $v\varepsilon$ is 7.5) the probability of registering four or five counts per interval could be even higher than that of obtaining doubles or even triple counts as evident from the last column of Table 1.

4. Results of Neutron Multiplicity Measurements

Neutron Multiplicity measurements were carried out both with a large cathode area Milton Roy type Pd–D₂O electrolytic cell [3,5] as well as some gas/plasma loaded TiD₂ targets. In these “first attempt” experiments conducted in 1989 only the frequency spectrum type analysis was performed. Unfortunately the overall neutron detection efficiency was only around 1–1.5%, primarily due to the poor geometrical arrangement of the detector assembly with respect to the source of neutrons. Table 2 shows the multiplicity distribution of neutron counts of both the foreground and background detector channels taken over a 63 h background run. It may be seen that no multiplicities beyond doubles were recorded. In general the equipment was found to function very satisfactorily, with the no-LENR-source (background) counts both of the foreground detector as well as the background detector strictly obeying Poisson statistics.

One of the unexpected surprises however, as already commented upon, was that both a shut off but previously operated electrolytic cell, as well as stand alone TiD₂ targets, emitted neutrons even in an unperturbed state. In all these runs the neutron yield was in the form of distinct spikes superimposed on a steady background.

The first frequency distribution measurements with an operating Milton Roy cell were conducted from 12 June 1989

Table 2. Experimentally observed multiplicity spectrum of background counts in two different neutron detector channels over a 63-h period (Counting interval 20 ms).

Multiplicity of counts	Frequency	
	BF ₃ Bank	He ³ Bank
0	750035	743948
1	339	6413
2	1	14
3	0	0
4–20	0	0
N_0	0.023 cps	0.13 cps
$N_0\tau$	5×10^{-4}	0.0086

onwards. An initial neutron emission episode lasting ~ 5 min duration occurred about 30 min after commencement of electrolysis and this was followed by two more such episodes about an hour later. The cell current was then switched off (evening of 14 June) but surprisingly three additional short neutron emission episodes occurred within a few hours of electrolysis being terminated. During these episodes, the neutron count rates were in the range of ~ 0.5 –1.7 cps, which corresponded to between 4 and 14 times that of the background value of ~ 0.12 cps. In four out of the above six episodes, count multiplicities of 2, 3, 4, 5 and even 10 were recorded at least once each. Throughout this run period lasting several days the background counter did not register any noticeable increase in count rate; nor did it record any multiple counts events.

On the evening of 16 June, an extended 2.5 h long neutron emission episode occurred in spite of the cell not having been operated for 52 h prior to that. The count rate during this wide neutron emission episode attained a value as high as 20 cps at the peak (between 19.45 and 19.55 h). Even the background neutron monitor which was 1.5 m away indicated a significant increase in count rate, commensurate with its efficiency for neutrons emanating from the Milton Roy cell. Table 3 presents the frequency distribution of neutron counts measured during this long episode. It may be seen that multiplicities of even five or more were registered several times. Close to the peak of the emission episode for example there were almost 20 such high multiplicity burst neutron emission events within a time span of 5 min (see data of 19.55 h).

A fresh attempt at neutron multiplicity measurements was made in summer 1994 with a newly procured Milton Roy cell. This time the electrolyte used was LiOD instead of NaOD which was used in the 1989 runs (The manufacturer had actually recommended only NaOD. This is being emphasized since use of LiOD could have had a bearing on the neutron production characteristics of the new Milton Roy cell.) We used a large annular neutron detector set up inside the central tube of which the electrolytic cell was mounted giving a neutron detector efficiency as high as $\sim 10\%$. For statistical analysis of the pulse train the improved artificial dead time technique discussed earlier was employed. The experiment was conducted over a two month period: The first 15 days were used to collect background data. The second one month was devoted to data collection with the operating new Milton Roy cell charged with LiOD electrolyte. For the last 15 days run LiOD electrolyte was replaced by LiOH (We thought we were doing a control run; but it turned out that the Pd cathodes were probably still charged with deuterium from the previous one month's LiOD run, as we shall see shortly.)

The variation of the neutron counts over the two month period clearly showed that with the LiOD electrolyte the average neutron count rate was systematically $\sim 10\%$ above the background values recorded during the no cell run of first 15 days [13]. But surprisingly during the last 15 days when the electrolyte had been replaced with LiOH the counts did not fall to background values immediately but rather decreased steadily over the next 15-day period, eventually attaining background levels, suggesting that it took 15 days for the deuterium inside the Pd cathode to be fully replaced

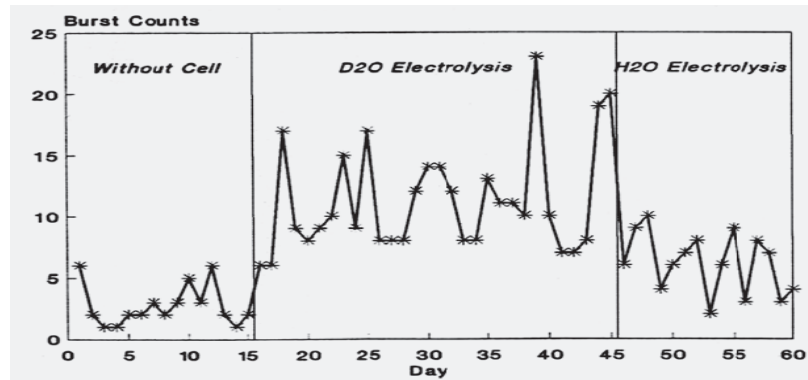


Figure 5. Daily variation of sum of burst component of neutron counts.

by hydrogen. Figure 5 reproduced from [13] presents the variation of the burst neutron counts component over the 60-day period as detected by the dead time technique discussed above. This too shows evidence of the slow replacement of D by H during the last 15 days.

Figure 6 presents the variation of the total integrated number of neutrons which were detected as bursts, observed over the entire 15 or 30 days period, as a function of the neutron multiplicity. (15-day counts have been normalized to 30-day period for comparison.) Here again the counts data during the third phase with LiOH electrolyte clearly displays evidence of significant non Poissonian multiplicity, due to deuterium still being embedded within the Pd metal.

Detailed descriptions of all these measurements and results are available in [2–7, 13,17]. In all these runs the foreground counter gave clear evidence of several higher order neutron multiplicity events. In many instances during the 1989 measurements, the peak of the multiplicity spectrum was in the 4 or 5 neutron pulses region. Since the overall neutron detection efficiency in those runs was only $\sim 1\%$ it implies that approximately 400–500 neutrons were produced

Table 3. Multiplicity distribution of neutron counts in 20 ms time bins from a Quiescent Milton Roy Cell: neutron emission episode of 16 June 1989.

Hours	Time															BF ₃ Counter bank (signal)			³He Counter bank (background)		
	1*	2*	3*	4*	5*	6*	7*	8*	9*	10*	11*	12*	13*	14*	15*	1*	2*	3*	1*	2*	3*
18.55	124	21	4	1	-	-	-	-	-	-	-	-	-	-	-	2	1	-			
19.00	54	9	1	-	-	-	-	-	-	-	-	-	-	-	-	1	-	-			
19.05	335	54	7	2	1	-	-	-	-	-	-	-	-	-	-	4	-	-			
19.10	320	82	10	-	-	-	-	-	-	-	-	-	-	-	-	5	-	-			
19.15	243	13	4	-	1	-	-	-	-	-	-	-	-	-	-	5	-	-			
19.20	315	35	3	1	-	-	-	-	-	-	-	-	-	-	-	4	-	-			
19.25	295	24	-	1	-	-	-	-	-	-	-	-	-	-	-	5	-	-			
19.30	492	51	3	2	-	-	-	-	-	-	-	-	-	-	-	4	-	-			
19.35	447	42	2	1	-	-	-	-	-	1	-	1	-	-	-	9	-	-			
19.40	104	13	4	-	-	1	-	-	-	-	-	-	-	-	-	5	-	-			
19.45	355	49	1	1	-	1	-	-	-	-	-	-	-	-	-	33	1	-			
19.50	395	99	16	2	-	-	-	-	1	-	-	-	-	-	-	22	3	-			
19.55	55	24	7	33	2	1	1	1	1	1	2	2	1	-	5	6	2	-			

* Starred numbers represent the multiplicity of counts obtained in a single 10 ms interval. The respective frequency of occurrence (per 1000 gated intervals) is given in the corresponding column below.

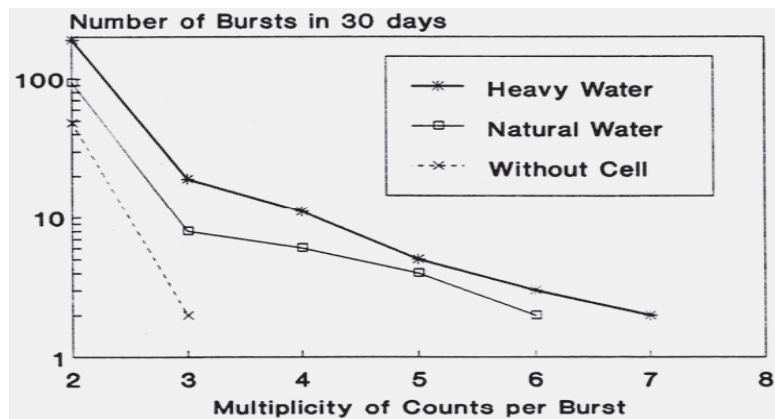


Figure 6. Variation of total number of counts of neutron pulses which passed through dead time gate over 30-day period as a function of multiplicity.

in each of those “explosive bursts”. In fact during the 16 June 1989 run with the first Milton Roy cell wherein the 2.5 h long neutron spike episode occurred multiplicities as high as 15 were recorded during the last 5 min interval (see Table 3.) implying that a burst of 1500 neutrons was produced in this flash incident.

In the 1994 campaign during the D₂O run with the new Milton Roy cell, in spite of the higher ($\sim 10\%$) neutron detection efficiency, the maximum multiplicity recorded was only around 8 counts, pointing to a burst strength of not more than 80 neutrons. It must however be noted that in this experiment the average magnitude of the neutron output was only $\sim 10\%$ above the background values and there were no clearly distinguishable spikes superimposed on the background values. In response to a possible criticism that a mere 10% above background levels could be “suspect”, it may be pointed out that the observation that when the LiOD was replaced with LiOH the neutron count rate steadily decreased to background values over a 15-day period clearly confirms that the neutrons were indeed produced by LENR processes [13].

5. Discussion and Conclusions

Thus on the whole there is unmistakable evidence that whenever LENR sources produce neutrons, a considerable fraction (6.5–25%) [6,12] of these are emitted in the form of bursts of strength varying from 20 to several 100s, the exact magnitude depending on the type of LENR source. The neutron detection efficiency (ε) however sets a lower limit to the magnitude of the burst strength that can be detected. For example, if ε is only 1% and one neutron count is registered during a one minute interval, this could have resulted either from 100 isolated events of single neutron emission during that one-minute interval or from a single burst of 100 neutrons, on account of the 1% detection efficiency. In other words it is possible that the balance 75–93.5% which although registered as singles counts, could still have resulted from burst neutron emission. This is a point that is seldom appreciated. Thus it would seem that the real fraction of neutrons emitted as bursts could have been much larger than the figures quoted above.

We are proposing in this paper that each of the hot spots wherein tritium was found to be concentrated could perhaps be associated with an NAE site of the type discussed in LENR literature [1]. Based on the BARC findings we therefore postulate that once an NAE is formed a rapid cascade of up to 10^{12} tritium producing nuclear reactions takes place in quick succession in this local site, in a sort of micro-nuclear explosion, during which process on an average for every ten million tritium nuclei generated one neutron is also emitted as a very low-probability offshoot side reaction event.

We then go on to further speculate that if neutrons and tritium could be produced in micro-nuclear explosions then

possibly other nuclear reactions such as those responsible for heat and helium as well as transmutation products could also possibly take place in similar micro-nuclear explosions. As noted earlier the observed craters in post run cathodes could be an indication of such events.

Indeed, as noted by Krivit [18] recently, there have been several unexplained “excess heat boil off” incidents accompanied by significant energy release reported in LENR literature over the last two decades, starting with a major explosion/meltdown incident involving a 1 cm cube Pd cathode that Fleischmann has discussed, all of which seem to suggest that “runaway mini nuclear explosions” have all along been suspected to happen in Pd samples heavily loaded with deuterium, but only on very rare occasions. A widely circulated but unpublished recent assessment of the LENR field carried out by the US Defense Intelligence Agency [19] has even raised the question: “If rapid explosive energy output can occur in one or several modes, could LENR serve as a high energy density explosive?”

In conclusion, it is once again emphasized that the main experimentally measurable parameter that can throw more light on these speculations is neutron multiplicity and hence statistical analysis experiments of the type described in this paper warrant serious attempts at replication. The key to successful observation of neutron multiplicity is however obtaining high neutron detection efficiency and use of the dead time method in conjunction with thermal neutron detectors embedded inside a neutron moderator block.

We do concede that our “claim” of simultaneous production of neutrons and tritium is a weak link in the arguments used to arrive at the micro-nuclear explosion hypothesis and certainly that too needs independent confirmation through further careful measurements.

Acknowledgements

The author wishes to place on record the significant contributions of his former colleagues and co-authors of many of the BARC papers referred to here, notably Drs. P.K. Iyengar, S.B. Degwekar, A. Shyam, T.C. Kaushik, R.K. Rout and L.V. Kulkarni.

References

- [1] E. Storms, *The Science of Low Energy Nuclear Reaction*, World Scientific, Singapore, 2007.
- [2] P.K. Iyengar, *Proc. 5th Int. Conf. on Emerging Nucl. Ener. Systems*, July 1989, Karlsruhe, Germany, 291, World Scientific, Singapore, 1989.
- [3] M. Srinivasan, Hot Spots, Chain events and micro-nuclear explosions, *Proc. 15th Int. Conf. on Condensed Matter Nuclear Science*, Oct. 5–9 2009, Roma, Italy. (2009)
- [4] P.K. Iyengar et al., *Fusion Technol.* **18** (1990) 32.
- [5] M. Srinivasan, *Low Energy Nuclear Reactions and New Energy Technology Sourcebook*, Vol. 2, Jan Marwan, Steven B Krivit (eds.), American Chemical Society, Oxford University Press, Oxford, 2009.
- [6] P.K. Iyengar, M. Srinivasan, *Proc. 1st Int. Conf. on Cold Fusion*, Salt Lake City, UT, USA, 1990.
- [7] M. Srinivasan, A. Shyam, S.B. Degwekar, L.V. Kulkarni, *Proc. 1st Int. Conf. on Cold Fusion*, Salt Lake City, UT, USA, 1990, p. 175.
- [8] R.E. Uhrig, *Random Noise Techniques in Nuclear Reactor Systems*, Ronald Press, New York, 1970.
- [9] R.K. Rout, A. Shyam, M. Srinivasan, A.B. Garg, V. Shrikande, *Fusion Technol.* **30** (1996) 273.
- [10] T.C. Kaushik, A. Shyam, M. Srinivasan, R.K. Rout, L.V. Kulkarni, *Indian J. Technol.* **28** (1990) 667.
- [11] M. Srinivasan et al., *Proc. Int. Workshop on Anomalous Nuclear Effects Deuterium/Solid Systems*. Brigham Young University, Provo UT, USA, 1990, American Institute of Physics, 1991.
- [12] R.K. Rout, M. Srinivasan, A. Shyam, V. Chitra, *Fusion Technol.* **19** (1991) 391.
- [13] A. Shyam, M. Srinivasan, T.C. Kaushik, L.V. Kulkarni, *Proc. 5th Int. Conf. on Cold Fusion*, Monte Carlo, Monaco 191, 1995.
- [14] M. Srinivasan, D.C. Sahni, *Nukleonik* **9** (1967) 155.
- [15] S.B. Degwekar, *Ann. Nucl. Energy* **16** (1989) 409.

- [16] S.B. Degwekar, M.Srinivasan, *Ann. Nucl. Energy* **20** (1993) 463.
- [17] P.K. Iyengar, M. Srinivasan, Paper A4 in Report BARC 1500, Dec. 1989, Bhabha Atomic Research Centre, Trombay, Bombay, 1989.
- [18] S.B. Krivit, Cold Fusion, Chapter in Encyclopedia on Electrochemical Power Sources, Vol. 2, Elsevier, Amsterdam, 2009, pp. 255–270.
- [19] B. Barnhart, Technology Forecast Report, DIA-08-0911-003, 13 Nov 2009, Unpublished.



Research Article

Review of Twenty Years of LENR Research Using Pd/D Co-deposition

Pamela A. Mosier-Boss*, Jack Y. Dea and Frank E. Gordon†

SPAWAR Systems Center Pacific, San Diego, CA 92152, USA

Lawrence P.G. Forsley

JWK International, Annandale, VA 22003, USA

Melvin H. Miles

Dixie State College, St. George, UT 84770, USA

Abstract

In the Pd/D co-deposition process, working and counter electrodes are immersed in a solution of palladium chloride and lithium chloride in deuterated water. Palladium is then electrochemically reduced onto the surface of the working electrode in the presence of evolving deuterium gas. Electrodes prepared by Pd/D co-deposition exhibit highly expanded surfaces consisting of small spherical nodules. Because of this high surface area and electroplating in the presence of deuterium gas, the incubation time to achieve high D/Pd loadings necessary to initiate LENR is orders of magnitude less than required for bulk electrodes. Besides heat, the following nuclear emanations have been detected using Pd/D co-deposition: X-ray emission, tritium production, transmutation, and particle emission. Experimental details and results obtained over a twenty year period of research are discussed.

© 2011 ISCMNS. All rights reserved.

Keywords: Nuclear products, Pd/D co-deposition

PACS: 14.20.Dh, 78.67.Rb, 68.35.Ct

1. Introduction

On March 23, 1989, Fleischmann and Pons announced, in a press conference, that their electrochemical cells were producing more heat than could be accounted for by chemical means. They speculated that the heat had a nuclear origin. The physics community noted that Fleischmann and Pons had not published their results in any journal prior to their announcement, there had been no reports of any replications of the effect, there was no mention of the generation

*E-mail: pam.boss@navy.mil

†Retired

of any nuclear ash, and that the reported results did not match theory. Despite these deficiencies, scientists, worldwide, went into their laboratories to replicate the Fleischmann–Pons results. A few scientists succeeded but a great many more failed. It is now known that failures were due to the fact that the experimental conditions necessary to achieve the effect, i.e., high D loading and high D flux inside the Pd lattice, had not been achieved.

Stanislaw Szpak, an electrochemist at the Navy laboratory in San Diego, was aware of the Fleischmann–Pons experiment prior to the press conference and knew about the long incubation times needed to fully load bulk Pd with D. To reduce the incubation time, he developed the Pd/D co-deposition process as a means of initiating low energy nuclear reactions (LENR). In this process, working and counter electrodes are immersed in a solution of palladium chloride and lithium chloride in deuterated water. Palladium is then electrochemically reduced onto the surface of the working electrode in the presence of evolving deuterium gas. In this communication, a review is presented of observations made using the Pd/D co-deposition process. The research efforts can be grouped into three time periods for the years encompassing 1989–1995, 1995–2005, and 2005 to present.

2. Summary of Results between 1989 and 1995

In the years between 1989 and 1995, the emphasis of the research was to characterize the deposit formed as the result of Pd/D co-deposition and to search for evidence of nuclear products.

2.1. Characterization of the Pd/D Deposit

The Pd formed as a result of Pd/D co-deposition is black and powdery. Figure 1a shows a scanning electron microscope (SEM) image of an electrode prepared by the Pd/D co-deposition process. It can be seen that the highly expanded surface consists of small spherical nodules [1,2]. Cyclic voltammetry [2,3] and galvanostatic pulsing [4] experiments indicate that, by using the co-deposition technique, a high degree of deuterium loading (with an atomic ratio $D/Pd > 1$) is obtained within seconds and maintained throughout the experiment. These experiments also indicate the existence of a D_2^+ species within the Pd lattice. Because an ever expanding electrode surface is created, non-steady state conditions are assured, the cell geometry is simplified because there is no longer a need for a uniform current distribution on the cathode, and long charging times are eliminated [5].

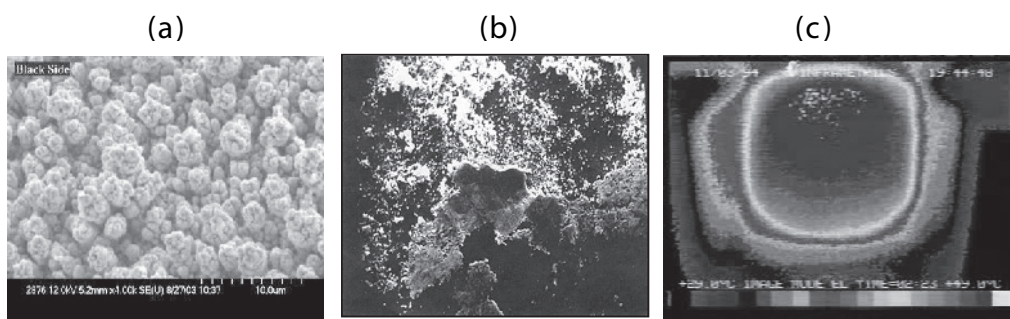


Figure 1. (a) SEM of the Pd deposit formed as the result of Pd/D co-deposition [6] (Reprinted with permission from *Eur. Phys. J. Appl. Phys.*). (b) SEM of the Pd film showing features consistent with Pd melting under water [7] (Reprinted with permission from *Phys. Lett. A*). (c) Infrared image of a cell during Pd/D co-deposition. The circular area in the center is the cathode.

2.2. Evidence of excess heat

In the early experiments, a thermocouple was soldered to the inside of a Cu cathode used as the substrate for Pd/D co-deposition. Another thermocouple was placed inside the cell between the cathode and the anode. Temperature measurements using these thermocouples during electrolysis showed that the cathode was hotter than the solution. These results indicate that the observed heat is not due to Joule heating. In an experiment using Ni screen as the substrate for Pd/D co-deposition, boil off of ~ 25 mL of solution was observed to occur in a five minute time period. A silver Pd film was observed on the cell wall adjacent to the Ni screen. SEM analysis of this silver film was done (Fig. 1b). According to the metallurgist, Gordon Chase, doing the analysis, the observed features were consistent with metal that had melted under water [8]. The melting point of palladium is 1554.9°C.

In 1994, infrared imaging of the cells was done at UCSD with the assistance of Massoud Simnad of UCSD and Todd Evans of General Atomics. In these experiments Pd/D co-deposition was done on a Ni screen that was in close proximity to a 100 μm thick acetate window [9]. The surface temperature distribution of the backside of the cathode was measured as a function of time using an infrared camera. Figure 1c shows an infrared image of the cell. The circular area is the cathode. It can be seen that the cathode is hotter than the surrounding liquid. It was observed that, unlike Joule heating, excess enthalpy generation occurs in the form of localized events in close proximity to the contact surface. It was also observed that, the higher the electrolyte temperature, the more frequent the events. In the limit, these events overlap to produce oscillating islands. The steepness of the temperature gradients indicates that the heat sources are located in close proximity to the electrode-solution contact surface.

2.3. Measurement of low intensity radiation and tritium content

In 1989, the Department of Energy (DoE) conducted a review of the phenomenon. The conclusions of the review were that the claims of excess heat were not convincing, that the excess heat was not shown to be associated with a nuclear process, and that the evidence of neutron emission was not persuasive. In the aftermath of the DoE review, we concluded that heat was not going to convince anyone that nuclear events were occurring inside the palladium lattice. Also heat does not provide any information as to the processes occurring inside the Pd lattice. For these reasons, the emphasis of our research shifted from heat to looking for nuclear emissions such as γ -/X-rays and tritium.

Pd/D co-deposition experiments were conducted inside lead caves while measuring gamma and X-rays, as a function of time, using a HPGe detector with an Al window and a Si(Li) detector with a Be window [1]. The cathodically polarized Pd/D system was observed to emit X-rays with a broad energy distribution and with an occasional emergence of recognizable peaks attributable to the Pd K_{α} and Pt L lines. As can be seen in Figure 2a, the emission of γ -/X-rays was sporadic and of limited duration. Photographic film is another detector that has been used to detect radiation. It is an example of a constantly integrating detector, meaning that once an event occurs it gets permanently recorded in the emulsion. Use of a constantly integrating detector is particularly advantageous when events occur sporadically or at low levels, which is true of the Pd/D system. Figure 2b shows photographic film that was placed on top of a thin plastic sheet that was in contact with a silver disk cathode that had been used in a Pd/D co-deposition experiment. The circular shape of the cathode is clearly seen as well as fogging inside the circular disk. The fogging is inhomogeneous indicating that some sites are more active than others.

Figure 3a shows a schematic of the experimental configuration used to monitor tritium in both the liquid and gas phases during electrolysis [10]. In these experiments, the D_2 and O_2 gases were recombined in a separate chamber. The tritium content in the liquid and gas phases were measured daily using the liquid scintillation technique. The measured data were compared to the amount expected based upon mass balance. The time dependence of tritium content of an open cell operating galvanostatically with intermittent sampling is given by the following expression [11]:

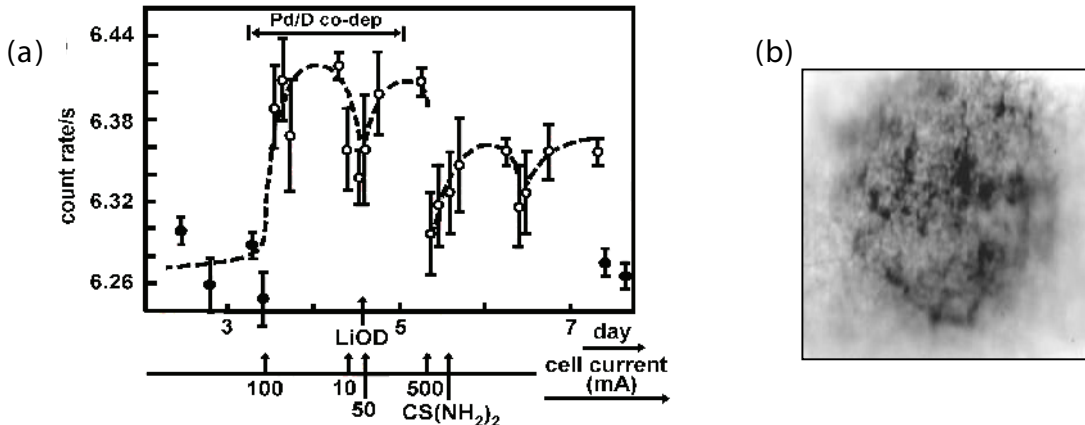


Figure 2. (a) Count rate during cathodic polarization of the Cu/Ag/Pd electrode as measured using a HPGe detector. The period of Pd/D co-deposition is indicated as well as the addition of LiOD and CS(NH₂)₂. (b) Fogging of photographic film after exposure to Pd deposited on an Ag disk cathode [6] (Reprinted with permission from *Eur. Phys. J. Appl. Phys.*). A thin Mylar sheet separated the film from the cathode.

$$f(t) = f(0) \left(\frac{m(0) - r(i)t}{m(0)} \right)^{S-1} + \frac{q}{(s-1)r(i)} \cdot \left\{ 1 - \left[\frac{m(0) - r(i)t}{m(0)} \right]^{S-1} \right\}, \quad (1)$$

where f is the tritium mass fraction, m is the mass of the electrolyte phase, $r(i)$ denotes the rate of change associated with the cell current, q is the rate at which tritium is added/removed, and S is the isotopic separation factor. Figure 3b shows the tritium distribution between the gas and liquid phases observed for one experiment. It was observed that tritium production occurred in bursts and sporadically. During a burst, the rate of tritium production was determined to be 3000–7000 atoms s⁻¹.

3. Summary of Results between 1995 and 2005

In the years between 1995 and 2005, calorimetric measurements were done. Pd/D co-deposition experiments were also done on piezoelectric crystals and triggering of nuclear effects, using external electric and magnetic fields, was examined.

3.1. Calorimetry

Calorimetry of cathodes prepared using Pd/D co-deposition was done by Me I Miles while he was on sabbatical at the New Hydrogen Energy (NHE) Laboratory in Sapporo, Japan [12,13]. He used an isoperibolic Dewar calorimetry cell. The cell was sufficiently tall enough to keep the Pd deposit from reaching the gas-liquid interface thereby preventing D₂ and O₂ recombination from occurring. Results indicated that excess enthalpy was generated during and after the completion of the co-deposition process. The rates of excess enthalpy generated using the co-deposition technique were higher than those obtained using Pd wires or other forms of Pd electrodes. Positive feedback and heat-after-death effects were observed. The rates of excess power generation were found to increase with an increase in both cell current and cell temperature.

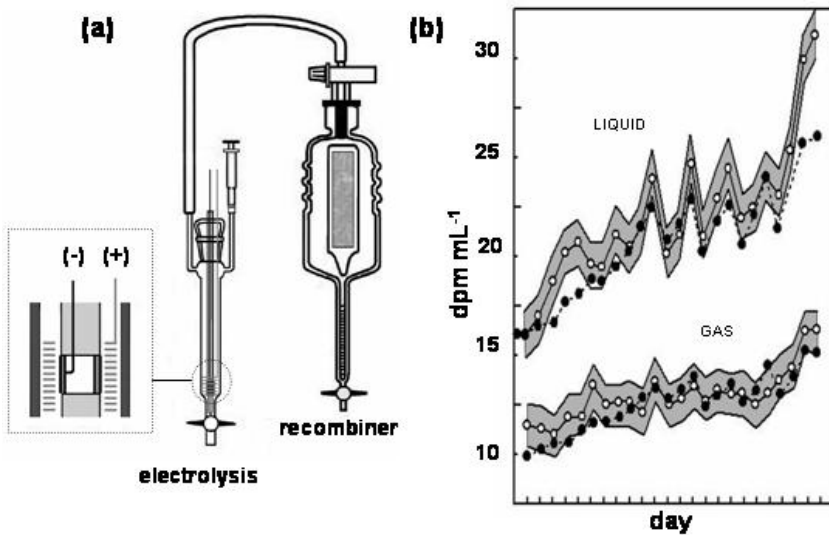


Figure 3. (a) Schematic of the electrolysis cell and recombining system used to monitor tritium in the gas and liquid phases during electrolysis. (b) Tritium content, in dpm mL^{-1} , for Pd/D co-deposition done on a Cu/Ag/Pd cathode. Open circles are the experimental data with the 2σ error bars, solid circles are the amount of tritium expected based upon the mass balance.

3.2. Hot spots and mini-explosions

In 2000, a LENR workshop was held at the then SPAWAR San Diego laboratory. In attendance was Lowell Wood from Lawrence Livermore National Laboratory. Upon seeing the infrared imaging video of the cathode prepared using the Pd/D co-deposition technique, he indicated that the hot spots could be the result of mini-explosions. He further suggested that a microphone in close proximity to the cathode may detect these mini-explosions. Rather than monitoring the experiment with a microphone, a Pb/Zr/Ti piezoelectric crystal was used as the cathode in Pd/D co-deposition. These transducers respond to both pressure and temperature. A schematic of the expected response is shown in Figure 4a. When a mini-explosion occurs, a shock wave, f_1 , will be created and heat, Q , will be dissipated. The shock wave is expected to be instantaneous and of short time duration. This shock wave will cause compression of the crystal. The heat will lag behind the shock wave and will cause the crystal to expand. An example of a single event during Pd/D co-deposition is shown in Fig. 4b. A sharp downward spike, indicative of compression caused by the shock wave from the explosion, is observed that is followed by expansion of crystal as the slower heat wave reaches the crystal.

3.3. Triggering: effect of external electric/magnetic fields

In 1993, Bockris et al. [14] reported on three methods of triggering anomalous heat in the Pd/D system. These methods included electrochemical stimulation in which heat bursts were initiated by pulsing the current, radio-frequency stimulation, and magnetic stimulation. Beginning in 2003, the use of external electric and magnetic fields to trigger nuclear processes in Pd/D co-deposition was explored. These efforts are still on-going.

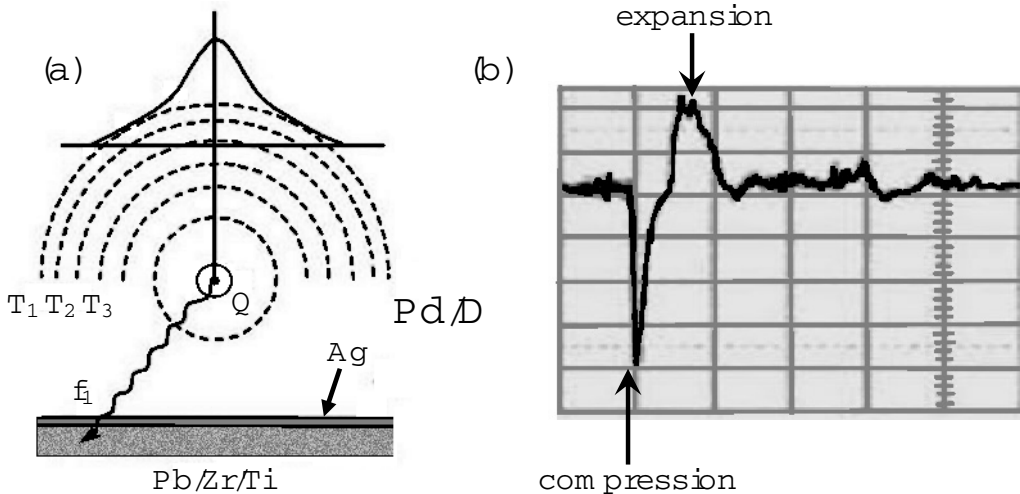


Figure 4. (a) Schematic of the events that should occur when a mini-explosion occurs during Pd/D co-deposition. (b) A recording of a single mini-explosion that was detected using a Pb/Zr/Ti piezoelectric crystal.

3.3.1. External electric fields

Figure 5a shows a schematic of the cell configuration used in the external electric field experiments [15]. Copper plates were attached on either side of the cell. A regulated high voltage source was used to apply 6000 V DC (with a $\sim 6\%$ AC component ripple) across these Cu electrodes. The electric field was applied after Pd/D co-deposition onto an Au foil cathode had been completed. The experiment was terminated after 48 h and the cathode was subjected to SEM analysis. Figure 1a shows an SEM image of the Pd deposit obtained in the absence of an external field. The deposit exhibits a cauliflower like morphology. After exposure to an external electric field, significant changes in the morphology of the Pd/D deposit were observed. Fractal features (Fig. 5b) were observed as well as dendritic growths, rods, wires, and craters (Fig. 5c). Micro-volcano like features, like those in Fig. 5d, were also observed. This kind of damage to metals is consistent with damage seen in materials such as ^{252}Cf which undergoes spontaneous fission. In ^{252}Cf , the volcano like eruptions result from large numbers of spontaneous fissions resulting in ‘spike damage.’

The features shown in Fig. 5b–d are suggestive of solidification of molten metal. If the energy needed to melt metal is of a nuclear origin, it should be reflected by the chemical composition of those features. When these features were subjected to further analysis using an energy-dispersive X-ray (EDX) analysis system, the following new elements were detected: Al, Mg, Si, Ca, and Zn [16]. The distribution of these new elements was not uniform and was only associated with these molten formations. This indicates that the new elements were not the result of contamination. In addition, Ca, Al, Mg, and Si cannot be electrochemically plated onto a cathode from an aqueous solution. This provides additional evidence that the new elements were the result of transmutation and not transportation.

3.3.2. External magnetic fields

Figure 6a shows a schematic of the cell configuration used in the current external magnetic field experiments [7]. In an external, magnetic field experiment conducted in 1993, an Au wire cathode was wrapped around a capillary tube housing a thermocouple. Another capillary tube, housing a second thermocouple, was placed between the cathode and anode. The orientation of the cathode was perpendicular to the magnetic field and not parallel as shown in Fig. 6a.

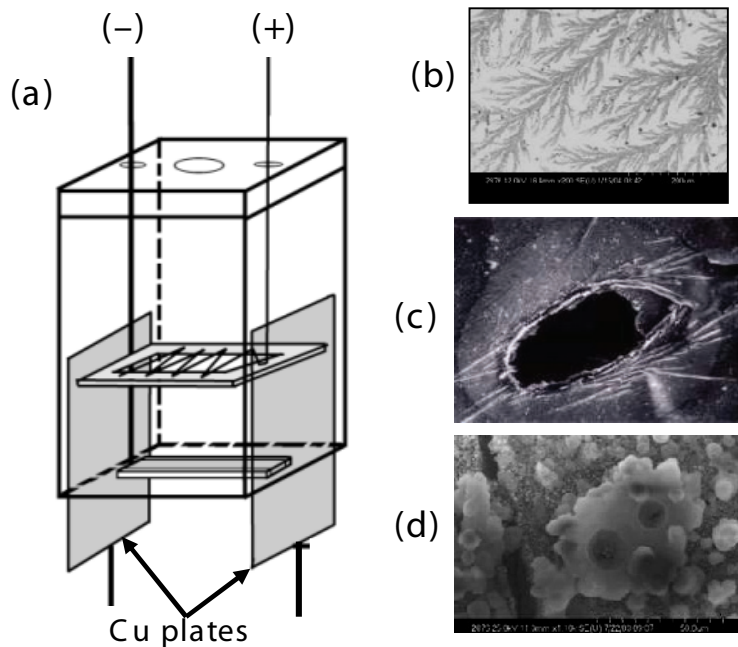


Figure 5. (a) Schematic of the cell used in the external electric field experiment. SEM images of the Pd deposit upon termination of the experiment showing (b) fractals, (c) craters [15] (Reprinted with permission from *J. Electroanal. Chem.*), and (d) micro-volcano like features.

After the Pd had finished plating out on the Au wire, an electromagnet was used to apply a 120 G field. Figure 6b shows the measured temperature response of the thermocouples. Before the electromagnet is turned on, it can be seen that the Au/Pd cathode was hotter than the solution. The temperature differential was approximately 1°C. When the electromagnet was turned on, the temperature of the cathode increased and the temperature differential between the cathode and solution was 3°C. These results were in agreement with what Bockris et al. had observed in his external magnetic field experiments [14].

SEM analysis of the Pd deposit exposed to a 2500 G magnetic field is shown in Fig. 6c. The Lorenz forces of the magnetic field have caused the Pd microglobules to form star-like features. EDX analysis of these features (Fig. 6d) shows the presence of Fe, Ni, Cr, and Al.

Miley and Shrestha [17] have done a compilation of reported transmutation results in LENR experiments. The experiments done include gas permeation of Pd films, electrolytic loading of Pd, and glow discharge. The new elements reported in these experiments are the same as those reported in Pd/D co-deposition. The fact that different experimentalists worldwide, using a variety of deuterium loading procedures, are observing the same elements adds further validation of the results.

4. Summary of Results between 2005 To Present

In 2004 at ICCF14 in Marseille France, George Miley of the University of Illinois Urbana suggested that Pd/D co-deposition experiments should be done using CR-39 as a detector. According to Miley, the CR-39 used in their experiments showed evidence of DD fusion particles. A search of the literature on CR-39 was done. Columbia Resin 39 (CR-39) is an optically clear, amorphous, thermoset plastic. The use of CR-39 to detect nuclear particles was first

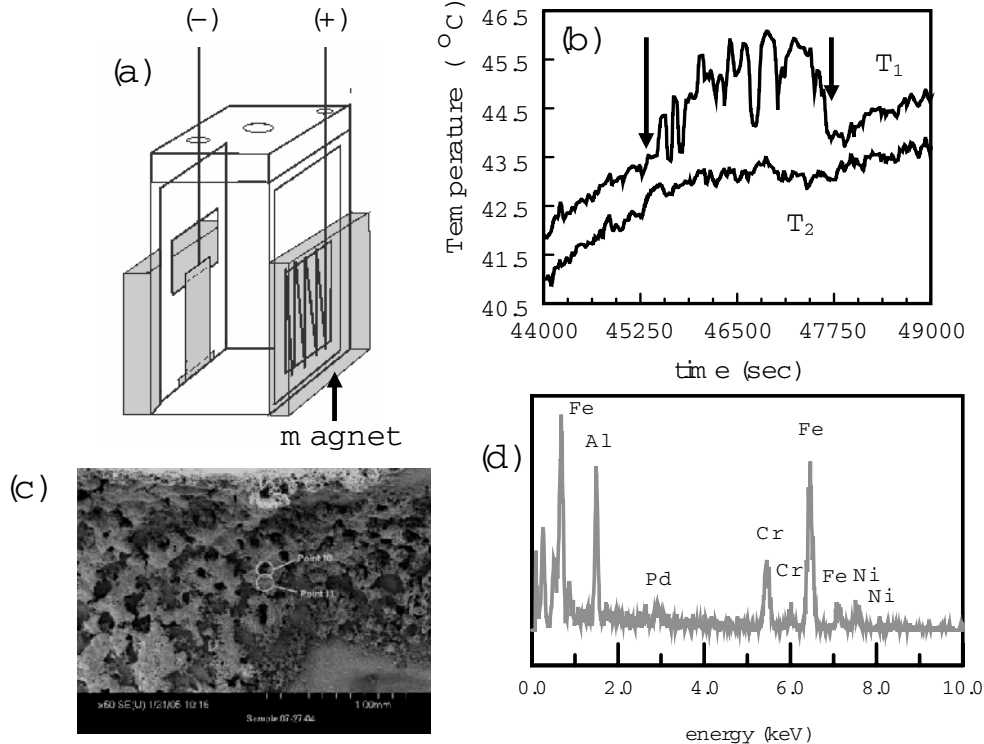


Figure 6. (a) Schematic of the cell used in the current external magnetic field experiment. (b) Temperature response of the Au/Pd cathode (T_1) and solution (T_2) for an experiment conducted in the presence of a 120 G magnetic field. Cell current was at -400 mA. Arrows indicate when the electromagnet was turned on and off. (c) SEM of Pd deposit exposed to a 2500 G external magnetic field. (d) Elemental analysis of point 10 in (c).

demonstrated by Cartwright et al. [18] in 1978. When an energetic, charged particle traverses through a solid state nuclear track detector (SSNTD) such as CR-39, it creates along its path an ionization trail that is more sensitive to chemical etching than the bulk material [18,19]. After treatment with a chemical etchant, tracks due to the energetic particles remain in the form of holes or pits which can be examined with the aid of an optical microscope. The size, depth of penetration, and shape of the track provides information about the mass, charge, energy, and direction of motion of the particle that created the track [20]. Besides detection of charged particles such as protons and alphas, CR-39 can also be used to detect neutrons [21]. In order to detect neutrons with CR-39, the neutron must either scatter or undergo a nuclear reaction with the proton, carbon, or oxygen atoms comprising the SSNTD to form a moving charged particle. It is the track of this neutron-generated charged particle that is revealed upon etching. While most neutrons will pass through without undergoing a reaction, approximately one in 100,000 neutrons passing through 1mm thick CR-39 will create such a track. Other advantages for using CR-39 in Pd/D co-deposition experiments are its integrating capability, which is good for events that occur in bursts or sporadically; the existence of a threshold for registration; ruggedness; insensitivity to electromagnetic noise; and resistance to chemical and mechanical damage.

4.1. Experimental configuration

Figure 7a shows linear energy transfer (LET) curves for charged particles traversing through water. When the cathode emits a charged particle, that charged particle has to traverse through a layer of water before it is registered by the detector. As can be seen, a thin layer of water between the cathode and the detector greatly impacts the charged particle. The larger the charge and size of the particle, the greater the reduction in energy as it travels through the water layer. Also, the deposit formed as a result of Pd/D co-deposition (Fig. 1a) has a cauliflower morphology that will cause the thickness of the water layer to vary. To minimize these effects, the CR-39 detector needs to be in close proximity to the detector as shown in the schematic in Fig. 7b.

4.2. Control experiments

Figure 8a shows damage observed in CR-39 used in a Pd/D co-deposition experiment conducted on an Ag wire in the presence of an external magnetic field. The damage coincides with the placement of the cathode indicating that the cathode is the source of the damage. While the degree of damage looks to be substantial, that is only because CR-39 is a constantly integrating detector. When an event occurs, it gets permanently stamped on the surface of the detector. The damage observed in Fig. 8a had accumulated over a two-week time period. At higher magnification (Fig. 8b) it can be seen that there are circular and elliptical tracks as well as small and large tracks. A triple track is circled. Such tracks result from a reaction that yields three particles of equal mass and energy. The significance of the triple tracks will be discussed *vide infra*.

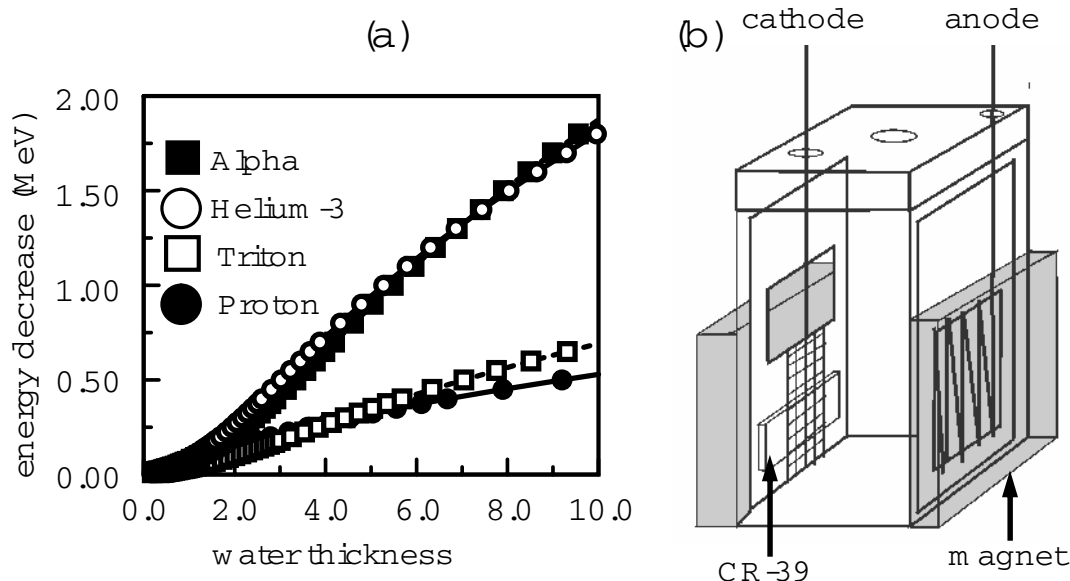


Figure 7. (a) LET curves for charged particles in water. (b) Schematic of the cell.

Figure 8c,d shows tracks obtained in CR-39 resulting from exposure to an ^{241}Am source and Pd/D co-deposition, respectively. The photomicrographs were obtained at $1000\times$ magnification. The top images were obtained by focusing the microscope optics on the surface of the detector and the bottom images are an overlay of two images taken at two

different focusing depths (surface and bottom of the pits). When the microscope optics are focused on the surface of the detector, the pits due to the alpha tracks are dark in color, Fig. 8c top image. Focusing inside the pits, a bright spot is observed, Fig. 8c bottom image. This bright spot is the endpoint of the particle that entered the detector [20]. Tracks have a conical shape. The bright spot inside the track is caused by the tip of the cone acting like a lens when the detector is backlit. These features, dark on the surface and bright spot inside, are diagnostic of a nuclear generated track. As seen in Fig. 8d, the pits obtained as a result of Pd/D co-deposition exhibit these same features. In contrast, features due to chemical damage are bright, shallow, irregular in shape, and exhibit no contrast.

A series of control experiments were conducted to show that the pits resulting from Pd/D co-deposition were not due to either radioactive contamination or to either chemical or mechanical damage [6]. The most notable experiment was replacing the PdCl_2 with CuCl_2 . For both systems, the same electrochemical reactions are occurring. At the cathode, a metal plates out on the electrode substrate and water is reduced to form deuterium gas. Oxygen and chlorine gas evolution occurs at the anode. The only significant difference is that metallic palladium absorbs deuterium and copper does not. Pits were observed for the Pd system and not the Cu. These results indicate that the pits are not due to chemical reactions with the evolving deuterium, oxygen, or chlorine gases; they are not due to the impingement of deuterium gas on the surface of the detector; and they are not due to the metal dendrites piercing into the surface of the detectors.

To determine the energies of the charged particles, experiments were conducted placing 6 μm thick Mylar between the cathode and the CR-39 detector [23]. Approximately 90% reduction in tracks was observed. LET curves indicate that the Mylar film cuts off <0.45 MeV protons and <1.45 MeV alphas. However, this does not take into account

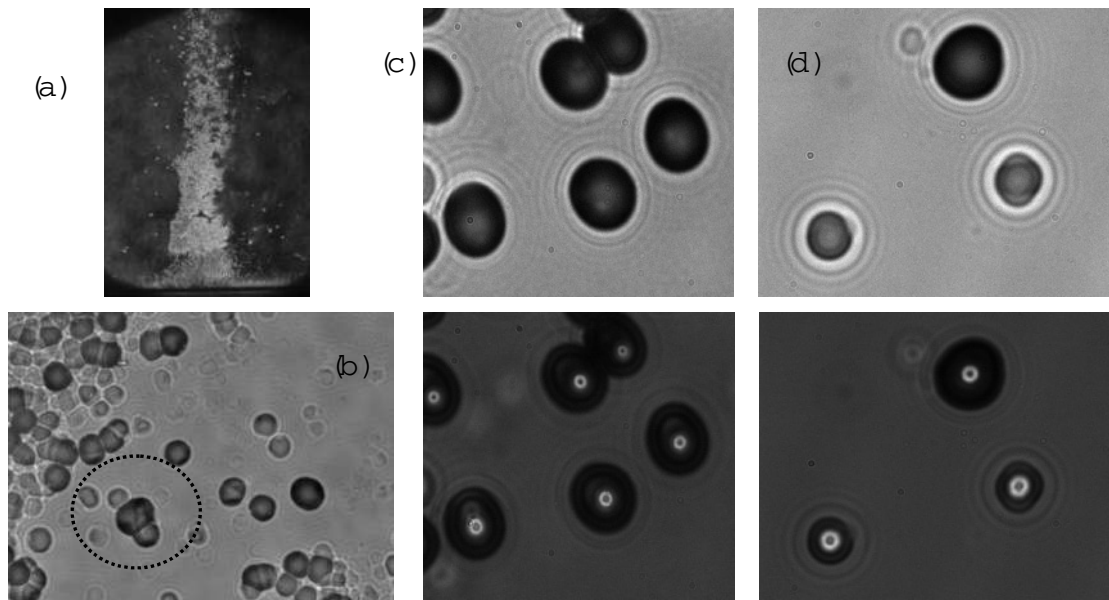


Figure 8. CR-39 photomicrographs of tracks obtained for Pd/D co-deposition done on an Ag wire in the presence of a magnetic field where (a) 20 \times magnification and (b) 500 \times magnification. A triple track is circled. (c) and (d) are photomicrographs obtained at 1000 \times magnification where (c) are tracks resulting from exposure to an ^{241}Am source and (d) are Pd/D co-deposition tracks. In (c) and (d) the top images were obtained by focusing the microscope optics on the surface of the detector and the bottom images are an overlay of two images taken at two different focusing depths (surface and bottom of the pits).

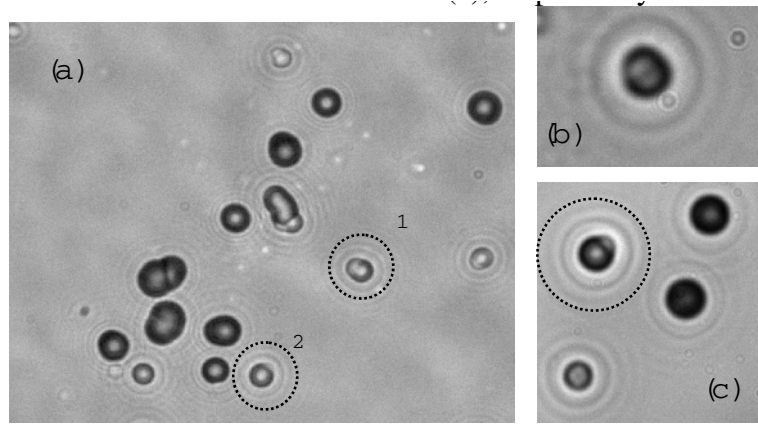


Figure 9. (a) Pd/D co-deposition tracks at $500\times$ magnification. (b) and (c) ~ 1 MeV alpha tracks obtained by placing $24\ \mu\text{m}$ of Mylar between a CR-39 detector and an ^{241}Am source. Images (b) and (c) taken with a magnification of $1000\times$. [23] (Reprinted with permission from *Eur. Phys. J. Appl. Phys.*)

the water layer the particle needs to traverse before it reaches the Mylar film. Given the cauliflower-morphology of the Pd deposit, the water film varies between 0 to $10\ \mu\text{m}$. Taking the water layer into account, the charged particles are primarily $<0.45\text{--}0.97\ \text{MeV}$ protons and $<1.45\text{--}3.30\ \text{MeV}$ alphas. Figure 9 compares Pd/D co-deposition tracks with ~ 1 MeV alpha tracks. The Pd/D co-deposition tracks, Figure 9a, are primarily circular in shape. There are some elliptically shaped tracks, two of which are circled. Figure 9b,c shows ~ 1 MeV alpha tracks. Like the Pd/D co-deposition tracks, these tracks are primarily circular in shape. This indicates that particles traveling at $\sim 90^\circ$ angle normal to the surface have sufficient energy to get through the water layer and Mylar to impinge on the detector. Particles traveling at oblique angles are blocked. The elliptical ~ 1 MeV tracks in 9(b) and circled track in 9(c) look similar to tracks Nos. 1 and 2 in 9(a), respectively.

4.3. Effect of cathode substrate

It was found that the cathode substrate influences the nuclear emissions observed in Pd/D co-deposition. When Pd/D co-deposition was done on a Ni screen in the absence of either an external electric or magnetic field, no tracks were observed in the CR-39 detector [6]. Instead the impression of the Ni screen was observed on the detector. It has been shown that CR-39 can be used in X-ray microscopy [24]. In the contact soft X-ray microscopy technique, the transmission X-ray image of a biological cell was recorded as latent damage on the CR-39 detector. After etching, the image of the cell was revealed as a relief on the polymer. To determine the effect of X and gamma rays on CR-39, experiments were done by exposing Cu-screen covered CR-39 detectors to a ^{137}Cs gamma ray source and to the X-ray source of an X-ray diffractometer. After etching, the impression of the Cu screen was observed in the detectors. These results were similar what was observed in the Ni-screen, no external field, Pd/D co-deposition experiments and suggest that the observed Ni screen damage is due to X-rays/gamma rays. However, when the Pd/D co-deposition experiments on Ni screen were done in the presence of either an external electric or magnetic field, tracks were obtained [6]. In contrast to the Ni screen experiments, tracks were obtained in the CR-39 detectors in Pd/D co-deposition on Ag, Au, and Pt wires in both the presence and absence of an external electric/magnetic field.

To further illustrate the effect of cathode substrate on the observed emissions, Pd/D co-deposition, in the absence of an external electric/magnetic field, was done on the cathode shown in Fig. 10. Half the cathode was a bare Ni screen

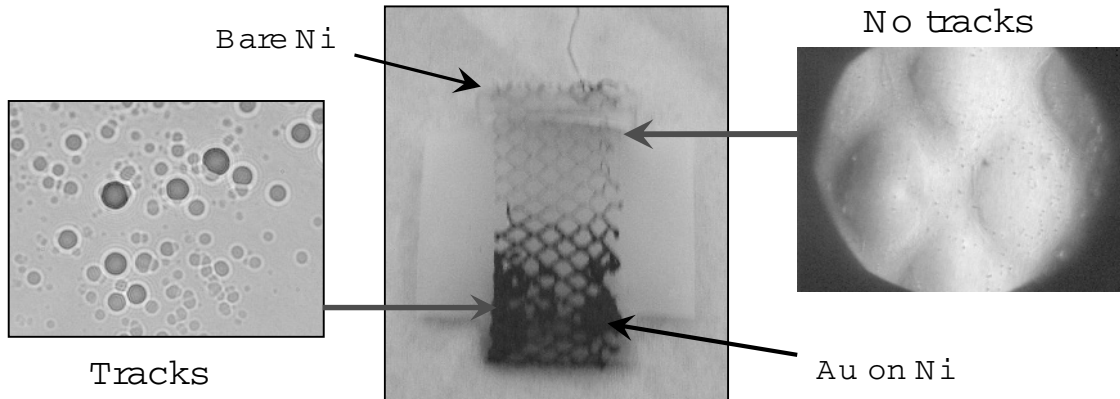


Figure 10. Results obtained on a CR-39 detector used in a Pd/D co-deposition experiment done in the absence of an external field. A photograph of the cathode is shown in the middle. Photomicrographs of the CR-39 are shown.

whereas the other half was Au electroplated onto the Ni screen. Based on prior experimental results, the expectation for this experiment was that the CR-39 detector in contact with the bare Ni would show an impression of the Ni screen whereas tracks would be observed on the Ni/Au half. Figure 10 summarizes the results. Microscopic examination after etching showed that, for the bare Ni half of the cathode, no tracks were observed. Instead, the impression of the Ni screen was observed on the surface of the detector. In contrast, tracks were observed on the Ni/Au half of the cathode. As both halves of the cathode experienced the same experimental conditions, it is difficult to explain such disparate results on chemical damage or radioisotope contamination.

4.4. Evidence of neutrons

In addition to tracks on the front surface of the CR-39 detectors used in Pd/D co-deposition experiments, tracks have also been observed on the backside (Fig. 11a). The detectors are 1 mm thick. The LET curves indicate that the only particles that can go through 1 mm thick CR-39 are >40 MeV alphas, >10 MeV protons, or neutrons. Figure 11b shows tracks in CR-39 created upon exposure to a ^{238}PuO fission source. The tracks are very similar to those shown in Fig. 11a and suggest that the backside tracks are due to neutrons. Specifically, the tracks in Fig. 11a,b are circular in shape. Some tracks are circular with small tails that are due to recoil protons that have exited the CR-39 at an oblique angle. In Fig. 11a,b, there are smaller shallower tracks. These are latent tracks which are due to neutron recoils deeper inside the detector. Additional etching will expose these recoil proton tracks that are deeper inside the plastic as shown in Fig. 11c. The top, $50\ \mu\text{m}$ diameter track was a surface track. After etching away an additional $53\ \mu\text{m}$ of the detector, the two recoil proton tracks deeper inside become visible.

Figure 8b shows a triple track that is circled. In SSNTDs such as CR-39, these triple tracks are indicative of DT neutrons causing a carbon atom to shatter into three alpha particles [25–28]. Figure 11d shows a triple track obtained from a different Pd/D co-deposition experiment. The left hand image of Fig. 11d was obtained by focusing the microscope optics on the surface of the detector. The three lobes of the triple track are clearly visible. The right hand photomicrograph shown in Fig. 11d is an overlay of two images taken with the microscope optics focused on the surface of the detector and the bottom of the pits. From this image, three particles breaking away from a center point are clearly visible. Figure 11e shows a DT neutron generated triple track that is very similar to the Pd/D co-deposition triple track shown in Fig. 11d. The number of triple tracks observed in Pd/D co-deposition is low. At most five to ten total such tracks have been detected on both the front and back surfaces of the detector. Both symmetric and asymmetric triple

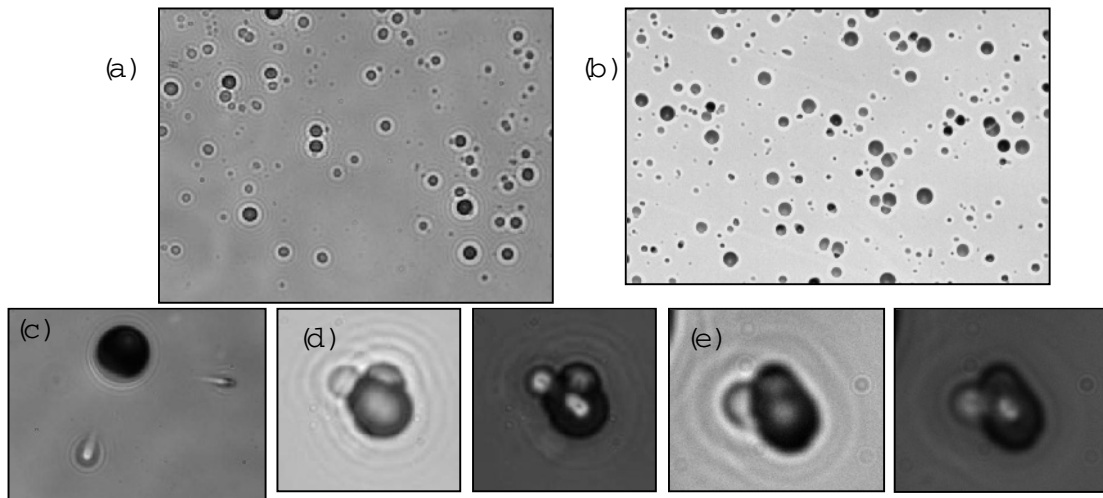


Figure 11. (a) Tracks on the backside of a CR-39 detector used in a Pd/D co-deposition experiment. (b) Tracks in CR-39 caused by neutrons from a ^{238}PuO fission source. (c) Results of sequential etching showing deeper proton recoil tracks. The black, $50\ \mu\text{m}$ diameter track on top is a surface track. Triple tracks obtained as a result of (d) Pd/D co-deposition and (e) exposure to DT neutrons. Left hand images in (d) and (e) obtained with the microscope optics focused on the surface of the detector. Right hand images in (d) and (e) are an overlay of two images taken at two different focusing depths (surface and bottom of the tracks). (c) and (d) reprinted with permission from *Naturwissenschaften* [29].

tracks have been observed in the CR-39 detectors used in Pd/D co-deposition experiments. The most likely source of the neutrons responsible for the triple tracks is DT fusion inside the Pd lattice.

5. Reproducibility

The SSC-Pacific results using Pd/D co-deposition have been replicated by others. Forsley did infrared imaging of a Ni screen cathode during Pd/D co-deposition and saw that the cathode was hotter than the solution. He also observed that the heat was not homogeneous but occurred as ‘hot spots.’ Excess heat production in the Pd/D co-deposition system was first measured by Miles [12] and then replicated by Letts [30]. Bockris et al. observed bursts of tritium in the gas and liquid phases using Pd/D co-deposition [31]. Their results were similar to those reported by Szpak et al. [10]. The CR-39 results have been replicated by Kowalski [32], Tanzella et al. [33], and Williams [32]. However, there has been some disagreement as to the origins/interpretations of the tracks observed in the CR-39 detectors used in the Pd/D co-deposition experiments. In particular, Kowalski has stated that the tracks are too large to be due to alpha particles [32,34]. However, both track modeling and the results shown in Figure 9 indicate that the Pd/D co-deposition generated tracks have the same size and shape as $\sim 1\ \text{MeV}$ alpha tracks. Figure 12 shows a side-by-side comparison of Pd/D co-deposition generated tracks and tracks created in CR-39 exposed to a $\sim 1\ \text{MeV}$ alpha source. The tracks are indistinguishable from one another.

Tanzella et al. [33] also conducted experiments placing a 6 μm Mylar film between the CR-39 detector and the cathode. While a $\sim 90\%$ reduction was observed in the SSC-Pacific experiments [23], Tanzella et al. reported a 99.9% decrease. Kowalski [34] has suggested that this difference is significant. A number of experimental factors, such as the proximity of the wires to the Mylar film, surface area, etc. could explain the reported differences between the SRI and the SSC-Pacific results. In their analysis of Tanzella’s CR-39 detectors, Lipson et al. only scanned under-dense track regions to better quantify the energy of the charged particle and recoil tracks. This will result in an undercounting

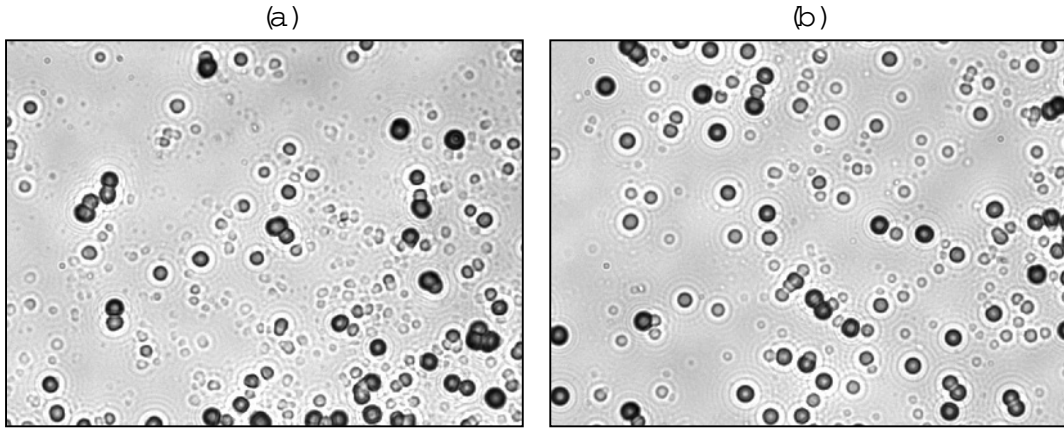


Figure 12. Photomicrographs obtained at 500 \times magnification for (a) Pd/D codeposition tracks and (b) \sim 1 MeV alpha tracks. (a) and (b) reprinted with permission from *J. Condensed Matter Nucl. Sci.* [35].

of tracks. Also different cathode substrates were used in the two experiments. The cathode substrate used in the SRI experiment was Ag while the SSC-Pacific experiment used Pt and Au wires in series. As discussed *vide supra*, the cathode substrate used in the co-deposition process does affect the emission of the energetic particles. Kowalski [34] has also stated that the particles reported by Tanzella et al. [33] were identified as 2.5 MeV protons. This is not correct. Using a sequential etching protocol, the tracks were attributed to proton recoils resulting from the interaction of the detector with fast neutrons. The energy of the neutrons responsible for these recoils was determined to be 2.5 MeV.

6. Conclusions

Using the Pd/D co-deposition technique developed by Stanislaw Szpak, we have detected excess heat, gamma and X-ray emissions, tritium production, transmutation, charged particles, and neutrons. Taking all the data together, we have compelling evidence that nuclear reactions are stimulated by electro-chemical processes. To date, these observations have been published in 22 peer-reviewed journal papers and two peer-reviewed symposium books.

Acknowledgments

This work was funded by the SPAWAR Systems Center Pacific ILIR and S and T Initiatives Programs, the Defense Threat Reduction Agency (DTRA), and JWK Corporation. The authors acknowledge the contributions of Dr. Stanislaw Szpak, retired from SPAWAR Systems Center Pacific, who pioneered the Pd/D co-deposition process. The authors would like to thank Massoud Simnad and Todd Evans for their assistance in conducting the infrared imaging experiments; Gordon Chase for his analysis of the cathode after the thermal runaway; M. Ashraf Imam of NRL for SEM analysis of cathodes; and Mark Morey, Jim Tinsley, and Paul Hurley of National Security Technologies, LLC for exposing CR-39 to a DT neutron source. They would also like to thank Dr. Gary Phillips, nuclear physicist, retired from the Naval Research Laboratory, for valuable discussions in interpreting the CR-39 data. Finally, they would like to thank Lowell Wood and George Miley for suggesting experiments to detect mini-explosions and energetic particles.

References

[1] S. Szpak, P.A. Mosier-Boss, *Phys. Letts. A* **221** (1996) 141–143.

- [2] S. Szpak, P.A. Mosier-Boss, S.R. Scharber, J.J. Smith, *J. Electroanal. Chem.* **337** (1992) 147–163.
- [3] S. Szpak, P.A. Mosier-Boss, S.R. Scharber, J.J. Smith, *J. Electroanal. Chem.* **380** (1995) 1–6.
- [4] S. Szpak, P.A. Mosier-Boss, J.J. Smith, *J. Electroanal. Chem.* **379** (1994) 121–127.
- [5] S. Szpak, P.A. Mosier-Boss, J.J. Smith, *J. Electroanal. Chem.* **302** (1991) 255–260.
- [6] P.A. Mosier-Boss, S. Szpak, F.E. Gordon, L.P.G. Forsley, *Eur. Phys. J. Appl. Phys.* **40** (2007) 293–303.
- [7] S. Szpak, P.A. Mosier-Boss, J.J. Smith, *Phys. Lett. A* **210** (1996) 382–390.
- [8] Gordon Chase, Private communication.
- [9] P.A. Mosier-Boss, S. Szpak, *Nuovo Cimento Soc. Ital. Fis. A* **112** (1999) 577–587.
- [10] S. Szpak, P.A. Mosier-Boss, R.D. Boss, J.J. Smith, *Fusion Technol.* **33** (1998) 38–51.
- [11] S. Szpak, P.A. Mosier-Boss, R.D. Boss, J.J. Smith, *J. Electroanal. Chem.* **373** (1994) 1–9.
- [12] S. Szpak, P.A. Mosier-Boss, M. H. Miles, M. Fleischmann, *Thermochimica Acta* **410** (2004) 101–107.
- [13] S. Szpak, P.A. Mosier-Boss, M. H. Miles, *Fusion Technol.* **36** (1999) 234–241.
- [14] J. O'M. Bockris, R. Sundaresan, Z. Minevski, D. Letts, Triggering of heat and sub-surface changes in Pd–D systems, *The Fourth International Conference on Cold Fusion*, Lahaina, Maui, 1993.
- [15] S. Szpak, P.A. Mosier-Boss, C. Young, F.E. Gordon, *J. Electroanal. Chem.* **580** (2005) 284–290.
- [16] S. Szpak, P.A. Mosier-Boss, C. Young, F.E. Gordon, *Naturwissenschaften* **92** (2005) 394–397.
- [17] G.H. Miley, P.J. Shrestha, Transmutation reactions and associated low-energy nuclear reactions effects in solids, in *Low-Energy Nuclear Reactions Sourcebook*, Vol. I, J. Marwan, S.B. Krivit (eds.), Washington D.C., American Chemical Society, 2008, pp. 173–218.
- [18] B.G. Cartwright, E.K. Shirk, P.B. Price, *Nucl. Instr. Meth.* **153** (1978) 457.
- [19] J.R. Bhakta, G.D. Hardcastle, J.C.H. Miles, *Radiation Measurements* **30** (1999) 29.
- [20] D. Nikezic, K.N. Yu, *Materials Sci. Eng. R* **46** (2004) 51.
- [21] J.A. Frenje et al., *Rev. Sci. Instrum.* **73** (2002) 2597.
- [22] G.W. Phillips et al., *Radiat. Prot. Dosim.* **120** (2006) 1.
- [23] P.A. Mosier-Boss, S. Szpak, F.E. Gordon, L.P.G. Forsley, *Eur. Phys. J. Appl. Phys.* **46** (2009) 30901: 1–12.
- [24] K. Amemiya et al., *Nucl. Instrum. Meth. Phys. Rev. B* **187** (2002) 361.
- [25] S.A.R. Al-Najjar, A. Abdel-Naby, S.A. Durrani, *Nuclear Tracks* **12** (1986) 611.
- [26] A.M. Abdel-Moneim A. Abdel-Naby, *Radiation Measurements* **37** (2003) 15.
- [27] J.K. Palfalvi, et al., *Radiation Measurements* **40** (2005) 428.
- [28] L. Saj.-Bohus, et al., *Radiation Measurements* **40** (2005) 442.
- [29] P.A. Mosier-Boss, S. Szpak, F.E. Gordon, L.P.G. Forsley, *Naturwissenschaften* **96** (2009) 135–142.
- [30] D. Letts, Personal communication.
- [31] J. O'M. Bockris, C.-C. Chien, D. Hodko, Z. Minevski, Tritium and helium production in palladium electrodes and the fugacity of deuterium therein, *The Third International Conference on Cold Fusion*, Nagoya, Japan, 1992.
- [32] L. Kowalski, *Eur. Phys. J. Appl. Phys.* **44** (2008) 287.
- [33] A.G. Lipson, A.S. Roussetski, E.I. Saunin, F. Tanzella, B. Earle, M. McKubre, Analysis of the CR-39 detectors from SRI's SPAWAR/Galileo type electrolysis experiments #7 and #5. Signature of possible neutron emission, *Proceedings of 8th International Workshop on Anomalies in Hydrogen/Deuterium Loaded Metals*, J. Rothwell, P. Mobberley (eds.), 2008, pp. 182–203.
- [34] L. Kowalski, *J. Condensed Matter Nucl. Sci.* **3** (2010) 1.
- [35] P.A. Mosier-Boss, F.E. Gordon, L.P.G. Forsley, *J. Condensed Matter Nucl. Sci.* **3** (2010) 4.



Research Article

Bose–Einstein Condensate Theory of Deuteron Fusion in Metal

Yeong E. Kim *

Purdue Nuclear and Many-body Theory (PNMBT) Group, Department of Physics, Purdue University, West Lafayette, IN 47906, USA

Abstract

Theory of Bose–Einstein condensation nuclear fusion (BECNF) has been developed to explain many diverse experimental results of deuteron induced nuclear reactions in metals, observed in electrolysis and gas loading experiments. The theory is based on a single conventional physical concept of Bose–Einstein condensation of deuterons in metal and provides a consistent theoretical description of the experimental results. The theory is capable of explaining most of the diverse experimental observations, and also has predictive powers as expected for a quantitatively predictive physical theory. It is shown that the fusion energy transfer to metal can be accomplished by the stopping power of metal without invoking hypothesis of fusion energy transfer to metal lattice vibrations. It is also shown that observed anomalous tritium production can be explained by a sub-threshold resonance reaction mechanism. The basic concept and important features of the BECNF theory is presented, and theoretical explanations of the experimental observations are described. Key experimental tests of theoretical predictions are proposed and discussed.

© 2011 ISCMNS. All rights reserved.

Keywords: Bose–Einstein Condensation, Deuteron fusion in metal, Nano-scale materials, Sub-threshold resonance reaction

PACS: 24.10.-i, 24.10.Cn, 24.30.-v, 61.46.-w, 89.30.Jj

1. Introduction

Two decades ago, Fleischmann and Pons reported excess heat generation in electrolysis experiment using the negatively polarized Pd/D–D₂O system [1]. Since then, many others have reported experimental observations of excess heat generation and anomalous nuclear reactions occurring in metal at ultra low energies from electrolysis experiments [2] and gas-loading experiments [2–4]. These anomalous reaction rates cannot be explained using the conventional theory of nuclear reactions in free space, which predicts extremely low nuclear reaction rates at ultra low energies (≤ 10 eV) due to the Gamow factor arising from the Coulomb repulsion between two charged nuclei undergoing nuclear-reaction process.

Recently, a consistent conventional theoretical explanation [5] is provided for the anomalous results observed for deuteron induced nuclear reactions in metal at ultra low energies. The theory is capable of explaining most of the experimental observations, and provides theoretical predictions that can be tested experimentally for the confirmation of the theory. A detailed description of the theoretical explanation, based on the theory of Bose–Einstein condensation

*E-mail: yekim@purdue.edu

nuclear fusion is presented along with suggested experimental tests of predictions of the theory and a discussion of the scalability of the fusion rates based on the theory.

2. Anomalous Experimental Results

The conventional deuterium fusion in free space proceeds via the following nuclear reactions:

- {1} $D + D \rightarrow p (3.02 \text{ MeV}) + T (1.01 \text{ MeV})$,
- {2} $D + D \rightarrow n (2.45 \text{ MeV}) + {}^3\text{He} (0.82 \text{ MeV})$,
- {3} $D + D \rightarrow {}^4\text{He} + \gamma (23.8 \text{ MeV})$.

The cross-sections (or reaction rates) for reactions {1} and {2} have been measured by beam experiments at intermediate energies ($\geq 10 \text{ keV}$). The cross-sections for reactions {1}–{3} are expected to be extremely small at low energies ($\leq 10 \text{ eV}$) due to the Gamow factor arising from Coulomb barrier between two deuterons. The measured cross-sections have branching ratios: $(\sigma\{1\}, \sigma\{2\}, \sigma\{3\}) \approx (0.5, 0.5, 10^{-6})$.

From many experimental measurements by Fleischmann and Pons [1], and many others [2–4] over 20 years since then, the following experimental results have emerged. At ambient temperatures or low energies ($\leq 10 \text{ eV}$), deuterium fusion in metal proceeds via the following reactions:

- {4} $D(m) + D(m) \rightarrow p(m) + T(m) + 4.03 \text{ MeV (m)}$,
- {5} $D(m) + D(m) \rightarrow n(m) + {}^3\text{He}(m) + 3.27 \text{ MeV (m)}$,
- {6} $D(m) + D(m) \rightarrow {}^4\text{He}(m) + 23.8 \text{ MeV (m)}$,

where m represents a host metal lattice or metal particle. Reaction rate R for {6} is dominant over reaction rates for {4} and {5}, i.e., $R\{6\} \gg R\{4\}$ and $R\{6\} \gg R\{5\}$.

Experimental observations reported from electrolysis and gas-loading experiments are summarized below (not complete):

- [a] The Coulomb barrier between two deuterons are suppressed.
- [b] Excess heat production (the amount of excess heat indicates its nuclear origin).
- [c] ${}^4\text{He}$ production commensurate with excess heat production, no 23.8 MeV γ -ray.
- [d] More tritium is produced than neutron $R\{4\} \gg R\{5\}$.
- [e] Production of nuclear ashes with anomalous rates: $R\{4\} \ll R\{6\}$ and $R\{5\} \ll R\{6\}$.
- [f] Production of hot spots and micro-scale craters on metal surface.
- [g] Detection of radiations.
- [h] “Heat-after-death”.
- [i] Requirement of deuteron mobility ($D/\text{Pd} > \sim 0.9$, electric current, pressure gradient, etc.).
- [j] Requirement of deuterium purity ($H/D \ll 1$).

All of the above experimental observations are explained either quantitatively or qualitatively in terms of theory of Bose–Einstein condensation nuclear fusion (BECNF) in the previous publication [5] and this paper. In this paper, additional theoretical explanations are provided for the *observations* [a]–[d] in later sections. Theoretical explanations of other *observations* such as “Heat-after-death” [h] have been described in [5].

3. Deuteron Mobility and Bose–Einstein Condensation of Deuterons in Metals

Development of Bose–Einstein condensate theory of deuteron fusion in metal is based upon a single hypothesis that deuterons in metal are mobile and hence are capable of forming Bose–Einstein condensates.

3.1. Deuteron mobility in metal

Experimental proof of proton (deuteron) mobility in metals was first demonstrated by Coehn in his hydrogen electro-migration experiment [7,8]. The significance of Coehn's experimental results [7] is emphasized by Bartolomeo et al. [9]. A theoretical explanation of Coehn's results [7] is given by Isenberg [10]. The Coehn's experimental fact is not well known in review articles and textbooks.

There are other experimental evidences [11–15] that heating and/or applying an electric field in a metal causes hydrogens and deuterons in a metal to become mobile, thus leading to a higher density for quasi-free mobile deuterons in a metal. It is expected that the number of mobile deuterons will increase, as the loading ratio D/metal of deuterium atoms increases and becomes larger than one, $D/\text{metal} \geq 1$.

Mobility of deuterons in a metal is a complex phenomenon and may involve a number of different processes [15]: coherent tunneling, incoherent hopping, phonon-assisted processes, thermally activated tunneling, and over-barrier jump/fluid like motion at higher temperatures. Furthermore, applied electric fields as in electrolysis experiments can enhance the mobility of absorbed deuterons.

3.2. BEC fraction of deuterons in metal

Fraction of deuterons in a metal satisfying BEC condition can be estimated as a function of the temperature. The BEC condensate fraction $F(T) = N_{\text{BE}}/N$ can be calculated from integrals,

$$N_{\text{BE}} = \int_0^{E_c} n(E)N(E)dE \quad \text{and} \quad N = \int_0^{\infty} n(E)N(E)dE$$

where $n(E)$ is either Bose–Einstein or Maxwell–Boltzmann distribution function, $N(E)$ is the density of (quantum) states, and E_c is the critical kinetic energy of deuteron satisfying the BEC condition $\lambda_c = d$, where λ_c is the de Broglie wavelength of deuteron corresponding to E_c and d is the average distance between two deuterons. For $d = 2.5 \text{ \AA}$, we obtain $F(T = 300 \text{ K}) \approx 0.084$ (8.4 %), $F(T = 77.3 \text{ K}) \approx 0.44$ (44%), and $F(T = 20.3 \text{ K}) \approx 0.94$ (94%). At $T = 300 \text{ K}$, $F = 0.084$ (8.4%) is not large enough to form BEC since motions of deuterons are limited to several lattice sites and the probability of their encounters are very small. On the other hand, at liquid nitrogen (77.3 K) and liquid hydrogen (20.3 K) temperatures, probability of forming BEC of deuterons is expected to be $\Omega \approx 1$. This suggests that experiments at these low temperatures can provide tests for enhancement of the reaction rate R_t , Eq. (4) (described in Section 4) as predicted by BECNF theory.

4. Bose–Einstein Condensate Theory of Deuteron Fusion in Metal

For the BEC theory of deuteron fusion in metal, we make one basic assumption that mobile deuterons in a micro/nano-scale metal particle form a BEC state. The validity of this assumption is to be verified by independent experimental tests suggested in this paper. Because of the above assumption, the theory cannot be applied to deuterons in bulk metals, which do not provide well-defined localized trapping potentials for deuterons.

For applying the concept of the BEC mechanism to deuteron fusion in a nano-scale metal particle, we consider N identical charged Bose nuclei (deuterons) confined in an ion trap (or a metal grain or particle). Some fraction of trapped deuterons are assumed to be mobile as discussed above. The trapping potential is 3-dimensional (nearly sphere) for nano-scale metal particle, or quasi 2-dimensional (nearly hemi-sphere) for micro-scale metal grains, both having surrounding boundary barriers. The barrier heights or potential depths are expected to be an order of energy ($\leq 1 \text{ eV}$) required for removing a deuteron from a metal grain or particle. For simplicity, we assume an isotropic harmonic potential for the ion trap to obtain order of magnitude estimates of fusion reaction rates.

N -body Schrödinger equation for the system is given by

$$H\Psi = E\Psi \quad (1)$$

with the Hamiltonian H for the system given by

$$H = \frac{\hbar^2}{2m} \sum_{i=1}^N \Delta_i + \frac{1}{2} m\omega^2 \sum_{i=1}^N r_i^2 + \sum_{i < j} \frac{e^2}{|\mathbf{r}_i - \mathbf{r}_j|} \quad (2)$$

where m is the rest mass of the nucleus. Only two-body interactions (Coulomb and nuclear forces) are considered since we expect that three-body interactions are expected to be much weaker than the two-body interactions.

Electron degrees of freedom are not explicitly included, assuming that electrons and host metal atoms provide a host trapping potential. In the presence of electrons, the Coulomb interaction between two deuterons can be replaced by a screened Coulomb potential in Eq. (2). Hence, Eq. (2) without the electron screening effect represents the strongest case of the reaction rate suppression due to the Coulomb repulsion.

The approximate ground-state solution of Eq. (1) with H given by Eq. (2) is obtained using the equivalent linear two-body method [16,17]. The use of an alternative method based on the mean-field theory for bosons yields the same result (see Appendix in [18]). Based on the optical theorem formulation of low energy nuclear reactions [19], the ground-state solution is used to derive the approximate theoretical formula for the deuteron–deuteron fusion rate in an ion trap (micro/nano-scale metal grain or particle). The detailed derivations are given elsewhere including a short-range nuclear strong interaction used [18,20].

Our final theoretical formula for the nuclear fusion rate R_{trap} for a single trap containing N deuterons is given by [5]

$$R_{\text{trap}} = 4(3/4\pi)^{3/2} \Omega S B \frac{N^2}{D_{\text{trap}}^3} \propto \Omega \frac{N^2}{D_{\text{trap}}^3}, \quad (3)$$

where N is the average number of Bose nuclei in a trap/cluster, D_{trap} is the average diameter of the trap, $B = 2r_B/(\pi\hbar)$, $r_B = \hbar^2/(2\mu e^2)$, and S is the S -factor of the nuclear fusion reaction between two deuterons. For $D(d, p)T$ and $D(d, n)^3\text{He}$ reactions, we have $S \approx 55 \text{ keV-barn}$. We expect also $S \approx 55 \text{ keV-barn}$ or larger for reaction {6}. $B = 1.4 \times 10^{-18} \text{ cm}^3/\text{s}$ with S in units of keV-barn in Eq. (3). $SB = 0.77 \times 10^{-16} \text{ cm}^3/\text{s}$ for $S = 55 \text{ keV-barn}$. Only one unknown parameter is the probability of the BEC ground state occupation, and the S -factor. We note that $\Omega \leq 1$.

The total fusion rate R_t is given by

$$R_t = N_{\text{trap}} R_{\text{trap}} = \frac{N_D}{N} R_{\text{trap}} \propto \Omega \frac{N}{D_{\text{trap}}^3} \quad (4)$$

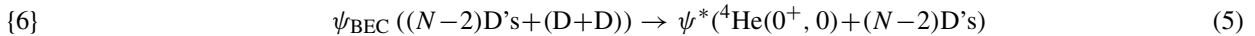
where N_D is the total number of deuterons and $N_{\text{trap}} = N_D/N$ is the total number of traps. Eq. (4) shows that the total fusion rates, R_t , are very large if $\Omega \approx 1$.

Equations (3) and (4) provide an important result that nuclear fusion rates R_{trap} and R_t do not depend on the Gamow factor in contrast to the conventional theory for nuclear fusion in free space. This could provide explanations for overcoming the Coulomb barrier and for the claimed anomalous effects for low-energy nuclear reactions in metals. This is consistent with the conjecture noted by Dirac [21] and used by Bogolubov [22] that boson creation and annihilation operators can be treated simply as numbers when the ground state occupation number is large. This implies that for large N each charged boson behaves as an independent particle in a common average background potential and the Coulomb interaction between two charged bosons is suppressed. This provides an explanation for the *observation* [a]. There is a simple classical analogy of the Coulomb field suppression. For a uniform charge distribution in a sphere, the electric field is a maximum at the surface of the sphere and decreases to zero at the center of the sphere.

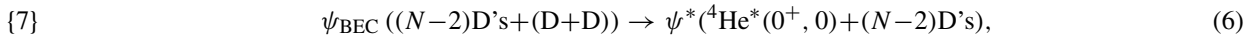
5. Theoretical Explanation of Anomalous ${}^4\text{He}$ Production (the *observations* [b] and [c])

Above the ground-state of ${}^4\text{He}$, there are five excited continuum states, ${}^4\text{He}^*$ (J^π, T), below the ($\text{D} + \text{D}$) threshold energy [23]: ($0^+, 0, 20.21 \text{ MeV}$), ($0^-, 0, 21.01 \text{ MeV}$), ($2^-, 0, 21.84 \text{ MeV}$), ($2^-, 1, 23.33 \text{ MeV}$), and ($1^-, 1, 23.64 \text{ MeV}$). In this paper, we consider reaction rates for two exit channels to ${}^4\text{He}$ ($0^+, 0, 0.0 \text{ MeV}$) and ${}^4\text{He}^*$ ($0^+, 0, 20.21 \text{ MeV}$) states.

For a single trap (or metal particle) containing N deuterons, the deuteron-deuteron fusion can proceed with the following two reaction channels:



and



where ψ_{BEC} is the Bose–Einstein condensate ground state (a coherent quantum state) with N deuterons and ψ^* are final excited continuum states. ${}^4\text{He}$ in Eq. (5) represents the ground state with spin-parity, 0^+ , while ${}^4\text{He}^*$ in Eq. (6) represents the 0^+ excited state at 20.21 MeV with the resonance width of $\Gamma(T + p) = 0.5 \text{ MeV}$ above the ${}^4\text{He}$ ground state [23]. It is assumed that excess energy (Q -value) is absorbed by the BEC state and shared by $(N - 2)$ deuterons and reaction products in the final state. It is important to note that reaction {6}, described by Eq. (5), cannot occur in free space due to the momentum conservation, while reaction {7} described by Eq. (6) can occur with $Q = 0$ in free space without violating the momentum conservation, due to the resonance width of $\Gamma(T + p) = 0.5 \text{ MeV}$ [23] for the 20.21 MeV state of ${}^4\text{He}^*$.

For micro/nano-scale metal particles, the above consideration shows that excess energies (Q) lead to a micro/nano-scale firework type explosion, creating a crater/cavity and a hot spot with fire-work like star tracks. The size of a crater/cavity will depend on number of neighboring Pd nanoparticles participating in BEC fusion almost simultaneously. Hot spots and craters have been observed in experiments reported by Srinivasan et al. [24] and others. This provides a theoretical explanation of *observation* [f].

We now consider the total momentum conservation for reaction {6} described by Eq. (5). The initial total momentum of the initial BEC state with N deuterons (denoted as D^N) is given by $\vec{P}_{\text{D}^N} \approx 0$. Because of the total momentum conservation, the final total momenta for reaction {6} is given by

$$\{6a\} \quad \vec{P}_{\text{D}^{N-2} {}^4\text{He}} \approx 0, \quad \langle T_{\text{D}} \rangle \approx \langle T_{{}^4\text{He}} \rangle \approx Q(6)/N,$$

where $\langle T \rangle$ represents the average kinetic energy.

For the reaction {6} with Eq. (5), the average kinetic energy for each deuteron is $\langle T \rangle = Q(6)/N = 23.85 \text{ MeV}/N$. For the case of 5 nm Pd trap, the number of deuterons in the trap is $N = \sim 4450$, and $\langle T \rangle \approx 5.36 \text{ keV}$. With this deuteron kinetic energy of $\sim 5.36 \text{ keV}$, a question arises whether the hot-fusion reactions {1} and {2} can occur as the secondary reactions to the primary reaction {6}. Since the secondary reactions {1} and {2} have not been observed, there have been speculations such as a hypothesis that the fusion energy of 23.85 MeV is transferred to metal lattice vibrations thus producing heat. In the following a more convincing alternative explanation is described that transfer of the fusion energy of 23.85 MeV to the metal is accomplished as the energy loss of energetic (5.36 keV) deuteron due to the stopping power of the metal.

Experimental values of the conventional hot-fusion cross section $\sigma(E)$ for reaction {1} or {2} have been conventionally parameterized as [25]

$$\sigma(E) = \frac{S(E)}{E} \exp[-(E_G/E)^{1/2}], \quad (7)$$

where E_G is the “Gamow energy” given by $E_G = (2\pi\alpha Z_D Z_D)^2 M c^2 / 2$ or $E_G^{1/2} \approx 31.39 \text{ keV}^{1/2}$ for the reduced mass $M \approx M_D/2$ for reactions {1} or {2}. The value E is measured in keV in the center-of-mass (CM) reference frame. The S factor, $S(E)$, is extracted from experimentally measured values [26] of the cross section $\sigma(E)$ for $E \geq 4 \text{ keV}$ and is nearly constant [27]; $S(E) \approx 52.9 \text{ keV-barn}$, for reactions {1} or {2} in the energy range of interest here, $E \leq 100 \text{ keV}$.

The probability $P(E_i)$ for a deuteron to undergo the conventional hot-fusion reaction {1} or {2} while slowing down in the deuterated palladium metal can be written as [28]

$$\begin{aligned} P(E_i) &= 1 - \exp \left[\int dx n_D \sigma(E_{DD}) \right] \approx \int dx n_D \sigma(E_{DD}) \\ &= n_D \int_0^{E_i} dE_D \frac{1}{|dE_D/dx|} \sigma(E_{DD}). \end{aligned} \quad (8)$$

Values E_D and E_{DD} are the deuteron kinetic energies in the LAB and CM frames respectively, ($E_{DD} = E_D/2$). The stopping power [29] for deuterium in PdD for $E_D \leq 20 \text{ keV}$ is given by [28]

$$\frac{dE_D}{dx} = 3.70 \times 10^{-15} n_{pd} \sqrt{E_D} \text{ eV} \cdot \text{cm}^2 \quad (9)$$

for deuterium in palladium and

$$\frac{dE_D}{dx} = 0.89 \times 10^{-15} n_D \sqrt{E_D} \text{ eV/cm}^2 \quad (10)$$

for deuterium in deuterium. Therefore, the stopping power for deuterium in PdD is given by the sum of Eqs. (9) and (10),

$$\frac{dE_D}{dx} = 3.1 \times 10^5 \sqrt{E_D} \text{ keV/cm}, \quad (11)$$

for $n_{pd} = 6.767 \times 10^{22} \text{ cm}^{-3}$ and $n_D = n_{pd}$. If we use Eq. (11) and the conventional extrapolation formula for $\sigma(E)$ given by Eq. (7), the integration in Eq. (8) can be performed analytically to yield the following expression for Eq. (8) [28]:

$$P(E_i) = 1.04 \times 10^{-6} \exp(-44.40/\sqrt{E_i}), \quad (12)$$

where E_i is in keV (LAB), for reactions {1} or {2} assuming equal branching ratios (50% each).

For the case of 5 nm diameter Pd particle containing ~ 4450 deuterons, Eq. (12) with $E_i = 5.36 \text{ keV}$ yields $P(5.36 \text{ keV}) \approx 0.49 \times 10^{-14}$ per deuteron. Therefore, the total fusion probability for 4450 deuterons is $P_{\text{total}} \approx 2.2 \times 10^{-11}$, yielding a branching ratio of $R\{1\}/R\{6\} \approx R\{2\}/R\{6\} \approx 10^{-11}$. Tritium production from {1} and neutron production from {2} are both negligible. Even for the case of $E_i \approx 20 \text{ keV}$ with a 3.2 nm Pd particle containing ~ 1200 deuterons, $P(20 \text{ keV}) 0.5 \times 10^{-10}$, and the total fusion probability is $P_{\text{total}}(20 \text{ keV}) \approx 0.6 \times 10^{-7}$. Therefore, the fusion energy of 23.85 MeV in {6} is transferred to the metal by the stopping power of the metal without appreciable production of T and n from {1} and {2}.

6. Theoretical Explanation of Anomalous Tritium Production (the *observation [d]*)

There have been many reports of anomalous tritium and neutron production in deuterated metal from electrolysis experiments [30–34] and gas/plasma loading experiments [24, 35–40]. The reported branching ratio of $R(T)/R(n)$ ranges from 10^7 to 10^9 in contrast to the conventional free-space reactions branching ratio of $R\{1\}/R\{2\} \approx 1$. In this

section, we present a theoretical explanation of this anomalous tritium production based on the BECNF theory, utilizing a sub-threshold resonance ${}^4\text{He}^*$ (0^+) state at 20.21 MeV with a resonance width of $\Gamma(T + p) = 0.5$ MeV as shown in Fig. 1.

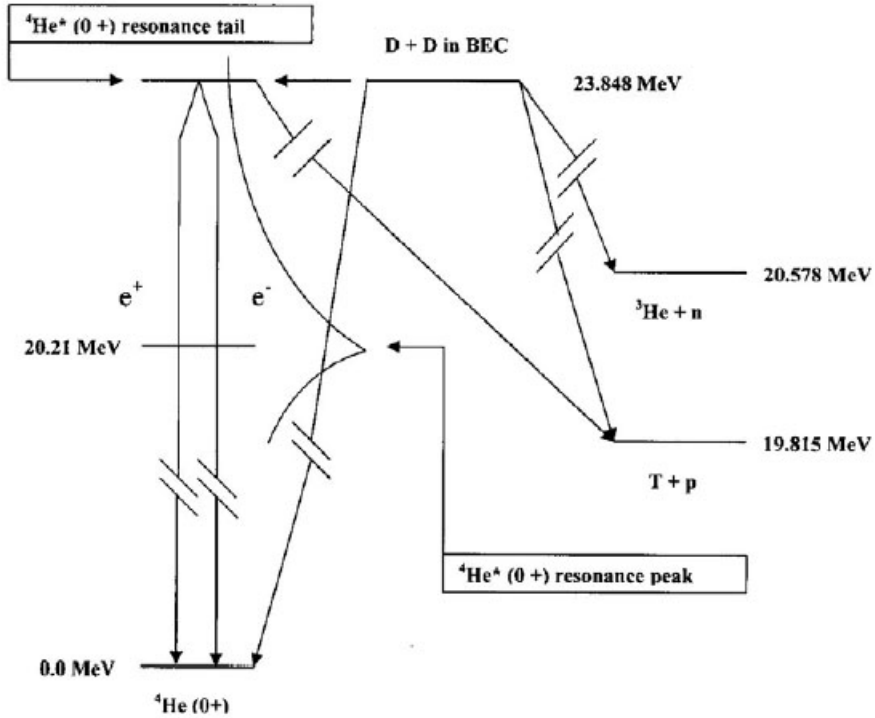


Figure 1. Energy levels of nuclei $A = 4$.

In Fig 1, reaction channels {4}–{7} are shown. Decay channels {7a} and {7b} (described below) are also shown. Due to a selection rule derived in [5], both {4} and {5} are suppressed, and we have $R\{4\} \ll R\{6\}$ and $R\{5\} \ll R\{6\}$. In free space, {6} would be forbidden due to the momentum conservation. For this section (Eqs. (13)–(15)), we use a new energy level scale, which sets $E = 0$ for $(D + D)$ state, and $E = -23.85$ MeV for the ${}^4\text{He}$ ground state. Q -value remains the same since $Q = E_i - E_f$.

Reaction {7}, described by Eq. (6), can proceed via a sub-threshold resonance reaction [41,42]. The cross section for the sub-threshold resonance reaction is given by Breit–Wigner expression [42]

$$\sigma(E) = \pi \tilde{\lambda}^2 w \frac{\Gamma_1(E)\Gamma_2}{(E - E_R)^2 + (\Gamma/2)^2}, \quad (13)$$

where $\tilde{\lambda} = \lambda/2\pi$, $\lambda = h/mv$ (de Broglie wavelength), w is a statistical factor, E_R is the sub-threshold resonance energy. Γ_2 is a partial decay width and Γ is the total decay width to the final states. If E is measured from the threshold energy $E = 0$ of $(D + D)$ state, $E_R = (20.21 \text{ MeV} - 23.85 \text{ MeV}) = -3.64 \text{ MeV}$.

After combining Eq. (7) with Eq. (13), the $S(E)$ factor can be written as

$$S(E) = E \exp\left(\sqrt{E_G}/\sqrt{E}\right) \pi \tilde{\chi}^2 w \frac{\Gamma_1(E)\Gamma_2}{(E - E_R)^2 + (\Gamma/2)^2}. \quad (14)$$

From Eq. (14), we obtain the $S(E)$ factor near zero energy as [41]

$$S(E) = \frac{\pi^2 \hbar^4}{4\mu^2 R_n^2 K_1^2(x)} w \theta_0^2 F_{BW}(E), \quad F_{BW}(E) = \frac{\Gamma_2}{(E - E_R)^2 + (\Gamma/2)^2}, \quad (15)$$

where μ is the reduced mass in units of atomic mass unit (931.494 MeV), R_n is the nuclear radius, and $K_1(x)$ is the modified Bessel function of order unity with argument $x = (8Z_1Z_2e^2R_n\mu/\hbar^2)^{1/2}$. We note that $F_{BW}(ER)$ is a maximum at $E = E_R = -3.64$ MeV. At $E = 0$, $F_{BW}(0)$ is reduced to $F_{BW}(0) = 0.47 \times 10^{-2} F_{BW}(E_R)$. Equation (15) shows that the $S(E)$ factor has a finite value at $E = 0$ and drops off rapidly with increasing energy E . θ_i^2 is the reduced width of a nuclear state, representing the probability of finding the excited state in the configuration i , and the sum of θ_i^2 over i is normalized to 1. The dimensionless number θ_i^2 is generally determined experimentally and contains the nuclear structure information.

For the entrance channel, $D + D \rightarrow {}^4\text{He}^*(0^+, 0, 23.85 \text{ MeV}, Q = 0)$, there are two possible decay channels as shown in Fig. 1:

$$\{7a\} \quad {}^4\text{He}^*(0^+, 0) \rightarrow T(1.01 \text{ MeV}) + p(3.02 \text{ MeV}),$$

$$\{7b\} \quad {}^4\text{He}^*(0^+, 0) \rightarrow {}^4\text{He}(0^+, 0, 0.0) \text{ (ground state)},$$

$S(E)$ factors are calculated from Eq. (15) using $E = 0$ at a tail of the ${}^4\text{He}^*(0^+, 0)$ resonance at 20.21 MeV. $E = 0$ corresponds to 23.85 MeV above ${}^4\text{He}(0^+, 0)$ ground state. The calculated $S(E)$ can be used in Eqs. (3) and (4) to obtain the total fusion reaction rate. We will estimate $S(E)$ factors for the decay channels, (7a) and (7b), using Eq. (15) in the following.

For the decay channel {7a}, $\Gamma_2 = \Gamma\{7a\} = 0.5 \text{ MeV}$ [23]. When this value of Γ_2 is combined with other appropriate inputs in Eq. (15), the extracted S -factor for the decay channel {7a} is $S\{7a\} \approx 1.4 \times 10^2 \theta_0^2 \text{ keV-barn}$ for $E \approx 0$. In [5], it was shown that the neutron production rate $R\{5\}$ is suppressed, i.e. $R\{5\} \ll R\{6\}$ due to a selection rule. Since $({}^3\text{He} + n)$ state has a resonance width of $\Gamma_2({}^3\text{He} + n) = 0$ [23], this value of $S\{7a\}$ may provide an explanation of the reported branching ratio of $R(T)/R(n) \approx 10^7 - 10^9$ [24, 30–40] or $R(n)/R(T) \approx 10^{-7} - 10^{-9}$.

If we assume $S\{6\} \approx 55 \text{ keV-barn}$ (this could be much larger), we expect the branching ratio $R\{7a\}/R\{6\} = R(T)/R({}^4\text{He}) \approx 2.6 \theta_0^2 \approx 2.6 \times 10^{-6}$ if $\theta_0^2 \approx 10^{-6}$. Experimental measurements of $R(T)/R({}^4\text{He})$ are needed to determine θ_0^2 . If $S\{6\} (= S({}^4\text{He}))$ is determined to be larger from future experiments, $R(T)/R({}^4\text{He})$ is reduced accordingly. From a previous section, we have theoretical prediction that $R(n)/R({}^4\text{He}) < 10^{-11}$. Combining this with the above theoretical prediction of $R(T)/R({}^4\text{He}) \approx 2.6 \theta_0^2$, we have $R(n)/R(T) < 0.38 \times 10^{-11}/\theta_0^2$. If we assume $\theta_0^2 \approx 10^{-6}$, we have $R(n)/R(T) < 0.38 \times 10^{-5}$, which is consistent with reported values of $10^{-7} \approx 10^{-9}$.

For the decay channel {7b} ($0^+ \rightarrow 0^+$ transition), γ -ray transition is forbidden. However, the transition can proceed via the internal $e^+ e^-$ pair conversion. The transition rate for the internal electron pair conversion is given by

$$\omega = \frac{1}{135\pi} \left(\frac{e^2}{\hbar c}\right)^2 \frac{\gamma^5}{\hbar^5 c^4} R_N^4, \quad R_N^2 = \left| \langle \psi_{\text{exc}}, \sum_i r_i^2 \psi_{\text{g.s.}} \rangle \right| \approx R_n^2 \phi_0, \quad (16)$$

where γ is the transition energy, R_n is the nuclear rating, and $\phi_0 = \langle \psi_{\text{exc}} | \psi_{\text{g.s.}} \rangle$. Eq. (16) was derived by Oppenheimer and Schwinger [43] in 1939 for their theoretical investigation of $0^+ \rightarrow 0^+$ transition in ${}^{16}\text{O}$. The rate for the internal electron conversion is much smaller by many order of magnitude.

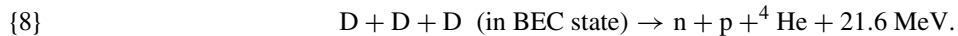
For our case of $0^+ \rightarrow 0^+$ transition {7b}, we obtain $\omega \approx 1.75 \times 10^{13} \phi_0^2/\text{s}$, and $\Gamma\{7b\} = \hbar\omega \approx 1.15 \times 10^{-2} \phi_0^2 \text{ eV}$ using appropriate inputs in Eq. (16). Using $\Gamma_2 = \Gamma\{7b\} = 1.15 \times 10^{-2} \phi_0^2 \text{ eV}$ in Eq. (15), the extracted S-factor for decay channel {7b} is $S\{7b\} \approx 3.3 \times 10^{-6} \theta_0^2 \phi_0^2 \text{ keV-barn}$ for $E \approx 0$, yielding a branching ratio, $R\{7b\}/R\{7a\} \approx S\{7b\}/S\{7a\} \approx 2.4 \times 10^{-8} \phi_0^2$. Experiments are needed for testing this predicted branching ratio.

7. Theoretical Explanations of Anomalous Neutron Production

Experimental observation of $R(n)/R(T) \approx 10^{-7}$ – 10^{-9} [24,36–40] is anomalous since we expect $R(n)/R(T) \approx 1$ from “hot” fusion reactions, {1} and {2}. In this section, we explore nuclear reactions producing neutrons at anomalously low rates.

There are three possible processes that can produce neutrons. The first process is the secondary “hot” fusion reaction {2} producing 2.45 MeV neutrons as discussed with Eqs. (7)–(12). The rate for this secondary reaction is extremely small, $R\{2\}/R\{6\} = R(n)/R(^4\text{He}) < 10^{-11}$, as shown previously.

The second process is a 3D BECNF reaction. In [5], it is shown that both reactions {4} and {5} are suppressed due to a selection rule [5]. It was also suggested that the following 3D BECNF is possible:



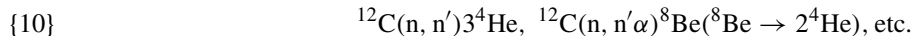
This reaction is a secondary effect since the probability for {8} is expected to be much smaller than the 2D BECNF reaction {6}; it is suppressed further due to the selection rule described in [5].

The third process is a “hot” fusion reaction $\text{T}(\text{d}, \text{n})^4\text{He}$,



induced by 1.01 MeV T produced from reaction {7a}. Since the cross-section for reaction {9} is large and a maximum (several barns) at $E_{\text{D}} \approx 100 \text{ keV}$ [44], neutrons from this process may contribute substantially to the branching ratio $R(n)/R(T) = 10^{-7}$ – 10^{-9} .

Energetic neutrons from the reaction {9} described above could induce the following reactions:



as reported recently by Mosier-Boss et. al. [45].

To test the above theoretical interpretation, based on the process {9}, we need to measure/detect (i) tritium production, (ii) Bremsstrahlung radiations from energetic electrons going through metal, (iii) 0.51 MeV γ -rays from e^+e^- annihilation, (iv) energetic electrons from e^+e^- pair production, (v) γ -rays from the following reaction:



and (vi) γ -rays from reaction {12} induced by 0.3 MeV protons from {7a}:



The cross-section for {11} with thermal neutrons is $\sim 0.5 \text{ mb}$.

8. Proposed Experimental Tests of Theoretical Predictions

8.1. Experimental test for metal particle size

The first experimental test of the BEC mechanism for deuterium fusion with nano-scale Pd particles was carried out in 2002 with Pd blacks loaded by high-pressure deuterium gas [46] in our laboratory in the Physics Building at Purdue University. The result of this experiment shows no excess heat production. This may be because Pd nano-particles (Pd

Blacks) used had too large sizes (80–180 nm) and were clumped together (not isolated). The recent report of deuteron gas-loading experiment by Arata and Zhang [3] show positive results of observing excess heat and ${}^4\text{He}$ production using ~ 5 nm Pd particles imbedded in ZrO_2 and purified deuterium. The recent experimental results by Kitamura et al. [4] using ~ 10 nm Pd particles have confirmed the results of Arata and Zhang [3], and also is consistent with one of theoretical predictions of the BECNF theory [5]. The theoretical prediction is that the reaction rate for smaller palladium particles is expected to be greater than the reaction rate for larger palladium particles, R (smaller Pd) $> R$ (larger Pd). Their experimental data shown in Fig. 3(a) (~ 104 nm Pd particles) and Fig. 3(c) (~ 10 nm Pd particles) in their paper [4] is consistent with the above prediction. Their data in Fig. 3(c) are also consistent with the requirement of deuteron mobility in metal (the *observation* [i] described in [5] (in this case the reaction occurs only when the pressure gradient exists).

8.2. Experimental test for anomalous tritium production

For experimental tests of the sub-threshold resonance reaction described in Section 6, it is desirable to carry out high-sensitivity detections of weak signals (i) of Bremsstrahlung radiations from energetic electrons going through metal and (ii) of 0.51 MeV γ -rays from e^+e^- annihilation, as well as (iii) ${}^4\text{He}$ production, during tritium production experiments to test the predicted branching ratio $R\{7b\}/R\{7a\} \approx S\{7b\}/S\{7a\} \approx 10^{-8}\phi_0^2$, and also to determine the branching ratio $R\{7a\}/R\{6\}$ which in turn can provide information on θ_0^2 for $S\{7a\}$ and also $S(E)$ for reaction {6}.

8.3. Experimental test for fusion-rate enhancement at low temperatures

As discussed in a previous section, the BEC fraction and the probability Ω of the BEC ground-state occupation will increase at lower temperatures. This increase of Ω will enhance the total fusion rate R_t , Eq. (4). This prediction can be tested by carrying out experiments at low temperatures. For an example, thermal cycling experiment [24] and other experiments [35–40] should be repeated with micro/nano-scale Titanium particles.

8.4. Experimental test for fusion-rate enhancement at high pressures

High pressures will shorten the average distance between two deuterons in metal, thus enhancing the BEC fraction and hence Ω . This enhances the total fusion rates R_t , Eq. (4). This prediction can be tested by carrying out experiments at high pressures.

The null results reported by Baranowski et al. [47] and Silvera and Moshary [48] from their high-pressure deuterium gas-loading experiments may be due to their use of bulk metals. It is desirable to carry out similar experiments with micro/nano-scale metal particles.

8.5. Experimental tests for fusion-rate enhancement with ultra-high density deuteron clusters

Recently, Lipson et al. [49,50], Holmlid et al. [51], and Miley et al. [52] have been developing ultra-high density deuteron clusters on palladium thin film with densities approaching $10^{24}/\text{cm}^3$ corresponding to an average distance $d = 1 \text{ \AA}$ between two deuterons satisfying the BEC requirement at ambient temperature. This ultra-high density deuteron clusters could be used as test beds for BECNF theory as described above and also as test beds for BEC of deuterons in metal described below.

8.6. Experimental tests of Bose–Einstein condensation of deuterons in metal

BECNF theory is based on one single physical hypothesis that mobile deuterons in a metal/grain/particle form a Bose–Einstein condensate. Therefore, it is important to explore experimental tests of this basic hypothesis.

For the atomic Bose–Einstein condensate, many properties of the BE condensate have been investigated both experimentally and theoretically [53]. Gross-Pitaevskii theory [53], based on Gross-Pitaevskii equation and its extensions, provides a consistent theoretical description of the experimental observations (i)–(iv) listed below.

- (i) Determination of critical velocity for superfluidity of BEC [54].
- (ii) Determination of dynamic structure factor by Bragg scattering experiment [55,56].
- (iii) Observation of rotation/quantized vortices [57].
- (iv) BEC on optical lattices [58].
- (v) Josephson effect [59] as a signature of superfluidity (experimental tests yet to be done) [53,60].

It is desirable to carry out similar experiments (i)–(v) for investigating properties of the Bose–Einstein condensate of deuterons in micro/nano-scale metal grains or particles. However, BEC of deuterons in metal are imbedded with electrons in metal lattice, which acts as a trap, while the atomic BEC is created in a magnetic trap. Therefore, we do not know theoretically to what extent Gross-Pitaevskii theory for the atomic BEC is applicable to the BEC of deuterons in metal. We need to develop an appropriate theory (or theories) as well as carrying out experimental tests.

However, there is a simple basic fundamental experimental test of the BEC and superfluidity of deuterons in metal: measurement of the diffusion rates of deuterons and protons in metal at low temperatures. Theoretical prediction is that the diffusion rate of deuterons is expected to be larger than that of protons at lower temperatures in metal.

One of the advantages of carrying out experiments for observing the BEC of deuterons in micro/nano-scale metal particles is that the modern nano-fabrication techniques allow us to fabricate them in multitude with great precision in one-dimension, two-dimension, and three-dimension. This capability will allow us to produce the BEC of deuterons in metal (A) in a double-well potential trapping two Bose–Einstein condensates for studying the Josephson effect ((v) above), and also (B) in lower-dimensional traps to study the BEC in one-dimension and two-dimension.

9. Potential Applications to Other Phenomena

There are other potential applications of the BEC of deuterons to other related phenomena listed in the following: (i) transient acoustic cavitation fusion [61,62], (ii) transmutation [63–66], and (iii) high-temperature superconductivity in deuterated metals and alloys [67]. These applications will be described in future publications. For proton–metal transmutations [63], we may have to reformulate the BECNF theory based on BEC of molecular Bosons (H_2 's) or Bosons formed by pairing of two protons in metals.

In 2005, Szpak et. al. [66] reported presence or “new” elements (Al, Mg, Ca, Si, Zn, ...) from an operating $Pd//D_2O, Li^+, Cl^-//Pt$ cell placed in an external electrostatic field. Their observation implies nuclear transmutation of a new kind.

Fusion of N deuterons (ND's) in BEC state is possible, but its probability would be much less than that of fusion of two deuterons (2D). Possible multi-deuteron BEC fusion reactions for formation of Ca, Si, Al, and Mg are: 20 D's \rightarrow 40 Ca + 297.6 MeV, 14 D's \rightarrow 28 Si + 205.4 MeV, 13 D's \rightarrow 26 Al + 177.9 MeV, and 12 D's \rightarrow 24 Mg + 171.6 MeV. Independent experiments are needed to test the results reported by Szpak et. al. [66] and the above theoretical interpretation.

10. Summary and Conclusions

Based on a single physical concept of Bose–Einstein condensation of deuterons in metal, theory of Bose–Einstein condensation nuclear fusion (BECNF) is developed to explain deuteron-induced nuclear reactions observed in metal. It is shown that the BECNF theory is capable of explaining qualitatively or quantitatively all of ten experimental observations (listed in Section 2) reported from electrolysis and gas-loading experiments.

It is shown that the fusion energy transfer to metal can be accomplished by the stopping power of metal without invoking a hypothesis of fusion energy transfer to metal lattice vibrations. It is also shown that observed anomalous tritium production can be explained by incorporating a sub-threshold resonance reaction mechanism into the BECNF theory.

The BECNF theory has also predictive powers as expected for a quantitatively predictive physical theory. Experimental tests of theoretical predictions are proposed and discussed, including tests of the basic hypothesis of Bose–Einstein condensation of deuterons in metal. Experimental tests are needed not only to test theoretical predictions, but also to improve and/or refine the theory, which are needed for designing reproducible experiments and for scaling up BECNF processes for potential practical applications.

References

- [1] M. Fleischman, S. Pons, Electrochemically induced nuclear fusion of deuterium, *J. Electroanal. Chem.* **261** (1989) 301; Errata, *J. Electroanal. Chem.* **263** (1989) 187.
- [2] P.L. Hagelstein et al., New physical effects in metal deuterides, *Proceedings of ICCF-11*, Marseille, France, Condensed Matter Nuclear Science, World Scientific, Singapore, 2006, pp. 23–59, and references therein.
- [3] Y. Arata, Y.C. Zhang, *J. High Temp. Soc.* **34**(2) (2008) 85.
- [4] A. Kitamura et al., *Phys. Lett. A* **373** (2009) 3109, and references therein.
- [5] Y.E. Kim, Theory of Bose–Einstein condensation mechanism for deuteron-induced nuclear reactions in micro/nano-scale metal grains and particles, *Naturwissenschaften* **96** (2009) 803 and references therein.
- [6] S. Pons, M. Fleischmann, Heat after death, *Trans. Fusion Technol.* **26** (Dec. 1994) 87.
- [7] A. Coehn, Proof of the existence of protons in metals (with discussion), *Z. Electrochem.* **35** (1929) 676–680.
- [8] A. Coehn, W. Specht, Ueber die Beteiligung von Protonen an der Elektrizitätsleitung in Metallen (Role of protons in electric conductivity of metals), *Z. Phys.* **83** (1930) 1–31.
- [9] C. Bartolomeo, M. Fleischmann, G. Larramona, S. Pons, J. Roulette, H. Sugiura, G. Preparata, Alfred Coehn and After: The α , β , γ of the Palladium–Hydrogen System, *Trans. Fusion Technol.* **26** (Dec. 1994) 23.
- [10] I. Isenberg, The ionization of hydrogen in metals, *Phys. Rev.* **79** (1950) 736.
- [11] B. Duhm, Diffusion of hydrogen in palladium, *Z. Phys.* **94** (1935) 435–456.
- [12] Q.M. Barer, *Diffusion in and through Solids*, Cambridge University Press, New York, NY, 1941.
- [13] J.F. Macheche, J.-C. Rat, A. Herold, Study of hydrogen–metal systems: Potential induced by the diffusion of hydrogen in palladium, *J. Chim. Phys. Phys. Chim. Biol.* **73** (1976) 983–987.
- [14] F.A. Lewis, Palladium–hydrogen system 2, *Platinum Met. Rev.* **26** (1982) 20–27, 70–78, 121–128.
- [15] Y. Fukai, *The Metal–Hydrogen System*, Second Edition, Springer, Berlin, Heidelberg, New York, 2005.
- [16] Y.E. Kim, A.L. Zubarev, Ground state of charged bosons confined in a harmonic trap, *Phys. Rev. A* **64** (2001) 013603-1.
- [17] Y.E. Kim, A.L. Zubarev, Equivalent linear two-body method for Bose–Einstein condensates in time-dependent harmonic traps, *Phys. Rev. A* **66** (2002) 053602-1.
- [18] Y.E. Kim, A.L. Zubarev, Ultra low-energy nuclear fusion of Bose nuclei in nano-scale ion traps, *Italian Phys. Soc. Proc.* **70** (2000) 375.
- [19] Y.E. Kim, Y.J. Kim, A.L. Zubarev, J.H. Yoon, Optical theorem formulation of low-energy nuclear reactions, *Phys. Rev. C* **55** (1997) 801.
- [20] Y.E. Kim, A.L. Zubarev, Nuclear fusion for Bose nuclei confined in ion traps, *Fusion Technol.* **37** (2000) 151.
- [21] P.A.M. Dirac, *The Principles of Quantum Mechanics*, Second Edition, Chapter XI, Section 63, p. 235, Clarendon Press, Oxford, 1935.
- [22] N. Bogolubov, On the theory of superfluidity, *J. Phys.* **11** (1966) 23–29.
- [23] D.R. Tilley, H.R. Weller, G.M. Hale, Energy level of light nuclei $A = 4$, *Nucl. Phys. A* **541** (1992) 1.
- [24] M. Srinivasan et al., Observation of tritium in gas/plasma loaded titanium samples, *AIP Conf. Proc.* **228** (1990) 514.
- [25] W.A. Fowler, G.R. Caughlan, B.A. Zimmerman, Thermonuclear reactions rates, *Annu. Rev. Astron. Astrophys.* **5** (1967) 525; see also Thermonuclear reaction rates II, *Annu. Rev. Astron. Astrophys.* **13** (1975) 69.

- [26] A. von Engel, C.C. Goodyear, Fusion cross-section measurements with deuterons of low energies, *Proc. R. Soc. A* **264** (1961) 445.
- [27] A. Krauss, H.W. Becker, H.P. Trautvetter, C. Rolfs, Low energy fusion cross-sections of D + D and D + ${}^3\text{He}$ reactions, *Nucl. Phys.* **465** (1987) 150.
- [28] Y.E. Kim, Surface reaction mechanism for deuterium–deuterium fusion with a gas/solid-state fusion device, *Fusion Technol.* **19** (1990) 558–566; *AIP Conf. Proc.* **228** (1990) 807.
- [29] H.H. Anderson, J.F. Ziegler, *Hydrogen Stopping Powers and Ranges in All Elements*, Pergamon Press, New York, 1977.
- [30] E. S.C. Talcott, Electrolytic tritium production, *Fusion Technol.* **17** (1990) 680.
- [31] K. Cedzynska, S.C. Barrowes, H.E. Bergeson, L.C. Knight, F.W. Will, Tritium analysis in palladium with an open system analytical procedure, *Fusion Technol.* **20** (1991) 108.
- [32] F.G. Will, K. Cedzynska, D.C. Linton, Reproducible tritium generation in electrochemical-cells employing palladium cathodes with high deuterium loading, *J. Electroanal. Chem.* **360** (1993) 161; Tritium generation in palladium cathodes with high deuterium loading, *Trans. Fusion Technol.* **26** (Dec. 1994) 209.
- [33] J.O'M. Bockris, C.-C. Chien, D. Hodko, Z. Minevski, Tritium and helium production in palladium electrodes and the fugacity of deuterium therein, *Frontiers Science Series No. 4, Proceedings of the Third International Conference on Cold Fusion*, H. Ikegami (ed.), October 21–25, Nagoya, Japan, Universal Academy Press, Tokyo, Japan, 1993, p. 23.
- [34] R. Szpak, P. A. Mosier–Boss, R. D. Boss, J. J. Smith, On the behavior of the Pd/D system: evidence for tritium production, *Fusion Technol.* **33** (1998) 38–51.
- [35] A. DeNinno, A. Frattolillo, G. Lollobattista, L. Martinis, M. Martone, L. Mori, S. Podda, F. Scaramuzzi, Emission of neutrons as a consequence of titanium–deuterium interaction, II *Nuovo Cimento* **101A** (1989) 841.
- [36] T.N. Claytor, D.G. Tuggle, H.O. Menlove, P.A. Seeger, W.R. Doty, R.K. Rohwer, Tritium and neutron measurements from a solid-state cell, LA-UR-89-3946, October 1989, Presented at the NSF-EPRI workshop.
- [37] T.N. Claytor, D.G. Tuggle, H.O. Menlove, P.A. Seeger, W.R. Doty, R.K. Rohwer, Tritium and neutron measurements from deuterated Pd–Si, *AIP Conference Proceedings* 228, Anomalous Nuclear Effects in Deuterium/Solid Systems, S. Jones, F. Scaramuzzi, D. Worledge, Provo Utah (eds.), 1990, p. 467.
- [38] T.N. Claytor, D.G. Tuggle, S.F. Taylor, Evolution of tritium from deuterided palladium subject to high electrical currents, *Frontiers Science Series No. 4, Proceedings of the Third International Conference on Cold Fusion*, H. Ikegami (ed.), October 21–25, Nagoya, Japan., Universal Academy Press Tokyo, Japan, 1993, p. 217.
- [39] T.N. Claytor, D.G. Tuggle, S.F. Taylor, Tritium Evolution from various morphologies of deuterided palladium, *Proceedings of the Fourth International Conferences on Cold Fusion*, T.O. Passel (ed.), December 6–9, 1993, Maui, Hawaii, EPRI-TR-104188-V1 Project 3170, Vol. 1, 1994, p. 7–2.
- [40] T.N. Claytor et al., Tritium production from palladium alloys, *Proceedings of ICCF-7*, 1998, p. 88.
- [41] C.E. Rolfs, W.S. Rodney, *Cauldrons in the Cosmos: Nuclear Astrophysics*, Chapter 4, University of Chicago Press, Chicago, 1988.
- [42] J.M. Blatt, V.F. Weisskopf, *Theoretical Nuclear Physics*, John Wiley and Sons, 1952, 8th Printing, 1962.
- [43] J.R. Oppenheimer, J.S. Schwinger, *Phys. Rev.* **56** (1939) 1066.
- [44] G.S. Chulick, Y.E. Kim, R.A. Rice, M. Rabinowitz, Extended parameterization of nuclear-reaction cross sections for few-nucleon nuclei, *Nucl. Phys. A* **551** (1993) 255–268.
- [45] P.A. Mosier–Boss, S. Szpak, F.E. Gordon, L.P.G. Forsley, Triple tracks in Cr-39 as the result of Pd–D Co-deposition: evidence of energetic neutrons, *Naturwissenschaften* **96** (2009) 135; Characterization of Tracks in CR-39 Detectors as a Result of Pd/D Co-deposition, *Eur. Phys. J. Appl. Phys.* **46** (2009) 30901.
- [46] Y.E. Kim, D.S. Koltick, R. Pringer, J. Myers, R. Koltick, *Proceedings of ICCF-10*, Massachusetts, USA, 2003, Condensed Matter Nuclear Science, World Scientific, Singapore, 2006, pp. 789–799.
- [47] B. Baranowski et al., Search for ‘cold fusion’ in some Me–D systems at high pressures of gaseous deuterium, *J. Less-Common Met.* **158** (1990) 347.
- [48] I. F. Silvera, E. Moshary, Deuterated palladium at temperatures from 4.3 to 400 K and pressures to 105 kbar: search for cold fusion, *Phys. Rev. B* **42** (1990) 9143.
- [49] A. G. Lipson, A.G. Lipson, B. J. Heuser, C. Castano, G.H. Miley, B. Lyakhov, A. Mitin, Transport and magnetic anomalies below 70 K in a hydrogen-cycled Pd foil with athermally grown oxide, *Phys. Rev. B* **72** (2005) 212507.

- [50] A.G. Lipson, B.J. Heuser, C.H. Castano, A. Celik-Aktas, Observation of low-field diamagnetic contribution to the magnetic susceptibility of deformed single crystal PdHx, *Phys. Lett. A* **339** (2005) 414–423.
- [51] L. Holmlid, H. Hora, G.H. Miley, X. Yang, *Laser and Particle Beams* **27** (2009) 529.
- [52] G.H. Miley, H. Hora, X. Yang, Condensed matter ‘cluster’ reactions in LENRs, *Proceedings of the 14th International Conference on Condensed Matter Nuclear Science*, Washington, DC, 2008.
- [53] L. Pitaevskii, S. Stringari, *Bose–Einstein Condensation*, Clarendon Press, Oxford, 2003.
- [54] R. Onofrio et al., Observation of Superfluid flow in a Bose–Einstein Gas, *Phys. Rev. Lett.* **85** (2000) 228 and references therein.
- [55] J. Steinger et al., Bragg spectroscopy of a Bose–Einstein condensate, *Phys. Rev. Lett.* **82** (1999) 4569.
- [56] J. Steinhauser et al., Excitation spectrum of a Bose–Einstein condensate, *Phys. Rev. Lett.* **88** (2002) 120407-4.
- [57] F. Chevy et al., Inferometric detection of a single vortex in a dilute Bose–Einstein condensate, *Phys. Rev. A* **64** (2001) 031601 and references therein.
- [58] P. Pedri, et al., Expansion of a coherent array of Bose–Einstein condensates, *Phys. Rev. Lett.* **87** (2001) 220401.
- [59] B.D. Josephson, Possible new effects in superconductive tunneling, *Phys. Lett.* **1** (1962) 251.
- [60] L. Pitaevskii, S. Stringari, Thermal vs. quantum decoherence in double well trapped Bose–Einstein condensates, *Phys. Rev. Lett.* **87** (2001) 180402-1 and references therein.
- [61] R.S. Stringham, in the *Proceedings of ICCF-7* (1990), ICCF-10 (2003), ICCF-14 (2008).
- [62] A.G. Lipson, V.A. Klyuev, B.V. Deryaguin et al., *Sov. Tech. Phys. Lett.* **61**(10) (1990) 763.
- [63] G.H. Miley, P. Shrestha, Review of transmutation reactions in solids, *Proceedings of ICCF-10*, Boston, Massachusetts, Condensed Matter Nuclear Science, World Scientific, Singapore, 2006, pp. 361–378.
- [64] Y. Iwamura et al., *Jpn. J. App. Phys.* **41** (2002) 4642–4648.
- [65] Y. Iwamura et al., *Proceedings of ICCF-11*, Marseille, France, Condensed Matter Nuclear Science, World Scientific, Singapore, 2006, pp. 339–350.
- [66] S. Szpak et al., Evidence of nuclear reactions in the Pd lattice, *Naturwissenschaften* **92** (2005) 394.
- [67] P. Tripodi et al., Temperature coefficient of resistivity at compositions approaching PdH, *Phys. Lett. A* **276** (2000) 122–126.



Research Article

Energy Exchange Using Spin-Boson Models with Infinite Loss

Peter L. Hagelstein *

Research Laboratory of Electronics, Massachusetts Institute of Technology, Cambridge, MA, 02139, USA

Irfan U. Chaudhary

Department of Computer Science and Engineering, University of Engineering and Technology, Lahore

Abstract

From experiment we know that energy is produced in the Fleischmann–Pons experiment, and that commensurate ${}^4\text{He}$ is observed, with about 24 MeV per helium atom. From the absence of neutrons in experiments producing excess heat, we know that the helium nuclei are born with less than 10 keV energy on average. This results in the key theoretical problem associated with the Fleischmann–Pons experiment: where does the energy go? In the lossy spin-boson model, a large energy quantum is converted into many small quanta. Here we present a new analysis of the lossy spin-boson model.

© 2011 ISCMNS. All rights reserved.

Keywords: Excess power, Fleischmann–Pons effect, Lossy-spin boson model, Phonon exchange

1. Introduction

Since the first days after the initial announcement of Fleischmann and Pons in 1989 [1,2], we have been drawn to the problem of how an energy quantum at the nuclear scale (MeV) is split up into a very large number of smaller quanta at the atomic scale (meV). The basic problem which received much attention in the early years was the absence of deuteron–deuteron fusion neutrons in amounts commensurate with the energy observed, which was taken as evidence that no commensurate deuteron–deuteron fusion reactions occurred [3]. We now recognize that this observation is symptomatic of a much larger version of the problem. Cells producing excess heat have in some cases been monitored for neutrons, gammas, and X-rays with the result that very little radiation of any kind is observed correlated with excess power [4]. Consequently, we are driven to the conclusion that there are essentially no energetic particles of any kind produced commensurate with the energy observed.

To date, only one product has been shown to be correlated with excess power in amounts commensurate with the energy: ${}^4\text{He}$ atoms in the gas, with about one helium atom observed for every 24 MeV of energy produced [5–7]. In light of the comments above, we became interested in the question of how much energy the ${}^4\text{He}$ atom is born with,

*E-mail: plh@mit.edu

in order to be consistent with experimental observations. For example, there have been proposals that two deuterons come together in the vicinity of a Pd nucleus, creating a ${}^4\text{He}$ nucleus which is born with nearly 24 MeV following a recoil with the Pd (as commented on in [4], and similar to the mechanism discussed in [8]). In another proposal, four deuterons come together to make two ${}^4\text{He}$ nuclei, each of which carries away about 24 MeV in kinetic energy [9]. Since energetic ${}^4\text{He}$ nuclei would subsequently collide with other nuclei [10], we should be able to determine from experiment on average how much energy that the ${}^4\text{He}$ nuclei are born with from observations of secondary radiation correlated with excess power.

We carried out a set of simple calculations for neutron, X-ray, and gamma-ray yields for a wide range of initial ${}^4\text{He}$ energies [4]. We found that the most sensitive diagnostic is secondary neutron production from deuteron–deuteron fusion following a hard collision of a ${}^4\text{He}$ nucleus with a deuteron. We then looked through a large number of papers to find experiments where excess power was observed under conditions where neutron emission was monitored. A modest number of such experiments have been reported, and in the majority of these experiments there is no correlation between neutron emission and excess power. From an analysis of the experimental papers, it was possible to estimate upper limits for the number of source neutrons produced per unit energy to be between 0.008 and 0.8 n/J, which correspond to initial ${}^4\text{He}$ energies between 6.2 and 20.2 keV [4].

We can conclude from this that theoretical proposals like those mentioned above, which result in energetic ${}^4\text{He}$ nuclei, are inconsistent with experiment. A natural response might be to suggest that perhaps the ${}^4\text{He}$ nuclei pushes off a lighter particle, resulting in less kinetic energy (a neutrino in [11], and an electron in [8]). In this case, the lighter particle will carry most of the energy. We can get a rough estimate of the minimum ${}^4\text{He}$ recoil energy for any light particle by estimating the recoil energy in the case of a photon. Assuming that momentum is conserved, the ${}^4\text{He}$ nucleus would have a momentum of roughly

$$P = \frac{\hbar\omega}{c} \quad (1)$$

and a corresponding recoil energy of

$$E = \frac{P^2}{2M} = \frac{(\hbar\omega)^2}{2Mc^2} = 76 \text{ keV.} \quad (2)$$

As a result, we are able to rule out all proposed mechanisms in which the end result is ${}^4\text{He}$ and another particle with energy and momentum conserved, as inconsistent with experiment (since the secondary neutron yield for 76 keV alphas should have been seen).

1.1. Connection with theory

This argument is powerful, and it allows us to make progress on theory in several ways. If we know a certain class of models is inconsistent with experiment, then we can use our time more productively looking at models that are not inconsistent with experiment. In order to develop models that can be consistent with experiment, we need to understand new kinds of reaction mechanisms that work differently from the simple Rutherford billiard ball model, in which local conservation of momentum and energy dictates that product particles must be energetic. People have thought about this problem for several years, and we are in a position to summarize some of the different lines of thought that have resulted.

In light of the comments above, there seem to be three basic possibilities: (a) we can imagine a scenario in which the energy produced is somehow spread among a large number of particles initially, as a new kind of many-particle effect [12,13]; (b) perhaps the reaction initially creates a small number of energetic particles, which then slow down (in a new way that does not lead to secondary radiation) and exchange energy with a large number of particles; or (c) the

reaction energy is transferred initially in some way to a phonon mode, or some other low energy degree of freedom. Each of these possibilities individually would constitute a revolution in nuclear physics and condensed matter, if real.

At present, there is no known physical system that works as (a), in which direct coupling of a large reaction energy occurs between one system and a very large number of particles. The number of particles under discussion in the case of deuterons would be 24 MeV divided by the associated upper limit from experiment combined with a yield calculation, which in this case is under 1000 eV [14]. Hence, the first possibility imagines the direct coupling of 24 MeV to more than 24,000 deuterons. It may be that such energy redistribution might be possible in a tightly coupled system with much stronger particle–particle interactions, but it is very hard to see how this scenario might work in the PdD environment. While this kind of mechanism is discussed by Kim in [12,13], a calculation that demonstrates that such an effect can occur at a finite rate has to our knowledge not yet been given. We might also consider energy transfer to the Pd subsystem since it is coupled much more strongly; but even so, the Pd–Pd interactions are very weak compared to what would be required for direct distribution of 24 MeV.

The possibility that new physics might be involved in the slowing down of an energetic particle as in (b) can be contemplated. Working against this kind of approach is the problem of obtaining consistency with observations of secondary radiation, specifically secondary neutrons. The basic problem is that Rutherford scattering between a charged energetic particle (such as an alpha particle) and a deuteron is very efficient at producing energetic deuterons, which then have a high probability of subsequently producing neutrons from deuteron–deuteron fusion reactions. To be consistent with the observed lack of secondary neutron emission for MeV alphas, the secondary neutron yield would have to be reduced by 4–5 orders of magnitude [4]. If the initial alpha energy were 10 MeV or more, then the predicted yield of neutrons from deuteron break up reactions is nearly 10 orders of magnitude higher than observed. Experiments that have focused on the slowing down of charged particles over the past seventy years have unfortunately not provided evidence for the kind of large enhancement that would be required.

We have focused over the past decade or more on models in which the energy is transferred to low energy degrees of freedom as in (c). Working against the approach is the fact that there are no previous observations of similar effects in the nuclear physics literature. However, a somewhat similar effect is known in other areas. If we consider the basic problem to be one of converting a large energy quantum associated with a two-level system (representing nuclear energy levels) into a large number of low-energy oscillator quanta (representing a phonon mode), then there is the beginning of a precedent in the NMR and atomic physics literature [15]. In the multiphoton regime of the spin-boson model [16], coherent energy exchange occurs between two-level systems with a large transition energy and an oscillator with a low characteristic energy [17,18]. This basic effect has been observed experimentally [19]. The problem that we face is that this anomalous coherent energy exchange effect is very weak in the spin-boson model; coherent energy exchange is possible only when the large quantum is divided into a few tens of low energy quanta. In order to split a very large MeV quantum into a much larger number of oscillator quanta, we require a model something like the spin-boson model, but this new model must have a much stronger version of the effect to be relevant to the Fleischmann–Pons excess heat observations.

In the sections that follow, we will consider the lossy spin-boson model in the limit of infinite loss [20–22]. The spin-boson model augmented with loss is capable of a much stronger anomalous energy conversion effect than the conventional spin-boson model. The finite loss version of the model in our view is relevant to experiment, but it is complicated; if we make the loss infinitely fast, then the resulting model simplifies considerably, and allows us to quantify it in a useful way.

2. Spin-boson model

In the basic spin-boson model, a two-level system is coupled to an oscillator with linear coupling (the two-level system can make a transition up or down, coupled with an increase or decrease of one oscillator quantum). This model is very

popular in the atomic physics literature (several hundred papers have been published on it), mostly because it provides a test problem for new mathematical techniques. The following Hamiltonian describes the model [16]

$$\hat{H} = \Delta E \frac{\hat{S}_z}{\hbar} + \hbar\omega_0 \hat{a}^\dagger \hat{a} + U (\hat{a}^\dagger + \hat{a}) \frac{2\hat{S}_x}{\hbar}. \quad (3)$$

The first term describes the two-level system energy with transition energy ΔE , the second describes the oscillator with a characteristic frequency of ω_0 , and the last term accounts for linear coupling between the two systems.

In the multiphoton regime (where the characteristic energy of the oscillator is much less than the transition energy of the two-level system), the states that are coupled in the Hamiltonian are off of resonance, since the energies of the two individual systems are highly mismatched. Our intuition might suggest that no energy exchange is possible under such conditions, since the energy levels of the two systems are not matched. Nevertheless, many analyses carried out over the past 50 years have shown that coherent energy exchange can occur. The reason for this is that there can be a weak indirect coupling between distant states that are resonant with each other, resulting in a finite rate for coherent energy exchange as long as the two-level system energy (including the coupling) is matched to an odd number of oscillator quanta [17,18].

2.1. Nuclear levels and phonon mode

We might think about this model in relation to the Fleischmann–Pons excess heat effect. In this case, the two-level system might represent nuclear energy levels; the ground state of the two-level system might stand in for the ground state of a nucleus, and the excited state of the two-level system might stand in for an excited nuclear state. The oscillator in the two-level system might represent one phonon mode.

It is possible to use a spin-boson model to investigate what happens when these two systems are coupled. For the model to be relevant there needs to be some coupling so that a transition between the two nuclear states can occur if a phonon is exchanged. In general we would expect the nuclear states not to care whether the phonon modes (which the nucleus is part of) are excited or not. There are, however, some special cases where we would expect coupling to occur [23]. A phonon mode is going to care about the mass of a nucleus; hence if a nucleus is made up of a superposition of states with different masses, then we might expect that phonon exchange might occur if the mode is highly excited in association with transitions between these different states.. Alternatively, if there is a D₂ molecule embedded in the lattice, a phonon mode is going to notice if it makes a transition to a ⁴He atom. In both of these cases, it would be plausible to use a spin-boson model to begin analyzing what happens if phonon exchange becomes possible.

Intuitively, we would not expect much to happen in either case. When off-resonant states mix, we can usually use second-order perturbation theory to compute the level shifts, and how much mixing occurs. The spin-boson model in this application would predict a shift of the nuclear levels sufficiently small as to be unmeasurable. The probability that the nuclear transition energy could be converted into vibrational energy in the spin-boson model for this example can be evaluated directly, and the result is that no coherent energy exchange can take place. We conclude that within the context of the spin-boson model nothing interesting happens.

3. Lossy Spin-Boson Model

We have argued for several years that when the spin-boson model is augmented with loss that things change qualitatively [20–22]. In this case, we are interested in the Hamiltonian

$$\hat{H} = \Delta E \frac{\hat{S}_z}{\hbar} + \hbar\omega_0 \hat{a}^\dagger \hat{a} + U (\hat{a}^\dagger + \hat{a}) \frac{2\hat{S}_x}{\hbar} - i \frac{\hbar\hat{\Gamma}(E)}{2}. \quad (4)$$

The first term in this case represents many two-level systems, the second term accounts for the oscillator as before, the third term describes linear coupling with the oscillator (which mediates transitions between all of the different two-level systems on equal footing), and the last term accounts for loss.

For coherent energy exchange in the multiphoton regime, we have shown explicitly that severe destructive interference occurs in the basic spin-boson model in the limit of weak coupling, resulting in a very slow associated rate. This destructive interference is lifted in the lossy version of the model, especially under conditions where the loss is very strong [21]. As such, the lossy version of the spin-boson model is very efficient at exchanging energy coherently under conditions where a large two-level system quantum is split up into many small oscillator quanta; it constitutes a new kind of model in this regard that we have not encountered previously in physics.

3.1. Coupling between nearly degenerate states

There is a joke in which a mathematician, a physicist, and an engineer each sees a fire breaking out; the mathematician realizes that a solution exists, and walks away; the physicist reduces it to a previously solved problem, and also walks away; and the engineer rolls up his sleeves and puts the fire out. In the sense of this joke, as applied physicists, we would like to reduce the problem to one previously solved. So, our focus then is finding some well known previously solved problem that is like this one, which perhaps would allow us to have some intuition about how the new model works.

As it turns out, there is a classic physics problem, which is something like the new model, that allows us to understand the new model simply. In the lossy spin-boson model, we are interested in the coherent dynamics which govern transitions between nearly degenerate states. But almost the same mathematical problem occurs when we consider the coherent dynamics of an electron in the conduction band of a crystal semiconductor. We can use our intuition about this well known problem then in order to understand how the lossy spin-boson model works.

Consider for example an idealized set of atoms next to one another in one dimension, each with the same energy level, with the possibility of electron tunneling between neighbors. The evolution equation for the probability amplitudes $c_n(t)$ at each site can be written as

$$i\hbar \frac{d}{dt}c_n(t) = -Vc_{n-1}(t) - Vc_{n+1}(t). \quad (5)$$

This, by itself, is almost enough for us to recognize that the electron will evolve pretty much as a free particle with an effective mass. We might develop an energy band by working with eigenfunctions of the problem

$$c_n(t) = e^{-iEt/\hbar} e^{ikna} \quad (6)$$

and then substituting to obtain

$$E = -2V \cos(ka), \quad (7)$$

where a is the lattice constant for this idealized model. The conduction band in this case is locally parabolic around $k = 0$, so that the dispersion relation is almost the same as a particle in free space. We can approximate the discrete probability amplitudes with a continuous wavefunction

$$\begin{aligned} c_n(t) &\rightarrow \psi(na, t) \\ c_{n\pm 1}(t) &\rightarrow \psi((n \pm 1)a, t) \rightarrow \psi(na, t) \pm a \left(\frac{\partial \psi}{\partial x} \right)_{x=na} + \frac{a^2}{2} \left(\frac{\partial^2 \psi}{\partial x^2} \right)_{x=na} + \dots \end{aligned} \quad (8)$$

which allows us to approximate the evolution equation as a Schrodinger equation

$$i\hbar \frac{\partial}{\partial t} \psi(x, t) = -2V\psi(x, t) - Va^2 \frac{\partial^2}{\partial x^2} \psi(x, t). \quad (9)$$

The effective mass in this model can be obtained from

$$\frac{\hbar^2}{2m^*} = a^2 V. \quad (10)$$

The continuum limit of this problem is that of a free particle in a constant potential. This allows us to use our intuition about free particle dynamics to understand the more complicated problem of coupling between a set of ordered degenerate states. Because we have so much intuition about this problem, we would have little problem extending our intuition if there was an additional potential that depended on the position n , or if the coupling coefficients varied slowly with n .

3.2. Lossy spin-boson model as a nearly degenerate state problem

To proceed, we would like to find a way to recast the lossy spin-boson model into a form in which it looks like a set of ordered nearly degenerate states with coupling between neighbors. In the absence of coupling, the states are not degenerate; we may write them as

$$E_{M,n} = M \Delta E + n \hbar \omega_0. \quad (11)$$

In general there are many states, and only a few of them might have roughly the same energy. For example, if the transition energy were exactly 11 times larger than the oscillator energy, then we would have the same energy if we increase the number of oscillator quanta n by 11 each time we decreased the number of excited states of the two-level systems by 1. But then this would leave us with all kinds of states that have different energies, and which are not degenerate.

We can accomplish this by using a second-order formulation. We separate out all of the states that are nearly degenerate, and focus on them; all of the other states we eliminate algebraically. For example, the eigenvalue equations for two sets of expansion coefficients are

$$\begin{aligned} E\mathbf{c} &= \mathbf{H}_a \cdot \mathbf{c} + \mathbf{V}_{ab} \cdot \mathbf{d}, \\ E\mathbf{d} &= \mathbf{H}_b \cdot \mathbf{d} + \mathbf{V}_{ba} \cdot \mathbf{c}, \end{aligned} \quad (12)$$

where \mathbf{c} is a vector of coefficients of the degenerate states that we want to focus on, and \mathbf{d} is a vector of coefficients for all of the other states. We can focus on the \mathbf{c} vector by eliminating the \mathbf{d} vector to obtain

$$E\mathbf{c} = \mathbf{H}_a \cdot \mathbf{c} + \mathbf{V}_{ab} \cdot (E - \mathbf{H}_b)^{-1} \cdot \mathbf{V}_{ba} \cdot \mathbf{c}. \quad (13)$$

This problem now describes an ordered set of nearly degenerate states with coupling between neighbors. The indirect coupling between neighbors is included naturally in this formulation. All that remains is to understand the shifts and couplings of the resulting nearly degenerate states.

4. Results

We have carried out a variety of calculations using this general approach, and the results are interesting. There is a scaling law apparent within this model that we found from our first few calculations, which will help us in what follows to understand the results more simply. Our focus in what follows is on the special case where the loss is infinite for all basis states with an energy less than a cut-off energy we selected.

4.1. Scaling

There are a relatively small number of parameters that appear in the augmented spin-boson model in the limit of infinite loss, which will make it easier for us to understand. Perhaps the most important parameter for our discussion is the ratio of the transition energy to the oscillator energy, which will appear in our discussion in connection with the number of oscillator quanta Δn which is exchanged for a two-level system quantum. The strength of the coupling between the two systems is also important, and we have found that a useful measure of this can be developed through the dimensionless coupling parameter g defined according to

$$g = \frac{\max \left(\left| i \hat{H} | f \right\rangle \right)}{\Delta E} \rightarrow \frac{(N+1)U\sqrt{n_0}}{2\Delta E}, \quad (14)$$

where N is the number of two-level systems. The number of two-level systems by itself constitutes an important additional parameter of the model.

One way to think about scaling in this model is to start with a problem in which the number of quanta Δn to be transferred is fixed, and then imagine that we would like to see what happens when we vary the number of two-level systems N or the coupling strength g . If we fix g and look at models with different N , we find that the energy offsets of the nearly degenerate states are very similar. As we increase the number of two-level systems, then the states become more and more nearly degenerate as the maximum offset remains constant. Also, the maximum indirect coupling between nearly degenerate states remains approximately fixed in this limit. Hence, if we compute results for one such model, the answer will be very similar to other models with different values of N .

We have found another concept that is very helpful in understanding these models. The details of the local coupling between the nearly degenerate states seem to depend only on the local coupling strength of the original problem when N is large. As a result, we can assume that all of the coupling matrix elements are the same locally (as a function of the number of excited two-level systems) in the initial Hamiltonian, to get approximate values for the shifts and indirect coupling matrix elements for the nearly degenerate states. We find that these approximate values are very close to the exact ones computed for the full problem. Since this seems to work, it allows us to focus on the level shifts and indirect coupling matrix elements as a function of g for this simpler uniform problem. Instead of having to analyze each version of the model separately, all we really need is to characterize the shift and indirect coupling matrix elements as a function of the dimensionless coupling strength g to understand most of what is important about the model.

4.2. Indirect coupling between neighboring states

By far the most important result from this model is the indirect coupling strength between neighboring nearly degenerate states. Results are shown in Figure 1 for the scaled indirect coupling matrix element as a function of the dimensionless coupling strength g .

Several features of these results are of interest to us here. To begin with, these indirect coupling coefficients are important for coherent energy exchange between the two-level systems and the oscillator, because the maximum rate at which two-level system transitions occur is proportional to this matrix element. When we scale the matrix element by the number of oscillator quanta exchanged Δn , the resulting scaled matrix element is proportional to the rate at which individual oscillator quanta are exchanged.

When g is small, the coupling is weak, and the matrix elements scale as

$$\frac{V_{\text{eff}}}{\Delta E} \rightarrow A(\Delta n)g^{\Delta n}. \quad (15)$$

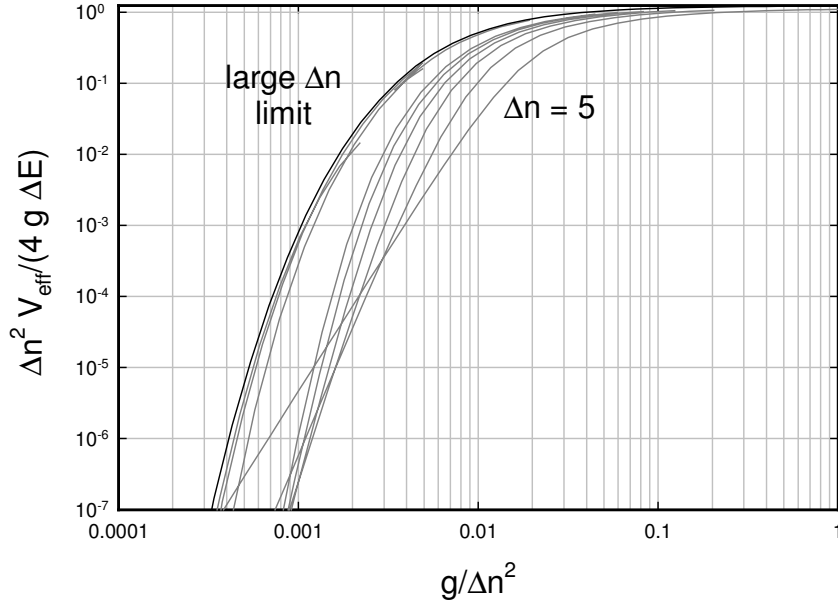


Figure 1. Scaled indirect coupling matrix element as a function of the scaled dimensionless coupling parameter g for different odd Δn , including 5, 7, 9, 11, 15, 51, 101, 151 (grey); also shown is the large Δn limit (black).

From perturbation theory we know that $A(3)$ is $9/8$, in agreement with the numerical calculations. For larger values of Δn , an approximate fit is given by

$$A(\Delta n) = a e^{b\Delta n} \quad (16)$$

with $a = 0.3139\Delta E$, and $b = 0.3441$. When g is somewhat above unity for modest Δn , the nearest neighbor indirect coupling matrix element is roughly

$$V_{\text{eff}} \rightarrow 4.8 \frac{g\Delta E}{\Delta n^2} = 4.8 \frac{g\hbar\omega_0}{\Delta n}. \quad (17)$$

We have found that in the limit of large Δn , it is possible to express the indirect coupling matrix element in terms of a universal function according to

$$\frac{\Delta n^2 V_{\text{eff}}}{4g\Delta E} = \Phi\left(\frac{g}{\Delta n^2}\right), \quad (18)$$

where the universal function Φ can be fit according to

$$\ln \Phi(y) = \frac{a_{-3}}{y^3} + \frac{a_{-2}}{y^2} + \frac{a_{-1}}{y} + a_0 \quad (19)$$

with the fitting parameters

$$\begin{aligned} a_{-3} &= -2.11317 \times 10^{-10}, & a_{-2} &= 1.8517 \times 10^{-6}, \\ a_{-1} &= -0.00899174, & a_0 &= 0.208444. \end{aligned} \quad (20)$$

This result is plotted in Fig. 1 to compare with the finite Δn results.

In connection with coherent energy exchange in the Fleischmann–Pons experiment, this result begins to clarify some of the issues. In this case Δn is very large (on the order of 10^8 – 10^9). Consequently, we expect that when g is small, the indirect coupling matrix element will be essentially zero, consistent with no coherent energy exchange. We would not expect any coherent energy exchange below $g/\Delta n^2 = 10^{-4}$ for large Δn .

5. Discussion

In the Fleischmann–Pons experiment, energy is produced by some new physical process that results in ${}^4\text{He}$ as a reaction product. Nuclear reactions as understood in the nuclear physics literature lead to energetic reaction products as a consequence of Rutherford-style conservation of energy and momentum. Due to the absence of energetic reaction products observed in the Fleischmann–Pons experiment, we know that the ${}^4\text{He}$ is born with sufficiently low energy so as to be inconsistent with any reasonable extrapolation of Rutherford reaction kinetics. Based on this kind of consideration alone, we can conclude that our attention should be focused on new reaction schemes that split up the nuclear energy quantum into a very large number of small quanta. At present, there seem to be two basic ways that this might be done. One approach is being pursued by Kim [12,13], where the reaction energy is proposed to be converted to kinetic energy of a large number of deuterons in a way that remains to be clarified. The other approach is through a coherent energy exchange mechanism with a condensed matter degree of freedom, such as a phonon or plasmon mode.

Many years ago we noticed that models with coupled two-level systems and an oscillator, augmented with loss, could dramatically improve the rate at which coherent energy exchange occurs in the multiphonon regime [24]. Over the years we have explored this effect using a number of different tools, including quantum flow calculations, periodic lattice models, and coupling between nearly degenerate states. In the case of the quantum flow calculations, we were able to demonstrate coherence under conditions where up to 10^4 phonons were exchanged by brute force numerical calculations. The periodic lattice calculations are useful for quantifying the threshold effect.

A few years ago, we made an effort to connect our approach with results in the conventional literature on coherent energy exchange in the spin-boson model [17,18]. In this case, we were able to develop a rotation that allowed the problem to be analyzed as a set of nearly degenerate states with dominant nearest neighbor coupling. By viewing the lossless version of the problem in this way, we were able to analyze coherent energy exchange in the multiphonon limit systematically for weak and moderate coupling.

We have been interested in recent years in extending this style of analysis to the lossy version of the problem. In the results discussed briefly in this paper, we have succeeded. Perhaps the most important feature of this kind of analysis is that we have identified scaling laws that make the system much simpler to understand. As a result, we are able to present results for the indirect coupling matrix elements systematically for models with different numbers of exchanged phonons. These indirect matrix elements determine nearly everything about how fast coherent energy exchange occurs in the models.

We have not emphasized the dramatic increase in the rate of coherent energy exchange with loss as compared to the lossless case, but this issue deserves some comment here. One way to see this is in the definition of the dimensionless coupling parameter g for the two problems: the definition of g appropriate for the lossy problem is larger essentially by the number of two-level systems than the definition in the lossless case. This means that in the lossless problem, the energy coupling effects act the same if one two-level system is coupled to the oscillator, or if one million two-level systems are coupled. In the lossy version of the problem, the presence of the additional two-level systems increases the dimensionless coupling strength in proportion to the number of them. Hence it is much easier for a physical system to act like a strongly coupled system if it behaves similarly to the spin-boson model augmented with loss.

In a sense, this captures what is special about the model. We know that only a strongly coupled system is going to be capable of splitting up a large quantum into a very large number of small quanta. The physical coupling between the atoms in PdD does not seem to be strong enough by at least six orders of magnitude to do the job. In the lossless

spin-boson model, the energy exchange process is nearly the same as the coupling between one two-level system and the oscillator. Not only would we need the transition matrix element for single phonon exchange to be on the order of 24 MeV to get into the strong coupling limit, but once there we would at most be able to split a 24 MeV quantum into smaller quanta on the order of 1 MeV. However, in the spin-boson model augmented with loss, whether the coupling is strong (or not) is determined in part by the magnitude of the phonon exchange matrix element, and in part by the number of two-level systems involved (and their excitation). Hence, we can have a strongly coupled system in this case if the individual local interaction matrix element is much less than 24 MeV, as long as the effect of all of the individual transitions in the system add up in phase (which occurs in this kind of model if the phonon mode wavelength is long), and if there are a lot of them.

We have focused on the spin-boson model augmented with loss in this paper since the energy exchange part of the problem is clearly the most important. Our overall model for excess heat in the Fleischmann–Pons experiment involves two sets of two-level systems instead of one, so the associated model is more complicated. In the event that the excitation transfer step is the bottleneck, then this step limits the reaction rate for the overall model. Our calculation of this transition matrix element seems to be consistent with the transition rates needed to account quantitatively for the observed rates of excess power. The related computation of the energy exchange rate has been for us much more difficult, since it has become clear than pretty much all excited states which can be coupled to be consistent with the requirement that phonon exchange occurs.

Some of our colleagues have expressed displeasure with the model, arguing that any significant nuclear excitation in such a model would be lost immediately. A feature of the model worthy of comment in this regard is that the indirect coupling between states in this model occurs through off-resonant states that are in energy deficit. Although it remains to be demonstrated explicitly that this results in the stabilization of these states, the associated intuition is that the system is going to have trouble decaying if it does not have enough energy to decay.

Other colleagues have misunderstood energy exchange in this kind of model, talking about a very energetic phonon being emitted. Such language is unhelpful. Instead, the way this model works is that the coupled system undergoes a very large number of rapid sequential excitation and de-excitation steps, exchanging one low energy oscillator quantum at a time; this occurs in a coherent process similar to that already described in the spin-boson model, and observed in experiment.

References

- [1] M. Fleischmann, S. Pons, M. Hawkins, *J. Electroanal. Chem.* **261** (1989) 301–308; errata **263** (1990) 187.
- [2] M. Fleischmann, S. Pons, M.W. Anderson, L.J. Li, M. Hawkins, *J. Electroanal. Chem.* **287** (1990) 293–348.
- [3] J.R. Huizenga, *Cold Fusion, The Scientific Fiasco of the Century*, University of Rochester Press, Rochester, NY, 1992.
- [4] P.L. Hagelstein, *Naturwissenschaften* **97** (2010) 345.
- [5] M.H. Miles, R.A. Hollins, B.F. Bush, J.J. Lagowski, R.E. Miles, *J. Electroanal. Chem.* **346** (1993) 99–117.
- [6] M.H. Miles, Correlation of excess enthalpy and helium-4 production: A review, *Proceedings 10th International Conference on Cold Fusion*, 2003, pp. 123–131.
- [7] P.L. Hagelstein, M.C.H. McKubre, D.J. Nagel, T.A. Chubb, R.J. Hekman, New physical effects in metal deuterides, *Proceedings 11th International Conference on Cold Fusion*, 2005, pp. 23–59.
- [8] P. Kalman, T. Keszthelyi, D. Kis, *Eur. Phys. J. Appl. Phys.* **44** (2008) 297–302.
- [9] A. Takahashi, Tetrahedral and octahedral resonance fusion under transient condensation of deuterons at lattice focal points, *Proceedings of the 9th International Conference on Cold Fusion*, 2002, pp. 343–348.
- [10] A. Takahashi, T. Inokuchi, Y. Chimi, T. Ikegawa, N. Kaji, Y. Nitta, K. Kobayashi, M. Taniguchi, Experimental correlation between excess heat and nuclear products, *Proceedings of the 5th International Conference on Cold Fusion*, 1995, pp. 69–78.
- [11] X.Z. Li, Q.M. Wei, B. Liu, S.L. Ren, *J. Cond. Mat. Nucl. Sci.* **1** (2007) 11–15.
- [12] Y.E. Kim, *Naturwissenschaften* **96** (2009) 803–811.

- [13] Y.E. Kim, Bose–Einstein condensate theory of deuteron fusion in metal, Purdue Nuclear and Many-Body Theory Group, Preprint PNMBTG-1–10, 2010.
- [14] P.L. Hagelstein, *J. Cond. Mat. Nucl. Sci.* **3** (2010) 35.
- [15] M. Forre, *Phys. Rev. A* **70** (2004) 013406.
- [16] C. Cohen-Tannoudji, J. Dupont-Roc, C. Fabre, *J. Phys. B Atom. Mol. Phys.* **6** (1973) L214.
- [17] P.L. Hagelstein, I.U. Chaudhary, *J. Phys. B Atom. Mol. Phys.* **41** (2008) 035601.
- [18] P.L. Hagelstein and I. U. Chaudhary, *J. Phys. B Atom. Mol. Phys.* **41** (2008) 035602.
- [19] D. Fregenal, E. Horsdal-Pedersen, L.B. Madsen, M. Forre, J.P. Hansen, V.N. Ostrovsky, *Phys. Rev. A* **69** (2004) 031401(R).
- [20] P.L. Hagelstein, I.U. Chaudhary, Progress on phonon exchange models for excess heat in metal deuterides, *Proceedings of the 13th International Conference on Cold Fusion*, 2007, 590–606.
- [21] P.L. Hagelstein, I.U. Chaudhary, Models relevant to excess heat production in Fleischmann–Pons experiments, Low-energy nuclear reactions sourcebook, ACS Symposium Series 998, 2008, pp. 249–267.
- [22] P.L. Hagelstein, I.U. Chaudhary, Excitation transfer and energy exchange processes for modeling the Fleischmann–Pons excess heat effect, *Proceedings of the 14th International Conference on Cold Fusion*, 2008, p. 579.
- [23] P.L. Hagelstein, I.U. Chaudhary, M. Melich, R. Johnson, A theoretical formulation for problems in condensed matter nuclear science, *Proceedings of the 14th International Conference on Cold Fusion*, 2008, p. 596.
- [24] P.L. Hagelstein, A unified model for anomalies in metal deuterides, *Proceedings of the 9th International Conference on Cold Fusion*, 2002, pp. 121–134.



Research Article

Concerning the Role of Electromagnetism in Low-energy Nuclear Reactions

Scott R. Chubb*

Infinite Energy Magazine, 9822 Pebble Weigh Ct., Burke, VA 22015, USA

Abstract

Considerable confusion has resulted in the “debate” (and lack of “debate”) about whether or not Low-Energy Reactions (LENR) can take place. A key reason for this has involved the lack of a cogent argument, based on fundamental physical ideas, involving electromagnetism. In this paper, I re-examine this question. In fact, a cogent argument does exist, based on resonant electrodynamics, and its more general formulation, involving quantum electrodynamics. Lessons learned from this and their relevance are key to understanding the most salient effects, including the Infra-Red (IR) results from the SPAWAR experiments, and Mitchell Swartz’s experiments. The associated arguments suggest that magnetic effects that have only been indirectly applied may be used to trigger LENR in particular situations. A new experiment, based on this line of reasoning, is suggested.

© 2011 ISCMNS. All rights reserved.

Keywords: Cold fusion, Energy band states, Ion band states, Quantum electrodynamics

PACS: 03.65.XP, 03.75-b, 03.75Kk, 03.75.LM, 03.75.Nt

1. Introduction

Talbot Chubb and I suggested in 1989 that deuterons (d's), in fully loaded palladium deuteride (PdD), could behave very differently than in free space, by occupying the kinds of states (energy band states) that electrons occupy in periodically ordered solids [1,2]. Based on this conjecture, we suggested that the normal rules about fusion might not apply to the cold fusion (CF) claims by Fleischmann and Pons (FP). Because d's are bosons, on the length scales associated with conventional electromagnetism, implicit in this hypothesis, we were also suggesting that by occupying the lowest energy (band) state, the d's could form a Bose Einstein Condensate (BEC). At the time we made this suggestion, confusion about its relevance resulted [3] because it was widely believed that BEC's could form only at very low temperatures, as opposed to a situation in which they are induced (as in the case of laser-cooling of alkali vapors) dynamically through the presence of externally applied forces. In addition, our suggestion was not widely publicized for two reasons: The experiments were not widely believed to be valid; and Perceptions about the limitations of conventional energy band theory.

*E-mail: chubbscott@mac.com

Implicitly, as well, it was widely believed that in the initial experiments by FP, conventional fusion reactions were taking place. But because in conventional fusion, the dominant reactions ($d + d \rightarrow ^3 \text{He} + n$ and $d + d \rightarrow ^3 \text{H} + p$) are mediated by the strong force, the collision process inherently occurs over nuclear scale dimensions, and details about the nature of the reaction process far from the reaction are not important. Then, a static electromagnetic interaction (EMI) applies because the reacting particles have high velocity. This is relevant in these kinds of situations, but this certainly does not have to be relevant in a solid because in a solid, time-dependent changes involving many particles can become relevant. In fact, the relevant reaction in the FP results and in other experiments involving excess heat appears to involve the creation of ^4He . Although ^4He rarely occurs in conventional fusion, it is produced but through a reaction ($d + d \rightarrow ^4 \text{He} + \gamma$) that is mediated by the electromagnetic force, and in this reaction (as a consequence) details about the behavior of the reacting particles far from the location of the reaction play an important role in initiating it.

Although the initial band theory idea that Talbot Chubb and I proposed seemed to be preposterous at the time, by responding to the critics, new ideas evolved from our thinking. A key point in what we developed is associated with the potential relevance of finite size and finite time-scales, as they might apply in band theory. A natural generalization of band theory, in fact, does exist [4], which is associated with the underlying formalism that Felix Bloch used, in his formulation of transport phenomena, which involves multiple-scattering theory, as opposed to the conventional “picture” that has been used to introduce ideas related to band theory. When this alternative picture is used, finite size effects can be introduced in a manner that can explain how, through many-body effects associated with a finite solid, a form of ($d + d \rightarrow ^4 \text{He} + \gamma$) reaction can occur in which the gamma ray can be suppressed.

In fact, a cogent argument does exist, based on resonant electrodynamics, and its more general formulation, involving quantum electrodynamics (QED), that explains this last effect, as well as conventional energy band theory. The associated logic, which is quite general, is based on a generalization of multiple scattering theory. As in the case of extending band theory to finite systems, I developed [5–7] this generalization in response to the critics of our initial theory.

A particular limit, involving near-resonant electrodynamics in a solid, which is most relevant in the situation in which d 's occupy energy band states, can be related to a physical effect: that when periodic order is approximately preserved in a solid, the lowest energy excitations of the solid occur through resonant forms of interaction, involving elastic recoil, in which the solid as a whole moves rigidly. These occur when all of the particles in the solid move at once, without their relative separations being altered, except at the boundaries of the solid, where translational symmetry is broken.

This last picture has been partially summarized elsewhere [8,9]. But a complete summary has not appeared previously. Specifically, details about how it relates to understanding how the gamma ray (in the ($d + d \rightarrow ^4 \text{He} + \gamma$) reaction) can be suppressed have not been discussed. This is done in Section 4 of this paper. Because confusion has existed [3] about the initial formulation of our model [1,2], it seems appropriate to provide some background about it. This is done in Section 2. In addition, in this section, some background information is presented about two other QED models (by Schwinger and Preparata), that includes comments about deficiencies in these models, which resulted from a lack of information about the relevance of (the QED of) the ($d + d \rightarrow ^4 \text{He} + \gamma$) reaction, and the fact that ^4He is produced at levels in the excess heat experiments that are consistent with a form of this last reaction in which the gamma ray is converted into alternative forms of energy.

In discussing the relevant physics of this last reaction, I point out that a degree of confusion exists concerning the relevance of conventional Gamow tunneling ideas in the associated dynamics. Because confusion has existed about this, it is appropriate to provide additional background material that clarifies what is known quantum mechanically about the reaction and why Gamow tunneling does not apply. This is covered in Section 3. This material, in turn, provides a useful way to introduce the material (associated with how the gamma ray can be suppressed) found in the fourth section. Here, I also explain how magnetic effects potentially can trigger CF excess heat.

2. Background

At the time we initially proposed the Ion Band State idea (in which d's would occupy energy band states), we were motivated by work that I did, based on a model developed by Fox [10] on a form of BEC that is created dynamically. The particular problem involved the possible formation of a BEC consisting of excitons [10]. In the physical situation associated with this form of BEC, the condensation evolves after excitons are created. In particular, an exciton is created when an electron is excited by light into a higher energy state in an insulator or semi-conductor in such a way that its energy is not large enough for it to “escape” from the location completely, where it was located initially. When this occurs, an idealized picture becomes appropriate in which the electron and the “electronic-hole” (associated with the location where the electron was located initially) move together, in a manner that can be thought of as resulting from the motion of a quasi-particle.

The idealized limit in which excitons possibly can form occurs when there are only a small number of them interacting with each other and a periodic structure (a crystal lattice). (The atoms in a lattice are symmetrically located in such a way that each atom is periodically displaced relative to the others.) Then, when the excited electron is not too localized, an exciton can form, in which the electron and electronic-hole effectively “see” a periodic potential, just as electrons in the valence and conduction bands in an insulator or semi-conductor see a periodic potential. As a consequence, both the electron and electronic-hole, associated with the exciton, occupy an energy band state, similar to the kinds of (valence and conduction band) states electrons occupy.

As a consequence, the process in which an isolated, excited state electron would decay occurs over a considerably longer period of time than occurs in a situation in which it has been located in an atom, and the composite electron/electronic-hole pair wanders around the lattice in a way that is similar to the way electrons wander around the lattice. The excitons can be viewed as bosons because electronic-holes are treated as being fermions (as a result of the excitation process) and (like d's), each electron/electronic-hole pair obeys Bose–Einstein statistics. In the unconventional idea of extending this kind of limit to d's interacting with a lattice, we argued that, if a comparable picture might apply to d's in Ion Band States (in which effectively, the electronic-hole in an exciton could be replaced by a neutron and the electron by a proton) the associated proton-neutron pair implicitly could interact with the lattice and with other, comparable proton-neutron pairs over very different time scales than when the associated interaction occurs with d's in free space.

Also implicitly, by treating each d as a boson, we assumed a form of Born–Oppenheimer separability [11] between atomic- and nuclear-scale processes (similar to the Born–Oppenheimer Separability (BOS) between electronic and nucleus degrees of freedom that occurs in molecules), in which the dominant forms of interaction that occur were mediated electromagnetically in both the nuclear- and atomic-scale dimensions. In doing this, we suggested that the Gamow factor, tunneling picture that was commonly viewed as being relevant need not apply. Implicitly, in our initial idea that an Ion Band State (IBS) model and our use of BOS might apply, we were invoking the idea the electromagnetic forces (as opposed to the strong force) were mediating the associated nuclear reaction.

As I mentioned in the Introduction, confusion about our theory developed in part because of perceived limitations of conventional band theory. In fact, the motivation for the initial model, which involved studying exciton condensation, is related to a deeper many-body problem that implicitly involves quantum electrodynamics (QED). In addressing the critics of our theory, I also demonstrated that conventional energy band theory also could be derived from QED. This fact has not been widely appreciated, possibly because energy band theory, traditionally, is presented as a semi-classical limit of a phenomenological, single-particle theory. In my reformulation of the energy band problem, I demonstrated that it can be derived as a particular limit (that preserves periodic order) of the more general QED many-body problem [4–7].

In the particular application of our IBS theory to CF[4–7], we initially identified a very particular limit where it should apply: near full-loading ($x \rightarrow 1$ in PdD_x). This limit, which preserves periodic order, is consistent with IBS

formation (as a result of the anti-bonding character of the electronic states of PdD) when small variations in loading ($x = 1 \pm \delta$, $\delta \ll 1$) take place [7]. Thus, we predicted that high-loading would be required. We also predicted that the dominant product in heat-producing electrodes would be ^4He , and that the ^4He would be found, without high energy particle emission [1,2,11], primarily in the surface regions and outside heat-producing electrodes. We made these three predictions prior to experimental observations of the associated effects.

During the initial stages of the CF debate, two other theorists (Schwinger [12] and Preparata [13]) also suggested models that directly [13] and indirectly [12] invoked QED. It is potentially of merit to recognize that in addition to our theory, in these theories [12,13], ideas were presented that could explain how the reactions could proceed without high energy particles being produced. At the time, both Preparata [13] and Schwinger [12] suggested that different reactions from the one that produces ^4He could be involved, although Preparata pointed out that ^4He could be produced in the excess heat experiments. It is also potentially noteworthy that separately we [1,2,11] and Preparata [14] suggested that the ^4He would be created but would be found primarily outside heat-producing electrodes.

In fact, at this early stage in the associated research, the fact that ^4He was being produced and at the appropriate levels to account for the heat was not known. In addition, considerable confusion existed concerning a subtlety associated with how ^4He might be produced, even in the conventional fusion reactions. In particular, in order for this reaction to take place, the possible wave function describing the behavior of the interacting d's must possess Bose exchange symmetry (i.e., the d's must be bosons) on length scales associated with EMI, far from the location of the reaction. A key assumption in our initial formulation of the IBS theory was that this kind of behavior be maintained on all length scales. In fact, once this assumption is made, it follows that the allowable final state must possess an even number of proton-neutron pairs when the initial state possesses an even number of proton-neutron pairs [1,2,11,15]. (This approximate selection rule was the basis of our prediction that the dominant by-product in the heat-producing reaction would be ^4He .) An important point is that, as discussed in the next section, it is known that not only is it required that in the $(\text{d} + \text{d} \rightarrow ^4\text{He} + \gamma)$ reaction, the d's have to possess Bose exchange symmetry far from the reaction, but the reaction obeys other selection rules: the transition is quadrupolar (it involves a change in angular momentum $\Delta J = 2\hbar$) and also requires that the initial and final states have vanishing spin [16].

The associated physics is very different than in conventional fusion, where, by assumption, a static Coulomb barrier is used to explain how same-charged, heavy hydrogen nuclei ($-\text{d}$'s) can have appreciable overlap. In this conventional picture, d's initially approach each other with such a high velocity that their momenta do not change appreciably, except when their separation approaches nuclear scale, where they are allowed to interact dynamically entirely through the strong force, and the EMI can be treated, entirely statically, based on the standard (WKB), Gamow tunneling formula.

These assumptions apply to the most frequently observed $(\text{d} + \text{d} \rightarrow ^3\text{H} + \text{p}$ and $\text{d} + \text{d} \rightarrow ^3\text{He} + \text{n}$) reactions, which occur when two proton-neutron pairs collide at a point, where the two pairs can be viewed as forming an “excited state” of a ^4He nucleus, in which the dynamical changes are dominated by the strong force. In this limit, the distinction between protons (p's) and neutrons (n's), at the point of nuclear contact, effectively (except through differences in kinetic energy, associated with changes in mass that do not relate to time-dependent EMI effects), is inconsequential, and the normal, intuitive picture that nuclear physicists have applies: The most frequent reactions occur when the amount of nuclear energy that is released is minimized. (This last, intuitive idea was also assumed by Schwinger and Preparata.)

When the associated picture applies, the WKB tunneling model can be used to estimate the rate of nuclear reaction. Here, the rate of reaction can be calculated from the relationship,

$$\tau = f_{\text{astro}} \times G_T, \quad (1)$$

where f_{astro} (the astrophysical factor) depends entirely on the strong force and on quantities that have nuclear scale dimension, while G_T (referred to as the Gamow factor), which depends on the initial velocity v and electrostatic

repulsion (at the point of contact) between the d's, can be evaluated using the Gamow tunneling formula[15]:

$$G_T = \exp\left(-\frac{2\pi\alpha}{\beta}\right), \quad (2)$$

where $\beta = \frac{v}{c}$, c is the speed of light and $\alpha = \frac{1}{137} = \frac{e^2}{\hbar c}$ is the fine structure constant.

3. Importance of QED (as Opposed to the Coulomb Barrier) in $d + d \rightarrow \alpha + \gamma$

Based on the intuitively appealing idea that tunneling applies and that energy release is minimized, most nuclear physicists assume that the least common reaction ($d + d \rightarrow \alpha + \gamma$) occurs infrequently because the energy release (23.8 MeV) is considerably (7–8 times) larger than it is in the remaining reactions. In fact, this picture is not right. Important details about time-dependent, EMI effects, which are responsible for the fact that the $d + d \rightarrow \alpha + \gamma$ reaction occurs rarely (a fact that was not appreciated even by Schwinger[13] and Preparata[12]), have been ignored. In particular, the fact that EMI plays a central role in this reaction is known because although $d + d \rightarrow \alpha + \gamma$ rarely occurs, the reverse reaction (the photo-dissociation process: $\gamma + \alpha \rightarrow d + d$) has been studied in detail.

As discussed elsewhere [9,16], it is known, implicitly, as a consequence, as opposed to the conventional picture, involving a static Coulomb barrier, and the common, intuitive idea that the large energy release that is involved is responsible for the reaction occurring infrequently, an alternative model applies. In particular, the selection rules, alluded to in the last section, exist and a well-defined electromagnetic transition is involved in the photo-dissociation process. The analysis shows quite conclusively [16] that the reaction can be explained as resulting from a well-characterized (quadrupolar) transition, in which the total spin of the final state d's vanishes, and that it is necessary to include the effects of EMI (and the requirement that the d's obey Bose Einstein statistics) on length- and time- scales that are far from the location of the photo-dissociation process. In QED, the rate of any transition is proportional to the absolute square of the associated transition matrix element. Thus, by construction, the theory requires that a transition rate forward in time be equal to the comparable rate for a transition backward in time, and the common intuition, that this reaction is suppressed because of the large energy release, is wrong.

An important point has and continues to be the role of time-dependent effects in QED phenomena. The potential relationship of these EMI effects in potential nuclear fusion reactions, and in LENR, involving $d + d \rightarrow {}^4\text{He}$ is not widely appreciated because it is commonly believed that the charge-neutral, strong force potential provides the time-dependent dynamics associated with the reaction.

An important reason for this is that, as outlined above, the importance of the effect of QED in $d + d \rightarrow \alpha + \gamma$ is not widely appreciated because this reaction, superficially, appears to be dominated by strong force effects since it conserves isospin and also because it is believed, as a consequence, that it occurs infrequently because the energy from the reaction is so much larger than the comparable reaction energies associated with the other reactions. The possible importance of QED in the LENR situation, and the possibility that approximate periodic order in this situation might be important, in solids, has not been widely considered probably because the conventional theory, of periodically ordered solids, that is commonly used, involves a semi-classical limit that does not include the possibility that, effectively, many channels for de-excitation can become possible through resonant phenomena in which an approximately ordered lattice is allowed to move and accelerate rigidly. In this situation, in principle, all of the charged particles in a particular region can “move” together at once, in such a way that the separation between any two particles does not change. In fact, collisions between charged particles at the “boundaries” of such a region with “particles” outside the region introduce forms of coupling that limit the extent and lifetime of these forms of “rigid-body” motion. Because it is never possible to identify where the “boundary” of such a region occurs, implicitly, the lowest energy excitations that result from these forms of approximate symmetry occur through resonant EMI processes, in which momentum and energy are conserved globally, and the perturbations (from collisions) that result occur when the net flux of each kind of particle into and away from

the “ordered” region vanishes. Possible coupling between different configurations involving different center-of-mass velocities (and momenta) necessarily can result in forms of approximate degeneracy, and (as a consequence) many alternative forms of partial excitation and de-excitation can take place.

In free space, comparable forms of coupling are not present. As summarized elsewhere [9] and below, in a finite solid, through these kinds of effects, the “single γ ray” can be converted into many (lower frequency) photons. Also, as discussed elsewhere [8,9] through the Zener/ionic breakdown model, the phenomenon can occur through a time-dependent process, involving a form of coherent tunneling, in which the necessary changes in momentum for triggering the reaction can increase in magnitude with time.

4. The QED of $d + d \rightarrow {}^4\text{He}$ in Cold Fusion

As mentioned in the Introduction, in Cold Fusion (CF), a variant of the helium-4 (α particle) producing fusion reaction (which rarely occurs in conventional fusion) appears to be dominant. As I pointed out in the last two sections, most nuclear physicists assume the conventional form of this reaction occurs infrequently because it creates considerably more energy than the other fusion reactions and that the most frequent reactions minimize the amount of energy that is released. This assumption is wrong. It does not include subtleties involving EMI. It does apply when d 's have high velocity, initially, and collide at a point, provided they are not “prepared” (through EMI), in a particular way. As discussed elsewhere [9] in qualitative terms, in a solid, richer forms of time-dependent EMI can take place through non-linear coupling between photons, electrons, their spins, and other charged particles. Further complicating the problem is the fact that the α ray that one would expect to be present in the normal ${}^4\text{He}$ (α -particle) producing reaction can appear and disappear through adsorption and emission by electrons and other charged particles in the associated environment, that can (and must, in most situations) result in “parametric down-conversion” (PDC) processes [9], even in relatively small crystals.

In particular, PDC processes occur through non-linear forms of coupling between a single photon and matter that result in the photon being split into two or more (and possibly many, many more) entangled (lower frequency—potentially considerably lower frequency) photons. These kinds of effects are known to occur when photons propagate through insulators. In these situations, because the scattering processes occur only at a small number of points, the possibility of massive PDC processes that can create many photons from a single photon has not been observed. Also, the theoretical basis of the process, though well-understood, has been limited to two photons, primarily because the fields that are involved do not include significant coupling to the kinds of cooperative forms of electronic excitation that are possible in metals, such as the recoil effect, discussed below.

In larger metal crystals, typically, the associated forms of coupling rapidly attenuate any electromagnetic wave propagation, and because approximate boundary conditions can be used in these kinds of situations, the possibility of observing and understanding PDC processes, involving one or more (optical) photons, has not been investigated. As discussed below and elsewhere [9], when more precise boundary conditions are invoked, in finite lattices, elastic forms of resonant coupling become possible. Because it is never possible to define the boundary of a solid, precisely, in principle, it is never possible to determine if a portion of the solid moves rigidly (or actually accelerates) through a process in which the available momentum from an applied field (static or dynamic) rigidly couples to the center of mass of a collection of atomic centers and electrons. This means a potentially huge degeneracy can result, provided the applied field is sufficiently weak, and the crystal has finite extent (but has a characteristic nano-scale dimension). As discussed in the present section of the paper, this, in principle, can result in the possibility of a large number of different photons, with varying, but well-defined frequencies, being produced.

This possibility implies that through these PDC processes, the γ ray associated with the conventional $d + d \rightarrow \alpha + \gamma$ reaction can be converted into many different optical, IR, microwave, or lower frequency forms of radiation, coherently or incoherently. As a consequence, the “ α ” particle (henceforth referred to as ${}^4\text{He}$, when it occurs in lower energy

environments <1000 eV but as an “ α ” particle when its energy is greater than this) can be “emitted” with negligibly small energy.

In a previous paper [9], I provided an initial argument that explains how this might take place, in smaller, approximately ordered, crystals. The associated PDC effects possibly can explain how a static magnetic or electric field could lead to localized phenomena, associated with the emission of higher energy α particles that apparently have been observed in experiments [17] associated with replicating the SPAWAR protocol [18]. This possibility was explained in this earlier paper [9], based on a form of Bragg Resonant scattering, in which the “photons” are effectively “trapped” as result of the kinds of effects, suggested by Giuliano Preparata. The simplest way of explaining how this can take place involves forms of scattering that are allowed to take place in one particular region of space, but not in other regions of space.

Good reasons exist for associating these kinds of effects, with an entirely counterintuitive limit, in which the lowest forms of momentum and energy conservation, are required to obey a form of symmetry, Bloch symmetry, that is related to periodic order, that, as a consequence, can lead to forms of resonant coupling, similar to Bragg Scattering in solids that can create an imbalance in momentum that can create the kinds of effects that Giuliano Preparata intuitively identified.

Here, in general terms, resonant scattering can take place, along the lines that Giuliano Preparata intuitively recognized. Specifically, matching conditions, associated with situations in which many particles and photons approximately share a common phase, resulting from conservation of momentum and energy, can be imposed. This can occur through the requirement that many of the potentially radiation-emitting particles receive and transmit their signals in a way that can constructively interfere and cause a positive form of feed-back, very similar to the resonant laser-like effect that he suggested was involved. In the most basic form of radiation-emitting situation that appears to be relevant in PdD, how this occurs is closely related to how the deuterons can become coupled coherently. In the simplest situation, this involves forms of charge and current conservation that are non-local. This can occur as the stoichiometry of PdD_x effectively varies between $x = 1 + \delta$ and $x = 1 - \delta$ (provided δ is sufficiently small), as a result of the strongly anti-bonding nature of the electronic states near the Fermi energy of PdD, when an applied DC field (or pressure), which is required to confine the D, within the lattice, is maintained for a sufficiently long period of time, and collisions are effectively stifled. The associated coupling occurs through a highly polarized bond that, in larger crystals, involves the lowest energy acoustic phonons, which, as envisioned by Giuliano Preparata, can be viewed as a form of semi-classical oscillation of the electromagnetic zero (or “trapped photons”) of the solid [21].

An important point is that in a finite crystal of PdD, discretely defined forms of momentum (P_{cm}) can be transferred rigidly to the center-of-mass of all or a portion of the solid, through resonant processes, that, in larger crystals, mimic the kind of oscillation, envisioned by Preparata. An illustrative example of how this can occur involves a 1-dimensional lattice, with real boundaries, defined by a set of unit cells, each separated from the others by an integer (**n**) multiple of the lattice constant **a**. Constructive interference can occur whenever an integer multiple (**m**) of the deBroglie wavelength (λ_d) equals **a**, or **na**. The allowable coupling (which is defined by $P_{\text{cm}} = \hbar/\lambda d$) as a consequence, associated the lowest energy fluctuations, from rigid translations, involves size dependent forms of momentum transfer. Effectively, the associated EMI can be viewed as involving a form of antenna, defined by **na/m**. In the reference frame that is stationary with respect to the lattice, as illustrated in a previous paper [8], when there are **2N** unit cells in the lattice, the kinds of rigid translations that are consistent with these lowest energy fluctuations occur when, for $\mathbf{j} = \mathbf{m}$ or $\mathbf{j} = \mathbf{n}$, $-\mathbf{N} + \mathbf{1} \leq \mathbf{j} \leq \mathbf{N}$ or $-\mathbf{N} \leq \mathbf{j} \leq \mathbf{N} - \mathbf{1}$.

The basis for this relationship involves a form of degeneracy, associated with the potential, rigid motion of a lattice, alluded to above. Here, in the periodically ordered regions, the electromagnetic fields resonantly scatter, between many possible wave lengths, without altering the energies of particles in the lattice, within the reference frame that is stationary with respect to the lattice. (The lattice is defined by the requirement that each unit cell is electromagnetically neutral.) However, outside the lattice, in the reference frame that is stationary with respect to any externally applied (static) fields, the lattice is allowed to move. Each possible velocity or acceleration that can take place without causing

a collision defines a possible energy band state (through the associated wave-vector) that is degenerate with respect to the others. The presence of any form of collision has the potential of removing these degeneracies. When interaction with the external region, outside the lattice, is sufficiently weak but persists for a sufficiently long time, the differences in energy that result from collisions, can be quite small. This means that a continuum or quasi-continuum of states exist that can potentially couple either to an external electromagnetic field or one associated with potential nuclear reactions (which technically occur in regions external to the lattice since in the immediate vicinity of reactions, net charge is allowed to accumulate).

One potential mechanism for triggering these effects (that appears to be consistent with many of the experiments) involves a situation (in which x varies between $1 + \gamma$ and $1 - \gamma$, in PdD_x) that occurs when ionic charge enters and leaves the solid. Then, instantaneously, charge need not be conserved locally within the solid since it is impossible to measure either the charge or current. Also when this occurs, a form of broken gauge symmetry [4] can take place (resulting from finite size effects), in which portions of the “lattice” can appear to not conserve charge, as a consequence of many charged particles moving in lock-step in a way that is contrary to the conventional situation in which charge is conserved locally, and the associated response, referred to as gauge symmetry, cannot be violated locally [4]. As a consequence, in the interior regions of a solid, charge conservation can occur non-locally, but at the boundaries and outside this region, this is not possible. The possibility that such a region can exist and be important in potential fusion reactions has been ignored in the theoretical pictures that have formed the basis for rejecting CF-related phenomena.

At the boundaries of solids, these kinds of effects can occur in situations in which the associated momentum and energy can grow with increasing time. In particularly unusual situations, associated with PdD_x (as x varies between $1 + \delta$ and $1 - \delta$), fluctuations in charge (of d's and electrons into and away from the lattice for values of x immediately above and below the value $x = 1$) can cause this kind of effect to occur because the net electron–deuteron charge that is allowed to enter the lattice can increase (when x is above the value $x = 1$) and decrease (when x is below the value $x = 1$), as a consequence of the strongly anti-bonding behavior of the electrons, and the associated electron, energy band states (near the Fermi energy) in PdD . As a result, in a finite metallic PdD lattice, a form of “preparation” can take place (involving, effectively, a form of dissociation between the nucleus of each D from its electron). This can occur provided the fluctuations in charge into and away from the lattice are sufficiently small, occur over a sufficiently long period of time, and can result in possible nuclear effects.

This kind of effect can alter possible forms of nuclear fusion in PdD because the $d + d \rightarrow \text{helium-4} + 23.8 \text{ MeV}$ reactions (in a host material) are allowed to occur, provided momentum is allowed to change sufficiently rapidly (even in a quasi-discontinuous manner, for example, through wave function cusps [15]). An important point, in this context, is that even classically, when a particle has mass m , velocity v , charge q , momentum

$$mv = p - \frac{q}{c} A,$$

as opposed to the situation associated with a static, time-independent Coulomb potential situation, where $mv = p$. In particular, in the more general situation associated with the two reactions, $d + d \rightarrow {}^4 \text{He} + 23.8 \text{ MeV}$ and $d + d \rightarrow \alpha + \gamma$, non-local effects are required. In more general situations, it follows from basic electro-dynamic considerations that simply by stressing a metal, with a sufficient force, in particular ways, as the metal approaches nano-scale dimension, potentially new effects, through resonant EMI, can occur that potentially can induce a spectrum of X-rays, lower frequency forms of light (including the kinds of IR forms of heat, observed by Mitchell Swartz [19] and in the SPAWAR experiments [20], and microwaves), and/or phonons. Thus, in any nano-scale PdD “crystal,” as opposed to a static, electrostatic, “Coulomb” barrier, being involved in $d + d \rightarrow {}^4 \text{He}$ (or α -particle) reactions, for example, a more sophisticated, time-dependent QED barrier is probably involved. In general terms, involving larger crystals, Giuliano Preparata [13,21] recognized this possibility (that the barrier that prevents fusion in free space should be very different in solids). But superficially, it appears that he relied on an over-simplified model, in which interactions with charged matter are treated semiclassically through a modified form of free particle interaction.

In fact, in a more realistic theory [8,9], based on a generalization of the conventional semi-classical model of (electron and ion [15]) energy band theory (which, in the case of electrons, is known to accurately describe heat and charge transport), the simplest approximation of the most relevant picture shares many of the intuitive features of the plasma picture suggested by Giuliano Preparata. Important differences exist. Giuliano Preparata assumed well-defined boundaries exist in a solid, so that the lattice could be treated as being stationary with respect to its external environment. In a real solid, it is never possible to determine precisely where the lattice begins and ends, where its boundaries are located, and whether or not it is in motion. The generalized energy band picture that applies to finite lattices is considerably richer because it includes quantum mechanical effects that are implied by these facts.

Starting from these assumptions, in the previous paper [9], the more general theory was used to suggest a number of effects, including the possibility that in the SPAWAR co-deposition experiments, the emission of high energy particles might be related to the orientation of the applied fields. This earlier paper presented an intuitive picture of the underlying QED.

In particular, the concept of “trapped photons,” as envisioned by Preparata, was introduced, and a more general feature of their behavior, that explains how momentum can be conserved non-locally, coherently, through lattice recoil, was identified, through a generalized form of resonant Bragg scattering. Implicitly, the relevant physics of this involves a many photon, coherent state. For this reason, a more complete description of the microscopic physics involves assumptions about the representation of the manyphoton wave function. In order to incorporate Bragg resonance into the multi-photon state, it is sufficient to require that when a photon possesses wave-vector \vec{k} , it also possesses the wave-vector $\vec{k} + \vec{G}$, where

$$|\vec{k}| = |\vec{k} + \vec{G}|, \quad (3)$$

\vec{G} is a reciprocal lattice vector, and the angular frequency of the photon, ω_0 , is given by $\omega_0 = c|\vec{k}|$. In a sufficiently large lattice, Eq. (3) can be required to be valid provided

$$2|\vec{K}| \geq |\vec{G}|. \quad (4)$$

If there are M values of \vec{G} ($\equiv \vec{G}_i, i = 0, M - 1$) that satisfy Eq. (4), the requirement that the multi-photon state $\Psi_{\vec{k}}(x_1, \dots, x_M)$ possess photons with wave-vectors \vec{k} and $\vec{k} + \vec{G}_i$ (for each value of i , with $\vec{G}_0 \equiv 0$) can be imposed through the relationship,

$$\begin{aligned} \Psi_{\vec{k}}(x_1, \dots, x_M) \equiv & \int d^3k_1 \dots d^3k_M \langle \vec{k}_1, \dots, \vec{M}|\vec{k}, \vec{k} + \vec{G}_1, \dots, \vec{k} + \vec{G}_{M-1} \rangle \\ & \times \Phi_{\vec{k}_1}(x_1) \Phi_{\vec{k}_2}(x_2) | \dots \Phi_{\vec{k}_M}(x_M), \end{aligned} \quad (5)$$

where

$$\langle \vec{k}, \vec{k} + \vec{G}_1, \dots, \vec{k} + \vec{G}_{M-1} \rangle = \frac{1}{\sqrt{M!}} a_{\vec{k}}^+ a_{\vec{k} + \vec{G}_1}^+ \dots a_{\vec{k} + \vec{G}_{M-1}}^+ |0\rangle, \quad (6)$$

is the multi-photon eigenstate associated with the occupation of (single) photons with wave-vectors \vec{k} and $\vec{k} + \vec{G}_i$, for all values of i , and

$$\langle \vec{k}_1, \dots, \vec{k}_M | = \langle 0 | a_{\vec{k}_1}^+ a_{\vec{k}_2}^+ \dots a_{\vec{k}_M}^+ \frac{1}{\sqrt{M!}} \quad (7)$$

is an eigenstate of an arbitrary M -photon state (in which each frequency is singly occupied). In Eqs. (6) and (7), respectively, the symbols $a_{\vec{q}}^+$ and $a_{\vec{q}}$ are used to denote creation and annihilation operators, and in Eq. (5), each function $\Phi_{\vec{k}_j}(x_j)$ can be constructed (as shown below) according to the condition that it possess Bloch symmetry using multiple scattering theory.

Equations (5)–(7) apply when at most each photon frequency is occupied by a single photon. With minor modifications (involving changes in the prefactor $\frac{1}{\sqrt{M!}}$), a more general relationship can be constructed that includes the possibility for multiple photon occupation of each photon frequency. An important point is that the overlap between wave functions of the form given by Eq. (5) with the interaction (electromagnetic) potential $V_{Int} = -\frac{e}{c} \vec{J} \bullet \vec{A}$, defined by the currents \vec{J} and vector potential \vec{A} , potentially involves all photons that have wave-vectors \vec{k} and wave-vectors \vec{G} that satisfy Eq. (4). For this reason, as opposed to the situation associated with the conventional $d + d \rightarrow \alpha + \delta$, in which the transition involves a single 23.8 MeV gamma ray, in the situation involving Bragg resonant, trapped photons, the transition is required to involve many photons.

Furthermore, using multiple scattering theory, it is possible to show that the associated wave function has appreciable overlap with many different nuclei, at many different locations in space. For these reasons (that many photons are involved and because overlap occurs involving many nuclei), it is not necessary for appreciable energy and/or momentum to become localized anywhere inside the lattice. As a consequence, implicit in the microscopic physics is the result that high energy particle emission not only is unnecessary, but it is unlikely.

The explicit application of multiple scattering theory (to derive each wave function $\Phi_{\vec{k}_j}(x_j)$) involves requiring that $\Phi_{\vec{k}_j}(x_j)$ satisfy the Helmholtz equation,

$$(\nabla^2 + k_j^2) \Phi_{\vec{k}_j}(x_j) = 0, \quad (8)$$

in a particular region (the interstitial region) of space (which can have infinitesimal extent) and the inhomogeneous wave equation,

$$(\nabla^2 + k_j^2) \Phi_{\vec{k}_j}(x_j) = -\frac{4\pi}{c} J, \quad (9)$$

in the remaining region (the Muffin Tin region). Then, by introducing the Green's function $G(r-r')$ for the Helmholtz equation, it is possible to relate values of Φ in the Interstitial (IS) region to the integral of the product ($J \times G$) of the current density (J) in the Muffin Tin (MT) region with G , and the values Φ and its normal derivative along the boundaries of the MT region using the identity,

$$\begin{aligned} \Phi_{\vec{k}_j}(r)|_{r \in IS} = & \int_{\text{MT boundary}} dA \hat{n} \bullet \{-\nabla_{r'} G(r-r') \Phi_{\vec{k}_j}(r') + G(r-r') \nabla_{r'} \Phi_{\vec{k}_j}(r')\} \\ & + \frac{4\pi}{c} \int_{\text{MT Region}} d^3 r' G(r-r') J(r'). \end{aligned} \quad (10)$$

Here, \hat{n} is a unit vector pointing in the direction normal to the boundary of the MT region, and

$$G(r-r') \equiv G_{k_j}(r-r') = \frac{c}{4\pi} \frac{\cos(k_j|r-r'|)}{|r-r'|} = \frac{c}{4\pi} k_j \Sigma_L n_l(k_j r^>) j_l(k_j r^<) Y^* L(\hat{r}) Y_L(\hat{r}), \quad (11)$$

where $r^>(r^<)$ is $|r'|(|r|)$ when $|r'| > |r|$ and $r^>(r^<)$ is $|r|(|r'|)$ when $|r| > |r'|$, $k_j \equiv |\vec{k}_j|$, respectively, n_j and j_l are l^{th} order spherical Neumann and Bessel functions, $Y_L(\hat{r}) = Y_{l,m}(\hat{r})$ denotes a spherical harmonic, evaluated in the direction of the unit vector \hat{r} (where the index $L = (l, m)$ is used to signify the two values l and m associated with each spherical harmonic).

To make further progress, we introduce the physics associated with lattice recoil. In particular, in the idealized limit associated with a situation in which the lattice moves elastically and rigidly (and the particle–particle separations do not change within the lattice), effectively, regions where charge can accumulate can occur at locations where d's occupy IBS's (and are not part of the lattice); while elsewhere, charge does not accumulate. The recoil effect can be introduced by allowing the locations where charge can accumulate to move relative to locations where it does not accumulate.

Within this approximation, a second interstitial region (where the possible electromagnetic fields also satisfy a Helmholtz equation) is required. It begins at the boundary of each nuclear region, which surrounds a location where d's can have appreciable overlap and extends to the boundary of each MT, where the frequency of each potential photon is Doppler shifted by an amount equal to a suitable frequency associated with the conditions that are responsible for the recoil. This last condition is satisfied (in the non-relativistic limit) when the angular frequency ω in this second IS region satisfies the equation,

$$\omega_0(1 - \beta_{CM}) = \omega = cG_i, \quad (12)$$

where G_i is one of the reciprocal lattice vectors that satisfies Eq. (4), $\beta_{CM} = \frac{v_{CM}}{c}$ is the velocity of the center-of-mass of the lattice (v_{CM}) that results from the recoil process, divided by the speed of light (c), and, as in Eq. (3), $\omega_0 = ck_j$. Again, within the context of this last approximation, a slightly modified version of Eq. (11) (in which k_j is replaced by $\frac{\omega}{c} = G_i$) can be used to determine $\Phi_{k_j}(x)$, and the values $\Phi_{k_j}(x)$ at the boundary of each MT in the MT region can be computed, using this second equation.

Because the MT region in Eq. (10) extends throughout the lattice (specifically, there is at least one MT in each unit cell), implicitly, appreciable overlap can occur between values of $\Phi_{k_j}(x)$ inside the IS region that are located in different unit cells. This result becomes more transparent if we apply multiple scattering theory, as it is used in conventional energy band theory [22]. In particular, to do this, we impose the boundary condition that each wave function $\Phi_{k_j}(x)$ possesses Bloch symmetry, $\Phi_{k_j}(x + R_n) = e^{i\vec{k}_j \cdot \vec{R}_n} \Phi_{k_j}(x)$ (R_n = Bravais lattice vector). As a consequence, it is possible to re-express both integrals on the right-hand side of Eq. (10) (using conventional expansions that are used in energy band theory [22]) in terms of quantities that have comparable magnitude throughout the lattice.

Besides explaining how non-local, reduced energy and momentum processes can result when “trapped photon” states are involved, because these states possess Bloch symmetry, they can couple coherently to the electronic and ionic band states coherently in the kinds of situations associated with PdD. As a result, small changes, associated with coupling between photons that occupy these kinds of states with the solid and (as a consequence) with externally applied fields can take place. A particularly interesting case involves a situation involving an applied magnetic field. In particular, even small, external magnetic fields might play an important role in triggering excess heat, provided they have a suitable orientation.

A particular situation that might apply in this context involves applying a constant magnetic field \vec{B} parallel to the surface. When this occurs, the spins of d's in IBS's, in principle, can couple coherently to \vec{B} (through the Zeeman effect) in such a way that preferentially their precession can induce states that have vanishing spin normal to the surface. This in turn can result in a preferential orientation for possible nuclear reactions in directions that are also normal to the surface. Furthermore, through a form of NMRlike coupling in which a second, external (RF) field is applied normal to the surface, a resonant condition can be established (associated with flipping the spins of the d's that occupy IBS's). Essentially, the optimal way of performing this kind of experiment involves introducing an RF field, that has an angular frequency Ω_L that matches the Larmor frequency of the applied magnetic field ($\Omega_L = \frac{e|\vec{B}|}{m_d c}$, where m_d = deuteron mass) associated with flipping each deuteron spin. This could help to trigger excess heat because to preserve periodic order ${}^4\text{He}$ has to be removed from the solid [1,2,11].

Acknowledgments

I would like to acknowledge valuable conversations with Talbot Chubb, Mitchell Swartz, David Nagel, and Dennis Letts. Partial support of this work was provided by the New Energy Foundation.

References

- [1] S.R. Chubb, T.A. Chubb, Distributed Bosonic States and Condensed Matter Fusion, Naval Research Laboratory Memorandum Report 6600, 1990. <http://newenergytimes.com/Library/1990ChubbS-NRLReport6600.pdf>
- [2] T.A. Chubb, S.R. Chubb, Nuclear Fusion in a Solid via a Bose Bloch Concentrate, Naval Research Laboratory Memorandum Report 6617, 1990. <http://newenergytimes.com/Library/1990ChubbT-NRLReport6617.pdf>
- [3] D. Lindley, The embarrassment of cold fusion, *Nature* **344** (1990) 375.
- [4] S.R. Chubb, Role of Broken Gauge Symmetry in Transport Phenomena Involving Neutral and Charged Particles in a Finite Lattice, <http://arxiv.org/abs/cond-mat/0512363v1>.
- [5] S.R. Chubb, T.A. Chubb, Theoretical Framework for Anomalous Heat and ${}^4\text{He}$ in Transition Metal Systems, *Proc. ICCF8*, 385 (2000). <http://www.lenr-canr.org/acrobat/ChubbSRtheoretica.pdf>
- [6] S.R. Chubb, T.A. Chubb, Relationship between microscopic and macroscopic interactions in low energy nuclear reactions: Lessons learned from $D + D \rightarrow {}^4\text{He}$, *Proc ICCF9*, 57 (2003). <http://www.lenr-canr.org/acrobat/ChubbSRrelationsh.pdf>.
- [7] S.R. Chubb, Nuts and Bolts of the Ion Band State Theory, *Proc ICCF10*, 735 (2005). <http://www.lenr-canr.org/acrobat/ChubbSRtheoretica.pdf>
- [8] S.R. Chubb, Roles of Approximate Symmetry and Finite Size in the Quantum Electrodynamics of $d + d \rightarrow {}^4\text{He}$ in Condensed Matter Nuclear Science, in *8th International Workshop on Anomalies in Hydrogen/Deuterium Loaded Metals*, W. Collis (ed.), Italy, International Society of Condensed Matter Nuclear Science, 2007.
- [9] S.R. Chubb, Resonant Electromagnetic Interaction in Low Energy Nuclear Reactions, in *Low-Energy Nuclear Reactions Sourcebook*, J. Marwan, S.B. Krivit (eds.), Washington, D.C., American Chemical Society, 2008, pp. 99–123.
- [10] David Fox, private communication.
- [11] S.R. Chubb, T.A. Chubb, Lattice Induced Nuclear Chemistry. in *Anomalous Nuclear Effects. in Deuterium/Solid Systems*, S.E. Jones et al. (eds.), AIP Conference Proceedings 228, American Institute of Physics, New York, NY, 1991, pp. 691–710.
- [12] J. Schwinger, *Proc. ICCF1*, 1990, pp. 130–136.
- [13] G. Preparata, *Proc ICCF1*, 1990, pp. 91–97.
- [14] M.H. Miles, Excess Heat and Helium Production in Palladium and Palladium Alloys, in *Spawarsyscom SSC TR 1862*, vol. 1, P.A. Mosier-Boss, S. Szpak (eds.), San Diego, Naval Space Warfare System Center, 2002, pp. 19–30. <http://lenr-canr.org/acrobat/MosierBossthermaland.pdf>
- [15] S.R. Chubb, T.A. Chubb, Ion-band state fusion: reactions, power density, and the quantum reality question, *Fusion Technol.* **24** (1993) 403 . T.A. Chubb, S.R. Chubb, Cold Fusion as an Interaction Between Ion Band States , *Fusion Technol.* **20** (1991) 93.
- [16] D.R. Thompson, *Nucl. Phys.* **A154** (1970) 442. Thompson cites the relevant experimental information.
- [17] S.B. Krivit, Extraordinary Courage: Report on Some LENR Presentations at the 2007 American Physical Society Meeting. <http://www.newenergytimes.com/news/2007/2007KrivitS-ExtraordinaryCourage.pdf>.
- [18] S. Szpak, P.A. Mosier-Boss, F.E. Gordon, *Naturwissenschaften* **94** (2007) 511–514.
- [19] M. Swartz, presented at The 2009 Advanced Colloquium on Lattice Assisted Nuclear Reactions, Cambridge, MA, June 2009. Also private communication.
- [20] S. Szpak, S., P.A. Mosier-Boss, F.E. Gordon, Polarized D^+ /Pd-D₂O System: Hot Spots and Mini-Explosions, *Proc. ICCF10*, (2006). <http://www.lenr-canr.org/acrobat/SzpakSpolarizedd.pdf>
- [21] Giuliano Preparata, QED Coherence in Matter. New Jersey, World Scientific, 1995, pp. 25–40. Ibid, pp. 153–178. And private communication.
- [22] Antonios Gonis, William H. Butler, *Multiple Scattering in Solids*, Springer-Verlag, New York, 2000, pp. 282.



Research Article

Weight of Evidence for the Fleischmann–Pons Effect *

Rodney Johnson and Michael Melich †

W.E. Meyer Institute of Systems Engineering Naval Postgraduate School, Monterey, CA 93943, USA

Abstract

Cravens and Letts [1] have analyzed a portion (167 papers) of the published literature reporting on D₂O electrolysis experiments such as Fleischmann and Pons's (FP). They identify four criteria for what constitutes a “proper” FP experiment and state that experiments that satisfy all four criteria are likely to succeed in producing excess heat, while those that do not are likely to fail. This paper presents results of using a Bayesian network for probabilistic analysis of this claim. Consideration of a small subset of the papers (12) is sufficient to give a likelihood ratio of about 28 to 1 in favor, and this number appears to grow generally rapidly, though not monotonically, as more papers are added to the set.

© 2011 ISCMNS. All rights reserved.

Keywords: Bayesian networks, Cold fusion, Fleischmann–Pons effect, Weight of evidence

PACS: 01.30.Rr, 02.50.Cw, 25.45, 82.45.

1. Introduction

Some of us, when asked why we tend to accept the reality of the Fleischmann–Pons effect (FPE), reply with the statement:

“It’s not any one experiment; it’s the number and variety of confirmations by independent researchers around the world.”

Independent replication is considered as an important step in acceptance of new experimental results. We here report an attempt to model in formal terms the intuition that¹ if a number of published reports have a significant probability of being right about excess heat, then “having a lot dramatically increases the probability.”

We use Bayesian probability theory, a discipline with a long history of use in dealing precisely and systematically with uncertain information. (This dates back at least to its use by Laplace in comparing imperfect astronomical

*The views expressed herein are those of the authors and not necessarily those of the US Government, Department of Defense, Department of the Navy, or the Naval Postgraduate School.

†E-mail: melich@alumni.rice.edu

¹ . . . to paraphrase an anonymous reviewer of this article.

observations in celestial mechanics with Newton's gravitational theory. We are persuaded in part by the arguments of Jaynes [2].²) Specifically we use a *Bayesian network* (see the subsection with that title) a tool for dealing with complex sets of interrelated propositions. Here we have a proposition, "the FPE is real" with other propositions concerning a number of pertinent reports, each singly open to doubt but together sufficient in some cases to convert initial skepticism into acceptance.

We summarize results in terms of the *weight of evidence* (see the subsection with that title) a quantity that indicates how one should modify a probability assessment in the light of new evidence. Readers will each bring their own prior information to the table. Those who give a sufficiently low prior probability to the FPE will remain unpersuaded after taking the contents of the literature into account, though they should be less skeptical than before. Those who give a probability of flat-out 0 will retain that value, having precluded the possibility of learning. Those who already accept the FPE will find confirmation of their assessment. And those who are not sure of their probability assignment may find help in giving it a numerical value (see subsection "Weight of Evidence" and the references there to Jaynes and I.J. Good.)

1.1. Cravens—Letts database

Cravens and Letts [1] report a study of 167 selected papers concerning heat generation in "classical" Fleischmann–Pons electrolytic systems: cells with Pd cathodes in D₂O-based electrolyte. The list spans the years 1989–2007 and is non-exhaustive mainly because papers were included only if available in digital form. The authors rated the papers, when possible, according to four *yes/no* "enabling criteria," related to (1) cathode loading, (2) good chemical procedures, (3) operating current densities, and (4) non-equilibrium operation. (See the paper [1] for details.) In addition they assigned a *yes/no* value according to whether excess power was reported. They successfully rated 122 of the 167 papers and, after statistical analysis, concluded that production of excess power was highly correlated with the number of criteria satisfied—very likely if all four were met and less likely if fewer were met.

1.2. What is the problem?

We are interested in questions such as:

"Given that in paper #1, where all 4 criteria were met, heat was observed, and in paper #2, where only 2 criteria were met, no heat was observed, and . . . in paper #167, . . . heat was observed, then what can we say about the probability that the FP effect is 'real'?"

In condensed-matter nuclear science in general we face multiple observations and experimental results, and multiple conjectures and hypotheses that might explain them. To illustrate, consider the propositions:

- A: Nuclear reactions occur at low temperature in solids.
- B: Excess heat is observed.
- C: Helium production is observed.
- D: Emission of energetic particles is observed.

Then *B*, *C*, and *D* are observations that can serve as evidence in support for *A*, considered as a hypothesis. Likewise, consider propositions:

²"In this workshop we are venturing into a smoky area of science where nobody knows what the real truth is. [Always in such fields] supreme self-confidence takes the place of rational arguments. Therefore we will try to avoid dogmatic assertions . . . We think that the original viewpoint of James Bernoulli and Laplace [about probability] offers some advantages today in both conceptual clarity and technical results for currently mysterious problems."—Jaynes [3]

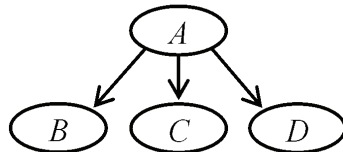


Figure 1. Multiple support for a hypothesis.

- E*: Known nuclear reactions & quantum many-body effects.
- F*: “New physics”.³
- G*: Error/deception.
- H*: Excess heat is reported.

Then *E*, *F*, and *G* are alternative hypotheses that might explain observation *H*. The relations between the propositions are shown schematically in Figs. 1 and 2. These are simple *Bayesian networks*; see the subsection below with that title.

2. Bayesian Methods

In general there may be more complicated interrelations (as in Fig. 3). We need help in thinking quantitatively about such problems, and probability theory provides tools for doing so. *Bayes’s rule* (or *Bayes’s theorem*) is a fundamental rule of probability, used in updating the probability of a proposition in the light of new information. There are various methods based on it (called “*Bayesian*”), including *Bayesian networks*, which allow representing complex relations between propositions and making inferences concerning their probabilities.

2.1. Rules for probability

The degree of credence we accord to a proposition is (or should be) subject to change when we learn new relevant information. In formal terms, if *A* is a proposition to which we have initially assigned a probability $P(A)$, and we then obtain new information in the form of a proposition *B*, we update the probability of *A* to a quantity $P(A|B)$, the *conditional probability* of *A*, given *B*. One also uses the terms *prior* and *posterior* probabilities for $P(A)$ and $P(A|B)$, respectively. The process could continue, of course. Obtaining further new information, say *C*, leads to $P(A|BC)$, and so on. In this section we collect some basic rules, prominent among them Bayes’s theorem, for dealing with conditional probabilities. We recommend the textbook by Jaynes [2] for (along with much else) a thorough discussion of what we here touch on lightly.

2.1.1. Bayes example problem

It is common in textbooks to introduce Bayes’s theorem with an example: medical screening. Say you are a doctor screening for an uncommon but serious disease, where “uncommon” means:

1% of people in the general population have the disease.

Also suppose there is a quite reliable test for the disease:

³... whatever we might choose to mean by the phrase. The propositions listed here are informal, abbreviated, and intended primarily as illustration.

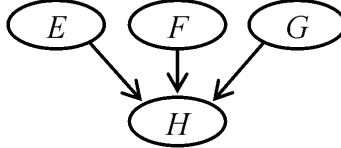


Figure 2. Alternative explanations.

98% of people with the disease will test positive;
 95% of those without the disease will test negative.

You give one of your patients the test as part of a routine physical, and the results come back positive. Do you tell the patient: “There is a 98% chance that you have a serious disease”?

We will see that the probability is actually closer to 16.526%, or about one chance in six, *not* 98%. Your patient is probably healthy. (Expensive or risky treatment is unjustified. But more testing is mandatory; ignoring a 1 in 6 chance amounts to Russian roulette.)

We express the given information symbolically:⁴

D : disease T : test positive
 D' : no disease T' : test negative

$P(D) = 0.01$: probability of disease in the absence of test results
 $P(D|T)$: the conditional probability of disease, given positive test results

We want $P(D|T)$. We have $P(D)$ and two other conditional probabilities:

$P(T|D) = 0.98$: probability of a positive test, given that the disease is present
 $P(T'|D') = 0.95$: probability of a negative test, given that the disease is absent

2.1.2. Rules

We collect here some basic rules of probability theory. These will be used in evaluating $P(D|T)$.

Product rule: probability that A and B are both true

$$P(AB) = P(A)P(B|A) = P(B)P(A|B)$$

Bayes's rule:

$$P(A|B) = P(B|A)P(A)/P(B)$$

Sum rule:

$$P(B) = P(B|A)P(A) + P(B|A')P(A') + P(B|A'')P(A'') + \dots$$

where

$$A, A', A'', \dots$$

⁴In general (as in the “sum rule” of the next sub-subsection) we use a notation such as A, A', A'', \dots to denote a set of propositions exactly one of which is true. Here we assume that D and D' are such a set (one either has the disease or one doesn't) and likewise for T and T' (only two test results are possible: positive and negative). In this special case of just two alternatives, one can read the prime symbol as logical negation: *not-D* for D' and *not-T* for T' .

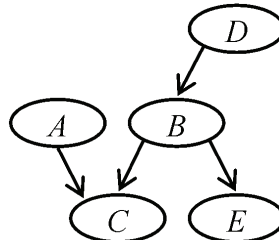


Figure 3. Bayesian network.

are an exhaustive set of mutually exclusive propositions – that is, one must be true, but no two can be true at once.

The sum rule is useful for evaluating the denominator $P(B)$ on the right-hand side of Bayes's rule. Some variants of these rules can be useful; we may use

$$P(A|B) = P(AB)/P(B) \quad (1)$$

in place of Bayes's rule as just given, and we may use the sum rule in the form

$$P(B) = P(AB) + P(A'B) + P(A''B) + \dots \quad (2)$$

2.1.3. Solution of example problem

Applying Bayes's rule to the previously given probabilities gives

$$P(D|T) = P(T|D)P(D)/P(T) = 0.98 \times 0.01/P(T)$$

and the sum rule gives

$$\begin{aligned} P(T) &= P(T|D)P(D) + P(T|D')P(D') \\ &= 0.98 \times 0.01 + 0.05 \times 0.99 \\ &= 0.0098 + 0.0495 = 0.0593 \end{aligned}$$

where we have used the fact that $P(T|D') = 1 - P(T'|D') = 1 - 0.95 = 0.05$. Finally,

$$P(D|T) = 0.98 \times 0.01/0.0593 = 0.16526$$

which is the stated result of 16.526%, or about one chance in six.

2.2. Bayesian networks

A Bayesian network is a graphical representation of complex relations between propositions; it allows inferences concerning their probabilities. Figure 3 shows an example slightly more general than the ones shown in Figs. 1 and 2.

A Bayesian network consists of nodes connected by arrows. Loops, as in Fig. 4, can lead to contradictions and are not allowed. (This means that the network is a *directed acyclic graph*.) With each node is associated a “random variable” (such as A, B, C, \dots in Fig. 3). By calling a variable such as A “random” we mean simply that:

- (1) There is a set of possible values $\{a_1, a_2, \dots, a_n\}$, so that the propositions $A = a_1, A = a_2, \dots, A = a_n$ form an exhaustive set of mutually exclusive propositions; and
- (2) We can talk about probabilities (perhaps conditional) of these propositions, e.g. $P(A = a_i), P(B = b_j|A = a_i)$.

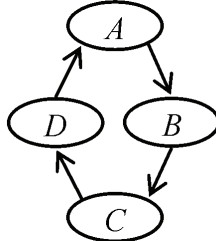


Figure 4. Loop (not allowed).

True-false proposition, such as D and T of the medical screening example, are included (see Fig. 5); the set of values is just $\{true, false\}$.

Arrows indicate conditional dependence. If there is an arrow from a node X to a node Y , we call X a parent of Y . Thus the parents of C in Fig. 3 are A and B . A variable has a probability distribution conditional on its parents. In the case of A , B , and C , this means that conditional probabilities $P(C = c|A = a, B = b)$ are given for all values a , b , and c in the value sets of A , B , and C , respectively. This generalizes in a straightforward way to any number of parents. For a node without parents, such as A , we require the unconditional probabilities $P(A = a)$ for each a .

Bayesian networks can be used for updating our probabilities for values of some variables when we obtain new information in the form of values for other variables. This generalizes the medical screening example. There, we learned the value $T = true$ for the test result, making it no longer uncertain. Consequently we could update our probability for D , disease, from the prior value $P(D)$ to the posterior value $P(D|T = true)$. Analogously, if we learn values for some of the variables, say C and E , in the more elaborate network of Fig. 3, we can ask how the new information affects the probabilities for the values of other variables, such as B .

To begin, in terms of the conditional and unconditional probabilities associated with the nodes, we can write an expression for the joint probability distribution for the entire set of variables; for the illustrative network of Fig. 3, this is the set of probabilities $P(A = a, B = b, C = c, D = d, E = e)$ that $A = a$ and $B = b$ and $C = c$ and $D = d$ and $E = e$, where a , b , c , d , and e range over their respective value sets. We show this in a shorthand notation, writing A for $A = a$, B for $B = b$, etc., so that the desired set of probabilities is denoted by $P(ABCDE)$; they are then given by:

$$P(ABCDE) = P(A)P(B|D)P(C|AB)P(D)P(E|B). \quad (3)$$

In general there is one factor for each node, consisting of the associated probability expression (conditional or unconditional).

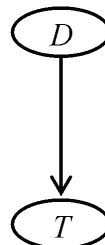


Figure 5. Medical screening example.

From this we can calculate other conditional probabilities such as $P(B|CE)$, for example: the updated probabilities for B , given that we have learned values for C and for E . By Eq. (1), the alternative form of Bayes's rule given above, we can write:

$$P(B|CE) = P(BCE)/P(CE). \quad (4)$$

We can get the numerator, $P(BCE)$, by using essentially the alternative form of the sum rule, Eq. (2) above: sum (3) over the variables that do not occur in $P(BCE)$:

$$P(BCE) = \sum_{a,d} P(A = a, B, C, D = d, E).$$

Likewise we get the denominator by summing over B as well:

$$P(CE) = \sum_{a,b,d} P(A = a, B = b, C, D = d, E) = \sum_b P(B = b, C, E).$$

And the last two equations allow us to compute the desired quotient in (4).

For more information about Bayesian networks, see the textbook by Jensen [4], for example. There are also useful on-line tutorials by Breese and Koller [5] and by Murphy [6].

Software support is necessary for work with networks of any substantial size. For the work reported here we took advantage of a Java applet written by Yap, Santos et al. [7] at the University of British Columbia and made available for download. This allows one to draw a network by means of a graphical interface, enter conditional probabilities in tabular form, set observed values for selected nodes, and display the resulting probabilities for other nodes.

2.3. Weight of evidence

For inference about a *yes/no* proposition, a formulation of Bayes's theorem in terms of *odds* and *likelihoods ratios* can be useful. First, a bit of terminology: The quantities $P(B|A)$, $P(B|A')$, $P(B|A'')$, ... that occur in the sum rule (under "Rules" above) are called the *likelihoods* of A , A' , A'' ,⁵ For a pair of alternatives, A and A' , the quotient $P(B|A)/P(B|A')$ is called the likelihood ratio. When these are the only alternatives, we have $P(A)/P(A') = P(A)/(1 - P(A))$; this quantity is the (prior) odds for A and denoted by $O(A)$. Similarly, the posterior odds for A are $O(A|B) = P(A|B)/P(A'|B)$.

Now write Bayes's rule for A and for A' :

$$P(A|B) = P(A)P(B|A)/P(B)P(A'|B) = P(A')P(B|A')/P(B)$$

and divide the first equation by the second. The factors of $P(B)$ cancel, and we get:

$$P(A|B)/P(A'|B) = [P(A)/P(A')][P(B|A)/P(B|A')].$$

The left-hand side is the posterior odds for A , the first factor on the right is the prior odds, and the second factor is the likelihood ratio. Thus:

$$O(A|B) = O(A)[P(B|A)/P(B|A')],$$

which we can state as:

⁵Recall that A, A', A'', \dots form an exhaustive set of mutually exclusive propositions. "Likelihood" is used in a technical sense. The terminology is unfortunate because it may give the impression that the likelihoods are conditional probabilities of A, A', A'', \dots , which they are not; in particular they need not sum to 1.

$$\text{“posterior odds} = \text{prior odds} \times \text{likelihood ratio”}$$

If the “evidence” B consists of several observations B_1, B_2, \dots that are independent in the sense that $P(B_1 B_2, \dots | A) = P(B_1 | A)P(B_2 | A)\dots$ and $P(B_1 B_2, \dots | A') = P(B_1 | A')P(B_2 | A')\dots$, then the equation generalizes to

$$O(A | B_1 B_2, \dots) = O(A)[P(B_1 | A)/P(B_1 | A')][P(B_2 | A)/P(B_2 | A')]\dots$$

Taking logs of all the factors gives an additive version. Thus taking a new piece of independent evidence B_i into account just increments the log of our odds for A by

$$\log[P(B_i | A)/P(B_i | A')]$$

which is called the *weight of evidence* for A provided by B_i (see [8, 2, pp. 91 ff.]).

If one starts with noncommittal prior odds of 1:1, evenly balanced between acceptance and rejection of a proposition, then the likelihood ratio of the evidence gives ones posterior odds. On the other hand, one can view the reciprocal of the likelihood ratio as a “critical prior”: the prior odds such that the evidence would bring us to posterior odds of 1:1. In this latter role, the likelihood ratio can help us in assigning a numerical value to our prior odds for a proposition; imagine a successions of independent repetitions B_1, B_2, \dots of an experiment with a given likelihood ratio and ask how many successful outcomes would bring us to a state of uncertainty, poised between acceptance and rejection (see [8, 2, Ch. 5]).

Our task will be to evaluate the likelihood ratio (equivalently, the weight of evidence) for the proposition that “the FP effect is real” provided by Cravens and Letts’s ratings of a subset of the papers in their database.

2.4. Estimating probabilities

In the medical example we were given the values $P(T|D) = 0.98$, $P(T'|D') = 0.95$, $P(D) = 0.01$. In practice such numbers are often gotten from a study: give the test to some people known to have the disease, and observe that about 98% test positive. The numbers are known only with some uncertainty, e.g. “The fraction of people with the disease who test positive is in the range 0.980 ± 0.002 with probability 68%. This seems to be saying that $P(T|D)$ is in a certain range with a certain probability. What do we mean by the probability of a statement about other probabilities?⁶.

Our treatment of Cravens and Letts’s evidence will involve probabilities that are not known in advance but are estimated from the data. To illustrate the considerations involved, we present a simple problem.

The “biased coin” problem concerns a coin for which the probability p of heads is some arbitrary number between 0 and 1, not known to us and not necessarily 0.5. It is not at all clear how one could construct such an object in practice,⁷ so it may be better to think of a game spinner with two sectors, marked H and T , with H containing a fraction p of the circle (Fig. 6). If we spin so that the probable location of the pointer is uniformly distributed over the circle, the probability of its showing heads is p .

Now write H_p for the proposition that the size of the H sector is p , and suppose that this unknown size was chosen at random (uniformly) between 0 and 1 (Fig. 7). We are now dealing with continuous probability distributions; $P(H_p)$ is a probability *density*, not a discrete value, and satisfies $\int P(H_p)dp = 1$ rather than $\sum_p P(H_p) = 1$.

⁶The need to take systematic account of uncertainties in our information is ubiquitous and has a long history—cf. our previous mention of Laplace ([9, 2, Ch. 5])

⁷We might try loading a coin by making it of two layers with lead on one side and aluminum on the other. This turns out not to be effective; see [2, Chapter 10.3], “How to cheat at coin and die tossing.” Jaynes shows in fact that the probability of heads is not just an intrinsic physical property of the coin and may have little to do with quantities such as the displacement of the center of gravity of the coin from its geometrical center.

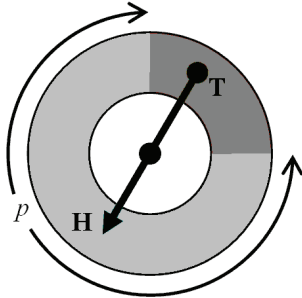


Figure 6. “Biased coin” spinner.

Suppose we spin once and observe a head. What is our new probability for H_p , given E_{11} : one head in one trial? Bayes’s rule for continuous probability distributions gives:

$$P(H_p|E_{11}) = P(E_{11}|H_p)P(H_p)/P(E_{11}) = p/P(E_{11})$$

Here $P(E_{11}|H_p)$ is p , because that’s what H_p says: the probability of getting a head is p . And $P(H_p)$ is 1 by assumption. The continuous version of the sum rule (“Rules” above) gives

$$\begin{aligned} P(E_{11}) &= \int_0^1 P(E_{11}|H_p)P(H_p)dp = \int_0^1 pdp = 1/2 \\ P(H_p|E_{11}) &= 2p \end{aligned} \tag{5}$$

as in Fig. 8.

Now the probability of heads on the next trial is:

$$P(\text{“one more head”}|E_{11}) = \int_0^1 P(\text{“one more head”}|E_{11}H_p)P(H_p|E_{11})dp$$

The first factor in the integrand is p , and equation (5) gives the second. So

$$P(\text{“one more head”}|E_{11}) = \int_0^1 2p^2 dp/3$$

We can continue making trials and updating our probability distribution for H_p . With the notation E_{mn} = “ m heads observed in n trials,” we obtain the general formula:

$$P(H_p|E_{mn}) = [(n+1)!/m!(n-m)!]p^m(1-p)^{n-m}$$

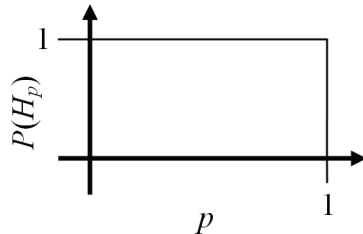


Figure 7. Uniform prior $P(H_p)$.

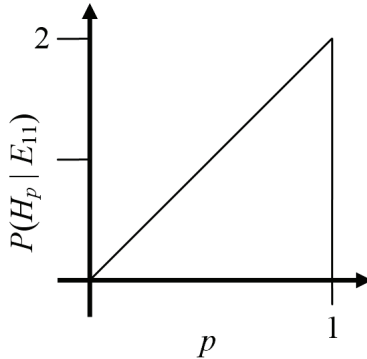


Figure 8. One head in one trial observed.

and the formula for the probability of heads on the next trial is:

$$P(\text{"one more head"} | E_{mn}) = (m + 1)/(n + 2).$$

This is Laplace's *rule of succession*: with a uniform prior for H_p and m "successes" out of n independent trials, the probability μ of success on the next trial is given by

$$\mu = (m + 1)/(n + 2)$$

The successive posterior distributions peak up more and more sharply as the number of trials increases (Fig. 9). The width of the peak is 2σ , where the standard deviation σ is given by

$$\sigma = \sqrt{\mu(1 - \mu)(n + 3)}$$

and the mean μ is as just given. For a derivation of σ , see Eq. (6.35) in [2].

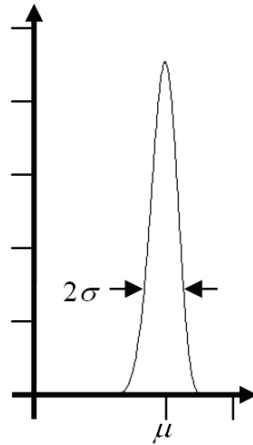


Figure 9. Peak shape.

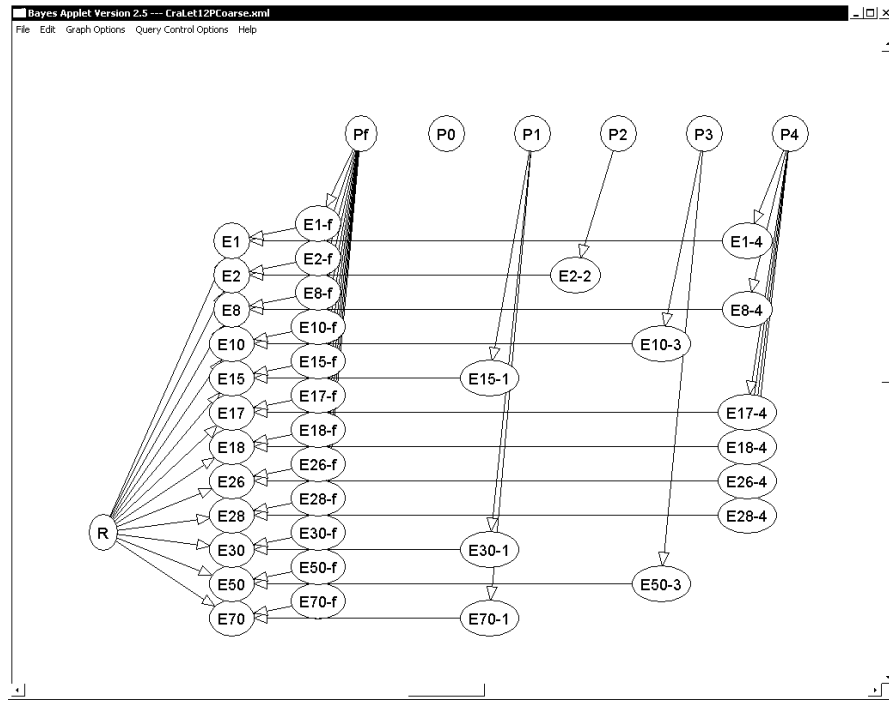


Figure 10. Network for twelve selected papers (initial configuration).

The assumption of a uniform prior may or may not be justified, depending on available information. But if the prior is continuous and non-zero near μ , the shape of the posterior will often be found to resemble Fig. 9.

3. Problem Setup

The network we developed is shown in Fig. 10 as displayed by the applet [7] that was mentioned at the end of the subsection “Bayesian Networks”. Node R is the proposition of interest – roughly speaking, “is the FP effect ‘real’?” The nodes E_1, E_2, \dots, E_{70} refer to the results published in the set of papers selected for initial consideration; the subscripts are index numbers of the papers in the Cravens–Letts [1] database. The other “ E ” nodes are auxiliary nodes associated with the papers, and the “ P ” nodes are various probabilities to be estimated from the data by means illustrated in the previous subsection.

Table 1. $P(R)$

R	
True	False
0.5	0.5

3.1. Selected papers

Cravens and Letts [10] suggested eight papers for initial consideration: those numbered 2 through 28 in the following list; these were deemed to represent particularly significant or influential early positive and negative results. To these we added the initial Fleischmann–Pons report (#1) and three arbitrarily selected later papers (#30, #50, #70).

#	Cri	Heat	Citation
1	4	Yes	M. Fleischmann & S. Pons, <i>J. Electroanal. Chem.</i> 261 (2, part 1) 301–308 (Apr. 10, 1989).
2	2	No	R. D. Armstrong et al., <i>Electrochimica Acta</i> 34 (9) 1319–1322 (Sep. 1989).
8	4	Yes	R. C. Kainthla et al., <i>Electrochimica Acta</i> 34 (9) 1315–1318 (Sep. 1989).
10	3	No	N. S. Lewis et al., <i>Nature</i> 340 (6234) 525–530 (Aug. 17, 1989).
15	1	No	D. E. Williams et al., <i>Nature</i> 342 (6248) 375–384 (Nov. 23, 1989).
17	4	Yes	A. J. Appleby et al., <i>Proc. First Ann. Conf. Cold Fusion</i> , 32–43 (Mar. 1990).
18	4	Yes	Y. Arata & Y.-C. Zhang <i>Proc. Japan Acad. B</i> 66 (1) 1–6 (1990).
26	4	Yes	S. Guruswamy & M. E. Wadsworth, <i>Proc. First Ann. Conf. Cold Fusion</i> , 314–327, (Mar. 1990).
28	4	Yes	T. Lautzenheiser & D. Phelps, <i>Amoco Production Company Research Report T-90-E-02, 90081ART0082</i> (Mar. 1990).
30	1	No	G. R. Longhurst et al., <i>J. Fusion Energy</i> 9 (3) 337–343 (Sep. 1990)
50	3	Yes	V. C. Noninski & C. I. Noninski, <i>Fusion Technology</i> 19 (2) 364–368 (Mar. 1991)
70	1	No	T. I. Quickenden & T. A. Green, <i>J. Electroanal. Chem.</i> 344 (1–2) 167–185 (Jan. 15, 1993).

The numbers under “#” are the index numbers of the papers in Cravens and Letts’s database. The numbers under “Cri” give the number of enabling criteria satisfied by the paper. A Yes or No under “Heat” indicates whether excess heat was reported.

3.2. Network propositions

Proposition R can also be phrased as “the experimental treatment makes a difference”. We consider two alternatives:

- $R = \text{false}$: the probability of observing excess heat is the same (P_f) regardless of whether all, some, or none of Cravens and Letts’s enabling criteria are satisfied. This would imply that reported observations of excess heat are the result of error, deception, or extraneous factors.
- $R = \text{true}$: the probability of observing excess heat has one of several values (P_0, \dots, P_4), depending on the number of enabling criteria that are satisfied.

E_i states that excess heat was reported in paper number i of the data base.

E_{if} states that excess heat was reported in paper number i in case $R = \text{false}$. Its truth value is irrelevant in case $R = \text{true}$. Its conditional probability is simply the value of P_f .

E_{in} states that excess heat was reported in paper number i in case $R = \text{true}$, where n is the number of enabling criteria met by the paper. Its truth value is irrelevant in case $R = \text{false}$. Its conditional probability is simply the value of P_n .

Nodes E_{if} and E_{in} exist to simplify the expression of the conditional probabilities of E_i , rather than for any intrinsic interest of their own. E_i is *true* if either (1) R and E_{in} are both *true* or (2) R is *false* and E_{if} is *true*; E_i is *false* otherwise. The E_{if} and E_{in} nodes could be eliminated and E_i made directly dependent on R , P_f , and P_n at the expense of expanding Table 2 to a table with 50 rows.

Table 2. $P(E_i | RE_{if} E_{in})$

R	E_{if}	E_{in}	E_i	
			True	False
True	True	True	1	0
True	True	False	0	1
True	False	True	1	0
True	False	False	0	1
False	True	True	1	0
False	True	False	1	0
False	False	True	0	1
False	False	False	0	1

3.3. Network variables

P_f is the probability of excess heat being reported in case $R = \text{false}$.

P_n is the probability of excess heat being reported in an experiment satisfying n of the enabling criteria ($n = 0, \dots, 4$) in case $R = \text{true}$.

P_f and P_0, \dots, P_4 are probabilities to be estimated from the data by means illustrated under ‘‘Estimating Probabilities’’ above. Ideally they would each be described by a continuous probability density on the interval from 0 to 1. Because of practical limitations of the software, we used fairly coarse discrete approximations.

3.4. Probability tables

The prior and conditional probabilities for the nodes of the network are specified in tabular form.

We set the prior probability of R equal to 0.5, as shown in Table 1, giving prior odds of 1. Consequently the posterior odds are equal to the likelihood ratio. (See subsection ‘‘Weight of Evidence’’.) This makes it easy to determine the weight of evidence from the program outputs.

The conditional probability of E_i is specified as in Table 2. This simply makes E_i agree with E_{if} when R is false and with E_{in} when R is True. The actual probability values are those of E_{if} in the first case and E_{in} in the second.

The conditional probabilities of E_{in} are given in Table 3; the same values apply also for E_{if} . The probability of E_{in} , given P_n , is by definition simply the value of P_n ; and the probability of E_{if} , given P_f , is the value of P_f .

The prior probabilities of P_n ($n = 0, \dots, 4$) are shown in Table 4, and the same values apply for P_f . They are all the same: a coarse discrete approximation to a uniform distribution on the unit interval.

Table 3. $P(E_{in} | P_n)$

P_{in}	E_{in}	
	True	False
0.1	0.1	0.9
0.3	0.3	0.7
0.5	0.5	0.5
0.7	0.7	0.3
0.9	0.9	0.1

Table 4. $P(P_n)$

P_n				
0.1	0.3	0.5	0.7	0.9
0.2	0.2	0.2	0.2	0.2

4. Results

After entering the probability tables in the nodes of the network of Fig. 10, we successively declared “observed” values for the nodes E_i , starting with *true* for E_1 and finishing with *false* for E_{70} . The final state of the network is shown in Fig. 11. Display of the probability distributions of the nodes R and P_f , P_0 , ..., P_4 , has been enabled.

The posterior probabilities for $R = \text{true}$ and $R = \text{false}$ are 0.9655 and 0.0345, corresponding to posterior odds of 27.99. This then is the final value of the likelihood ratio, since we started by setting the prior odds to 1.0. The value of the likelihood ratio is plotted in Fig. 12 as a function of the number of papers taken into account, from 1 paper (#1 only), through 12 papers. The notations across the top show for each point the number of enabling criteria met and whether excess heat was observed.

The likelihood ratio for R , give 1 paper, is 1.0, exactly equal to the prior value of 1.0 with no papers at all (not plotted). With one paper, the distributions of P_f and P_4 were identical—a bit biased toward high values, as the first paper (#1) reported heat. There was not yet a basis for choosing between the two. Adding a second paper (#2, reporting no heat) increased the ratio to about 1.47. Thereafter the trend is generally upward with increasing steepness, but with a conspicuous glitch at the 11th paper (#50). The two neighboring papers, #30 and #70, reported *no* for excess heat, yet

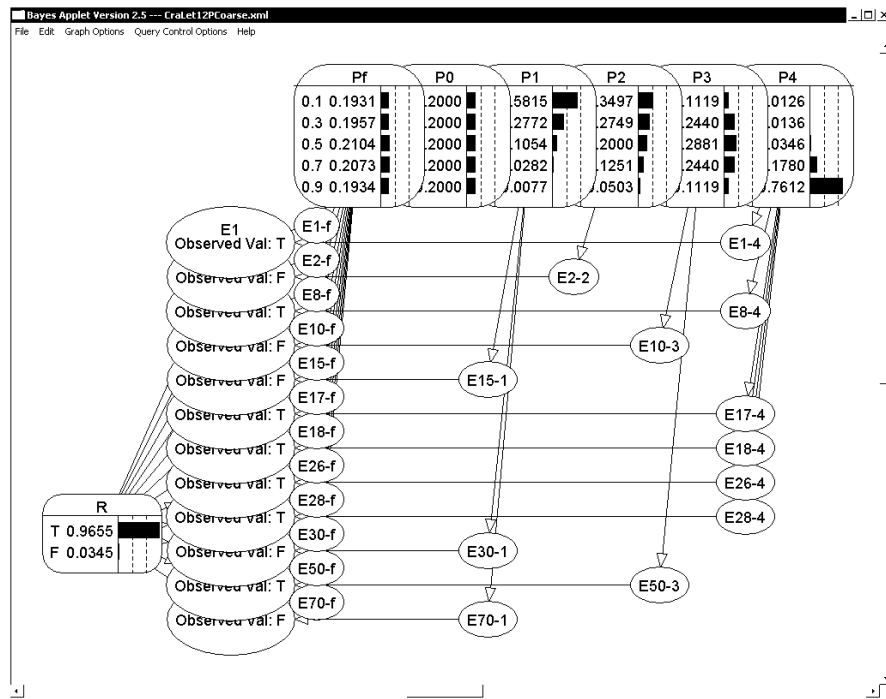


Figure 11. Final configuration of network for twelve selected papers.

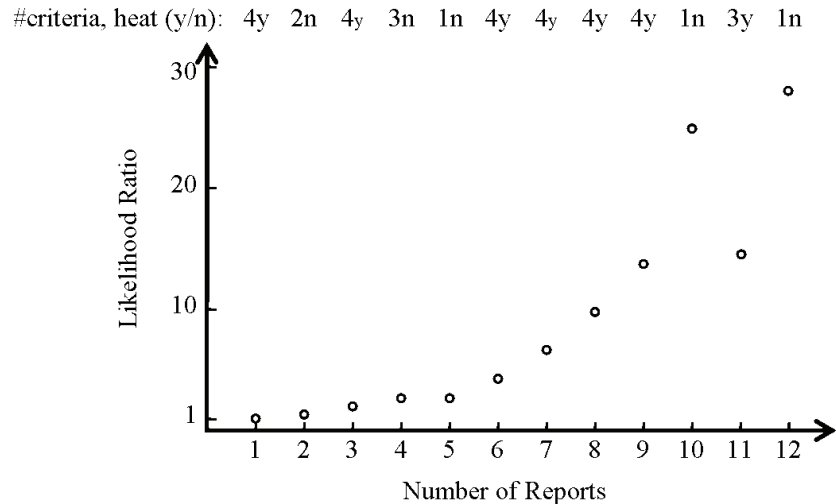


Figure 12. Change in likelihood ratio as more and more papers are taken into account.

their inclusion increased the likelihood ratio for R . On the other hand, paper #50, though positive for heat, nevertheless decreased the likelihood ratio for R . A possible explanation is that only one previous paper had met exactly 3 of the 4 criteria, and that one was negative for heat. This disagreement, one *no* and one *yes* for heat, made the case “3 criteria met” appear “random” and so apparently decreased the likelihood ratio for R . This underscores the fact that R is asking whether *the experimental treatment makes a difference*. The observation of no heat when some of the criteria are not met can serve as evidence for R just as well as the observation of heat when all are met.

In the final configuration, the posterior distribution for P_4 was strongly biased toward high values, as shown in Fig. 11, and as one would expect. P_3 was symmetrically distributed, somewhat peaked near 0.5, as for that case the evidence was balanced, with one paper positive for heat and one negative. P_1 and P_2 were biased toward low values, again as one would expect. P_0 was flat, unchanged from its prior, as no evidence was included bearing on the case of 0 criteria met. The distribution of P_f was quite flat, close to its prior, as the probability for $R = \text{false}$ was estimated as being rather small. Note that if R were definitely known to be *true*, the value of P_f would be irrelevant, and we would expect it to be equal to its prior.

Twelve papers is a small enough sample that no particular significance should be attached to the particular final numerical value of 27.99 for the likelihood ratio for R , though the qualitative behavior of Fig. 12 is suggestive. Moreover, the set of 12 is not a representative sample of the data base; some were selected for historical significance. In particular, papers #10 and #15 are accounted by Cravens and Letts [1] as “the most important papers in the field of Condensed Matter Nuclear Science” for their early and lasting negative impact.

It would be desirable in the future to include substantially more papers – ideally all that were successfully rated according to criteria met and presence of heat. The present scheme lumps together all papers that meet the same number of criteria. It would be desirable to consider particular subsets of the four criteria, rather than simply the count, expanding the number of cases from 5 to 16. The ability to handle substantially more papers might make that feasible.

Acknowledgments

The authors gratefully acknowledge the support of the Defense Threat Reduction Agency for this work.

References

- [1] D. Craven, D. Letts, The enabling criteria of electrochemical heat: beyond a reasonable doubt, in *Proc. 14th International Conference on Condensed Matter Nuclear Science* (ICCF-14), Washington, D.C., August 10–15, 2008.
- [2] E.T. Jaynes, *Probability Theory: the Logic of Science*, Cambridge, UK: Cambridge University Press, 2003.
- [3] E.T. Jaynes, Probability in quantum theory, in *Complexity, Entropy, and the Physics of Information, SFI Studies in the Sciences of Complexity*, vol. VIII, W.H. Zurek (ed.), Addison-Wesley, 1990, pp. 381–403.
- [4] F.V. Jensen, *Bayesian Networks and Decision Graphs*, Springer-Verlag, New York, 2001.
- [5] J. Breese, D. Koller, Tutorial on Bayesian networks, <<http://ai.stanford.edu/~koller/BNtut/BNtut.ppt>>, 1997.
- [6] K. Murphy, A brief introduction to graphical models and Bayesian networks, <<http://www.cs.ubc.ca/~murphyk/Bayes/bnintro.html>>, 1998.
- [7] A. Yap, J.R. Santos et al., CIspace Group, Laboratory for Computational Intelligence, University of British Columbia, available for download under Belief and Decision Networks at <<http://www.aispace.org/downloads.shtml>>; see also Terms of Use at <<http://www.aispace.org/about.shtml>>.
- [8] I.J. Good, *Probability and the Weighing of Evidence*, London: C. Griffin, 1950.
- [9] E.T. Jaynes, Confidence intervals vs. Bayesian intervals, in *Foundations of Probability Theory, Statistical Inference, and Statistical Theories of Science*, vol. II, edited by W. L. Harper and C. A. Hooker, Dordrecht, Netherlands: D. Reidel Publishing Company, 1976, pp. 175–257.
- [10] D. Craven, D. Letts, Private communication.



Research Article

Tunneling Beneath the ${}^4\text{He}^*$ Fragmentation Energy

Andrew Meulenberg *

National Advanced IPv6 Centre, Universiti Sains Malaysia, 11800 Penang, Malaysia

Krityunjai P. Sinha †

Department of Physics, Indian Institute of Science, Bangalore 560012, India

Abstract

The repulsive Coulomb barrier between deuterium nuclei is reduced in length and height by a catalytic mechanism involving optical phonons and electric fields in a lattice. If this mechanism induces the formation of $\text{D}^- \text{D}^+$ pairs, the tightly bound and energetic electron pair (a “lochon” in the D^- ion) becomes an attractive force between the nuclei. The lattice constraints and slow collision processes force the ions into a near 1-D configuration within the lattice that deepens the electron ground-state potential well. This permits the electron pair to remain closely bound to one deuteron and to do work in bringing the $\text{D}^- \text{D}^+$ pair together. The work done reduces the nuclear-mass deficit (transferring it to electron kinetic and field energy) and that, along with the reduced Coulomb repulsion of the nuclear protons, brings down the helium nuclear-energy levels of the fusing pair and raises the ${}^4\text{He}$ fragmentation level. The proposed model accounts for the observations in condensed-matter nuclear science (CMNS) of excess heat (in both p–p and d–d reactions) and the differing observations (or for the absence) of tritium, ${}^3\text{He}$, neutrons, and ${}^4\text{He}$. The variation (unpredictability) of results (inherent in the many experiments) and evidence for transmutation, heretofore stumbling blocks to acceptability of CMNS, is now perhaps a validation of its existence. All major observed CMNS processes are addressed by the model.

© 2011 ISCMNS. All rights reserved.

Keywords: CMNS, Catalyst, Deuterium, LENR, Phonon-assisted, Tight-binding

PACS: 21.10.Dr Binding energies and masses, 25.10.+s Nuclear reactions involving few nucleon systems, 25.30.-c Lepton-induced reactions, 25.60.Pj Fusion reactions, 25.90.+k Other topics in nuclear reactions: specific reactions, 27.10.+h $A \leq 5$

1. Introduction

The Fleischman–Pons effect, observed in a palladium lattice electrolytically loaded with deuterium, is a release of energy greatly in excess of that possible by chemical means. The explanation proposed for the effect (a low-kinetic-energy nuclear-fusion of two-deuterium atoms) and the experimental results violated three known aspects of deuteron (d–d) fusion in Nuclear Physics. These are:

*E-mail: mules333@gmail.com

†E-mail: kpsinha@gmail.com

1. *Ultra-low probability of reaction*: Tunneling of deuterons must occur through a much longer and higher inter-nuclear Coulomb barrier than could be penetrated at the rates required to provide the excess heat observed.
2. *Fragmentation and fragmentation ratio*: The high fragmentation rates that would result from conventional penetration of the d-d Coulomb barrier and the formation of an excited ${}^4\text{He}$ nucleus (${}^4\text{He}^*$) are not observed. The fragmentation ratio, n:p, from $\text{D}+\text{D} \Rightarrow {}^3\text{He}+\text{n}$ and $\text{D}+\text{D} \Rightarrow \text{T} + \text{p}$ is expected to be $\sim 50:50$ (neutron + ${}^3\text{He}$ and proton + ${}^3\text{H}$ emission are considered to be nuclear “ash”).
3. *Decay paths from excited states of ${}^4\text{He}$* : No energetic gamma rays from direct de-excitation of fused D-D nuclei to the ${}^4\text{He}$ ground state (or products from another mechanism for delivering nuclear energy to the lattice) are observed.

Furthermore, subsequent low-energy-nuclear-reaction (LENR) research has often failed to reproduce the effect, has produced a large variety of (instead of consistent) results, and has provided strong evidence of changes in elemental composition (transmutation [1]) that is not possible from simple fusion reactions. Various models have been proposed to support the multiple experimental results and to overcome the arguments against a nuclear process. Few have been able to answer all of these challenges. None has yet been accepted, even by a large number of LENR researchers.

The present authors have developed a model ([2–5] reviewed briefly below) to solve the first of these problems using accepted physics of the solid state for the greater stability (perhaps cyclic) of charged sites relative to uncharged sites in some crystal lattices [6]. This knowledge was applied to the PdD lattice to suggest paired electrons in the same state (i.e., s-orbit in a D^- ion) becoming a local-charged Boson – the “lochon” – and the resulting $\text{D}^- \text{D}^+$ ion pairs being attractive rather than being repelled by the normal d-d Coulomb barrier [7]. The present work shows how extension of this lochon model supports the reduction in total energy of the colliding nucleons, and thereby explains most of the other experimental results observed in the field (including items 2 and 3 above).

The next sections describe the Lochon model, its extension, and its implications - from the PdD lattice sites, to the d-d near-field, and to the nuclear-interaction region. The nuclear issues are then addressed along with the mechanisms whereby the extended model is able to explain even the unexpected observations of LENR. Two appendices provide details of the extended-lochon process and address some applicable semi-classical physical-property issues of electrons and orbits that are never mentioned in quantum-mechanics texts and papers. A final appendix mentions a mathematical construction for a deep, bosonic, atomic orbital that might be verified by the experimental LENR results and the extended-lochon model.

2. Lochon Model

We have previously presented a model whereby the repulsive Coulomb barrier between hydrogen (deuterium) nuclei is reduced in height and length, perhaps by orders of magnitude [2]. This lochon-catalyzed-fusion mechanism, involving longitudinal optical phonons and local electric fields (internally or externally generated) in a crystal lattice that induce the formation of $\text{D}^- \text{D}^+$ pairs, increases the low-energy-tunneling probability by more than 100 orders of magnitude relative to that predicted from models based on multi-MeV deuteron-beam experiments [2].

We are dealing with a composite system (PdD_x) where two types of atoms or ions exist. Thus the primary lattice is palladium and the sub-lattice is hydrogen (deuterium). However, for our situation, the most relevant modes may be the interface phonon modes. The solutions to the quantum mechanical equations representing this system correspond to localized optical-phonon modes near the interface. The optical phonon mode of interest has the deuterons, beating against each other at the sub-lattice phonon frequency ($\sim 10^{14}/\text{s}$). The reduced dimensionality at an interface, or at a linear defect, deepens the potential well, thus creating higher-frequency phonon modes. These higher-energy modes create resonant electrostatic fields that are strongly coupled with the electrons confined in the layer. The addition of laser stimulation [2] increases the resonant phonon-field amplitudes, the $\text{D}^- \text{D}^+$ pair production, and the energy at which the local Coulomb barrier is encountered. This external resonant field can be adjusted to selectively stimulate the

higher-frequency modes and the counter moving deuteron modes. Phonon-induced electron pairing in a deepened well provides a basis for filling the deuteriums electron ground-state s-orbital that further localizes the pair [8] and binds it to a deuteron during its resonant oscillations within a lattice site.

The proposed electron pair would result in sub-lattice $D^- D^+$ pairs [9] and become more than strong screening; it would become an attractive force between the nuclei [5]. Thus, as the deuterons approach each other closely and deeply penetrate the D^- distributed-electron Coulomb field, the residual proton-proton (or d-d) Coulomb barrier is found to be much reduced, in height as well as in length. With the resulting enhanced barrier-penetration probability, the energy level of nuclei with reasonable tunneling probability may drop from the multi-100 keV range down into the many eV range, thus leading to low-energy nuclear reactions.

In this early version of our model (which was only concerned with the barrier penetration problem), normal tunneling of deuterons is into resonant excited ${}^4He^*$ nuclear states at energy levels above the fragmentation levels [10]. Thus, even if the Coulomb barrier is overcome by the tightly-bound electron pair and fusion is possible, the major observations of LENR (e.g. more heat than accounted for by neutron producing reactions) are not possible. This requirement of tunneling into states above fragmentation is dictated by the mass deficit ($Q = 23.8$ MeV [11]) between the two colliding D atoms and the resultant 4He atom. Therefore, even with no incident kinetic energy, a deuteron pair has too much mass energy to tunnel beneath the fragmentation levels [12] at 20.6 and 19.8 MeV above the 4He ground state. Nevertheless, the model was successful in providing a mechanism (with mathematical predictions of fusion rates consistent with observation) to counter arguments against LENR (item 1 above).

3. Extended Lochon Model

In a more detailed study of the lochon model, new and unexpected effects are found. Just as slow-motion photography can reveal unsuspected processes, the study of low-energy collisions between charged particles (i.e., eV compared to MeV) has provided some surprises. It is the non-equilibrium conditions of a “slow” $D^- D^+$ collision in a linear sub-lattice or lattice defect that provides a possible answer to the nuclear ash problem of CMNS (item 2 above). The deuteron motion is slow relative to the bound-electron motion. This distinction allows us to separate their actions and use the Born–Oppenheimer approximation to solve for the electron quasi-steady-state parameters, step-by-step, as the $D^- D^+$ pair approach each other over the lattice barrier separating them (and afterwards, Appendix A).

The D–D molecular potential well deepens as an extended D_2 molecule is being confined to two dimensions (Fig. 1) [13] by the lattice and Coulomb fields. During this process, the electron potential well also deepens (by reduced dimensionality and by the quadratic Stark effect from the confining lattice electric fields). A deepening of the electron potential wells does not necessarily mean that the electrons go deeper into the well; they must lose total energy to do that (although they gain kinetic energy in the process). However, being in a ground state ($l = 0$, with no lower energy states having angular momentum) they cannot directly radiate photons or generate phonons. (This would be a highly forbidden transition, since both processes require a change in angular momentum of $\Delta l = 1$). Because of the differences in resonant frequencies involved, indirect radiation of energy (via near-field coupling with lattice phonons) is slow. Nevertheless, in a critical concept provided by Tom Barnard [14], a mechanism is provided whereby these electrons may dissipate energy as the separation of the D–D $^+$ pair is reduced.

Since work is done by the electrons during this movement (they transfer energy to the deuterons), they fall further into the deuterons deepening Coulomb potential well. Part of this work is a result of “lochon drag,” which is analogous to phonon drag effects [15] on electrons in a lattice. Being deeper in the well means that one or both of the paired electrons is less likely to transfer to the potential well of the other deuteron during the process. This is a critical assumption of the model [16].

Since this electron pairing is a possible state, quantum mechanics can calculate its energy relative to that of zero or single-electron occupancy [6]. However, the probability of being in that state depends on the energy of the electron

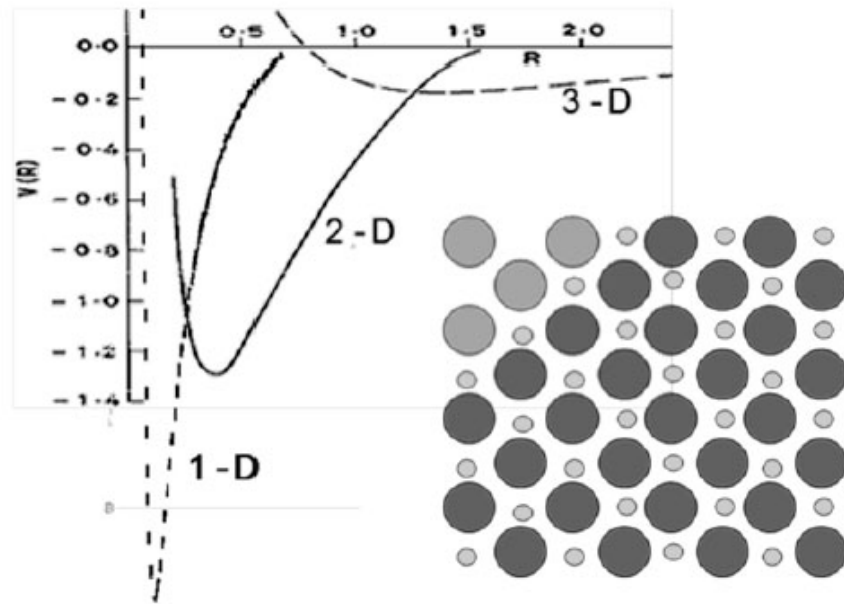


Figure 1. Molecular potential well for 3-D, 2-D, and 1-Dimension hydrogen-molecule configurations using atomic units ($R = 0.53 \text{ \AA}$ and $V(R) = 27.2 \text{ eV}$). The PdH lattice represented here (in planar view) includes an interface at which the tri-linear H sub-lattice is reduced in dimensionality.

pair and the local Fermi levels and electric fields; and these in turn depend on the recent history of the $D^- D^+$ pair. This is thus a time-dependent calculation. A consequence of the electron pairing in this model is that a portion of the electric-field energy of the $D^- D^+$ pair can be converted into work to overcome the lattice barrier (many-eV range) and the d-d Coulomb barrier (keV to MeV range) as they get closer. The effect of unpaired electrons, relative to that of paired electron(s), for LENR has been explored and found to be of little consequence.

3.1. Slow interactions

Nuclear physics collision experiments are diabatic. The equilibrium electron-energy levels do not have time to change before the event is over. On the other hand, the critical portion of the $D^- D^+$ interaction in a lattice is adiabatic. The “slow” motion of the converging deuterons allows hundreds of electron orbital cycles to occur during each step and therefore allows the electrons time to experience and respond to the changing fields. Furthermore, nuclear physics experiments are unlikely to see any of this $D^- D^+$ pairing effect unless the target deuterons have a reasonable probability of being in the negative ion state at the moment of collision. On the other hand, under the influence of lattice optical-phonon motion, that moment may be precisely when this state is most likely. A deuteron-beam experiment would have only a low statistical probability of involving a negative deuterium ion. Also, the mathematical interpretation of nuclear physics experiments under its low-energy (e.g. $\sim 5 \text{ keV}$) collision conditions would only indicate a higher Coulomb screening [17]. This interpretation *may be* appropriate for a deuteron with bound electrons. However, there are aspects of the LENR experimental results and of this model that any nuclear physics experiment is unlikely to see.

As the bound electrons move deeper into the D^- Coulomb potential well, the cancellation of external electric fields (of the electron and proton) reduces the external field energy (potential energy) and therefore the “size” and (initially

very slightly) the mass of the charged particles [18]. Since energy is conserved, part of this loss in field energy goes into the increased kinetic energy of the electrons (T_e), part into the increased kinetic energy of the deuterons (T_d), and part into increasing the inter electron–deuteron electric fields as the oppositely charged particles move closer together (Appendix A). However, just as the electrons do work in bringing the deuterons together, the deuteron and electron pairs must have work done on them to move them closer together. Thus, there are compensating field contributions from the e–e and d–d interactions as well. The net result of this 3 or 4-body interaction is that the tightly-bound, energetic, electrons (lochon or $e^\#s$) and deuterons lose total energy (they have more KE, but have moved even deeper into the local Coulomb wells). With proximity, the D^-D^+ attractive Coulomb potential grows, and collapse of the D^-D^+ pair is accelerated. Nevertheless, the initial energy expended in overcoming the lattice barrier keeps the D^-D^+ pair in the adiabatic regime (at low velocity) until the pair gets very close (~ 10 pm?). As the pair gets still closer together, the D^-D^+ Coulomb potential dominates the lattice barrier and the closing velocity increases. However, during this same period, the electron kinetic energy also increases greatly so that the relative velocities (electron to deuteron) are maintained in the adiabatic regime.

The electron's kinetic-energy-increase and their movement deeper into the Coulomb well about the deuteron causes them and their orbit to “shrink” (Appendices B and A). The electron deBroglie wavelength decreases with increased velocity and, as it spirals in, its external-field energy is further “cancelled” by that of the proton. With an increase in energy from the T_e = multi-eV range of electrons in sub-lattice deuterium atoms to the keV range of a bound electron as it approaches the deuteron, the deBroglie wavelength is reduced by an order of magnitude. As the $e^\#$ kinetic energy increases to the 100 keV range, the wavelength drops by $10\times$ again and approaches that of the electron Compton radius. However, by this time, the peak electron field (and therefore the electron center of “mass”) has shifted to within 100s of Fermi of the nucleus.

3.2. Electron–proton interaction in the 1–10 fm range

As the electron moves even closer to the nucleus (within 10 fm), its instantaneous kinetic energy continues to increase; but, it begins to lose its identity and may no longer be considered a separate entity (Fig. 2). The $e^\#-p$ pair has become a relativistic rotating dipole field (monopole + quadrupole field, if two bound electrons are present). The cancelled charge far-field energy has been replaced by near-field, electromagnetic and relativistic-mass energy. In support of this proposed semi-classical kinematic model for the (brief?) existence of tightly bound electron pairs, recent mathematical work [19] uses a solution of the Klein–Gordon equation to indicate the possibility of a deep energy level [20] in the hydrogen atom (Appendix C) for a charged boson, such as the lochon.

Figure 2a shows the consequences of electron–proton proximity on the electric potential (assuming stationary charges) as an example of the size/shape change effect mentioned above and in Appendix B. (Resolution of Fig. 2b is insufficient to show details at the sub-fm scale.) In the 60 fm range and assuming the classical-electron radius ($r_e = 2.82$ fm), the electron and proton potentials are clearly delineated. At 10 fm, the potentials significantly alter each other and the “effective” charge is less than 1 for either of the particles (the dipole approximation still works). As the ($e^\#p$) pair shrinks further, the electric field of the electron is progressively cancelled by that of the proton and the residual proton-charge radius is limited to femtometers. The fact that there is any residual charge is attributable to the extra mass and relativistic nature of the proton's inner structure.

What do these changes mean to the problem at hand? To first order, we'll assume that the *changes* in electron size, fields, and deBroglie and Compton radii can be ignored. The electron will be considered as a classical charge. We will treat the proximate electron–proton as a small dipole rather than the large structure that would result from using the deBroglie or Compton radii. The Heisenberg Uncertainty Principle, as applied to the tightly bound electrons(s), will be modified by the proximate presence of the proton(s) so that the kinetic energies required to shrink free electrons to nuclear sizes are no longer in the 100 MeV range.

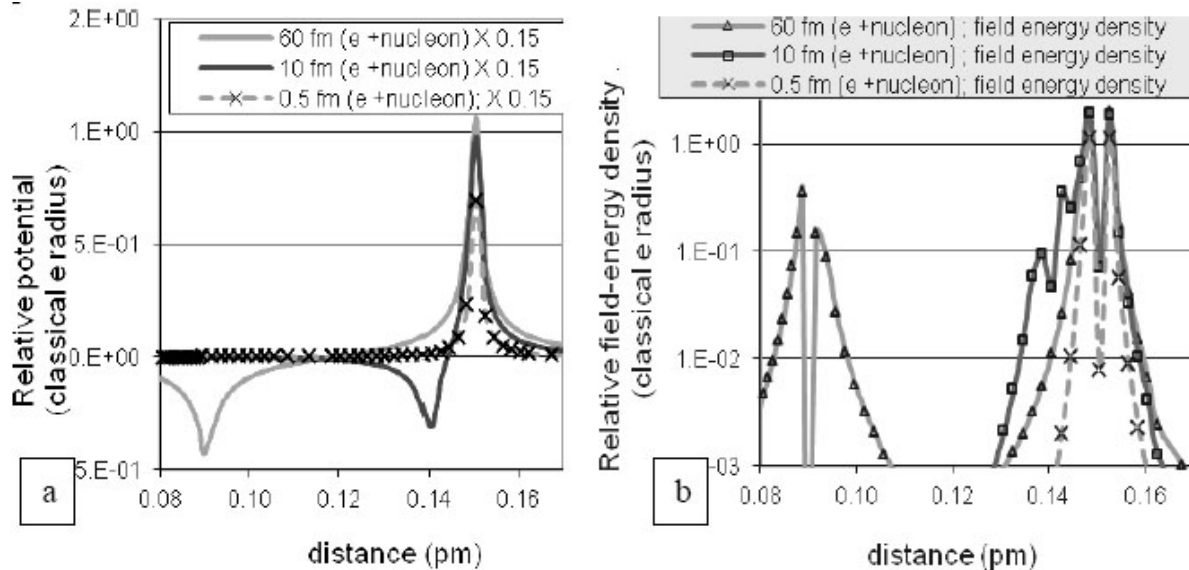


Figure 2. (a) Electric potential between, and (b) EM mass-energy distribution of, an electron (assuming a classical radius) and proton separated by 60, 10, and 0.5 fm. Note change in “size” of both particles as they approach each other and the change in vertical scale between (a) and (b).

We have shown how the Coulomb-barrier problem might be solved with the lochon model and laid a foundation for the D–D nuclear interaction with the help of tightly bound, highly energetic electron pairs (lochons). Now we further extend the model to see how it affects the nuclear interaction.

3.3. Nuclear interactions

Examining the traditional D–D to ${}^4\text{He}^*$ transition (Fig. 3, where $*$ indicates an excited state of the nucleus), we see the broad transition region (bracketed) beyond 23.8 MeV above the ${}^4\text{He}$ ground state. This “ Q ” value (broad arrow at 23.8) is the energy difference that corresponds to the mass difference between the deuterium pair and the ${}^4\text{He}$ atom. Even with the improbable event of D–D tunneling from zero kinetic-energy states, the excess mass of the deuterium atoms would put the deuterons into this high level. These excited ${}^4\text{He}^*$ states are above the fragmentation levels at \sim 20.6 and 19.8 MeV (dashed arrows). While fragments from both levels have been observed in LENR experiments, the radiation fluence levels are not nearly high enough to explain the excess heat observed. Furthermore, the measured concentration levels of ${}^4\text{He}$ have been orders of magnitude higher than would be expected from standard theory and, in some cases, have been high enough to account for the observed heat if all excited-state energy (\sim 24 MeV) is converted to thermal energy [21]. How could this happen? Since the observed data is not possible within the known framework of nuclear physics, something else must be going on.

This figure, which shows the excited states of ${}^4\text{He}$ as well as the fragmentation and minimum D–D input energy levels, indicates that there are no energy levels below the ${}^3\text{H} + \text{p}$ fragmentation level. Thus, even if a helium nucleus were to be excited into a heretofore-unobserved meta-stable state below the 20.2 MeV level, it might still fragment rather than decay back to the ${}^4\text{He}$ ground state. Likewise, in a d–d interaction, if fusion via normal tunneling were to take place, it would be resonance tunneling into one of the many levels above the broad arrow at 23.8 MeV. Decay from these excited states would almost always give nearly equal probabilities of fragmentation into the p or n fragmentation channels.

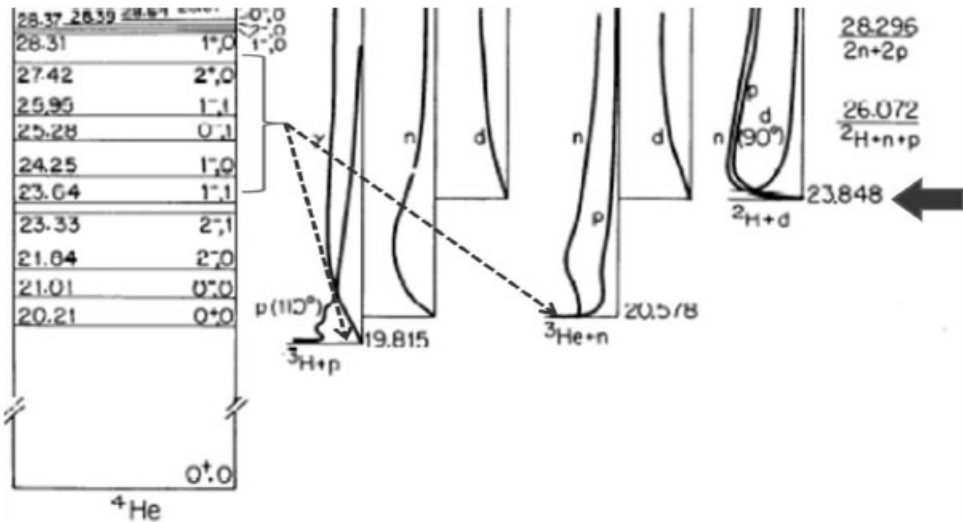


Figure 3. Energy levels and possible decay branches associated with conventional D–D to ${}^4\text{He}^*$ fusion reactions, as well as the excited states and fragmentation and minimum d–D input energy levels of ${}^4\text{He}$ [10]. Note that these values include the mass energy of the atomic electron(s).

However, if the excited state is able to more quickly decay to one of the levels below 23.8 MeV, the fragmentation probability begins to shift to favor the proton channel. This enhanced decay into the lower excited states could be an explanation for reduced levels of neutrons for the heat generated. However, it does not explain reduced levels of energetic protons.

3.4. Reduced energy ${}^4\text{He}^*$

With the ability of deuterons to be drawn from an appropriate PdD lattice site through the lattice and nuclear-Coulomb barriers to an adjacent reduced-energy nucleus (Appendix A) of a D^- ion, the possibility of a low-energy excited compound nucleus becomes real. With the lochon (the shrunken-orbit electron pair – as indicated by the superscript #) rather than with the normal atomic electrons, the excited (but lochon-neutralized) helium-4 nucleus may not have sufficient energy to fragment. Since gamma decay is highly forbidden, how does ${}^4\text{He}^{*\#}$ shed the excess energy to get to the ${}^4\text{He}$ ground state? It is proposed that existence of this condition and the subsequent decay process is the basis for the experimental observations of CMNS.

Depending on the actual energy of the excited (compound) nuclei, the decay process could include fragmentation, or not. Since there may be no standard resonance states of this compound nucleus, the final tunneling could be into a range of energy levels. This variability would account for the observations in CMNS of excess heat, in both p–p and d–d reactions, and the observations (or absence) of tritium, ${}^3\text{He}$, neutrons, and ${}^4\text{He}$ in the d–d reaction. The unpredictability of experimental results has been a major problem for CMNS. It now may be a validation of the extended-lochon model. Furthermore, this proposed mechanism accounts for observed “transmutation,” something that many CMNS investigators did not accept for a long time.

To see how this “new” process can occur, we must take a closer look at the details behind Fig. 3. If an appropriate state existed below ~ 19 MeV, then any fragmentation would become unlikely. We propose a non-fragmentation mechanism that does not rely on a new state below 20 MeV. This mechanism of tightly bound electron(s) could shift the

existing ${}^4\text{He}$ ground and excited nuclear states down and it demonstrates how the fragmentation levels can be shifted up in energy.

The key to the mechanism is the lochon, which during the collision process attains significant energy (keV to MeV range); but, being tightly bound in an $l = 0$ ground state, it does not radiate. If it survives the final tunneling of the d^+ through the thin residual $\text{D}^{-\#}$ (actually d^+ plus lochon) Coulomb barrier, it may have attained MeV energies from the work done at the expense of the D^- Coulomb potential energy. Thus, it is very tightly bound and the lochon, the D^- nucleus, and the deuteron all have had mass converted into kinetic and field energy. Since the average lochon orbital radius is so small, even in a circular orbit, the orbital angular momentum is much less than \hbar . (so that the $l = 1$ state is not available). With the lochon being spin-coupled electrons in a filled s-orbital, there is no spin-flip possible to provide angular momentum sufficient to generate a photon. Therefore, no photonic radiation is possible and there is no violation of the uncertainty principle as the lochon orbit and size both shrink during the D^- - D^+ collision.

Once the D^+ is inside the D^- Coulomb barrier, the situation is different from that of the normal d-d scattering problem. The normal situation compares the mass difference between ${}^4\text{He}$ and 2D, which is just the same as that between ${}^4\text{He}^{++}$ and 2d. In our case, the electrons and protons in the helium nucleus with a tightly bound electron pair and the free deuterium atoms are different animals. (${}^4\text{He}^*$ is the excited state with normal atomic electrons, and ${}^4\text{He}^{*\#}$ is ${}^4\text{He}^*$ with shrunken-orbit electrons.) The external Coulomb field of these “shrunken-orbit” electrons (a source of their mass) is nearly zero, and a comparable amount has been subtracted from the proton(s) fields. This mass–energy equivalent has been converted into kinetic energy [22] and into the interactive-field energies (mutual attractions and repulsion of the electrons and protons).

The nuclear potential is much different also. The Coulomb barrier between the lochon-altered protons (now electric dipoles) is almost gone. Thus, they can be much closer together. (In the d-d case, all 4 nucleons can then be closer together.) Since most of the normal nucleon wavefunction is outside the d-d nuclear well, the depth of the ${}^4\text{He}^{*\#}$ nuclear potential well with which the nucleons are bound is increased by the loss of Coulomb repulsion and the gain in time spent in the well (increased wavefunction overlap). As a consequence, the “effective” depth of the nuclear well is further increased, the ground and excited-state energies become lower, and the energy required to break apart the excited nucleus is higher. If we look at Fig. 4 (with this information applied to Fig. 3), we see that the whole column on the left is moved down (the energy levels may split and, depending on the model used to describe the new nucleon-dipole or light proton, their values will be different) and everything on the right (except for the arrow) is moved up.

The Q arrow at 23.8 MeV moves down with the column; because, while the energy distribution of the ${}^4\text{He}^\#$ and ${}^4\text{He}^{*\#}$ (which states may never actually exist) is different from that of ${}^4\text{He}$ and ${}^4\text{He}^*$, the mass difference between ${}^4\text{He}^\#$ and 2D $^\#$, is still nearly the same (the protons have lost about the same mass that the lochon has gained). Thus, the deuterons tunnel into nearly the same states that they would have without the energy reduction. However, with the tightly bound lochon, the states are no longer the same states. And, if they were stable states, they would be shifted down in energy (along with the ground state if it exists with the lochon).

4. Fragmentation

Do the ${}^4\text{He}^{*\#}$ fragmentation levels really rise above the 23.8 MeV D–D energy level? Well, the elimination of nucleon Coulomb repulsion is considered to decrease the ground-state level by about 0.73 MeV (but that is based on comparisons of isomers differing by only one atomic number). If we consider a lochon in the nuclear region, the difference resulting from the double-negative charge could be 1–2 MeV (the increase in nuclear binding energy, which also raises the relative fragmentation energies by at least that amount). Since fragmentation energy is a strong function of inter-nucleon distance, and the lochon has such a great impact on that, this energy could easily go up by another MeV or two. So the answer is seen in Fig. 4. The lowest “ ${}^4\text{He}^{*\#++}$ + lochon” fragmentation level is above not only \sim 22.8 MeV, it may be above the $Q^\# = 23.8$ MeV value. The number of fragmentation levels of the lochon-neutralized nucleus may

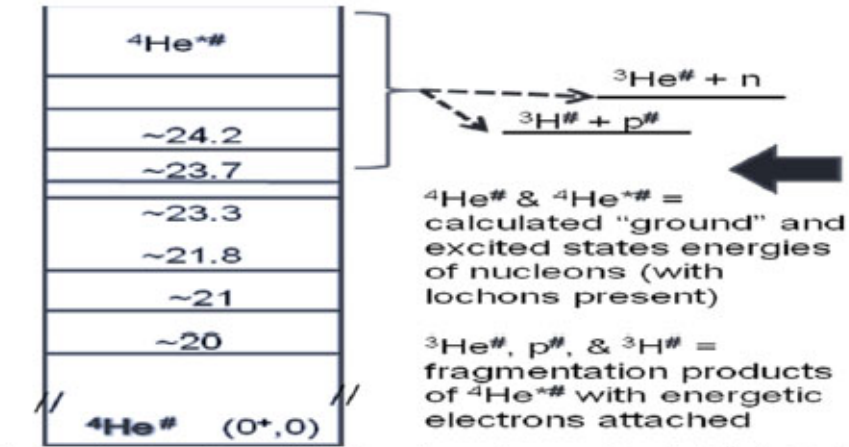


Figure 4. Energy levels and possible decay branches associated with the lochon model $D + D$ to ${}^4\text{He}^{*\#}$ fusion reactions and minimum $D + D$ input energy levels of ${}^4\text{He}^*$. Note that these values include the tightly bound-electron-induced adjustments to the nuclear potential and the mass energy of the atomic and shrunken-orbit electrons.

be increased because the neutrons and tightly bound electrons can be divided in multiple ways among the two protons involved. These levels can be considered as representative of centrifugal barriers since it takes increased kinetic energy and angular momentum to get to them.

This lochon modification of the compound nucleus (${}^4\text{He}^{*\#}$) energy levels can thus explain the absence (or change in ratio) of fragmentation in LENR identified as item 2 in the introduction.

5. Alternative Decay Paths

Perhaps important for the reduction of fragmentation is the number of accessible shrunken-orbit nuclear-energy levels proposed to be now below the fragmentation levels. Any occupied levels above the ${}^3\text{He}^*$, p^* , and ${}^3\text{H}^*$ fragmentation levels are transitory (rapidly fragmenting or decaying to these lower-energy levels). In addition to their normal decay processes (which do not compete well with fragmentation), the excited nucleons may reach lower-energy stable levels by transferring their kinetic energy to their tightly bound electrons. These electrons couple this energy to the nearby atomic electrons or the lattice (via near-field radiation, phonon, and plasmon interactions). In the presence of this new decay process, normal decay processes from excited-nuclear levels ${}^4\text{He}^{*\#}$ to the fragmentation or lower levels is inhibited and becomes a low-probability process.

An important point to note is that the new energy-transfer process to and through the tightly bound electrons is not rapid. It is steady. But, even for states above fragmentation levels, this initial decay process may compete well against fragmentation. Furthermore, the presence of the tightly bound electron(s) interferes with “normal” decay processes that depend on stable resonance states (e.g., gamma decay) and/or angular momentum (e.g., fragmentation). The steady process means that the total time for decay to ground is long, relative to normal decay modes. However, it “drains” EM field energy necessary for the formation of gamma rays and utilizes the angular momentum that would allow fragmentation. While it is slowing these processes, it lowers the nuclear energy below the fragmentation levels and interferes with the stability of the lower nuclear states shown in Fig. 4. Thus, as long as the tightly bound electrons are present, the helium nucleus is not in a normal state and the indicated excited levels are only representative and cannot be considered real.

The presence of a lochon so-greatly reduces the Coulomb barrier to fusion, that non-zero-angular-momentum ${}^4\text{He}^{\#*}$ states might become accessible. These states are more accessible via shrunken-orbit electrons and their decay through normal processes (e.g., gamma decay to lower levels, or to the ground state) could more readily compete with fragmentation. Nevertheless, it is unlikely that gamma decay from such states (or direct tunneling to the stable-fragments) could compete with the energy decay process from proximity coupling through, or in the presence of, the tightly bound electron(s) or lochon.

During the p–p or d–d lochon-enhanced fusion process, the lochon could divide or perhaps attain energies in the MeV range from coupling with the protons accelerating in the nuclear potential. These rapidly accelerating and decelerating electrons would then radiate Bremsstrahlung or would proximity couple their energy to the adjacent Pd electrons [23]. This extended-collision/radiation process lasts:

1. Until the neutral entity (${}^2\text{He}^{*\#}$ or ${}^4\text{He}^{*\#}$) drifts into a neighboring nucleus in a transmutation process;
2. Until one (or more) of the shrunken-orbit electrons combines with a proton ($\text{p} + \text{e} \Rightarrow \text{n} + \nu$, via the p–e–p, p–2e–p, etc. reactions); or,
3. Until ejection of the energetic electron(s) from the nucleus and the (D or ${}^4\text{He}$) ground state is reached.

Thus, the last of the introductory arguments against cold-fusion have been addressed.

6. Conclusion

The Lochon Model provides a basis for penetration of the nuclear Coulomb barrier in low-energy p–p and d–d fusion reactions. Depending on the actual energy of the excited (compound) nuclei and the number of tightly bound electrons, $\text{e}^{\#}$, still attached (0, 1, or 2) after the nuclear Coulomb barrier has been penetrated, the decay process could include fragmentation, or not. This extension of the model accounts for the observations in CMNS of excess heat, in both p–p and d–d reactions. It also explains the observations (or their absence) of tritium, ${}^3\text{He}$, neutrons, and ${}^4\text{He}$ in the d–d reaction. The ability of the tightly bound lochon - to alter energy levels in the nuclear potential wells and fragmentation energies of the excited ${}^2\text{H}^{\#*}$ and ${}^4\text{He}^{\#*}$ atoms - permits decay to the ${}^2\text{H}$ or the ${}^4\text{He}$ ground states or allows sufficient time as a shrunken-orbit atom or neutral nucleus for transmutation of lattice atoms or impurities.

Variation of observed results of LENR is thus based on the number of tightly bound, energetic electrons remaining within the nuclear region after initial D^-D^+ fusion and during the subsequent decay process. The Extended Lochon Model, in its present form, may explain all observed LENR processes (model-predicted levels and observability of Bremsstrahlung and any neutrinos must still be determined), but not necessarily the best means of, or materials for, producing them. That comes next.

Acknowledgments

This work is supported in part by HiPi Consulting, New Market, MD, USA; by the Science for Humanity Trust, Bangalore 560094, India; by the Science for Humanity Trust Inc, Tucker, GA, USA; and by the Indian National Science Academy.

Appendix A: Development of Electron Coupling into Tight Orbits

For the reasons stated above and in our earlier work, the D^-D^+ pairs are formed within the loaded PdD lattice (or interface and defect regions). This phonon-induced charge polarization is a maximum during the closest encounter of the deuteron ions. At this point, the monopole–monopole interaction is highest and the resulting E field can exceed the phonon field, to strip one or both electrons from the D^- ion. This exchange thus forms molecular deuterium (perhaps only temporarily, if the lattice barrier separates the molecule rather than drawing it into one lattice site).

This appendix addresses the electron energies and their exchanges assuming that the electrons are maintained as a pair long enough to move too deep into the D^- potential well to be removed by the D^+ E field until after Coulomb barrier penetration. The problem is addressed as a monopole–monopole interaction with the deepening electron energy levels treated as a modified Stark Effect. (The electron-energy levels in the D^- ion deepen in the E fields produced by the lattice and then by the D^+ ion.)

Of importance to the lochon model is the fact that the electrons in the D^- do work and, thereby, move deeper into the Coulomb potential well. Therefore, we need to compare the change in potential between the D^- and D^+ ions (ΔV_{dd}) relative to the work done in bringing them closer together (from l_1 to l_2) by a small distance, $\Delta l = l_1 - l_2$. In the simplest model, for the conditions of a $D^- D^+$ Coulomb attraction much greater than phonon effects and for a dielectric constant of ϵ ,

1. Change in potential: $\Delta V_{dd} = -e^2(1/l_1 - 1/l_2)/\epsilon = \sim (e^2/\epsilon(l_1 l_2))\Delta l$. (Thus, for small Δl , $I_1 = \sim l_2 = \sim l \Rightarrow \Delta V_{dd} = \sim (e^2/\epsilon l^2)\Delta l$.)
2. The force between the ions: $F_{dd} = -dV_{dd}/dl = -e^2/\epsilon l^2$.
3. Work by each deuteron ion: $\Delta W_1 = \Delta W_2 = F_{dd} * \Delta l/2 = \sim (-e^2/\epsilon l^2)(\Delta l/2)$.

The $\Delta l/2$ term comes from the near-equal masses of the D^- and D^+ . The work done by the D^- electrons equals that done by the D^+ ion. Each ion moves the other by $\frac{1}{2}$ the change in total separation distance Δl . The total work of the D^-D^+ system ($\Delta E_{dd} = \Delta W_1 + \Delta W_2$) is approximately the potential difference between l_1 and l_2 . We can look further into the conservation of energy to see where the work comes from. The D^+ ion does work by converting some of its field energy into kinetic energy (and in overcoming the lattice barrier early in the process). The D^- ion does the same; but, what field energy is converted? It must be the negative portion.

The lochon provides the negative charge and therefore the D^- ion portion of the work and field energy to bring the deuterons together and to give them kinetic energy to overcome the lattice barrier. In providing this energy, the lochon drops deeper into the D^- potential well and gains kinetic energy. These distances of the changing lochon orbits (charge = $-2e$, mass = 2 electron masses) relative to the D^- nucleus equal r_1 and r_2 with $r_1 > r_2$. Things are different from above because we are now looking at many electron orbits rather than only a portion of a single phonon cycle. The D^- nucleus does not significantly change its KE relative to the lochon during a decay of the lochon orbit. Therefore the lochon does almost no work on its deuteron nucleus in the D^- center-of-mass system. (It does not move the deuteron within this system; but, it moves the whole D^- relative to the D^+ .) However, the nucleus does work on the lochon. The lochon gains $\Delta V_{dl}/2$ in KE from the orbit decay and (from the virial theorem) can do the same amount of work on the D^-D^+ ion pair. Again, assuming that the D^-D^+ interaction energy greatly exceeds that of the lattice barrier:

4. Δ in potential (D^- nucleus & lochon): $\Delta V_{dl} = -2e^2(1/r_1 - 1/r_2)/\epsilon = 2e^2/(r_1 r_2) * \Delta r$.
5. Work done in decay of D^- electrons: $\Delta W_{dl} = \Delta V_{dl}/2 = \sim (e^2/\epsilon r^2)\Delta r$.

Assuming that the model holds, and if $\Delta V_{dl}/2 = \Delta W_1 = \Delta V_{dd}/2$ (e.g., if $\Delta r/r^2 = \Delta l/2l^2$) and $l > 2r$, then $\Delta l > 8\Delta r$. Thus, unless early in the process the lochon has moved deeply into its potential well, the inter-deuteron distance rapidly shrinks to the lochon orbit radius [24] ($l = r$) and will share the bound electrons. Sharing the electrons (lochon) between the deuterons will increase the size of the electron distribution and eliminate the D^-D^+ Coulomb attraction. If the electron orbit has shrunk prior to the transition from D^-D^+ to $D-D$, the now tightly bound electrons still provide better screening than that from free electrons or from normal molecular electrons. Furthermore, the momentum of the deuterons will continue to close the deuteron gap and thereby further shrink the electrons' (now molecular) orbit. The later the sharing of electrons, the deeper the electrons will be in their potential well, the higher the deuteron momenta, and the smaller the Coulomb barrier that must be tunneled through. Therefore, the phonon-induced collision process at the lattice barrier is the starting point that can lead to, or block, the proposed extended-lochon model.

The deuterium sites in PdD are highly confined by the Pd lattice and screened from each other by the Pd-lattice electrons. Thus, the initial conditions are not amenable to any simple analysis. Since, work done by the bound-electron pair in overcoming the lattice barrier may be critical to the model; it must be addressed in a more sophisticated manner than is possible in this paper.

As described here, the lochon motion to deeper regions of the D^- potential well (i.e., to tighter orbits with increased kinetic energy) can proceed without any radiation. Nevertheless, mass energy of both deuterons is lost (Appendix B). The process of shifting between the normal D^- ion in a lattice site to a “reduced-energy-nucleus” ion at the lattice barrier is reversible (unless, or until, the deuteron nuclear potentials overlap) and can continue to oscillate at the phonon frequency. However, with sufficient deuteron and boson energies within the Coulomb wells, energetic-lochon-catalyzed fusion may occur as described in the text. Alternatively, the “shrunken” electron orbits at the point near deuteron collision may allow closer approach of the D^-D^+ pair and the resultant stronger coupling would permit the small D^+ ion to be drawn into the D^- ion’s lattice site. The now-allowed proximity of the deuterons, one perhaps with electrons in the metastable nought orbit (Appendix C), can thereby provide boson-catalyzed fusion (similar to muon-catalysed fusion).

Appendix B: Electron Size in the Nuclear Regions

This appendix addresses the “size” of an electron as it must be pictured in its interaction with protons at nuclear distances. It is based on the presently-accepted model that the mass of the electron is totally electromagnetic [25]. Furthermore, the electrostatic field defining the charge is assumed to be the dominant EM component. The proton’s external EM field is identical to that of the electron. Therefore, if size is based on charge field alone, the electron and proton would be the same size. However, since the Compton radius is based on total mass and proton mass from the charge field is only a very small percentage of the proton mass energy, this useful radius is much smaller for the proton than is that for the electron. On the other hand, when the electron and proton are close together, other things come into play. Of major importance is the “collapse” of electron size as its far-field component is cancelled by that of the proton and the long-range monopole potential becomes only the short-range potential of a dipole (Fig. 2a). Other things happen as the electron and proton approach one another.

The additional kinetic energy of tightly bound electrons $e^{\#}$ means that an electron “size,” based on the deBroglie radius ($\lambda_{dB}/2\pi$), shrinks as $\lambda_{dB} = h/mv$. While this is actually related to the time-averaged electron-charge distribution in an orbit, not any actual electron size itself, there is still a frequency associated with the orbit and thus the deBroglie wavelength. Since frequency is related to energy and energies are additive, the deBroglie frequency (related to the deBroglie wavelength, $v_{dB} = v/\lambda_{dB}$) is added to the Compton frequency (related to the Compton wavelength, $v_C = c/\lambda_C$) and the summation provides a higher frequency (hence energy: $E_t = h(v_1 + v_2)$) that gives a smaller electron radius. (This shrinking is a basis for association with the momentum/size relationship of the Heisenberg Uncertainty Principle.)

A poor understanding of the various relationships between electron size and time-averaged charge distribution is a common source of some miscalculations of Coulomb screening by electrons. For example, tunneling is considered to be instantaneous. Therefore, screening by an electron “cloud” is not an average value, but a statistical probability of finding an electron at a given location at the instant of tunneling. This appendix provides some further insight into different usages of electron sizes.

If the much larger Compton electron radius is assumed, rather than the classical radius, one might think that the change in electron shape and effective charge begins much further from the proton. However, in Fig. 2a, because the plotted potential is a $1/r$ function (and the total energy and charge is fixed), the actual amplitude and shape of the exterior electron field cannot change with the model. The difference must be in the definition, not in the particle. With a Compton radius of 384 fm (0.384 pm), the statement would then be that the electron’s “size” extends much further to the extremities of the field than does the classical-electron radius of 2.82 fm. If the potential “inside” the chosen electron

radius is different, then the field in that region will change and the magnitude of the total field must be renormalized to provide the total mass/field energy of the electron.

Assuming that the electron mass is entirely electromagnetic in origin and that the field-energy density is proportional to the field squared, then the mass-distribution of the electron can be pictured as much more localized than that of the potential distribution (Fig. 2b). (Field \mathbf{E} is proportional to the derivative of the potential, giving $1/r^2$ dependence. This implies that energy density E , proportional to \mathbf{E} squared, varies as $1/r^4$.) The external-EM portion of the proton energy can be pictured in a similar manner. (Remember that this charge-field component is only about 0.05% of the total proton mass.) Because of the great increase in localized mass density relative to the potential, Fig. 2b is shown as a semi-log plot of the non-relativistic charge-field energy only. If the proton's mass energy (held to be relativistic-field energy by one author - AM) were included in the figure, it would extend 3 orders of magnitude above the curves shown. Expanding the resolution of the electron EM mass profile (not shown), one could see that the classical radius includes >99% of the mass energy. The Compton radius of the electron extends to some very-low value of field or potential. The electric potential at the 0.15 fm Compton radius of the proton is still very high (Fig. 2a).

Assuming that charge particles are not singularities, the electric potential must be finite and must reverse at the center of the charges. Therefore the field-energy density goes to zero at this point. However, as the electron approaches the proton at 10 fm distance in Fig. 2b, this electric-field density (mass) of the electron disappears. The electron may no longer have an identity. Nevertheless, when the electron gets close enough to the proton to eliminate any sign of the electron's negative charge, there is still a residual positive charge of the proton. The difference in near-field "charge" between the electron and proton is a relativistic effect. This is a result of the need to have the $1/r$ potential continue to a smaller radius for the proton than for the electron. It takes energy to do this.

The figures described above are for localized charges. They indicate that, when the electron is within Fermis of the proton, its field-energy density disappears. Where does it come from and where does it go? It comes from the proton and electron electrostatic fields and goes into motion of the altered and residual field energy (mass and/or charge). Unless energy is radiated away, or is transferred in some other form, it is bound to the "compound structure" and acts as energy-equivalent mass. However, the moments of inertia, magnetic moments, etc. of the structures are altered and energy can be stored in the new angular motion. For an isolated electron–proton structure, this has little consequence (also it is an extremely short-lived condition - a single transit by the electron?) However, for colliding p^+p^- or D^+D^- structures (where the closely bound electrons may exist for hundreds of orbits or more), it means that the nucleon wave-functions are altered.

Appendix C: Nought-orbits ($n = 0$)

In 2005, Jan Naudts posted a paper [19] on the arXiv entitled "On the Hydrino State of the Relativistic Hydrogen Atom." He showed that there was a solution to the Klein-Gordon (K-G) equation that is generally rejected as being non-physical. This solution adds a new atomic orbital at close to mc^2 . Since the K-G equation pertains to Bosons, not Fermions, Naudts suggested that the question of square integrability of the Dirac equation (which blocks Fermions from that level) might be the non-physical requirement instead and thus the K-G solution could be used to support such a level for Fermions as well. Two papers [26,27] have rejected both suggestions; but, a third [28] has accepted the K-G solution as real.

Applying this information to our model and assuming the additional K-G solution to be valid (at least for bosons), the reality of the bound electron pair (the lochon) as a boson means that this level is available as a physically real lower-energy state (the $n = 0$ or nought-orbital). This level will not be explored further here (such as the effects of a doubly charged boson on the solution). However, neither the $n = 1$ ground state nor the $n = 0$ nought orbit has sufficient angular momentum to permit photonic-energy transfer. Therefore, it is still a forbidden photonic transition. Nevertheless, as a viable, tightly bound, relativistic-electron state, the nought level can be reached by the model described in this paper

and it provides additional basis for the extended-lochon theory of low-energy nuclear reactions. This could be a critical point for both the Coulomb barrier penetration and the energy level at which the H–H or D–D fusion begins.

A potential importance of this nought orbit is the fact that it provides an intermediate stage for fusion via a mode that is well-known physics - muon-catalysed fusion. Since the $n = 0$ electron-orbit radius is ~ 400 fm (at ~ 507 keV), $n = 0$ hydrogen would be smaller than muonic hydrogen. But, just as a filled orbital H^- ion is larger than the neutral atom, the lochonic $n = 0$ hydrogen ion would be larger than a neutral nought-orbit atom. On the other hand, the nought-orbit molecule ($H^+ + H^-$, or $H_2^{\#}$) might be smaller than the muonic hydrogen molecular ion (and perhaps ionically bound rather than covalently bound). Details must be presented elsewhere; but, the implications for nought-orbit hydrogen and molecules for lattice mobility, lattice-site double occupancy, and muon-catalysed-type fusion are immense. Whether this is an unreal, a competitive, an incidental, or an assisting process is still to be determined.

References

- [1] Y. Iwamura et al., Transmutation Reactions Induced by D2 Gas Permeation Through Complexes (P/CaO/Pd), *14th Int. Conf. on Cold Fusion* (ICCF), Washington, DC, 10 August 2008; and Y. Iwamura, M. Sakano, T. Itoh, *Jpn. J. Appl. Phys.* **41** (2002) 4642–4648.
- [2] K.P. Sinha, A. Meulenberg, Laser stimulation of low-energy nuclear reactions in deuterated palladium, *Current Sci.* **91** (2006) 907, arXiv:cond-mat/0603213, accessed 28 June 2010.
- [3] K.P. Sinha, A. Meulenberg, Lochon catalyzed D–D fusion in deuterated palladium in the solid state, *Nat. Acad. of Sc. (India) Letters* 30(7&8) (2007), arXiv:0705.0595v1 accessed 28 June 2010.
- [4] K.P. Sinha, A. Meulenberg, A model for enhanced fusion reaction in a solid matrix of metal deuterides, ICCF-14, International Conference on Condensed Matter Nuclear Science. Washington, DC, 2008. <http://www.lenr-canr.org/acrobat/SinhaKPAmodelfore.pdf>.
- [5] A. Meulenberg, K.P. Sinha, Tunneling beneath the $^4\text{He}^*$ fragmentation Energy, *ICCF-15, International Conf. on Condensed Matter Nuclear Science*, Rome, Italy, 2009.
- [6] P.W. Anderson, *Phys. Rev. Lett.* **34** (1975) 953.
- [7] K.P. Sinha, *Infinite Energy* **29** (2000) 54.
- [8] No attempt is made to describe the electron orbits of a two-electron atom in a lattice. This is difficult enough for such an atom in free space [e.g., G. Tanner, K. Richter, J. M. Rost, *Rev. Mod. Phys.* **72** (2000) 497–544]. We know the orbits exist, but not what they look like. We have assumed a quadrupole, rather than a dipole configuration.
- [9] Presence of D^- ions and $D^- D^+$ pairs in the loaded-PdD lattice has not yet been sought or confirmed.
- [10] A. Krauss, H.W. Becker, H.P. Trautvetter, C. Rolfs, K. Brand, *Nuc. Phys. A* **465** (1) 150–172.
- [11] Useful definitions of terms in the paper that are not familiar to all readers may be accessed on the Wikipedia. http://en.wikipedia.org/wiki/Muon-catalyzed_fusion#Process <http://en.wikipedia.org/wiki/Born-Oppenheimer>; http://en.wikipedia.org/wiki/Phonon_drag; http://en.wikipedia.org/wiki/Adiabatic_theorem; http://en.wikipedia.org/wiki/Mass_deficit;
- [12] A. Takahashi, N. Yabuuchi, *ICCF-13 International Conf. on Condensed Matter Nuclear Science*, June '07, Sochi, Russia. <http://www.lenr-anr.org/acrobat/TakahashiAdeuteronst.pdf>.
- [13] S.H. Patil, *J. Chem. Phys.* **118** (2003) 2197.
- [14] Tom Barnard, Private Communication, & <http://www.ichaphysics.com/>.
- [15] C. Kittel, *Introduction to Solid State Physics*, 7th Edition., John Wiley and Sons Inc., 1996.
- [16] The proposed existence of $D^- D^+$ pairs in a lattice is based on accepted physics [6]. Mechanisms proposed for electrons and their ground state moving deeper into an atomic or molecular potential well are seldom discussed.
- [17] F. Raiola et al., *Eur. Phys. J. A* **19** (2004) 283–287 and A. Huke et al., *Eur. Phys. J. A* **35** (2008) 243–252.
- [18] Electron mass is considered to be entirely from electromagnetic-field energy. Therefore, the electric-field energy of the proton must also be mass-equivalent energy.
- [19] J. Naudts, On the hydrino state of the relativistic hydrogen atom. <http://arxiv.org/abs/physics/0507193> accessed 28 June 2010.
- [20] For an electron, the total energy = E_o = rest mass – binding energy = $\sim \alpha m_o c^2 = \sim (1/137)511 \text{ keV} = \sim 3.7 \text{ keV} \Rightarrow$ binding

energy = \sim 507 keV. For a lochon, the binding energy = \sim 1 MeV.

- [21] M. Mckubre, F. Tanzella, P. Tripodi, P.L., Hagelstein, *Proc. of ICCF8*, 70, 3 (2000).
- [22] Treatment of the kinetic energy of a reduced-field, relativistic, electron is beyond the scope here.
- [23] K.P. Sinha, A. Meulenberg, Radiative-field quantum-coupling between closely-spaced surfaces. <http://arxiv.org/abs/0902.0682> accessed 28 June 2010.
- [24] These simplified calculations assume circular electron orbits. No corrections have been made for the deepening of the orbit as the system approaches a 1-dimensional geometry and for the stark effect. On the other hand, neither is there a correction for the stretching of the electron orbit toward the D⁺, from proximity effects of the D[−] D⁺ potential well or for the linear electron orbit that makes r_{max} of the linear orbit greater than r_{avg} of the circular orbit.
- [25] E. Fermi, Correction of a Contradiction between Electrodynamic and Relativistic Electromagnetic Mass Theories, *Nuovo Cimento* 25, 159–170 (1923). Translation at: <http://www34.homepage.villanova.edu/robert.jantzen/mg/fermi/fermi4c.pdf>
- [26] N. Dombey, *Phys. Lett. A* **360** (2006) 62.
- [27] A.S. de Castro, *Phys. Lett. A* **369** (2007) 380.
- [28] T. Nadareishvili, A. Khelashvili, Some problems of self-adjoint extension in the Schrodinger equation. <http://arxiv.org/abs/0903.0234> accessed 28 June 2010. ... but the solution (b.2) again satisfies (2.1) in the (2.10) and therefore the hydrino (additional) states must be retained.



Research Article

Ultra-High Density Deuteron-cluster Electrode for Low-energy Nuclear Reactions

George H. Miley* and Xiaoling Yang

Department of Nuclear, Plasma and Radiological Engineering, University of Illinois, Urbana-Champaign, Urbana, IL 61801, USA

Heinrich Hora

Department of Theoretical Physics, University of New South Wales, Sydney, Australia 2052

Abstract

This paper reviews new and previous theoretical and experimental studies of the possibility of nuclear events in clusters created in multilayer thin film electrodes, including the correlation between excess heat, transmutations, and the cluster theory that predicts it. As a result of this added understanding of cluster reactions, a new class of electrodes is under study. These electrodes are designed to enhance cluster formation and subsequent reactions. Two approaches are under development. The first employs improved loading–unloading techniques, intended to obtain a higher volumetric density of sites favoring cluster formation. The second is designed to achieve Rydberg Matters. Various methods of exciting (triggering) cluster reactions are also discussed. Based on these insights, the design of Low-energy Nuclear Reaction (LENR) power cells is proposed. While still in the research stage, this approach promises ultimate development of “green” nuclear powered “batteries” offering remarkable energy densities well beyond present technology. © 2011 ISCMNS. All rights reserved.

Keywords: Deuterium cluster, Electrolysis, Glow discharge, Laser triggering, Low-energy nuclear reaction, Rydberg matter

PACS: 25.90.+k

1. Introduction

Recent research has developed a technique for imbedding ultra-high density deuterium “clusters” (50–100 atoms per cluster) in various metals and its compound such as Palladium (Pd), and Iron oxide (Fe) [1]. Experiments have shown that in Pd these condensed matter state clusters approach metallic conditions, exhibiting super-conducting properties while, in crystal defects of iron oxide, cluster states with deuterium densities of up to 10^{29} per cm^3 have been achieved [2] as shown from measurements of the emission of 630 eV deuterium ions during laser irradiation. This supports the hypothesis that these clusters are in an inverted Rydberg state.

*E-mail: ghmiley@uiuc.edu

The discovery of these clusters potentially has a revolutionary impact on Low-energy Nuclear Reactions (LENRs), which rely on excitation and reaction of the dense deuterium at room temperature without added compression as done in hot fusion. Although our previous research at the University of Illinois at Urbana-Champaign (UIUC) has recorded a net power through either electrical charging or deuteron ion-beam irradiating of deuterium loaded thin film electrodes, the power output was too low to be utilized for a practical power supply application. Work described here is now focussed on increasing the volumetric density of cluster sites in the electrodes to boost the net power output. There is strong evidence that this approach, if successful, will finally enable a useful LENR power cell.

In this article we first review the previous studies of ultra high density deuterium clusters, including early thin film electrodes for LENR at UIUC, then address recent studies of increasing the cluster densities in various electrode materials. Several ways of triggering cluster LENRs will also be discussed. It is proposed that these developments provide a “path” to the development of practical LENR power cells.

2. Early Thin Film Electrode for LENR at UIUC-Cluster Implications

Our initial studies of LENRs involved thin films coated on a flat alumina substrate as illustrated conceptually in Fig. 1. In this design, a double-layer Pd/Ni thin film, at 8000 Å and 1000 Å, respectively, sputtered on ceramic Al_2O_3 substrate [3], was used as a cathode. The design forces an electrical current flow parallel to the thin film surface so that a high current density and high proton flow rate are obtained simultaneously with a high deuterium density [3]. By using this electrode, the excess heat evolution during electrolysis runs was detected by a high sensitivity open-type calorimeter in a fixed temperature of $28.0 \pm 0.05^\circ\text{C}$ [4]. Smooth Pt sheets were used as cathodes in “Reference” runs, since Pt does not produce excess heat in light water electrolysis [5]. In these experiments, ca. 20% excess heat was measured. In typical cases the excesses heat evolution from the cathode at $I = 200$ mA continues for ~ 15 days.

The excess heat measured is correlated with the observation of reactions causing nuclear transmutations, attributed to proton–metal initiated reactions [6]. Such a correlation for these LENR transmutation reactions are equivalent, in principle, to the correlation of He-4 with excess heat that is reported for heavy water–Pd experiments where a D–D reaction is postulated. Interestingly, a recent study by Widom and Larsen claims that their theoretical transmutation calculations reasonably well match these results (see Fig. 3 in [7]). The situation where heavy water is used instead of light water, as reported in some other LENR studies (see [8]), is less clear but again appears to involve proton–metal reactions. In that case, p-metal reactions could occur simultaneously with D–D reactions. More study is needed to resolve all of the possible reactions involved in this important regime.

In order to obtain further proof of nuclear reactions in the thin-film cathodes [9], the detection of nuclear radiation accompanying the electrochemical loading of those cathodes is desirable. Although we have observed time-integrated rates of MeV proton and alpha emission during these electrolysis runs [10], time dependent emission rate measurements

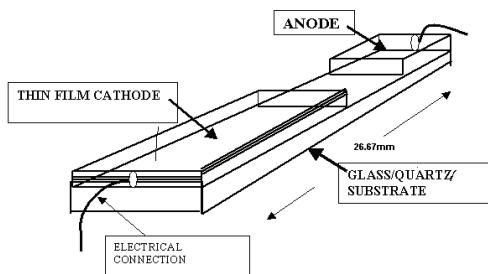


Figure 1. Recent work uses a unique integrated thin film plate-type electrode.

would be highly desirable to understand the reaction correlations. Unfortunately, it is hard to apply electronic SSB and X-ray detectors directly to the cathode during an electrolysis experiment since the emission rates are low compared to background interference. Thus, the technique using non-electronic detectors (CR-39 and thermal luminescence detector (TLD)) was employed to allow in-situ measurement of energetic charged particles and X-rays during the electrochemical loading of the flat-plate Pd-thin film cathodes. The total counts of tracks from protons and alphas after subtraction of background counts are statistically significant. In the control experiment with CR-39 detector attached to the thin film NiO_x (obtained by annealing of Alumina/Ni(4000A) sample in air atmosphere), where despite of the high voltage applied ($U \sim 10.0$ V), the electrolysis current in the cell was very low ($I \sim 1.0$ mA), and no tracks with $d < 7.8 \mu\text{m}$ were detected whereas, in the active electrode runs, numerous tracks with $d > 7.8 \mu\text{m}$ are clearly visible.

In summary, the observation of MeV particle emissions, combined with the transmutations and excess heat measurements, provide extremely strong evidence for nuclear reactions occurring in the thin films during electrolysis. These results, combined with recent observations of localized ultra-high density deuterium clusters in electrodes of this type have led us to consider the new “cluster” approach to power producing LENR power cells described here.

3. Ultra-High Density Deuterium-cluster Formation and Reaction Theory

3.1. Deuterium-cluster formation in palladium foils

In 1999, Nellis pointed out that it should be possible to form solid metallic hydrogen from H atoms since hydrogen may be considered to be the lightest alkali metal [11]. Recently, we achieved ultra-high-density metallic-like hydrogen and deuterium states through electrochemically loading-unloading H/D into a thin metal film, such as palladium (Pd) [1,12]. During the repeated loading-unloading process, the metal lattice expands significantly to form dislocation defects (Fig. 2). The diameter of the dislocation defects is around two burgers vector, while their length depends on the dimensions of the palladium film. The dislocation defects inside the metal form a potential trap for deuterium which then collects there to form ultra-high density clusters. The existence of ultra-high density H/D clusters in the palladium foil has been demonstrated through several different types of experimental methods [1,12]. Briefly, temperature programmed desorption (TPD) measurements suggest that the local loading ratio of hydrogen ($[\text{H}]/[\text{Pd}]$) within the dislocation loops is 1.8. Both a direct resistance measurement and measurements using a super-conducting quantum interference device (SQUID) indicate an H-loaded sample exhibits type-II superconductivity. These results suggest that hydrogen (or deuterium) inside the dislocation loop in a condensed metal-like state has an ultrahigh density.

3.2. Cluster reaction theory

Independently from the last year's results on clusters, the generation of deuterium clusters in a Bose–Einstein state has been fundamental to the explanation of the reaction product distribution observed in the earlier transmutation

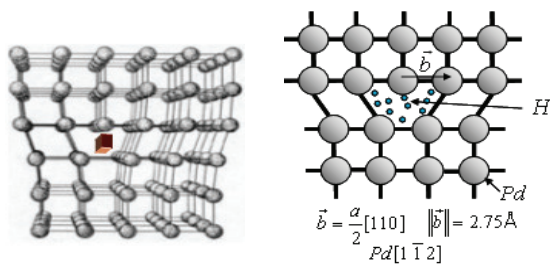


Figure 2. Scheme of edge dislocation loops in Pd containing condensed H/D.

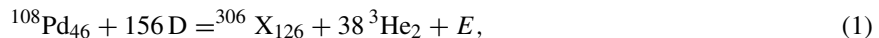
experiments [13,14] as summarized in [15]. The state of the deuterium clusters with about 2 pm nuclear distance in a Bose–Einstein condensation was shown [14,15] as the way that the transmutation product distributions could be generated by the reaction of a palladium nucleus with a cluster of 156 deuterons [15] ([16] see Eq. (10)). An essential point is that the deuterons have a Maxwell distribution in the palladium and profit from their Coulomb screening factor 14 [17] within the background of the conduction electrons. Then, the deuterons can move within the metal and within the interior of the inner electron clouds of the palladium atoms like neutral particles, comparable to neutrons within distances d of about 2 pm. The deuteron charge, i.e. Columbic repulsion, only occurs over shorter distances, allowing strong tunneling and reactions in the cluster.

The 2-pm nuclear distance is sufficient for nuclear reactions (see Fig. 1 of [16]) to occur within times of kilo- to mega-seconds (ks to Ms) as evident from inverse beta decay. The Bose–Einstein state prevents any localization between the deuterons within the 10 pm diameter cluster, such that the reaction with all 156 deuterons could happen as soon as the cluster surface reaches a 2-pm distance from a neighboring palladium nucleus. A screening factor of 14 was derived earlier [16] from an evaluation of reliable D–D reaction experiments in palladium [18] and measured later in a very sophisticated way directly in palladium [19,20]. The reason for the “clinging or clustering together” of the screened deuterons is discussed in [16] and assumed to be a type of molecular force possibly due the Casimir effect, which assumes a significant value at the very short 2 pm distance.

Prior to realizing the connection of the clustering mechanism of deuterium to the UIUC transmutation experiments, the formation of high density states in defects was of strong interest at UIUC. This leads to the experiments noted earlier where localization of 100 or more deuterium atoms within the small defect volume was measured from SQUID responses implying superconducting properties of this new localized state when a large number of crystal voids (Schottky defects) are artificially generated [1,12,21].

Another approach to clusters in void-defects of solids was the discovery of cluster states with ultra-high deuterium densities of up to 10^{29} per cm^3 in near-surface crystal defects of iron oxide. This was found [22] from measurements of the emission of 630 eV deuterium ions during laser irradiation with the conclusion that these clusters are in an inverted Rydberg state. It may be assumed that the clusters in these surface defects are related to the ones we have described relative to the defects formed by loading–unloading methods [1]. One difference is that the latter is located in the interior of the palladium, though they may be associated with the dislocation “anchor” at the film interfaces. In addition to the present interest in LENR, we have shown that these clusters in solids with very high deuterium densities is also of interest for experiments with high temperature nuclear fusion where they are compressed to cause high reaction rates using laser compression [23,24].

The reaction of the deuterium clusters was initially proposed to proceed via a compound nucleus by Miley 1997 [25] and was compared with various exothermal compound nuclear reactions [26,27]. The minimum of the element distribution was shown to resemble the fission reaction of uranium [15,16] and in addition [13,14] even showed a small local maximum as predicted by the Maruhn–Greiner theory where the compound nucleus is an excited state (unexcited uranium does not produce the small local maximum as well known from measurements [15,16]). The reaction of a deuterium cluster with 156 deuterons may then result in



where E is the energy release. The mass per nucleon expressed in proton masses in X is derived to be 1.004946 (ignoring the minor contribution associated with E). This compares favorably with the value of uranium 1.0001868 or with the very low value for iron 0.9988376.

A key point is that [15] the precise measurement of the element distribution has the local Maruhn–Greiner maximum at 155, not at the nucleon number 153 predicted by a classical extrapolation of magic numbers. However, the nucleus X with 126 protons and 180 neutrons represents a double magic number case where all well known magic numbers up to 126 agree with the derivation from the LENR measurements [15] giving the new number 180 [28]. This alternative

theory of the magic numbers based on these LENR measurements leads to a 3^n ($n = 1, 2, 3, \dots$) relation for a nuclear shell model. This allows resolution of a long standing issue in quark structure which could not distinguish between magic numbers of 184 vs. 180 [28].

3.3. Rydberg matter formation in surface defects of iron oxide

The relationship between the deuterium clusters observed in the UIUC experiments [1] and the surface states shown to be inverted Rydberg Matter (RM) [22] is important and now under study. This will be briefly described here. The generation of Rydberg matter in the universe as interstellar clusters has been discussed over recent years. These are molecular structures where the electrons are in orbital states with a quantum number $m = 1$ or higher. It is difficult to produce these states in the laboratory because the atoms needed for joining to a molecule require an energetic excitation much higher than the molecular binding energy. However, the statistics in interstellar space does permit this. Such RM clusters in space cannot be detected by spectroscopic methods but may be dark matter which is only measured by gravitation. Indeed, this may be the dark matter predicted to have some concentration inside and near the discs of galaxies.

A special method was developed by Holmlid et al. [22] to use the catalytic property at the surface of ion oxide. In voids of the crystal defects it is possible that hydrogen or deuterium atoms obtain a $m = 1$ excitation, leading to a RM molecular compound. It is calculated [22] that the proton distance of 74 pm in a H–H molecule with covalent binding is changes into a distance

$$d = 150 \text{ pm} \quad (2)$$

in the RM state. This state is a metallic modification of hydrogen H(1) where the number one expresses the $m = 1$ state [29]. Its generation by a low-pressure catalytic process was first obtained through clever use of iron oxide [30].

The inverted RM is using an inversion of the role of the electron and proton to form a hydrogen atom. The normal atom is based on the electric field of a central proton and the electron is attracted by this field. In Bohr's model, the electron is considered in a point mechanical treatment as rotating with an angular momentum p at a radius r such that the quantum relation

$$rp + nh/(2\pi) = n\hbar \quad (n = 1, 2, 3, \dots) \quad (3)$$

is fulfilled. This rotation is not true in the ground state for $n = 1$ because the electron would then emit energy by radiation. This problem was solved by Schrodinger's quantum mechanics where the electron orbiting is possible only for $n = 2$ and higher. The merit of both models should not be ignored. The transition of a rotating electron from a higher to lower orbit described the radiation emission to arrive at the measured times of about 10^{-8} s spontaneous emission. This was possible in the quantum mechanical description only by Dirac's introduction of the quantization of the electromagnetic field energy density (second quantization).

A quantum mechanical extension of Bohr's model is possible in the following way for exclusion of his orbiting problem for $n = 1$. The electric field energy gained by an electron when falling into the proton depends on the distance r and can be compared with the Fermi–Dirac energy for squeezing the electron into a sphere of radius r . The difference of the exponents of the energies arrives at a radius where both energies are the same. This is just the value [31].

$$r_B = \hbar^2/(me^2) \quad (4)$$

of the Bohr radius where m is the rest mass and e the electric charge of an electron ([31] see Section 2.3). Using this model, the measured polarization shift of spectral lines in plasma (Inglis–Teller effect) for hydrogen can be theoretically explained [32] with higher accuracy than by the earlier derived model by Griem.

The inverted hydrogen atom occurs when an electron produces the central electric field and the proton (or deuteron) falls into the electron until a radius is reached where the electric field energy gained is equal to the increase of the

Fermi–Dirac quantum energy. The radius is then different from the normal case by the square root of the ratio of the mass of the proton p or deuteron D , see the equations between 2.16 and 2.17 of [32].

For the distance d , Eq. (2), in Rydberg cluster, the distance d^* in the inverted deuterium RM cluster $D(-1)$ is then expressed with the deuteron mass m_D

$$d^* = (m/m_D)^{1/2}d. \quad (5)$$

Remarkably, this value is 2.5 pm as was initially calculated [22] from the orbital motion within the clusters.

The direct experimental proof of this distance was obtained from measurements using laser irradiation of the catalytic produced $D(-1)$ clusters [22]. The mechanism is described in Fig. 3. Photons from a laser beam irradiate the cluster and photo-electrically removing electrons at binding centers for the deuterons in the inverted RM. The remaining deuterons are then to repel each other by Coulomb repulsion causing a Columbic Explosion (CE) and are subsequently emitted into the vacuum above the iron oxide. Time of flight (TOF) measurements show energies of 630 eV. This corresponds to an initial distance of the deuterons in the cluster of

$$d_{\text{exp}}^* = 2.3 \text{ pm}. \quad (6)$$

In Section 4.3, a quantum theoretical explanation of the laser produced electron emission process is given, fitting the parameters obtained in this experiment. The small discrepancy between Eq. (5) and (6) may be a way to analyze some properties of the inverted Rydberg state of $D(-1)$. The threshold of the laser intensity is found to be close to

$$I_{\text{thre}} = 10^{10} \text{ W/cm}^2 \quad (7)$$

for a wave length of 565 pm. It should be noted that this experiment did not work with $H(1)$ and $H(-1)$ RM at the low intensities (7). This indicates that the $D(-1)$ clusters are in a Bose–Einstein condensation state which is not normally possible with protons as fermions while deuterons are bosons. As suggested by Kim [33], at the densities involved pseudo bosons may form allowing condensation. While the density of the deuterons in the clusters of the inverted RM state of $(D-1)$ based on the measured deuteron distance (6) corresponds to a value of about 10^{29} cm^{-3} , somewhat higher than estimated for our volumetric cluster, the two still may be related.

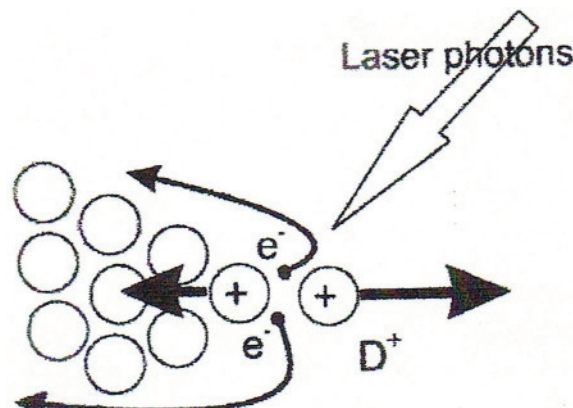


Figure 3. A pictorial representation of the Coulomb repulsion of deuterons in the cluster after removal of electrons by laser produced virtual quivering. Two electrons are excited into higher localized non-shielding orbital states by the laser pulse [2] leaving the remaining deuterons to be accelerated to the time-of-flight measured 630 eV energy by Coulomb forces, as Coulomb explosion CE.

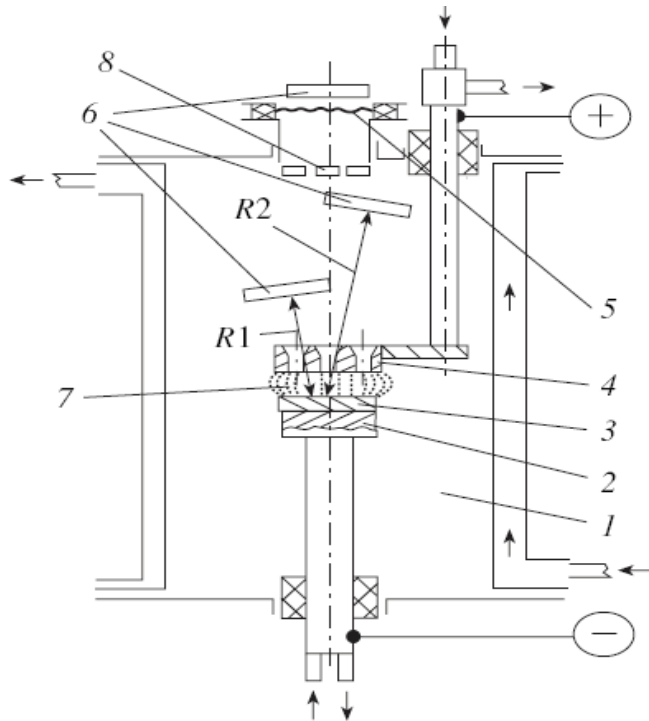


Figure 4. Schematic diagram of the glow discharge setup: (1) vacuum chamber; (2) cathode holder; (3) cathode; (4) anode; (5) Be window; (6) CR-39 detectors; (7) glow discharge region; (8) thermoluminescent detectors (TLDs) with 15- to 300- μm -thick Be filters. (b) Schematic diagram of the experiments with open cathode: (view A) TLDs with Be filters of different thickness; (1) cathode; (2) anode; (3) Be filters; (4) TLDs or pinhole camera; (5) metal holder of detectors; (6) 15- to 300- μm -thick Be filters. [35]

4. Excitation Methods for Cluster LENR

4.1. Electrolysis

LENR first gained attention in 1989 when Pons and Fleischmann reported that nuclear fusion was produced during electrolysis of heavy water on a palladium (Pd) electrode. They reported excess heat production of a magnitude of which the only possible sources were thought to be nuclear processes. They further reported measuring small amounts of nuclear reaction byproducts, including neutrons and tritium. These reports raised hopes of a cheap and abundant source of energy. Since then, the experimental results from various research groups, have shown support of the initial Pons and Fleischmann's measurement.

4.2. Glow discharge experiments

An alternative possibility for studying the D–D reaction yield is offered by the experiments with a high-current pulsed discharge in deuterium. The results of previous experiments [34] showed that pulsed glow discharge makes it possible to obtain ions with the energies within 0.8–2.5 keV and current densities within 300–600 mA/cm² at a deuterium pressure of 1–10 Torr.

The current density used for the bombardment of the cathode (target) surface in glow discharge is three orders of

magnitude higher than those using accelerators. Preliminary estimates show that high-current bombardment of the cathode with deuterium ions in a high current glow discharge can provide detection of the D–D reaction products even at $E \leq 1$ keV for exposures not exceeding several tens of hours (not possible with normal accelerator-target reaction measurements due to the current limitations of ion accelerators). This low-energy cross section data is relatively unexplored. However, it is not only vital information for LENRs, but also for fusion in astrophysical objects.

Figure 4 shows a schematic diagram of the experimental setup and the arrangement of detectors. Using this setup, intense directional X-ray emission has been observed from metal targets (Pd and Ti) in a pulsed high current (100–400 mA) and low-voltage (1.0–2.0 keV) deuterium/hydrogen glow charge. X-ray measurements showed an intense ($I_x = 10^{13} - 10^{14} \text{ s}^{-1} \cdot \text{cm}^{-2}$) soft X-ray emission (with a mean energy of quantum $E_x = 1.2\text{--}1.5$ keV) directly from the Pd or Ti cathode. The X-ray yield is strongly dependent on a deuterium diffusivity in the surface layer of the cathode, and the emission can be associated with enhanced electron screening effects at metal surfaces and interfaces and a coherent oscillation of this screening layer.

4.3. Low-energy laser excitation of RM matter

Low-energy laser excitation may be another way of exciting LENR reactions in RM mater. This requires development of efficient methods for coupling the laser photon energy with the inverted RM state of D(-1) clusters in order to remove electrons, and cause the D-atom in the cluster to fuse. The mechanisms to explain removal of the electrons by the laser field from the inverted surface RM state of D(-1) clusters, Fig. 1, is explained from the oscillation of the electron in an electromagnetic field (quiver motion at laser irradiation) in combination with a quantum relation to obtain a correspondence principle for the electromagnetic interaction [36].

A free electron in space, e.g. in a plasma, quivers in a laser field with the amplitude E of the laser field having a maximum elongation

$$r = eE/(m\omega^2) \quad (8)$$

with a maximum momentum $p = mv$ from the quiver velocity v

$$p = mv = eE/\omega, \quad (9)$$

where ω is the radian frequency of the laser. Indeed, free electrons in a vacuum perform the quiver motion as detected also from Thomson scattering where oscillation energy of the electrons

$$\varepsilon_{\text{osc}} = (eE/\omega)^2/(2m). \quad (10)$$

is the quiver energy.

A basic difference between this analysis and classical point mechanical motion in vacuum occurs when it is bound in an unexcited hydrogen atom or any bound state including the Rydberg state. If the laser field has a sufficiently high intensity $I > I_i$ above the ionization threshold I_i in vacuum, the electron will be ionized and then follow the quiver motion where I_i is defined by the ionization energy ε_i . At lower intensities photon interaction of the laser light can occur quantum-electro-dynamically with the electron in the hydrogen atom by resonance for energy levels given by energy eight-values of the quantum states of the electron within the bound atom. At these lower intensities one cannot describe the electron interaction with the photons in the point-mechanical classical way as quiver motion. Nevertheless, the correspondence to the quiver motion might be considered as a virtual oscillation (with all caution not to overstress this description until it is studied further). It is therefore interesting to see when the product of the length of the quiver motion, r of Eq. (8), with the momentum $p = mv$, Eq. (9) reaches the value of Planck's constant h

$$rmv = \hbar = h/(2\pi). \quad (11)$$

This quantum relation permits substitution of the laser field E of the quiver velocity v in Eq. (9) with the quiver energy (10) to arrive at

$$\varepsilon_{\text{osc}} = \hbar^2 / (2mr^2). \quad (12)$$

For low-laser intensities, this can be considered as a “virtual” quiver motion of the electron which is fundamentally different from the quantum states of the electron when bound in the atom. Based on this virtual description, it is interesting to see what happens if r assumes the value of the Bohr radius, Eq. (4). This arrives at a value of a “Bohr”-quiver oscillation energy

$$\varepsilon_{\text{B,osc}} = me^4 / (2\hbar^2) = \alpha^2 mc^2 / 2 = 13.6 \text{ eV}; \alpha = e^2 / (\hbar c) \quad (13)$$

using the vacuum speed of light c and the fine structure constant α . This is just the ionization energy of hydrogen. It is worth noting that this value is simply expressed by the fine structure constant α and the electron rest energy mc^2 . It is remarkable that this ionization energy for hydrogen marks a border line between the classical and the quantum mechanical state now expressed by the quiver motion, i.e. by the virtual electron oscillation.

The state of the inverted Rydberg cluster D(-1) [22] with distance d^* of 2.3 pm between the deuterons (as measured from the 630 eV energy of the emitted deuterons with the TOF mass spectrometer) is a rather complicated quantum state for the electrons and deuterons. In fact, it is the state of the electron of an unexcited hydrogen atom. Using the radius $r^* = d^*/2 = 1.15 \text{ pm}$ as a first approximation in the inverted Rydberg deuterium cluster in the same way as the Bohr radius (4) was used for hydrogen, we arrive at a virtual oscillation energy for the electron for “ionization” from the bound state in the inverted Rydberg state cluster.

$$\varepsilon_{\text{DD,osc}} = \varepsilon_{\text{B,osc}}(m_e/m_D)[d/(2r_B)]^2. \quad (14)$$

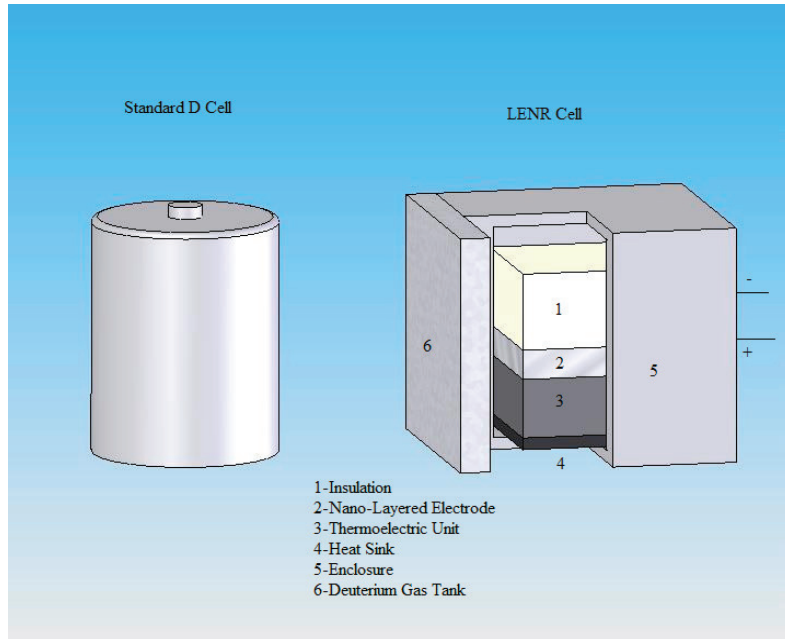


Figure 5. Small LENR battery – design based on present experimental data base.

The laser intensity for producing a quiver energy $\varepsilon_{B,osc}$ for the boron ionization Eq. (14) at the wave length 565 pm is $2.298 \times 10^{14} \text{ W/cm}^2$ resulting with the same ratios as Eqs. (13) and (14) to arrive at a laser intensity

$$I^* = 3.1 \times 10^{10} \text{ W/cm}^2. \quad (15)$$

This is close to the measured threshold in the experiment. We assumed an ad hoc distance d^* for the inverted D-clusters in these calculations in order to work with the radius $r^* = d^*/2$ according to Fig. 1. The correct value may be somewhat different, leading to a slightly different threshold I^* . When very precise measurements of the threshold intensity are at hand, the more precise elongation of the virtual quivering in the D (-1) cluster could be calculated and may give more important information about the inverted Rydberg state of the D-clusters which definitely will not be a “clumping” together of spheres of the kind illustrated schematically in Fig. 1, but with much more complicated structures. This result and the corresponding theory also provide exciting new insights to the correspondence principle of electromagnetic interactions [36].

It is very important to realize that the measured [22] $d^* = 2.3 \text{ pm}$ value is lower than the initially expected theoretical value. This shows qualitatively that the radius of an inverted deuterium atom is larger than for an inverted Rydberg state of free deuterium. This confirms the implied overlap between the cluster members with neighboring states within the D (-1) state under the assumption of a cubic deuteron lattice structure in the cluster. The degree of overlap can be defined quantitatively from this type of analysis and should be carefully studied when more precise measurements are obtained.

The very low emission energy of the electron in D(-1) is understandable from the comparison of the model described in Fig. 1 where the binding is much weaker than in a hydrogen atom, cf. the model in Section 2.3 of [31]. Compared to the very long time of the resonance transition of electrons in atoms, the virtual-quiver-model ionization process is indeed extremely fast, roughly in the femto-second range. The electric field amplitude of the laser of 10^{10} W/cm^2 is $2.7 \times 10^6 \text{ V/cm}$ in good consistence to a laser driven field emission process. The laser intensity threshold near 10^{10} W/cm^2 for removing the electrons in the inverted Rydberg state for the subsequent 630-eV Coulomb explosion of the deuterons arrives at the virtual electron oscillation energy in full analogy to the ionization of hydrogen. This represents a characteristic of the correspondence principle of electromagnetic interaction [36]. It is a further example of the different mechanisms when transitioning from the classical to the quantum mechanical range as first noted when explaining the Schwarz–Hora effect [37,38].

5. A Potential Power Cell Using Gas Loading

While these clusters have extremely local high density, the low fractional volume of the clusters (which is where the LENRs would occur) limits total reactions over the electrode to low levels. The development of materials with abundant nano- or micro-structures may solve this problem, allowing a high volumetric density of cluster sites, i.e. a high cluster “packing fraction”. The idea is that the dislocation loops mainly form at the near surface of the material. Nano- or micro-structures feature with large surface area, thus providing more room for dislocation formation. If high volumetric densities of cluster sites can be created via methods outlined earlier, a high reaction rate per cc should result in a competitive power cell at small size. We term the electrode designed to achieve a “massive cluster electrode” (MCE) for controlled cluster reactions.

To avoid use of expensive materials, the power unit may ultimately use different structures. Dislocations can also form in materials other than Pd such as Nickel with direct hydrogen charge [39]. It is encouraging that higher hydrogen loading at dislocation cores than in the bulk material has been reported. Hydrogen interactions at dislocations in Silicon have been extensively studied [40], but no work has yet been done to investigate application of LENRs. As the understanding of the technology of H/D condensation in the defects of solid materials continues to grow, development of a family of possible host materials is only a matter of time.

Based on the prior excess heat measurements described earlier, local power densities exceeding a kW/cm^3 are possible, promising very high energy density power units. Since the radiation emitted (protons, alphas, and X-rays) are not very penetrating (do not escape the cell structure) and no long lived radioactive reaction products are observed, LENR power units would be a remarkable “green” nuclear technology. A sketch of a small Dcell equivalent LENR battery is shown in Fig. 5.

The cell shown has a deuterium gas “fuel” tank attached. Gas loading is used rather than electrolysis for compactness. Heat flow is directed to the outer casing through a thermoelectric element using an insulation and heat sink design. Modular sections connected in series allow a 1.5 V output at 0.1 A. This type of battery must be used in devices where natural convection air cooling or other heat flow dissipates heat from the battery casing. The battery run time is determined by the amount of deuterium stored. Refilling of the depleted tank is done by pump down and gas injection through a filtered line connected to a “filling station”. The unit shown is designed for 1000 A h per gas fill. The main technological step needed before construction of this battery is to finish development of the nano-layered electrode structure described earlier.

6. Conclusion

While LENR D-cluster studies are still in the research stage, there is mounting evidence that this technology may lead to a very attractive “green” power unit. If so, small self-powered battery-like units could be constructed with very high energy densities, well beyond present 1000 W·h/kg battery technology. Power densities would also be formidable. This revolutionary development would drastically impact the distributed mobile power industry. Much more R&D is needed, however, to achieve this vision, not only will this allow a radical new energy technology, but it will develop a whole new science related to these unique cluster states in metals. Preliminary experimental studies with the Bose–Einstein condensed ultra-high density deuteron clusters have been performed at the LANL TRIDENT Petawatt Laser with the goal of generating high energy (MeV) deuteron beams from the embedded deuterium clusters [41]. Such ultra-intense laser interactions provide important insight into the cluster states present in the targets (equivalent to the electrodes when used for LENR). This work, while not directly LENRs, uses the condensed matter cluster aspect to enhance Inertial Confinement Fusion (ICF) and ultimately has a similar goal of producing fusion energy without emission of radioactive radiation [42–44].

Acknowledgements

Important contributions to this paper from L. Holmlid are gratefully acknowledged. The paper is dedicated to the memory of Andrei Lipson who participated in many of the studies and who unexpectedly passed away late last year. Support for parts of the work by a NPL Associate, INC. Plasma Physics grant and by the New York Community Trust was essential to the effort.

References

- [1] A. Lipson, B.J. Heuser, C. Castanov, G. Miley, B. Lyakov, A. Mittin, Transport and magnetic anomalies below 70 K in a hydrogen cycles Pd foil with a thermally grown oxide, *Phys. Rev. B* **72** (2005) 212507/1–6.
- [2] S. Badei, L. Andersson, L. Holmlid, High-energy Coulomb explosion in ultra-high dense deuterium: Time-of-flight mass spectrometry with variable energy and flight length, *Int. J. Mass Spectr.* **282** (2009) 70–76.
- [3] G.H. Miley, H. Hora, E.G. Batyrbekov, R.L. Zich, Electrolytic cell with multilayer thin-film electrodes, *Trans. Fusion Technol.* **26** (1994) 313.
- [4] G.H. Miley, H. Hora, A. Lipson, S.O. Kim, N. Luo, C.H. Castano, T. Woo, Progress in thin-film electrode research at the University of Illinois, *The 9th International Conference on Condensed Matter Nuclear Science*, 2002.

- [5] E. Storms, How to produce the Pons–Fleischmann effect, *Fusion Technol.* **29** (1996) 261.
- [6] C.H. Castano, A.G. Lipson, S.O. Kim, G.H. Miley, Caloremetric measurements during Pd–Ni thin film–cathodes electrolysis in $\text{Li}_2\text{SO}_4/\text{H}_2\text{O}$ solution, in *the proceedings of ICCF-9*, Beijing, China, 19–24 May, 2002.
- [7] A. Widom, L. Larsen, Nuclear abundances in metallic hydride, <http://www.newenergytimes.com/Library/2006WidomANuclearAbundancesInMetallicHydride.pdf>, (2006).
- [8] G.H. Miley, G. Selvaggi, A. Tate, M. Okuniewski, M.J. Williams, D. Chicea, H. Hora, J. Kelly, Advances in Thin-Film Electrode Experiments, in *the proceedings of 8th International Conference on Cold Fusion, ICCF-8*, Villa Marigola, Lerici, Italy, May 21–26, 2000.
- [9] G.H. Miley, Emerging physics for a breakthrough thin-film electrolytic cell power unit, in *the proceeding of Space Technology Application and International Forum (STAIF-99)*, M.S. El- Genk (ed.), AIP conference proceedings, vol. 458, 1999, p. 1227.
- [10] Lipson, A.G., Roussetski, A.S., Miley, G.H., Castano, C., In-situ charged particles and X-ray detection in Pd thin film-cathodes during electrolysis in $\text{Li}_2\text{SO}_4/\text{H}_2\text{O}$, in *the proceedings of ICCF-9*, Beijing, China, 19–24 May, 2002.
- [11] W.J. Nellis, Metastable solid metallic hydrogen, *Philosophical Magazine Part B* **79** (1999) 655–661.
- [12] G. Lipson, B.J. Heuser, C.H. Castano, A. Celik-Aktas, *Phys. Lett. A* **339** (2005) 414–423.
- [13] G.H. Miley, J.A. Patterson, *J. New Energy* **1** (1996) 11.
- [14] G.H. Miley, G. Narne, M.J. Williams, J.A. Patterson, J. Nix, C. Cravens, H. Hora, Progress in New Hydrogen Energy, M. Okamoto (ed.), *New Energy and Industrial Technology*, Tokyo, 1997, p. 629.
- [15] G.H. Miley, H. Hora, K. Philberth, A. Lipson, P.J. Shrestha. Radiochemical comparisons on low energy nuclear reactions and uranium. In *Low-Energy Nuclear Reactions and New Energy Technologies Source Book*, vol. 2, J. Marwan, S.B. Krivit (eds.), American Chemical Society/Oxford University Press, Washington DC, 2009, pp. 235–252. ISBN 978-0-8412-2454-4.
- [16] H. Hora, G.H. Miley, Maruhn–Greiner maximum from uranium fission for confirmation of low energy nuclear reactions LENR via a compound nucleus with double layer magic numbers, *J. Fusion Energy* **26** (2007) 347, 349–354.
- [17] H. Hora, J.C. Kelly, J.U. Patel, M.A. Prelas, G.H. Miley, J.W. Tompkins, Screening in cold fusion derived from D–D reactions, *Phys. Lett. A* **175** (1993) 138–143.
- [18] M.A. Prelas, F. Boody, W. Gallaher, E. Leal-Quiros, D. Mencin, S. Taylor, *J. Fusion Energy* **9** (1990) 309.
- [19] K. Czerski, A. Huke, A. Biller et al., *Europhys. Lett.* **54** (2001) 449.
- [20] K. Huke, P. Cerski, Heide et al., *Phys. Rev. C* **78** (2008) 015803.
- [21] G.H. Miley, X. Yang, Deuterium cluster target for ultra-high density, *Fusion Sci. Technol.* **56**(1) (2009) 511.
- [22] S. Badiei, L. Andersson, L. Holmlid, High-energy Coulomb explosion in ultra-high dense deuterium: Time-of-flight mass spectrometry with variable energy and flight length, *Int. J. Mass Spectr.* **282** (2009) 70–76.
- [23] L. Holmlid, H. Hora, G.H. Miley, X. Yang, Ultrahigh-density deuterium of Rydberg matter clusters for inertial confinement fusion targets, *Laser and Particle Beams* **27** (2009) 529–532.
- [24] P.U. Andersson, L. Holmlid, Ultra-dense deuterium: a possible nuclear fuel for inertial confinement fusion (ICF), *Phys. Lett.* A doi:10.1016/j.physleta.2009.06.046.
- [25] G.H. Miley Transact, *Am. Nucl. Soc.* **76** (1997) 155.
- [26] H. Hora, J.A. Patterson, d- and p-Reactions in low energy nuclear fusion, *Transmutation and Fission, Transact. Am. Nuclear Soc.* **76** (1997) 144–145.
- [27] H. Hora, G.H. Miley, J.C. Kelly, Current trends in international fusion research, *Proceedings of the Third Symposium*, E. Panarella (ed.), NRC Research Press, National Research Council of Canada, Ottawa, ON K1A 0R6 Canada, 2002 p. 527; H. Hora, G.H. Miley, F. Osman, *Astrophys. Space Sci.* **298** (2005) 247; H. Hora, G.H. Miley, *Czechosl. J. Phys.* **50** (2000) 433.
- [28] N. Ghahramani, H. Hora, G.H. Miley, K. Philberth, F. Osman, Nuclear magic numbers based on a quark-like model is compared with the Boltzmann distribution model from nuclear abundance in the universe and low energy nuclear reactions, *Phys. Essays* **21** (2008) 201; H. Hora, N. Ghahramani, G.H. Miley, M. Ghanaatian, M. Hooshmand, K. Philberth, F. Osman, Quark-gluon model for magic numbers related to low energy nuclear reactions, *Low Energy Nuclear Reactions and New Energy Technologies Source book*, Vol. 2, J. Marwan, S. B. Krivit (eds.), American Chemical Society, Oxford University Press, Washington, DC. ISBN 978-0-8412-2454-4.
- [29] R. Chau, A.C. Mitchell, R.W. Minich, W.J. Nellis, *Phys. Rev. Lett.* **90** (2003) 245501.
- [30] S. Badiei, L. Holmlid, *J. Phys. B: At. Mol. Opt. Phys.* **39** (2006) 4191.
- [31] H. Hora, *Plasmas a High Temperature and Density*, Springer, Heidelberg, 1991.

- [32] H. Hora, B.I. Henry, Polarization shift of spectral lines in high density plasmas, *Opt. Comm.* **44** (1983) 218–222.
- [33] Y.E. Kim, Theory of Bose–Einstein condensation mechanism for deuteron-induced nuclear reactions in micro/nano-scale metal grains and particles, *Naturwissenschaften* **96**(7) (2009) 803–11.
- [34] A.B. Karabut, Ya. A. Kucherov, I.B. Savvatimova, *Phys. Lett. A* **170** (1992) 265.
- [35] A.G. Lipson, A.S. Rusetski, A.B. Karabut, G. Miley, D–D Reaction enhancement and X-ray generation in a high-current pulsed glow discharge in deuterium with titanium cathode at 0.8–2.45 kV, *J. Exp. Theoret. Phys.* **100**(6) (2005) 1175–1187.
- [36] B.W. Boreham, H. Hora, Energy spectra of electrons emitted from laser irradiated low density gas and the correspondence principle of electromagnetic interaction, *Laser and Particle Beams* **13** (1995) 71–85.
- [37] H. Schwarz, H. Hora, Modulation of an electron wave by a light wave, *Appl. Phys. Lett.* **15** (1969) 349–351.
- [38] H. Hora, P.H. Handel, New experiments and theoretical development of the quantum modulation of electrons (Schwarz–Hora effect), *Advances in Electronics and Electron Physics*, P.W. Hawkes (ed.), Acad. Press, New York, vol. 69, 1987, pp. 55–113.
- [39] J. Alami, J. Creus, X. Feaugas, Influence of the plastic strain on the hydrogen evolution reaction on polycrystalline nickel electrodes in H₂SO₄, *Electrochimica Acta* **51**(22) (2006) 4716–4727.
- [40] M.I. Heggie, S. Jenkins, C.P. Ewels, P. Jemmer, R. Jones, P.R. Briddon, Theory of dislocations in diamond and silicon and their interaction with hydrogen, *J. Phys.: Condens. Matter* **12** (2000) 10263–10270.
- [41] X. Yang, G.H. Miley, K.A. Flippo, H. Hora, Energy enhancement for deuteron beam fast ignition of a pre-compressed inertial confinement fusion (ICF) target, *Phys. Plasmas* **18** February (2011).
- [42] H. Hora, G.H. Miley, M. Ghoranneviss, B. Malekynia, N. Azizi, X.-T. Hem, Fusion energy without radioactivity: laser ignition of solid hydrogen–boron(11) fuel, *Energy and Environment Sci.* **3** (2010) 479–486.
- [43] Yuandi Li, Nuclear Power without radioactivity, *Highlights in Chem. Technol.* **7**(10) (2010).
- [44] Heinrich Hora, Clima Problems and Solutions: Solar Cells, Nuclear Power and Lasers with New Methods (in German) S. Roderer Publisher, Regensburg/Germany 2010 ISBN 978-3897837157.



Research Article

Progress in Condensed Cluster Fusion Theory *

Akito Takahashi †

Technova Inc., Uchisaiwaicho 1-1-1, Chiyodaku, Tokyo, Japan

Abstract

The theoretical models on Condensed Cluster Fusion in the dynamic ordering process of deuterons in condensed matter (especially PdDx lattice) have been elaborated in three steps in the period from 1989 to 2009. The present paper briefly reviews theoretical modeling, mathematical formulation and quantitative estimations of multi-body deuteron fusion rates, time-dependent screening effect by electron clouds, and time-dependent size of condensing clusters as 4D/TSC. TSC is the tetrahedral symmetric condensate and key idea for clustering and dynamic condensation. Final products of 4D fusion are mainly ^4He nuclei with 2–5 MeV main component and 23.8 MeV minor component.

© 2011 ISCMNS. All rights reserved.

Keywords: Condensed cluster fusion, Deuteron cluster fusion, 4D Fusion, Helium-4, Tetrahedral symmetric condensate, Time-dependent condensation

PACS: 89.20.-a

1. Introduction

Major questions concerning theoretical modeling of the process of experimentally claimed “radiationless excess heat with ^4He ash” as condensed matter nuclear effects (CMNE) are as follows.

- (A) How can the mutual Coulombic repulsion between deuterons be overcome at low deuteron energy, so as to attain significant levels of deuteron-related fusion?
- (B) How can the ^4He generation channel be predominant?
- (C) How can hard radiations be suppressed?
- (D) What kind of environments in/on condensed matter are conducive to CMNE?

Many theoretical efforts in the past have concentrated on questions A and D, and controversial answers have been provided for questions B and C. We focus on question B “The major ash of ^4He due to a two-body deuteron fusion

*Note: This paper is a modified version of Section 3 of the author's previous review paper, “Potential Clean Energy by Condensed Cluster Fusion”, to be published in Infinite Energy Magazine 2010.

†E-mail: akito@sutv.zaq.ne.jp.

reaction cannot be expected" is undoubtedly true, as far as concerned the emission of particles in final state interactions by fusion reactions, commonly seen in nuclear physics. This means that we need to invent some new nuclear processes in condensed matter to explain ${}^4\text{He}$ production in correlation with excess heat. Takahashi has argued that the direct coupling of an excited nucleus in the final state interaction with a lattice (e.g., a metal–deuteride system) to transfer the nuclear excitation energy directly to the lattice (vibration) is impossibly difficult [1,6,16].

There are, in principle, several ways to get to certain lower excited states of ${}^4\text{He}^*$ (probably the assumed levels of 20.21 MeV as noted by Swartz [17] or the Schwinger–Preparata P-wave state [18], as shown in Fig. 1. See Fig. 1 for ${}^4\text{He}$ level charts and related reactions. One simple way is excitation by incident gamma-rays with energy more than 20.21 MeV, which may show resonance photon absorption at $E_\gamma = 20.21$ MeV with some narrow energy width (maybe of the order of several tens of meV). Another way is by using the p + t reaction with $(20.21 - 19.814) = 0.396$ MeV relative kinetic (beam) energy. Conventional d + d reactions cannot go there since the ${}^4\text{He}^*$ excited energy with zero relative kinetic energy is 23.8 MeV. So, Swartz [17] assumed that this 3.6 MeV difference — (23.8 minus 20.21) — was due to the hypothetical Phuson interaction (the feasibility is discussed below). In any case, the assumed 20.21 MeV state of 'special d–d fusion' should be reached through the d + d strong interaction, and therefore we need to consider the competition among n-, p- and gamma-emission channels with their own partial energy widths, because we have to start or compete with the $\langle d - d \rangle$ admixture state by d + d to ${}^4\text{He}^*$ ($E_x = 23.8$ MeV) or by-passed routes. We therefore need to treat the competition among particle emission break-ups and gamma (or electromagnetic) transitions. To treat only the photon channel is consequently misleading. We stress that, in the p + t break-up channel, the [t] channel, is dominant due to its large partial energy width, defeating the gamma-ray emission transition, the [γ] channel, for the 20.21 MeV state of ${}^4\text{He}$ if this were attained in the d–d interaction in condensed matter at all (the author however regards it as very pessimistic to construct a feasible model considering this possibility).

We cannot change the branching ratios after the (virtual) intermediate compound state ${}^4\text{He}^*$ ($E_x = 23.8$ MeV + E_k) with very short life (on the order of 10^{-22} s), since no force-exchange bosons can transfer energy (or any information) from the intermediate compound nucleus to surrounding nuclei, atoms or lattices – all of which are located at distances larger than 0.1 nm. We need to consider a time length for the force-exchange boson (the photon for an electromagnetic interaction) of more than 3×10^{-19} s, which is very much longer than the life time 10^{-22} s of ${}^4\text{He}^*$ ($E_x = 23.8$ MeV + E_k). The branching ratios, $[n]/[t]/[\gamma]$ of d–d fusion should therefore almost maintain at constant values, $0.5/0.5/10^{-7}$ for $E_k = 0.025$ eV to about 100 keV. (See Fig. 2 for an illustration of this feature of the branching.) Here E_k is the relative kinetic energy of the d–d interaction.

To change out-going channels, namely branching ratios, we need the participation of a Third Interaction with the d–d strong interaction process during the initial interaction state. The third interaction should be effective enough to quantitatively change the virtual intermediate excited state of ${}^4\text{He}^*(E_x)$, or other deuteron-related compound nuclei states.

As discussed in detail in the literature [16] on possible third interactions to change the out-going channels (branching ratios), we can conclude:

- (1) The lowest excited energy of ${}^4\text{He}^*$, intermediate compound nucleus, by two body d + d fusion reaction is 23.8 MeV. Lower excited energy than 23.8 MeV is forbidden by kinematics. As a result, the $[n]/[t]/[{}^4\text{He}]$ branching ratios become almost constant at: $0.5/0.5/10^{-7}$ for $E_k = 0$ eV to 100 keV (relative kinetic energy of reaction).
- (2) If a ${}^4\text{He}^*(E_x)$ state with $E_x < 19.8$ MeV occurs, the final product becomes ${}^4\text{He}$ in a ground state, after electromagnetic transition. To realize this process in view of d + d reactions, there should exist a third coupling field which must reach more than 4 MeV difference of energy ($23.8 - 19.8$) of the d–d system in the initial state interaction.
- (3) A many-body interaction process between the d + d pairing and the third field of photon–phonon coupling in the lattice of condensed matter may be considered. Due to the very short range force of the d + d strong interaction

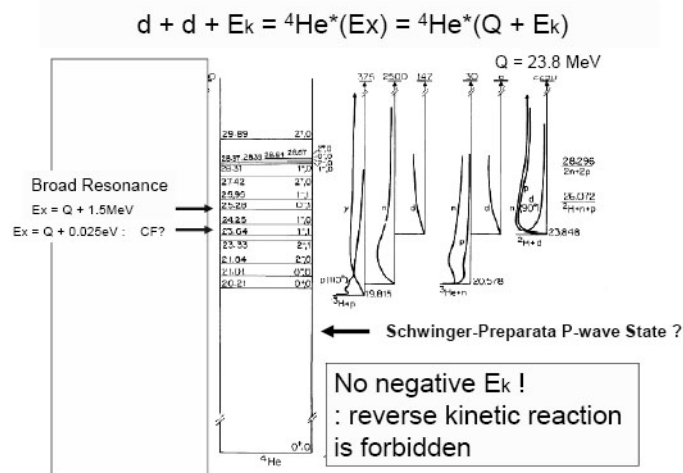


Figure 1. DD ($d + d$) reaction and energy levels of ${}^4\text{He}$.

and its very short life time as a virtual intermediate compound state, no processes have ever been proved to remove the 4 MeV gap-energy [7–14]. Moreover, the field coupling constant of electromagnetic interaction looks too weak, of the order of 10^{-2} relative to the strong interaction, to drastically change the state of $d + d$ strong interaction for fusion. Quantitative studies on transition probabilities for proposed models [7–15] will be further needed.

(4) Deuteron-cluster fusion, i.e., 4D fusion, may produce ${}^4\text{He}$ as a major final ash of the reaction. To realize the conditions for 4D fusion, the microscopic ordering/constraint process for the dynamic Platonic symmetry must be satisfied. The EQPET/TSC model is one of these theoretical models, although it requires further investigation to become established [1–6].

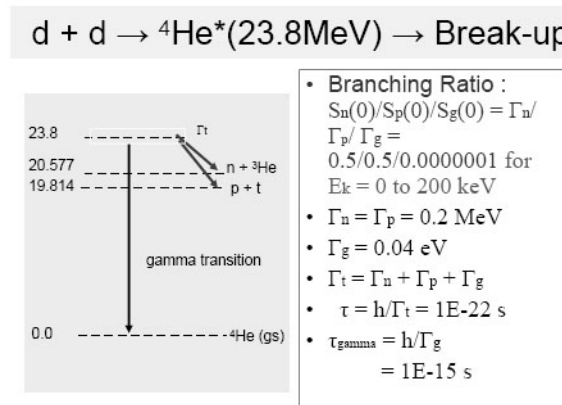


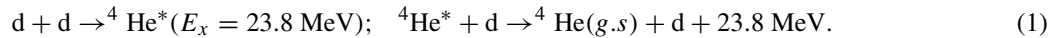
Figure 2. Break-up (out-going, decay) channels of $d + d$ fusion.

This theoretical model treats a process of “condensed cluster fusion” of multi-body deuteron interactions in condensed matter.

2. Brief Explanation of Condensed Cluster Fusion Models

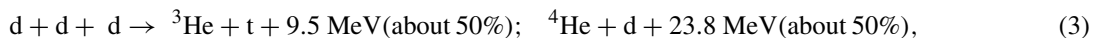
2.1. Step 1: Multi-body deuteron fusion models

Just two weeks after the announcement of the Fleischmann–Pons “cold fusion” experiment [25] claiming large excess heat evolution without corresponding intense neutron emission from the heavy-water electrolysis using Pd cathodes, the author submitted a short note to the *J. Nucl. Sci. Technol.* [19] proposing a three-body deuteron interaction, 3D fusion, considering the following D-catalyzed cascade reaction channel to produce the main ash of ${}^4\text{He}$,



Ordinary $\text{d} + \text{d}$ (2D) fusion should have two main outgoing channels with a 50%/50% branching ratio, the $\text{n} + {}^3\text{He} + 3.27 \text{ MeV}$ channel and the $\text{p} + \text{t} + 4.03 \text{ MeV}$ channel should have very small branching ratios ($10^{-5}\%$) of the electromagnetic transition, ${}^4\text{He(g.s.)} + \gamma + 23.8 \text{ MeV}$, in the range of low deuteron kinetic energy. For this reason, it is reasonable to consider that a third hadronic interaction should participate in the $\text{d} + \text{d}$ strong interaction to realize a main branch of the ${}^4\text{He}$ producing reaction.

The quantitative model of Eq. (1) meets, however, a difficulty in predicting a high level reaction rate, due to the very short life time (about 10^{-22} s) of ${}^4\text{He}^*$ ($E_x = 23.8 \text{ MeV}$), from proven nuclear physics knowledge. The model was therefore elaborated [20,21] to the “simultaneous” 3D and 4D fusion models in the dynamic environment of the PdD lattice with excited D-harmonic oscillators (phonons) to be able to predict more than several watts/cc-PdD excess heat with ${}^4\text{He}$ ash ($23.8 \text{ MeV/}{}^4\text{He}$). It also predicted much less (of the order of 10^{-6} – 10^{-12} of helium yield) of tritium and neutron production. Fusion reactions by transient deuteron clusters were modeled to take place as the following competition processes of 2D, 3D and 4D fusions.



The formation of transient clusters of 2D, 3D and 4D was modeled to approximately quantify the concept shown in Fig. 3. Deuterons sit at O-sites as Einstein oscillators (harmonic oscillators), and have Gaussian wave function for the ground state (energy eigenvalue is 32 meV) [20]. At higher phonon-excited states, D-wave function changes to form a “U” shape distribution to enhance the probability of multiple deuterons meeting around the T-site. Fusion rates for 3D and 4D formation can overtake 2D fusion rates at high phonon excited states [20].

A time-window of about 50 fs was conceived for a transient 4D cluster formation with about 10 GHz lattice plasma-oscillation under D-phonon excitation [21]. We have also roughly estimated D-cluster formation probabilities, as shown in Fig. 4, as a function of D-phonon energy (one phonon = 64 meV, namely 0.064 eV). Competing fusion rates were then estimated, as shown in Fig. 5.

Later, we considered electron spin combinations (in Step 2 [1]) and the Platonic symmetries (in Step 3 [4,5]) for D-cluster formation. We also later found by using Langevin equation analyses [4–6] that the initial time window for 4D/TSC formation with a much shorter time interval of $1.0 \times 10^{-18} \text{ s}$ was enough for further 4D/TSC condensation. Also, a very small 4D cluster formation probability of 10^{-11} can already be realized for 4D fusion rates to meet a

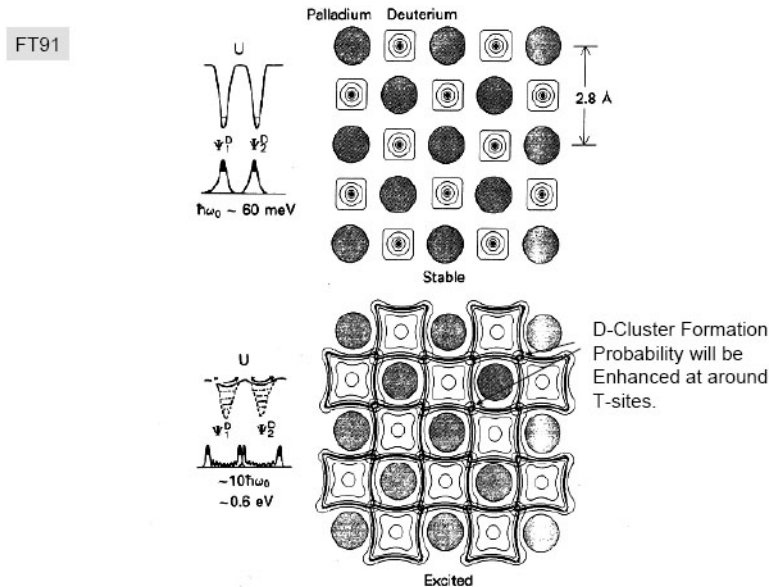


Figure 3. Modeling of transient D-cluster formation under a D-harmonic oscillator in the PdD lattice [21].

1 W/cm³ level of nuclear heat-power level. Henceforth, we need to re-quantify cluster formation probabilities with more sophisticated solid state physics (or surface physics) modeling.

However, our Step-1 theory can already explain why deuteron-related nuclear reactions with observable excess heat level and ⁴He main ash are possible with apparently radiation-less nuclear products. To prove the super-screening scenario of mutual Coulomb barriers among deuterons, we need further elaboration of Steps 2 and 3.

2.2. Step 2: EQPET/TSC models

Elaboration of EQPET/TSC (electronic quasi-particle expansion theory/tetrahedral symmetric condensate) models were reviewed more in detail in our recent papers [1,2]. There, we proposed a multi-body deuteron fusion process by formation of Tetrahedral Symmetric Condensates (TSC) and Octahedral Symmetric Condensates (OSC). Some numerical results were given by EQPET analyses, which could explain the 3–78 W/cm³ heat-power level with 1.0×10^{11} f/s/cm³ to 1.0×10^{13} f/s/cm³ of ⁴He-atoms production by 4D and 8D fusion reactions, with neutron production rates smaller than 10 neutrons/s/cm³. There remain, however, open questions as to where TSC is formed. We have proposed two mechanisms, as transient motion forming deuteron-clusters with short lifetimes (60 fs). In the near surface region of the PdD_x cathode, deuterium full loading ($x = 1$; PdD) may be attained by electrolysis, gas discharge or gas-permeation, at least locally. No experimental techniques have been developed to measure local distribution of the x -value, although we know that it would be vital information. At very small densities (namely 1 ppm, as assumed in our papers [20,21]), PdD₂ states may exist.

Trapped D in a Bloch potential has discrete energies with 32 meV ground state and 64 meV of one phonon energy for excited states. Over 0.22 eV, all D-ions in the lattice diffuse out of the solid if excitation happens at every O-site. Following the classical Drude model, transient clusters of TSC can be formed with certain probabilities, by excitation with an external UV or an EUV laser, in limited places, such as near the surface region. An illustration of a possible

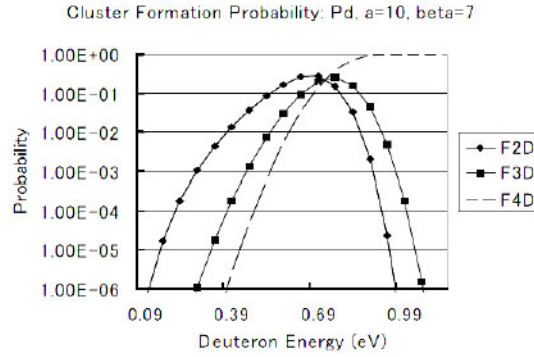


Figure 4. Estimation of 2D, 3D and 4D cluster formation probabilities around T-sites in the PdD lattice as a function of D-phonon excitation energy.

state of 4D/TSC ($t = 0$) formation at a focal point (T-site in this case) is shown in Fig. 6.

In EQPET models, we assume that the total 4D wave function can be expanded by a linear combination of partial wave functions of dde* type molecules with regular electron states $e(1,1)$ and electronic quasi-particle states as $e^*(2,2)$ Cooper pair, $e^*(4,4)$ quadruplet, and so on.

$$|\Psi_N\rangle = a1|\Psi_{(1,1)}\rangle + a2|\Psi_{(2,2)}\rangle + a4|\Psi_{(4,4)}\rangle + a6|\Psi_{(6,6)}\rangle + a8|\Psi_{(8,8)}\rangle \quad (5)$$

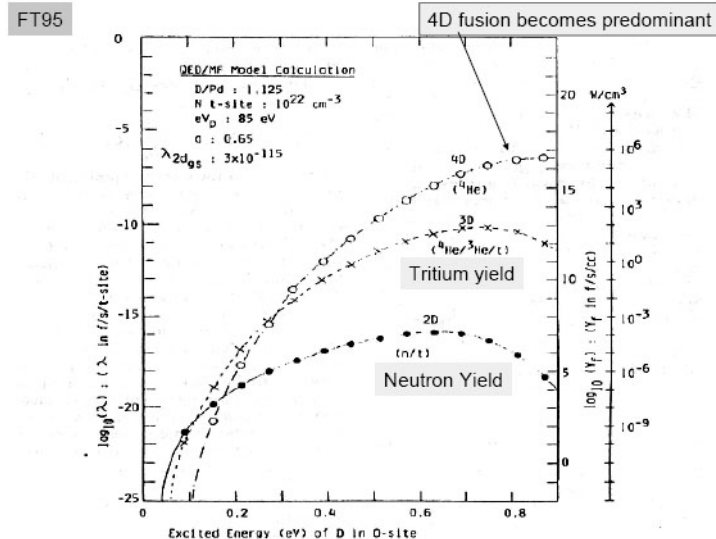


Figure 5. Comparison of logarithmic fusion rates between 2D, 3D and 4D fusions in PdD as a function of D-phonon excitation energy (from Fig. 4 [20]).

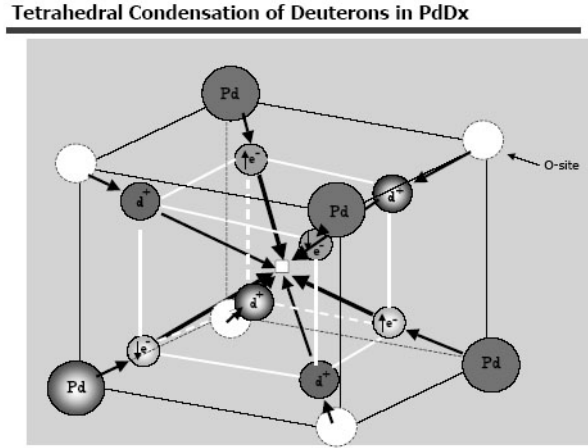


Figure 6. Illustration of initially formed 4D/TSC ($t = 0$) around some T-sites in a PdD lattice under D-phonon excitation; 4 centers of electron waves are drawn with “e[−]” and will form tetrahedra by an exchange interaction of a 1s electron from d⁺ and a 5s (or 5f) electron from Pd[−] states.

The modal fusion rate is defined [21] as,

$$\lambda_N = a1^2\lambda_{(1,1)} + a2^2\lambda_{(2,2)} + a4^2\lambda_{(4,4)} + a6^2\lambda_{(6,6)} + a8^2\lambda_{(8,8)}, \quad (6)$$

$$\lambda_{nd(i,j)} = v(S_{nd}/E_d) \exp(-n\Gamma_{(i,j)}). \quad (7)$$

The modal fusion rate given by Eq. (6) for 4D fusion is attributed almost 100% to the quadruplet EQPET molecule dde*(4,4) state. Therefore, the accuracy of this model is closely related to what the minimum size state of 4D/TSC is. Screening energies for d–d reactions are compared in Table 1. The estimated fusion rates are shown in Table 2.

Subsequently, we have considered that the squeezing motion of TSC can be more simply treated by a semi-classical model, because of the three-dimensional constrained motion of 4d and 4e particles in the TSC into the central focal point. Every QM particle-center in the TSC can undergo a central squeezing motion with the same velocity, to keep charge neutrality of the total TSC system – in other words, to satisfy the minimum system energy state (as calculated by the variational principle of quantum mechanics, QM). Therefore, this squeezing motion can be treated approximately by Newtonian mechanics until the point at which four deuterons get into the range (about 5 fm) of the strong nuclear interaction. When four electrons start to separate at the minimum TSC state, four deuterons suddenly start to feel the mutual Coulomb repulsion. The nuclear interaction at this stage can be approximately treated by the STTBA (Sudden Tall Thin Barrier Approximation) [1]. We obtained: $\lambda_{4d} = 2.3 \times 10^{-4} \text{ f/s/cl}$ at the TSC-minimum state. This microscopic fusion rate is 10^7 times larger than that given in Table 2. We consider therefore that the EQPET model may have given significant underestimation for the 4D fusion rate when the rigid constraint of motion in the three-dimensional TSC motion in condensed matter is attained, as shown in Fig. 7.

TSC squeezes from about 100 pm size to its minimum-size of about 10–20 fm diameter and behaves as a charge-neutral pseudo-particle. The life time of TSC is estimated as the time difference from the 100 pm size state to a minimum size with a velocity of the order of 10^5 cm/s ; we obtain about 60 fs. (This was later found to be much shorter (1.4 fs) in Step 3 [4–6].)

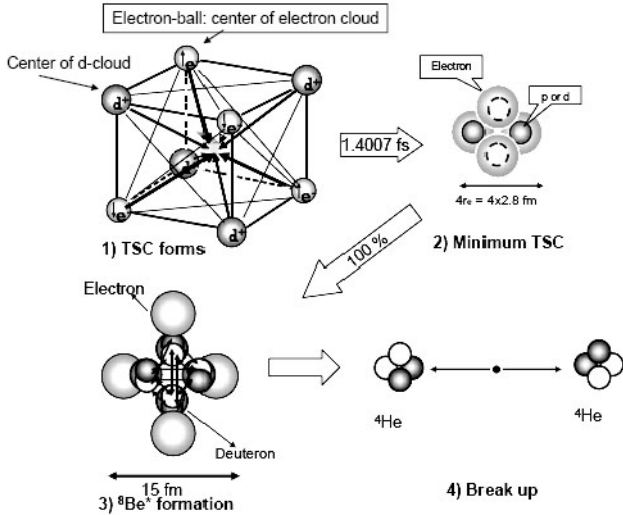


Fig. 4: Illustration of 4D/TSC squeezing motion and 4D cluster fusion

Figure 7. Schematic steps of 4D/TSC condensation motion; (1) TSC ($T = 0$) is just formed, (2) TSC gets to the minimum size state after about 1.4 fs condensation time [4–6], (3) strong interaction among 4D forms a ${}^8\text{Be}^*$ intermediate excited nucleus, (4) ${}^8\text{Be}^*$ undergoes a final state interaction to break up (from [4], Fig. 4).

2.3. Step 3: D-Cluster dynamics and fusion rate by Langevin equation

To explain the apparent hard-radiation-free excess heat with ${}^4\text{He}$ ash in CMNS experiments, especially in dynamic PdDx systems, we have done a series of studies to model D-cluster (or multi-body deuteron) fusion reaction mechanisms in 1989–2009, thus arriving at our latest theory in Step 3 studies based on quantum-mechanical Langevin equations [4–6] (stochastic differential equations).

The basics of the methods with Langevin equations for D-cluster dynamics, especially for the D-atom, D_2 molecule, D_2^+ ion, D_3^+ ion, 4D/TSC (tetrahedral symmetric condensates) and 6D²-OSC (octahedral symmetric condensates) are given in our latest papers [5,6] which are included in the LENR Source book Vols. 1 and 2.

First, one-dimensional Langevin equations for D-clusters with the R_{dd} (d–d distance) are formulated under the Platonic symmetry [6] of multi-particle D-cluster systems with deuterons and quantum-mechanical electron centers. Under the orthogonally coupled Platonic symmetry for a Platonic deuteron-system and a Platonic electron system,

Table 1. Screened energies for various EQPET molecules.

$e^*(m^*/me, e^*/e)$	Screening Energy U_s (eV)		b_0 (pm)	
	dd^*	dd^*e^*	dd^*	dd^*e^*
(1, 1); Normal electron	36	72	40	20
(2, 2); Cooper pair	360	411	4	2
(4, 4); Quadruplet	4000	1108	0.36	1.3
(8, 8); Octal coupling	22154	960	0.065	1.5
(208, 1); muon	7579	7200	0.19	0.20

dynamic equations should be treated for many-body systems of deuterons and electrons with metal atoms. Systems with more than four deuterons plus four 1s electrons of deuterium atoms plus 40 4d-shell electrons of four Pd atoms in an fcc lattice plus surrounding lattice atoms under D-phonon excited states should be considered in the model. A simple one-dimensional Langevin equation for the internuclear d–d distance R_{dd} can be formulated, as shown in [4–6]. Considering the mean values taken from the Langevin equation with the weight on quantum mechanical wavefunctions for electrons and deuterons, we could further derive a time-dependent one-dimensional Langevin equation for the expectation value $\langle R_{dd} \rangle$, which is nonlinear, but could be solved by the Verlet's time step method [4,5]. We showed [5,6] that only 4D(or H)/TSC can condense ultimately to a final, very small charge neutral entity with about 10–20 fm radius. At the final stage of 4D/TSC condensation in about 2×10^{-20} s, 4D fusion with two ${}^4\text{He}$ products takes place with almost 100% probability, according to our HMEQPET calculation [4,5] for barrier factors and fusion rate formula using Fermi's first golden rule.

Basic Langevin equations for a Platonic symmetric D-cluster having N_e d–d edges and N_f faces of d–d–e (D_2^+) or d–e–d–e (D_2) type are written as in Eq. (8). Here, R is the d–d distance and m_d is the deuteron mass, V_s is the d–d pair trapping potential of either a d–e–d–e or a d–d–e type molecule. The first term on the right-hand side of Eq. (8) is the total Coulomb force of the D-cluster system, and $f(t)$ is the fluctuation of force for which we introduce a quantum mechanical fluctuation of deuteron positions under condensation motion. The quantum mechanical effect of electron clouds is incorporated as the second term on the right-hand side as “friction” in the Langevin equation for the D_2 molecule, $N_e = N_f = 1$. For the D_3^+ ion which is known to be stable in a vacuum, $N_e = 3$ and $N_f = 6$ are given. For 4D/TSC, $N_e = 6$ and $N_f = 6$ are given. For 6D $^{2-}$, $N_e = 12$ and $N_f = 24$ are given. By taking a QM ensemble average with d–d pair wave functions, assumed to have Gaussian distributions, we derived the Langevin equation for 4D/TSC as shown in Eq. (9). By taking QM ensemble average of Eq. (10), we obtained Eq. (13). And we obtained the time-dependent TSC-cluster trapping potential as Eq. (14).

A similar Langevin equation and trapping potential were also derived for the 6D $^{2-}$ molecule. We compare the central potential curve (at $R' = R_{dd}$) in Fig. 8. We find that 4D(H)/TSC can condense ultimately to a very small charge neutral entity and has no stable or ground state. This may be the reason that we do not observe D_4 molecules in nature. On contrary, the 3D $^+$ molecule and the 6D $^{2-}$ molecule have stable ground states. Equation (13) was numerically solved by the Verlet method [4], and shown in Fig. 9.

Time-dependent barrier penetration probabilities are given as a function of R_{dd} , since we have a one-to-one relation between the elapsed time and $R_{dd}(t)$.

$$N_e m_d \frac{d^2 R}{dt^2} = -\frac{k}{R^2} - N_f \frac{\partial V_s}{\partial R} + f(t), \quad (8)$$

$$6m_d \frac{d^2 R_{dd}(t)}{dt^2} = -\frac{11.85}{[R_{dd}(t)]^2} - 6 \frac{\partial V_{s2}(R_{dd}(t); 1, 1)}{\partial R_{dd}(t)} + \langle f(t) \rangle + f'(t), \quad (9)$$

$$f'(t) = f(t) - \langle f(t) \rangle, \quad (10)$$

$$f(t) = \left[-\frac{\partial \Delta E_c(R_{dd})}{\partial R_{dd}} \right] \bmod [X^2(R'_{dd}; R_{dd}(t))], \quad (11)$$

$$X^2(R'_{dd}; R_{dd}(t)) = \frac{1}{\sqrt{2\pi\sigma^2}} \exp[-(R'_{dd} - R_{dd}(t))^2/(2\sigma^2)], \quad (12)$$

$$6m_d \frac{d^2 \langle R_{dd} \rangle}{dt^2} = -\frac{11.85}{\langle R_{dd} \rangle^2} - 6 \frac{\partial V_s(\langle R_{dd} \rangle; m, Z)}{\partial \langle R_{dd} \rangle} + 6.6 \left\langle \frac{(R' - R_{dd})^2}{R_{dd}^4} \right\rangle, \quad (13)$$

$$V_{tsc}(R' : R_{dd}(t)) = -\frac{11.85}{R_{dd}(t)} + 6V_s(R_{dd}(t); m, Z) + 2.2 \frac{|R' - R_{dd}(t)|}{[R_{dd}(t)]^4}. \quad (14)$$

Table 2. Typical results of EQPET/TSC for fusion rates, power levels and products, for TSC in PdDx, assuming $N_{4D} = 10^{22}$ (1/cm³).

Cluster	Microscopic fusion rate (f/cl/s)	Macroscopic yield (f/s/cm ³), Power (W/cm ³)	Ash (fusion products)
2D	1.9×10^{-21}	19 (f/s/cm ³), 1.9×10^{-11} (W/cm ³)	Neutron; 10 n/s/cm ³
3D	1.6×10^{-13}	1.6×10^9 (f/s/cm ³), 1.6×10^{-3} (W/cm ³)	Tritium; 8×10^8 t/s/cm ³
4D	3.1×10^{-11}	3.1×10^{11} (f/s/cm ³), 3.1 (W/cm ³)	Helium-4; 3×10^{11} h/s/cm ³

The fusion rate is calculated by the following Fermi's golden rule [21],

$$\lambda_{nd} = \frac{2}{\hbar} \langle W \rangle P_{nd}(r_0) = 3.04 \times 10^{21} P_{nd}(r_0) \langle W \rangle. \quad (15)$$

Here P_{nd} is the barrier factor for a nD-cluster and $\langle W \rangle$ is the averaged value of the imaginary part of the nuclear optical potential [2]. The extrapolation of the $\langle W \rangle$ value to 4d fusion was made by using the scaling law $\langle W \rangle \propto (\text{PEF})^5$ with PEF value which is given in units of the derivative of a one pion exchange potential (OPEP) (the simple case of the Hamada–Johnston potential [6] for the pion exchange model for the nuclear strong interaction). We obtained the next value of 4D fusion yield per TSC generation, as:

$$\eta_{4d} = 1 - \exp \left(- \int_0^{t_c} \lambda_{4d}(t) dt \right). \quad (16)$$

Using time-dependent barrier factors as given in [3–5], we obtained $\eta_{4d} \cong 1.0$. This result means that: *We have found that 4D fusion may take place with almost 100% yield per a TSC generation, so that the macroscopic 4d fusion yield is given simply by the TSC generation rate Q_{tsc} in the experimental conditions of CMNS.*

However, when we consider that the deuteron has spin-parity 1^+ and combinations of 4d have total spin state 4, 3, 2, 1 and 0, the 4d fusion with outgoing channel to two ${}^4\text{He}$ (0^+ : gs) particles is forbidden, by spin-parity conservation (for S-wave in/out channels), except for the 0^+ spin-parity state ($T = 0$). This result will be explained elsewhere in detail, including P-wave and D-wave states with isospins.

The ultimate condensation is possible only when the double Platonic symmetry of 4D/TSC is kept in its dynamic motion. A sufficient increase (super screening) of the barrier factor is also only possible as far as the Platonic symmetric 4D/TSC system is kept. Therefore, there should be always four deuterons in the barrier penetration and the fusion process, so that the 4d simultaneous fusion should take place predominantly. The portion of 2D (usual) fusion rate is considered to be negligible [4,6]. Typical nuclear products of 4D fusion are naively predicted to be two 23.8 MeV α -particles. But the final state interaction of ${}^8\text{Be}^*$ is complex and yet to be studied. There may be dominant outgoing channels via excited states of fragmented composite particles, such as ${}^4\text{He}^*$ and ${}^6\text{Li}^*$, which would produce ${}^4\text{He}$ -particles (α -particles) mostly in the 2–5 MeV region. These α -particles are difficult to detect in liquid-phase D-loading cells, and also somewhat difficult even in gas-loaded cells, due to attenuation of particles in liquid, gas and solid phases. Fragmentation may occur “symmetrically” as ${}^4\text{He}^*(E_x) + {}^4\text{He}^*(E_x) + (47.6 \text{ MeV} - 2E_x)$, or “asymmetrically” as ${}^4\text{He}(\text{g.s.}) + {}^4\text{He}^*(E_x) + (47.6 \text{ MeV} - E_x)$. If E_x is the first excited state 20.21 MeV (see Fig. 2), ${}^4\text{He}^*(E_x = 20.21 \text{ MeV})$ breaks up to t(1.8–3.4 MeV) + p(0.6–2.2 MeV) only. This triton may cause secondary DT (d + t) reactions in its slowing down in PdDx matter and the emission of energetic neutrons in the 10–17 MeV region, which may explain the SPAWAR triplet tracks [22–24]. There is possible minor channel emission of 1–5 MeV deuterons and protons. If ${}^8\text{Be}^*$ has odd spin-parity (3-), 46 keV α -particles may be final products after the electromagnetic transition by many QED photons to lattice [26].

We consider lastly the principle of dynamic condensation motion of TSC in view of the Heisenberg uncertainty principle. At the starting condition of 4D/TSC ($t = 0$), the d-d distance R_{dd} was estimated to be the same value

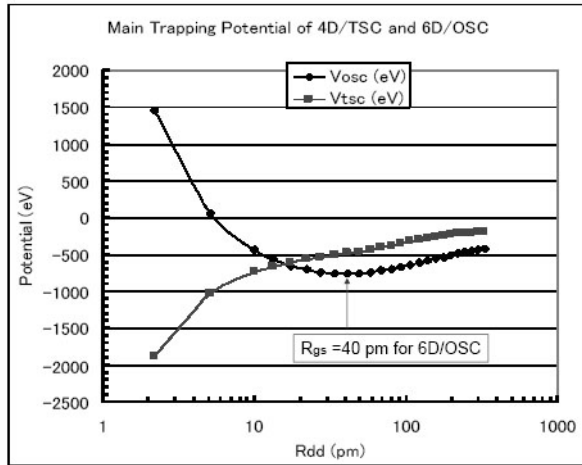


Figure 8. Comparison of cluster trapping potentials for 4D/TSC and 6D²⁻/OSC. TSC condenses ultimately to a very small R_{dd} value ($R_{dd} - \text{min} = 20 \text{ fm}$), while OSC converges at $R_{dd} = 40 \text{ pm}$ (corresponding to the ground state).

(74.1 pm) as that of the D₂ molecule. At this starting point, the mean electron kinetic energy of one “d–e–d–e” face EQPET molecule of the TSC six faces was 17.6 eV. During the non-linear condensation of TSC, the size of “d–e–d–e” EQPET molecule decreases from $R_{dd} = 74.1 \text{ pm}$ at $t = 0$ to $R_{dd} = 20.6 \text{ fm}$ at $t = 1.4007 \text{ fs}$. From the uncertainty principle, the electron wave length should decrease accordingly to the decrement of R_{dd} . At $t = 1.4007 \text{ fs}$, the mean kinetic energy of electron for “d–e–d–e” EQPET molecule was estimated [4] to be 57.6 keV. Considering the relations, $\lambda = \hbar/(mv)$ of the de Broglie wave length and (kinetic-energy) = $\frac{1}{2}mv^2$, we understand that the effective quantum mechanical wave length of trapped electrons in TSC has decreased dramatically during the 1.4007 fs condensation time. The estimated trapping potential depth of TSC at $t = 1.4007 \text{ fs}$ was -130.4 keV . This is understood as an adiabatic state in very short time interval (about 10^{-20} s) to trap such high kinetic energy (57.6 keV) electrons in a very deep (-130.4 keV) trapping potential, in order to satisfy the uncertainty relation. By the way, the mean kinetic energy of relative d–d motion was estimated to be 13.68 keV at this adiabatic state, which is also diminished relative to the deuteron wave length trapped in the adiabatic TSC potential. In this way, a very short R_{dd} (in other words, super screening of the mutual Coulomb repulsion) was realized in the dynamic TSC condensation to give a very large 4D simultaneous fusion rate. It is also worthwhile to point out that the simultaneous 4D fusion in the final stage interval, about $2 \times 10^{-20} \text{ s}$, of the TSC-minimum state should take place with a relative kinetic energy about 10 keV, by chance, similar to the target plasma temperature of the DT plasma-fusion device (ITER, for instance). In this sense, the 4D condensed cluster fusion is not “cold fusion”.

3. Concluding Remarks

How to super-screen the Coulomb barrier, how to obtain ⁴He ash and why there are no apparent hard radiations, these are questions that are fundamentally resolved by the 4D/TSC dynamic condensation motion. The Langevin equation-based analysis can be extended for neutral clusters, such as 6D/OSC and 8D/HSC, with further elaboration of the modeling. We can name Condensed Cluster Fusion Models for these processes as proposed and quantitatively studied in the last 20 years.

Future works should include:

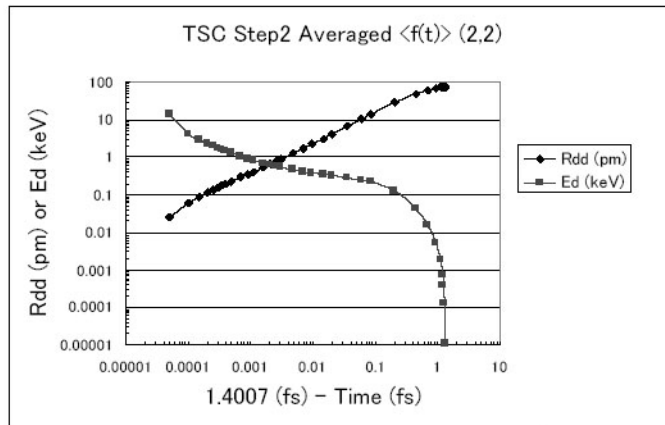


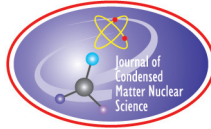
Figure 9. Numerical solution of Eq.(13) by the Verlet method⁴. Time is reversed starting from the condensation time at 1.4007 fs.

- (1) How to enhance the 4D/TSC ($t = 0$) rate in the nano-structure of metal–deuterium systems? This should be investigated, since this gives key information on the stimulation-conditions in experiments. The TSC formation process in regular PdD lattices under external stimulation, on the surface sub-nano-holes (we will show in separate paper elsewhere) of nano-particles or nano-structure samples or interfaces with incoming deuteron (or D₂) flux should be modelled or experimentally tested.
- (2) Details of the ⁸Be* final state interaction and out-going channels should be studied. This compound excited state may have a complex final state interaction to various out-going channels as symmetric and asymmetric fragmentations and $\alpha + ^4\text{He}^*(E_x < 47.6 \text{ MeV}) + (47.6 \text{ MeV} - E_x)$, gamma-transition of ⁸Be*(47.6 MeV – E_γ) + $E\gamma$ and minor channels of n, p, and t emission, etc. Lower excited states of ⁸Be* have many out-going channels to ⁴He(g.s) + ⁴He(g.s). Combinations of spin-parities and isospins are complex. Charged particle spectroscopy and experimental particle-identification should be cross-checked with such theoretical predictions.

References

- [1] A. Takahashi, *J. Condensed Matter Nucl. Sci.* **1** (2007) 129–141.
- [2] A. Takahashi, N. Yabuuchi, *J. Condensed Matter Nucl. Sci.* **1** (2007) 106–128.
- [3] A. Takahashi, N. Yabuuchi, Study on 4D/TSC condensation motion by non-linear Langevin equation, in *LENR Source Book*, vol. 1, J. Marwan, S. Krivit (eds.), Washington, DC, American Chemical Society, 2008, pp. 57–83.
- [4] A. Takahashi, The basics of deuteron cluster dynamics as shown by a Langevin equation, in *LENR Source Book*, vol. 2, J. Marwan, S. Krivit (eds.), Washington, DC, American Chemical Society, 2009, pp. 193–217.
- [5] A. Takahashi, *J. Condensed Matter Nucl. Sci.* **2** (2009) 33–44.
- [6] A. Takahashi, ‘*Cold Fusion 2008, Mechanisms of condensed cluster fusion*, (in Japanese)’, Tokyo, Kogakusha, 2009. ISBN978-4-7775-1361-1.
- [7] Y. Kim, *Naturwissenschaften* **96** (2009) 803–811.
- [8] X.Z. Li, Multiple scattering of deuterium wave function near surface of palladium lattice, in *Condensed Matter Nuclear Science*, A. Takahashi, K. Ohta, Y. Iwamura (eds.), World Scientific, Singapore, 2006, pp. 482–493.
- [9] X.Z. Li, B. Liu, Q.M. Wei, S.X. Zheng, D.X. Cao, *J. Fusion Energy* **23** (2004) 217–221.
- [10] P. Hagelstein, Unified phonon-coupled SU(N) models for anomalies in metal deuterides, in *Condensed Matter Nuclear Science*, P. Hagelstein, S. Chubb (eds.), World Scientific, Singapore, 2006, pp. 837–870.

- [11] P. Hagelstein, Phonon exchange models: some new results, in *Condensed Matter Nuclear Science*, J.P. Biberian (ed.), World Scientific, Singapore, 2007, pp. 743–768.
- [12] S. Chubb, Framework for understanding LENR processes using conventional condensed matter physics', in *Condensed Matter Nuclear Science*, P. Hagelstein, S. Chubb (eds.), World Scientific, Singapore, 2006, pp. 646–664.
- [13] T. Chubb, Bloch ions, *Condensed Matter Nuclear Science*, J.P. Biberian (ed.), World Scientific, Singapore, 2007, pp. 665–676.
- [14] H. Hora, G. Miley, X.Z. Li, J.C. Kelly, F. Osman, Low energy nuclear reactions resulting as picometer interactions with similarity to K-shell electron capture, in *Condensed Matter Nuclear Science*, J.P. Biberian (ed.), World Scientific, Singapore, 2007, pp. 822–837.
- [15] A. Takahashi, M. Ohta, T. Mizuno, *Jpn. J. Appl. Phys.* **41** (2001) 7031–7046.
- [16] A. Takahashi, N. Yabuuchi, Deuterons-to- ${}^4\text{He}$ Channels, in *Condensed Matter Nuclear Science, ICCF13 Proceedings*, Y. Bazhutov (ed.), Publisher Center MATI Tsiolkovsky Moscow Technical University, 2008, pp. 569–578. ISBN 978-5-93271-428-7.
- [17] M. Swartz, *Fusion Technol.* **31** (1997) 228–236.
- [18] G. Preparata, *Trans. Fusion Technol.* **26** (1994) 397–407.
- [19] A. Takahashi, *J. Nucl. Sci. Technol.* **25** (1989) 558–560.
- [20] A. Takahashi, T. Iida, H. Miyamaru, M. Fukuura, *Fusion Technol.* **27** (1995) 71–85.
- [21] A. Takahashi, T. Iida, F. Maekawa, H. Sugimoto, S. Yoshida, *Fusion Technol.* **19** (1991) 380–390.
- [22] P.A. Mosier-Boss, S. Szpak, F.E. Gordon, L.P.G. Forseley, *Eur. Phys. J. Appl. Phys.* **46** (2009) 30901.
- [23] P.A. Mosier-Boss, S. Szpak, F.E. Gordon, L.P.G. Forseley, *Naturwissenschaften* **96** (2009) 135–142.
- [24] P.A. Mosier-Boss, S. Szpak, F.E. Gordon, L.P.G. Forseley, *Eur. Phys. J. Appl. Phys.* **44** (2008) 291–295.
- [25] M. Fleischmann, S. Pons, *J. Electroanal. Chem.* **261** (1989) 301.
- [26] A. Takahashi, *Trans. Fusion Technol.* **26** (1994) 451–454.



Research Article

Inhibition of LENR by Hydrogen within Gas-loaded Systems

Dennis Cravens*

P.O. Box 1317, Cloudcroft, New Mexico, USA

Abstract

This paper develops a model of reaction kinetics for Low-energy Nuclear Reactions (LENR) for gas loaded systems. The method is patterned after mathematics used in Michaelis–Menten kinetic models, which are standard in enzyme catalytic studies. Hydrogen is found to inhibit the deuterium reaction rates and can be explained by mixed inhibition kinetics where the hydrogen both competes with deuterium at the active sites requiring higher concentrations of deuterium for a given reaction rate and it also undergoes non-competitive inhibition, which alters the maximum rate of the reaction. This kinetic model predicts that hydrogen contamination would require higher loading ratios for similar reaction rates or heat production and also such contamination may lower ultimate heat production due to hydrogen active site complex productions.

© 2011 ISCMNS. All rights reserved.

Keywords: Gas loading, Inhibition, Kinetics

PACS: *****

1. Introduction

A large number of mechanisms have been put forth in the field of Low-energy Nuclear Reactions (LENR). Most of these have addressed the difficulty of achieving the conditions of close range reactions between nuclear species and pathways. The high-level energy must leave the reaction sites without disrupting active sites. Here we will take a novel approach from the view of phenomenology and be interested only in the kinetics of the reaction and not the mechanism. The most common tools used in seeking to understand LENR have been nuclear and solid state studies. Here we will try to use biophysical methods to reveal some of the kinetics and material interactions played by the catalytic nature of the problem. It is hoped that this will give new methods for understanding this complex phenomenon.

The author will borrow heavily from the mathematics developed for enzyme catalysis. These methods are standard within biophysics but seem to be somewhat unknown outside the area. It seems clear that LENR proceeds primarily through some catalytic interaction between deuterium and some catalytic active host. In many ways its kinetics are similar to enzyme reactions where two substrate species have to seek out an enzyme, be accepted at an active site, react, and then release the product(s). The Michaelis–Menten kinetics developed within biophysics was developed to handle

*E-mail: Physics@tularosa.net

problems with these properties. This method dates back to 1913 [1] and was developed on the simple assumption that some reactions can proceed only when a catalyst and a substrate come in contact and their concentrations change slowly.

2. Kinetic Model and Mathematical Development

The kinetics of enzyme systems is well treated in most enzyme and biophysics texts [2]. We will adopt most of such mathematics directly but our terminology will be different since the product of concern here is heat, and we will be using inorganic active sites instead of enzymes, and nuclear species instead of substrates. Since many of our readers will be unacquainted with enzyme studies, we will use the simplistic “lock and key” analogy to help clarify by analogy. The catalytic agent is the “lock” and the reacting agent is the “key” in this analogy. The two have to connect correctly at the same place and time for there to be a reaction.

For the LENR events to proceed by a process similar to Michaelis–Menten kinetics we assume that (1) once the reaction occurs it is irreversible, (2) the reaction takes place quickly with few or no intermediate steps once correct conditions are present, (3) the reactions are rare enough that they do not significantly alter the deuterium concentration as the reactions proceed, and (4) the reactions do not appreciably alter the number of active sites. These are equivalent to the assumptions used in the standard Michaelis–Menten kinetics.

We will be addressing only the reactions within the host lattice and not the loading at the surface. It should be kept in mind that a more realistic treatment can be produced if the model were to be expanded to treat the loading process. Here we will only be considering processes that occur after loading of the sample. The kinetic reaction becomes:



Where M denotes the active site on or within the metal host, D_2 denotes deuterium (either entering as a D_2 molecule or in two events from separate D 's), MD_2 denotes the deuterium active host complex, and P the product (here heat and any “nuclear ash”). k_1 denotes the forward reaction rate and $k-1$ the reverse reaction rate for forming the deuterium/host complex. k_2 denotes the forward reaction rate for the production of the products. Notice there is no reverse reaction rate expected for the high-energy reaction of LENR. That is to say the large energy release by the reaction prevents back reactions from the nuclear ash returning to deuterium species.

For this series of experiments we will be interested in the rate of production of the heat, which is our primary product. Our experimental variable will be the concentration of our reactant, D_2 and later the concentration of our inhibitor H_2 . The well known result for the rate of product production for such kinetics is:

$$d[P]/dt = V_0 = k_2[MD_2] = k_2[M][D_2]/(K_m + [D_2]) = V_{\max}[D_2]/(K_m + [D_2])$$

or in the Lineweaver–Burk linear form for plotting,

$$1/V_0 = K_m/(V_{\max}^*[D_2]) + 1/V_{\max}.$$

For the value of

$$K_m = (k-1 + k_2)/k_1.$$

The value of $d[P]/dt = V_0$ represents the production rate of heat and nuclear ash. We did not attempt to measure the nuclear ash but could easily record the temperature differential in our experiments. The value of V_{\max} is the maximum rate that can be expected if all our active sites are saturated with deuterium and nothing else alters them nor competes with deuterium to occupy the active regions. This would yield our highest possible heat production rate if we had no inhibition of the active sites, the deuterium availability was not limited, and the products could leave without disruption of the process. This would predict that the reciprocal of the heat production in our LENR system is expected to obey a

hyperbolic curve in regards to concentration of deuterium present at our active sites, and that we can expect large changes from changes in the deuterium concentrations for lower “loading ratios” and then smaller changes due to alterations in the concentrations past the $[D_2] = K_m$ value. The high slope and the rapid change of reaction rate to a plateau value indicate that K_m must be relatively small and hence: $K_1 > K_2$. That is to say that the binding of the deuterium to the active site is much easier than the progression to the production of heat via any possible nuclear channels. This is consistent with most LENR results. That is to say, the chemical binding is easy but the nuclear reactions more difficult, and the reaction is more predominant above some minimum concentration of deuterium [3].

However, most LENR systems are not as clean and simple as this. Hydrogen is a common contaminant, is very hard to remove from the experiments, will compete with deuterium for the active sites, alter the active sites so the deuterium cannot be bound, and may even bind to the deuterium active site complex in such a way as to prevent reactions from proceeding to completion.

Such conditions are common considerations in enzyme and catalytic systems. When this is admitted into the mathematics, the Michaelis–Menten kinetics must be modified. When an inhibitor competes directly with the reactant for the active site, the standard approach is called competitive inhibition. Then the modified production rate must be altered to:

$$V_i = V_{\max}[D_2]/\{K_m(1 + [I]/K_i) + [D_2]\}.$$

Notice that the K_m is simply modified by the factor $(1 + [I]/K_i)$ where the $[I]$ is the concentration of the competitive agent and K_i is its complex dissociation constant. When there is no inhibitor, $[I]$ we recover our original kinetics. When its dissociation constant is non-zero, the modification can become significant. The formation enthalpies are -19.1 kJ/mol for palladium hydride and -17.3 kJ/mol for the deuteride at 298 K [4]. Thus, in our case the hydride from the active complex is more stable than deuterium by about 2 kJ/mol. This means that a small amount of hydrogen can significantly reduce the overall reaction rate since it could slowly replace deuterium at the active site as the more stable configuration. Once bound it is not likely to freely dissociate from the active complex. In practice, the contamination by hydrogen would be revealed by a requirement to have higher loading ratios before attaining similar heat production rates. In that case, we would expect some researchers to have difficulty in seeing significant heat production if hydrogen contamination occurred, and that some would experience no results unless very high-loading ratios were achieved. In our lock and key analogy, it would be equivalent to having many fake useless keys mixed with our good keys so that the time needed to unlock the locks increases. You could enhance your chances of finding a good key by simply adding more good keys to the mix even if you cannot remove the bad ones. In this case, higher deuterium loading should increase the production rate of heat up to some maximum that is set by the number of active sites (number of locks).

Where heat is our measure of rate of reaction, $1/V_0$ becomes described by the linear equation:

$$1/V_0 = \{K_m(1 + [I]/K_i)\}/(V_{\max}^*[D_2]) + 1/V_{\max}.$$

This is a “linear” form used in plotting such kinetics. In our case, this allows our model to form a complex with the active site with hydrogen that does not lead to the production of heat. The fundamental assumption in the derivation of such model is that there are some active sites that are occupied by hydrogen instead of deuterium that do not lead to the production of heat.

Non-competitive inhibition occurs when the inhibitor forms a complex containing both the reactant and the active site. In our case that would be equivalent to a D and H occurring at an active site and not being able to proceed to the production of heat. In enzyme systems such non-competitive inhibition signifies that the binding of the inhibitor at one area of catalyst creates a complex that prevents reactions to take place. This would seem to signal in our case that the presence of hydrogen would cause more tightly bound hydrogen–hydrogen or deuterium–hydrogen pairs at the active site that would prevent reactions. In our lock and key analogy, this is like having some bad keys getting stuck in some

of the locks. Your maximum production rate is dropped since some of the locks are taken out of commission for some of the time. Even if you add more good keys (deuterium) you will never recover your higher rates.

In that case, the constant $1/V_{\max}$ term also must be altered by the factor containing the concentration of the inhibitor, $1 + [I]/K_i$.

And the overall equation becomes:

$$1/V_0 = \{K_m(1 + [I]/K_i)\}/(V_{\max}^*[D_2]) + \{1 + [I]/K_i\}/V_{\max}.$$

For this work, we note that the rate of product production is proportional to our observed temperature differential,

$$d[P]/dt = V_0 \text{ or } 1/V_0 = a/\Delta T$$

and the concentration of the reactant is proportional to the deuterium partial pressure, P_d ,

$$[D_2] = b^* P_d.$$

The modification due to the inhibitor can be set to a constant for a set hydrogen partial pressure or concentration,

$$c = \{1 + [I]/K_i\}.$$

The values a , b , and c are constants chosen to allow easy unit conversion. The value of c is constant and set for specific experimental conditions since the value of K_i is not easily obtained directly. The overall equation then becomes:

$$a/\Delta T = (c^* K_m)/(V_{\max}^* b^* P_d) + c/V_{\max}.$$

This is our general expression for “mixed inhibition” at a set temperature and inhibitor concentration. It allows for both the inhibition by direct competition with hydrogen for the active site and the production of a hydrogen/deuterium/active site complex that would prevent or slow the reaction rates. If we are correct in our assumed kinetics, we should get a series of approximately linear Lineweaver–Burk plots, which have higher slopes and higher intercepts as the inhibitor concentration is increased.

3. Experimental

A series of experiments were run with a range of deuterium and hydrogen gas ratios and pressures. The material containing the active sites was produced by BCT partners and contains predominately Pd and Ni held within fine Y stabilized zirconium oxide proton conductive material with inclusions of ppm of rare earths, lanthanides and nickel. They use a proprietary method of production but it is generally described as production by underwater sparks in a reductive circulating solution of heavy water. The solution is further reduced with hydrazine, filtered (Millipore–0.22 μm) and the fines are recovered by vacuum distillation at 45°C. Five grams of the powder was placed in each small sheathed gas cylinder (typically used as CO₂ cartridges – Genuine Innovation – 12 g, 14 ml volume) – see Fig. 1. These were fitted with a cap and thermistor feed-throughs. Deuterium and hydrogen gases were produced by electrolysis of water/heavy water solutions at a range of various relative concentrations. Pre- and post-calibration runs were made with sand and Ar for each cylinder and thermistor assembly. All cylinders were pressurized to the same total 74 kPa (slightly above atmospheric at the lab’s altitude) by addition of Ar; the ratio of hydrogen, deuterium, and argon was varied so that the effect of changing deuterium partial pressures could be studied. The cylinders were simultaneously lowered into a constant temperature oil bath held at 80.0°C. The temperature differential between the internal temperature of the cylinder and the oil bath was recorded for each. The differential was recorded each minute and the average over 60 min. The standard deviation of the data points taken each minute was used to make error bar estimates.

The use of gas loading of powdered sample in LENR is well known [5]. The material used for this series was a fine powder – see Fig. 2.

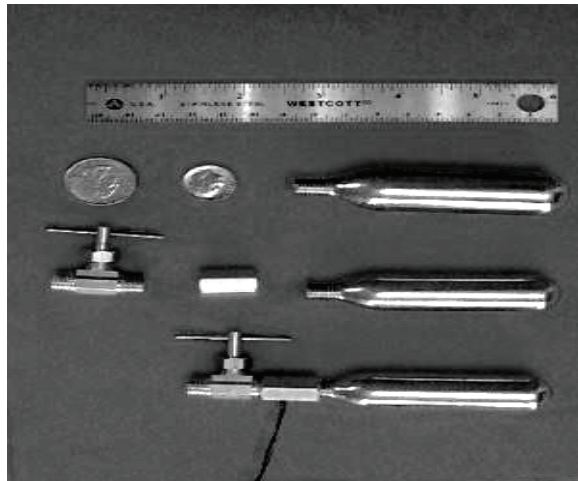


Figure 1. Palladium lattice. The big spheres are Pd atoms, their distance was set equal to 4; the octahedral sites lie on the same plane just in between two Pd atoms; the tetrahedral sites are positioned on a different plane at a relative distance of 2.828 Å.

4. Results

The results of the series of experiments can be seen in Table 1 and Lineweaver–Burk (LB) Plots in Fig. 3. This is a linear form of the Michaelis—Menten equation and produces a straight line with the equation $y = mx + c$ with a y -intercept

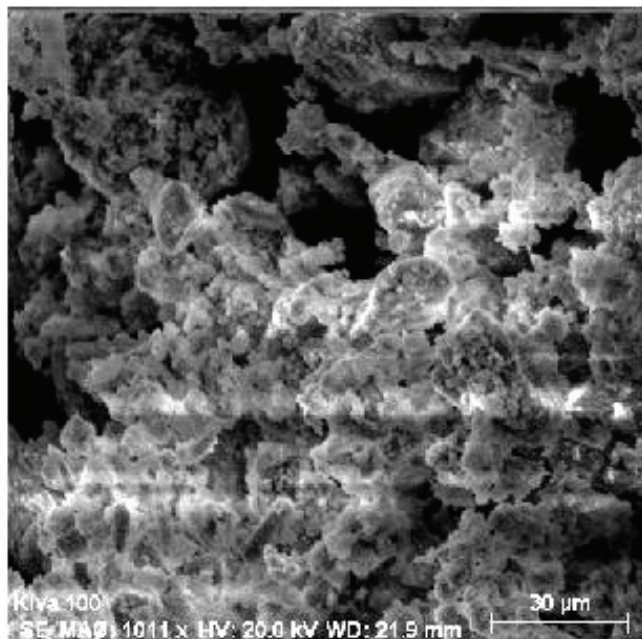


Figure 2. The electron micrograph shows the general size of the material used in the runs. All runs used the same material and 5 g sample size so the number and concentration of the active sites would remain approximately the same for easy comparisons. Photo courtesy of Edmund Storms.

equivalent to $1/V_{\max}$ or its modified form due to inhibitors and the extrapolated x -intercept of the graph representing $-1/K_m$. The extrapolated y -intercept is the case where an infinite concentration of deuterium would be available. Our units for the LB Plot are nonstandard since most enzyme and catalytic systems use molarities of chemical species in solution. Here we will use the reciprocal of the thermal output power for our y -axis as seen by our temperature differential between the sample inside its sheathed cylinder and the oil bath. Since our product of interest is heat, the differential is useful because it directly relates to the thermal power and hence the rate of “product” production. Likewise, instead of the standard molar concentrations used in most plots we will be using the partial pressures of the gases in units of kPa. Although the partial pressures were varied, the total pressure was always adjusted to 75 kPa, which was slightly above atmospheric pressure at lab elevation. The mathematical form is the same since the temperature differential versus partial pressure is the same form as rate of product production versus molar concentration.

From the LB plot in Fig. 3, it can be seen that there is an increase in the effective K_m due to the competition of hydrogen with deuterium for the active sites. The apparent increase in the effective K_m is indicative of competitive inhibition. This means that some active sites can be occupied either in part or totally by the hydrogen and there are fewer sites available for the deuterium pairs to proceed to the desired products. If this were the only role of the inhibitor, then the rate could recover by just increasing the concentration (pressure of gas) of the deuterium.

It can also be seen from the LB plot that the V_{\max} is also lowered. This is indicative of non-competitive inhibition where the binding of the inhibitor is more tenacious than the reactants. Thus it appears that hydrogen not only competes with the deuterium in competitive inhibition but also, once bound, is not as easily separated from the active site as the deuterium. This leads to a lowering of the amount of heat generated per time (power) produced by our reaction. Hydrogen thus both competes for the active sites so that fewer deuterium–deuterium reactions can take place and ties up some active sites so that fewer sites are available for deuterium exchanges and thus lowers the ultimate temperature difference that can be reached by the reaction. When both competitive and non-competitive inhibition occurs, it is termed mixed inhibition. Mixed inhibition seems to be the case for these LENR gas-loading experiments. There is also a possibility that there is some product inhibition, which occurs when the accumulation of the product (for example He) inhibits the reaction. This must be investigated by using longer time runs than available in this experiment. It is likely that the role of the small particle size and elevated temperature may overcome some problems incurred by product inhibition. Dynamic changes in gas pressures may also limit such product inhibition. In our lock and key analogy, it is like having some locks break once opened. Until some of the nuclear ash is removed, some active sites are useless and the production rate starts to fall as time progresses.

Table 1. This shows the temperature differential seen at various partial pressures of deuterium and for various partial pressures of hydrogen. The remaining gas pressure was adjusted to a total of 75 kPa by addition of Argon. The estimated error bars for the temperature differentials is 0.04°C as seen from the time variation of the data readings over one hour. Error bars are not shown on the plot since reciprocals of the data points are plotted.

Deuterium Pressure kPa	Delta T with		
	0 kPa hydrogen	10 kPa hydrogen	20 kPa hydrogen
2	0.23	0.08	0.00
5	0.33	0.13	0.00
10	0.40	0.14	0.05
20	0.43	0.17	0.06
30	0.48	0.17	0.06
40	0.48	0.17	0.06
50	0.50	0.17	0.07
60	0.51	0.16	0.07

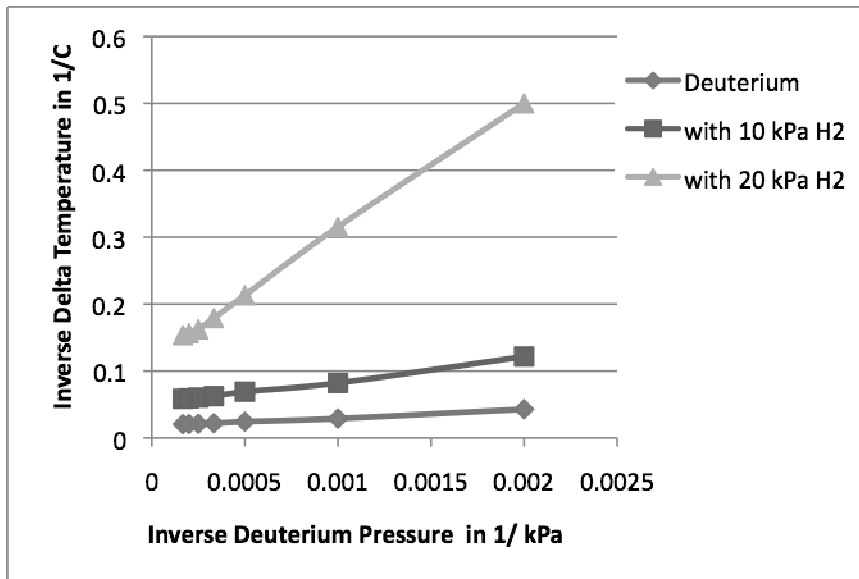


Figure 3. This is a plot of 1/differential temperature ($^{\circ}\text{C}$) versus 1/deuterium pressure (kPa). As the hydrogen partial pressure increases the reaction rate decreases. The greater slope with increasing hydrogen pressure shows that the effective K_m increases, which lowers the reaction rates. The y-intercept also increases with increased hydrogen concentration, which signals a change in the effective V_{max} . This is indicative of hydrogen being bound more strongly than deuterium at the active site.

5. Discussion

The results show that hydrogen inhibits production of heat in LENR gas loaded systems by both competing for active sites and causing stable hydrogen/deuterium/active site complexes. This indicates that care should be taken to exclude the lighter hydrogen isotope from LENR gas loaded experiments. Practical advice would be to assure no cross contamination during preparation and the use of high vacuum and purging runs between any hydrogen and deuterium runs. Further preliminary experiments not included here would indicate that dynamic loading conditions, higher temperatures and higher surface area to mass metal hosts seem to give better results. That is to say the active sites for this series of experiments may reside on the surface interface between the deuterium gas and the catalytic host material and the reaction rate constants may be temperature dependent. This will be covered in a future extension of the kinetic model presented here.

Although this paper was designed to address LENR gas loaded systems, it is worthwhile to know that applications can be made to electrolytic systems. For example see run NRL684 in [6]. A close up of the relative part can be seen in Fig. 4.

In this experiment, Letts replaced D_2O with H_2O in an active co-deposited cell. There was an immediate disturbance due to the fluid replacement and then the cell first returns nearly to its original power levels. Then after about 30 min a steady drop was observed in “excess power” to about half the original value, then another slower decline to zero after about 9 h was observed. In light of this study, this seems to indicate that the first drop is due to the competitive portion of the inhibition from free exchange of H and D at the surface. This can be fairly fast since it involves the loading of the active sites from the solution. The second longer decline may be due to the non-competitive inhibition due to H slowly replacing, binding, and tying up active sites. One prediction of this model would be that the original power levels could be partially and temporarily recovered by increasing the current density during the competitive inhibition decline

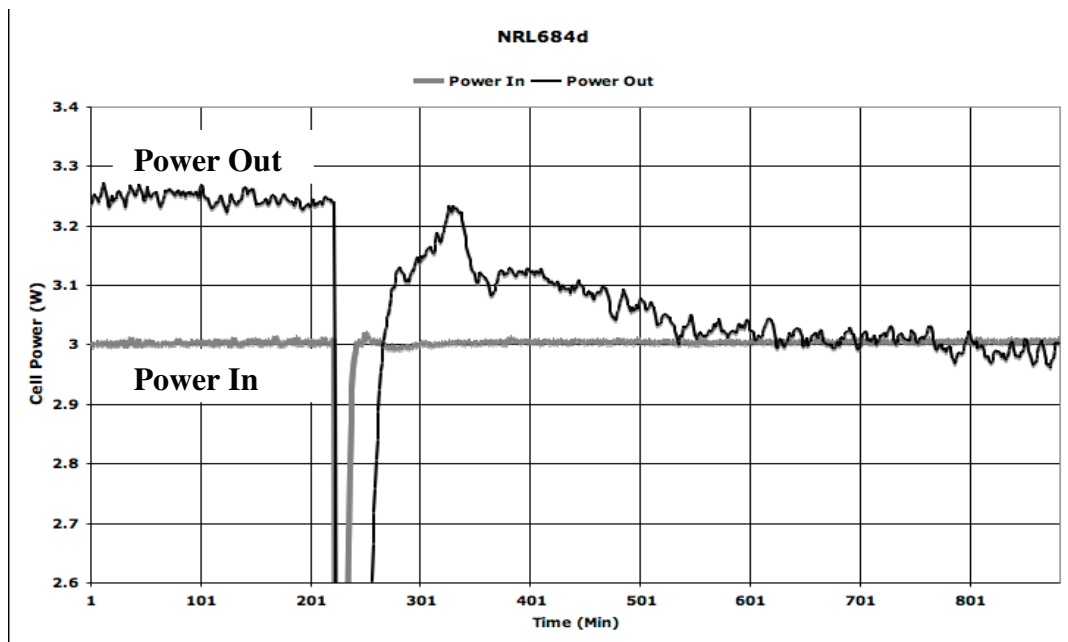


Figure 4. This is taken from Dennis Letts' work and is included elsewhere in this book. It is an electrochemical co-deposited run with the power in held at 3 W except during water addition. At point 210 the heavy water was replaced with natural abundance water. The system recovers for a while near point 310. There is then a first rapid decline over 30 min possibly due to competitive inhibition and finally a gradual decline to about point 800. This is perhaps due to slow replacement by H at the active sites as may be expected from non-competitive inhibition.

but not after the long non-competitive decline. Also it can be expected from this model that reversing the current and re-populating the active sites with hydrogen would destroy its heat production until completely cleaned of hydrogen.

It is refreshing to find that practical general guidelines and directions to the LENR process can be achieved from simple methods that avoid the assumptions of nuclear mechanisms and theories.

Acknowledgements

The author thanks Dr. Edmund Storms for the SEMS analysis and Dr. Tom Claytor for the XRF analysis and Dennis Letts for the data and plot for Fig. 4. LENR is rich with individuals who help each other and share analysis and work. It is only by such cooperation that the field has survived over 20 years with little or no funding.

References

- [1] L. Michaelis, M. Menten, *Biochemische Zeitschrift* **49** (1913) 333–369.
- [2] R. Copeland, *Evaluation of Enzyme Inhibitors*, Wiley-Interscience, UK, 2005.
- [3] M.C.H. McKubre et al., Excess Power Observations in Electrochemical Studies of the D/Pd System; The Influence of Loading, *Third International Conference on Cold Fusion, "Frontiers of Cold Fusion"*, Nagoya Japan: Universal Academy Press Inc., Tokyo, Japan, 1992.
- [4] T. Flanagan et al., *J. Less-Common Metals* **172–174** (1991) 42–55.

- [5] A. Takahashi et al., Deuterium Gas Charging Experiments with Pd Powders for Excess Heat Evolution (II) Discussions on Experimental Results and Underlying Physics, in *The 9th Meeting of Japan CF-Research Society*, Shizuoka, Japan, 2009.
- [6] D. Letts, *Co-deposit methods*, elsewhere in this book.



Research Article
Dynamics in Pd–H(D) Systems

Antonella De Ninno *

C.R. ENEA Frascati, Department FIM-FISLAS, via Enrico Fermi 27, 00044 Frascati, Rome, Italy

Abstract

PdH(D) shows many peculiar aspects which make it unique both for solid state and for LENR physics. Its most surprising characteristic is that it behaves like a stable dense plasma consisting of H(D) nuclei which can be well explained on the basis of an appropriate many-body model.

© 2011 ISCMNS. All rights reserved.

Keywords: Lattice dynamics, Low-energy nuclear reactions, Material science

PACS: 63;64;52;24

1. Introduction

The Pd/H(D) system is historically the first that had attracted research activities [1] because it represents one of the most transparent and instructive models for a metal–hydrogen system. Palladium hydride shows many interesting features, most of them not explained yet.

Perhaps the most intriguing conundrum is the effective charge of hydrogen inside the lattice and whether it can migrate under the action of an electric field. It has been shown by Alfred Cöhn [2] that the dissolved hydrogen get ionized when it enters into the lattice and settle in its equilibrium position in ionic form. Ionization may actually occur just at the surface of the crystal and ions reach their equilibrium positions later on [3].

Moreover, the Pd–H system exhibits a complex phase diagram: at room temperature and pressure hydrogen is in a gas like situation within the Pd lattice when $H/Pd \leq 0.02$ (α -phase); increasing the loading a new phase, named β -phase, emerges coexisting with the α -phase; in the β -phase hydrogen is confined in the octahedral sites of the Pd lattice. When $H/Pd \sim 0.6$, the b -phase extends to the whole lattice.

In Fig. 1, it is shown the Pd lattice where Pd atoms occupy the fcc (face centered cubic) positions. Two equilibrium positions are allowed to the solute atoms: the octahedral position along the minimum distance between Pd atoms, and the tetrahedral position at the center of a tetrahedron having four Pd atoms at its vertex. The octahedral sites correspond to the minimum energy position of the empty Pd lattice, however, increasing the loading, the energy bands of PdH undergo a severe modification.

*E-mail: deninno@frascati.enea.it

Experimental evidence [4] shows that a new phase in which hydrogen migrates from octahedral to tetrahedral positions in the lattice exists. In fact, the volume expansion due to hydrogen absorption shows that, when $H/Pd \sim 0.8$, the rate $\Delta V/V$ changes pointing towards a different occupation of hydrogen in the lattice.

Evidence for a structural and electronic phase transition, we will call it $\beta \rightarrow \beta'$ in the next, is also provided by measuring the number of charge carriers in the Pd–H system [5] which undergoes an unexpected change when $H/Pd \geq 0.83$. It has been found that each hydrogen entering the Pd lattice in the β -phase contributes with about 0.75 electrons to the conduction band, whereas for $x = H/Pd$ exceeding a threshold each hydrogen contributes with more than four electrons to the conduction band; since the hydrogen has only one electron on its own it must persuade more than three Pd electrons to jump into the higher energy band, so that the hydrogen that enters the lattice causes a local reshuffling of the Pd electronic bands.

The electrical resistivity $\rho(x)$ of the Pd–H system as a function of x shows an increase of the carrier and/or mobility over a certain threshold [6] too. In the coexistent $\alpha - \beta$ region, $\rho(x)$ increases almost linearly with the hydrogen content up to the value where the $\beta - \beta'$ transition occurs: then it decreases quite sharply reaching the value ρ_0 of the pure Pd metal.

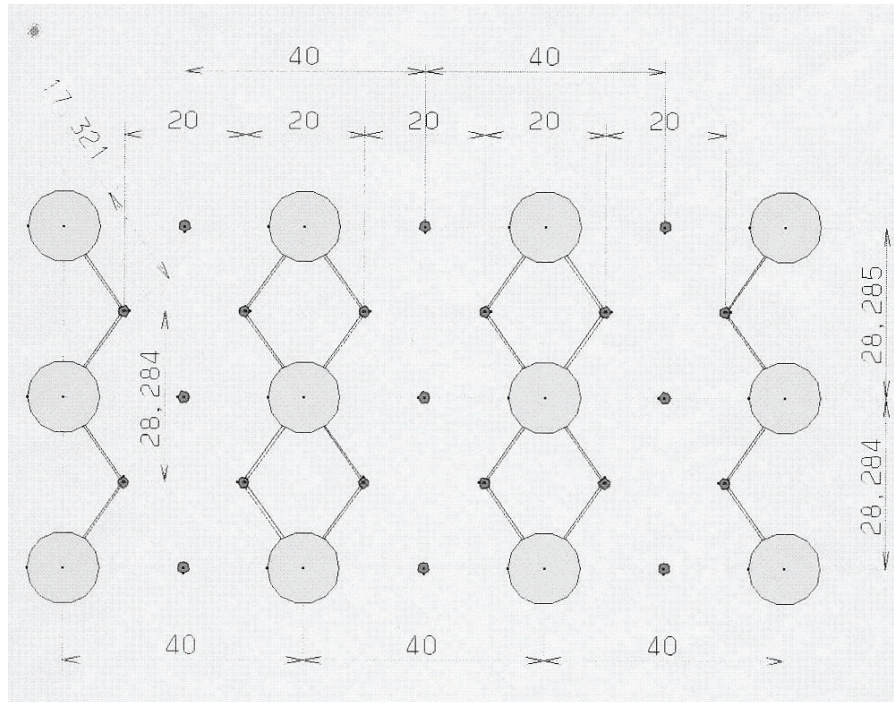


Figure 1. Palladium lattice. The big spheres are Pd atoms, their distance was set equal to 4 Å; the octahedral sites lie on the same plane just in between two Pd atoms; the tetrahedral sites are positioned on a different plane at a relative distance of 2.828 Å.

2. Hydrogen Kinetics in Palladium

In spite of such a puzzling picture, the understanding of hydrogen dynamics inside the solid state lattice is a very important task both for theoretical physical chemistry, for applications in the fields of hydrogen fuel cycle and for LENR researches. As mentioned above, the most interesting state of the Pd/H system starts at a specific loading threshold which is not easy to obtain. During the isothermal loading process, the solute gradient inside the metal suffers from a thermodynamic force influenced by all the fields that can affect the free energy of the solute.

The diffusion flux is described by the general equation:

$$J = -M \cdot c \cdot \text{grad } \mu,$$

where c is the hydrogen concentration, M the mobility related to D , the diffusion coefficient, by the Einstein relation and μ is the chemical potential. The stress induced by the hydrogen diffusive flux causes an inhomogeneous distribution of the solute. Kandasamy [7] showed that a suitable strain can stop the diffusion of hydrogen caused by the concentration gradient, in fact the previous equation is modified as follows:

$$J = -D \left(\nabla c - \frac{c \bar{V}}{RT} \nabla \sigma \right),$$

where \bar{V} is the molar volume of hydrogen in the metal and σ the stress field.

It is well known that during the loading expanded β areas grow near the α areas. In this region of coexistence very strong deformation fields are generated at the border between the two phases, due to the different lattice parameters. This process is highly irreversible because of the energy dissipation involved in the generation of dislocations. Calculations performed for a cylindrical Pd cathode show that the maximum shear stress is obtained on the surface at the beginning of the diffusion process. This means that the loading is abruptly limited to a thin slab underneath the surface, as a consequence, the loading path is very important to determine the final concentration profile inside the metal [8].

The coexistence phase allows the strain gradient to grow and introduces into the system a stress energy which can prevent any further intake of hydrogen, however, an appropriate path on p – c – T diagram can skip the coexistence region and improve the loading [9]. In Fig. 2, it is shown the comparison between two loading procedures: (a) electrolysis of LiOH solution using Pd wire; (b) the Pd wire has been pre loaded at high (>34 bar) pressure and ($>270^\circ\text{C}$) temperature and then used as a cathode in LiOH electrolysis with the same parameters as in the former case. Above the point $P = 34$ bar and $T = 270^\circ\text{C}$ which is the critical point on the p – c – T diagram, the co-existence phase does not exist anymore. The results clearly show that the loading ratio is 20% higher than usual.

A further increase of the concentration can be reached if the stress is allowed to relax with suitable loading procedure both in gas phase and in electrolysis [10]. Figure 3 shows that switching the current level between two values improves the loading ratio because the stress field is allowed to relax during the low-current phase.

The experimental data show that the self-induced strain field arising from very steep concentration gradients is responsible for the well-known difficulty in obtaining reproducible high loading samples. In addition, possible damages induced by the loading process itself can modify the material during the experiment in an unpredictable way, resulting in poor reproducibility of the loading procedure.

3. Influence of Microstructure on Loading

To facilitate the loading avoiding the growth of an excessive strain it can be useful to prepare a material with intrinsic characteristics such as to minimize the gradients in the solute concentration. Since the hydrogen diffusion coefficient is orders of magnitude higher in the grain boundaries than in bulk, the diffusive process takes place in two steps: firstly, hydrogen is included in the grain boundaries where the diffusivity is higher, in a second step it diffuses inside the grain.

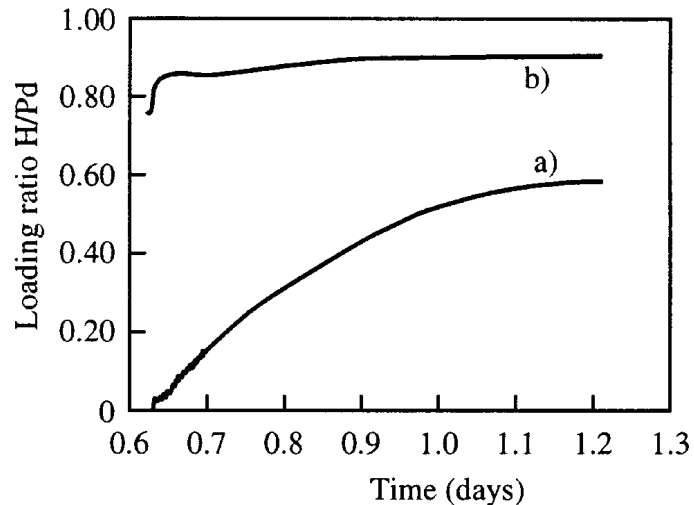


Figure 2. Concentration behavior vs time.(a) Pd sheet charged in electrolysis, $I = 10$ mA, (b) Pd sheet pre charged in H_2 gas and then in electrolysis with $I = 10$ mA.

The grain boundaries act as a source of hydrogen for the bulk where the actual diffusive process takes place. Thus the presence of a suitable network of grain boundaries enhances the kinetics and reduces the chemical potential gradient increasing the loading on the whole. The same mechanism works on thin films where the reduced dimensionality limits the growth of high stress fields, and the strains accumulated inside the film can be relaxed toward the substrate. The thin

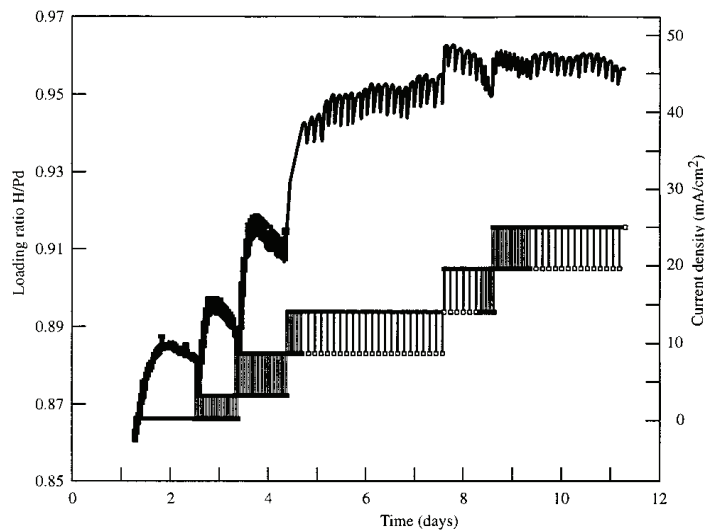


Figure 3. A further increase of the concentration value is obtained that allows the lattice to relax the stored stress fields temporarily decreasing the electrochemical action on the electrode surface: changing the electrolytic current between two values instead of using only the high level improves the loading.

film loading is complicated by the expansion of the lattice. In Pd, $\Delta l/l$ can reach 10%, under this condition the films loose their adhesion on the substrate and delamination occurs. In case several loading–unloading cycles are required the situation is even more difficult to be faced. Several “tricks” can be used to improve the adhesion to the substrate choosing appropriate buffer layers made out of several different layers in order to absorb part of the mechanical stress generated by the loading process.

Thermo-mechanical treatments and in particular cold working followed by baking can be used to modify the grain size in Pd samples. Grain size dimension can be changed both with the mechanical machining and with the thermal treatment, and it is possible, fixing one parameter, to obtain curves as those in Fig. 4 which shows a maximum of the loading ratio versus the grain size. Such a behavior implies that two different factors enhance the hydrogen diffusion into the lattice: smaller grain size reduces the strength of the stress field since the boundary network acts as fast hydrogen transporter through the sample; on the other hand the softening of the mechanical properties induced by larger grain size activates the stress relief mechanism based on plastic deformations. The combination of the two mechanisms enhances both diffusivity through short circuit path and stress relaxation by plastic deformations. Concentrations larger than 0.95 H/Pd and 0.90 D/Pd have been obtained in electrolytic loading of samples with about 50 μm grain size [11].

4. PD/H Systems in H Plasmas

It is known that an electric field causes the changes of Pd surface reactivity and, as a consequence, an increase of the stoichiometry of Pd/H can be measured. Di Pascasio et al. [12] studied the possibility to increase the hydrogen loading in a metallic material, Pd in particular, in presence of a hydrogen plasma. They found that the hydrogen confinement in Pd can be increased by exposing it to cold H plasma without changing any other parameter. The term “cold plasma” is used for plasmas having a low concentration of ions ($\sim 10^6 \text{ m}^{-3}$) in thermal equilibrium within the environment. Due to the low concentration of electrons the heat transfer is controlled by the neutral species. They concluded that a new thermodynamic condition is achieved in presence of a plasma, in particular, the thermodynamic condition of H inside

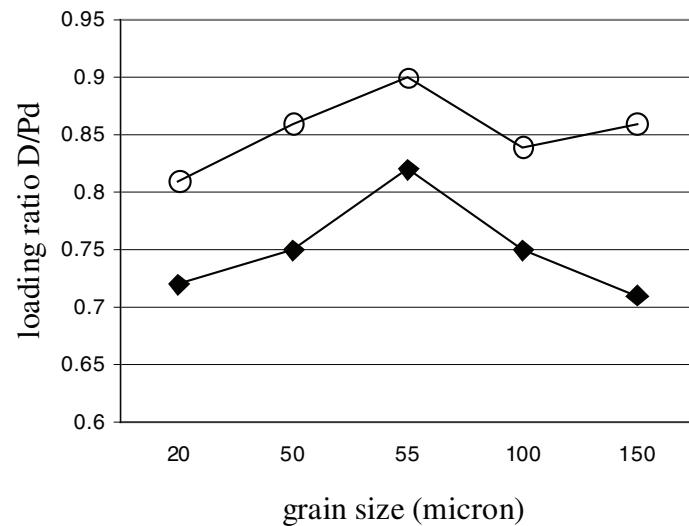


Figure 4. Loading ratio D/Pd vs. grain size. The two series refer to different values of reduction by cold rolling. Open circles: reduction rate = 1/5; black diamonds: reduction rate = 1/7. The annealing temperature was 900°C for both. Samples were loaded in electrolysis with a current density $i = 25 \text{ mA/cm}^2$.

Pd is affected by the presence of an external electric field even if the material characteristics are still that of a metal. Even Tomaszewska and Stepie [13] found that in presence of an external electric field Pd–H bonds seem to become stronger or, in a different view, the existence of an electric field decreases the activation energy required for hydrogen diffusion into the subsurface. More recently, an international team of researchers has developed a process using an electric field which can significantly improve hydrogen storage and release in/from materials [14].

In these reports, they came to the conclusion that, in a cold plasma, hydrogen inside the Pd lattice undergoes a transformation which affects the state, the number and the transport properties of both electrons and H ions.

A very interesting demonstration of external plasma effect on the loading of H in Pd can be observed inducing a corona discharge between two plane electrodes like those usually operating in electrolysis. The working electrode, a Pd coating 2 μm thick on a Si wafer, was grounded and a positive voltage was applied to the counter Pt bulk electrode. Both electrodes had a planar geometry with a 25.35 mm area, the gap between the electrodes was 4 mm. At the beginning of the experiment, the gap was filled with LiOH solution, the applied potential was kept well below the breakthrough voltage and the ordinary H loading occurred. As soon as the loading reached the threshold of the $\beta \rightarrow \beta'$ transition (see above), the solution was removed, the change of the electronic density on the Pd–H surface increased the number of secondary electrons involved and a negative corona discharge was formed. H^+ ions were accelerated with a high kinetic energy toward the working electrodes and impinged on Si trespassing the Pd coating. Removing the electrode from its housing and observing the surface with an optical microscope, a grid made out of very peculiar scratches was observed (Fig. 5a). The strange morphology of the scratches is quite hard to understand because it is perhaps the heritage of the polishing procedure of the Si wafer from which the electrode substrate was obtained. The same experiment carried out using a deposition of Pd on Vycor glass shows pits randomly distributed (Fig. 5b). A possible explanation is that tiny defects on the surface, although non visible before the discharge, have been amplified by the presence of the very high gradients of the electric field around the pins which, in turn, accelerate the ions within the limit of the plasma area. Inside the area delimited by two parallel scratches a very high temperature was reached by the Si (Fig. 5c) which appeared to be fused and resolidified. Cubic shapes with a pipe in the middle suggesting a re-crystallization process from the fused state can be seen (Fig. 5d) using the SEM analysis. The accelerated H^+ ions knocks with a very high energy on the surface producing very deep damages. Profilometry shows scratches as deep as 5 μm at the border of the structures shown in Fig. 5.

Besides the visual inspection of the sample, the Pd on Si cathodes were subjected to Rutherford Backscattering Spectroscopy (RBS) used for compositional thin film analysis (less than 1 μm) and to Elastic Recoil Detection Analysis (ERDA) which is an efficient technique for high resolution depth profiling of light elements, especially for detection of hydrogen depth profile. In Fig. 6 (a–c) the RBS analysis results are shown compared to simulations in order to get a quantitative evaluation. Figure 6a shows the comparison between a reference (not used in the experiment) sample of Pd on Si and the behavior expected for a 9000 Å thick Pd film; this is just to calibrate the instrument, 9000 Å is the bulk limit for the instrument. Figure 6b shows that, after the experiment described above, the Pd film was almost completely removed from the Si surface: the analysis fits the result obtained simulating a 40 Å thick film made out of a mixture of the metals used in the experimental set up; a bigger amount of Pd, about 300 Å thick film, was found on the back side of the Si wafer that was 1mm thick (see Fig. 6c). ERDA analysis, in Fig. 6d, shows the hydrogen content in a 6000 Å depth (the analyzed depth depends on the energy of the beam): signal below channel 200 accounts for the H_2 content in a 6000 Å layer beneath the surface whereas the peaks around channel 200 show the hydrogen adsorbed on the surface. An amount of hydrogen four times greater than in the reference was found on the surface exposed to the plasma, however, a much higher value was found on the backside surface. The small amount of hydrogen found inside the sample after the discharge can be ascribed to the very high reactivity of H^+ ions which react with other species and are subtracted to the analysis.

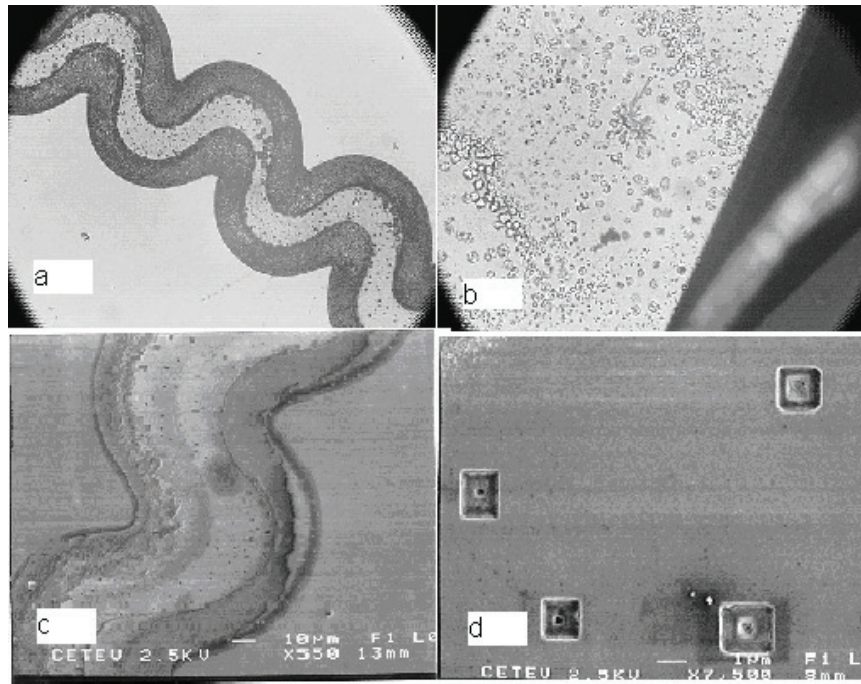


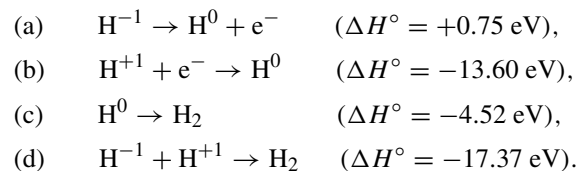
Figure 5. (a) Optical microscope image of a Pd on Si cathode exposed to negative corona discharge, (b) same as above but on Vycor glass substrate, (c) and (d) SEM images of the sample shown in (a) with different magnifications.

5. A Conceptual Discontinuity

Another surprising feature of the PdH system is the very high diffusion coefficient (about $10^{-7}\text{cm}^2\text{s}^{-1}$ for hydrogen in the α -phase) and the fact that the diffusion coefficients for deuterium, hydrogen and tritium are in the order $D_{\text{D}^+} > D_{\text{H}^+} > D_{\text{T}^+}$ different from what can be expected on the basis of a simple classical model of diffusion. Moreover, Dandapani and Fleischmann [15] reported a very high equilibrium H/D separation factor for H and D dissolution into Pd cathodes at high negative over potentials. They interpreted this fact in a way that the species behave like classical oscillators in the lattice, in other words, they are virtually unbounded. Since the delocalization depends on the occupancy by the protons of highly excited states, the above stated properties of deuterons inside Pd lattice: high diffusion coefficient, inverse isotopic effect, large oscillation in the lattice, implies that many-body interactions must come into play and supply the energy required to raise the H^+ to such excited states.

Even the analysis of the Born–Haber cycle for H in Pd requires some hypothesis “ad hoc”.

The rational chemical design of high-efficiency hydrogen Storage Metals (HSM) has to take into account the large difference between H^+ and H^- ions :



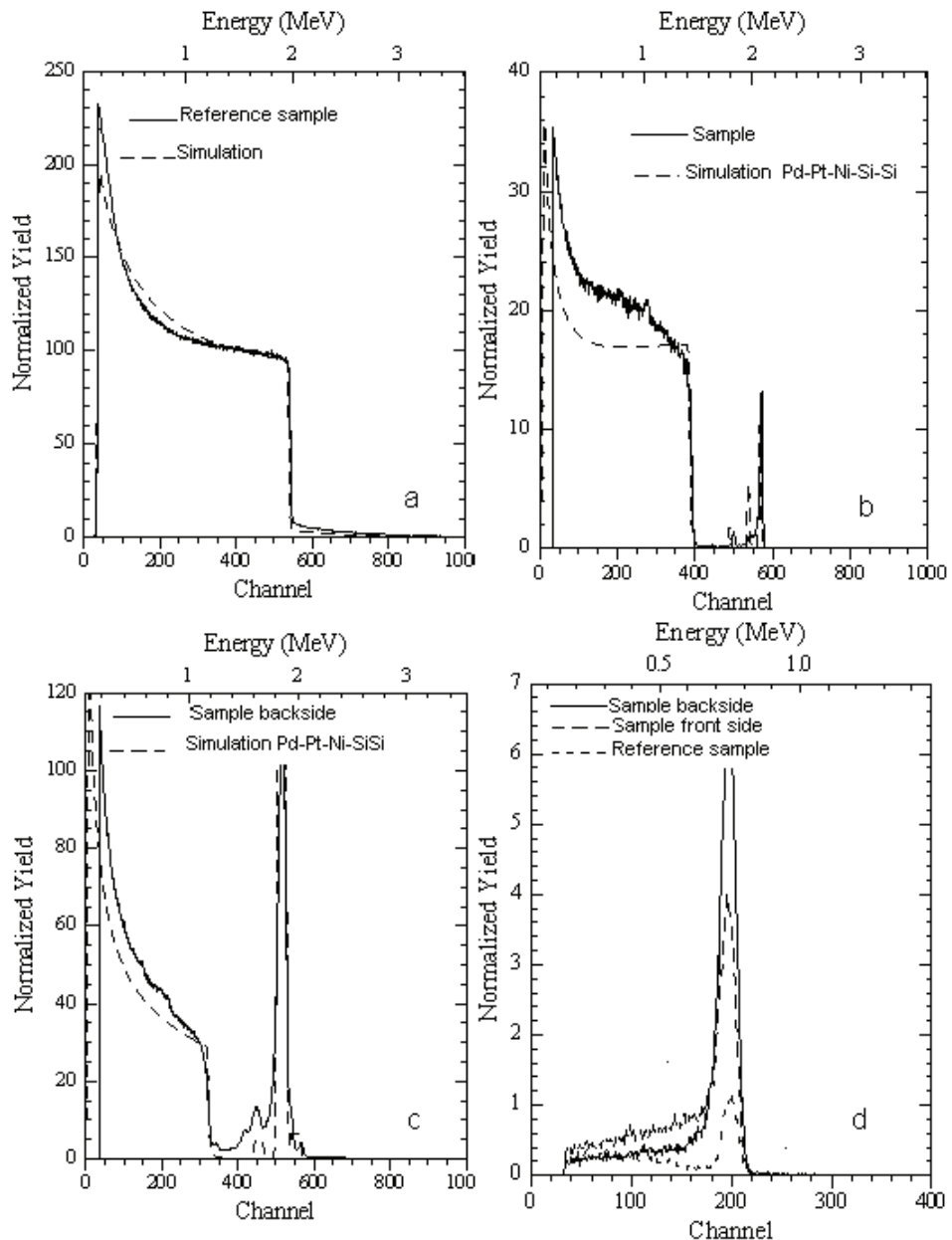
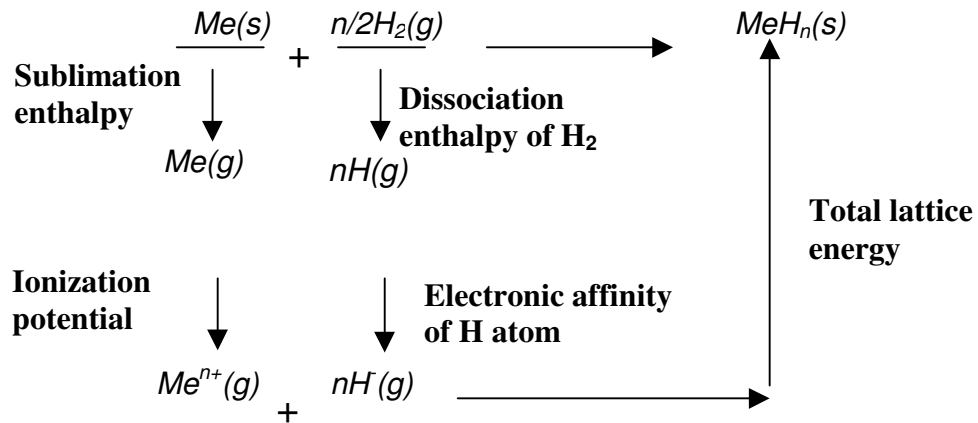


Figure 6. (a) RBS of Pd on Si compared with a simulation of 9000 Å thick slab of Pd; (b) RBS of the cathode exposed to negative corona discharge compared with a simulation of 40 Å of Pd-Pt-Ni Si on 20 000 Å of Si; (c) same as above but on back side of the sample compared with a simulation of 300 Å of Pd-Pt-Ni Si on 20 000 Å; (d) ERDA measures the hydrogen content in a 6000 Å depth. The peak shows the hydrogen content inside (on the left) and outside (on the right) the sample. See further details in the text.



Thus it is very important to state which is the real state of hydrogen inside the lattice, i.e. if it is in form of H_2 , H_+ or H_- . In 1929 Alfred Cöhn showed in an experiment on electromigration that hydrogen diffuses like a positive charge when it enters the Pd lattice. This result was confirmed by other authors [16,17] and the positive fractional charge was measured to be in the range of 0.3–0.7. Even modeling the electronic structure [18] confirms that the H drift appears to involve partially positive charged ions. Moreover, the same calculations show that, increasing the loading, H hopping through tetrahedral sites is energetically more promoted than through octahedral sites. The latter items may be just another sign of the $\beta \rightarrow \beta'$ transitions.

In order to behave like a (partially) positive ion inside the Pd lattice the hydrogen atom (or molecule) must find very strong electric fields in order to maintain itself in the ionized state (or to dissociate into two ions). The electric field inside the lattice must be able to produce a very high energy (13.6 eV over a distance of the Bohr radius 0.57 Å).

Clearly this requires a very peculiar electron distribution !

In a paper of 1994 [19], M. Fleischmann, S. Pons and G. Preparata wrote: “The hydrogen in the Palladium lattice is present as protons and the second surprising feature is that the extremely dense proton plasma is present in an electron concentration of 600–1000 M . . . we are driven to the conclusion that a satisfactory explanation of the stable existence of the dense plasma must be based on an appropriate many-body model”. They centered their statement on the analysis of the peculiarity in the Pd–H system described above.

As conclusion, Pd hydride behaves like a solid plasma inside a lattice. Such a perspective allows to explain the influence of an external electric field on hydrogen dynamics inside the Pd from a different point of view.

The chemical potential of hydrogen dissolved in Pd, in the α -phase can be set equal to

$$\mu_H = \mu_H^0 + RT \ln \left(\frac{x}{1-x} \right) + \Delta\mu_H, \quad (1)$$

where μ_H^0 is the standard chemical potential, $x = H/Pd$, the second term is the configurational term for the ideal statistic standard distribution among octahedral sites and the last one stands for the excess potential. At equilibrium the chemical potential of hydrogen in gas equals the chemical potential of hydrogen inside the lattice

$$\mu_H = \frac{1}{2}\mu_{H_2} + \frac{1}{2}RT \cdot \ln p_{H_2}$$

and, introducing the Sievert constant $K = \exp \left[\left(\mu_H^0 - \frac{1}{2} \mu_{H_2}^0 \right) / RT \right]$ one obtains

$$\ln(p_{H_2}) = \ln \left(K \cdot \frac{x}{1-x} \right) + \frac{1}{RT} (\Delta\mu_{H^+} + \Delta\mu_e).$$

The term $\Delta\mu_e$ represents the excess potential contribution of both protons and H^- electrons. It is straightforward to see that when the last term is omitted the equation represents the behavior in ideal solution state. This is actually true in the α -phase $x < 0.02$ where hydrogen is an ideal solid solution in the host lattice. Increasing the hydrogen concentration the elastic contribution $\Delta\mu_{H^+}$ generates a distortion in the octahedral cage which, in turn, introduces an attractive interaction between H-atoms and leads to the formation of clusters of high H density, namely the β -phase. From this point on, in case the rigid band model is assumed, the electronic contribution to the excess potential is due to the steep increase of the Fermi level caused by the electrons of the dissolved hydrogen, thus the loading is very hard to be increased.

The experimental findings listed above point toward the growth of a new phase at $x = x_{\beta'}$ (namely the β') where protons occupy the tetrahedral sites and become tentatively unbound. In this phase the second (configurational) term in Eq. (1) does not hold any more.

In case a potential V is applied to the metal, the excess potential $\Delta\mu_e$ will include its effect according to [20]

$$\Delta\mu : |e|z^*V. \quad (2)$$

In case the metal has a negative potential, the chemical potential of hydrogen inside the lattice fall below the chemical potential μ_{ext} of the hydrogen outside. The profile of the chemical potential μ is thus lowered by: (a) the phase transition and (b) the $\Delta\mu_e$ due to the voltage difference between inside and outside the metal. A new equilibrium point will be reached at $x' = x_{\text{eq}} + \delta x$, where the first term is related to the phase transition and the latter to the applied potential according to (2). Consequently, if we apply a negative potential to the Pd/H system when the system is in the new phase β' at $x \equiv x_{\beta'}$ a current flow j' adds up to the electrolytic current j_{el} :

$$j(x) = j_{\text{el}}(x) + j'(x) = j_{\text{el}} \left(1 + \frac{\mu(x_{\beta'}) - \mu(x)}{\mu(x') - \mu(x_{\beta'})} \right),$$

which disappears when $x \equiv x_{\beta'}$. It is worthwhile observing that the transverse field effect described above is not the longitudinal electric field generated by a voltage drop across the cathode accountable for electromigration.

A quantitative analysis of this effect can be obtained measuring the R/R_0 behavior during the LiOD electrolysis on a Pd strip, 1μm thick sputtered on Vycor glass (see Fig. 7). The deposition was shaped in such a way to have a high electric resistance (about 1.5 kΩ) so that the voltage drop across the cathode was maximized and the longitudinal current along the strip was limited. According to the well-known Baranowski relationship between the PdH(D) resistivity and the loading ratio it can be seen that the loading increases (the resistance decreases above $R/R_0 \sim 1.8$) whenever the voltage across the cathode increases.

In case the resistance of the cathode is not negligible (a strip, a wire, a patterned deposition) the electrostatic equation for the cell has the following solution:

$$V(z) = \frac{V_{\text{ac}}}{\cosh(\xi L)} \cosh[\xi(L-z)],$$

where z is the curvilinear coordinate, V_{ac} is the voltage drop between anode and cathode, L is the total length of the cathode and

$$\xi^2 = \frac{\rho_c}{\rho_{\text{el}}} \frac{1}{\delta d} F.$$

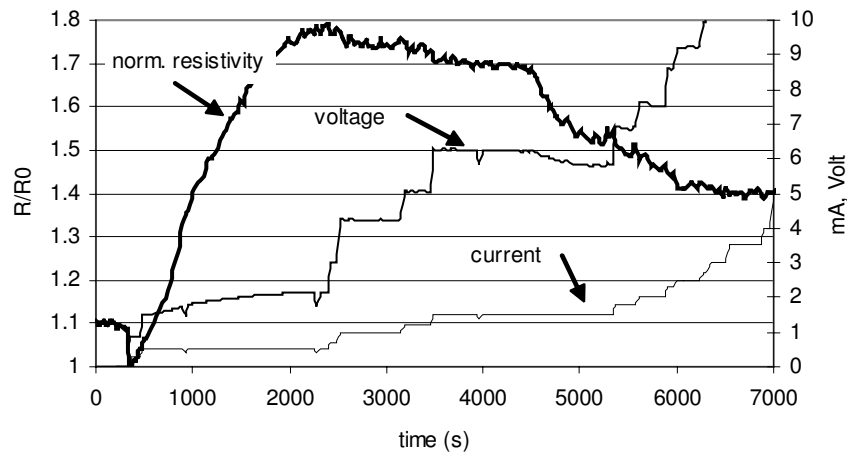


Figure 7. Normalized resistance of a Pd deposition on Alumina substrate in LiOD electrolysis.

F is a factor accounting for the cell geometry, δ the cathode thickness and d its width, ρ_c and ρ_{el} the electrical resistivity of the cathode and the cell.

This potential acts as a source of the additional current flux which is not uniform across the sample but depends on the distance of the point where the voltage V_{ac} is applied. The result is an inhomogeneous loading along the sample.

6. PD–H(D) System and Low-energy Nuclear Reactions

The above analysis of PdH(D) systems pictures a quite peculiar system looking like a *solid plasma*. This may answer the thoughtful question about the reality of Low-Energy Nuclear Reactions (LENR) in condensed matter. Such a question is usually asked in the context of Quantum Mechanics which shows that “Cold Fusion” should not be possible: nuclear physics of deuterons in the lattice (with a space–time scale six orders of magnitude smaller than the space–time scales of the lattice) *should not differ* from nuclear physics in vacuum. However since 1989 several scientists posed the problem in the framework of Quantum Electro Dynamics (QED). Preparata et al. [21] observed that the ground state in condensed matter involves the atoms/molecules of a macroscopic piece of matter in an intricate dynamical interplay mediated by large amplitude (classical) e.m. fields. This intuition was substantially shared by Julian Swinger [22], one of the fathers of QED: deuterons inside the Pd lattice can be described as a plasma in condensed matter having a strong electromagnetic coupling with the lattice. In such a picture LENR appear as a natural development of the very first concept of nuclear fusion.

The very first nuclear fusion reaction used 100-kV powerful gas discharge developed by Mark Oliphant, heavy water for the Deuterium was produced by Paul Harteck while the analysis of the cloud chamber was done by Lord Rutherford [23]. First attempts to develop the reaction into an energy source were done by Oliphant in 1937 who tried to produce extremely intense deuterium or deuterium–tritium beams from gas discharges, having an energy of about 100 keV, to hit targets containing deuterium or deuterium–tritium. These attempts were radically rejected by Spitzer (1957) who argued that such beam experiments do well result in fusion reactions but it is absolutely impossible to produce more energy by fusion than is put in for the beams. The Spitzer objection was that the ion energy goes mostly into heating of the electrons in the target, never permitting an exothermal fusion reaction. Spitzer’s option led to the

decision that instead of bombarding a cold target, one has to heat the reacting particles as in the sun, up to the plasma state at a temperature of dozens of million degrees so that ions do not lose their energy by collisions with electrons and the desired fusion reactions can take place. Following Spitzer's argument, the handling of the fusion plasma within the magnetic confinement is at a stage at which a test reactor ITER is going to be built by 2015, which may lead, hopefully, to a power station to supply 4 GW fusion energy output by 2040.

Spitzer's argument keeps its full validity as long as the beam-irradiated target remains at ordinary state of matter.

The basic concept of thermonuclear fusion is to produce extremely high temperature plasmas with a suitable density in order to sustain the reaction.

But, what if a solid-state plasma can be naturally available in nature at room temperature!

If we study the dynamics of particles moving as a screened ion gas in condensed matter we must pay attention to the boundary conditions due to the very complex disposition of the atoms and their electronic clouds in the equilibrium positions of the lattice. The dynamics of deuterons in the Pd lattice is similar to the motion of charged particles stored in a radiofrequency electric quadrupole trap subjected to the Mathieu's equations. Pd electrons of the outer bands oscillate around their equilibrium sites producing strong electric fields; due to the peculiar structure of the Pd lattice a radio frequency trap is formed among Pd atoms in (101) and (101) planes. It can be shown [24] that the combined effect of the trap force, electrostatic interaction, non linearity and damping produce, under proper conditions, the increase of the collision probability between quasi-free deuterons. The initial conditions, i.e. the deuterons density, their velocity and their initial coordinates determine the overall percentage of colliding particles. Thus experimental conditions able to affect the dynamics of deuterons in a way that an external electric field or a suitable deuteron flux from side to side can significantly increase the collision rate. This may explain the different experimental approaches to the phenomenon and the variety of experimental results in terms of nature and yield of nuclear products: (a) static approach means that the material has a very high loading ratio, at which a significant part of the lattice fulfills the condition described by Preparata et al. in [21]; (b) dynamical approach based on deuteron or D₂ gas flux through the Pd target.

Physical mechanisms responsible for the observed nuclear event have been proposed [25,26] but their discussion is out of the scope within this paper. From the above description of PdH(D) systems three major considerations result: (a) at high loading ratios a phase transition occurs so that hydrogen (or Deuteron) behave like almost unbound charged particles; the strong coupling of these particles with the electromagnetic field that exists inside the matter makes the familiar picture of nuclear reactions in vacuum unsuited to describe the energy release typical of a localized nuclear event; (b) hydrogen or Deuteron are in a quasi-plasma state and their dynamics inside the lattice is strongly influenced not only by the local structure of the lattice but also by their kinetic conditions. This may explain why so many different experimental approaches have been proposed so far to trigger LENR; (c) the energy resulting from a nuclear event is shared among several components which implies the existence of high energy classic fields which can, in turn, induce secondary nuclear reactions, such as transmutations.

Acknowledgments

The Author wish to thank Antonio Frattolillo, Emilio Del Giudice and Antonietta Rizzo who took part to the project on New hydrogen Energy supported by ENEA between 1999 and 2002. I also wish to thank Dr. Enrico Simonetti of CeTeV and Dott.ssa Rita Tonini of the Department of Physics of University of Modena and Reggio Emilia for the realization and the analysis of Pd films used in the plasma discharge experiments.

References

- [1] T. Graham, *Phil. Trans. Roy. Soc.* **156** (1866) 415.
- [2] Z. Cohn, *Elektrochem.* **35** (1929) 676.
- [3] A.H. Verbruggen, R. Griessen, J.H. Rector, *Phys. Rev Lett.* **52** (1984) 1625.

- [4] H. Peisl, Lattice strains due to hydrogen in metals, in *Hydrogen in Metals I*, Ch. 3, G. Alefeld, J. Volkl (eds.), Springer, Berlin, 1978.
- [5] R. Wisniewski, J. Rostocki, *Phys. Rev. B* **3**(2) (1971) 251.
- [6] G. Bambakidis, R.J. Smith, D.A. Otterson, *Phys. Rev.* **177** (1969) 1044.
- [7] K. Kandasamy, *Int. J. hydrogen Energy* **20** (1995) 455.
- [8] R. Felici, L. Bertalot, A. De Ninno, A. La Barbera, V. Violante, *Rev. Sci. Instrum.* **66** (1995) 3344.
- [9] A. De Ninno, A. la Barbera, V. Violante, *J. Alloys and compounds* **253–254** (1997) 181–184.
- [10] A. De Ninno, V. Violante, A. La Barbera, *Phys. Rev. B* **56**(5) (1997) 2417–2420.
- [11] A. De Ninno, M. Vittori Antisari, C. Giangiordano, *ICCF7 International Conference on Cold Fusion*, Vancouver, 1998, pp. 103–107.
- [12] Di Pascasio F., Gozzi D., Trionfetti C., *J. Appl. Phys.* **97** (2005) 043304.
- [13] A. Tomaszewska, Z.M. St. pie., XIII International Seminar on Physics and Chemistry of Solids IOP Publishing, *J. Phys. Conf. Series* **79** (2007) 012028.
- [14] J. Zhou, Q. Wang, Q. Sun, P. Jena, X.S. Chen, *PNAS* **107** (2010) 2801–2806.
- [15] B. Dandapani, M. Fleischmann, *J. Electroanal. Chem.* **39** (1972) 323.
- [16] A. Herold, J.C. Rat, *Bull. Soc. Chim. Fr.* **1** (1972) 80.
- [17] M. Tamaki, S. Hara, I. Kondoh, K. Yoneda, A. Tsuruno, H. Kobayashi, *Nucl. Instrum. Meth. Phys. Res. A* **377** (1996) 166.
- [18] N. Luo, G.H. Miley, A.G. Lipson, *Appl. Surface Sci.* **219** (2003) 167–173.
- [19] M. Fleishmann, S. Pons, G. Preparata, *Il Nuovo Cimento* **107**(1) (1994) 143–156.
- [20] M. Cola, E. Del Giudice, A. De Ninno, G. Preparata, *ICCF8 International Conference on Cold Fusion*, SIF Conference Proceed. Vol. 70, F. Scaramuzzi (ed.), SIF, Bologna, 2000, pp. 349–356.
- [21] T. Bressani, E. Del Giudice, G. Preparata, *Nuovo Cimento* **101A** (1989) 845.
- [22] J. Schwinger, Nuclear energy in an atomic lattice, In *Proceedings of the First Annual Conference on Cold Fusion*, Salt Lake City – Utah, March 28–31, 1990, pp. 130.
- [23] M.C. Oliphant, P. Harteck, Lord Rutherford, *Nature* **113** (1934) 413.
- [24] V. Violante, A. De Ninno, *Fusion Technol.* **31** (1997) 219–227.
- [25] see “Theory, Mechanism and Modeling” in *Low Energy Nuclear Reaction Sourcebook*, Jan Marwan, Steven B. Krivit (eds.), ACS Symposium Series 998, 2008, pp. 39–122.
- [26] A. Widom, L. Larsen, *Eur. Phys. J. C* (2006) (DOI) 10.1140/epjc/s2006-02479-8.



Research Article
Model for Sonofusion

Roger S. Stringham *

First Gate Energies, PO Box 1230, Kilauea, HI 96754, USA

Abstract

Experimental cavitation sonofusion results needed a mechanism to explain the measured ${}^4\text{He}$ and heat produced. A model is introduced based on high-density low-energy transient astrophysical behavior, creating an environment for fusion events by forming electron free clusters. The cluster's low temperature and high density are shown to be essential to the fusion environment.
© 2011 ISCMNS. All rights reserved.

Keywords: Bubble, Calorimetry, Cavitation, Cluster, Ejecta, Fusion, Fusion products, Jet, Picosecond, Transient high-density plasma

PACS: 47.55.df, 45.50.Tn, 47.15.Uv, 44.90.c

1. Introduction

The sonofusion model is based on the concept of producing very high-density relatively cool transient environments for BEC (Bose Einstein Condensate) fusion events and has some similarities to muon fusion [1]. Environments of black dwarf stars that are cooling have a similar density. The collapse of a transient cavitation bubble is followed by the control of a natural progression of events ending in sonofusion products. The bubbles are produced using ceramic piezo resonating ultrasound devices [2–5] that enable DD fusion events in nm and sub nm size clusters in target foils via a picosecond electromagnetic (EM) implosion pulse. Some advances in hot inertial confined fusion in the last several years support cavitation produced clusters [6] but of a scale more than a trillion times larger. The acoustic driven transient cavitation bubbles produce very high energy densities and D_2O dissociation is in an EM compressing high-density plasma that is found in the transient cavitation bubble jet and cluster (see Fig. 1). Sonofusion experiments have produced fusion products ${}^4\text{He}$ and heat measured by mass spectroscopy and calorimetry [7] as well as ejecta sites, and transmutation [8]. Scanning electron microscope (SEM) and inductively coupled plasma mass spectrometry, have measured ejecta sites and their transmutation. Some early work indicates ${}^{108}\text{Pd} \rightarrow {}^{112}\text{Cd}$, alpha addition. The model is speculative but explains most experimental results and draws from advances in astrophysics, nano and atomic physics, pulsed laser physics, inertial confined fusion physics, and muon fusion physics.

Sonofusion requires a strong enough acoustic field to produce collapsing bubbles in D_2O . The temperature and pressure adjustments control the reactor. The process starts with a million-fold collapse of the cavitation bubble's

*E-mail: firstgate@earthlink.net

Cluster Squeeze to Fusion

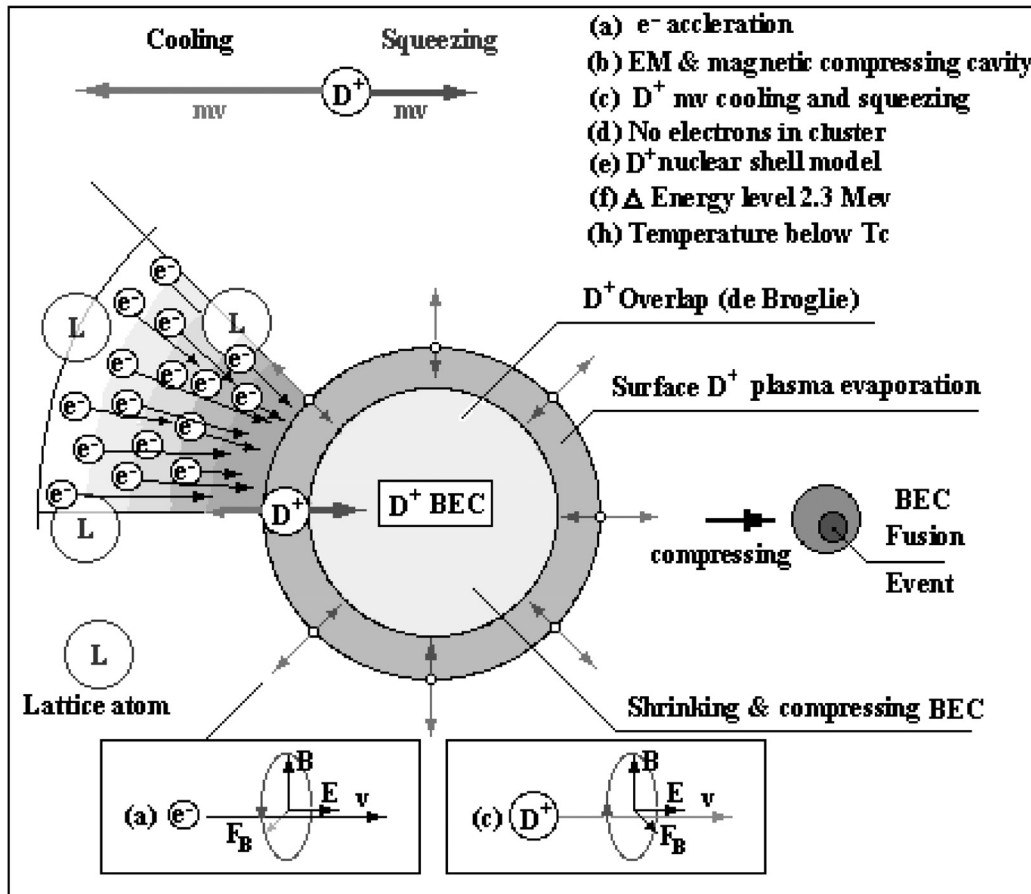


Figure 1. After the jet implants deuterons and electrons into the target lattice, a transient cluster cavity is formed. The scale for this 1,000,000 deuteron cluster shows a 1 nm diameter, at a high density, being squeezed by pressures that far exceed the coulombic escape pressure. As compression continues, the cluster contents are cooled well below their BEC critical temperature, T_c . The cluster is cooled by surface ablation and/or evaporation to form a BEC environment for DD fusion to products of ${}^4\text{He}$ and heat. Fusion occurs when the deuteron separation in the cluster approaches 10^{-12} m. There would be several random target foil atoms (L) in the surrounding EM field that donate some of their electrons to the free electron cloud surrounding the cluster.

volume, a few microseconds or less in duration. This produces the potential for a 1 millionfold increase in the energy density in the transient cavitation bubble's adiabatic collapse, and in its final stage it produces sonoluminescence and jet. Z-pinch compression of the bubble jet of dense D^+ and e^- plasma follows. The jet implants and there is a brief charge separation (Fig. 1). Accelerating electrons (a) facilitate the cluster's EM implosion pulse (b) create a dense cluster of electron free deuterons (d). The cluster is EM squeezed and evaporatively cooled to form a BEC (c). The population of local accelerating electrons towards the cluster center (a) creates a surrounding imploding EM cavity picosecond pulse (b) with the magnetic field parallel to the cluster surface. The electric field is parallel to the electron velocity

with a compression pressure much greater than the coulomb escape pressure during the picosecond pulse duration. About half of the total cluster's population pops from the surface during this picosecond EM pulse. This occurs as the cluster's surface deuterons evaporate helped by positive charge repulsion. The evaporative cooling removes heat from the interior deuterons of the cluster and counters its compression heating. These escaping deuterons may be too hot to react with the incoming electrons and ultimately will become hydrides of the surrounding target foil lattice. The continued pressure produces an environment for fusion events not unlike muon fusion (a DD₁ BEC). The cluster's BEC nature gets help from the cooling evaporation of its contents of the remaining compressed deuterons in the cluster that produces significant de Broglie overlap and a much higher T_c (transition temperature) than the temperature of the cluster (h). The T_c is controlled by the 2.3 MeV (f) energy difference between the cluster's ground state and the next energy level supports the nuclear shell model (e).

The time line, Fig. 2, shows the sequence of events for one TCB cycle at the reactor's piezo acoustic resonance. The transient cavitation bubble's isothermal growth, its pseudo adiabatic violent collapse, its sonoluminescence emission and its high-density jet formation depend on this frequency (1–25 μ s). The jet accelerates from the remnants of the collapsed transient cavitation bubble and implants into the target foil. A charge separation preserved by a small portion of the implanted deuterons is prevented from Coulombic disbursement by accelerating free electrons rushing to the cluster with a squeezing pressure much larger than the Coulombic escape pressure.

This implosion pressure, the EM pulse, squeezes the cluster to a density approaching that of muon fusion and white or black dwarf stars. If fuel is present these would be fusion producing densities. At the same time the surface of the cluster is eroding as plasma-evaporation of surface deuterons are expelled from the cluster. The momentum lost via deuteron evaporation is equal to and opposite to the compression gain of the remaining cluster contents. This helps keep the BEC cluster cool ($\lambda_{BEC} = k/T^{1/2}$). These deuterons interact with the flood of EM accelerating electrons directed to the center of the cluster. The evaporating deuterons may interact with an electron (14.7 eV producing a deuterium atom) or pass into the surrounding lattice as a hydride. The EM picosecond pulse compresses the cluster contents towards muon densities and fusion.

The cooling of the natural boson's interior deuterons keeps the cluster's electron free system at its extremely high ΔE of 2.3 Mev. The deuteron's nuclear shell model dissociation energy is the next energy level with respect to its ground state. This ΔE is more than a million times greater than that for a deuterium atom with its electron. This gives a broad temperature range for the BEC cluster to exist well below its million-degree (T_c) transition temperature. The BEC cluster's existence depends on its high transition temperature range. When the EM squeeze produces enough density, one or more fusion events occur in the cluster and are destroyed initiating a spherical heat pulse and ejecta, shown in Fig. 2. The heat pulse reaching the target lattice surface ejects useful heat, ⁴He, and vaporous target foil into the D₂O. This occurs in the order of 10 ps and is acoustic frequency dependent [7].

2. Sonofusion Experimental

The velocity of the collapsing bubble surface interface is about Mach 6 where sonoluminescence emission occurs [9]. The velocity of the squeezed z-pinch jet as it implants into the foil at about 20 Mach is several times that of the collapsing transient cavitation bubble interface boundary in D₂O. A SEM photo of the target foil surface in an aborted run shows the 100 μ m impact crater of an accelerating 1 μ m particle caught by the surface tension at the interface of a collapsing transient cavitation bubble and jet. The impact crater fits the expectation of a micro impact of the 1 μ m particle [10].

Some of the measured experimental data gathered over a 20 year period were calorimetry, mass spectrum analysis, MS, scanning electron microscope analysis, SEM, and inductively coupled plasma mass spectrum analysis. All devices used for sonofusion were devised for some sort of calorimetry measurements. Usually the technique used was a D₂O flow-through type with a variable resistance heater in the reactor flow that could be switched on and adjusted to continue the power input that maintains the steady-state temperature in the reactor. This matching of the input acoustic power

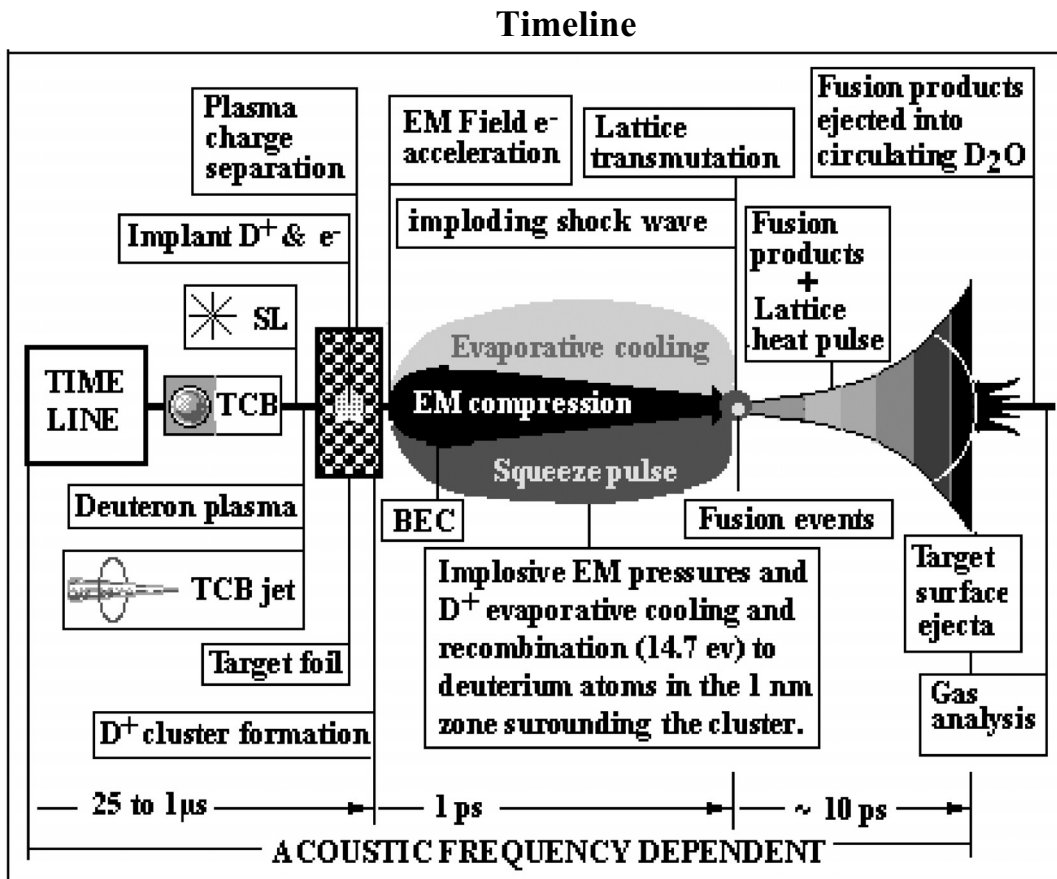


Figure 2. The time line above extends from the bubble initiation to the fusion ejection for a single cavitation bubble. There is a sequence of events that sets the time line for a fusion event and product ejecta. During the first microseconds, depending on frequency, the target foil lattice, black dots, is implanted with deuterons and electrons from a dense jet plasma that is produced by an acoustically driven collapsing, transient cavitation bubble, TCB. The deuteron jet that forms because of the bubble collapse is implanted into the target foil and the initial impact separation of free electrons produces EM forces to form clustered deuterons, with a high transition temperature. The cluster of deuterons is EM squeezed and cooled to a BEC where a fusion event occurs producing ⁴He and heat. This implantation to fusion period is a picosecond event. The resulting ⁴He and heat are ejected via a spherical heat pulse made up primarily of vaporized target lattice.

to the resistance power showed the imbalance of the input power to the output power and was the measurement of the excess heat produced. These were comparative power inputs with power errors of 1–3 W in input and output measurements that relied on acoustic power measurements and their efficiencies. The efficiencies of piezo inputs can be measured by comparing the run mode to the calibration mode. Thermocouples placed at various interior and exterior points of the reactor allowed for steady-state calibration temperature measurements with the reactor in the calibration and running mode.

Three reactors MII, MIII and MVI with frequencies of 20, 46, and 1600 kHz were used to produce data that fashioned the model. Figure 3a is the MII reactor showing the dual cavitation systems, the H₂O and the D₂O, the top system containing the target foil. Figure 3b is the open MII reactor with the 5 × 5 × 0.01 cm in the 0.5 cm thick reaction cavity.

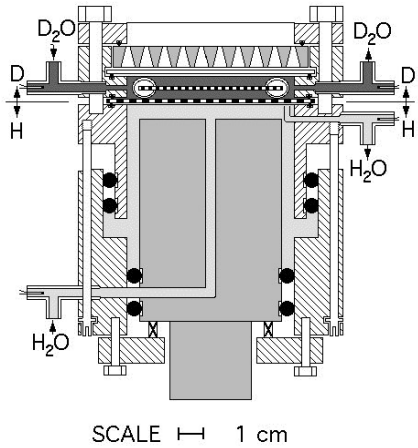


FIGURE 3 a. The M II reactor - top detail.

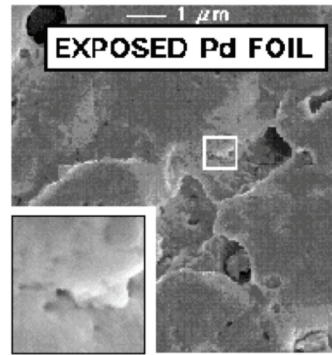


FIGURE 3 c. SEM of target foil.

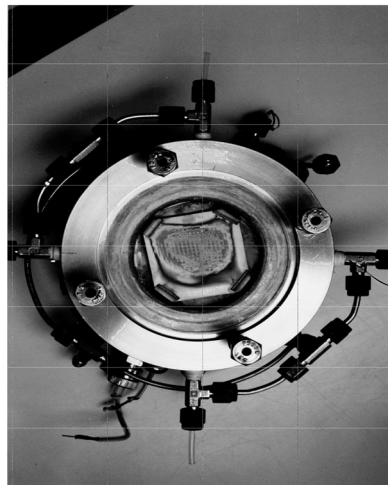


FIGURE 3b. The MIII reactor –Ti target foil.

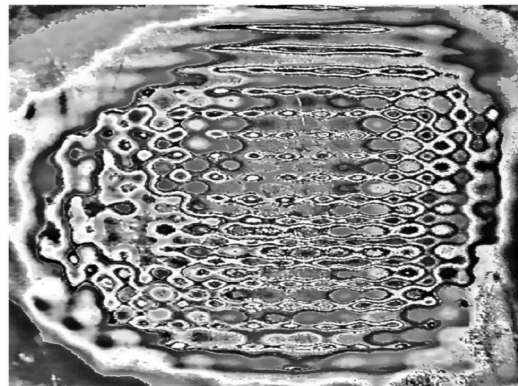


FIGURE 3d. Detail of Ti target foil.

Figure 3. Experimental apparatus and exposed target foils.

Figure 3c,d is exposed target foils from the 46 kHz systems. SEM, photo of a Pd foil and an optical photo of the TiO_x thin film surface of iridescent color of a Ti foil are shown [10].

SEM photos of exposed target foils showed the extreme temperature surface effects of localized melting and volcano like ejecta sites. Ejecta sites 50–10 000 nm in diameter, depend on the acoustic frequency, with the larger sites filled with recondensed 1 μm spheres of target foil metal. Some larger volcano-like vents showed vent linings of sub-micrometer hemispheres. Not many of the total number of foils were examined by SEM, but all exposed foils had visual changes that varied from slight to 80% destruction. John Dash of Portland State University took the first SEM photo of a Pd foil in 1993. Several foils were examined at the Scanning meeting in Monterey, CA in 1996. In the year 2000, Pd and Ti

foils were examined by SEM and photographed by Jane Wheeler of Charles Evans Lab in Sunnyvale, CA 2000 and later in 2003 a 1.6 MHz foil was examined. Lorenza Moro of SRI examined some of the same foils in the year 2000 [11].

The mass spectrum measurements of reactor gases for ${}^4\text{He}$ were made at SRI by Dave Thomas and later by Fran Tanzella; at the Bureau of Mines in Amarillo, TX by Tom Davidson; and at the DOE in Canoga Pk., CA by Brian Oliver [12]. These measurements were made from 1990 to 1995 with varying degrees of success.

In 1990 Dr. S. Tam of Balazs Analytical Lab, in Sunnyvale CA, dissolved a small portion of an exposed Pd foil in nitric acid, and examined it by inductively coupled plasma mass spectroscopy [8]. The measurements showed the presence of ${}^{112}\text{Cd}$ not found in the non-exposed foil. This was explained as ${}^{108}\text{Pd}$ picking up an alpha and a couple of electrons to yield ${}^{112}\text{Cd}$. Other Cd isotopes were not found.

In the fall of 1994, X-ray analysis at the Naval Research Lab in Washington, DC by George Chambers of exposed and unexposed Pd foils showed clearly the swelling and rearrangement of Pd lattice atoms. The gravimetric measurements by Ed Storms at his laboratory in Santa Fe, NM of cavitation exposed Pd foils at 46 kHz showed no change in weight. This was an unexpected result; no D loading of the Pd lattice. Pd foils were Au electroplated and non-plated $50 \times 50 \times 0.1$ mm foils and showed no measurable D loading from weight measurements before and after cavitation exposure. X-ray and the gravimetric measurements pointed to the fact that even if the Pd lattice was permanently expanded, the D was not present as shown by the gravimetric measurements. We know that D_2 , ${}^4\text{He}$, and DOOD were measured by MS in the gases collected from the reactor that were ejected into the circulating D_2O (see Table 1). Brian Oliver, DOE laboratory in 1994, also measured some ${}^4\text{He}$ via MS of selected milligram samples from exposed Pd target foils. Only small amounts of ${}^4\text{He}$ were found. It is this experimental data gathered over 20 years of experiments that strives for an explanation of the heat and ${}^4\text{He}$ and needs a model as a guide for the next critical experimental procedures that will help open the door to a useful device.

Table 1. Table of MS Data From Gases Collected From Three Runs.

Brian Oliver at the DOE laboratory at the Rocketdyne facilities in California did a series of mass spectrum measurements of three 50 cm^3 stainless steel gas sample volumes labeled 4-1, 4-2, and 4-3. Sample 4-1 was a standard run – background ${}^4\text{He}$. Sample 4-2, a Ti target foil run showed ${}^3\text{He}$ and ${}^4\text{He}$ [12]. Sample 4-3 was a Pd foil run showing ${}^4\text{He}$. (${}^3\text{He}$ data not shown [10])

Sample	Measured ${}^4\text{He}$ (10^{14} atoms)	${}^4\text{He}$ in sample (10^{14} atoms)	${}^4\text{He}$ Concentration (ppm)
4-1A	0.2506	4.623	0.471
4-1B	0.2436	4.760	0.484
4-1C	0.2237	4.621	0.470
		Mean ($\pm 1\sigma$)	0.475 ± 0.008
4-2A	0.7696	31.31	2.548
4-2B	0.7521	31.37	2.552
4-2C	0.7357	31.46	2.560
		Mean ($\pm 1\sigma$)	2.55 ± 0.01
4-3A	188.2	7483.0	553.5
4-3B	182.6	7447.0	550.9
4-3C	178.3	7460.0	553.5
		Mean ($\pm 1\sigma$)	551.8 ± 1.0

3. Outside Experimental Support

The implanting jet initiated by the cavitation bubble collapse is very much like the imploding wire and the z -pinch. An example is the frozen deuterium thread in a vacuum where a bank of condensers discharges a powerful energy jolt producing a crushing magnetic field pressure to the thread. This thread implosion's transient environment approached that needed for fusion events. The high velocity transient cavitation bubble jets are similar to the imploding wires and frozen threads of deuterium atoms, but sonofusion has an advantage passing through the dielectric D_2O and not the vacuum of the wire and thread [13]. The sonofusion jets are on the order of 10^{16} times less in volume.

Back lighting inertial confined fusion experiments at Massachusetts Institute of Technology and the University of Rochester, measured the density, electric field, and magnetic field of an imploded 2.7 mm gold covered sphere of deuterium via focused lasers. The squeezed contents of the sphere measured 300 gm/cm^3 , the electric field at 10^9 V/m , and B field at 10^2 T [6]. There is a tremendous advantage using the much smaller inertial confined sonofusion system and its nanometer scale that takes advantage of derived atomic forces. The sonofusion cluster is 10^{22} times smaller in volume than the 2.7 mm back lighting sphere.

Work in Sweden where Leif Holmlid's group used a femtosecond pulsed laser focused on liquid D produced transient densities equivalent to that of muon fusion [14]. The transient high densities 3 00,000 times those of water were produced with a deuteron separation similar to those of muon fusion. These densities were produced in his laboratory by passing the pulsed femtosecond laser beam into deuterium. This is the density that sonofusion needs to approach to be effective. Its advantage is that the number of transient cavitation bubbles formed in a microsecond can lead to millions of clusters in target foils.

Muon fusion represents extreme densities, deuteron separation, which we hope to approach with sonofusion experiments [15]. The densities or deuteron spacing are the same as those found in white and black dwarf stars due to their gravitational pressures. At these densities sonofusion needs just a picosecond or less to consummate a DD fusion event. The density or separation between deuterons in DD_μ^+ is around 10^{36} D/cm^3 or a separation of 10–12 m.

The DOE funded much of the outside supporting research that also supports the sonofusion model. Some international laboratories and universities research support sonofusion's experimental data, but those results need to be scaled down to the nano dimensions of sonofusion's natural transient cavitation bubble collapse.

3.1. The transient cavitation bubble (TCB)

Start with the cavitation bubble that has enough acoustic energy to rapidly grow isothermally followed by a catastrophic pseudo adiabatic collapse producing very high energy densities. This bubble is known as a TCB (transient cavitation bubble). The final stage of the TCB collapse produces sonoluminescence and a jet of the bubble's contents. See Fig. 2 [7,16–18]. As the TCB collapses, the energy density is inversely related to the change in the bubble's radius cubed where a one hundred fold radius decrease is a million fold increase in energy density. For H_2O or D_2O liquid this effect is aided by high frequencies, surface tension, and smaller TCB. The symmetry of this process is not present as the TCB oscillates during its microsecond collapse. Also during the collapse process the collapsing TCB does lose some mass so it deviates from the ideal of a pure adiabatic nature. During the TCB collapse process, the formation at the bubble's interface of small proto jets form the resonant oscillation. During the bubble's collapse its surface is in continuous deformation [19]. When observed by Mie scattering, this process is smoothed out showing a curve of time vs. bubble radius change at an accelerating rate [9]. The single bubble sonoluminescence uses a much less intense acoustic field so the same bubble cycles through millions of growth and collapse cycles without a terminal collapse and is in a continuous cycle process using less acoustic energy than the TCB mode. If the TCB acoustic input is too intense, the TCB is lost to frothing. Acoustic power couples to the temperature and external pressure.

3.2. The jet

The jet contents are high-density dissociated deuterons and electrons from the transient cavitation bubble. Some high mass ions of Ar and O will be pinched off from the high velocity jet on its short journey to the target foil. D^+ and e^- have a small collision profile. The cavitation jets photographed by several bubble research programs [20,21] are the cause of much erosion damage. This jet damage arises from the increased energy density from the violent adiabatic collapse of a transient cavitation bubble. These bubbles that form a resonance population will grow isothermally to 10 times their initial radius. Those bubbles will be involved in a near adiabatic collapse process. This energy density is transferred as the high density partial plasma to an accelerating EM z-pinched jet originating from the last stage of the bubble shell or interface of the collapsing transient cavitation bubble. The velocity of the jet coming from the last stage from the bubbles interface at 6 Mach [9] is squeezed by the EM z-pinch and via the jet's sheath electrons just before its implantation into the target foil [5]. The jet gains more velocity by its release from its interface and the EM z-pinch squeeze in the water dielectric. This velocity was estimated to be in the neighborhood of 30 Mach with the squeeze on the jet [22]. It is ironic that the very phenomenon, the z-pinch, that hobbles the Tokomak type reactors is the one that makes sonofusion work.

3.3. Jet implantation

As the z-pinch, high density jet impacts the target foil lattice, the electrons enter first followed by the deuterons. The jet's impact lattice penetration carries the electrons deeper into the lattice than the deuterons but is influenced by deuteron Coulombic forces. Any entering deuterium atoms with loosely bound electrons will lose their electrons via lattice stripping. The deuterons are separated from the cloud of free electrons for a femtosecond or less creating a charge separation and the condensing into a proto-cluster. From this chaotic mixture an EM pulse focuses on the forming cluster. The EM implosion pulse is in place before the Coulombic repulsion can disperse many of the clustering deuterons. These clusters probably range in deuteron number from 1000 to a million with a limit placed on the smallest number by the absence of gamma radiation that is suppressed by the unique properties within the BEC of the cluster. A BEC mass is larger than that of μDD^+ muon ion that produces a gamma fusion product. A BEC size of a 1000 deuterons should be enough to disperse the heat of DD fusion events to the lattice heat pulse. The lattice is probably locally disordered where the sub surface cluster is formed, a volume of a cubic nm or less. See Fig. 2. Before coulomb forces disperse deuterons, a compression EM pulse larger than the coulomb repulsion squeezes the cluster contents to 1/10 its original radius (see Fig. 1).

3.4. The cluster and compression

The cluster is transient and free of electrons. This is very important to the formation of the high temperature BEC. The cluster is a transient entity having a low temperature probably below 100,000 K and a compressed volume of more than $10^{31} D^+/m^3$. An imploding picosecond EM pulse pressure much greater than the Coulombic escape pressure surrounds the cluster cavity. A cluster, spin 1, of deuteron bosons and a cluster mass of a million deuterons has an energy difference of 2.3 Mev between its ground level and its next energy level. This is in accordance to the nuclear shell model of a deuteron. The properties of the cluster are those of a BEC. The presence of the BEC is made possible by the ablative or evaporative cooling and the inertial implosion pressures of the single escaping surface deuterons from the cluster. This evaporative loss of energy from the cluster, potentially millions of Kelvin from the mass loss evaporating deuterons from the cluster involves as many as one-half of the total of initial cluster deuterons. The cluster's cooling keeps the BEC well below its transient transition temperature increasing the deuteron overlap. Keeping the cluster in a BEC phase for the fusion event opens up new possibilities for fusion channels. The cluster's deuterons, although surrounded by other deuterons, do not individually feel their charge and tend to behave as neutral particles except at the cluster's

surface (all being repulsed equally). As long as the EM pulse confines the cluster this will be true. The deuterons escaping from the cluster during the imploding EM spherical pulse are a cooling mechanism for the remaining interior deuterons of the cluster (see Fig. 1). The gray outer circle of the cluster represents surface deuterons that may be lost to evaporation.

The EM implosion pulse of one picosecond surrounds the cluster cavity in the lattice with an electric field moving in the direction of the center of the cavity and cluster. And the pulse's free electron acceleration generates magnetic field lines that are tangent to the cluster surface and perpendicular to the electric field as the EM pulse squeezes the cluster's contents. The magnetic field's lines accelerate perpendicularly towards the surface of the cluster with a spherical squeeze. The electric field pressure squeeze is much like the squeeze of the *z*-pinch of the jet but is a spherical compression. Added to compression of the cluster and opposed to evaporation inertia is the momentum of the lost deuterons directed to the cluster center following the direction of the electron electric field pressure [23]. These compressions are similar to the large laser inertial confined fusion systems using back lighting. If a 10-fold cluster radius compression occurs, it leads to a 10^{34} D^+/m^3 density in the cluster contents approaching that of muon fusion.

3.5. The fusion

At some point during the cluster compression the cluster density will be enough to initiate DD fusion events. The transient cluster dynamics within the EM pulse time frame of a picosecond will produce one or more DD fusion events. It may be initiated by a shockwave or by just the increasing density of the cluster via the imploding EM pulse and is enough to produce a DD fusion environment. The heat of fusion is distributed to the cluster's deuteron mass because of its boson BEC properties. This occurs before any gamma radiation can form. Experimentally sonofusion showed an absence of any measured gamma or other radiation from laboratory setups at EQuest Sciences, Los Alamos National Lab, or Stanford Research International. For example, our LANL experiments show in the sample Pd 4-3 in Table 1 that there were 452 ppm ^4He produced that were collected in the gas phase via a 50 cm^3 sample volume in a 20 h period in the laboratory's atmosphere air. The ^4He production of 10^{18} atoms would be a potential gamma source of $1.6 \times 10^5 \text{ Gy/h}$ dispersed spherically and 4.5 Gy/h (Gy = Gray) where this amount is fatal to one-half the population [24]. No gammas were measured and nobody has suffered adverse radiation effects working on these experiments.

3.6. The heat pulse and ejecta

The fusion destroyed cluster forms an intense heat pulse that makes its way through the lattice to its surface as a spherical lattice hot spot that ejects its contents. The vaporized target foil and the remnants of a vaporized cluster that includes the deuterons, the heat, and the ^4He are ejected into the circulating D_2O . The ejected heat pulse contents are ejected into the flowing D_2O surrounding the target foil with the gases distributed in the gas phase and throughout the D_2O . The formation of D_2 and D_2O and some DOOD were measured by mass spectrum analysis [7]. The heat carried by the ejecta was transferred into the flowing D_2O and also in contact with the target foil surface. The sonofusion heat as the product of ^4He fusion events was transferred to the circulating D_2O to be used for some designated utility. The advantages of sonofusion are its ease in the use of transient cavitation bubbles produced at a rate of billions per second, its lower cost, and its small size compared to a very complex inertial confined fusion systems. The comparison between the known inertial confined fusion and sonofusion systems shows heat removed from billions of clusters per second make up in quantity for what they lack in size. This is also true for the economics of the two systems.

3.7. The ejecta site

There are SEM photos of a number of the cavitation exposed target foils that show the extent of the damage and the frequency of ejecta sites and their population distribution [3,5,17]. There are maybe six of sixty target foils that have

been examined by SEM. The population distribution of the various diameter sizes (diameters equals depth for the average heat pulse) of ejecta sites covering the surface of the target foils and plotted as the number vs. diameter shows a size cut off and also a maximum number for ejecta sites that are single fusion events. The energy of a single fusion event is about the energy of the smallest ejecta volume. The SEM of the target foil surface shows many ejecta sites, as many as thirty per one square μm (see Fig. 3c). There is a timeline of target foil ejecta activity and the instant the acoustic power is shut down, one sees the ever-changing ejecta site population frozen in the target foil at that instant, between acoustic cycles [25]. The next acoustic cycle the surface would have changed the target surface. Every acoustic cycle alters the target foil surface with a new generation of ejecta sites. The target foil damage at lower frequencies, 20 to 46 kHz, was substantial, but at 1.6 MHz the damage was difficult to measure with the SEM [11].

3.8. The target foils

The target foils exposed to the sonofusion environment have been varied. The surface areas were mostly $5 \times 5 \times 0.01$ cm thick for the 20 and 46 kHz systems or $1 \times 1 \times .01$ cm for the 1.6 MHz systems. The foils were of many elements and their alloys. The following is a partial list of sonofusion materials: Cu and CuB, C as Graphite, Ti and Ti alloys, V, Ni and Ni alloys, Pd and PdB, Ag, and stainless steel. Many of these target foils showed evidence of excess heat suggesting that more than one type of lattice could be used in the sonofusion process. The acoustic frequency changes produce different characteristics in surface damage to target foils [14]. The higher frequency of 1.6 MHz shows more SL, but less target foil damage, and just single fusion event per ejecta sites form smaller clusters. The target foils show other acoustic surface alteration via coloration, addition to surface as MD_x and MO_x [10], and concentrated cavitation damage related to standing waves induced into the foil from the propagating frequencies 20, 46 and 1600 kHz. The cavitation patterns etched acoustically into the foil surface were a function of mass, thickness, area shape, and composition (see Fig. 3d).

3.9. The D_2O

The advantage of using D_2O rather than other deuterium containing molecules is that when D_2O is dissociated it will cycle back as D_2O , DOOD , and D_2 and will remain at one low degraded steady-state mixture. But, for example, $(\text{CD}_3)_2\text{CO}$ will dissociate into many species including the above and continue to degrade into a mixture quite different than initial deuterated acetone (CO , CD_4 , CD_3CD_3 , CD_3OC , $(\text{CD}_3)_4\text{C}$, etc.). A better fluid than D_2O in this respect is liquid hydrogen, but it is difficult to work with. D_2O has the added advantage of hydrogen (deuterium) bonding and high surface tension. Another possibility is as a circulating fluid of HgD and other MD_x in a non-metallic system, perhaps a ceramic.

H_2O and D_2O systems of D bosons and H fermions have complexities and unknowns of mixed deuteron clusters. This introduces the addition of jet implanted protons and deuterons producing fermion and bosons and clusters. If protons are added to the cluster, it will maintain its boson character if the protons are added as pairs, H_2 bosons, maintaining the cluster's BEC character. If this is the case, it helps explain excess heat found in mixed system of D_2O and H_2O .

3.10. Many bubbles

The model discussed above involves the path of one bubble, one jet, and one cluster. However, sonofusion is a multi-bubble system. Billions of bubbles are produced each second and some of the bubble population will qualify as transient cavitation bubbles. These bubbles, if near to the target foil boundary will implant the foil with one or more deuteron clusters. These billions of clusters implanted per second each producing ${}^4\text{He}$ and fusion heat from the sonofusion reactor

is a source of useable heat. It is the sum of trillions of cluster events per second initiated by the transient cavitation bubbles that supplies a constant flow of heat that holds more promise as an alternate energy source for heating when compared to the complexities of a back-lighting inertial confined fusion event [6].

4. Discussion

The purpose of the model is to present a possible path to fusion derived from the various experimental results obtained over the last 21 years. Sonofusion starts with controlling the natural phenomenon of the cavitation of D_2O . The transient cavitation bubble is controlled by manipulation of the parameters temperature, pressure, and acoustic input. The adjusted parameters produce transient cavitation bubbles that adiabatically collapse producing high-density jets that implant into target foils [26]. With lattice stripping and impact range difference, the electrons and deuterons are separated with Coulombic attractive forces of a compressing nature overcoming the Coulombic repulsion forces of dispersion for a picosecond. During the ensuing picosecond EM imploding pulse generation compresses cluster density to the point of DD fusion. The very small clusters at the higher acoustic frequencies and clusters with 1000 to 1 million deuterons and volumes of $0.3\text{--}1\text{ nm}^3$ with starting densities of $10^{31\text{--}33}\text{ deuterons m}^{-3}$ are delivered by high velocity target foils implanting dense deuteron plasma jets. The clusters are squeezed by a picosecond EM pulse and a deuteron evaporative pressure that combines to compress these small clusters to 1/10 their original implant diameter. Densities that approach those of muon fusion are reached during the EM picosecond pulse. The muon fusion μDD molecule is separated by 10^{-12} m at a density of $10^{36}D^+\text{m}^{-3}$. This transient density has been produced in deuterium by Leif Holmlid of the University of Gothenburg in Sweden using a femtosecond pulsed laser to irradiate liquid deuterium [14]. His group has created transient densities of three hundred thousand times that of water and a deuteron separation distance of $2.3 \times 10^{-12}\text{ m}$.

The heat pulse from the fusion event is produced in the BEC cluster. The cluster is a BEC with a very high transient temperature of more than 106 K due to its ΔE of 2.3 Mev, between the nearest energy levels. In the separation of the deuterium proton from its neutron, noting there are no electrons in the cluster, there are no other energy levels available other than dissociation for the shell model's proton and neutron of deuteron nucleus. Cooling the cluster via plasma evaporation of deuterons from the cluster surface at a rate will compensate for compression heating of the BEC cluster contents. The cluster compression is more complex as the individual electrons are also coupled to lattice atoms, other electrons, plasma of evaporated deuterons, as well as the cluster. Most of the accelerating electrons are probably within a nm of the cluster surface. The deuteron cluster being the focus of accelerating free electrons produce the electric field. What happens to these fermions in this electric field as this picosecond implosive pulse advances to the cluster? The cluster cavity surrounded by compressing magnetic field lines encapsulates the cluster of deuterons. The dense electrons in a shrinking phase space may form Cooper like fermion pairs, bosons, altering the amount of available space during the squeeze pulse.

Fusion in a BEC environment leads to a 4He and heat product with no gamma radiation. The gamma radiation requires the time period one cycle of a 24 MeV gamma but the heat of fusion in the BEC cluster will be distributed immediately throughout the BEC mass of deuterons. Fusion must occur before the deuteron population disappears via plasma evaporation and coulomb repulsion becomes dominant. This should be something less than a picosecond. The BEC will accept the heat of fusion and is ready for transfer to the target lattice before the mechanism for gamma production can occur. The transfer occurs as the fusion event destroys the deuteron cluster. This heat of fusion is transferred to the lattice target as a spherical heat pulse erupting from the target surface as an ejecta site. The 4He , heat, target foil, and other minor products are found in the circulating D_2O and can be collected from the gas phase for analysis.

Some of the damage to the foil looks like heavy clusters dropping through the target foil due to a cluster's transient million fold gravity and density increase. The bubble is such a good energy concentrator that it has been considered

the underlying cause in other modes of fusion, particularly hot fusion producing neutrons and excess heat. This does not appear to be the case for sonofusion.

The sonofusion model been examined as a 1-D ray array of spherically focused accelerating free electrons directed towards the D^+ cluster surface.

5. Summary

Inertial confined fusion, hot fusion, has some similarities to sonofusion. Comparing their high densities, compression, and EM fields show that a lot is gained by sonofusion being smaller and faster. One must overcome the compression heating to maintain the properties of the BEC sonofusion clusters. Half of the total cluster deuterons, see Fig. 1, evaporate in a picosecond removing heat from the remaining cluster deuterons. The T_c for these clusters will be high because of the large energy between the electron free cluster's ground state and its next energy level of the deuteron's nuclear shell model. These conditions preserve the BEC cluster for a picosecond. The sonofusion energy density of a W/g is very high. In another direction, if the reactor's piezo geometry is altered, it may be a possible source for ambient superconductivity. The key to fusion and superconductivity is the transient nature and the staying power of the BEC cluster.

Sonofusion uses the leverage of natural processes to produce the high density implanting z-pinch jet and the picosecond BEC cluster. The initial chaotic electron deuteron implanting impact condenses this mixture via EM pressures organizing the clusters. These relatively cool, extremely high transient density BEC clusters (close to those of muon fusion) produce measured fusion products of heat and $4He$. Sonofusion can be developed into a large utility or a portable hand held power system. It is an ideal space energy system with its low fuel-mass to energy ratio, and has the flexibility to be scaled up to megawatt or down to milliwatt outputs.

Acknowledgments

Help and encouragement has come from many people: Dick America, Jim Rieker, Joe McDowell, Fran Tanzella, Joel Garbon, and Julie Wallace.

References

- [1] L.W. Alvarez et al., *Phys. Rev.* **105** (1957) 1127.
- [2] R.S. Stringham, *ICCF-7 Proceedings*, F. Jaeger (ed.), Vancouver, BC, Canada, April 19–24, 1998, pp. 361–365.
- [3] R. Stringham, *ICCF-8 Proceedings*, F. Scaramuzzi ed. Lerici, LaSpezia, Italy, May 21–26, 2000, pp 299–304.
- [4] R.S. Stringham, *IEEE Proceedings*, Sendai, Ultra Sonic Symposium, Japan, Vol. 2, Oct. 5–8, 1998, pp. 1107–1110.
- [5] R.S. Stringham, *Proceedings ICCF-9*, Xing Z. Li (ed.), Tsinghua University, Beijing, China, May 19–24, 2002, pp. 323–328.
- [6] R.D. Petrasso et al., *Science* **319** (Feb. 2008) 1223–1225.
- [7] R. Stringham, When bubble cavitation becomes sonofusion, ACS #238, Envro. Div., *New Energy Tech. Sym.*, Salt Lake City, Utah, March 16–20, 2009.
- [8] R.S. Stringham, Data presented at ICCF-4 Conference, Lahaina, Maui, HI, Dec.6–9, 1993.
- [9] K.R. Weninger, P.G. Evens, S.J. Putterman, *Phys. Rev. E* **61**(2) (2000) 3.
- [10] R.S. Stringham, *ICCF-15 Proceedings*, V. Violante (ed.), Rome, Italy, Oct 5–9, 2009, to be published.
- [11] R.S. Stringham, Sonofusion Model, ACS #239, Envro. Div., *New Energy Tech. Sym.*, San Francisco, CA, Mar. 2010. To be published, ACS Sourcebook #3.
- [12] B. Oliver, DOE MS analysis of 4He and 3He in target metals and collected gases for EQuest Sciences, report, “Helium Analysis of Target Metals” B. M. Oliver, 1995, Rockwell, International, Canoga Park, CA, 91309.
- [13] M.A. Liberman, J.S. De Groot, A. Toor, R.B. Spielman, *Physics of High-Density Z-Pinch Plasmas*, Springer-Verlag, NY, QC718.5. 1998, pp. 45–48, 19 and 238–241.

- [14] L. Holmlid, Transient high densities of deuterium, <http://nextbigfuture.com/2009/05/university-of-gothenberg-making.html>.
- [15] J.D. Jackson, Catalysis of nuclear reactions between hydrogen isotopes by μ^- -mesons, *Phys. Rev.* **106** (1957) 330.
- [16] R.S. Stringham, *ICCF-7 Proceedings*, Poster, F. Jaeger (ed.), Vancouver, BC, Canada, April 19–24, 1998, pp. 361–365.
- [17] R.S. Stringham, *ICCF-10 Proceedings*, P. Hagelstein, S. Chubb (ed.), Boston, USA, Aug. 24–29, 2003, pp. 233–246.
- [18] R.S. Stringham, *ICCF-11 Proceedings*, J.P. Biberian (ed.), Marseilles, France, Oct. 31–Nov. 5, 2004, pp. 238–252.
- [19] R.E. Apfel, video of cavitation jets, *Proceedings of the joint J. Acoust. Soc. Am. and Japan Acoust. Soc.*, Honolulu, HI, 1998.
- [20] Y. Tomita, A. Shima, *Acoustica* **71** (1990) 161.
- [21] M.P. Felix, A.T. Ellis, *Appl. Phys. Lett.* **19** (1971) 484, and W. Lauterborn, H. Bolle, *J. Fluid Mech.* **72** (1975) 391.
- [22] B.P. Barber, S.J. Puttermann, *Phys Rev. Lett.* **69** (1992) 26.
- [23] R.S. Stringham, *ICCF-14 Proceedings*, D. Nagel, M. Melich (eds.), Wasington DC, USA, Oct. 5 – 9, 2008, to be published.
- [24] The health risk of g-rays. http://en.wikipedia.org/wiki/Ionizing_radiation#Limiting_exposure.
- [25] R.S. Stringham, *ACS book, LENR sourcebook*, vol. 2, J. Marwan, S. Krivit (eds.), 2009.